

Sequential Microwave-Ultrasound Assisted Extraction of Flavonoid from *Moringa oleifera*: Product Characteristic, Antioxidant and Antibacterial Activity

Aji Prasetyaningrum, Bakti Jos, Ratnawati Ratnawati, Nur Rokhati, Teguh Riyanto, and Gian Restu Prinanda*

Department of Chemical Engineering, Faculty of Engineering, Universitas Diponegoro, Jl. Prof. H. Soedarto SH, Tembalang, Semarang 50275, Indonesia

* Corresponding author:

email: gianrestuprinanda@gmail.com

Received: May 13, 2021

Accepted: January 3, 2022

DOI: 10.22146/ijc.65252

Abstract: *Moringa oleifera* leaves contain secondary metabolites in flavonoid compounds known to prevent several diseases. Therefore, appropriate extraction methods are required to produce extracts with a high yield of flavonoids from *Moringa*. In this study, the extraction from *Moringa* leaves was carried out using the sequential microwave/ultrasound-assisted extraction (MUAE) method compared with sequential ultrasound/microwave (UMAE), microwave (MAE), ultrasound (UAE), and maceration (ME). The effects of the time, temperature, and percentage of ethanol were studied on total flavonoid content using AlCl_3 colorimetric assay. The extracts were analyzed by Scanning Electron Microscopy (SEM), Fourier Transforms Infrared Spectrophotometry (FTIR), and High-Performance Liquid Chromatography (HPLC). The antioxidant and antibacterial activities were tested using DPPH-scavenging and disc diffusion methods. The results of SEM surface analysis on various extraction methods show differences on each surface. The FTIR spectrum showed the presence of flavonoid O-H at 3200 cm^{-1} , C=O at 1621 cm^{-1} , and C-O at 1019 cm^{-1} . In the results of HPLC, MUAE extracts 16.70 mg/100 g flavonoid quercetin at the retention time of 4.5 min, with the highest total flavonoids (2.89 mg QE/g), the highest antioxidant activity (IC_{50} 72.31 $\mu\text{g/mL}$), and highest antibacterial activity (*S. aureus* 7 mm, *E. coli* 2 mm).

Keywords: *Moringa oleifera*; quercetin; microwave; ultrasound; antioxidant

■ INTRODUCTION

Moringa oleifera is a tropical and subtropical plant belonging to the Moringaceae family. *Moringa* is one of the most vital medicinal and pharmaceutical plants, containing various useful nutrients such as potassium, iron, phosphorus, calcium, vitamin A, vitamin D, and essential amino acids [1]. In addition, *Moringa* leaves extracts exhibit antioxidant, anti-hypertensive, and anti-cancer effects [2]. Tannins, steroids, triterpenoids, flavonoids, saponins, interquinones, and alkaloids are antioxidant agents found in *Moringa* leaves [3]. In addition, biologically active compounds such as flavonoids (myricetin, quercetin, kaempferol, 3-O-glucoside kaempferol) were also found in *Moringa* [4].

Conventional extraction methods such as maceration are popular for bioactive compound

extraction. However, a large amount of solvent and a long extraction time are required [5]. In recent years, several advanced extraction techniques have been developed. In order to extract flavonoids from natural sources, microwave, ultrasound, pulsed-electric field, pressured liquid, and supercritical fluid have been used [6-7]. Ultrasound-assisted extraction (UAE) is preferable for the extraction of natural products. UAE can increase the extraction mass transfer rate caused by the resulting cavitation in the material. The short extraction process is achieved as the solubility of the analyte in the extraction media increases as surface tension and solvent viscosity decrease, boosting extraction efficiency. The polymeric structure of the cell wall is destroyed, allowing more bioactive chemicals from plant material to enter the liquid extraction phase

[5]. Microwave-assisted extraction (MAE) has been widely used to extract secondary metabolites from plants due to the shorter extraction time, less solvent required, and high extraction yield. MAE is equivalent to other current extraction techniques, such as supercritical fluid extraction from a technical standpoint; however, it has economic and practical advantages because it is easy to operate and requires simple sample preparation techniques [8]. MAE can reduce solvent use and extraction time while increasing extract yield. Microwaves are used in MAE to heat and evaporate water from the cell. As a result, the cell swells, stretches, and ruptures, allowing the metabolic component to leave and be extracted by the solvent [9]. UAE and MAE can be considered as one of the most effective extraction strategies for extracting bioactive chemicals from plant materials, such as flowers, due to their high extraction efficiency [10], fruits [11], leaves [5], bark [12], seeds [13], and pods [14].

Combining two or more extraction techniques, such as microwave extraction (MAE) and ultrasound (UAE), can speed up processing time and be more efficient than single extraction [15]. In order to speed up the extraction process and liberate the targets from the matrix in a short amount of time, simultaneous irradiation with ultrasound and microwave energy can be used [16]. Ultrasound and microwave radiations could speed up the extraction procedure and enhance the extraction of bioactive compounds [17]. When the mass transfer mechanism is improved, the extraction time is reduced indeed [18]. Ultrasound/microwave-assisted extraction (UMAE) uses UAE as pre-treatment and is continued by MAE for simultaneous irradiation as an essential upgrade of UAE [19]. The acoustic cavitation effect of ultrasonic causes a higher content of bioactive compounds, followed by internal heating in plant cells with microwave irradiation [20]. The reverse version with MAE as pre-treatment and continued with UAE approach resulted in greater levels of extractable bioactive chemicals due to the effect of internal heating within the plant cells caused by microwave irradiation followed by sonic cavitation [21]. Microwave-ultrasound-assisted extraction (MUAE) is a cost-effective and time-saving extraction method that

employs ultrasound and microwave technology compared to other new extraction technologies such as pressurized liquid extraction, supercritical fluid extraction, enzyme-assisted extraction, and pulsed electric field extraction [22]. MUAE can provide the high activation energy or impact energy required for the extraction process while also limiting or preventing the degradation of the bioactive compounds in the extract [19].

To the best of our knowledge, no comprehensive study reported on the effects of sequential microwaves/ultrasound on the quality and quantitative properties of flavonoids extracted from Moringa leaves. Therefore, this study aims to determine the effect of various extraction methods such as UAE, MAE, UMAE, and MUAE on variations in extraction time, temperature, and percent solvent on the quantification of total flavonoids and quercetin in Moringa leaves. In addition, the effects of different extraction methods were studied on antibacterial and antioxidant activities.

■ EXPERIMENTAL SECTION

Materials

The leaves of Moringa leaf powder bought from Herbology (Bogor, Indonesia), The chemical such as ethanol (96% purity, CAS 64-17-5 Merck, Germany), AlCl₃ (CAS 7446-70-0 Merck, Germany), potassium acetate (CAS 127-08-2 Merck, Germany), DPPH (2,2-Diphenyl-1-picrylhydrazyl) (CAS 1898-66-4 Merck, Germany), quercetin (CAS 117-39-5 Merck, Germany), kaempferol (CAS 520-18-3 Merck, Germany), myricetin (CAS 529-44-2 Merck, Germany), rutin (CAS 153-18-4 Merck, Germany), apigenin (CAS 520-36-5 Merck, Germany), rhamnetin (CAS 90-19-7 Merck, Germany), luteolin (CAS 491-70-3 Merck, Germany), metylluteolin (20243-59-8 Merck, Germany), galocatechin (CAS 3371-27-5 Merck, Germany), gallic acid (CAS 149-91-7 Merck, Germany), nutrient agar (SKU: 70148-100G, Sigma-Aldrich, USA), *Escherichia coli* (FNCC media agar *E. coli*, Nanobio Laboratory, Indonesia), and *Staphylococcus aureus* (FNCC media agar *S. aureus*, Nanobio Laboratory, Indonesia).

Instrumentation

The equipment used in this study included a glass funnel, measuring cup, beaker, Erlenmeyer, test tube, vial bottle, glass stirrer, dropper pipette, 5 mL measuring pipette, measuring flask, separating funnel, ose needles, condenser, round bottom flask, vial bottles, analytical scales (OHAUS PA224), Microwave (MGC20100S, Beko, Polish), Ultrasound (JP-010S, Skymen, USA), SEM (JSM-6510 LA, JEOL, Japan). The characterization was used FTIR spectrophotometer (Spectrum Two L160000A, PerkinElmer, USA), UV-Vis spectrophotometer (Model ENF-24/F, Shimadzu, Japan), and HPLC (Prominence LC-20, Shimadzu, Japan). The experimental setup of microwave and ultrasound is depicted in Fig. 1.

Procedure

Extraction of Moringa leaf

Moringa powder was extracted at a solid/liquid ratio of 1:25 (g/mL). This study used a modified microwave extractor (MGC201000S, Beko, Poland) with a digital timer, temperature control, and a power of 200 W. The ultrasound extractor (model JP-010S, Skymen, USA), a timer (0–30 min), an ultrasonic with an output of 80 Watts, and a frequency of 40 kHz. UAE and MAE applied are guided by Jitan et al. [23] with minor modifications. Sequential MUAE and UMAE are guided by the research of Yu et al. [10] by alternating microwave first pre-treatment and then continued with ultrasound and vice versa. Extraction variable such as time (0, 5, 10, 20, 25,

30 min), temperature (30, 40, 50, 60, 70, 80 °C), and the solvent concentration of ethanol (0, 10, 20, 30, 40, 50, 60, 70, 80, 90%). Immediately after treatment, the mixture of Moringa was cool at room temperature. Furthermore, the extract was then filtered using Whatman 42 filter paper. The extract was collected in amber glass bottles and stored at refrigeration temperature.

Scanning electron microscopy (SEM) analysis

A scanning electron microscope was utilized to examine the morphology of Moringa extract extracted from UAE, MAE, UMAE, and MUAE. At a magnification of 1000 times, the surface and cross-section of the Moringa extract were photographed for morphological purposes.

Fourier transform infrared spectroscopy (FTIR) analysis

FTIR was used to examine the functional groups of Moringa extract extracted from UAE, MAE, UMAE, and MUAE. The extract samples were ground, and KBr was used to press the highly dispersed powders. The formed pellets were then used for FTIR spectroscopy measurements at 4000–500 cm^{-1} .

Total flavonoids determination

Total flavonoids were analyzed using the aluminum chloride colorimetric method with slight modification, according to Mukhriani et al. [24]. Quercetin was used to make the calibration curve. First, 10 mg of quercetin was dissolved in ethanol 96% and

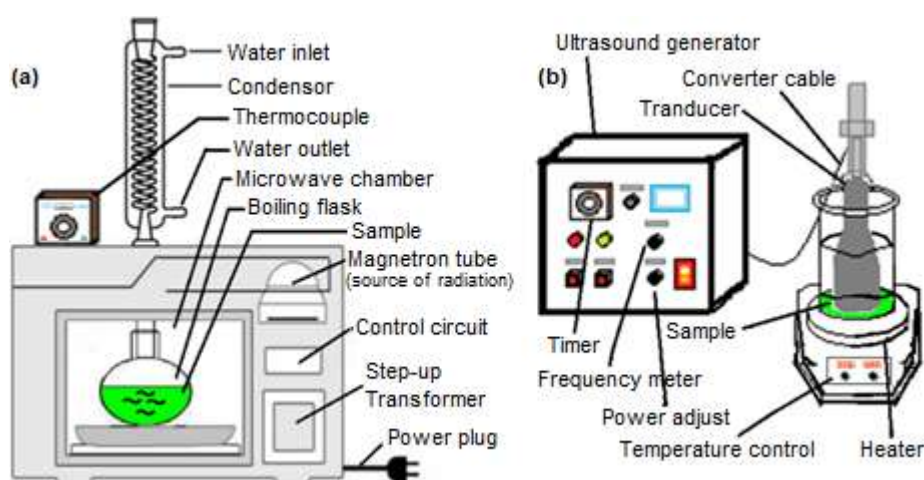


Fig 1. The schematic device of (a) Microwave extraction and (b) Ultrasound extraction

diluted to 100, 200, 300, 400, and 500 µg/mL. Next, 1 mL of each concentration of standard solutions, as well as 1 mL of UAE, MAE, UMAE, and MUAE extracts, were mixed with 1 mL of 2% aluminum chloride (AlCl₃) and 1 mL of 120 mM potassium acetate (CH₃COOK). The mixture was incubated at room temperature for 30 min. The absorbance was measured at 430 nm against a blank without AlCl₃ using UV-vis spectrophotometer. Total flavonoid content was calculated and expressed in quercetin equivalent (mg QE/g). Total flavonoid content = $(x \times v \times fp) / g$. Where x is the quercetin concentration from the standard curve (µg/mL), fp is the dilution factor, v is the extract volume (mL), and g is the extract weight (mg).

High-performance liquid chromatography (HPLC) analysis

Prominence LC-20 was used for the HPLC analyses. Shim-pack XR-ODSII column (150 mm × 3 mm ID) was used to separate the compounds at room temperature. Moringa extracts were injected into the HPLC column with a concentration of 0.10 g/L. The relative area was estimated using quercetin, kaempferol, myricetin, rutin, apigenin, rhamnetin, luteolin, metylluteolin, gallic acid (0.20 g/L) as the internal standard to explain probable changes in the instrument's analysis to the results of UAE, MAE, UMAE, and MUAE extracts.

Assays of antioxidant activity using the DPPH method

The antioxidant activity was determined using the DPPH scavenging technique modified from Tristantini et al. [25]. Initially, a 1 mM DPPH solution was prepared by dissolving 3.80 mg in 100 mL of ethanol. Next, 2 mL of UAE, MAE, UMAE, and MUAE extracts were added to 2 mL of 1 mM DPPH. The absorbance level was determined at 517 nm after 30 min of incubation in darkness. A UV-Vis spectrophotometer was used for analysis. A DPPH solution without adding the sample extract was utilized as a control. The results were expressed in percentage. The following formula was used to calculate the DPPH free radical scavenging assay: % DPPH scavenging activity = $(\text{absorbance of control} - \text{absorbance of sample}) / (\text{absorbance of control}) \times 100$. A calibration curve was used to determine the amount of DPPH in each well. The proportion of DPPH that remains is compared to the extract concentration to determine the

number of samples needed to achieve a 50% reduction in DPPH or inhibition concentration of 50% (IC₅₀). The IC₅₀ value of a very strong antioxidant activity is less than 50 g/mL [26].

Antibacterial test using disc-diffusion method

The antibacterial test was carried out by the disk diffusion method by calculating the inhibition zone produced from the extract against bacteria growing in a petri dish. In this test, *E. coli* as Gram-negative bacteria and *S. aureus* as Gram-positive bacteria were used. One loop of bacterial colonies (*E. coli* and *S. aureus*) from nutrient agar (NA) was diluted using sterile 0.9% NaCl solution to have turbidity, according to Mc. Farland (107–108 CFU/mL). A sterile cotton swab is inserted into a tube containing a bacterial suspension, then streaked evenly on the agar medium (in a petri dish). A total of 20 µL of Moringa sample solution (UAE, MAE, UMAE, and MUAE extract) was injected into blank disk paper using a micropipette. After the solution was completely absorbed, the sample's disc paper was placed on media nutrient agar (MNA) 1 containing *E. coli* and MNA 2 containing *S. aureus* test bacteria, and then incubated at 37 °C for 24 h. The clear zone formed around the disc indicates that the sample can inhibit bacterial growth, and its diameter can be known.

RESULTS AND DISCUSSION

Morphological Activity

The SEM results are shown in Fig. 2, which reveals the surface changes in the samples. Analysis of the solid characteristics of the extract from Moringa begins with surface analysis with SEM. SEM is used to see the effect of extraction technology on the surface of Moringa. The Moringa had distinct physical alterations due to the various extraction procedures. Moringa cell walls were slightly perforated after extraction by UAE, as shown in Fig. 2(a). UAE extract showed wrinkled surfaces and observable plant cell perforations. UAE can enhance extraction by using sonic cavitation, which breaks down cell walls, allowing solvents to penetrate plant material and release intracellular compounds. Fig. 2(b) shows the situation of more extensive cell wall rupture obtained from MAE.

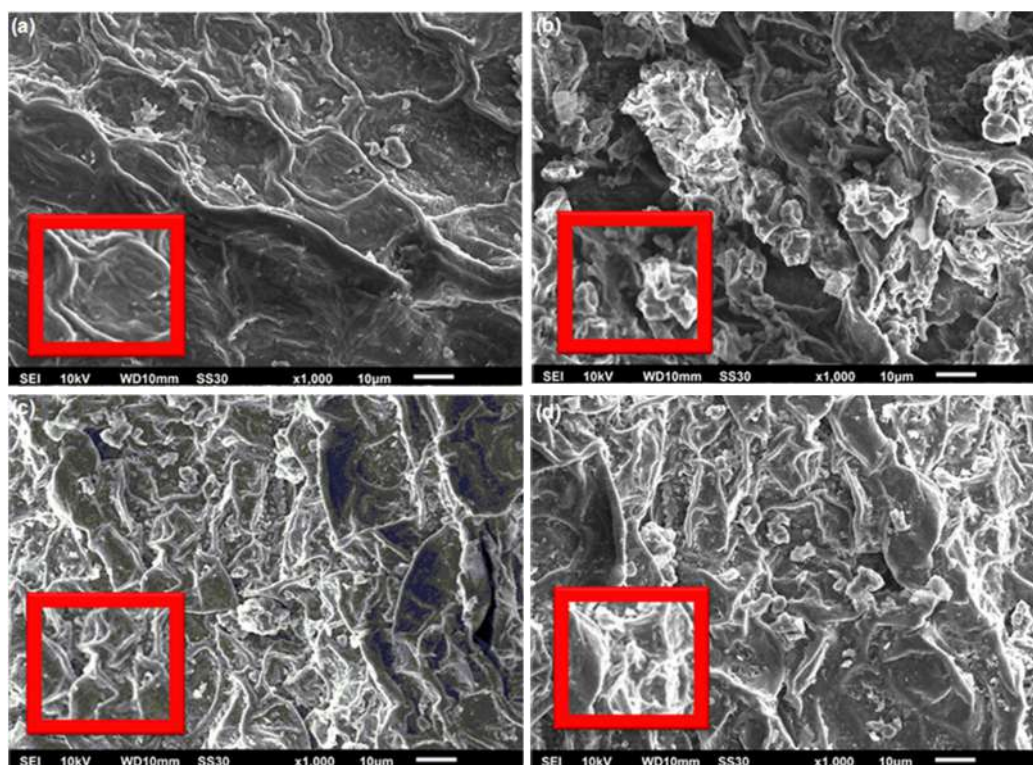


Fig 2. SEM results of UAE (a), MAE (b), UMAE (c), and MUAE extract (d)

Microwaves have a greater effect on cell wall rupture than ultrasound. In the MAE process, non-ionizing electromagnetic energy is applied directly to the raw material allowing rapid heating of solvents and suspensions due to the rapid energy delivery transformation. Ion conduction and dipole rotation cause dissolved ions to migrate due to this heating enhancing the solvent's penetration into the matrix, making it easier to retrieve the target chemical [7]. The microstructure of the ruptured tissue in the treatment using sequential UMAE and MUAE, as shown in Fig. 2(c, d), showed more

extensive damage or rupture of the cell wall indicated by a rougher surface. The diffusion rate of flavonoid compounds in cells increases on a rougher surface, and the solvent could completely extract flavonoid compounds [27].

FTIR Analysis

The functional group transformation of the functional groups in the UAE, MAE, UMAE, and MUAE, was also observed using FTIR spectra on the Moringa extract (Fig. 3). Table 1 and Fig. 3 show the FTIR

Table 1. Moringa FTIR wavenumber results compared with standard quercetin

Functional group	Wavenumber (cm ⁻¹)					
	Quercetin	Fresh Moringa	UAE	MAE	UMAE	MUAE
-OH (alcohol)	3340	3314	3278	3271	3314	3282
C=O	1711, 1666	1738	1737	1745	1738	1735
C=C	1656, 1510	1616	1648, 1605	1630	1652; 1625	1621
-OH (bend)	1379	1433	1413	1416	1427	1409
C-OC	1310, 1242, 1160	1319, 1113	1316, 1147	1325, 1158	1315, 1160	1317, 1162
C-H (aromatics)	938, 820, 600	628	594	595	614	595
C-H (stretch)	2924, 2880	2942, 2831	2917, 2849	2917	2940; 2834	2918; 2835
C-O (stretch)	1110, 1057	1021	1027	1022	1019	1019

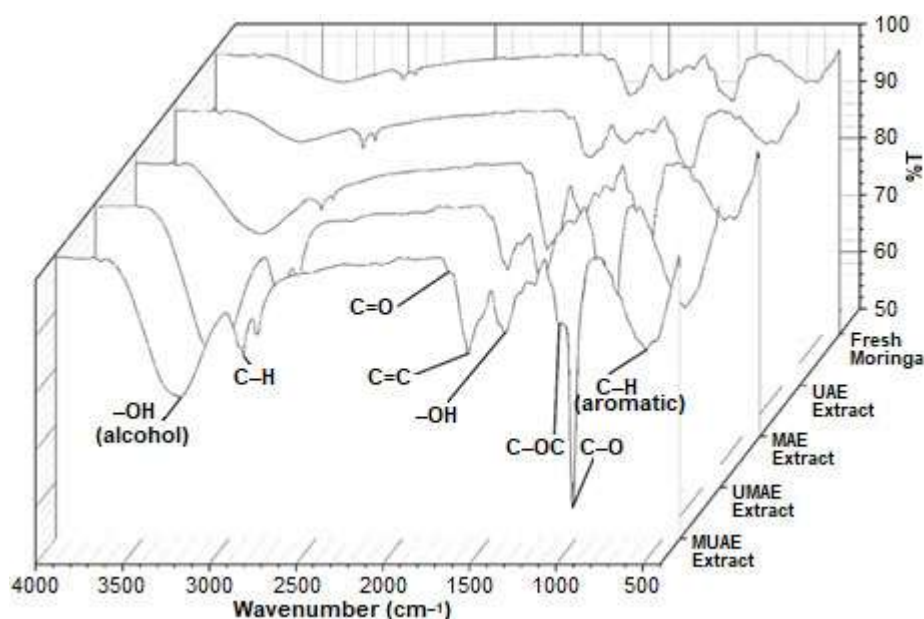


Fig 3. FTIR spectra on fresh Moringa, UAE, MAE, UMAE, and MUAE extract

result of Moringa extract. From the FTIR results in all extraction methods found the absorption of aryl ketonic strain (C=O) at 1735–1845 cm^{-1} , aromatic ring stretching (C=C) was found at 1605–1652 cm^{-1} , bending of the phenol (C–OH) at 1409–1433 cm^{-1} , and stretching in the aryl ether ring (C–OC) at 1113–1325 cm^{-1} .

For the flavonoid group, the presence of carboxylic acids (O–H) is indicated by peaks at 3000–2700 cm^{-1} , and the presence of an ester functional group (C=O) is indicated by one peak in the region 1770–1668 cm^{-1} [28]. The flavonoid structure of quercetin is shown in Fig. 4.

Moringa had phenolic O–H peaks at 3321.96 cm^{-1} , C=C alkene peaks at 1657.50 cm^{-1} , phenol C–OH stretching at 1237.05 cm^{-1} , and C–OC bending vibrations at 1057.68 cm^{-1} [9]. The stretching of the OH group was identified in the FTIR spectra of pure quercetin in its characteristic band at 3406 and 3283 cm^{-1} , while the phenol function's OH bending was detected at 1379 cm^{-1} . Aromatic ring stretching C=C was detected at 1610, 1560, and 1510 cm^{-1} . Absorption of aryl ketonic strain C=O was clearly visible at 1666 cm^{-1} . In-plane C–H flexural bands in aromatic hydrocarbons were detected at 1317 cm^{-1} . The bands at 1263, 1200, and 1165 cm^{-1} are caused by C–O stretching (the aryl ether ring, C–O in phenols, and C–OC). Out-of-plane flexural bands (C–H aromatics) were seen at 933, 820, 679, and 600 cm^{-1} , respectively [29].

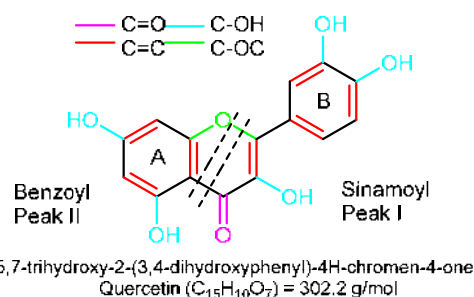


Fig 4. Functional groups in the flavonoid quercetin

It can be concluded that the difference in the extraction method has no significant effect on the flavonoid functional groups of Moringa plants. Functional group results from FTIR results show quercetin compounds in all Moringa leaf extraction methods

Effect of Extraction Time on Total Flavonoids

The time for extraction has an impact on the flavonoid content. Therefore, the extraction period is extended to allow the solvent to permeate more deeply into plant cells and extract more flavonoids. The results of the total flavonoids with variation extraction time are shown in Fig. 5.

The total flavonoids with variation extraction time are shown in Fig. 5. The longer the extraction takes, the extraction content will increase gradually and reach the highest value total flavonoids (for UAE of 2.26 mg QE/g,

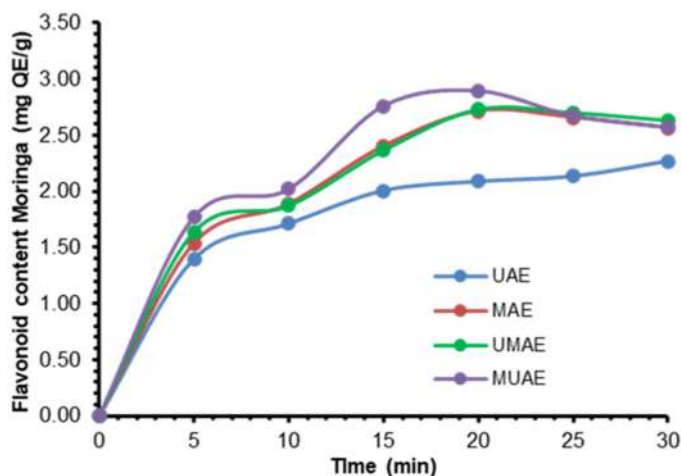


Fig 5. Extraction time effect on total flavonoids of UAE, MAE, UMAE, and MUAE extract

MAE of 2.71 mg QE/g, UMAE of 2.72 mg QE/g, and MUAE of 2.89 mg QE/g). According to total flavonoids results using the microwave, this technique can get extraction yield faster and more efficiently than ultrasound.

The increase in flavonoid content is due to the longer the solvent process, the higher the ability for the solvent to bind flavonoid compounds. In the ultrasound and microwave methods, cavitation and inner heat damage the plant cell wall so that the flavonoids present in the vacuole can be extracted out of the cell [30-31]. Sequential extraction techniques can increase efficiency because the fresh solvent is supplied in each extraction, which improves solubility [32]. However, generally, the flavonoid content in the extract is limited so that the extraction power will decrease at a certain time. It has been reported that the maximum time extraction in MAE was 15–20 min [33].

At the same yield, UMAE reduced the extraction time by 98.66% and 19.89%, respectively, compared to maceration and MAE [22]. UMAE is improved with the help of acoustic cavitation and certain fast microwave heating, the extraction time is shorter, the required volume of solvent required is less, and the yield UMAE is higher (97%) when compared with UAE (89%). It is because the internal heat of UMAE radiation breaks vacuole cells in plant cells faster, allowing flavonoids to be extracted more easily, as opposed to cavitation ultrasound

alone, which takes longer [34]. Sequential UMAE (UAE as pre-treatment) get higher yield (31.88%) when compared with MAE (27.81%), UAE (17.92%), and maceration (19.16%) [35]. MUAE extract (MAE pre-treatment) tended to be higher (7.85 mg QE/g) than UMAE (UAE pre-treatment) (6.55 mg QE/g), MAE (4.79 mg QE/g), and UAE (6.23 mg QE/g) [10].

Effect of Temperature on Total Flavonoids

From the results of time variations, the total flavonoid test at temperature variations was carried out at 20 min of the extraction process. The total flavonoids with variation temperature results are shown in Fig. 6. As the temperature rises, the extraction content rises with it, eventually reaching its maximum value total flavonoids (for UAE 2.26 mg QE/g, MAE 2.72 mg QE/g, UMAE 2.71 mg QE/g, and MUAE 2.89 mg QE/g).

As the solvent temperature rose, it came into contact with the free water molecules in Moringa, causing further cell damage and mass transfer. The flavonoid content increases when the temperature ranges from 30 to 50 °C, this is because heat can damage the extracted plant cell tissue so that the active components released will increase, but the subsequent increase results in structural changes resulting in a decrease in the detected compounds. Total flavonoids decreased when the temperature was higher than 50 °C [36]. Compared to UAE and MAE, sequential UAE + MAE was a much higher yield [20].

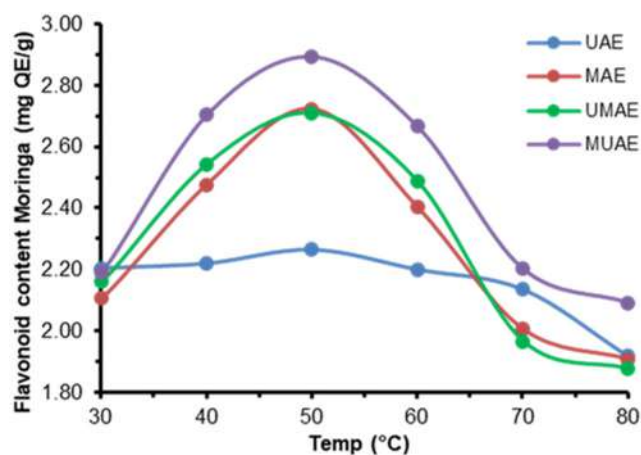


Fig 6. Temperature effect on the total flavonoids of UAE, MAE, UMAE, and MUAE extract

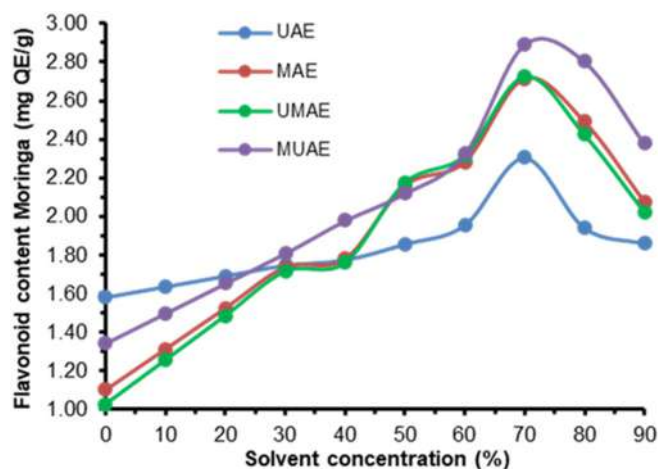


Fig 7. Effect of solvent concentration on the total flavonoids of UAE, MAE, UMAE, and MUAE extract

Effect of Solvent Concentration on Total Flavonoids

One of the driving factors for extraction is ethanol concentration, which is a crucial metric for assessing extraction efficiency. From the results of time and temperature variations, the total flavonoid test at ethanol concentration variations was carried out at 50 °C for 20 min of the extraction process. The total flavonoids with variation solvent concentration are shown in Fig. 7. In flavonoid test results, the ethanol concentration affected the total flavonoid content. The higher the extraction content will increase gradually and reach the highest value total flavonoids (for UAE of 2.30 mg QE/g, MAE of 2.71 mg QE/g, UMAE of 2.72 mg QE/g, and MUAE of 2.89 mg QE/g). The flavonoid content increases when the solvent concentration is between 50 and 70% (v/v). The best ethanol-water ratio was found in the range of 65–75% when Moringa was extracted at a temperature of 55–65 °C [37]. With a 70% solvent ratio in MAE, total flavonoids of 1.90 mg QE/g tended to be higher than 1.72 and 1.70 mg QE/g obtained by UAE and maceration, respectively [11]. The range of ethanol concentrations decreased significantly when ethanol was 70–80% (v/v) because chlorophyll was dissolved into the extract so that the yield of flavonoids that the solvent could extract was reduced. Higher solvent concentrations also can change the polarity of the solvent and affect the total solubility of flavonoids, resulting in a decrease [38]. If the solvent used is 96% concentrated ethanol, then the chlorophyll will

also be extracted, and the extract will become very thick so that the extraction rate is reduced [39].

HPLC Analysis

Furthermore, the extract of Moringa was analyzed using HPLC to determine the main components of the flavonoid quercetin in Moringa extract using the UAE, MAE, UMAE, and MUAE methods. Fig. 8 illustrates the HPLC spectra of various Moringa extraction processes.

The HPLC results for flavonoid quercetin in the UAE extract at a retention time (RT) of 4.21–4.60 min to get a yield of 39.58 ppm, for the MAE extract quercetin was found at RT 4.79 min to get a yield of 41.48 ppm, for the UMAE extract quercetin was found at RT 4.66 min got a yield of 11.97 ppm, and for the MUAE extract quercetin was found at RT 4.51 min to get a yield of 16.70 ppm. Research by Sukmawati et al. [40] found a quercetin range in RT 4.18–4.56 min, and RT is the minimum time required for the fluid mixture to be separated by gravity in the HPLC apparatus. The HPLC results for flavonoid kaempferol in the UAE extract at a retention time (RT) of 6.14 min to get a yield of 1.38 ppm. For the MAE extract, kaempferol was found at RT 6.02–6.42 min to get a yield of 14.81 ppm. For the UMAE extract, kaempferol was found at RT 5.23–6.43 min got a yield of 22.73 ppm, and for the MUAE extract, kaempferol was found at RT 5.10–6.33 min to get a yield of 22.84 ppm. Therefore, MUAE can extract more flavonoid kaempferol than UMAE, MAE, and UAE. In the sequential MUAE, it was found that the peak of other compounds at RT 3.54 was 289 ppm, which is thought to be the myricetin compound that was detected in HPLC analysis. This phenomenon was also reported in Shervington's study of flavonoid HPLC analysis from Moringa leaves, which found myricetin at RT 3.60 min, quercetin at RT 4.80 min, and kaempferol at RT 6.70 min [41]. Myricetin, quercetin, and kaempferol are the main flavonoids contained in Moringa. Other flavonoids such as apigenin, rhamnetin, and luteolin are found in smaller levels [42]. HPLC analysis of Moringa leaves revealed 26.20 ppm myricetin at 4.35 min, 5 ppm quercetin at 5.89 min, and 41.50 ppm kaempferol at 6.44 min [4]. Consequently, with the above information and the

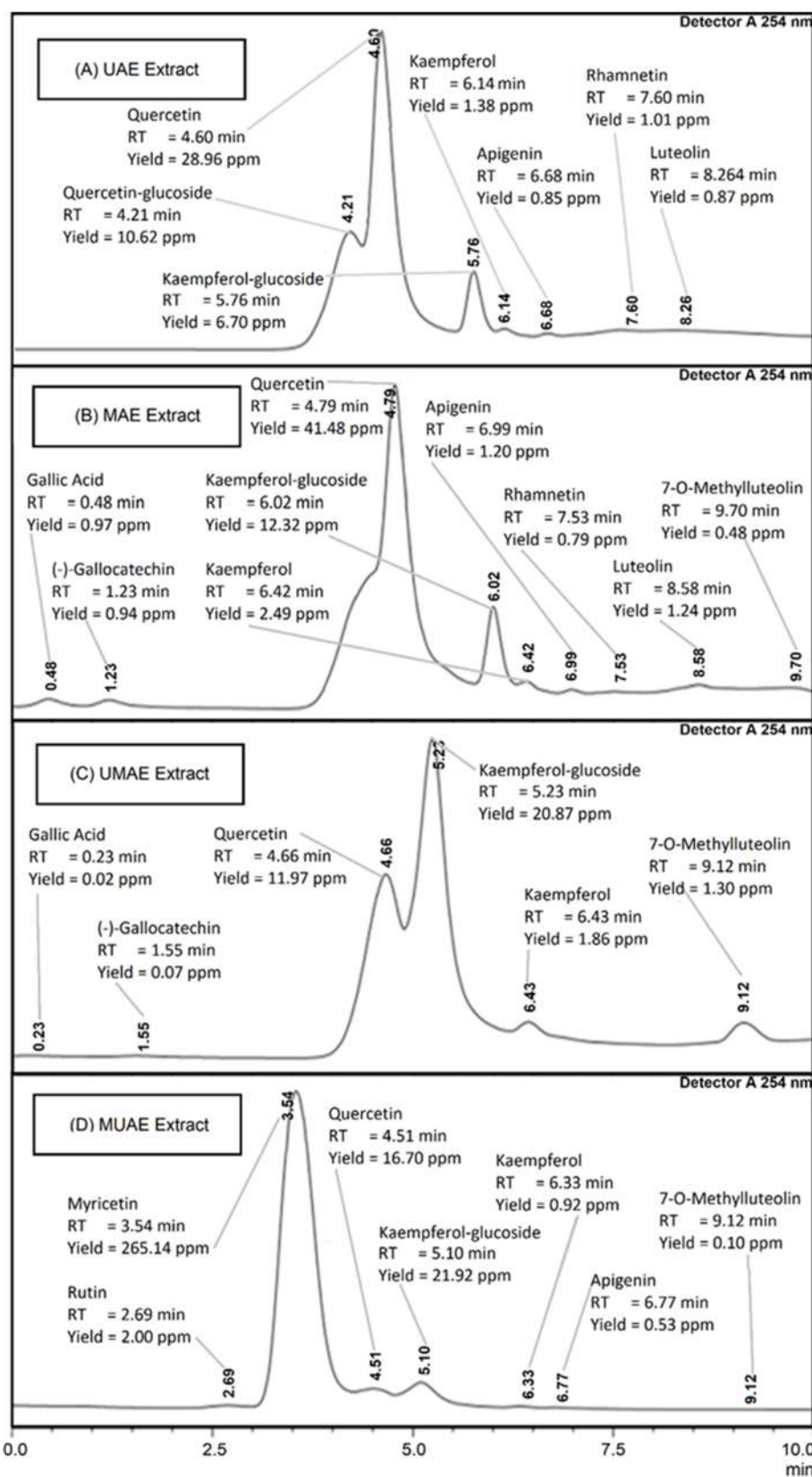


Fig 8. Spectra HPLC on UAE (A), MAE (B), UMAE (C), and MUAE (D) extract

comparison of the extraction method, we found that microwaves can extract more quercetin content, and sequential microwave-ultrasound can extract more flavonoids with reasonable efficiency.

Total Antioxidant Activity

UAE had the lowest antioxidant activity than MAE, UMAE, and MUAE, similar to the total flavonoid content results. Fig. 9 depicts the DPPH method's antioxidant test results.

Based on Fig. 9, the results of the extraction of Moringa by UAE, MAE, UMAE, and MUAE showed an increase in the % of antioxidants to the initial concentration of the sample. Table 2 shows the antioxidant activity and IC_{50} result of Moringa extract.

In this study, standard quercetin obtained IC_{50} of 39.34 $\mu\text{g/mL}$. The results of Moringa extraction by UAE ($IC_{50} = 87.83 \mu\text{g/mL}$), MAE ($IC_{50} = 80.21 \mu\text{g/mL}$), UMAE ($IC_{50} = 76.54 \mu\text{g/mL}$), and MUAE ($IC_{50} = 72.31 \mu\text{g/mL}$). All extraction methods yielded IC_{50} values of less than 100, indicating that the antioxidants extracted are potent antioxidants. The DPPH method was chosen because it is a method that is straightforward, easy, quick, and sensitive and only testing necessitates a tiny sample product. The DPPH method's quantitative evaluation of antioxidant activity is based on a change in the intensity of the purple color of the DPPH, which is proportional to the DPPH solution's concentration. The absorbance at the maximal wavelength of DPPH will change as a result of the color change when measured using UV-Vis spectrophotometry so that the value of free radical scavenging activity will be known, which is expressed by the IC_{50} value [43]. IC_{50} range of 150–200 $\mu\text{g/mL}$ is a weak antioxidant, the IC_{50} range of 100–150 $\mu\text{g/mL}$ is a

moderate antioxidant, the IC_{50} range of 50–100 $\mu\text{g/mL}$ is a strong antioxidant, and the IC_{50} range is < 50 $\mu\text{g/mL}$ is a very strong antioxidant [25]. Compared to maceration and MAE, UMAE increased antioxidant activity by 11.71% and 2.60%, respectively [22].

Antibacterial Test Using the Disc Diffusion Method

Bacteria such as *E. coli* (gram-negative) and *S. aureus* (gram-positive) were tested against UAE, MAE, UMAE, and MUAE extracts. Based on Table 3, the extract from Moringa extraction using UAE, MAE, UMAE, and MUAE have antibacterial activity on *E. coli* and *S. aureus*.

Table 3 shows the results of the inhibition zone diameter. The antibacterial test results of moringa extract with MUAE against *S. aureus* were found to be higher than other methods. In addition, MUAE extract can also affect Gram-negative bacteria such as *E. coli*. because the

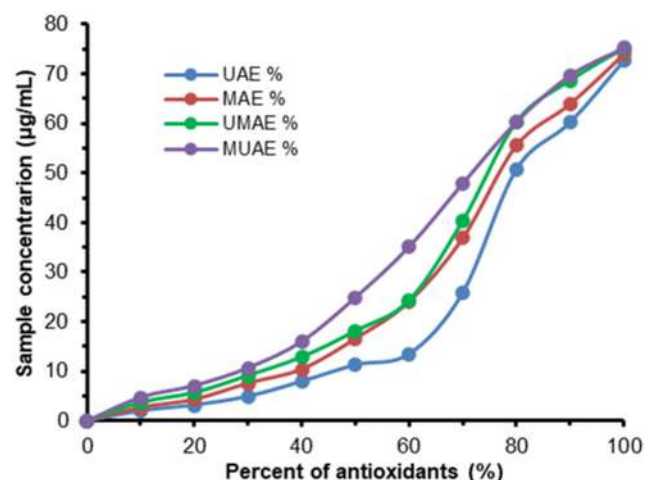


Fig 9. Antioxidant activity of UAE, MAE, UMAE, and MUAE extracts

Table 2. Results of antioxidant activity (%) and IC_{50} of Moringa extract

Concentration ($\mu\text{g/mL}$)	Antioxidant Activity (%)				
	Quercetin	UAE	MAE	UMAE	MUAE
60	71.43	13.48	24.05	24.30	35.11
70	71.77	25.88	36.87	40.34	47.87
80	77.54	50.79	55.55	60.30	60.31
90	81.06	60.25	63.94	68.65	69.67
100	82.44	72.66	73.93	75.14	75.21
IC_{50}	39.34	87.83	80.21	76.54	72.31

Table 3. Results of antibacterial activity of Moringa using the Disc Diffusion method

Bacteria test sample	Obstacles zone (mm)			
	UAE	MAE	UMAE	MUAE
<i>E. coli</i>	2	1	2	2
<i>S. aureus</i>	4	4	5	7

structure of the bacterial cell wall influences the sensitivity of bacteria to antibacterial. Gram-positive bacteria, as an example *S. aureus*, are more susceptible to antibacterial than Gram-negative bacteria because their cell walls are simpler than Gram-negative bacteria's, making it easier for antibacterial compounds to enter Gram-positive bacteria cells [44]. Therefore, the inhibition zone in *S. aureus* is larger than in *E. coli*.

■ CONCLUSION

The selection of the Moringa extraction method can affect the content of bioactive compounds and their biological activities. In total flavonoid content found that MUAE get more flavonoid content with 2.89 mg QE/g > UMAE with 2.73 mg QE/g > MAE with 2.71 mg QE/g > UAE with 2.30 mg QE/g. The best extraction conditions were found at 50 °C for 20 min and 70% ethanol. SEM scan of Moringa morphological extract showed cell damage or rupture of the results of cell extraction with ultrasonic and microwave indicated by a rougher surface, so it is expected that flavonoid compounds in cells (in plants located in vacuoles) can be extracted completely by solvents. In all samples, the FTIR spectrum of Moringa extract showed the presence of flavonoid C=O at 1621 cm⁻¹ and C-O at 1019 cm⁻¹, which was in accordance with the standard flavonoid quercetin spectrum. HPLC analysis found that MAE gets more quercetin content with 41.48 ppm > UAE with 28.96 ppm > MUAE with 16.70 ppm > UMAE with 11.97 ppm. Antioxidant test with DPPH showed that MUAE gets the highest antioxidant activity in the Moringa extract with an IC₅₀ of 72.31 µg/mL and the highest antibacterial with obstacles zone for 2 mm *E. coli*, and 7 mm *S. aureus*. Ultrasonic and microwave technology are beneficial for extracting flavonoids in Moringa.

■ ACKNOWLEDGMENTS

The authors acknowledge the Ministry of Education,

Culture, Research and Technology of the Republic of Indonesia (Kemdikbudristek) for the financial support through Penelitian Terapan Unggulan Perguruan Tinggi (PTUPT) 2021, with contract number: 225-138/UN7.6.1/PP/2021.

■ AUTHOR CONTRIBUTIONS

Aji Prasetyaningrum conceived and designed the experiments, Bakti Jos contributed reagents, materials, and analysis tools, Ratnawati analyzed and interpreted the data, Nur Rokhati revised the manuscript, Teguh Riyanto wrote the paper, and Gian Restu Prinanda performed the experiments. All authors agreed to the final version of this manuscript.

■ REFERENCES

- [1] Benarima, A., Laouini, S.E., Seghir, B.B., Belaiche, Y., and Ouahrani, M.R., 2020, Optimization of ultrasonic-assisted extraction of phenolic compounds from *Moringa oleifera* leaves using response surface methodology, *Asian J. Res. Chem.*, 13 (5), 307–311.
- [2] Vongsak, B., Sithisarn, P., Mangmool, S., Thongpraditchote, S., Wongkrajang, Y., and Gritsanapan W., 2013, Maximizing total phenolics, total flavonoids contents and antioxidant activity of *Moringa oleifera* leaf extract by the appropriate extraction method, *Ind. Crops Prod.*, 44, 566–571.
- [3] Hilwatullisan, Zaman, M., Husaini, A., and Chodijah, S., 2020, Diversification of biscuit product using *Moringa oleifera* flour as an additional source of nutrition, *J. Phys.: Conf. Ser.*, 1500, 012047.
- [4] Kamarudin, A.A., Saad, N., Sayuti, N.H., Razak, N.A.A., and Esa, N.M., 2020, Enhancement of phenolics and antioxidant activity via heat assisted extraction from *Moringa oleifera* using response surface methodology and its potential bioactive constituents, *Malays. J. Med. Health Sci.*, 16 (2), 83–90.
- [5] Pollini, L., Tringaniello, C., Ianni, F., Blasi, F., Manes, J., and Cossignani, L., 2020, Impact of ultrasound extraction parameters on the antioxidant properties of *Moringa oleifera* leaves, *Antioxidants*, 9 (4), 277.

- [6] Rocchetti, G., Blasi, F., Montesano, D., Ghisoni, S., Marcotullio, M.C., Sabatini, S., Cossignani, L., and Lucini, L., 2019, Impact of conventional/non-conventional extraction methods on the untargeted phenolic profile of *Moringa oleifera* leaves, *Food Res. Int.*, 115, 319–327.
- [7] Rodríguez-Pérez, C., Gilbert-López, B., Mendiola, J.A., Quirantes-Piné, R., Segura-Carretero, A., and Ibáñez, E., 2016, Optimization of microwave-assisted extraction and pressurized liquid extraction of phenolic compounds from *Moringa oleifera* leaves by multiresponse surface methodology, *Electrophoresis*, 37 (13), 1938–1946.
- [8] Sin, K., Baraoidan, W.A., and Gaspillo, P.D., 2014, Microwave-assisted extraction of phenolic compounds from *Moringa oleifera* Lam. leaves using response surface methodology as optimization tool, *Philipp. Agric. Sci.*, 97 (1), 36–42.
- [9] Izza, N., Dewi, S.R., Setyanda, A., Sukoyo, A., Utoro, P., Al Riza, D.F., and Wibisono, Y., 2018, Microwave-assisted extraction of phenolic compounds from *Moringa oleifera* seed as antibiofouling agents in membrane processes, *MATEC Web Conf.*, 204, 03003.
- [10] Yu, J., Lou, Q., Zheng, X., Cui, Z., and Fu, J., 2017, Sequential combination of microwave- and ultrasound-assisted extraction of total flavonoids from *Osmanthus fragrans* Lour. flowers, *Molecules*, 22 (12), 2216.
- [11] Keshavarz, B., and Rezaei, K., 2020, Microwave- and ultrasound-assisted extraction of phenolic and flavonoid compounds from konar (*Ziziphus spinachristi*) fruits, *Int. Food Res. J.*, 27 (1), 47–55.
- [12] Tanase, C., Domokos, E., Coşarçă, S., Miklos, A., Imre, S., Domokos, J., and Dehelean, C.A., 2018, Study of the ultrasound-assisted extraction of polyphenols from beech (*Fagus sylvatica* L.) bark, *BioResources*, 13 (2), 2247–2267.
- [13] Kothari, V., Gupta, A., and Naraniwal, M., 2012, Comparative study of various methods for extraction of antioxidant and antibacterial compounds from plant seeds, *J. Nat. Rem.*, 12 (2), 162–173.
- [14] Fithri, N.A., Fitrya, Shabrina, T., Akbari, A., and Yulanri, D., 2019, Antioxidant activity analysis and standardization of *Parkia speciosa* (petai) pods ethanol extract, *Sci. Tech. Indones.*, 4 (1), 5–10.
- [15] Wang, T., Li, W., and Li, T.X., 2017, Microwave-ultrasonic synergistic extraction of crude sepolysaccharides from Se-enriched tea, *Key Eng. Mater.*, 737, 360–366.
- [16] Wu, D., Gao, T., Yang, H., Du, Y., Li, C., Wei, L., Zhou, T., Lu, J., and Bi, H., 2015, Simultaneous microwave/ultrasonic-assisted enzymatic extraction of antioxidant ingredients from *Nitraria tangutorun* Bobr. juice by-products, *Ind. Crops Prod.*, 66, 229–238.
- [17] Nour, A.H., Oluwaseun, A.R., Nour, A.H., Omer, M.S., and Ahmed, N., 2021, “Microwave-Assisted Extraction of Bioactive Compounds (Review)” in *Microwave Heating*, IntechOpen, London, UK, 1–31.
- [18] Vinatoru, M., Mason, T.J., and Calinescu, I., 2017, Ultrasonically assisted extraction (UAE) and microwave assisted extraction (MAE) of functional compounds from plant materials, *TrAC, Trends Anal. Chem.*, 97, 159–178.
- [19] Liew, S.Q., Ngoh, G.C., Yusoff, R., and Teoh, W.H., 2016, Sequential ultrasound-microwave assisted acid extraction (UMAE) of pectin from pomelo peels, *Int. J. Biol. Macromol.*, 93, 426–435.
- [20] Pongmalai, P., Devahastin, S., Chiewchan, N., and Soponronnarit, S., 2015, Enhancement of microwave-assisted extraction of bioactive compounds from cabbage outer leaves via the application of ultrasonic pre-treatment, *Sep. Purif. Technol.*, 144, 37–45.
- [21] Liang, Q., Chen, H., Zhou, X., Deng, Q., Hu, E., Zhao, C., and Gong, X., 2017, Optimized microwave-assistant extraction combined ultrasonic pre-treatment of flavonoids from *Periploca forrestii* Schltr. and evaluation of its anti-allergic activity, *Electrophoresis*, 38 (8), 1113–1121.
- [22] Mahdi, A.A., Rashed, M.M.A., Al-Ansi, W., Ahmed, M.I., Obadi, M., Jiang, Q., Raza, H., and Wang, H., 2019, Enhancing bio-recovery of bioactive compounds extracted from *Citrus medica* L. Var. *sarcodactylis*: Optimization performance of

- integrated of pulsed-ultrasonic/microwave technique, *J. Food Meas. Charact.*, 13 (3), 1661–1673.
- [23] Al Jitan, S., Alkhoori, S.A., and Yousef, L.F., 2018, Phenolic acids from plants: Extraction and application to human health, *Stud. Nat. Prod. Chem.*, 58, 389–417.
- [24] Mukhriani, Sugiarna, R., Farhan, N., Rusdi, M., and Arsul, M.I., 2019, Kadar fenolik dan flavonoid total ekstrak etanol daun anggur (*Vitis vinifera* L), *ad-Dawaa' J. Pharm. Sci.*, 2 (2), 95–102.
- [25] Tristantini, D., Ismawati, A., Pradana, B.T., and Jonathan, J.G., 2016, Pengujian aktivitas antioksidan menggunakan metode DPPH pada daun tanjung (*Mimusops elengi* L.), *Prosiding Seminar Nasional Teknik Kimia "Kejuangan"*, UPN Veteran Yogyakarta, 17 March 2016, G1, 1–7.
- [26] Marjoni, M.R., and Zulfisa, A., 2017, Antioxidant activity of methanol extract/fractions of senggani leaves (*Melastoma candidum* D. Don), *Pharm. Anal. Acta*, 8 (8), 1000557.
- [27] Jahromi, S.G., 2019, "Extraction Techniques of Phenolic Compounds from Plants" in *Plant Physiological Aspects of Phenolic Compounds*, IntechOpen, London, UK, 1–18.
- [28] Thirugnanasambandham, K., 2017, Ultrasound-assisted extraction of oil from *Moringa oleifera* Lam. seed using various solvents, *Energy Sources, Part A*, 40 (3), 343–350.
- [29] Catauro, M., Papale, F., Bollino, F., Piccolella, S., Marciano, S., Nocera, P., and Pacifico, S., 2015, Silica/quercetin sol–gel hybrids as antioxidant dental implant materials, *Sci. Technol. Adv. Mater.*, 16 (3), 035001.
- [30] Um, M., Han, T.H., and Lee, J.W., 2018, Ultrasound-assisted extraction and antioxidant activity of phenolic and flavonoid compounds and ascorbic acid from rugosa rose (*Rosa rugosa* Thunb.) fruit, *Food Sci. Biotechnol.*, 27 (2), 375–382.
- [31] Pimentel-Moral, S., Borrás-Linares, I., Lozano-Sánchez, J., Arráez-Román, D., Martínez-Férez, A., and Segura-Carretero, A., 2018, Microwave-assisted extraction for *Hibiscus sabdariffa* bioactive compounds, *J. Pharm. Biomed. Anal.*, 156, 313–322.
- [32] Chaves, J.O., de Souza, M.C., da Silva, L.C., Lachos-Perez, D., Torres-Mayanga, P.C., da Fonseca Machado, A.P., Forster-Carneiro, T., Vázquez-Espinosa, M., González-de-Peredo, A.V., Barbero, G.F., and Rostagno, M.A., 2020, Extraction of flavonoids from natural sources using modern techniques, *Front. Chem.*, 8, 507887.
- [33] Akhtar, I., Javad, S., Yousaf, Z., Iqbal, S., and Jabeen, K., 2019, Review: Microwave assisted extraction of phytochemicals an efficient and modern approach for botanicals and pharmaceuticals, *Pak. J. Pharm. Sci.*, 32 (1), 223–230.
- [34] Sasongko, A., Nugroho, R.W., Setiawan, C.E., Utami, I.W., and Pusfitasari, M.D., 2018, Aplikasi metode non konvensional pada ekstraksi bawang Dayak, *JTT*, 6 (1), 8–13.
- [35] Bagherian, H., Ashtiani, F.Z., Fouladitajar, A., and Mohtashamy, M., 2011, Comparisons between conventional, microwave- and ultrasound-assisted methods for extraction of pectin from grapefruit, *Chem. Eng. Process.*, 50 (11-12), 1237–1243.
- [36] Narsih, and Agato, 2018, Efek kombinasi suhu dan waktu ekstraksi terhadap komponen senyawa ekstrak kulit lidah buaya, *JGT*, 7 (1), 75–87.
- [37] Fombang, E.N., Nobossé, P., Mbofung, C.M.F., and Singh, D., 2020, Optimising extraction of antioxidants from roasted *Moringa oleifera* Lam. leaves using response surface methodology, *J. Food Process. Preserv.*, 44 (6), e14482.
- [38] Efthymiopoulos, I., Hellier, P., Ladommatos, N., Russo-Profilo, A., Eveleigh, A., Aliev, A., Kay, A., and Mills-Lamprey, B., 2018, Influence of solvent selection and extraction temperature on yield and composition of lipids extracted from spent coffee grounds, *Ind. Crops Prod.*, 119, 49–56.
- [39] Cvitković, D., Lisica, P., Zorić, Z., Repajić, M., Pedisić, S., Dragović-Uzelac, V., and Balbino, S., 2021, Composition and antioxidant properties of pigments of Mediterranean herbs and spices as affected by different extraction methods, *Foods*, 10 (10), 2477.
- [40] Sukmawati, Widiastuti, H., and Miftahuljanna, 2019, Analisis kadar kuersetin pada ekstrak etanol

- daun miana (*Plectranthus Scutellarioides* (L.) R.Br.) secara HPLC (High Performance Liquid Chromatography), *As-Syifaa Jurnal Farmasi*, 11 (1), 38–44.
- [41] Shervington, L.A., Li, B.S., Shervington, A.A., Alpan, N., Patei, R., Muttakin, U., and Mulla. E., 2018, A comparative HPLC analysis of myricetin, quercetin and kaempferol flavonoids isolated from Gambian and Indian *Moringa oleifera* leaves, *Int. J. Chem.*, 10, 28–35.
- [42] González-Burgos, E., Ureña-Vacas, I., Sánchez, M., and Gómez-Serranillos, M.P., 2021, Nutritional value of *Moringa oleifera* lam. leaf powder extracts and their neuroprotective effects via antioxidative and mitochondrial regulation, *Nutrients*, 13 (7), 2203.
- [43] Julianawati, T., Hendarto, H., and Widjiati, 2020, Penetapan total flavonoid, aktivitas antioksidan dan karakterisasi nanopartikel ekstrak etanol daun kelor (*Moringa pterygosperma* Gaertn.), *Jurnal Penelitian Kesehatan Suara Forikes*, 11 (1), 49–54.
- [44] Sari, R., Muhani, M., and Fajriaty, I., 2017, Uji aktivitas antibakteri ekstrak etanol daun gaharu (*Aquilaria microcarpa* Baill.) terhadap bakteri *Staphylococcus aureus* dan *Proteus mirabilis*, *PSR*, 4 (3), 143–154.

Supplementary Data

This supplementary data is a part of paper entitled "Fabrication of Alginate-Based Electrospun Nanofibers for Carbon Dioxide Removal".

Table S1. Chemical structure assignments of FTIR analysis

Wavenumber (cm ⁻¹)	Characteristic bands	Wavenumber (cm ⁻¹)	Characteristic bands
Alginate		Natural Zeolites	
1033	-C-O-C	462	O-Si-O
1419	O=C-O- (symmetric)	794	Si-O (allotropic)
1635	O=C-O- (asymmetric)	1049	Al-O
3448	-O-H	1635	Si-O
		3448	-O-H
PVA		Activated Zeolites	
848	-C-H isotactic	462	O-Si-O
1095	-C-O	794	Si-O (allotropic)
1342	-C-H	1072	Al-O
1442	O=C-O- (symmetric)	1635	Si-O
1635	-C=O	3448	-O-H
2939	-C-H		
3448	-O-H		
Alg/PVA NFs		Alg/PVA/Z NFs	
848	-C-H isotactic	617	Si-O-Si(Al)
1095	-C-O	848	-C-H isotactic
1327	-C-H	1095	-C-O
1427	O=C-O- (symmetric)	1327	-C-H
1604	-C=O	1427	O=C-O- (symmetric)
2908	-C-H	1620	Si-O
3286	-O-H	2939	-C-H
		3317	-O-H

Table S2. Five isotherm models adopted in this study

Models	Isotherm equation	Linearized equation	Curve plot
Langmuir	$q_e = \frac{q_m K_L C_e}{1 + K_L C_e}$	$\frac{C_e}{q_e} = \frac{1}{q_m} C_e + \frac{1}{K_L q_m}$	C_e vs. C_e/q_e
Freundlich	$q_e = K_F C_e^{1/n}$	$\log q_e = \log K_F + \frac{1}{n} \log C_e$	$\log C_e$ vs. $\log q_e$
Dubinin-Radushkevich (DR)	$q_e = q_s E^{(-K_{DR} \varepsilon^2)}$, where $\varepsilon = RT \ln \left(1 + \frac{1}{C_e}\right)$	$\ln q_e = \ln q_s - (K_{DR} \varepsilon^2)$, $E = \frac{1}{\sqrt{2K_{DR}}}$	ε^2 vs. $\ln q_e$
Temkin	$q_e = B \ln (K_T C_e)$, where $B = \frac{RT}{b_T}$	$q_e = B \ln K_T + B \ln C_e$	$\ln C_e$ vs. q_e
Elovich	$\frac{q_e}{q_m} = K_E C_e E^{-\frac{q_e}{q_m}}$	$\ln \frac{q_e}{C_e} = \ln K_E q_m - \frac{1}{q_m} q_e$	q_e vs. $\ln \frac{q_e}{C_e}$

Fabrication of Alginate-Based Electrospun Nanofibers for Carbon Dioxide Removal

Adhitasari Suratman^{1*}, Desi Nur Astuti¹, Ryan Jonathan¹, Agus Kuncaka¹, and Yusril Yusuf²

¹Department of Chemistry, Faculty of Mathematics and Natural Sciences, Universitas Gadjah Mada, Sekip Utara, Yogyakarta 55281, Indonesia

²Department of Physics, Faculty of Mathematics and Natural Sciences, Universitas Gadjah Mada, Sekip Utara, Yogyakarta 55281, Indonesia

* **Corresponding author:**

email: adhitasari@ugm.ac.id

Received: July 6, 2021

Accepted: January 26, 2022

DOI: 10.22146/ijc.67349

Abstract: A fabrication of eco-friendly and low-cost adsorbent materials is reported for CO₂ removal. Alginate nanofibers (NFs) adsorbents were prepared by incorporating poly(vinyl alcohol) (PVA) into alginate solutions via electrospinning technique from alginate biopolymers. Smooth-surfaced Alg/PVA NFs were obtained with a specific surface area of 9.197 m² g⁻¹. Zeolite (Z) was impregnated into polymer solutions to enhance the properties and performances of alginate nanofibers. Alg/PVA/Z NFs appeared to be rougher with a specific surface area of 25.998 m² g⁻¹. Both adsorbents offered great potential for CO₂ adsorbent in the future. The adsorption isotherms of Alg/PVA NFs followed the Langmuir model with optimum CO₂ adsorption capacity of 3.286 mmol g⁻¹ and Alg/PVA/Z NFs followed Dubinin-Radushkevich model with optimum CO₂ adsorption capacity of 10.710 mmol g⁻¹.

Keywords: electrospinning; nanofibers; alginate; poly(vinyl alcohol) (PVA); zeolites; carbon dioxide

■ INTRODUCTION

Over the past decades, fossil fuel combustion has elevated the atmospheric CO₂ concentration up to 416.87 ppm as of December 2021 [1]. Excessive release of carbon dioxide leads to global warming, which causes a threat to the environment and public health. Hence, it is essential to reduce carbon emissions. Carbon Capture and Separation (CCS) is a main technology for managing and mitigating CO₂ emissions. There are several pathways for CCS, such as pre-combustion, post-combustion, and oxy-fuel combustion [2]. Post-combustion is currently the most favored approach for capturing CO₂. Several post-combustion methods are available, including adsorption, absorption, membrane, and cryogenic. Among various methods, adsorption is preferable due to its cost-effective process, high CO₂ adsorption capacity, and low-energy requirement. Many studies have been conducted to develop adsorbent materials for carbon capture, such as carbonaceous materials (activated carbons, carbon nanotubes, graphene), biochar, zeolites, Metal-Organic

Frameworks (MOFs), Zeolitic Imidazolate Frameworks (ZIFs), and nanomaterials [2].

Nanomaterials, such as nanofibers offer higher specific surface area, which have a high potential for carbon dioxide removal. There are various fabrication methods to produce nanofibers, however, electrospinning is currently the most versatile technique for manufacturing nanofibers on an industrial scale. Electrospinning involves the electrohydrodynamic principle, in which a droplet of liquid is electrified to form a jet, followed by stretching and elongation to form nanofibers [3].

Electrospun nanofibers have exhibited prospective properties as adsorbent materials for carbon capture owing to their high porosity, high specific surface area, unique structure, good interconnectivity, tunable pore size, good mechanical properties, low gas resistance, and rapid kinetics reaction [3]. Various electrospun nanofibers adsorbent have been developed for CO₂ adsorption from diverse materials such as biopolymers [4-5], synthetic polymers [6-9], carbons [10-14], MOFs

[15-16], amine sorbents [17-18], metals oxides and ceramics [19-20].

In the past years, biopolymers-based adsorbents such as alginate have gained immense interest due to increased ecological and environmental concerns. Alginate consists of linear unbranched anionic polysaccharides of (1-4)-linked β -D-mannuronic acid (M) and α -L-guluronic acid (G) monomers which can be extracted from seaweed, specifically alginophyte seaweed species [21]. Seaweed cultivations are dominated by Asian countries, in which Indonesia is the major producers alongside China, Japan, Korea, and the Philippines. In 2016, Indonesia was listed as the second-largest seaweed producers with 38.7% of the global production, only topped up by China with 47.9% [22]. According to Presidential Regulation No. 33/2019, Indonesia has the potential to cultivate seaweed on 1.5 million hectares, in which estimation of alginophyte seaweed production can reach more than 240 thousand tons per year. Taking advantage of the abundant seaweed resources, the alginate can be one alternative of biodegradable biopolymers, low-cost sources, and generally non-toxic to the environment [23].

Alginate has been investigated for various applications, including CO₂ adsorption, because of its high hydrophilicity resulting from its hydroxyl and carboxyl groups [24]. Since alginate is polyelectrolyte, it is quite challenging to produce electrospun nanofibers from pure alginate solutions. However, these restrictions and processing limitations can be improved by introducing carrier copolymers into the alginate solution. One of the most commonly used copolymers is poly(vinyl alcohol) (PVA). PVA is a semi-crystalline hydrophilic polymers that is biocompatible with alginate, non-toxic, biodegradable, with thermal stability, and many carbonyl groups that can bind carbon dioxide molecules [21,25-26].

Another adsorbent that also has been broadly studied for CO₂ removal is zeolites. Zeolites are microporous crystalline aluminosilicate minerals that consist of silicate $[\text{SiO}_4]^{4-}$ and aluminate $[\text{AlO}_4]^{5-}$ tetrahedrons connected by oxygen atoms, forming a box-like structure with a molecular size of 0.5–1.2 nm. Zeolite exhibits excellent carbon capture performance as it has

high CO₂ adsorption capacity and selectivity at low pressure. Nevertheless, zeolite is very sensitive in the presence of water or moisture that causes greatly downgrade for CO₂ adsorption [27].

For long periods of time, zeolites have been exploited for environmental remediation with remarkable adsorption capacity, and yet, the materials classified as non-renewable resources that could generate secondary pollutant. On the other hands, alginate has been under spotlighted for carbon dioxide discharge since it is contained abundant hydroxyl and carboxyl groups also naturally biodegradable. Nonetheless, alginate performance still needed some improvement. Zeolites and alginate have been separately applied as CO₂ adsorbents, therefore, this study focused on combining extensive resources of alginate in Indonesia with natural zeolites obtained from local mining to synthesize eco-friendly carbon dioxide adsorbents. Afterward, an electrospinning technique was performed to fabricate alginate-zeolite nanofibers. Recently, utilizing nano-size zeolites have been reported. Many researchers have successfully fabricated zeolites nanofibers using the electrospinning technique [28-36]. Zeolites nanofibers have exhibited several advantages such as better performance and lifetime, improved mass transfer, higher selectivity, and minimized recovery and agglomeration issues [32].

■ EXPERIMENTAL SECTION

Materials

Na-Alginate (medium viscosity, vis. \geq 2000 cps), poly(vinyl alcohol) (PVA) (ave. Mw 70000–100000, fully hydrolyzed, vis. 11–14 cps), natural zeolite from Klaten (Central Java, Indonesia), HNO₃ 70%, Na₂EDTA 1 M, NaOH, HCl 37%, Sodium tetraborate (Na₂B₄O₇·10H₂O), CO₂ gas, phenolphthalein and methyl orange indicators. All chemicals and solvents were procured from Merck and Sigma Aldrich in pro-analytical grade and used as received without further purification.

Instrumentation

The electrospinning technique is set at 15 kV with a tip-to-collector distance of 15 cm at room temperature.

Conductivity-meter used is from ST10C-B (Ohaus). The Fourier transform infrared (FT-IR) used is from Shimadzu-Prestige 21 using the KBr pellet technique. Scanning Electron Microscopy-Energy Dispersive Spectroscopy (SEM-EDS) is from JEOL JSM-6510LA. Surface Area & Pore Size Analyzer is from Quantachrome Nova 1200e. CO₂ adsorption was investigated using a gas trapping system (Fig. 1).

Procedure

Synthesis Alg/PVA NFs

Alg/PVA NFs were synthesized following the procedure described by Islam and Karim (2010) [37]. Alg/PVA solutions were prepared by stirring alginate solution (2% w/w in double distilled water/DDW) and PVA solution (10% w/w in DDW) in various volume ratios (0:10, 1:9, 2:8, 3:7, and 4:6 v/v) for 2 h at room temperature. Alg/PVA solutions were electrospun for 2 h and collected on a grounded collector. As-spun Alg/PVA NFs were dried at room temperature and characterized using FTIR, SEM, and Surface Area & Pore Size Analyzer.

Synthesis zeolites modified Alg/PVA nanofibers (Alg/PVA/Z NFs)

Natural zeolite sieved 170 was demineralized by Na₂EDTA for 24 h and dealuminated using 8 M HNO₃ in water for 24 h. The pretreated zeolite was activated by calcination at 500 °C at a rate of 10 °C/min for 3 h in the air. Alg/PVA/Z NFs were fabricated by impregnating activated zeolites to the Alg/PVA solutions (2:8 v/v) with a various mass of zeolites 0.5–3.0% (w/w). The mixtures were electrospun for 2 h and collected on a grounded collector. As-spun Alg/PVA/Z NFs were dried at room temperature and characterized using FTIR, SEM, and Surface Area & Pore Size Analyzer.

Carbon dioxide capture

The capturing CO₂ gas was carried out using a gas trapping system at ambient temperature and pressure 1 atm (see Fig 1). The adsorption capacity of Alg/PVA NFs and Alg/PVA/Z NFs were analyzed by titrimetric method, in which carbon dioxide gas was trapped with NaOH solution. Initially, CO₂ gas was passed through the gas trapping system at a specific flow rate (10–50 mL min⁻¹) for a period of time (10–30 min) without the adsorbent

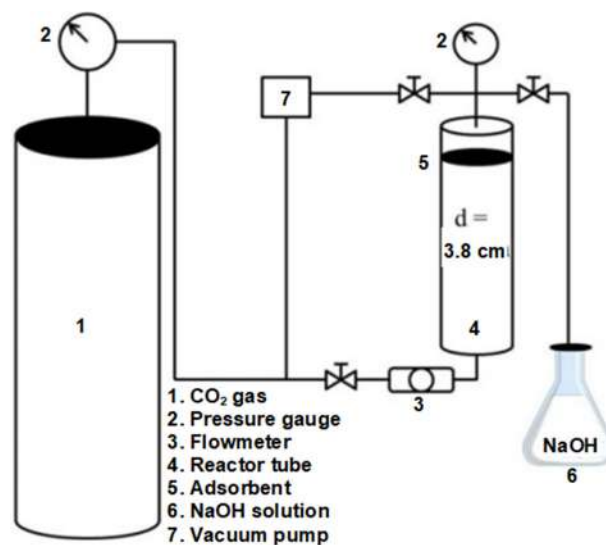


Fig 1. CO₂ adsorption process using gas trapping system

material. Afterward, Alg/PVA NFs and Alg/PVA/Z NFs adsorbent were placed in the reactor tube. Carbon dioxide then flowed into the reactor chamber at the same condition. The uncaptured CO₂ was trapped in NaOH 0.1 M and formed as Na₂CO₃. NaOH was titrated with HCl 0.1 M, and the concentration of uncaptured CO₂ was analyzed using back titration (Warder's method). Adsorption capacity of As-spun Alg/PVA NFs and Alg/PVA/Z NFs were conducted with various flowrates (10, 20, 30, 40, and 50 mL min⁻¹), contact time (10, 15, 20, 25, and 30 min), basis weight (i.e. electrospun time 1, 2, 3, 4, and 5 h), and mass of zeolites (0.5, 1.0, 1.5, 2.0, 2.5, and 3.0% (w/w)). The adsorption behaviors were analyzed using Langmuir, Freundlich, Dubinin-Radushkevich (DR), Temkin, and Elovich isotherm models (Table S2). The adsorption isotherm was studied using collected data for gas flowrates versus adsorption capacity.

RESULTS AND DISCUSSION

FTIR Characterization

As shown in Fig. 2, alginate showed characteristic peaks at 1033, 1419, 1635, and 3448 cm⁻¹ corresponding to the stretching of –C–O–C, symmetric –COO–, asymmetric –COO–, and O–H, respectively. The characteristic bands of pristine PVA were observed at 848 cm⁻¹ (C–H isotactic stretching), 1095 cm⁻¹ (C–O stretching), 1342 cm⁻¹ (C–H stretching), 1442 cm⁻¹

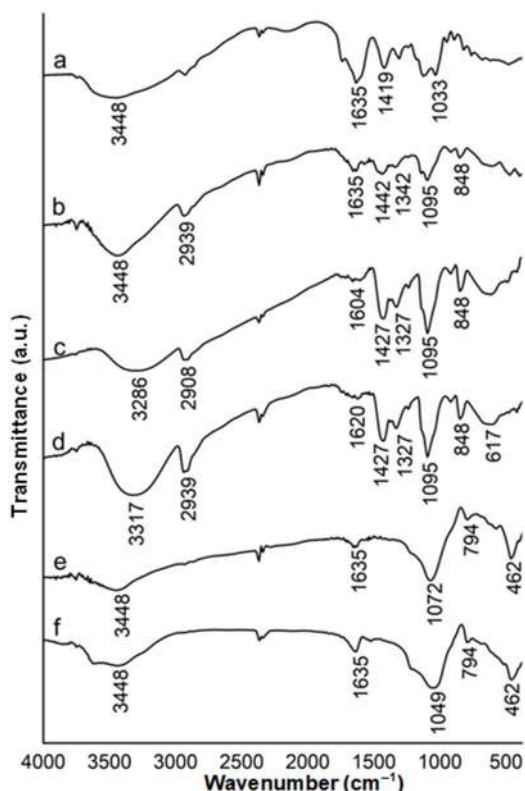


Fig 2. FTIR spectra of alginate (a), PVA (b), as-spun Alg/PVA NFs 2:8 (c), as-spun Alg/PVA/Z NFs 2:8:2.5 (d), activated zeolites (e), and natural zeolites (f)

(symmetric -COO- stretching), 1635 cm^{-1} (C–O stretching from acetate group), 2939 cm^{-1} (CH_2 stretching), and 3448 cm^{-1} (O–H stretching) [38]. Natural zeolites exhibited peaks at 462 cm^{-1} for bending vibration of O–Si–O, 794 cm^{-1} corresponds to an allotropic phase of SiO_2 . The vibration of Al–O bonds were shown at 1049 cm^{-1} . A band at 1635 cm^{-1} was associated with the Si–O bond. Hydroxyl groups were shown at 3448 cm^{-1} . After pretreatment, activated zeolites were seen with similar spectra of natural zeolites, but the Al–O vibration band shifted to 1072 cm^{-1} , indicating that the dealumination was successfully performed [39-40].

All as-spun Alg/PVA NFs exhibit similar bands as alginate and PVA, however, a few changed vibrations. For instance, Alg/PVA NFs 2:8 (Fig. 2(a)), O–H and C–O carbonyl stretching vibration shifted to lower band numbers at 3286 and 1604 cm^{-1} , respectively. These phenomena attributed to the fact that intermolecular interactions through hydrogen bonding between the

hydroxyl group of alginate and the etheric oxygen of PVA occurred (Fig. 3) [38]. The presence of zeolites in alginate-based nanofibers was represented by the bands in the range of $400\text{--}700\text{ cm}^{-1}$ for zeolites structural unit and 1620 cm^{-1} for Si–O bonds. Overall, as-spun Alg/PVA/Z NFs were also displayed to be shifted. Alg/PVA/Z NFs 2:8:2.5 showed the broadened peak of O–H stretching vibration was at lower wavenumber of 3317 cm^{-1} (the detailed assignment bands summarized in Table S1). This phenomenon could indicate that zeolite was interacted with alginate-PVA by polymers intermolecular interaction. Si(Al)–O from zeolites and O–H groups of PVA as well as alginate backbone interacted *via* hydrogen bonding (Fig. 4) [28,34].

Effect of Polymer Characteristic and Conductivity on Nanofibers Formation

There are three parameters that control the

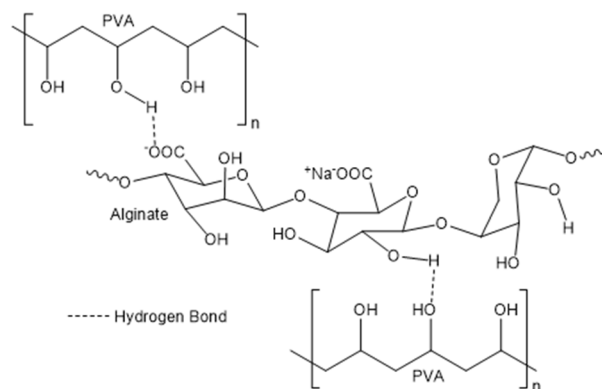


Fig 3. Illustrated representation of alginate-PVA intermolecular interactions

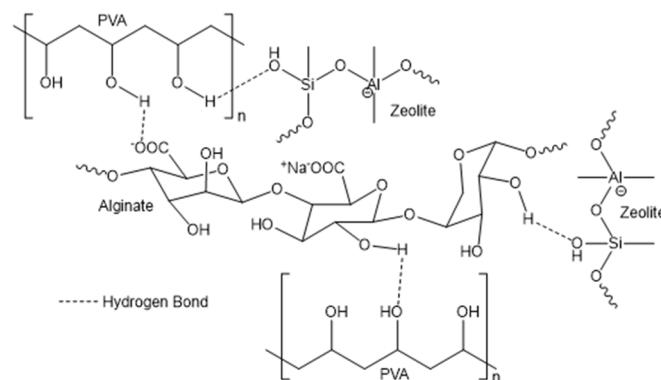


Fig 4. Illustrated representation of alginate-PVA-zeolites intermolecular interactions

dimension, structure, and morphology of nanofibers: solution, process, and ambient parameters. The parameters of solution were determined by polymer characteristics and solvents, such as polymer type, molecular weight, concentration, viscosity, surface tension, conductivity, and dielectric constant [41]. Natural polymers such as alginate were difficult to electrospun. The main reasons were due to polyelectrolyte character and low conductivity of pure alginate solution, as shown in Fig. 5 (volume ratio alginate to PVA of 10:0).

During the electrospinning process, polymer solution was fed into the syringe and ejected out as a spherical-shape droplet at the tip of the spinneret. A high voltage was applied to the droplet. When the electric field reached a certain threshold, the droplet was converted into a conical shape (i.e. Taylor cone). However, alginate solution could not be formed as a stable droplet. Polyelectrolyte character induced strong electrostatic repulsion that deformed the shape of the droplet and therefore inhibited the formation of Taylor cone. When the intensity of high voltage was increased, the repulsive

electrostatic forces overcame the surface tension, and the Taylor cone was then generated into a charged jet and thin fiber formed. However, polymers with low conductivity character lacked surface charge, which resulted in jet instability [3,21,41]. From the aforementioned explanations, it can be concluded that pure alginate solutions could not support electrospun and resulted in droplets form (Fig. 6(a)).

The formation of nanofibers can be improved by

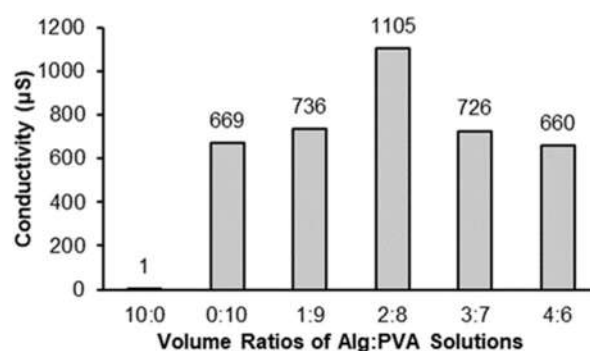


Fig 5. Conductivity values of various alginate/PVA solutions

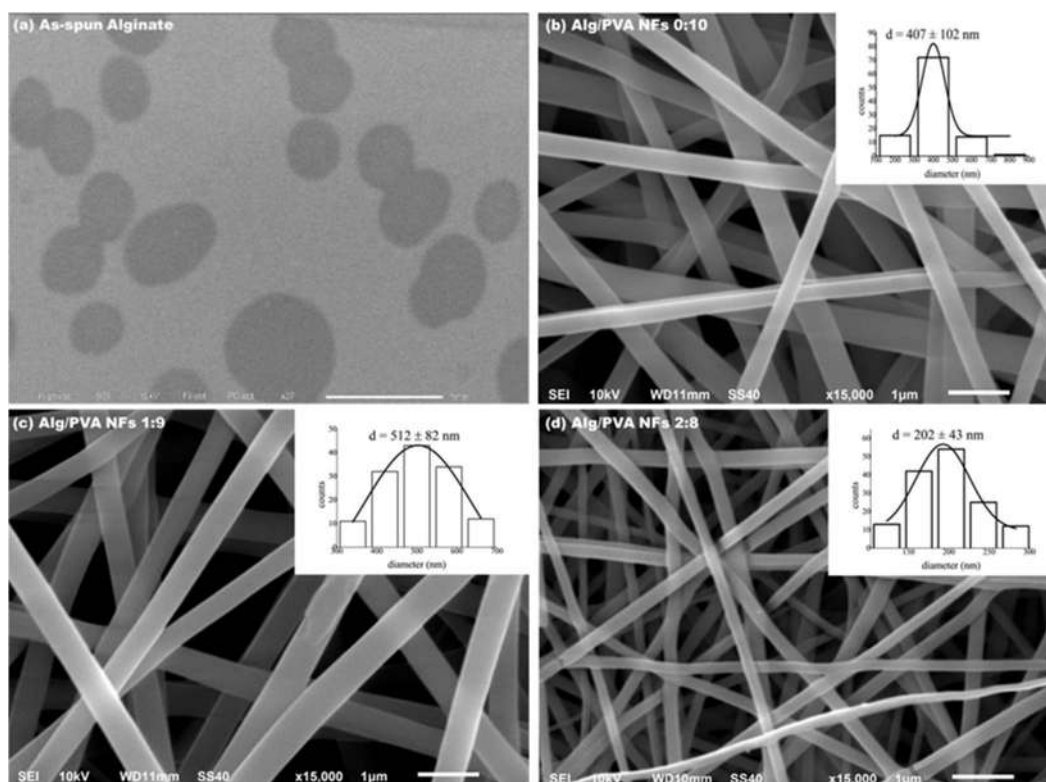


Fig 6. SEM images of as-spun alginate (a), as-spun Alg:PVA NFs volume ratios 0:10 (b), 1:9 (c), 2:8 (d), 3:7 (e), and 4:6 (f); insets show diameter of each nanofibers

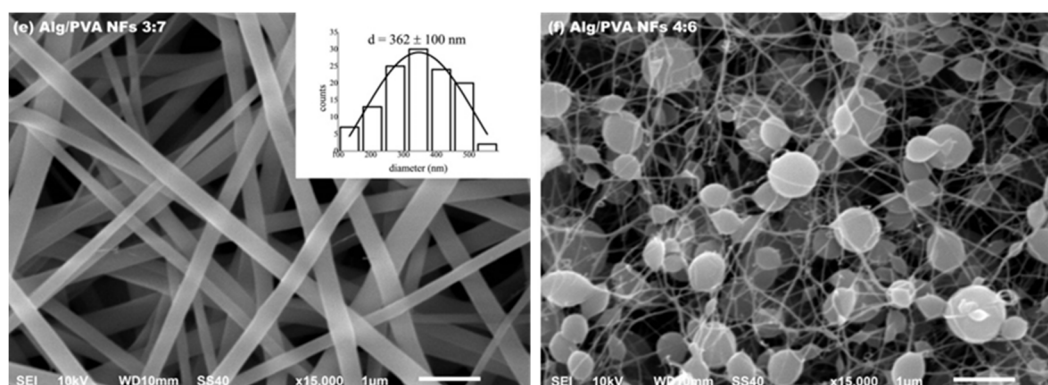


Fig 7. SEM images of as-spun alginate (a), as-spun Alg:PVA NFs volume ratios 0:10 (b), 1:9 (c), 2:8 (d), 3:7 (e), and 4:6 (f); insets show diameter of each nanofibers (*Continued*)

introducing PVA into alginate solutions. The Addition of copolymer reduced repulsion forces among polyanionic alginate molecules by breaking hydrogen bonds within alginate chains and thus enabled the formation of alginate nanofibers. PVA incorporation also increased solution conductivity because intermolecular bonds between alginate and PVA can lessen the rigidity of three-dimension structure and enhance the mobility of alginate chains [25-26]. Incorporated PVA into alginate solution with volume ratios Alg to PVA of 0:10, 1:9, 2:8, and 3:7 formed beadless nanofibers (Fig. 6(b-e)), but further increase alginate loading beyond that (4:6) resulted in beaded nanofibers (Fig. 6(f)) due to the dominance of polyelectrolyte nature of alginate solution. The most uniform, continuous, smooth-surfaced, and thinnest Alg/PVA NFs were obtained from Alg:PVA solution volume ratio 2:8 with an average diameter of 202 ± 43 nm.

Impregnation Porous Material on Electrospun Nanofibers

Impregnation of zeolite particles into Alg/PVA solutions disrupted the dynamic interactions within alginate and PVA and changed solution characteristics. When the amount of added zeolites increased, conductivity values gradually decreased (Fig. 7). Lower conductivity reduced the ability of the solutions to carry sufficient charges for nanofibers formation, as a result Alg/PVA/Z NFs appeared to be rougher and bigger in diameter, which can be seen in SEM analysis (Fig. 8(a,c,e)). Elemental analysis of Alg/PVA/Z NFs was carried out using SEM-EDS (Fig. 8(b,c,f)), revealing that

zeolites embedded into nanofibers structure. Mass percentage of particles increased as more zeolite was added into the solution. The high content of zeolites also generated lumps alongside nanofibers because of the particles aggregation [28-29,33,36]. The highest content of zeolites with minimized agglomeration and uniform Alg/PVA/Z NFs was obtained from a solution with a zeolite mass of 2.5% (w/w) with an average diameter of 250 ± 60 nm.

CO₂ Adsorption of Alginate-Based Nanofibers

The performance of Alg/PVA NFs for carbon capture was evaluated by varying morphologies, gas flowrates, contact times, and basis weight of the adsorbent. There are three different structural morphologies of nanofibers, namely smooth fiber, beads-on-string, and beads, in which affected the adsorption capacity of the materials. In respect to investigating the dependence of nanofiber morphologies

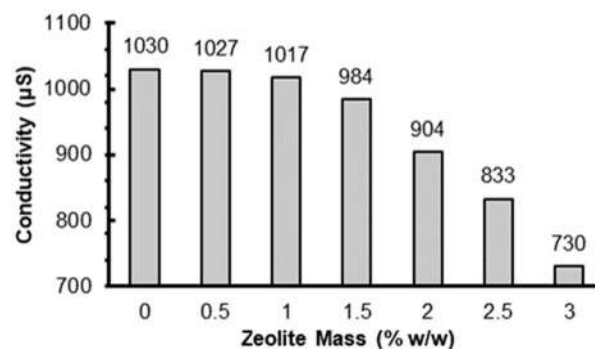


Fig 8. Conductivity values of alginate-PVA solution with different loading of zeolite particles

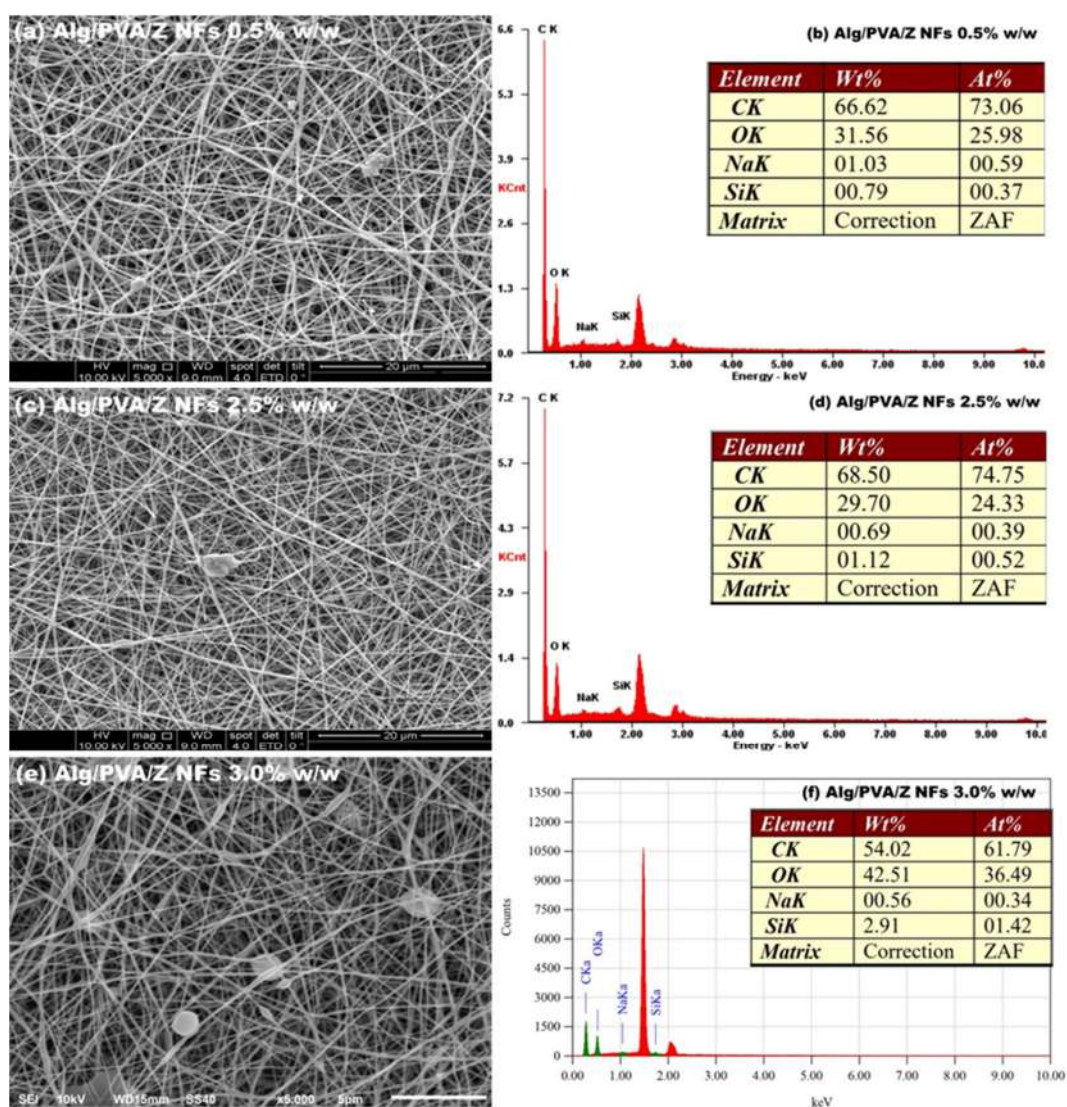


Fig 9. SEM images and EDX analysis of as-spun Alg/PVA/Z NFs with various zeolites mass: 0.5 (a, b), 2.5 (c, d), and 3.0 (e, f) % w/w

in CO₂ removal, a series of variation volume ratios alginate solution to PVA solution was conducted. As stated in the previous discussion, Alg/PVA NFs 0:10, 1:9, 2:8, and 3:7 formed beadless and smooth fiber morphology. As shown in Fig. 9(a), Alg/PVA NFs 2:8 with the finest diameter exhibited the largest adsorption capacity at 3.286 mmol g⁻¹. Apparently, thinner nanofibers had a higher total surface area, which influenced their enhanced ability to capture submicron particles and increased the higher filtration efficiency [42].

Pressure was another aspect that needed to be taken into consideration in carbon dioxide removal, which can

be achieved by varying flowrate (Fig. 9(b)) and contact time (Fig. 9(c)). Higher flowrate and contact time led to higher gas pressure inside reactor tube which caused lower adsorption capacity. High pressure tended to increase desorption rate over adsorption rate. The best flowrate and contact time about 20 mL min⁻¹ and 20 min, respectively. Additionally, adsorbent mass also influenced the CO₂ uptake. Mass of the resulted nanofibers is measured by basis weight, mass per unit area of the material. Variation of electrospun time (1, 2, 3, 4, and 5 h) could alter the basis weight of Alg/PVA NFs. When the basis weight was increased until 4955 g m⁻² (electrospun

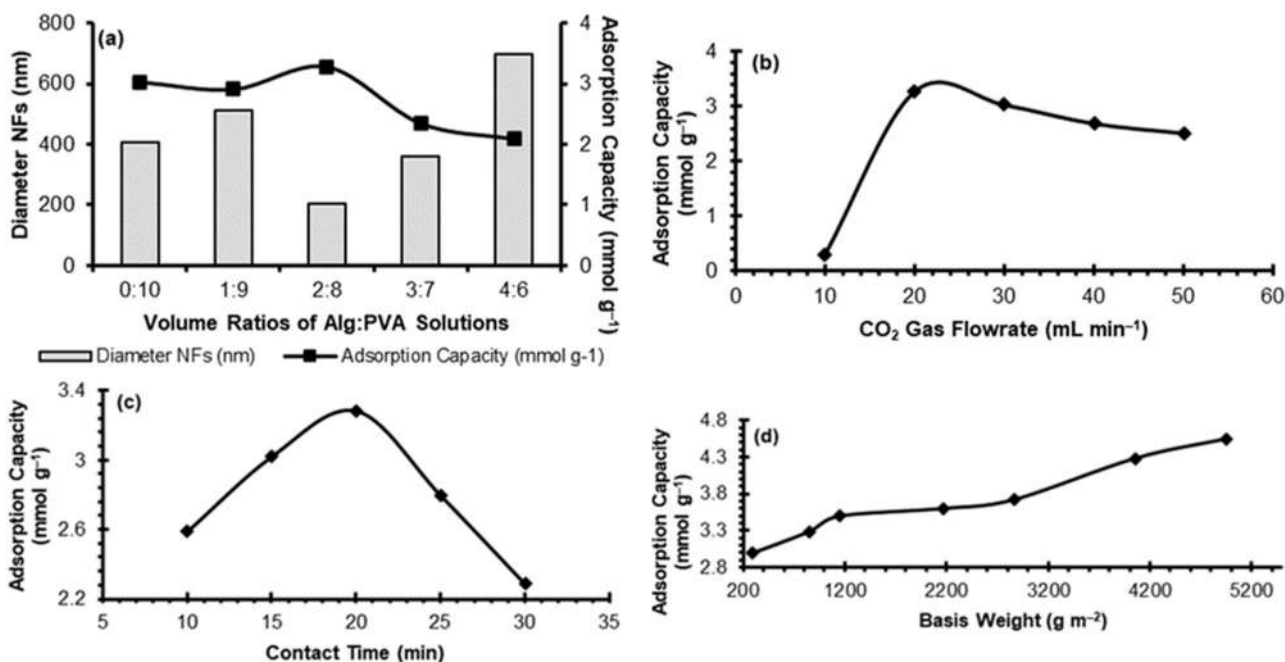


Fig 10. Adsorption capacity of Alg/PVA NFs 2:8 with various volume ratios of Alg/PVA solution (a), gas flowrate (b), contact time (c), and basis weight (d). All analysis carried out at ambient temperature and pressure 1 atm

time 5 h), the adsorption capacity increased up to 4.548 mmol g⁻¹ because the more enormous basis weight made the adsorbent denser and provided more active sites [43].

Influence of Zeolites on Adsorption Capacity

The specific surface area was a critical factor in carbon capture, hence zeolites were added into Alg/PVA solutions. Zeolites are well-known adsorbents for CO₂ removal. Zeolites properties and performances are affected by their particle sizes. When presented in nanoscale, zeolites have higher external surface area and more accessible active sites, therefore their performances would increase [31]. The adsorption capacities of

Alg/PVA/Z NFs were gradually enhanced with increase in zeolites loading. The maximum capacity was 10.710 mmol g⁻¹ which obtained from zeolites mass 2.5% (w/w). Further increase of zeolites load led to decreased in CO₂ adsorption capacity (Fig. 10(a)). High contains of zeolites produced beaded nanofibers with lower specific surface area and porosity of the resulted nanofibers. Zeolites were suitable adsorbents for low to moderate pressure. Therefore, raising gas flow rates created higher pressure conditions, resulting in decreased adsorption capacity due to the weak interaction between adsorbent-adsorbate became unstable. It led to more desorption of carbon dioxide molecules (Fig. 10(b)) [40].

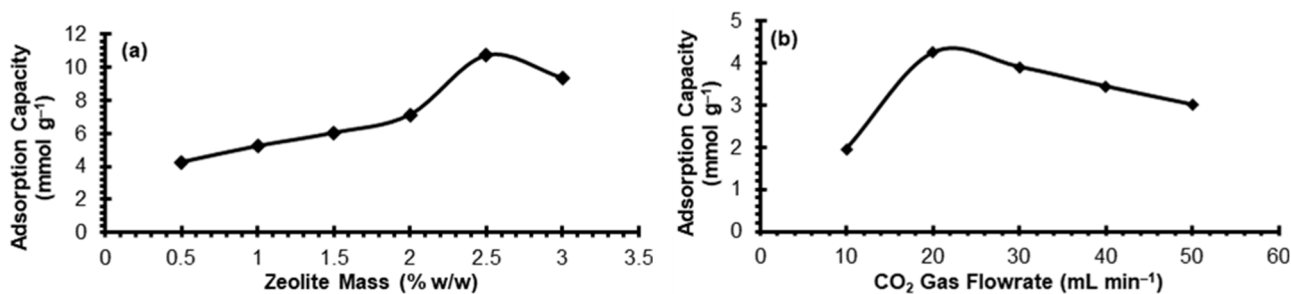


Fig 11. Adsorption capacity of Alg/PVA/Z NFs 2:8:2.5 with various zeolites loading (a) and gas flowrate (b). All experiments were done at ambient temperature and pressure 1 atm

In order to evaluate specific surface area of the adsorbents, N_2 adsorption isotherm were carried out at 77 K. As shown in Fig. 11, alginate-based nanofiber adsorbents exhibit Type I isotherm that indicating the typical microporous materials. The Brunauer-Emmett-Teller (BET) surface area was calculated to be 9.197 and 25.998 $m^2 g^{-1}$ for Alg/PVA NFs 2:8 and Alg/PVA/Z NFs 2:8:2.5, respectively. Zeolites porous structure increased specific surface area of the nanofibers and provided more active sites to capture CO_2 molecules. Consequently, at a relatively similar basis weight, Alg/PVA/Z NFs showed over than three times bigger adsorption capacity compared to Alg/PVA NFs.

Interaction between Alginate-Based Nanofibers and Carbon Dioxide

Alginate binds CO_2 through the carboxyl and hydroxyl groups within the chains [24]. Besides, CO_2 also can interact with the carbonyl group of PVA. The electron pair of the polymers carbonyl oxygen interacts with the carbon atom of carbon dioxide, in which the carbon atom of CO_2 molecules acts as an electron acceptor and lone pair electron of polymer carbonyl oxygen acts as an electron donor species [44]. FTIR spectra (Fig. 12) showed that after CO_2 adsorption, the carbonyl (1095 cm^{-1}) and symmetric carboxyl (1427 cm^{-1}) peaks of Alg/PVA NFs disappeared, also asymmetric $-COO-$ and $-OH$ stretching vibration shifted to higher wavenumber. The few changed peaks in FTIR spectra showed that Alg/PVA NFs binds CO_2 *via* hydrogen bond and Lewis acid-base interaction. There were two suggested configurations of Lewis acid-base interaction between polymers carbonyl groups and CO_2 : T-shaped geometry and bent T-shaped configuration [44].

Zeolites attract strongly to the gases with high quadrupole moment such as carbon dioxide *via* electric field produced by the cation of the zeolites. Interaction between zeolites framework structure and CO_2 molecules involved relatively weak intermolecular forces, namely Van der Waal's forces and electrostatic interaction [27,40,45].

Adsorption Isotherm Studies

The adsorption behaviors of alginate-based nanofibers were analyzed using Langmuir, Freundlich,

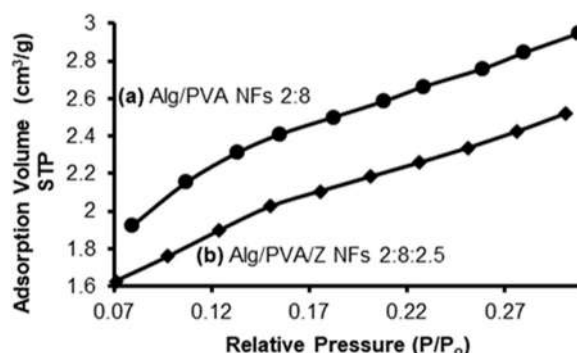


Fig 12. N_2 adsorption/desorption isotherm for CO_2 onto Alg/PVA NFs 2:8 (a) and Alg/PVA/Z NFs 2:8:2.5 (b)

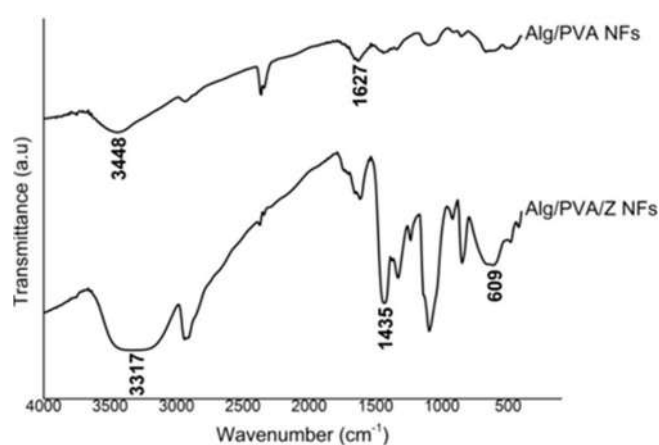


Fig 13. FTIR spectra of Alg/PVA NFs 2:8 and Alg/PVA/Z NFs 2:8:2.5 after CO_2 adsorption

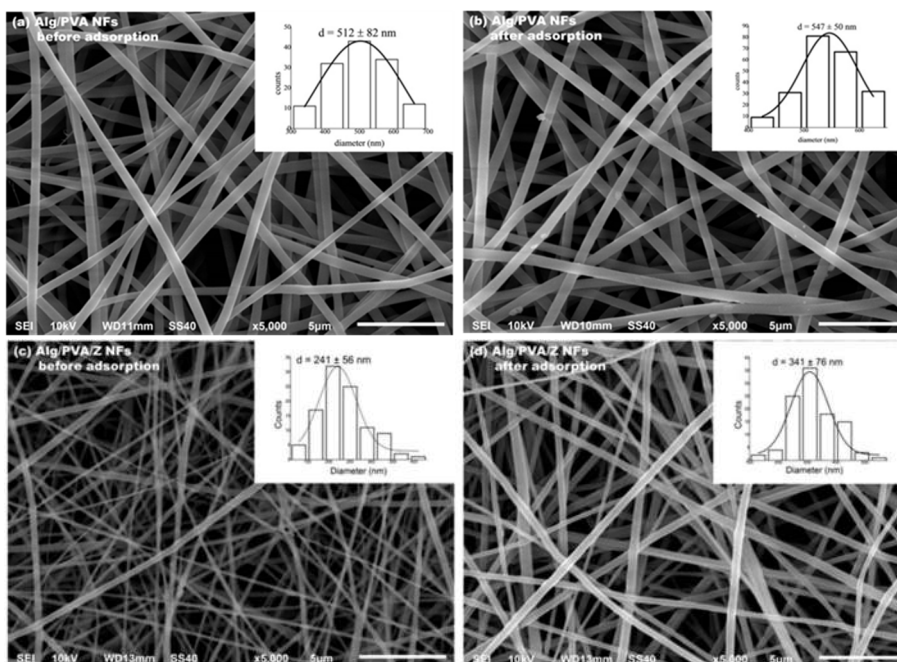
Temkin, Dubinin-Radushkevich (DR), and Elovich isotherm models [46]. See Table S2 for the detailed equations and curve plots.

Table 1 shows the result parameters and correlation coefficients (R^2) of each isotherm mode, a measure of goodness-of-fit, representing good linearity for a certain model relative to the other models. Plot C_e versus C_e/q_e of Alg/PVA NFs 2:8 gives the highest R^2 value (0.9999), revealing that Alg/PVA NFs 2:8 were fit the Langmuir isotherm model. Langmuir Isotherm is primarily designed to describe gas-solid phase adsorption. This isotherm was based on the assumption that CO_2 adsorption occurred on the homogeneous surface of Alg/PVA NFs 2:8 by monolayer sorption [46].

On the other hands, carbon dioxide adsorption onto Alg/PVA/Z NFs 2:8:2.5 showed good fitness of Dubinin-Radushkevich (DR) isotherm model as the plot of ϵ^2 versus $\ln q_e$ gives correlation efficient value close to

Table 1. Isotherm parameters for adsorption of CO₂ onto alginate-based nanofibers

Models	Parameters	Alg/PVA NFs	Alg/PVA/Z NFs
Langmuir	K_L , mmol^{-1}	-447.2222	1.3239
	q_m , mmol g^{-1}	2.484	12.6103
	R^2	0.9999	0.5923
Freundlich	K_F , $\text{mmol g}^{-1} \text{mmol}^{-1/n}$	1.3971	4.0435
	n	-12.7551	1.3770
	R^2	0.8641	0.9065
DR	K_{DR} , $\text{mol}^2 \text{kJ}^{-2}$	-2×10^{-9}	5×10^{-8}
	q_s , mmol g^{-1}	2.3936	7.2355
	R^2	0.904	0.9168
Temkin	K_T , mmol^{-1}	0.9998	1.0071
	b_T	-1.1031×10^4	9.5449×10^2
	R^2	0.8527	0.8965
Elovich	K_E	3.4060	-1.6955
	q_m , mmol g^{-1}	-0.2414	14.8148
	R^2	0.8725	0.2647

**Fig 14.** Morphological changes of Alg/PVA NFs 1:9 (a, b) and Alg/PVA/Z NFs 2:8:1.5 (c, d) before and after the adsorption process; insets show diameter of each nanofibers

unity. DR isotherm model is an empirical adsorption model that is generally applied to express adsorption mechanism with Gaussian energy distribution onto heterogeneous surfaces. The model was a semiempirical equation in which CO₂ adsorption follows a pore-filling mechanism through multilayer character involving Van

der Waal's forces of CO₂ gases on microporous zeolites inside Alg/PVA/Z NFs 2:8:2.5 [46].

Reusability of Alginate-Based Nanofibers

To understand the spontaneity of the adsorption process, the Gibbs free energy was calculated using the

following Eq. (1).

$$\Delta G^\circ = -RT \ln K_L \quad (1)$$

where ΔG° is Gibbs free energy (kJ mol^{-1}), R is gas constant ($8.314 \text{ J mol}^{-1} \text{ K}^{-1}$), T is the temperature (K), and K_L is Langmuir equilibrium constant. The result showed that the ΔG° values of Alg/PVA NFs 2:8 were $1.108 \text{ kJ mol}^{-1}$, obtained below 20 kJ mol^{-1} . These findings suggest that the CO_2 adsorption was followed by the physisorption mechanism [40].

Energy adsorption of Alg/PVA/Z NFs 2:8:2.5 could be calculated by the following equation:

$$E = \frac{1}{\sqrt{2K_{DR}}} \quad (2)$$

where E is energy adsorption (kJ mol^{-1}), and K_{DR} is Dubinin-Radushkevich equilibrium constant ($\text{mol}^2 \text{ kJ}^{-2}$). The value of E for Alg/PVA/Z NFs 2:8:2.5 were lower than 8 kJ mol^{-1} ($E = 3.162 \text{ kJ mol}^{-1}$). The calculated E represented the physical nature of the sorption [47]. Fig. 13 showed SEM images of alginate-based nanofibers and CO_2 adsorbed alginate-based nanofibers. All images displayed relatively unchanging surface morphology as well as diameter of the nanofibers (see the inset of Fig. 13).

■ CONCLUSION

Alginate is not able to electrospun from aqueous solutions because it possesses a polyelectrolyte characteristic. However, incorporating copolymer poly (vinyl alcohol) (PVA) 10% (w/w) into alginate solution (2% w/w) weakens the repulsive forces among polyanionic alginate chains, thus enabling alginate nanofibers formation. Alg/PVA NFs with uniform, continuous, smooth-surfaced nanofibers were obtained from Alg:PVA solution volume ratio 2:8 with average diameter of $202 \pm 43 \text{ nm}$ and specific surface area of $9.197 \text{ m}^2 \text{ g}^{-1}$. The Alg/PVA NFs for CO_2 capture was evaluated using a gas trapping system. The maximum adsorption capacity was $3.286 \text{ mmol g}^{-1}$, conducted within optimum conditions at flow rate and contact time about 20 mL min^{-1} and 20 min , respectively. To improve the properties and performances of alginate nanofibers, zeolite particles were impregnated into polymers solution. Impregnated zeolites altered nanofibers surface morphologies from smooth to rough fiber with an average

diameter of $250 \pm 60 \text{ nm}$ and enhanced specific surface area to $25.998 \text{ m}^2 \text{ g}^{-1}$. The optimum CO_2 adsorption capacity of Alg/PVA/Z NFs was $10.710 \text{ mmol g}^{-1}$. The adsorption behavior of resulting nanofibers was studied using five different isotherm models. Alg/PVA NFs showed the best linearity with Langmuir isotherm model with R^2 0.9999, and Alg/PVA/Z NFs was fit with in Dubinin-Radushkevich (DR) isotherm model. SEM images of nanofibers before and after the adsorption process displayed unchanging surface morphologies as well as the diameter of the nanofibers. The result of this study suggested that Alg/PVA NFs and Alg/PVA/Z NFs are promising candidates for CO_2 capture with high adsorption capacity that can be fabricated from eco-friendly and low-cost raw materials.

■ ACKNOWLEDGMENTS

The research was supported by the Ministry of Research, Technology and Higher Education of Indonesia under PUPT Project Grand No. 745/UN1-P/LT/DIT-LIT/2016.

■ REFERENCES

- [1] NOAA/ESRL, 2022, National Oceanic & Atmospheric Administration (NOAA)/Earth System Research Laboratory (ESRL) - Trends in Atmospheric Carbon Dioxide, <https://gml.noaa.gov/ccgg/trends/global.html>, accessed on March 22, 2022.
- [2] Hussin, F., and Aroua, M.K., 2020, Recent trends in the development of adsorption technologies for carbon dioxide capture: A brief literature and patent reviews (2014–2018), *J. Cleaner Prod.*, 253, 119707.
- [3] Xue, J., Wu, T., Dai, Y., and Xia, Y., 2019, Electrospinning and electrospun nanofibers: Methods, materials, and applications, *Chem. Rev.*, 119 (8), 5298–5415.
- [4] Marin, L., Dragoi, B., Olaru, N., Perju, E., Coroaba, A., Doroftei, F., Scavia, G., Destri, S., Zappia, S., and Porzio, W., 2019, Nanoporous furfuryl-imine-chitosan fibers as a new pathway towards eco-materials for CO_2 adsorption, *Eur. Polym. J.*, 120, 109214.

- [5] Jiamjirangkul, P., Inprasit, T., Intasanta, V., and Pagon, A., 2020, Metal organic framework-integrated chitosan/poly(vinyl alcohol) (PVA) nanofibrous membrane hybrids from green process for selective CO₂ capture and filtration, *Chem. Eng. Sci.*, 221, 115650.
- [6] Lin, Y.F., Ye, Q., Hsu, S.H., and Chung, T.W., 2016, Reusable fluorocarbon-modified electrospun PDMS/PVDF nanofibrous membranes with excellent CO₂ absorption performance, *Chem. Eng. J.*, 284, 888–895.
- [7] Zainab, G., Iqbal, N., Babar, A.A., Huang, C., Wang, X., Yu, J., and Ding, B., 2017, Free-standing, spider-web-like polyamide/carbon nanotube composite nanofibrous membrane impregnated with polyethyleneimine for CO₂ capture, *Compos. Commun.*, 6, 41–47.
- [8] Olivieri, L., Roso, M., De Angelis, M.G., and Lorenzetti, A., 2018, Evaluation of electrospun nanofibrous mats as materials for CO₂ capture: a feasibility study on functionalized poly(acrylonitrile) (PAN), *J. Membr. Sci.*, 546, 128–138.
- [9] Zainab, G., Babar, A.A., Iqbal, N., Wang, X., Yu, J., and Ding, B., 2018, Amine-impregnated porous nanofiber membranes for CO₂ capture, *Compos. Commun.*, 10, 45–51.
- [10] Hong, S.M., Kim, S.H., Jeong, B.G., Jo, S.M., and Lee, K.B., 2014, Development of porous carbon nanofibers from electrospun polyvinylidene fluoride for CO₂ capture, *RSC Adv.*, 4 (103), 58956–58963.
- [11] Nan, D., Liu, J., and Ma, W., 2015, Electrospun phenolic resin-based carbon ultrafine fibers with abundant ultra-small micropores for CO₂ adsorption, *Chem. Eng. J.*, 276, 44–50.
- [12] Heo, Y.J., Zhang, Y., Rhee, K.Y., and Park, S.J., 2019, Synthesis of PAN/PVDF nanofiber composites-based carbon adsorbents for CO₂ capture, *Composites, Part B*, 156, 95–99.
- [13] Chiang, Y.C., Wu, C.Y., Chen, Y.J., 2020, Effects of activation on the properties of electrospun carbon nanofibers and their adsorption performance for carbon dioxide, *Sep. Purif. Technol.*, 233, 116040.
- [14] Zainab, G., Babar, A.A., Ali, N., Aboalhassan, A.A., Wang, X., Yu, J., and Ding, B., 2020, Electrospun carbon nanofibers with multi-aperture/opening porous hierarchical structure for efficient CO₂ adsorption, *J. Colloid Interface Sci.*, 561, 659–667.
- [15] Zhang, Y., Zhang, Y., Wang, X., Yu, J., and Ding, B., 2018, Ultrahigh metal-organic framework loading and flexible nanofibrous membranes for efficient CO₂ capture with long-term, ultrastable recyclability, *ACS Appl. Mater. Interfaces*, 10 (40), 34802–34810.
- [16] Choi, C., Kadam, R.L., Gaikwad, S., Hwang, K.S., and Han, S., 2020, Metal organic frameworks immobilized polyacrylonitrile fiber mats with polyethyleneimine impregnation for CO₂ capture, *Microporous Mesoporous Mater.*, 296, 110006.
- [17] Zhang, Y., Guan, J., Wang, X., Yu, J., and Ding, B., 2017, Balsam-pear-skin-like porous polyacrylonitrile nanofibrous membranes grafted with polyethyleneimine for postcombustion CO₂ capture, *ACS Appl. Mater. Interfaces*, 9 (46), 41087–41098.
- [18] Abbasi, A., Nasef, M.M., Kheawhom, S., Faridi-Majidi, R., Takeshi, M., Abouzari-Lotf, E., and Choong, T., 2019, Amine functionalized radiation induced grafted polyolefin nanofibers for CO₂ adsorption, *Radiat. Phys. Chem.*, 156, 58–66.
- [19] Iqbal, N., Wang, X., Babar, A.A., Yu, J., and Ding, B., 2016, Highly flexible NiCo₂O₄/CNTs doped carbon nanofibers for CO₂ adsorption and supercapacitor electrodes, *J. Colloid Interface Sci.*, 476, 87–93.
- [20] Ali, N., Babar, A.A., Zhang, Y., Iqbal, N., Wang, X., Yu, J., and Ding, B., 2020, Porous, flexible, and core-shell structured carbon nanofibers hybridized by tin oxide nanoparticles for efficient carbon dioxide capture, *J. Colloid Interface Sci.*, 560, 379–387.
- [21] Jain, R., Shetty, S., and Yadav, K.S., 2020, Unfolding the electrospinning potential of biopolymers for preparation of nanofibers, *J. Drug Delivery Sci. Technol.*, 57, 101604.
- [22] FAO, 2018, *The Global Status of Seaweed Production, Trade and Utilization*, Globefish

- Research Programme, Volume 124, Food Agriculture Organization, Rome.
- [23] Anonymous, 2019, *Peraturan Presiden Republik Indonesia No. 3 Tahun 2019 tentang Peta Panduan (Road map) Pengembangan Industri Rumpun Laut Nasional Tahun 2018-2021*, Ministry of State Secretariat of the Republic of Indonesia, Jakarta.
- [24] Zhu, Y., Wang, Z., Zhang, C., Wang, J., and Wang, S., 2013, A novel membrane prepared from sodium alginate cross-linked with sodium tartrate for CO₂ capture, *Chin. J. Chem. Eng.*, 21 (10), 1098–1105.
- [25] Rošić, R., Pelipenko, J., Kocbek, P., Baumgartner, S., Bešter-Rogač, M., and Kristl, J., 2012, The role of rheology of polymer solutions in predicting nanofiber formation by electrospinning, *Eur. Polym. J.*, 48 (8), 1374–1384.
- [26] Mirtič, J., Balažić, H., Zupančič, Š., and Kristl, J., 2019, Effect of solution composition variables on electrospun alginate nanofibers: Response surface analysis, *Polymers*, 11, 692.
- [27] Abd, A.A., Naji, S.Z., Hashim, A.S., and Othman, M.R., 2020, Carbon dioxide removal through physical adsorption using carbonaceous and non-carbonaceous adsorbents: A review, *J. Environ. Chem. Eng.*, 8 (5), 104142.
- [28] Kim, H.G., and Kim, J.H., 2011, Preparation and properties of antibacterial poly(vinyl alcohol) nanofibers by nanoparticles, *Fibers Polym.*, 12 (5), 602.
- [29] Nawawi, M.S., Ahmad, M.R., Affandi, N.D.N., Sekak, K.A., and Ahmad, W.Y.W., 2013, Effect of zeolite presence and voltage variance on the fiber diameter of microporous PVA/zeolite nanofibrous membrane, *2013 IEEE Business Engineering and Industrial Applications Colloquium (BEIAC 2013)*, Institute of Electrical and Electronics Engineers (IEEE) Langkawi, Malaysia, 344–348.
- [30] Kang, D.H., and Kang, H.W., 2016, Surface energy characteristics of zeolite embedded PVDF nanofiber films with electrospinning process, *Appl. Surf. Sci.*, 387, 82–88.
- [31] Anis, S.F., and Hashaikeh, R., 2016, Electrospun zeolite-Y fibers: Fabrication and morphology analysis, *Microporous Mesoporous Mater.*, 233, 78–86.
- [32] Anis, S.F., Khalil, A., Saepurahman, Singaravel, G., and Hashaikeh, R., 2016, A review on the fabrication of zeolite and mesoporous inorganic nanofibers formation for catalytic applications, *Microporous Mesoporous Mater.*, 236, 176–192.
- [33] Bahi, A., Shao, J., Mohseni, M., and Ko, F.K., 2017, Membranes based on electrospun lignin-zeolite composite nanofibers, *Sep. Purif. Technol.*, 187, 207–213
- [34] Habiba, U., Afifi, A.M., Salleh, A., and Ang, B.C., 2017, Chitosan/(polyvinyl alcohol)/zeolite electrospun composite nanofibrous membrane for adsorption of Cr⁶⁺, Fe³⁺ and Ni²⁺, *J. Hazard. Mater.*, 322, 182–194.
- [35] Ji, S.H., Cho, J.H., Jeong, Y.H., Yun, J.D., and Yun, J.S., 2017, The synthesis of flexible zeolite nanofibers by a polymer surface thermal etching process, *Appl. Surf. Sci.*, 416, 178–182.
- [36] Ojstršek, A., Fakin, D., Hribernik, S., Fakin, T., Bračić, M., and Kurečić, M., 2020, Electrospun nanofibrous composites from cellulose acetate/ultra-high silica zeolites and their potential for VOC adsorption from air, *Carbohydr. Polym.*, 236, 116071.
- [37] Islam, M.S., and Karim, M.R., 2010, Fabrication and characterization of poly(vinyl alcohol)/alginate blend nanofibers by electrospinning method, *Colloids Surf., A*, 366 (1-3), 135–140.
- [38] Shalumon, K.T., Anulekha, K.H., Nair, S.V., Nair, S.V., Chennazhi, K.P., and Jayakumar, R., 2011, Sodium alginate/poly(vinyl alcohol)/nano ZnO composite nanofibers for antibacterial wound dressings, *Int. J. Biol. Macromol.*, 49 (3), 247–254.
- [39] Mozgawa, W., Król, M., and Barczyk, K., 2011, FT-IR studies of zeolites from different structural groups, *Chemik*, 65 (7), 671–674.
- [40] Pham, T.H., Lee, B.K., Kim, J., and Lee, C.H., 2016, Enhancement of CO₂ capture by using synthesized nano-zeolite, *J. Taiwan Inst. Chem. Eng.*, 64, 220–226.

- [41] Pelipenko, J., Kocbek, P., and Kristl, J., 2015, Critical attributes of nanofibers: Preparation, drug loading, and tissue regeneration, *Int. J. Pharm.*, 484 (1-2), 57–74.
- [42] Balgis, R., Kartikowati, C.W., Ogi, T., Gradon, L., Bao, L., Seki, K., and Okuyama, K., 2015, Synthesis and evaluation of straight and bead-free nanofibers for improved aerosol filtration, *Chem. Eng. Sci.*, 137, 947–954.
- [43] Matulevicius, J., Kliucininkas, L., Martuzevicius, D., Krugly, E., Tichonovas, M., and Baltrusaitis, J., 2014, Design and characterization of electrospun polyamide nanofiber media for air filtration applications, *J. Nanomater.*, 2014, 859656.
- [44] Kazarian, S.G., Vincent, M.F., Bright, F.V., Liotta, C.L., and Eckert, C.A., 1996, Specific intermolecular interaction of carbon dioxide with polymers, *J. Am. Chem. Soc.*, 118 (7), 1729–1736.
- [45] Zhao, L., Chen, Y., Wang, B., Sun, C., Chakraborty, S., Ramasubramanian, Dutta, P.K., and Ho, W.S.W., 2016, Multilayer polymer/zeolite Y composite membrane structure for CO₂ capture from flue gas, *J. Membr. Sci.*, 498, 1–13.
- [46] Ayawei, N., Ebelegi, A.N., and Wankasi, D., 2017, Modelling and interpretation of adsorption isotherms, *J. Chem.*, 2017, 3039817.
- [47] Raganati, F., Alfe, M., Gargiulo, V., Chirone, R., and Ammendola, P., 2018, Isotherms and thermodynamics of CO₂ adsorption on a novel carbon-magnetite composite sorbent, *Chem. Eng. Res. Des.*, 134, 540–552.

Bioactive Compound Profile and Biological Modeling Reveals the Potential Role of Purified Methanolic Extract of Sweet Flag (*Acorus calamus* L.) in Inhibiting the Dengue Virus (DENV) NS3 Protease-Helicase

Yuli Arif Tribudi^{1*}, Ayu Tri Agustin², Dian Eka Setyaningtyas³, and Dwi Gusmalawati⁴

¹Department of Animal Science, Faculty of Agriculture, Tanjungpura University, Jl. Prof. Hadari Nawawi, Pontianak 78121, West Kalimantan, Indonesia

²Medical Laboratory Technology Study Program, Politeknik Yakpermas Banyumas, Jl. Raya Jompo Kulon Sukoraja, Banyumas 53181, Indonesia

³National Research and Innovation Agency (BRIN), Jl. Raya Jakarta-Bogor, Cibinong, Bogor 16915, West Java, Indonesia

⁴Department of Biology, Faculty of Mathematics and Natural Sciences, Tanjungpura University, Jl. Prof. Hadari Nawawi, Pontianak 78121, West Kalimantan, Indonesia

* **Corresponding author:**

tel: +62-81333136886

email: yuliariftribudi@gmail.com

Received: August 9, 2021

Accepted: January 26, 2022

DOI: 10.22146/ijc.68317

Abstract: Dengue fever is an infectious disease caused by the dengue virus, and there is no yet effective drug to treat this disease successfully. Our study aimed to identify the bioactive compounds of *Acorus calamus* L. and its potential role in inhibiting dengue virus NS3 protease-helicase. Liquid Chromatography-Mass Spectrometry analyzed phytochemical constituents. Drug-likeness of the predominant compound methanol extract of *Acorus calamus* L. was investigated through the SWISS ADME server. Complex molecular interactions were investigated by Hex 8.0 docking program and Discovery studio 2016. Our study revealed that the five largest phytochemicals in the extract were acoric acid, acorone, acoradin, acoronene, and calamendiol. All predominant compounds are potent to be developed as drug candidates. Molecular docking results showed that the five compounds bind to the Arg599, Pro291, Lys388, Pro431, and His487 of the dengue virus NS3 protease-helicase, the ligand-binding site that plays an essential role in viral replication. The ligand-protein binding pattern exhibited hydrogen and hydrophobic interactions. The interaction of the acoradin-NS3 protease-helicase complex had the lowest binding energy of -299.7 kcal/mol. In summary, we conclude that *Acorus calamus* L. extract may have prospects as a drug for dengue virus infection.

Keywords: bioactivity; dengue viral infection; herb medicine; LC-MS; in silico

■ INTRODUCTION

Dengue is a global burden that infects about 96 million people each year with varying severity of symptoms worldwide. Indonesia is a tropical country with a high prevalence of dengue infection [1]. The agent of dengue is the dengue virus (DENV), transmitted through the mosquito vectors of *Aedes aegypti* and *Aedes albopictus* [2]. The infection of DENV is characterized by several clinical symptoms, including fever, headache, aches, nausea, and subsequent serious consequences such as dengue shock syndrome and morbidity. The high and rapid spread

of DENV poses a threat to public health.

Moreover, no antiviral agent successfully cured or prevented this disease nowadays [3-4]. The only dengue vaccine commercially available was CYD-TDV. This vaccine is known as a live-attenuated dengue vaccine to prevent serious infection in priorly infected people. However, the risk of terrible dengue may increase since CYD-TDV was given to individuals who had not previously been infected [5].

The infection of DENV belongs to the family Flaviviridae, consists of four serotypes, namely DENV-

1, DENV-2, DENV-3, and DENV-4. DENV contains a single-stranded RNA and positive polarity genome with 11 kb. The genome encodes both structural proteins and non-structural proteins. Non-structural protein 3 (NS3) is a non-structural protein that plays an essential role in the viral replication and capping RNA [4,6]. Several studies investigated the NS3 of the dengue virus as a molecular target of antiviral drugs against DENV infection [7-8].

Safe and effective vaccine development makes a prominent contribution to avoiding and treating DENV infection [8]. Several plants with antiviral activity might have prospects to be developed as drugs for DENV therapy, such as *Acorus calamus*, *Cymbopogon citratus*, and *Myristica fatua* [3]. Sweet flag (*Acorus calamus* L.) is one of the medicinal plants containing phenolic compounds, alkaloids, flavonoids, tannins, saponins, steroids, triterpenoids, and glycosides [9]. Traditionally, the rhizome of *A. calamus* L. has been beneficial to treat cough, fever, asthma, and digestive disorders [10]. In a previous study, methanol extract of *A. calamus* L. showed anti-dengue activity in vitro and in silico through inhibition of dengue virus NS5 [3]. Non-structural domain 5 of Methyltransferase (NS5) is an enzyme with multiple enzymatic functions enabling synthesis of the RNA synthesis, 5' RNA cap, and methylation [5]. However, the potential role of *A. calamus* L. methanol extract in inhibiting the NS3 protease-helicase protein is unknown.

Non-structural protein 3 (NS3) is a 69 kDa highly conserved protein among flaviviruses responsible for the viral replication cycle. NS3 consists of two domains, namely the N-terminal protease domain and the C-terminal RNA helicase domain. The N-terminal protease region is involved in cleaving viral polyprotein precursors into individual proteins. The C-terminal RNA helicase domain controls viral RNA synthesis and DENV genome replication [5]. This study aimed to characterize the phytochemical compounds of methanol extract of *A. calamus* L. rhizome using LC-MS analysis. Considering the previous elucidated biological functions, we identified drug-likeness and anti-dengue activity of methanol rhizome extract of *A. calamus* L. through in silico approach.

■ EXPERIMENTAL SECTION

Materials

The rhizome of *A. calamus* L. (local name: jeringau putih) was collected from 2nd Rasau Jaya village, Rasau Raya ditrics, Kubu Raya regency, Kalimantan Island, Indonesia. The chemicals used were methanol (95% chemical purity), Whatman paper grade 1, 0.01% hydrochloric acid in distilled water, and cellulose acetate 0.45 μm . The 3D structure of NS3 helicase-protease, acoric acid, acorone, acoradin, acoronene, and calamendiol was used in silico analysis.

Instrumentation

The instrumentations of a rotary evaporator and a centrifuge were used to extract *A. calamus* L. Extract was purified using a Sep-Pak C18 Vac cartridges, vacuum pump, or aspirator with 40 °C temperature, and stative clam. Shimadzu LCMS was used for characterized the phytochemical compounds of *A. calamus* extract.

Procedure

Extraction of *A. calamus* L. rhizome

The prepared sample was a fresh rhizome of *A. calamus* L. Before extraction, the refined rhizome is needed. Extraction was carried out using 95% methanol solvent [11]. After 24 h of maceration at room temperature, the residue was extracted with 95% methanol (1:5). The combined supernatant was filtered with Whatman paper grade 1, then concentrated using a rotary evaporator (40 °C) [12]. The supernatant was obtained from centrifugation at 5000 rpm for 20 min for purification [13].

Purification of *A. calamus* L. rhizome extract

Briefly, 12 mL of methanol 95% were poured into Sep-Pak C18 Vac cartridges, and then methanol was removed by pouring 18 mL of acidified distilled water. Liquid extract of 5–10 mL was running into the cartridge. Then, the solution was eluted by using methanol 95%. Methanol was evaporated with a rotary evaporator at 40 °C under vacuum conditions. The eluate was re-dissolved with acidified distilled water. Purified extract was stored at 4 °C for further analysis [14].

LC-MS profiling of methanolic extract of *A. calamus* L.

LC-MS analysis was performed using Shimadzu LCMS with the Shim Pack FC-ODS column (2 mm × 150 mm, 3 μm). The solvent consists of 0.01% HCl in water distillation and 95% methanol. We used a flow rate of 0.8 mL/min, maximum pump pressure (P) of 15 kgf/cm², the wavelength of 254 nm and 190 nm, the response time of 1 sec, AUX range of 2 AU/V, Lamp of D2 with positive polarity, LC stop time of 100 min, and probe temperature of 250 °C. Mass spectrophotometry (MS) was set as follows: full scan with a positive mode in the m/z 50–500 range. Maintained probe and a curved desolvation line (CDL) at 250 °C. Nitrogen as a nebulizer gas with a 1.5 mL/min flow rate, 1.5 kV gain detector, CDL voltage 25 V, and high voltage probe: +4.5 kV. Compounds are characterized based on the MS spectrum through the LC-MS Post-run Computer Program [15].

Data mining for molecular docking analysis

The target protein in this study is a DENV NS3 protease-helicase. Acoric acid, acorone, acoradin, acoronene, and calamendiol from the *Acorus calamus* L. determined as a ligand. The 3D structure of NS3 protease-helicase (PDB ID: 2WHX) was obtained from RSCB PDB (<https://www.rcsb.org/>). NCBI Pubchem Database (<https://www.ncbi.nlm.nih.gov/>) generates chemical structures of acoric Acid (CID: 15558302), acorone (CID: 5316254), acoradin (CID: 126324), acoronene (CID: 15558294), and calamendiol (CID: 12302239) with the SDF format. NS3 protease-helicase preparation includes removing water molecules or ligands using Discovery Studio Software. Then, energy minimization was performed using PyRx software. Furthermore, the docking results with the .pdb format were obtained using Open Babel [16].

Drug-likeness prediction

The biological function of acoric acid, acorone, acoradin, acoronene, and calamendiol of *A. calamus* L. as a drug candidate to treat dengue was investigated through the SWISS ADME server (<http://www.swissadme.ch>). Physicochemical, pharmacokinetics, and drug-likeness properties are determined to identify potential drug candidates. The Physico-chemical parameters studied are the number of H-bond acceptors, H-bond donors,

rotatable bonds, and iLOGP. Furthermore, pharmacokinetic constituents investigated were gastrointestinal absorption, Blood-Brain Barrier Permeability (BBB), and LogKp. Lipinski drug-likeness were analyzed using the SWISS ADME Server [17].

Molecular docking and visualization

Before conducting docking simulation, we validate compounds that really bind to the protein by biological activity prediction tool (<http://www.pharmaexpert.ru/passonline/>). Hex 8.0 program with Shape+Electro+DARS mode for molecular docking simulations was established. Docking results should be in the .pdb file. Briefly, visualization of the complex interaction of ligand-proteins was performed using the 2016 Discovery Studio program [18]. Furthermore, the binding side, type of chemical bond, and binding energy were determined [16].

RESULTS AND DISCUSSION

LC-MS Analysis of Methanol Extract of *A. calamus* L.

The health-beneficial properties of the rhizome *A. calamus* L. are related to the phytochemical component. The LC-MS approach for investigating chemical constituents in methanol rhizome extract of *A. calamus* L. was established. Our study showed 98 phytochemical compounds in the extract of *A. calamus* L. Chromatograms represent the compound component shown in Fig. 1. The predominant compound in the extract of *A. calamus* L. is acoric acid, acorone, acoradin, acoronene, and calamendiol (Table 1). In previous studies, *A. calamus* L. extract positively contain taxifolin-3-glucopopanoside, velutin, methyl digallate, γ-asarone, α-asarone, and β-asarone, which show antioxidant and

Table 1. The bioactive compound profiles of *A. calamus* L. extract with identities of compounds

Peak	Predominant compounds	RT (min)	Product ion (m/z)	Composition (%)
66	Acoric acid	9.086	268	4.0107
63	Acorone	7.291	236	3.6989
83	Acoradin	14.434	417	3.6989
62	Acoronene	7.279	234	3.4221
64	Calamendiol	7.326	238	3.0533

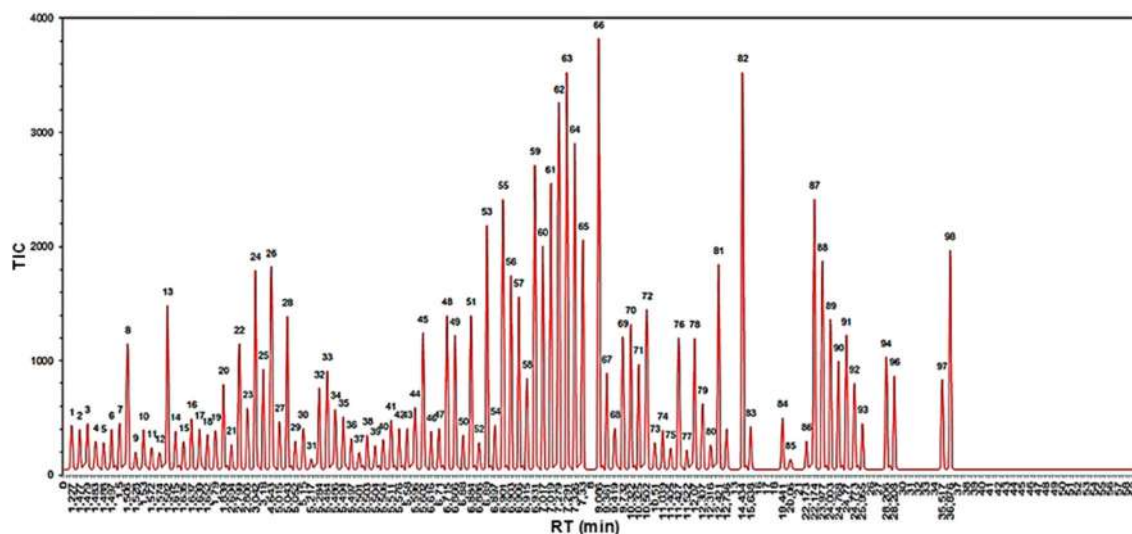


Fig 1. Chromatogram profile of *Acorus Calamus* L. extracts by LC-MS. Peaks show the bioactive compound profiles of *Acorus Calamus* L.

antifungal activity [10,19-20]. Phytochemical components variation is affected by several factors, including geographical, harvest time, solvent, and temperature of extraction [21].

The predominant compound was determined by chemical structure, retention time, composition, molecular weight, and mass spectrum. Acoric acid ($C_{15}H_{24}O_4$) has a molecular weight of 268.3530, indicated by m/z 268; acorone ($C_{15}H_{24}O_2$) with a molecular weight of 236.3550, established by m/z 236. Acoradin ($C_{24}H_{32}O_6$) has a molecular weight of 416.5140 appeared at m/z 417. Acoronene ($C_{15}H_{22}O_2$) and calamendiol ($C_{15}H_{26}O_2$) have a molecular weight of 234.3390 and 238.3710, with m/z of

234 and m/z 238, respectively (Fig. 2). Single-crystal x-ray diffraction studies show that the acoric acid is sesquiterpene from the acorone skeleton. A previous study reported extract ethanol rhizome of *A. calamus* L. (5 μ m and 10 μ m) have cell proliferation activities on SK-N-BE cell line [22]. In addition, methanol extract of *A. calamus* L. at a dose of 20 g/mL shows DENV-2 to 96.5% inhibitory activity in vitro. Acorone and calamendiol are sesquiterpenoids that may have pharmacological activities as an antifungal. A previous study confirmed that rhizome extract *A. calamus* L. has health benefits for treating disease so that the extract can be employed as a natural treatment [3].

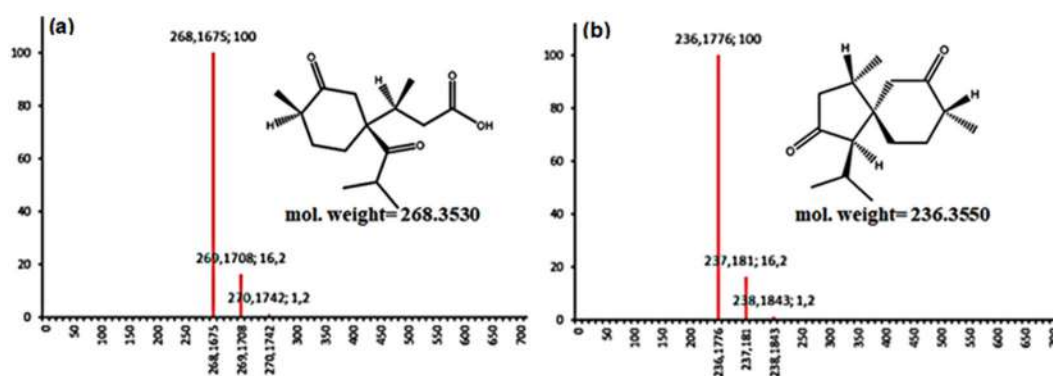


Fig 2. The mass spectra of the predominant compound of methanol rhizome extract of *A. calamus* L. acoric acid (a), acorone (b), acoradin (c), acoronene (d), and calamendiol (e). X-axis shows the m/z , and Y-axis indicates the absorbance (%)

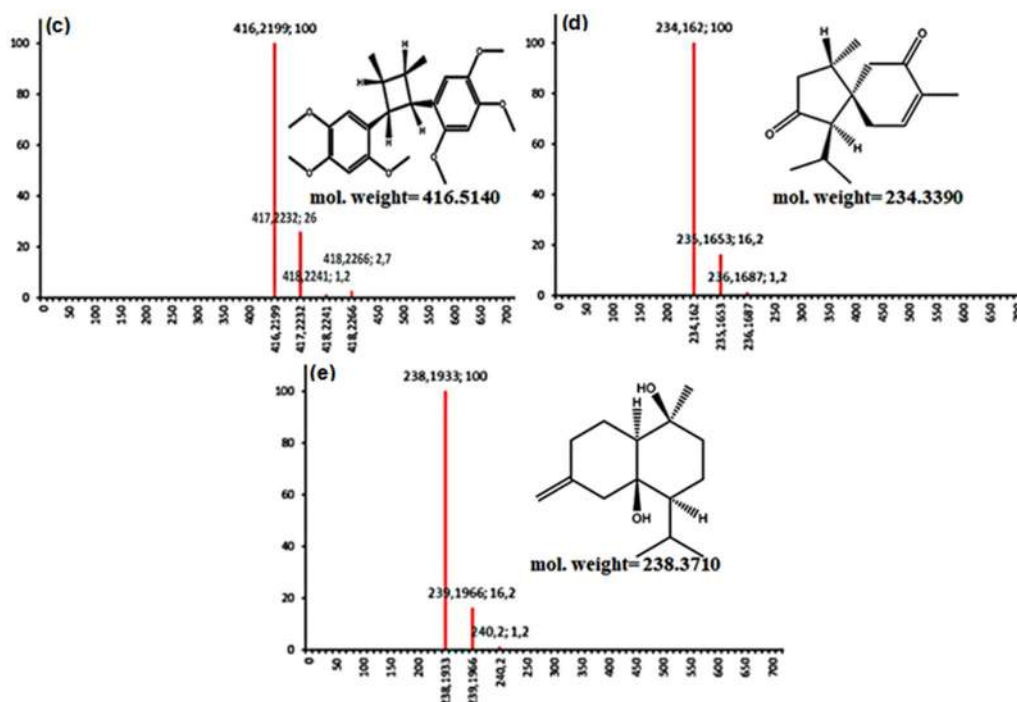


Fig 2. The mass spectra of the predominant compound of methanol rhizome extract of *A. calamus* L. acoric acid (a), acorone (b), acoradin (c), acoronene (d), and calamendiol (e). X-axis shows the m/z , and Y-axis indicates the absorbance (%) (Continued)

Physico-chemical Profile, Pharmacokinetics, and Druglikeness of Methanol Extract of *A. calamus* L.

The physicochemical properties of the predominant compounds (acoric acid, acorone, acoradin, acoronene, and calamendiol) of *A. calamus* L. extract are shown in Table 2. Functional groups, lipophilic properties, and the solubility of a natural compound determine the pattern of absorption, distribution, metabolism, and excretion in humans [17]. Based on ADME analysis, all compounds have good gastrointestinal (GI) and Blood-Brain Barrier (BBB) absorption. In addition, the value of skin permeation (KP) was -5.35 cm/sec to -6.65 cm/sec, indicating that the compound could pass through the skin barrier in humans.

Physicochemical is an important parameter related to drug activity. Molecules with a higher number of hydrogen bonds donors and acceptors in their structure may better prevent oxidative stress [16]. In this study, acoradin had the highest total number of hydrogen bonds. Compounds with a molecular weight of 130–725, H-bond donor: 0–6, H-bond acceptor: 2–20, log Kp: -2 to

6.5, and the number of rotatable bonds: 0–15 is considered to the drug clinically (Table 2). A compound with a GI value of more than 80% indicates high absorption capability. The drug's potential to be absorbed by the blood-brain barrier is an essential character related to side effects and drug efficacy. As long as the BBB value is more than 0.3, it exhibits that a compound can permeate the blood-brain barrier and be adequately distributed [23–24].

The drug-likeness analysis performs to investigate a molecule's ability to be a promising drug candidate [25]. One of the parameters for determining potential drug candidates is Lipinski. The Lipinski rule explains the criteria for drug candidates. There are molecular weights (500), high lipophilicity (≤ 5), hydrogen bond donors (≤ 5), hydrogen bond acceptor (≤ 10), and molar refractivity (40–130). At least, drug candidates should adhere to two of their criteria [26]. Based on drug-likeness, acoric acid, acorone, acoradin, acoronene, and calamendiol can be categorized as potent drug candidates (Table 2). After obtaining Lipinski results, we

Table 2. Physicochemical profile, pharmacokinetics, and drug-likeness predominant compounds from the extract of *A. calamus* L. by ADME analysis

Physicochemical properties	Acoric acid	Acorone	Acoradin	Acoronene	Calamendiol
H-bond acceptor	4	2	6	2	2
H-bond donor	1	0	0	0	2
Rotatable bond	5	1	8	1	1
Log P _{o/w} (iLOGP)	1.88	2.48	4.47	2.43	2.88
Pharmacokinetic components					
GI absorption	High	High	High	High	High
BBB permeability	Yes	Yes	Yes	Yes	Yes
CYP1A2 inhibitor	No	No	No	No	No
CYP2C19 inhibitor	No	No	No	No	No
CYP2C9 inhibitor	No	No	No	Yes	No
CYP2D6 inhibitor	No	No	Yes	No	No
CYP3A4 inhibitor	No	No	No	No	No
Log K _p (cm/s)	-6.65	-5.70	-5.35	-5.86	-6.01
Lipinski	Yes	Yes	Yes	Yes	Yes

investigated the potential role of the predominant compound of *A. calamus* L. as an anti-dengue agent through an *in silico* approach.

In silico Molecular Docking Analysis

Our study demonstrated molecular interactions between acoric acid, acorone, acoradin, acoronene, calamendiol, and non-structural protein NS3 protease-helicase. NS3 protease-helicase was determined as the protein target. The selected ligands include acoric acid, acorone, acoradin, acoronene, and calamendiol from extracts of *A. calamus* L. It was predicted to have a potential function as an anti-dengue drug agent through DENV NS3 protease-helicase binding interactions. Based on biological activity prediction, acoric acid, acorone, acoradin, acoronene, and calamendiol showed pharmacological effects as an antiviral with a Pa value of > 0.4.

The docking results showed five amino acid residues involved in the acoric acid-NS3 protease-helicase complex, namely Arg599, Leu429, Pro431, Pro291, His487 (Fig. 3(a)). Hydrogen bonds and hydrophobic stabilize these interactions. Acorone binds to Arg387, Pro431, Lys388, Arg599, Ile365, His487 residues in the RNA helicase domain of the NS3 protease-helicase. Hydrophobic and hydrogen bonds maintain Arg387, Pro431, Lys388, Arg599, Ile365, His487 residue (Fig. 3(b)). Acoradin and NS3 protease-helicase complex

involve Val544, His487, Glu490, Asp409, Ala606, Arg599, Lys388, Arg387, and Pro291. Hydrophobic and hydrogen bonds stabilize the acoradin and NS3 protease-helicase interactions (Fig. 3(c)). The occurrence of molecular complexes is due to non-covalent interactions such as hydrogen bonds, hydrophobicity, and Van der Waals. This binding is related to specific biological activity on the active site of the protein target [27].

The infection of DENV NS3 protease-helicase contains an N-terminal serine protease region with amino acid residues 1–168 and RNA helicase at residues 180–618 linked by 11 amino acids (residues 169–179). The enzyme consists of a trypsin-like serine protease domain with a catalytic triad of His51, Asp75, and Ser135 [4,6]. In this study, nine amino acid residues Ser364, Arg599, Ala602, Arg387, Pro431, Leu443, Arg599, Ile365, and His487, bind to acoronene. The acoronene and NS3 protease-helicase complex was established by hydrogen bond and hydrophobic interactions (Fig. 3(d)). The calamendiol and NS3 protease-helicase complexes had fewer interactions than the acoronene-NS3 protease-helicase complex (Fig. 3(e)). The docking results show that Arg599 and Lys388 are bonding with calamendiol through hydrophobic interaction by alkyl donor. Our study showed that the

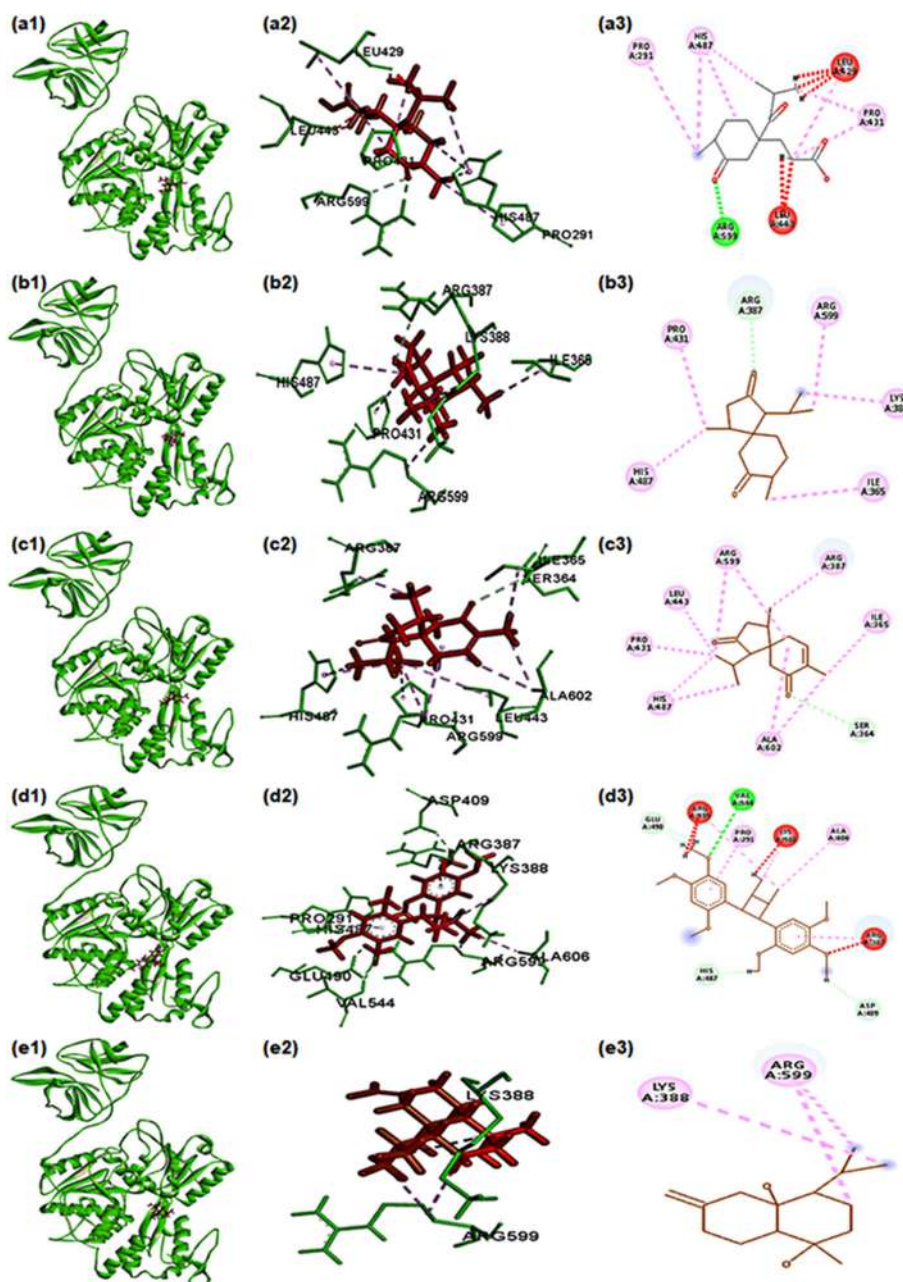


Fig 3. Molecular docking results from the interaction between acoric acid (a), acorone (b), acoradin (c), acoronene (d), and calamendiol (e) complexes with NS3 protease-helicase. Number 1 shows a visualization of the ligand-protein molecular complex. The 3D structure in number 2 and number 3 shows the 2D structure

five predominant compounds of methanol extract of *A. calamus* L. bind with the active site residues Arg599, Pro291, Lys388, Pro431, and His487 of NS3 protease-helicase. A previous study reported that Arg387, Lys388, and Arg599 residues are involved in the molecular interaction of NS3 protease-helicase inhibited by natural

compounds [4]. This result suggested that acoric acid, acorone, acoradin, acoronene, and calamendiol might disrupt the enzymatic activity of NS3 helicase-protease, so their function is responsible for the replication cycle could block. Ligand interaction, hydrogen, and hydrophobic effect may cause the protein fold to shift

into a nonfunctional protein [16]. In this study, NS3 helicase-protease signaling might be prevented by five predominant compounds of *A. calamus* L.

Besides chemical bonds, binding energy contributes to the stable molecular complex. Binding energy is formed when intermolecular interactions occur. Therefore, if the binding energy were lower, it would be easier for the molecules to interact. The amino acid residues and the chemical bond between the protein-ligand complex determine the binding energy [16]. Our study found that the acoradin and NS3 protease-helicase complexes required the lowest binding energy of -299.7 kcal/mol, so they could easily bind (Table 3). A hydrogen bond is the main contributor to the structure and ligand-receptor interaction. Furthermore, the efficacy and specificity of

the protein target are mainly assessed through hydrogen bonds [28]. In this case, the acoradin and NS3 protease-helicase interaction had the highest number of hydrogen bonds. Consequently, the acoradin and NS3 protease-helicase interaction had the lowest binding energy.

Previous research related to the exploration of anti-DENV investigated the potential activity of 12 compounds from the ethanol root extract of *A. calamus* L. Tatanan A compound was reported to have the highest anti-DENV capacity. In addition, cytotoxicity and cytopathogenic effects induced by DENV2 have successfully reduced (EC50 value of 3.9 M) [29]. Corresponding to the biological function of δ -Selinene and α -Caryophyllene of *Ipomoea batatas* L., exhibited inhibitory of the NS2B/NS3 protease catalytic domains

Table 3. Interaction between acoric acid, acorone, acoradin, acoronene, calamendiol, and NS3 protease-helicase

Interactions	Point interaction	Chemistry bond	Type	Energy binding (kcal/mol)
Acoric acid-NS3 protease-helicase	A:ARG599:HH12 - :LIG1:O	Hydrogen Bond	Conventional Hydrogen Bond	-247.1
	A:ARG599:CD - :LIG1:O	Hydrogen Bond	Carbon Hydrogen Bond	
	:LIG1:C - A:LEU429	Hydrophobic	Alkyl	
	:LIG1:C - A:PRO431	Hydrophobic	Alkyl	
	:LIG1:C - A:PRO291	Hydrophobic	Alkyl	
	:LIG1:C - A:PRO431	Hydrophobic	Alkyl	
	A:HIS487 - :LIG1	Hydrophobic	Pi-Alkyl	
	A:HIS487 - :LIG1:C	Hydrophobic	Pi-Alkyl	
Acorone-NS3 protease-helicase	A:ARG387:CD - :LIG1:O	Hydrogen Bond	Carbon Hydrogen Bond	-226.3
	:LIG1:C - A:PRO431	Hydrophobic	Alkyl	
	:LIG1:C - A:LYS388	Hydrophobic	Alkyl	
	:LIG1:C - A:ARG599	Hydrophobic	Alkyl	
	:LIG1:C - A:ILE365	Hydrophobic	Alkyl	
	A:HIS487 - :LIG1:C	Hydrophobic	Pi-Alkyl	
Acoradin-NS3 protease-helicase	A:VAL544:HN - :LIG1:O	Hydrogen Bond	Conventional Hydrogen Bond	-299.7
	:LIG1:H - A:HIS487:NE2	Hydrogen Bond	Carbon Hydrogen Bond	
	:LIG1:H - A:GLU490:OE1	Hydrogen Bond	Carbon Hydrogen Bond	
	:LIG1:H - A:GLU490:OE2	Hydrogen Bond	Carbon Hydrogen Bond	
	:LIG1:H - A:ASP409:OD1	Hydrogen Bond	Carbon Hydrogen Bond	
	A:ALA606 - :LIG1:C	Hydrophobic	Alkyl	
	:LIG1:C - A:ARG599	Hydrophobic	Alkyl	
	:LIG1:C - A:LYS388	Hydrophobic	Alkyl	
	:LIG1 - A:ARG387	Hydrophobic	Pi-Alkyl	
	:LIG1 - A:PRO291	Hydrophobic	Pi-Alkyl	

Table 3. Interaction between acoric acid, acorone, acoradin, acoronene, calamendiol, and NS3 protease-helicase (Continued)

Interactions	Point interaction	Chemistry bond	Type	Energy binding (kcal/mol)
Acoronene- NS3 protease- helicase	A:SER364:CA - :LIG1:O	Hydrogen Bond	Carbon Hydrogen Bond	
	A:ARG599 - :LIG1	Hydrophobic	Alkyl	
	A:ALA602 - :LIG1	Hydrophobic	Alkyl	
	A:ALA602 - :LIG1:C	Hydrophobic	Alkyl	
	: LIG1:C - A:ARG387	Hydrophobic	Alkyl	
	: LIG1:C - A:PRO431	Hydrophobic	Alkyl	-240.3
	: LIG1:C - A:LEU443	Hydrophobic	Alkyl	
	: LIG1:C - A:ARG599	Hydrophobic	Alkyl	
	: LIG1:C - A:ILE365	Hydrophobic	Alkyl	
A:HIS487 - :LIG1:C	Hydrophobic	Pi-Alkyl		
A:HIS487 - :LIG1:C	Hydrophobic	Pi-Alkyl		
Calamendiol- NS3 protease- helicase	: LIG1:H - :LIG1:O	Hydrogen Bond	Conventional Hydrogen Bond	
	: LIG1:C - A:ARG599	Hydrophobic	Alkyl	
	: LIG1:C - A:ARG599	Hydrophobic	Alkyl	
	: LIG1:C - A:LYS388	Hydrophobic	Alkyl	-241.3

*bold letters indicate donor atoms

(Ser135 and His51) through hydrophobic interactions [30]. Residue ~170–618 of dengue virus NS3 protease-helicase act encodes NTPase/RNA helicase and 5-RNA triphosphatase. Both enzymes are required for the replication and capping steps of viral RNA [31]. Our study revealed that acoric acid, acorone, acoradin, acoronene, and calamendiol from extracts of *A. calamus* L. have a potential role as anti-dengue through inhibition of the NS3 protease-helicase. This inhibition leads to disruption of RNA replication and translation activities to prevent and treat DENV infection.

■ CONCLUSION

This study confirmed 98 phytochemical compounds in methanol extract of *Acorus calamus* L. Acoric acid, acorone, acoradin, acoronene, and calamendiol were the five major compounds in the extract. These compounds show appropriate physicochemical, pharmacokinetics, and Lipinski rule as drug candidates. Furthermore, molecular docking results showed that acoric acid, acorone, acoradin, acoronene, and calamendiol might interfere with NS3 protease-helicase activity. Thus, the replication cycle of the dengue virus could be blocked.

■ AUTHOR CONTRIBUTIONS

Yuli Arif Tribudi contributed to conception and design, acquisition of data, analysis, and interpretation of data, drafting the article, critically revising the article for important intellectual content, final approval of the version to be published. Ayu Tri Agustin contributed to conception and design, data acquisition, analysis and interpretation of data, drafting the article. Dian Eka Setyaningtyas contributed to the acquisition of data, drafting the article. Dwi Gusmalawati contributed to the acquisition of data, drafting the article. All authors agreed to the final version of this manuscript.

■ REFERENCES

- [1] Zahid, K., Shakoore, S., Sajid, H.A., Afzal, S., Ali, L., Amin, I., Shahid, M., and Idrees, M., 2020, Advancements in developing an effective and preventive dengue vaccine, *Future Virol.*, 15 (2), 127–138.
- [2] Bhatt, P., Sabeena, S.P., Varma, M., and Arunkumar, G., 2021, Current understanding of the pathogenesis of dengue virus infection, *Curr. Microbiol.*, 78 (1), 17–32.

- [3] Rosmalena, R., Elya, B., Dewi, B.E., Fithriyah, F., Desti, H., Angelina, M., Hanafi, M., Lotulung, P.D., Prasasty, V.D., and Seto, D., 2019, The antiviral effect of Indonesian medicinal plant extracts against dengue virus in vitro and in silico, *Pathogens*, 8 (2), 85.
- [4] Halim, S.A., Khan, S., Khan, A., Wadood, A., Mabood, F., Hussain, J., and Al-Harrasi, A., 2017, Targeting dengue virus NS-3 helicase by ligand based pharmacophore modeling and structure based virtual screening, *Front. Chem.*, 5, 88.
- [5] Obi, J.O., Gutiérrez-Barbosa, H., Chua, J.V., and Deredge, D.J., 2021, Current trends and limitations in dengue antiviral research, *Trop. Med. Infect. Dis.*, 6 (4), 180.
- [6] Luo, D., Wei, N., Doan, D.N., Paradkar, P.N., Chong, Y., Davidson, A.D., Kotaka, M., Lescar, J., and Vasudevan, S.G., 2010, Flexibility between the protease and helicase domains of the dengue virus NS3 protein conferred by the linker region and its functional implications, *J. Biol. Chem.*, 285 (24), 18817–18827.
- [7] Basavannacharya, C., and Vasudevan, S.G., 2014, Suramin inhibits helicase activity of NS3 protein of dengue virus in a fluorescence-based high throughput assay format, *Biochem. Biophys. Res. Commun.*, 453 (3), 539–544.
- [8] Rather, I.A., Parray, H.A., Lone, J.B., Paek, W.K., Lim, J., Bajpai, V.K., and Park, Y.H., 2017, Prevention and control strategies to counter dengue virus infection, *Front. Cell. Infect. Microbiol.*, 7, 336.
- [9] Elshikh, M.S., Rani, E., Al Farraj, D.A., Al-Hemaid, F.M.A., Abdel Gawwad, M.R., Jeba Malar, T.R.J., Dyona, L., and Vijayaraghavan, P., 2022, Plant secondary metabolites extracted from *Acorus calamus* rhizome from Western Ghats, India and repellent activity on *Sitophilus oryzae*, *Physiol. Mol. Plant Pathol.*, 117, 101743.
- [10] Vadivel, V., Kausalya, J., Vidhyalakshmi, S., Sriram, S., Rajalakshmi, P., and Brindha, P., 2017, Phytochemical levels and antioxidant activity of traditionally processed Indian herbal mixture (*Acorus calamus*, *Curcuma aromatica* and *Zingiber officinale*), *Trop. J. Nat. Prod. Res.*, 1 (6), 262–269.
- [11] Chaubey, P., Archana, Prakash, O., Rai, K., Kumar, R., and Pant, A.K., 2017, *In vitro* antioxidant activity and total phenolic content of rhizome extracts from *Acorus calamus* Linn, *Asian J. Chem.*, 29 (11), 2357–2360.
- [12] Iancu, I.M., Bucur, L.A., Schroder, V., Mireşan, H., Sebastian, M., Iancu, V., and Badea, V., 2021, Phytochemical evaluation and cytotoxicity assay of Lythri herba extracts, *Farmacica*, 69 (1), 51–58.
- [13] Gusmalawati, D., Arumingtyas, E.L., Azrianingsih, R., and Mastuti, R., 2019, LC-MS analysis of carbohydrate components in Porang tubers (*Amorphophallus muelleri* Blume) from the second and the third growth period, *IOP Conf. Ser.: Earth Environ. Sci.*, 391, 012022.
- [14] Agustin, A.T., Safitri, A., and Fatchiyah, F., 2021, Java red rice (*Oryza sativa* L.) nutritional value and anthocyanin profiles and its potential role as antioxidant and anti-diabetic, *Indones. J. Chem.*, 21 (4), 968–978.
- [15] Lehotay, S.J., 2017, Utility of the summation chromatographic peak integration function to avoid manual reintegrations in the analysis of targeted analytes, *LCGC North Am.*, 35 (6), 391–402.
- [16] Agustin, A.T., Safitri, A., and Fatchiyah, F., 2020, An in silico approach reveals the potential function of cyanidin-3-o-glucoside of red rice in inhibiting the advanced glycation end products (AGES)-receptor (RAGE) signaling pathway, *Acta Inform. Med.*, 28 (3), 170–179.
- [17] Sivaraman, D., and Pradeep, P.S., 2020, Exploration of bioflavonoids targeting dengue virus NS5 RNA-dependent RNA polymerase: *In silico* molecular docking approach, *J. Appl. Pharm. Sci.*, 10 (5), 16–22.
- [18] Zubair, M.S., Anam, S., Maulana, S., and Arba, M., 2021, In vitro and in silico studies of quercetin and daidzin as selective anticancer agents, *Indones. J. Chem.*, 21 (2), 310–317.
- [19] Hermes, L., Römermann, J., Cramer, B., and Esselen, M., 2021, Quantitative analysis of β -asarone derivatives in *Acorus calamus* and herbal food products by HPLC-MS/MS, *J. Agric. Food Chem.*, 69 (2), 776–782.

- [20] Sidana, A., and Farooq, U., 2015, Evaluation of antileishmanial activity of plants used in Indian traditional medicine, *Bangladesh J. Pharmacol.*, 10 (2), 423–426.
- [21] Kurnianingsih, N., Ratnawati, R., Nazwar, T., Ali, M., and Fatchiyah, F., 2021, Purple sweet potatoes from East Java of Indonesia revealed the macronutrient, anthocyanin compound and antidepressant activity candidate, *Med. Arch.*, 75 (2), 94–100.
- [22] Li, J., Zhao, J., Wang, W., Li, L., Zhang, L., Zhao, X.F., Liu, Q.R., Liu, F., Yang, M., Khan, I., and Li, S.X., 2017, New acorane-type sesquiterpene from *Acorus calamus* L., *Molecules*, 22 (4), 529.
- [23] Pires, D.E.V., Blundell, T.L., and Ascher, D.B., 2015, pkCSM: Predicting small-molecule pharmacokinetic and toxicity properties using graph-based signatures, *J. Med. Chem.*, 58 (9), 4066–4072.
- [24] Berben, P., Bauer-Brandl, A., Brandl, M., Faller, B., Flaten, G.E., Jacobsen, A.C., Brouwers, J., and Augustijns, P., 2018, Drug permeability profiling using cell-free permeation tools: Overview and applications, *Eur. J. Pharm. Sci.*, 119, 219–233.
- [25] Wang, J., Ge, Y., and Xie, X.Q., 2019, Development and testing of druglike screening libraries, *J. Chem. Inf. Model.*, 59 (1), 53–65.
- [26] Benet, L.Z., Hosey, C.M., Ursu, O., and Oprea, T.I., 2016, BDDCS, the rule of 5 and drugability, *Adv. Drug Delivery Rev.*, 101, 89–98.
- [27] Zhang, Z., Fan, F., Luo, W., Zhao, Y., and Wang, C., 2020, Molecular dynamics revealing a detour-forward release mechanism of tacrine: Implication for the specific binding characteristics in butyrylcholinesterase, *Front. Chem.*, 8, 730.
- [28] Prasad, B.J., Sharavanan, P.S., and Sivaraj, R., 2019, Efficiency of *Oryza punctata* extract on glucose regulation: Inhibition of α -amylase and α -glucosidase activities, *Grain Oil Sci. Technol.*, 2 (2), 44–48.
- [29] Yao, X., Ling, Y., Guo, S., Wu, W., He, S., Zhang, Q., Zou, M., Nandakumar, K.S., Chen, X., and Liu, S., 2018, Tatanan A from the *Acorus calamus* L. root inhibited dengue virus proliferation and infections, *Phytomedicine*, 42, 258–267.
- [30] Kharisma, V.D., Probojati, R.T., Murtadlo, A.A.A., Ansori, A.N.M., Antonius, Y., and Tamam, M.B., 2021, Revealing potency of bioactive compounds as inhibitor of dengue virus (DENV) NS2B/NS3 protease from sweet potato (*Ipomoea batatas* L.) leaves, *Indian J. Forensic Med. Toxicol.*, 15 (1) 1627–1632.
- [31] Lai, H., Teramoto, T., and Padmanabhan, R., 2014, "Construction of dengue virus protease expression plasmid and in vitro protease assay for screening antiviral inhibitors" in *Dengue. Methods in Molecular Biology (Methods and Protocols)*, Eds. Padmanabhan, R., and Vasudevan, S., vol. 1138, Humana Press, New York, 345–360.

Effect of Physicochemical Process Variables on Natural Indigo Dye Production from *Strobilanthes cusia* Leaves by Response Surface Methodology

Edia Rahayuningsih^{1,2*}, Wachid Siti Fatimah², Mukmin Sapto Pamungkas^{1,2}, and Taranipa Marfitania²

¹Department of Chemical Engineering, Faculty of Engineering, Universitas Gadjah Mada, Jl. Grafika No. 2, Yogyakarta 55284, Indonesia

²Indonesia Natural Dye Institute (INDI), Integrated Research and Testing Laboratory (LPPT), Universitas Gadjah Mada, Sekip Utara, Yogyakarta 55281, Indonesia

* **Corresponding author:**

email: edia_rahayu@ugm.ac.id

Received: August 10, 2021

Accepted: February 21, 2022

DOI: 10.22146/ijc.68335

Abstract: The recovery process of indigoid compounds involves enzymatic hydrolysis of indigo precursors continued by oxidation reaction to synthesize indigo pigment. The purpose of this research was to evaluate the effect of physicochemical process variables, i.e., temperature, time, and pH aeration, on indigo yield from *Strobilanthes cusia* leaves. Small leaf pieces were immersed in distilled water and heated at temperatures (40, 50, and 60 °C) and duration (1, 2, and 3 h). The extract was aerated at different pHs (8, 10, and 12) to form the indigo product. The indigo concentration was quantified through a visible spectrophotometer and high-performance liquid chromatography (HPLC). The optimized condition for indigo production was studied using response surface methodology (RSM). Temperature, time, and interaction between temperature and time significantly affected the indigo yield. The optimized conditions for extraction of indigo dyes were determined to be at 60 °C for 1 h and pH 8 for maximizing the indigo yield. On that condition, the indigo concentration quantified by HPLC was 1.15% (w/v) which was lower than that by the spectrophotometry. By spectrophotometric analysis, the actual indigo content of 1.68% (w/v) on that optimum condition was close to the predicted indigo content of 1.77% (w/v) using RSM.

Keywords: indigo; *Strobilanthes cusia*; temperature; time; pH; response surface methodology

■ INTRODUCTION

Nowadays, one of the most polluting industrial sectors is the textile industry, producing large quantities of water pollutants contaminated with all types of chemicals. Indeed, the production of textile dyes is globally estimated at just over 10.000 tons annually, and around 100 tons annually of dyes are released into wastewater [1]. Approximately 7×10^7 tons of synthetic dyes are produced for the textile industry worldwide per year, of which nearly 10% of the dyestuffs are discharged to the environment as effluent after dyeing and processing [2]. Moreover, synthetic dye such as azo dyes that account for most textile dyestuffs is a cause of significant concerns. Most of them are highly toxic and carcinogenic [3].

To minimize the impact on health and the environment, natural dyes can be used as an alternative to reduce the use of synthetic dyes. Natural dyes can be derived from natural resources classified as insects or animals, minerals, fungi, and various plant parts, including roots, barks, leaves, flowers, and fruits [4-5]. As natural dyes are from renewable sources and biodegradable wastewater, they can sustain the environment [6]. In addition, natural dyes are generally less toxic and allergenic than synthetic dyes [7] and sometimes have a therapeutic effect on health [8].

Indigo, indigo-blue, or indigotin, is one of the most valuable sources of blue pigment and is extensively used [9-10]. Indigo dyes have been used for textiles coloration since prehistoric times, making them one of the oldest

dyes used by human beings [11]. Recently, indigo has become the most produced dye worldwide [12]. The production of indigo dye has been increased more than doubled from 22,000 tons per year in 2001 to 50,000 tons per year in 2011 due to its high global market demand. The indigo demand of 50,000 tons in 2011, 95% of the total production, was used to dye over 4 billion denim garments manufactured yearly [13-14].

There are a variety of temperate, tropical, and subtropical plants from many different species, genera, and families that can be hydrolyzed to form indigo dyes. *Indigofera sp.* is the most famous indigo-bearing plant which is mainly native to tropical and subtropical regions (India, Southeast Asia, and the Middle East). In temperate climates, Indigo dyes can also be produced from other species such as *Isatis tinctoria* or dyer's woad (Mediterranean, Western Asia, North America, and Europe) and *Polygonum tinctorum* (Japan and China). *Strobilanthes cusia* is a common alternative used in subtropical locations that have potential commercial value in sustainable indigo production and medicinal use [11]. *Strobilanthes cusia* (Nees) Kuntze or *Baphicacanthus cusia* (Nees) Bremek., a member of the family Acanthaceae, is an herbaceous plant native to many regions of Asia such as northeast India, Myanmar, Thailand, and southern China. This plant has been widely used as traditional herbal medicine and dye in southwest China [15-17]. *Strobilanthes cusia* is an indigo-rich plant that the main indigoid pigments were mostly synthesized in the leaves and stems of *Strobilanthes cusia* [18].

Indigo pigment can be formed by extracting the leaves of indigo-yielding plants. By steeping underwater, some indigo precursors such as indican (indoxyl- β -D-glucoside) and isatin B (indoxyl- β -ketogluconate) accumulated in the cell vacuole of leaves are hydrolyzed by the action of endogenous β -glucosidase. The products are indoxyl and glucose. In aerobic conditions, two molecules of indoxyl combine spontaneously to form indigo. However, isatin can be generated from the hydroxylation of indoxyl and decomposition of indigo in atmospheric oxygen. Condensation of indoxyl with isatin leads to indirubin as a side reaction of indigo biosynthesis [19-20].

A previous study revealed that some physicochemical parameters during fermentation, such as fermentation temperature, fermentation duration, pH, dissolved oxygen (DO), and redox potential of the fermented solution, played an essential role in indigo dye formation from *Indigofera* plant biomass [21]. Furthermore, there was also a study that focused on some parameters like concentration of substrate-indole, pH, and temperature to optimize the production of indigo pigment [22]. The traditional method successfully produced indigo dyes from plants that were performed by steeping the leaves of the plant in water and adjusting the pH during this process to form indigo [23]. However, the drawbacks of extracting dyes from plant material are time-consuming processes and low color value produced [24]. This method is less efficient, and the quality and quantity of products are variables [23,25]. Therefore, it is necessary to carry out further studies for optimizing the indigo extraction process to produce high-quality and quantity products with an efficient and eco-friendly process.

This study aims to understand the effect of physicochemical process variables, i.e., temperature, time, and pH aeration, on the formation of natural indigo dyes. The optimal condition of three parameters was run by using the full factorial design on response surface methodology (RSM).

■ EXPERIMENTAL SECTION

Materials

Strobilanthes cusia plants were obtained from a farmer in Temanggung, a regency located in Central Java, Indonesia. Indigo standard ($C_{16}H_{10}N_2O_2$, 95% purity) was purchased from Aurora Silk LLC (USA). Calcium oxide or quicklime (CaO) used to synthesize calcium hydroxide solution ($Ca(OH)_2$). Dimethyl sulfoxide or DMSO ($(CH_3)_2SO$, $\geq 99.95\%$ purity) was utilized for spectrophotometric analysis, which was purchased from Supelco Sigma-Aldrich Corporation. Acetonitrile (CH_3CN , 99.9% purity) utilized as a mobile phase for HPLC analysis was purchased from Merck (USA).

Procedure

Recovery of indigo from *Strobilanthes cusia*

The recovery process used in the experiment was based on the procedure conducted by Comlekcioglu et al. [26] with some modifications. The fresh leaves of *Strobilanthes cusia* were cleaned before being used. The leaves (5 g) were cut into smaller pieces, approximately 0.5 × 0.5 cm. Indigo precursors were hydrolyzed by putting the tiny leaves into the conical tube and adding 40 mL distilled water (leaves:distilled water = 1:8). This process was performed in anaerobic conditions so that the leaves were dipped underwater to exclude air. In this extraction process, there were several controlled parameters, namely temperature and time. The extraction process was carried out at 30, 60, and 90 °C for 1, 2, and 3 h, respectively. After the extraction process, the leaves were removed, and the extracts were quickly cooled to room temperature. The pH of the extract was adjusted to 8, 10, and 12, respectively, by adding a saturated solution of calcium hydroxide (0.1 g mL⁻¹), and the extract was aerated for 15 minutes using an aerator. The extract transforms its color from green-yellow into blue color after aeration is performed.

Quantification of indigo by visible spectrophotometry

The estimation of indigo yield in this experiment was quantified through a spectrophotometric method according to Puchalska et al. [27] and Qu et al. [28]. The indigo powder was dissolved in dimethyl sulfoxide (DMSO). The concentration of pure indigo was determined by the calibration curve method. The indigo concentration in an unknown sample was compared to a set of known concentrations of the standard sample. The standard indigo solutions were prepared in various concentrations (0, 25, 50, 100, and 200 ppm). Both standard indigo and unknown samples were dissolved in

DMSO. The samples were added 5 mL DMSO and diluted 50-fold. The absorbance of sample and standard was measured using Vernier-SpectroVis plus SVISPL spectrophotometer assisted with the Logger Lite program.

Quantification of indigo by high-performance liquid chromatography (HPLC)

HPLC analysis was performed to quantify the yield of pure indigo pigment and identify the primary component. Samples and standards were dissolved in dimethyl sulfoxide and analyzed by the HPLC system. Chromatographic separation was carried out with a reversed-phase column (octadecylsilane, C18) at room temperature with a flow rate of 1.0 mL/min under an isocratic flow of acetonitrile in 0–20 min. Products were detected and quantified using a UV detector at 600 nm.

Optimization of indigo extraction conditions

Response surface methodology (RSM) was performed using Design Expert 10.0.3 software to determine the optimal condition that provided the highest indigo yield. Three independent parameters, i.e., extraction temperature (A), extraction time (B), and pH of the extract before oxidation (C), were investigated. Each parameter was coded in three levels, as shown in Table 1. Extraction temperature was coded as -1, 0, and 1 which the actual value was 40, 50, and 60 °C, respectively. With the same coded values as extraction temperature, the actual value of extraction time was 1, 2, and 3 h, respectively, and the actual value of pH was 8, 10, and 12, respectively. Statistical analysis was performed on the experimental results by regression and analysis of variance (ANOVA). Response surfaces and contour plots of the model runs were also reported in this work. Furthermore, the desirability function was predicted to optimize the indigo yield.

Table 1. Experimental design for optimizing indigo yield

Independent parameter	Symbol	Unit	Level		
			-1	0	1
Extraction temperature	A	°C	40	50	60
Extraction time	B	Hour	1	2	3
pH before oxidation	C	N/A	8	10	12

RESULTS AND DISCUSSION

Quantification of Crude Indigo Dye

It can be understood from the result above (Fig. 1) that the addition of calcium hydroxide solution before the aeration process, which was defined as the increase in pH of the extract, increased extraction yields considerably. According to a previous report published, adding a small number of alkalis such as carbonate or calcium hydroxide into the extract could accelerate the oxidation reaction of indoxyl forms indigo and increase the indigo yield. However, an excess of alkali used could decrease the yield of indigo [29]. Calcium hydroxide also allowed the indigo suspension to sediment more rapidly and resulted in larger indigo particles [30].

The results in Fig. 1(a) show that there is a significant increase in crude indigo yield with the extended extraction time at the lower temperature (40 °C). It seems that increasing time in the extraction process can accelerate enzyme activity to break down indican as a major indigo

precursor to indoxyl. By contrast, increasing duration in hydrolysis reaction did not produce a considerable yield improvement at the higher temperature, as shown in Fig. 1(b) and 1(c). Even there is also a slight decline of indigo yield at a longer duration and higher temperature. It indicates that a lengthy extraction process at high temperatures may occur a loss of indigo [23].

Spectrophotometric Analysis

The concentration of pure indigo was examined using spectrophotometric analysis by dissolving in DMSO and the result is presented in Fig. 2. It is practically insoluble in water and many other common solvents, but some solvents will dissolve indigo to some extent. Indigo-blue was sufficiently unstable in DMSO, where the color of the solution could change over time from blue to purple or even red color. Gilbert 2007 also reported a red/brown color produced after 24 h when indigo-blue dissolved in DMSO [9]. The result (Fig. 2) reveals a maximum absorption wavelength of 616.9 nm,

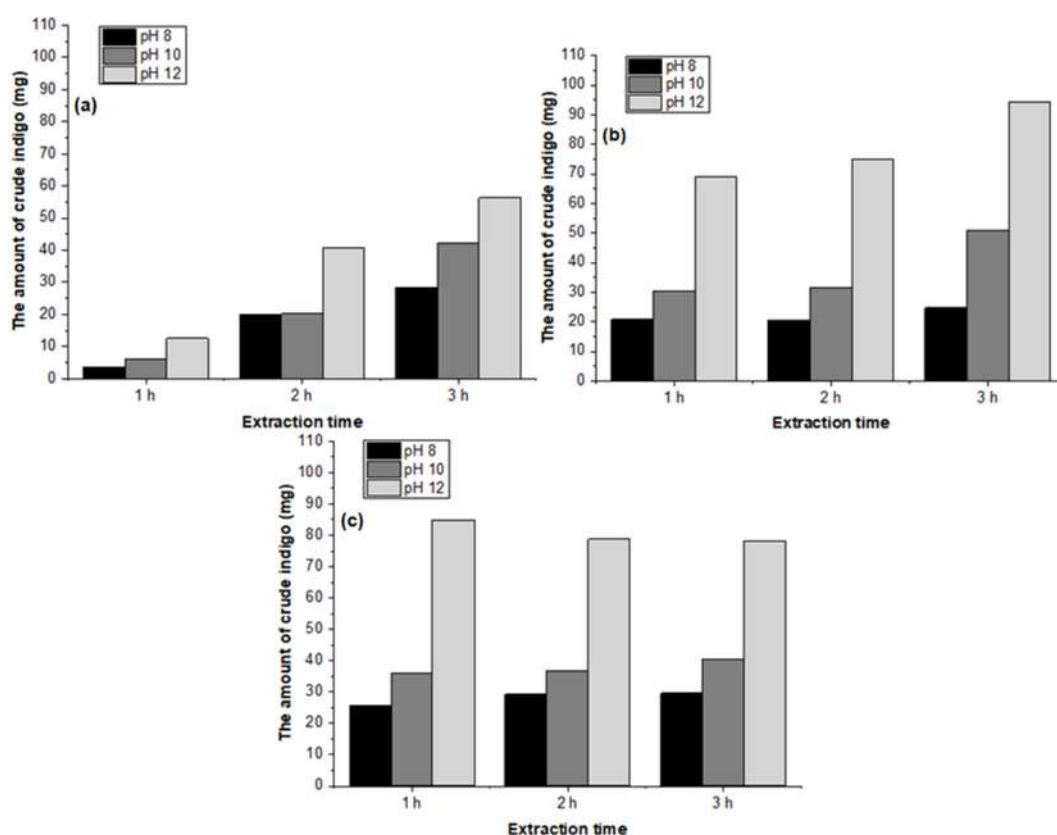


Fig 1. The amount of crude indigo yield at different pH (8, 10, and 12), extraction time (1, 2, and 3 h), and temperature: (a) 40 °C, (b) 50 °C, and (c) 60 °C

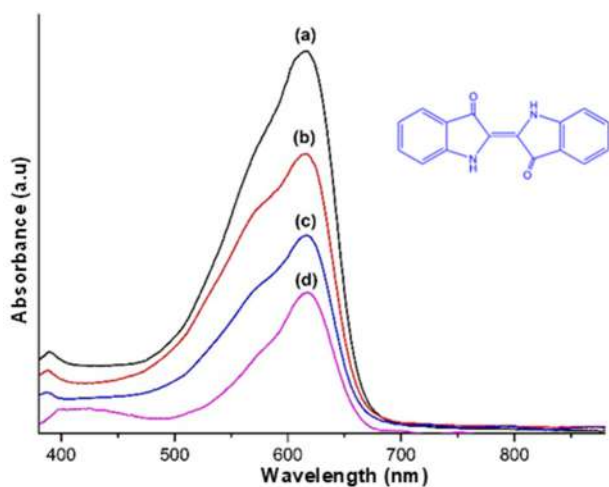


Fig 2. Visible absorption spectra of (a) extracted indigo-pH 8, (b) extracted indigo-pH 10, (c) extracted indigo-pH 12, and (d) indigo standard

indicating a maximum wavelength of indigo. In addition, the result shows that there is a broad spectrum of extracted indigo yield. The main factors that may cause the peak broadening are impurities such as calcium salts and various derivatives of indigo and indoxyl. The by-products of indigo synthesis, such as indirubin and isindirubin that produce red pigment, have maximum absorption at 540 nm and 552 nm, respectively [27].

Characterization of Natural Indigo Dye

The vibrational spectra of extracted indigo and standard indigo is presented in Fig. 3. The strong band at 3426 cm^{-1} usually is due to the N–H stretching. The strong exhibited at 1628 cm^{-1} is attributed to C=O stretching vibration. Other peaks at 1458 and 1404 cm^{-1} are assigned to the stretching vibration of the C=C aromatic ring. The absorption bands which appear at the region below 1320 cm^{-1} correspond to the deformation of N–H and C–H vibration [31].

Optimization of Indigo Extraction

ANOVA for the quadratic regression model is used to describe the relationship between indigo yield and independent variables. This model analysis shows that the response variable is adequately fitted to the regression model, a second-order polynomial equation. The equation of yield can be expressed in the following equation:

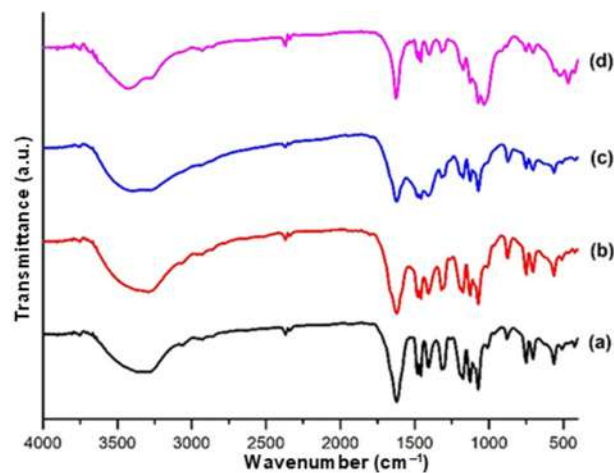


Fig 3. FT-IR spectra of a) extracted indigo-pH 8, (b) extracted indigo-pH 10, (c) extracted indigo-pH 12, and (d) indigo standard

$$Y = 1.19 + 0.44A + 0.15B - 0.07C - 0.24AB - 0.11AC - 0.054BC - 0.053A^2 - 0.014B^2 - 0.008406C^2$$

where Y represents the pure indigo yield as a function of studied independent variables, which are extraction temperature (A), extraction time (B), and pH before oxidation reaction (C).

In general, Table 2 is used to evaluate the significance level of each parameter toward the response variable, which is indigo concentration. A lower p-value ($p < 0.05$) and a higher F-value of each factor mean significantly affect the model. The results reveal that temperature and extraction time substantially influence the indigo yield, while pH is insignificant for this model. It indicates that pH has less influence on the increase of indigo yield. The highest F-value is for extraction temperature, indicating the most influential parameter to increase pure indigo yield. In addition, the interaction parameter between temperature and time (AB) provides statistical significance with a p-value equal to 0.25×10^{-2} . Conversely, the interaction between temperature and pH (AC) as well as time and pH (BC) are insignificant to the pure indigo yield.

In this study, the R^2 value of 0.8435 implies that 84.35% of the total variance is attributed to the response variable studied, which is the pure indigo yield. The predicted R^2 value reasonably agrees with the adjusted R^2 value because the difference between those data is less than 0.2. According to this regression analysis, the model

Table 2. Analysis of variance and regression of RSM

Source	Sum of squares	Df	Mean square	F value	p-value
Model	4.81	9	0.53	10.18	$< 1.00 \times 10^{-4}$
A-Extraction Temp.	3.45	1	3.45	65.70	$< 1.00 \times 10^{-4}$
B-Extraction Time	0.40	1	0.40	7.58	1.36×10^{-2}
C-pH	0.09	1	0.09	1.69	0.21
AB	0.66	1	0.66	12.62	0.25×10^{-2}
AC	0.16	1	0.16	3.02	0.10
BC	0.03	1	0.03	0.68	0.42
A ²	0.02	1	0.02	0.32	0.58
B ²	1.14×10^{-3}	1	1.14×10^{-3}	0.022	0.88
C ²	4.24×10^{-4}	1	4.24×10^{-4}	8.07×10^{-3}	0.93
Residual	0.89	17	0.05		
Corrected Total	5.71	26			
R ²					0.8435
Adjusted R ²					0.7606
Predicted R ²					0.5913
Adequate Precision					11.296

has a good precision value of 11.296. This value is greater than 4 so that the model meets the requirements for the optimization process. This good precision value measures the signal-to-noise ratio that compares the range of values predicted at the design point with the average prediction error. If it is greater than 4, the model has a signal that is strong enough to be used for optimization. In general, the results of the analysis show that most of the experimental results obtained are good enough to predict the concentration of extracted pure indigo (Fig. 4).

The interaction between temperature and time on the extraction process significantly affects the pure indigo yield, as shown in Table 2. At the lower temperature (40 °C), the higher extracted pure indigo yield was obtained at a longer extraction process. However, this process can be shortened by increasing the temperature, as presented in Fig. 5(a).

Fig. 5(b) and 5(c) show that the highest indigo yield is obtained at pH 8. At a relatively higher volume of the base added, indigo content decreased gradually. Russell and Kaupp [32] reported that indigo synthesized by the oxidation of indigo in basic conditions can involve the indoxyl radical as an intermediate. The effect of the excess base in a decline of the indigo yield can be rationalized by indolone formation in which the presence of base and

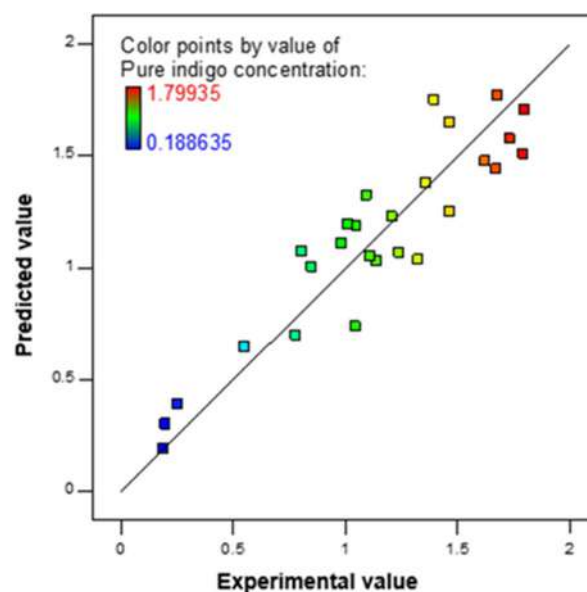


Fig 4. Predicted vs. experimental value for indigo yield (the straight line represents the predicted yield, and the points represent the experimental measurement)

oxygen may be converted to non-indigo products. Furthermore, adding the excess base can also reduce indigo purity by impurities such as calcium salts within the indigo product [30]. Some researchers also reported that the quantity of crude dye increased along with the increasing concentration of calcium hydroxide while

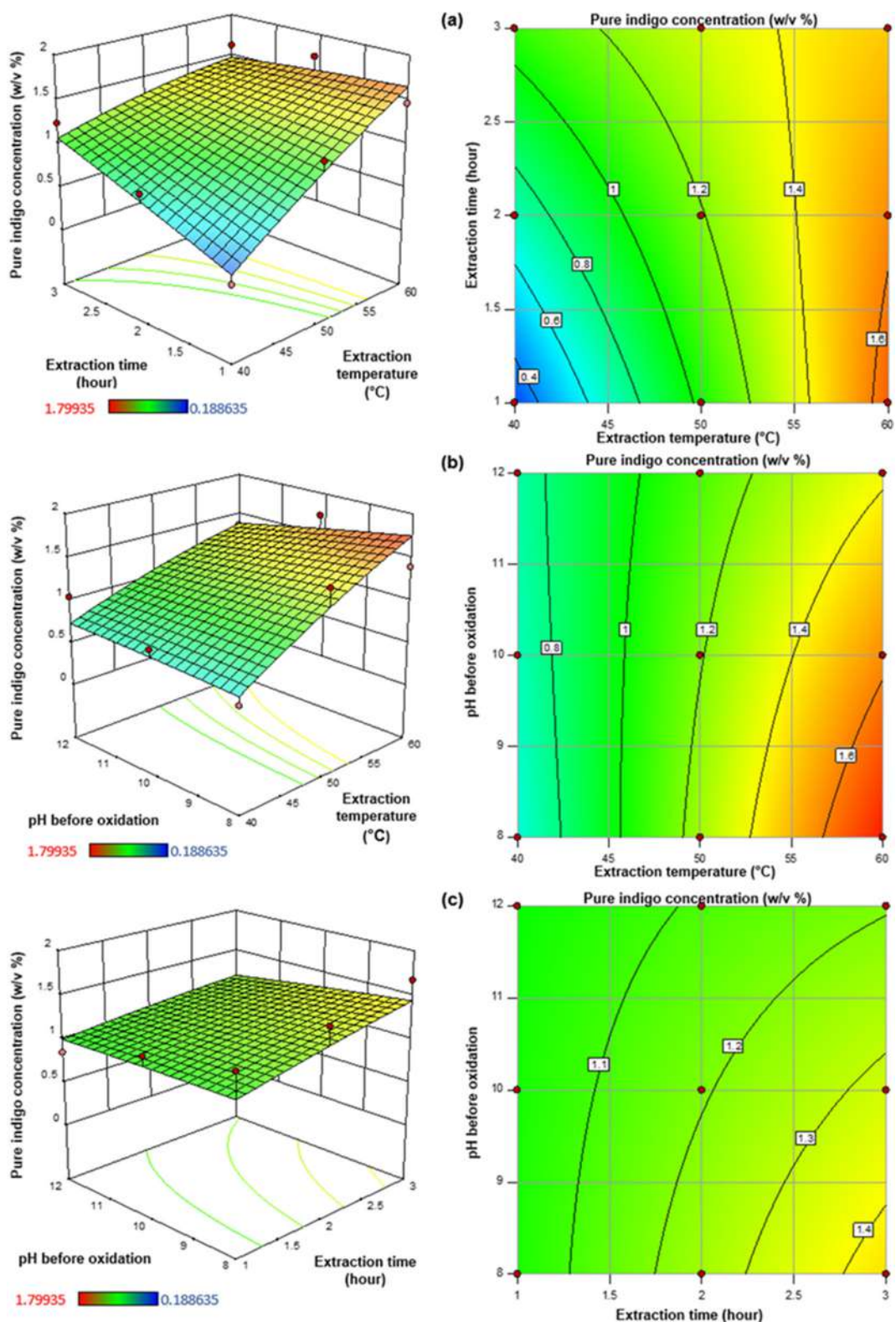


Fig 5. Response surfaces and contour plots of the pure indigo yield (w/v %) as a function of extraction temperature and time (a), extraction temperature and pH before oxidation reaction (b), extraction time and pH before oxidation reaction (c)

indigo content in the crude dye (% indigo per gram of crude dye) decreased [33]. A higher concentration of blue color could be achieved by declining the amount of lime [34].

Based on numerical optimization, the optimized process conditions for maximization of pure indigo concentration were achieved at 60 °C for one hour to break down indican to indoxyl and pH 8 to accelerate the reaction of indoxyl into indigo. An optimum indigo yield of 1.68% (w/v) was produced, which was adequately close to the predicted yield of 1.77% (w/v).

Determination of Natural Indigo Pigment by HPLC Analysis

Based on chromatogram data, there are a few impurities on the indigo sample compared to the indigo standard (Fig. 6). As shown in Table 3, the quantification of pure indigo shows some different results between the measurements using visible spectrophotometer and HPLC-UV. However, these findings provide a similar pattern. There is evidence to suggest that both Visible-spectrophotometry and HPLC-UV methods can accurately be used to determine the optimal variables that produce the highest pure indigo yield as long as both methods have the same tendency. The spectrophotometry has advantages over the HPLC method regarding analysis cost and instrumental operation, which is relatively inexpensive and easy to operate. However, compared to the spectrophotometric method, the HPLC method has greater sensitivity and higher precision. There are also

some disadvantages of spectrophotometry. Impurities in the sample cannot be eliminated, increasing the calculated concentration. As shown in Table 3, the estimation of indigo concentration by HPLC is lower than that by the spectrophotometric analysis.

CONCLUSION

In this study, natural indigo dyes have been successfully extracted from leaves of *Strobilanthes cusia*. In addition, the response surface methodology (RSM) based on the full factorial design was used to examine the optimal parameters from three independent factors on the indigo extraction. The results reveal that temperature and time are the most important factors influencing the amount of extracted pure indigo yield.

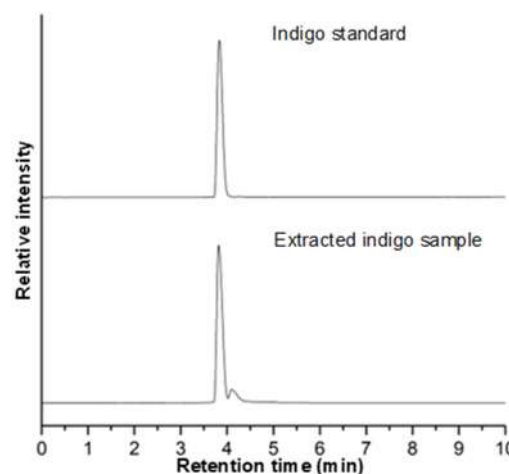


Fig 6. Chromatogram of the extracted indigo sample and standard

Table 3. Comparison of pure indigo concentration measured using Visible spectrophotometry and HPLC method

Sample	Control variables			Pure indigo yield (% w/v)	
	Extraction temp. (°C)	Extraction time (h)	pH before aeration	Visible-spectrophotometer	HPLC-UV
41A	40	1	8	0.19	0.22
42A	40	2	8	0.55	0.50
43A	40	3	8	0.80	0.64
51A	50	1	8	1.33	1.03
53A	50	3	8	1.67	1.09
61A	60	1	8	1.68	1.15
63A	60	3	8	1.80	1.18
63B	60	3	10	1.62	1.17
63C	60	3	12	1.21	0.95

Furthermore, an optimum of the pure indigo yield was achieved on conditions as follows: extraction temperature at 60 °C, extraction time of 1 h, pH before oxidation reaction of 8. Under that condition, the pure indigo yield of 1.68% (w/v) was experimentally obtained, which was a well fit for a predicted yield of 1.77% (w/v) by the regression model. This optimum condition could be used as a standard condition for natural dye extraction from *Strobilanthes cusia* leaves to provide the highest content of indigo dyes.

■ ACKNOWLEDGMENTS

This research was financially supported by Chemical Engineering Department, Faculty of Engineering, Universitas Gadjah Mada, and Riset Inovatif-Produktif (RISPRO) under contract number PRJ-103/LPDP/2019 between LPDP Ministry of Finance Indonesia and Directorate of Research Universitas Gadjah Mada.

■ REFERENCES

- [1] Semeraro, P., Rizzi, V., Fini, P., Matera, S., Cosma, P., Franco, E., García, R., Ferrándiz, M., Núñez, E., Gabaldón, J.A., Fortea, I., Pérez, E., and Ferrándiz, M., 2015, Interaction between industrial textile dyes and cyclodextrins, *Dyes Pigm.*, 119, 84–94.
- [2] Chandanshive, V.V., Kadam, S.K., Khandare, R.V., Kurade, M.B., Jeon, B.H., Jadhav, J.P., and Govindwar, S.P., 2018, *In situ* phytoremediation of dyes from textile wastewater using garden ornamental plants, effect on soil quality and plant growth, *Chemosphere*, 210, 968–976.
- [3] Ratna, and Padhi, B.S., 2012, Pollution due to synthetic dyes toxicity & carcinogenicity studies and remediation, *Int. J. Environ. Sci.*, 3 (3), 940–955.
- [4] Zerín, I., Farzana, N., Sayem, M., Anang, D.M., and Haider, J., 2020, “Potentials of natural dyes for textile applications” in *Encyclopedia of Renewable and Sustainable Materials*, Eds. Hashmi, S., and Choudhury, I.A., Elsevier, Oxford, 873–883.
- [5] Punrattanasin, N., Nakpathom, M., Somboon, B., Narumol, N., Rungruangkitkrai, N., and Mongkhohrattanasit, R., 2013, Silk fabric dyeing with natural dye from mangrove bark (*Rhizophora apiculata* Blume) extract, *Ind. Crops Prod.*, 49, 122–129.
- [6] Vankar, P.S., 2017, “Newer natural dyes for cotton” in *Natural Dyes for Textiles: Sources, Chemistry, Applications*, Woodhead Publishing, Cambridge, UK, 1–15.
- [7] dos Santos Silva, P.M., Fiaschitello, T.R., de Queiroz, R.S., Freeman, H.S., da Costa, S.A., Leo, P., Montemor, A.F., and da Costa, S.M., 2020, Natural dye from *Croton urucurana* Baill. bark: Extraction, physicochemical characterization, textile dyeing, and color fastness properties, *Dyes Pigm.*, 173, 107953.
- [8] Vankar, P.S., and Shukla, D., 2019, “Medicinal properties of natural dye plants” in *New Trends in Natural Dyes for Textiles*, Woodhead Publishing, Cambridge, UK, 283–347.
- [9] Gilbert, K.G., 2017, “Dyes” in *Encyclopedia of Applied Plant Sciences*, 2nd Ed., Eds. Thomas, B., Murray, B.G., and Murphy, D.J., Academic Press, Oxford, 368–373.
- [10] Li, S., Cunningham, A.B., Fan, R., and Wang, Y., 2019, Identity blues: The ethnobotany of the indigo dyeing by Landian Yao (Iu Mien) in Yunnan, Southwest China, *J. Ethnobiol. Ethnomed.*, 15 (1), 13.
- [11] Chavan, R.B., 2015, “Indigo dye and reduction techniques” in *Denim: Manufacture, Finishing and Applications*, Eds. Paul, R., Woodhead Publishing, Cambridge, UK, 37–67.
- [12] Głowacki, E.D., Voss, G., Leonat, L., Irimia-Vladu, M., Bauer, S., and Sariciftci, N.S., 2012, Indigo and Tyrian purple - From ancient natural dyes to modern organic semiconductors, *Isr. J. Chem.*, 52 (6), 540–551.
- [13] Pattanaik, L., Padhi, S.K., Hariprasad, P., and Naik S.N., 2020, Life cycle cost analysis of natural indigo dye production from *Indigofera tinctoria* L. plant biomass: a case study of India, *Clean Technol. Environ. Policy*, 22 (8), 1639–1654.
- [14] Hsu, T.M., Welner, D.H., Russ, Z.N., Cervantes, B., Prathuri, R.L., Adams, P.D., and Dueber, J.E., 2018, Employing a biochemical protecting group for a sustainable indigo dyeing strategy, *Nat. Chem. Biol.*, 14 (3), 256–261.

- [15] Gu, W., Zhang, Y., Hao, X.J., Yang, F.M., Sun, Q.Y., Morris-Natschke, S.L., Lee, K.H., Wang, Y.H., and Long, C.L., 2014, Indole alkaloid glycosides from the aerial parts of *Strobilanthes cusia*, *J. Nat. Prod.*, 77 (12), 2590–2594.
- [16] Lee, C.L., Wang, C.M., Hu, H.C., Yen, H.R., Song, Y.C., Yu, S.J., Chen, C.J., Li, W.C., and Wu, Y.C., 2019, Indole alkaloids indigodoles A-C from aerial parts of *Strobilanthes cusia* in the traditional Chinese medicine Qing Dai have anti-IL-17 properties, *Phytochemistry*, 162, 39–46.
- [17] Yu, H., Li, T., Ran, Q., Huang, Q., and Wang, J., 2021, *Strobilanthes cusia* (Nees) Kuntze, a multifunctional traditional Chinese medicinal plant, and its herbal medicines: A comprehensive review, *J. Ethnopharmacol.*, 265, 113325.
- [18] Xu, W., Zhang, L., Cunningham, A.B., Li, S., Zhuang, H., Wang, Y., and Liu, A., 2020, Blue genome: Chromosome-scale genome reveals the evolutionary and molecular basis of indigo biosynthesis in *Strobilanthes cusia*, *Plant J.*, 104 (4), 864–879.
- [19] Song, J., Imanaka, H., Imamura, K., Kajitani, K., and Nakanishi, K., 2010, Development of a highly efficient indigo dyeing method using indican with an immobilized β -glucosidase from *Aspergillus niger*, *J. Biosci. Bioeng.*, 110 (3), 281–287.
- [20] Qu, Y., Zhang, X., Ma, Q., Ma, F., Zhang, Q., Li, X., Zhou, H., and Zhou, J., 2012, Indigo biosynthesis by *Comamonas* sp. MQ, *Biotechnol. Lett.*, 34 (2), 353–357.
- [21] Dutta, S., Roychoudhary, S., and Sarangi, B.K., 2017, Effect of different physico-chemical parameters for natural indigo production during fermentation of *Indigofera* plant biomass, *3 Biotech*, 7 (5), 322.
- [22] Unde, V., and Mutnuri, S., 2014, Bio-catalytic production of indigo using biphasic organic solvent, *Discovery Biotechnol.*, 5 (13), 3–10.
- [23] Stoker, K.G., Cooke, D.T., and Hill, D.J., 1998, An improved method for the large-scale processing of woad (*Isatis tinctoria*) for possible commercial production of woad indigo, *J. Agric. Eng. Res.*, 71 (4), 315–320.
- [24] Das, H., and Kalita, D., 2016, “Fibers and dye yielding plants of Northeast India” in *Bioprospecting of Indigenous Bioresources of North-East India*, Eds. Purkayastha, J., Springer, Singapore, 77–99.
- [25] Vankar, P.S., 2017, “Innovative dye extraction methods” in *Natural Dyes for Textiles: Sources, Chemistry, Applications*, Woodhead Publishing, Cambridge, UK, 191–203.
- [26] Comlekcioglu, N., Efe, L., and Karaman, S., 2015, Extraction of indigo from some *Isatis* species and dyeing standardization using low-technology methods, *Braz. Arch. Biol. Technol.*, 58(1), 96–102.
- [27] Puchalska, M., Polec-Pawlak, K., Zadrozna, I., Hryszko, H., and Jarosz, M., 2004, Identification of indigoid dyes in natural organic pigments used in historical art objects by high-performance liquid chromatography coupled to electrospray ionization mass spectrometry, *J. Mass Spectrom.*, 39 (12), 1441–1449.
- [28] Qu, Y., Ma, Q., Zhang, X., Zhou, H., Li, X., and Zhou, J., 2012, Optimization of indigo production by a newly isolated *Pseudomonas* sp. QM, *J. Basic Microbiol.*, 52 (6), 687–694.
- [29] Darrac, P.P., and van Schendel, W., 2006, *Global Blue: Indigo and Espionage in Colonial Bengal*, University Press, Dhaka.
- [30] Garcia-Macias, P., and John, P., 2004, Formation of natural indigo derived from woad (*Isatis tinctoria* L.) in relation to product purity, *J. Agric. Food Chem.*, 52 (26), 7891–7896.
- [31] Ju, Z., Sun, J., and Liu, Y., 2019, Molecular structures and spectral properties of natural indigo and indirubin: Experimental and DFT studies, *Molecules*, 24 (21), 3831.
- [32] Russell, G.A., and Kaupp, G., 1969, Oxidation of carbanions IV. Oxidation of indoxyl to indigo in basic solution, *J. Am. Chem. Soc.*, 91 (14), 3851–3859.
- [33] Shin, Y., Yoo, D.I., and Kim, K., 2012, Process balance of natural indigo production based on traditional Niram method, *Text. Color. Finish.*, 24 (4), 253–259.
- [34] Purnama, H., Hidayati, N., Safitri, D.S., and Rahmawati, S., 2017, Effect of initial treatment in the preparation of natural indigo dye from *Indigofera tinctoria*, *AIP Conf. Proc.*, 1855, 020022.

Metabolite Profiling of Ebony (*Diospyros celebica* Bakh) Leaves and Wood Extracts Using LC-MS/MS

Dien Atin Boritnaban¹, Alfi Hudatul Karomah¹, Dewi Anggraini Septaningsih², Muhammad Majiudu², Fifi Gus Dwiyantri^{2,3}, Iskandar Zulkarnaen Siregar^{2,3}, and Mohamad Rafi^{1,2,4*}

¹Department of Chemistry, Faculty of Mathematics and Natural Sciences, IPB University, Jl. Tanjung Kampus IPB Dramaga, Bogor 16680, Indonesia

²Advanced Research Laboratory, Institute of Research and Community Services, IPB University, Jl. Palem Raya Kampus IPB Dramaga, Bogor 16680, Indonesia

³Department of Silviculture, Faculty of Forestry and Environment, IPB University, Jl. Lingkar Akademik Kampus IPB Dramaga, Bogor 16680, Indonesia

⁴Tropical Biopharmaca Research Center, Institute of Research and Community Services, IPB University, Jl. Taman Kencana No. 3, Bogor 16128, Indonesia

* **Corresponding author:**

email: mra@apps.ipb.ac.id

Received: August 19, 2021

Accepted: January 17, 2022

DOI: 10.22146/ijc.68529

Abstract: Ebony (*Diospyros celebica* Bakh) is an endemic forest tree species found in Sulawesi whose basic information on its metabolite profile is still lacking. The objective of this research was to separate and identify putatively metabolite present in the leaves and wood of ebony across Sulawesi. Separation and identification of ebony metabolites were carried out using UHPLC-Q-Orbitrap HRMS analysis. Using ultrasonication with ethanol as the extracting solvent, we used powdered ebony leaves and wood. The results showed that the metabolites contained in the leaves and wood of ebony were 59 metabolites. About 14 compounds were found in the leaves and wood, 21 compounds in the wood, and 24 compounds in the leaves. The identified metabolites are flavonoids, terpenoids, amino aldehydes, alkaloids, quinones, steroids, amino acids, fatty acids, and saccharides. Clustering of ebony using principal component analysis obtained leaves and wood groups using peak area of known compounds as the variable.

Keywords: *Diospyros celebica* Bakh; ebony; metabolomics; UHPLC-Q-Orbitrap HRMS

■ INTRODUCTION

Ebony (*Diospyros celebica* Bakh) is one of the endemic plants from Sulawesi, Indonesia. Ebony could be found in West Sulawesi, South Sulawesi, and Central Sulawesi [1]. Ebony wood is still a high economic value commodity made everyone seek the wood. Ebony is widely used as a material for luxury furniture, sculptures, carvings, fans, lathes, garnishing tools, brush bodies, luxury venire, wind instruments [2]. Another benefit of ebony wood was used as a non-synthetic preservative. It contains secondary metabolites that can be used in the health sector because it has several biological activities, such as antidiabetic, antibacterial, antifungal, and antiviral [3-6].

Utilization of ebony leaves may be an alternative to obtain secondary metabolites with various kinds of biological activities above. So, they would not cut down ebony because this wood is protected. However, those biological activities indeed come from secondary metabolites, which will differ in the composition and concentration in each part of the plant, such as leaves and stems. Therefore, research is needed to identify the different metabolites contained in ebony stems and leaves as initial information on the composition and concentration of the metabolites they have.

The different metabolites in the leaves and stems of ebony could be separated and identified using an LC-MS/MS-based metabolomics approach. LC-MS/MS is

used to analyze secondary metabolites' targeted and untargeted analysis. In addition, this instrument also has several advantages, such as high sensitivity and selectivity, can identify secondary metabolites in a relatively wide range, fast analysis time, and can separate large quantities of components with high resolution [7-8]. However, identifying metabolites using LC-MS/MS will produce complex data, so multivariate data analysis is needed to reduce data complexity [9].

In this study, the LC-MS/MS analysis results were evaluated using a multivariate analysis, such as the principal component analysis (PCA) method to describe the grouping pattern of metabolites contained in ebony leaves and wood extracts. A combination of LC-MS/MS with multivariate analysis has been reported to be able to classify metabolites based on plant parts extracted from the species *Andrographis paniculata* [10], *Chrysophyllum perpulchrum* [11], and *Harungana madagascariensis* [12], also used as an integrated strategy for quality control of *Dalbergia odorifera* [13]. However, no reported paper applies multivariate analysis to classify metabolites from ebony leaves and wood extracts. Therefore, this study aimed to identify metabolites from ebony leaves and wood extracts using LC-MS/MS and cluster them using PCA.

■ EXPERIMENTAL SECTION

Materials

The samples used in this study are ebony leaves and wood taken from three provinces in Sulawesi. We collected the ebony samples from several tree-growing sites in the three provinces, Batu Ampa and Sondoang from West Sulawesi, Pani Binangga, and Poso Pesisir from Central Sulawesi, Cani Sirenreng, and Bellabori from South Sulawesi. The collected samples were then composited in each location, so we have six ebony leaves and wood samples. All solvents (analytical or LC-MS grade) were purchased from Merck (Darmstadt, Germany).

Instrumentation

Separation of ebony metabolites are using an LC-MS/MS Thermo Scientific Vanquish Flex UHPLC

tandem Q Exactive Plus Orbitrap-High Resolution Mass Spectrometer (UHPLC-Q-Orbitrap HRMS) instrument (Thermo Fisher, Waltham, USA) equipped with ThermoXCalibur software and Compound Discoverer version 3.1 (Thermo Fisher, Waltham, USA). In addition, principal component analysis was carried out using the Unscrambler X version 10.1 (CAMO, Oslo, Norway).

Procedure

Extraction

Before being used for extraction, we pulverized all of the samples. The sample powder was extracted in ethanol at a ratio of 1:10 using ultrasonication for 30 minutes. The extract was then filtered, and the filtrate was analyzed using UHPLC-Q-Orbitrap HRMS to separate and identify metabolites.

Separation of ebony leaves and wood metabolites using UHPLC-Q-Orbitrap HRMS

Metabolites in ebony leaves and wood extracts were separated using the Vanquish Flex UHPLC-Q Exactive Plus Orbitrap-High Resolution Mass Spectrometer with Accucore C18 (100 × 2.1 mm, 1.5 μm) as the column. The mobile phase used is 0.1% formic acid in water (A) and 0.1% formic acid in acetonitrile (B) with a gradient elution system: 0.0–5.0 min (2–5 %B), 5.0–12.5 min (5–20 %B), 12.5–25.0 min (20–30 %B), 25.0–30.0 min (30–40 %B), 30.0–35.0 min (40–95 %B), 35.0–38.5 min (95 %B), 38.5–44.0 min (2 %B). The flow rate used was 0.25 mL/min with an injection volume of 2.5 μL. The ionization source used in the MS system is ESI, with positive and negative ionization modes in the *m/z* range of 100–1500. The capillary temperature used was 320 °C, spray voltage 3.8 kV, sheath gas and auxiliary gas flow rate 15 and 3 mL/min, and automatic gain control (AGC) 3 × 10⁶ and injection time set to 100 ms. The collision energy used is 18, 35, and 53 eV. The scan type used is full MS/dd MS² and full scan data set with a resolving power of 70,000 FWHM.

Data analysis

UHPLC-Q-Orbitrap HRMS data were processed using Compound Discoverer 2.2 with an in-house database collected from information on compounds in

the genus *Diospyros* to identify ebony leaves and wood extracts metabolites. Metabolites were identified through several stages, namely selected spectra stage, alignment retention time, detected unknown compounds, grouping unknown compounds, predicting processes, searching mass lists, filling gaps, normalizing areas, and marking background compounds. Ebony leaves and wood extract were then grouped by PCA using The Unscrambler X version 10.1. The variable used for grouping is the peak area of the identified compounds.

■ RESULTS AND DISCUSSION

Putative Identification of Ebony Leaves and Wood Metabolites

UHPLC-Q-Orbitrap HRMS was used to separate

and putative identification of ebony leaves and wood metabolites. Positive ionization mode obtained more detected metabolites than negative ionization mode. In addition, the ebony wood extract had a different chromatogram profile compared to the leaves extract, so the detected metabolites were also other, as shown in Fig. 1.

About 59 compounds were putatively identified in ebony leaves and wood extracts, consisting of 21 compounds identified only in the wood, 24 identified only in the leaves, and 14 identified in both wood and leaves (Fig. 2). The identified metabolites are flavonoids, terpenoids, amino aldehydes, alkaloids, phenolic acids, quinones, steroids, amino acids, fatty acids, and saccharides (Table 1).

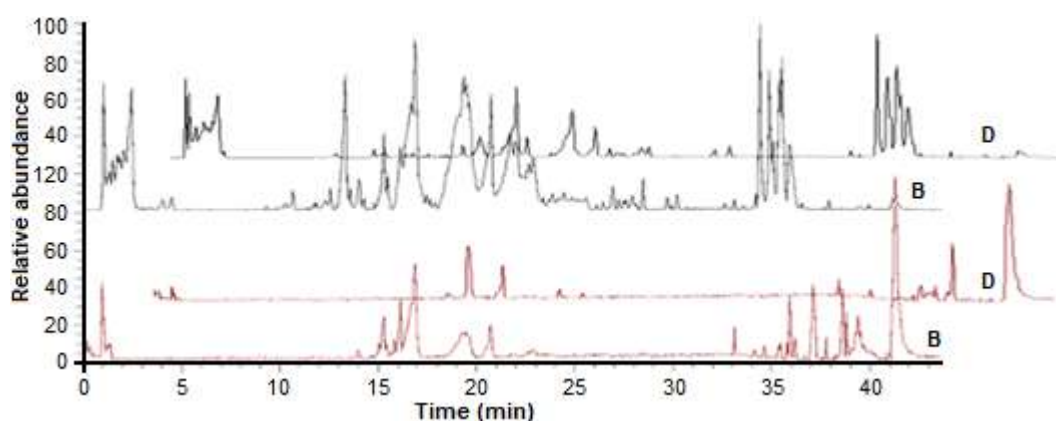


Fig 1. Representative chromatogram of ebony wood (B) and leaves (D) in positive ionization mode (black) and negative ionization mode (red)

Table 1. Putative identification of metabolite in ebony leaves and wood extracts

No	Name of Metabolites	RT	Formula	MW	Error mass (ppm)	Ion mode	MS-MS
Flavonoids							
1	Ethyl 1,3-dihydroxy-2-naphthoate	24.70	C ₁₃ H ₁₂ O ₄	232.0734	-0.86	[M+H] ⁺	233, 218, 190,161
2	Gibberellin A5*	15.01	C ₁₉ H ₂₂ O ₅	330.1456	-3.33	[M+H] ⁺	331, 313
3	3-Methylplumbagin*	21.90	C ₁₂ H ₁₀ O ₃	202.0627	-1.48	[M+H] ⁺	203, 188, 160
4	Rutin *	23.39	C ₂₇ H ₃₀ O ₁₆	610.1503	-5.08	[M+H] ⁺	611, 423, 329, 167
5	Kaempferol 3-(2''-galloylglucoside)	20.79	C ₂₈ H ₂₄ O ₁₅	600.0863	-1.67	[M+H] ⁺	601, 403, 287, 153
6	Diosindigo A*	34.48	C ₂₄ H ₂₀ O ₆	404.1252	-1.98	[M+H] ⁺	405,387,373,345
7	Apigenin*	14.34	C ₁₅ H ₁₀ O ₅	270.0521	-2.59	[M+H] ⁺	271, 253, 225, 211
8	Palomid 529*	35.37	C ₂₄ H ₂₂ O ₆	406.1413	-0.74	[M+H] ⁺	405, 390, 358, 357
9	Daidzein*	15.31	C ₁₅ H ₁₀ O ₄	254.0572	-2.76	[M+H] ⁺	255, 214, 185, 172
10	Kaempferol**	16.08	C ₁₅ H ₁₀ O ₆	286.0477	-2.45	[M+H] ⁺	287, 253, 201

Table 1. Putative identification of metabolite in ebony leaves and wood extracts (*Continued*)

No	Name of Metabolites	RT	Formula	MW	Error mass (ppm)	Ion mode	MS-MS
Terpenoids							
15	Hemigossypolone	16.24	C ₁₅ H ₁₄ O ₅	274.0838	-2.55	[M-H] ⁻	272, 151, 125
16	Betulinic acid	37.91	C ₃₀ H ₄₈ O ₃	456.3602	-3.07	[M-H] ⁻	455, 439, 421
17	(6aR,11aR)-3,9-Dihydroxypterocarpan	19.02	C ₁₅ H ₁₂ O ₄	256.0730	-2.73	[M+H] ⁺	257, 239, 211
18	(2S)-Naringenin	15.19	C ₁₅ H ₁₂ O ₅	272.0676	-3.31	[M+H] ⁺	273, 255, 197
19	Betulinaldehyde	39.52	C ₃₀ H ₄₈ O ₂	440.2891	-2.27	[M+H] ⁺	441, 315, 286
20	Pomolic acid*	37.68	C ₃₀ H ₄₈ O ₄	472.3899	-2.54	[M+H] ⁺	473, 437, 409, 313
21	Phlorisobutyrophenone *	11.46	C ₁₀ H ₁₂ O ₄	196.0733	-1.53	[M+H] ⁺	197, 151, 109, 72
22	Lupeol*	39.70	C ₃₀ H ₅₀ O	426.3847	-3.52	[M+H] ⁺	427, 409, 229, 217
23	Ursa-12,18-dien-3-ol**	39.54	C ₃₀ H ₄₈ O	424.3693	-2.83	[M+H] ⁺	426, 425, 407, 271
24	Marsformosanone**	36.86	C ₃₀ H ₄₆ O	422.3535	-3.32	[M+H] ⁺	423, 269, 243, 229
Amino Aldehydes							
25	Histidinal*	40.85	C ₆ H ₉ N ₃ O	139.0744	-1.44	[M+H] ⁺	140, 122, 81
Alkaloids							
26	2-Phenylethylamine**	5.37	C ₈ H ₁₁ N	121.0891	0	[M+H] ⁺	122, 105, 80
Phenolic acid							
27	Benzaldehyde	16.94	C ₇ H ₆ O	106.0419	0	[M+H] ⁺	107, 79, 77
28	Gallic acid	2.44	C ₇ H ₆ NO ₅	170.0205	-5.88	[M-H] ⁻	169,125, 97, 81
29	4-Hydroxy-2-oxopentanoate	40.95	C ₅ H ₈ O ₄	132.0424	-1.94	[M-H] ⁻	131,113, 88
30	2-Dehydropantoate	40.74	C ₆ H ₁₀ O ₄	146.0582	2.05	[M-H] ⁻	145, 118, 77
31	Methyl gallate*	8.30	C ₈ H ₈ O ₅	184.0362	-5.43	[M-H] ⁻	168, 139, 123
32	Ellagic acid*	15.03	C ₁₄ H ₆ O ₈	302.0059	-1.32	[M+H] ⁺	300, 283, 230
33	(S)-4-Hydroxymandelate	10.61	C ₈ H ₈ O ₄	168.0419	-2.38	[M+H] ⁺	169, 151, 109, 93
34	(R)-3-(3,4-Dihydroxyphenyl) lactate*	13.63	C ₉ H ₁₀ O ₅	198.0521	-3.53	[M-H] ⁻	197, 169, 140
35	4-Hydroxyphenylacetate*	12.69	C ₈ H ₈ O ₃	152.047	-1.97	[M+H] ⁺	153, 125, 111
36	(R)-2-Benzylsuccinate**	16.27	C ₁₁ H ₁₂ O ₄	208.0732	-1.9	[M+H] ⁺	209, 191, 177
37	p-Hydroxybenzoic acid**	14.01	C ₇ H ₆ O ₃	138.0314	-2.17	[M+H] ⁺	139, 111, 93, 65
38	p-Coumaric acid**	13.30	C ₉ H ₈ O ₃	164.0464	-5.49	[M-H] ⁻	163, 147, 119, 93
Quinone							
39	6-Methyl-8-hydroxy-1,4-naphthoquinone*	24.26	C ₁₃ H ₁₂ O ₅	248.0680	-2.02	[M+H] ⁺	249, 217, 161, 143
40	Xylopyrin*	19.65	C ₂₂ H ₁₈ O ₉	426.0937	-3.29	[M+H] ⁺	427, 275, 153, 108
41	3',5'-Diacetoxyacetophenone	16.08	C ₁₂ H ₁₂ O ₅	236.0683	-0.42	[M+H] ⁺	237, 193, 177
42	Demethylphylloquinol**	38.24	C ₁₅ H ₂₀ O ₄	438.3486	-2.74	[M+H] ⁺	439, 393, 249, 201
43	4-Prenylphlorisobutyrophenone**	10.21	C ₃₀ H ₄₆ O ₂	264.1356	-2.27	[M+H] ⁺	265, 247, 203, 187
44	Eremopetasinorone A **	12.29	C ₁₃ H ₁₈ O ₂	206.1303	-1.94	[M+H] ⁺	207, 189, 174, 149
45	Carnocin CP 5**	16.55	C ₂₃ H ₁₉ N ₃ O ₅ S	449.1030	-2.00	[M-H] ⁻	448, 327, 284, 255
Steroids							
46	4α-Hydroxymethyl-4β-methyl-5α-cholesta-8-en-3β-ol	39.97	C ₂₉ H ₅₀ O ₂	428.3645	-2.56	[M-H] ⁻	429, 219, 191, 165
47	3-Dehydroteasterone	39.04	C ₂₈ H ₄₆ O ₄	446.3383	1.51	[M+H] ⁺	447, 351, 191
48	4,4-Dimethylzymosterol	40.97	C ₂₉ H ₄₈ O	412.3695	-2.91	[M+H] ⁺	413, 395, 241

Table 1. Putative identification of metabolite in ebony leaves and wood extracts (*Continued*)

No	Name of Metabolites	RT	Formula	MW	Error mass (ppm)	Ion mode	MS-MS
49	3-(4-Ethylphenoxy)-4-oxo-4H-chromen-7-yl 2-furoate** Amino acid	26.99	C ₂₂ H ₁₆ O ₆	376.0938	-2.39	[M+H] ⁺	377, 257, 173
50	5-Aminopentanoate**	1.23	C ₁₅ H ₁₁ NO ₂	117.0789	-0.85	[M+H] ⁺	118, 101, 70
51	L-Tryptophan**	7.40	C ₁₁ H ₁₂ N ₂ O ₂	204.0895	-1.96	[M+H] ⁺	205, 188, 170, 149
52	L-Isoleucine**	1.90	C ₆ H ₁₃ NO ₂	131.0944	-4.58	[M+H] ⁺	132, 116, 86, 69
53	L-Phenylalanine**	3.26	C ₉ H ₁₁ NO ₂	165.0788	-1.20	[M+H] ⁺	166, 149, 131, 103
54	Ethyl 3,5-bis[(4-nitrobenzoyl) amino] benzoate** Fatty acid	14.32	C ₂₃ H ₁₈ N ₄ O ₈	478.1105	-3.76	[M-H] ⁻	477, 205, 163
55	(9S)-HPODE	34.84	C ₁₈ H ₃₂ O ₄	312.2298	-1.60	[M-H] ⁻	311, 275, 223
56	Colneleate**	35.48	C ₁₈ H ₃₀ O ₃	294.2190	-1.70	[M-H] ⁻	293, 275, 235, 183
57	Linoleate**	36.22	C ₁₈ H ₃₂ O ₂	280.2395	-2.50	[M+H] ⁺	281, 263, 245, 175
58	9,10-Epoxy-10,12Z,15Zoctadecatrienoate** Saccharide	33.63	C ₁₈ H ₂₈ O ₃	292.2032	-2.05	[M+H] ⁺	293, 278, 277, 249
59	Galactitol*	1.39	C ₆ H ₁₄ O ₆	182.0782	-3.30	[M-H] ⁻	181, 163, 131, 113

*) Only identified in the ebony wood extract

**) Only identified in ebony leaves extract

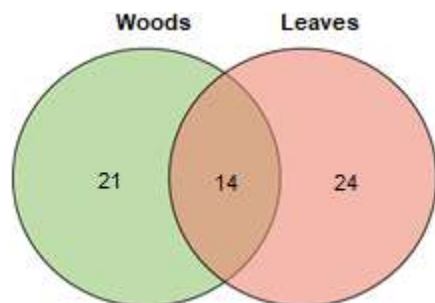


Fig 2. Venn diagram of the putatively identified compound in the ebony leaves and wood

Flavonoid

Flavonoids commonly give yellow color to higher plants, including ebony. In addition, flavonoids also play an important role as natural antioxidants and anticancer [14]. In ebony leaves and wood extracts, we identified ethyl 1,3-dihydroxy-2-naphthoate (1), a flavonoid compound detected at a retention time of 24.7 min. This compound was identified in the positive ionization mode with m/z 233 [M+H]⁺, 218 [M+H-CH₃]⁺, 190 [M+H-CH₃-CO]⁺, and 161 [M+H-CH₃-CO-COH]⁺.

Other flavonoid compounds putatively identified only in the ebony wood extracts were gibberellin A5 (2), 3-methylplumbagin (3), rutin (4), kaempferol 3-(2''-galloyl)glucoside (5), diosindigo A (6), apigenin (7), palomid 529 (8), daidzein (9). While those identified only in the leaves extracts were kaempferol (10), Kaempferol 3-glucuronide (11), (+)-dihydrokaempferol (12), quercetin 3-O-rhamnoside (13), epicatechin gallate (14).

Terpenoid

As we know, terpenoids function as a protector against microbes and insects [15]. So, maybe because of this, ebony wood is not easily damaged even if buried in the ground for decades. A total of five terpenoid compounds were identified in the leaves and wood extracts of ebony, consisting of hemigossypolone (15), betulinic acid (16), (6aR,11aR)-3,9-dihydroxypterocarpan (17), (2S)-naringenin (18), and betulinolaldehyde (19).

Compound (15) was identified at a retention time

of 35.8 and fragmented at m/z 272 $[M-H]^-$, 219 $[M-H-OH-CH-CH_2]^-$, and 203 $[M-H-OH-CH_2-CH_2-CH_3]^-$. In addition, three compounds were only identified in the wood extract, namely pomolic acid (20), phlorisobutyrophenone (21), and lupeol (22), as well as two compounds that were only identified in the leaf extract, namely ursal-12,18-dien-3-ol (23), marsformosanone (24).

Amino Aldehydes

In this study, histidinal (25) is a compound from the amino aldehyde group identified in the wood extract of ebony. This compound was detected at 40.9 min and fragmented at m/z 140 $[M+H]^+$, 122 $[M+H-H_2O]^+$, and 81 $[M+H-H_2O-C_2-NH_3]^+$.

Alkaloid

One compound from alkaloids that have been putatively identified in ebony leaves is 2-phenylethylamine (26). Compound (26) was detected at a retention time of 5.37 min. This compound was identified based on its fragmentation in the positive ionization mode with m/z 122 $[M+H]^+$, 105 $[M+H-NH_2]^+$, and 80 $[M+H-NH_2-C_2]^+$ [16].

Phenolic Acids

A total of five compounds from the phenolic acid group were putatively identified in the extracts of ebony leaves and wood. The five compounds are benzaldehyde (27), gallic acid (28), 4-hydroxy-2-oxopentanoate (29), 2-dehydropantoate, and (30). Benzaldehyde (27) was detected at a retention time of 16.9 min, with its fragmentation producing peaks at m/z 107 $[M+H]^+$, 79 $[M+H-CO]^+$, and 77 $[M+H-CO-H_2]^+$.

In addition, five other phenolic acid group compounds that were only identified in the ebony wood extract, namely methylgallate (31), ellagic acid (32), (S)-4-hydroxymandelate (33), (R)-3-(3, 4-dihydroxyphenyl) lactate (34), 4-hydroxyphenylacetate (35), and three compounds identified only in leaf extracts, namely (R)-2-benzylsuccinate (36), p-hydroxybenzoic acid (37), p-coumaric acid (38).

Quinone

A quinone is a group of compounds that gives a

unique color to ebony leaves and wood. Three compounds were identified in the wood extract, namely 6-methyl-8-hydroxy-1,4-naphthoquinone (39), xylopyrin (40), and 3',5'-diacetoxyacetophenone (41). Compound (42) was identified at a retention time of 24.26 min and fragmented to give m/z at 249 $[M+H]^+$, 217 $[M+H-CH_3-OH]^+$, 161 $[M+H-CH_3-OH-C_2O_2]^+$, and 143 $[M+H-CH_3-OH-C_2H_2O_2-O]^+$. At the same time, the ebony leaves extract contains four compounds from the quinone group consisting of demethylphyloquinol (43), 4-prenylphlorisobutyrophenone (43), eremopetasinorone A (44), carnocin CP 5 (45).

Steroid

Three compounds belonging to the steroid group were successfully detected and identified in the extracts of ebony leaves and wood, namely 4 α -hydroxymethyl-4 β -methyl-5 α cholesta-8-en-3 β -ol (46), dehydrotosterone (47), 4,4-dimethylzymosterol (48). The compound 4 α -hydroxymethyl-4 β -methyl-5 α cholesta-8-en-3 β -ol (46) was detected at a retention time of 40 min and fragmented at m/z 429 $[M-H]^-$, 219 $[M-H-C_{14}H_{25}-OH]^-$, 191 $[M-H-C_{14}H_{25}-OH-C_2H_4]^-$, and 165 $[M-H-C_{14}H_{25}-OH-C_4H_6]^-$ [11]. In addition, the compound 3-(4-ethylphenoxy)-4-oxo-4H-chromen-7-yl 2-furoate (49) was also identified, which was only detected in the ebony leaves extract.

Amino Acid, Fatty Acid, and Saccharide

Ebony leaves extract contains five amino acid group compounds, namely 5-aminopentanoate (50), L-tryptophan (51), L-isoleucine (52), L-phenylalanine (53), and ethyl 3,5-bis[(4-nitrobenzoyl) amino] benzoate (54). 5-aminopentanoate (55) was detected at a retention time of 1.23 min with its fragmentation yielding m/z at 118 $[M+H]^+$, 101 $[M+H-OH]^+$, and 70 $[M+H-OH-CO-H_2]^+$ [17].

(9S)-HPODE (56) was identified in ebony leaves and wood extracts. Linoleate (57) and 9,10-epoxy-10,12Z,15Zoctadecatrienoate (58) were fatty acids identified only in ebony leaf extract, while colneleate (56) was identified in ebony stem and leaf extracts. The colneleate compound 56 was detected at a retention time of 35.48 min. The fragmentation that occurred in this

compound (56) were m/z 293 [M-H]⁻, 275 [M-H-H₂O]⁻, 235 [M-H-H₂O-CH₂-H₂]⁻, and 183 [M-H-H₂O-CH₂-H₂-C₄H₄]⁻ [18].

Galactitol (59) is a saccharide group identified only in an ebony wood extract with a retention time of 1.39 min and fragmented at m/z 181 [M-H]⁻, 163 [M-H-H₂O]⁻, 131 [M-H-H₂O-CH₃-OH]⁻, and 113 [M-H-2H₂O-CH₃-OH]⁻.

Clustering of Ebony Leaves and Wood Extracts

Chromatogram profiles of ebony leaves and wood extracts from the three provinces in Sulawesi had relatively different separation profiles. However, it is not easy to distinguish it using eye visualization. Therefore, multivariate analysis, such as PCA, is needed to classify or differentiate leaves and wood extracts of ebony. The basic principle of clustering with PCA is to simplify variables by reducing dimensions and providing an overview of sample grouping through principal components (PC).

Fig. 3 shows the PCA score plot of the ebony extract using the peak area of identified compounds as the variable. The two main components often used in PCA analysis are PC1 and PC2. The two PCs show a diversity of data that can be explained by the variables used. In this study, the PCA results showed that leaves and wood extract of ebony could be separated with total variants from the two PC, which is about 85% (PC1 = 48% and PC2 = 37%). The two PCs can already explain most of the data

variability (at least 70%) [19]. The grouping of the ebony leaves and the wood extract was obtained in the PC2.

Evaluation of Analytical Performance

This study also evaluates the analytical performance to ensure the method used has good repeatability. The evaluated parameters are the repeatability of the retention time and the area of the peak numbers 40 and 7 analyzed for three days with three replications. The evaluation results show that the method used has good consistency based on the repeatability of retention time and band area. It has a % relative standard deviation (RSD) of less than 5% [20], as shown in Table 2.

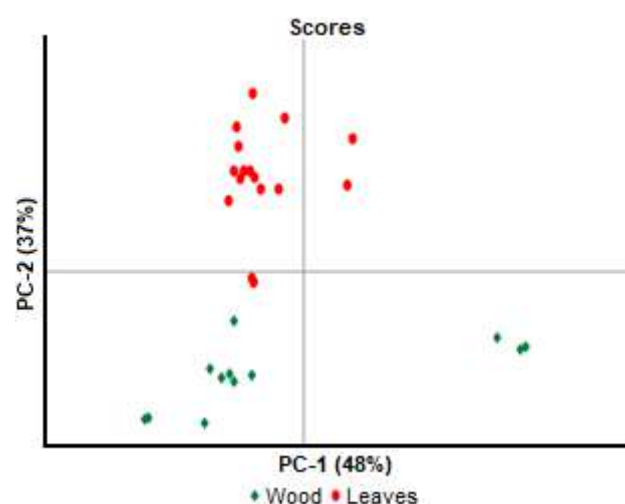


Fig 3. PCA plot of ebony leaves and wood extracts

Table 2. Evaluation of the analytical performance of the method (retention time and peak area of compound number 40 for wood and 7 for leaves)

Replication	Day 1		Day 2		Day 3	
	Wood	Leaves	Wood	Leaves	Wood	Leaves
Retention time						
1	19.86	14.12	19.73	14.15	19.81	14.09
2	19.74	14.12	19.76	14.12	19.85	14.07
3	19.75	14.09	19.82	14.06	19.78	14.09
Mean	19.78	14.11	19.77	14.11	19.81	14.08
% RSD	0.34	0.12	0.23	0.32	0.18	0.08
Peak area						
1	63462836	184356116	634798083	172252497	49589761	192765330
2	63218698	188160978	638253596	172375975	49769599	195513112
3	61695175	189204522	657139855	176205074	48694268	191175169
Mean	62792236	187240539	643397178	173611182	49351209	193151204
% RSD	1.53	1.26	1.87	1.23	1.17	1.14

■ CONCLUSION

Separation and putative identification of ebony leaves and wood extracts from three different provinces in Sulawesi, Indonesia, using LC-MS/MS, were successfully identified about 59 compounds. Approximately 14 compounds were identified in leaves and wood, 24 were identified only in leaves, and 21 in wood. Those compounds come from flavonoids, terpenoids, amino aldehydes, alkaloids, quinones, phenolic acids, steroids, amino acids, fatty acids, and saccharides. Therefore, PCA could cluster ebony leaves and wood extract with the total variants from PC-1 and PC-2 about 85% using the peak area of the identified metabolites.

■ ACKNOWLEDGMENTS

The authors gratefully acknowledged World Resources Institute (WRI) Forest Program grant (project code: 04682 periods 1 March 2019–30 September 2020) with the title "Timber tracking project IPB-WRI: a collection of physical timber reference material and setting up a reference data building pipeline for DNA of commercial timber species (*Diospyros celebica*. Bakh)" provided by Norwegian International Climate and Forest Initiative (NICFI).

■ REFERENCES

- [1] Karlinasari, L., Noviyanti, N., Purwanto, Y.A., Majiidu, M., Dwiyantri, F.G., Rafi, M., Damayanti, R., Harnelly, E., and Siregar, I.Z., 2021, Discrimination and determination of extractive content of ebony (*Diospyros celebica* Bakh.) from Celebes sland by near-infrared spectroscopy, *Forests*, 12 (1), 6.
- [2] Yuniarti, N., Syamsuwida, D., and Aminah, A., 2012, Dampak perubahan fisiologi dan biokimia benih eboni (*Diospyros celebica* Bakh) selama penyimpanan, *Jurnal Penelitian Hutan Tanaman*, 10 (2), 65–71.
- [3] Arianti, A., Budiarmo, E., Budi, A.S., and Kusuma, I.W., 2016, Analisis fitokimia ekstrak kayu eboni (*Diospyros celebica* Bakh), *Warta Rimba*, 4 (2), 61–68.
- [4] Kartini, K., Khumaidi, A., Khaerati, K., and Ihwan, I., 2018, Ekstrak etanol daun eboni menurunkan kadar glukosa darah tikus jantan yang diinduksi aloksan, *Jurnal Veteriner.*, 19 (3), 329–334.
- [5] Nugrahaini, A.W., Maulida, M.F., Khumaidi, A., 2020, Aktivitas antibakteri fraksi serbuk kayu eboni (*Diospyros celebica* Bakh.) terhadap *Escherichia coli* dan *Staphylococcus aureus*, *J. Sains Farm. Klin.*, 7 (3), 194–201.
- [6] Chen, J., Ni, C., Lou, J., and Peng, W., 2018, Molecules and functions of rosewood: *Diospyros celebica*, *Arabian J. Chem.*, 11 (6), 756–762.
- [7] Yang, Q., Zhang, A., Miao, J., Sun, H., Han, Y., Yan, G., Wu, F., and Wang, X., 2019, Metabolomics biotechnology, applications, and future trends: A systematic review, *RSC Adv.*, 9 (64), 37245–37257.
- [8] Zeki, Ö.C., Eylem, C.C., Reçber, T., Kır, S., and Nemutlu, E., 2020, Integration of GC-MS and LC-MS for untargeted metabolomics profiling, *J. Pharm. Biomed. Anal.*, 190, 113509.
- [9] Fan, M., Lian, W., Li, T., Fan, Y., Rao, Z., Li, Y., Qian, H., Zhang, H., Wu, G., Qi, X., and Wang, L., 2020, Metabolomics approach reveals discriminatory metabolites associating with the blue pigments from *Vaccinium bracteatum* thunb. leaves at different growth stages, *Ind. Crops Prod.*, 147, 112252.
- [10] Rafi, M., Karomah, A.H., Heryanto, R., Septaningsih, D.A., Kusuma, W.A., Amran, M.B., Rohman, A., and Prajogo, B., 2022, Metabolite profiling of *Andrographis paniculata* leaves and stem extract using UHPLC-Orbitrap-MS/MS, *Nat. Prod. Res.*, 36 (2), 625–629.
- [11] Baloglu, M.C., Llorent-Martínez, E.J., Aumeeruddy, M.Z., Mahomoodally, M.F., Altunoglu, Y.C., Ustaoglu, B., Ocal, M., Gürel, S., Bene, K., Sinan, K.I., and Zengin, G., 2019, Multidirectional insights on *Chrysophyllum perpulchrum* leaves and stem bark extracts: HPLC-ESI-MSⁿ profiles, antioxidant, enzyme inhibitory, antimicrobial and cytotoxic properties, *Ind. Crops Prod.*, 134, 33–42.
- [12] Llorent-Martínez, E.J., Ruiz-Riaguas, A., Sinan, K.I., Bene, K., Cordova, M.L.F., Picot-Allain, C., Mahomoodally, F., Saleem, H., and Zengin, G.,

- 2020, Exploring chemical profiles and bioactivities of *Harungana madagascariensis* Lam. ex Poir. leaves and stem bark extracts: A new source of procyanidins, *Anal. Lett.*, 53 (3), 399–412.
- [13] Sun, K., Su, C., Li, W., Gong, Z., Sha, C., and Liu, R., 2021, Quality markers based on phytochemical analysis and anti-inflammatory screening: An integrated strategy for the quality control of *Dalbergia odorifera* by UHPLC-Q-Orbitrap HRMS, *Phytomedicine*, 84, 153511.
- [14] Chin, S., Behm, C., and Mathesius, U., 2018, Functions of flavonoids in plant-nematode interactions, *Plants*, 7 (4), 85.
- [15] Tholl, D., 2015, Biosynthesis and biological functions of terpenoids in plants, *Adv. Biochem. Eng./Biotechnol.*, 148, 63–106.
- [16] Bjerrum, J.T., Wang, Y., Hao, F., Coskun, M., Ludwig, C., Günther, U., and Nielsen, O.H., 2015, Metabonomics of human fecal extracts characterize ulcerative colitis, Crohn's disease and healthy individuals, *Metabolomics*, 11 (1), 122–133.
- [17] Ponnusamy, K., Choi, J.N., Kim, J., Lee, S.Y., and Lee, C.H., 2011, Microbial community and metabolomic comparison of irritable bowel syndrome faeces, *J. Med. Microbiol.*, 60 (6), 817–827.
- [18] Eschen-Lippold, L., Rothe, G., Stumpe, M., Göbel, C., Feussner, I., and Rosahl, S., 2007, Reduction of divinyl ether-containing polyunsaturated fatty acids in transgenic potato plants, *Phytochemistry*, 68 (6), 797–801.
- [19] Ďuriš, V., Bartková, R., and Tírpáková, A. 2021, Principal component analysis and factor analysis for an Atanassov IF data set, *Mathematics*, 9 (17), 2067.
- [20] International Council for Harmonisation, 1995, *Validation of Analytical Procedures: Text and methodology Q2(R1)*, ICH Harmonised Tripartite Guideline, CPMP/ICH/381/95, Geneva.

Selecting Suitable Functionals and Basis Sets on the Study Structural and Adsorption of Urea-Kaolinite System Using Cluster Method

Nur Najwa-Alyani Mohd Nabil and Lee Sin Ang*

Faculty of Applied Sciences, Universiti Teknologi MARA, 02600 Arau, Perlis, Malaysia

* Corresponding author:

email: anglee631@perlis.uitm.edu.my

Received: September 6, 2021

Accepted: December 2, 2021

DOI: 10.22146/ijc.68599

Abstract: Kaolinite is an essential mineral with numerous applications across many sectors. One of them is in the agricultural industry, in which it is a crucial component in the method of controlled-release fertilizer. This manuscript reports the use of different functionals and basis sets on the structural and electronic properties of kaolinite's surface, intending to find reliable methods among those tested. Four different functionals, B3LYP, CAM-B3LYP, M06-2X, TPSSSTPSS, complemented with various basis sets, were used in this study. The results show that TPSSSTPSS complement with 6-311G** provides good agreement with previous research and experimental results among different functionals and basis sets used. The quantitative analysis was done to optimize the kaolinite molecule. Selected extrema points were used to place the urea molecule for the interaction of urea-kaolinite studies. The urea's interaction with kaolinite was reported at a different interaction site in the gas phase and different orientations of the urea molecule. Urea molecule was optimized above the Al-O and Si-O surfaces with their energy difference calculated. Our results showed that both surfaces act as promising adsorbents among the different orientations of the urea on both the Al-O and Si-O surfaces. However, Al-O, and Si-O had another preferable interaction site to the urea molecules.

Keywords: Density functional theory; kaolinite; urea; electrostatic potential surface; kaolinite-urea interaction

■ INTRODUCTION

Nowadays, controlled-release fertilizers (CRF) have become a new trend to minimize environmental pollution. CRF can control and delay the nutrients release in synchrony with the sequential needs of the plants. Thus, this type of fertilizer will enhance the efficiency of the uptake of the nutrients. Engineering designs are searching for an inexpensive chemical mineral that can be modified to achieve their target as CRF. Kaolinite is one of the materials that still generate interest in different research fields [1-5]. Kaolinite has been chosen as the nanostructure material to act as CRF due to its ability to reduce nutrient losses, increase nutrient-used efficiency and protect the environment [6-12].

Kaolinite has a layer with a large active surface area. Therefore, it can be exploited to enhance surface interaction with fertilizer elements. Kaolinite with chemical formula $\text{Al}_2\text{Si}_2\text{O}_5(\text{OH})_4$, as shown in Fig. 1, is a

1:1 dioctahedral phyllosilicate compound. A single-layer of kaolinite is a SiO_4 tetrahedral sheet and AlO_6 sheet, connected by oxygen atoms between the sheets. One hydrogen atom is bonded to the oxygen between the sheets (inner hydroxyl). In contrast, the other six hydrogen atoms are associated with the oxygen at the lower side of the AlO_6 sheet. This O-H is usually known as inner surface hydroxyl.

This paper focuses on both surfaces of AlO_6 (Al-O) and SiO_4 (Si-O) as they can function as H-acceptors in forming H-bonds to drive the intercalation of molecules [8].

Brindley and Robinson first reported the crystal structure of kaolinite (with non-H atoms) using powder X-ray diffraction [13]. However, earlier stages of research on kaolinite, show conflicting results on the structure of kaolinite, which then solved with space group C1 on both theoretical and experimental studies [14].

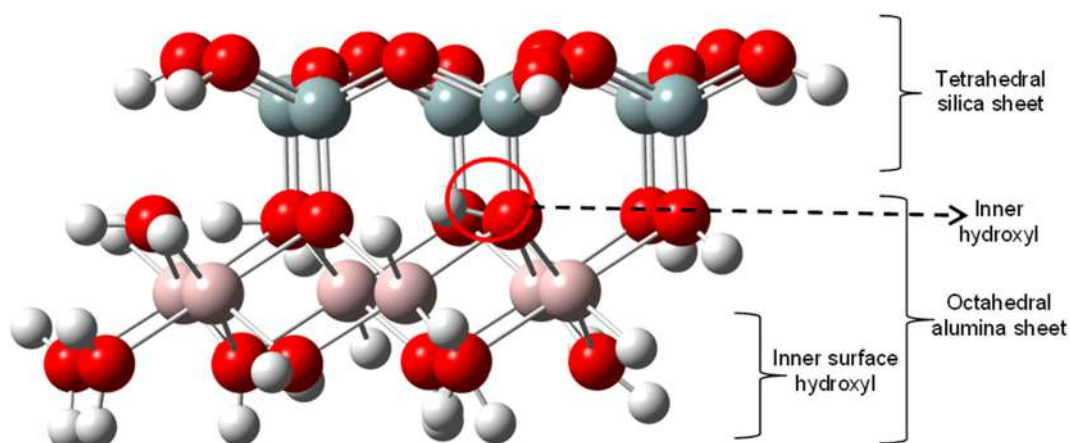


Fig 1. Kaolinite of one ring of the SiO_4 tetrahedral attached with one ring of the AlO_6 octahedral sheets (Red = oxygen, grey = silicon, pink = aluminum, and white = hydrogen)

Silicon, aluminum, and oxygen atoms' positions had resolved from the experimental view, except the determination of the exact positions of hydrogen, which is limited by the technique used. Furthermore, the weak interaction of X-rays with hydrogen atoms makes them unable to provide accurate hydrogen position information. The discrepancy of the experimental results could be due to different sample environments, sources of samples, and refinement methods. However, results from Bish et al. from the diffraction experiment have become a marker for computational studies [15].

Theoretical studies using the ab initio method or density functional theory have been performed on the atomic structure of kaolinite to complement the experimental data [14,16-22]. Here we focus on the

hydroxyl bonds of the kaolinite's surface as they are responsible for the adsorption with external molecules. Table 1 shows the different computational methods used with their hydroxyl bond lengths compared to the experimental data from Bish et al. study [15]. B3LYP function was used twice in the previous calculation where the kaolinite material used is in cluster compound [18-19]. It is convinced that B3LYP was more reliable functional than other DFT methods when dealing with OH group vibrational properties, especially when hydrogen bonds are present [19]. Castro and Martin studied different kaolinite sizes where no significant result showed affected from different sizes. Improvement of the basis set was made later. However, only inner hydroxyl bond length has a length different $\sim 0.01 \text{ \AA}$

Table 1. Hydroxyl bond length (in \AA) from previous theoretical studies of kaolinite

	Experimental Study		Computational Study					
	Bish et al. [20]	Hess and Saunders [21]	Hobbs et al. [23]	Balan et al. [22]	Castro and Martin [23]	Tosoni et al. [24]	Hu and Michaelides [25]	White et al. [16]
Computational method		HF/STO-3G HF/6-21G	CA-PZ/DZP	PBE/PW	RHF/3-21G*, B3LYP/3-21G* At different sizes of kaolinite	B3LYP/6-31G**	PBE/PW	GGA-BLYP/DNP
Inner hydroxyl bond lengths	0.974	0.99	0.994	0.980	0.962–0.993	0.969	0.974	0.974
Inner surface hydroxyl bond lengths *	0.976		0.991	0.975	0.963–0.987	0.964	0.969	0.972
	0.983					0.965	0.970	0.970
	0.979					0.962	0.969	0.970

*Some paper gives three different bond lengths for inner surface hydroxyl bond length

compared to Bish et al., while others are not much different from previous results. PBE was another function that was repetitively used in previous studies. It routinely predicts hydrogen bond strength better than the results obtained from other quantum chemistry methods with a large basis set. Results also show that PBE has less bond length than Bish et al. bond length than B3LYP functional results.

Besides confirming the kaolinite structure, research on the interaction between kaolinite's surface with guest molecules is also of interest [2,24-29]. Two types of approaches were used previously, either a) periodic model where the kaolinite is infinite, and calculation of interaction is in bulk view [2,24,28], and b) kaolinite is modeled with finite-size clusters [25-27,29-30]. For both approaches, urea is known as one of the guess molecules used to interact with the kaolinite for CRF purposes [11]. Therefore, an experimental-based study was done to find the properties of the urea-kaolinite compound [31-33]. Furthermore, further investigation by the computer simulation was done concerning the possible orientation of urea in the kaolinite-urea intercalation complex. It was pointed out that the dipole moment vectors of urea molecules tend to point towards the silica sheet. Thus, the character of the hydrogen bonds can be described more precisely in simulation [28,34]. However, these studies were done in a bulk mode where kaolinite is infinite, and many urea molecules are intercalated between kaolinite structures.

For this manuscript, the finite size of the kaolinite structure, as shown in Fig. 1, was applied. Previous studies have shown that systematically clustering a structure would lead its energy closer to the experimental values as the structure goes bigger [35]. However, the finite structure still gives out the same interaction potential as infinite structure [34]. To have systems that can react as infinite structures, commonly used in the theoretical study, is by terminating the dangling bond of the structure with hydrogen [2,24,28]. Thus, this article is set to build a kaolinite cluster model and further explore the adsorption properties of urea on the kaolinite surface.

■ COMPUTATIONAL DETAILS

For this study, the kaolinite structure is taken from

Bish et al. [15], where the structure of kaolinite is of a triclinic cell and belongs to the C1 space group (sub-class point group of triclinic crystal system). This study used a single ring of Si-O combined with a single ring of Al-O to represent the Si-O sheet and Al-O sheet of kaolinite, respectively. Dangling bonds were terminated by hydrogens, resulting in 72 atoms of kaolinite used in this study. The hydroxyl positions were completely optimized while other atoms were frozen to their original positions. The inner hydroxyl was labeled as OH₁₁₋₁₂ between the tetrahedral silica and octahedral alumina sheets. The inner surface hydroxyls are the hydrogen under octahedral alumina sheet was labeled as OH₁₃₋₁₄, OH₂₀₋₂₈, OH₁₉₋₃₈, OH₃₃₋₄₇, OH₄₂₋₄₈, and OH₅₁₋₅₂. Urea molecule was added at three different initial positions of the geometrically relaxed kaolinite cluster to study the interaction between the kaolinite and urea. Only the interaction site and urea were fully optimized, while other atoms were frozen throughout the calculation. Interaction sites are sites that are adjacent to the urea molecule. For example, as urea was placed on top of Si-O, only hydroxyl of Si-O, and urea were optimized. For this investigation, we assessed the capability of different sites to absorb urea molecules. However, only four of the most stable configurations were selected for analysis.

Different functionals of B3LYP, CAM-B3LYP, M06-2X and TPSS/PSS as implemented in Gaussian09 [36] combined with different basis sets (6-31G, 6-31G(d), 6-31G(d,p), 6-311G(d,p), 6-311++G(d,p) and DEF2-TZVP) were used in this study. The inclusion of the functional B3LYP with the 6-31G(d) basis set is due to its extreme popularity in adsorption on clay minerals and proper function for electrostatic interaction [25-27,29]. CAM-B3LYP functional is said to be advancement functional of B3LYP in the long-range calculation [37]. M05-2X was discussed in a previous study able to complement the result of B3LYP [38]. However, the newer and improved M06-2X had a lower bond length error than the M05-2X [39]. Thus, this study included these functions in the calculation of kaolinite. The interaction energy (IE) of optimized structure is calculated as the difference between the total

energy of complex and the whole energies of two separate molecules. The basis set superposition error (BSSE) was corrected by the empirical counterpoise method, and treatment of dispersion is included in this study. [40]. D3BJ gives less average error than non-dispersion corrected calculation and D3 dispersion-corrected DFT scheme [41]. The approach used in the current work can be referred to in our previous work [42].

RESULTS AND DISCUSSION

Energy Study

Fig. 2(a) shows the bond length of hydroxyl calculated in the gas phase with different basis set in B3LYP functional. All the hydroxyl bond lengths obtained are shorter than the Bish et al.. The smallest size basis set used in this study, 6-31G, produces the closest

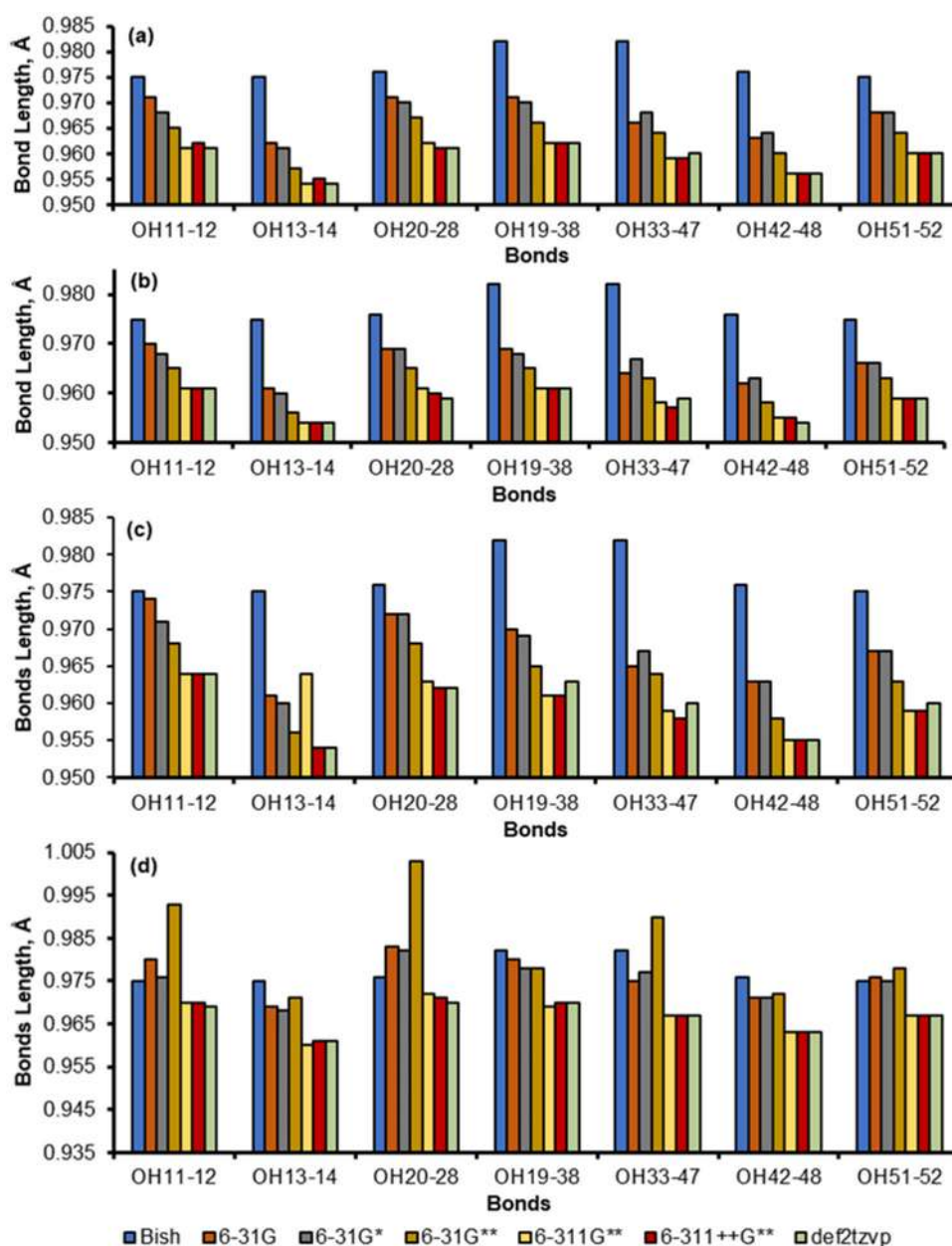


Fig 2. Hydroxyl bond lengths from different functionals and different basis sets. There are six basis sets being complemented with (a) B3LYP, (b) CAM-B3LYP, (c) M06-2X, and (d) TPSSTPSS functionals. The experimental value from Bish et al. is also included for comparison

value of experimental inner hydroxyl bond length (OH_{11-12} , 0.971 Å against 0.974 Å from Bish), compared to other larger basis sets used. Compared to the previous study of Tosoni et al. and Castro and Martin, the inner hydroxyl from B3LYP/6-31G in this study has the closest bond length to the experimental value [18-19]. For the inner surface hydroxyl bond in this study, the bond length is still in the same range as the previous research. Including polarization function (single or double) to this double zeta basis set shorten this bond length by about 0.007 Å at 6-31G* and by 0.010 Å at 6-31G**. The three triple zeta basis sets of 6-311G**, 6-311++G**, and DEF2-TZVP produce similar or equal bond lengths as the bar chart is flat. However, the bond length is 0.015 Å to 0.022 Å shorter than Bish et al.'s reported values. Adding diffuse function (++) to the triple zeta basis set does not provide any significant changes to the hydroxyl bond lengths if there are any at all. The results in Fig. 2(a) can be interpreted as the triple zeta basis set "stabilizes" the hydroxyl bond lengths, starting with 6-311G**.

Calculation using a different basis set with CAM-B3LYP, M06-2X, and TPSSTPSS functionals are shown in Fig. 2(b), 2(c), and 2(d). As is the case of B3LYP, all calculation of CAM-B3LYP and M06-2X functionals always has a bond length shorter than the experimental results. The same observations for B3LYP are also applicable here: for higher basis set 6-311G**, 6-311++G** and DEF2TZVP, hydroxyl bond lengths are a similar length and can be considered as consistent, and the diffuse and polarization functions do not give significant effect to the hydroxyl bond length.

Compared to the other functionals used, a few hydroxyl bond lengths under TPSSTPSS are more significant than the reported values. For example, double zeta basis set 6-31G** always resulted in the hydroxyl bond length longer than the experimental bond length, while the over- and under-estimation using 6-31G and 6-31G* are insignificant. Thus, the double zeta basis set provides fluctuated bond lengths and is unsuitable for describing the hydroxyl bond's length for the functional TPSSTPSS. However, the overall hydroxyl bond lengths of TPSSTPSS triple zeta basis sets are closer to the reported experimental values. The range difference is 0.006 to 0.015 Å, lower than the other functionals considered.

Fig. 3 shows the effect of the different functionals on the hydroxyl bond lengths, at basis set 6-311G**, since triple zeta basis set of 6-311G**, 6-311++G**, and DEF2TZVP do not show significant changes in the bond lengths (as seen in Fig. 2-3). Of the four functionals considered in this study, TPSSTPSS has the most hydroxyl bond length, similar to the experimental. For inner surface hydroxyl, this results still in the range with previous study bond length (refer to Table 1) as the hydroxyl bond length range from 0.961 – 0.971 Å. From this result, it shows that study on the kaolinite hydroxyl bond is reliable by using one ring with TPSSTPSS/6-311G** method.

A Quantitative Study of Kaolinite Electrostatic Surface Potential

The electrostatic potential (ESP) map is an essential

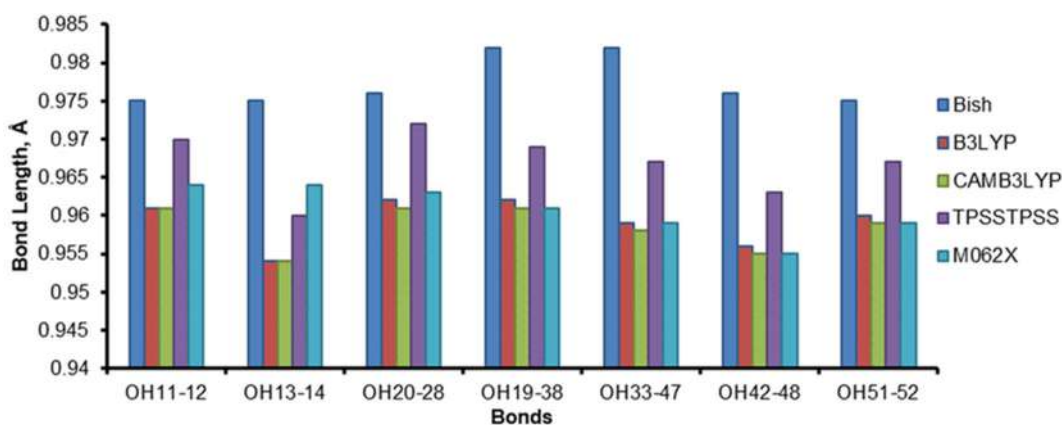


Fig. 3. Graph of various functional (basis set was fixed to 6-311G**)

tool for determining the physicochemical properties and explaining the interaction between molecules. However, in this report, an improvement of the potential map discussion for interaction between kaolinite and guest molecules was made. For the adsorption process of organic molecules, the ESP on the surface regions can provide information on the preferable site of the adsorption process. In Gaussview, ESP is represented using colors ranging from blue to red, in which blue indicates a positive surface, red is negative, and green is a neutral charge surface. The color represents the range of charges on the surface of kaolinite. This study also provides the maximum and minimum ESP values from the saddle point of energy range for maximum and minimum surfaces, as given in Table 2. The positive value in Table 2 shows that the site has less charge than the other place, and the negative value has more charges than the different areas of the map.

Fig. 4 shows the ESP surface of single ring kaolinite at Al-O top, Si-O top, and side views. It can be seen in Fig. 4 that the Si-O surface has a more robust red color surface compared to the Al-O surface, which indicates that the Si-O is an electron-deficient surface. It is due to the oxygen atoms on the Si-O surface. For the Al-O surface, the color varied from blue to yellow-reddish. Color changes are due to the structure of the Al-O surface having a variety of hydroxyl orientations. Some of the hydroxyls point out the kaolinite, shown as the blue surface, while others point to the middle of the kaolinite ring. For hydroxyl pointing to the center, the energy

contribution was included with sites atom (Al-O) and shown as yellow-reddish colored, which is less negative. Orientation of the hydroxyl at the Al-O was similar to previous experimental study results [43-44]. The middle ring hydroxyl of inner surface hydroxyl had tilted toward an empty octahedral site with one of it almost horizontal.

From Table 2, the maximum point appears more on the Al-O surface than the Si-O surface. The maximum points for Al-O surface are positive, ranging from 1.38 to 1.43 eV, while Si-O has a negative value of -0.60 eV for its maximum point. Minimum ESP value shows Al-O surface has energy range from -1.44 to 0.42 eV while Si-O surface has lower energy range from -2.04 to -1.86 eV. Energy differences on different surfaces indicate that the Al-O surface is an electron-abundant surface while Si-O is an electron-deficient kaolinite surface.

Table 2. Quantitative ESP energy of the kaolinite ESP surface

Site	Energy (eV)			
	Position	Maximum	Position	Minimum
Al-O	1	1.4094	1	0.4152
	2	1.3758	2	-1.2651
	3	1.4287	3	-1.4390
Si-O			1	-1.8637
	1	-0.5923	2	-2.0377
			3	-1.8642
			4	-1.9476

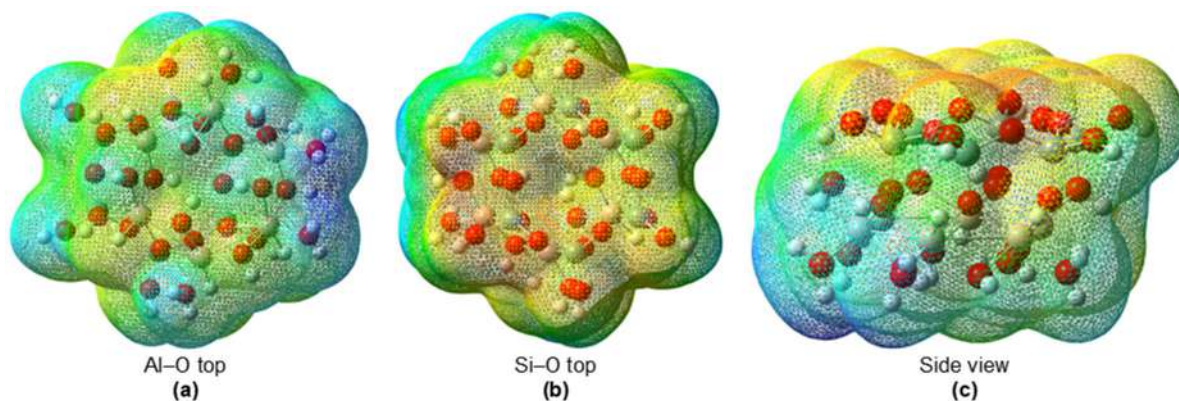


Fig 4. The ESP surface of the kaolinite

The location of the urea to study the interaction of kaolinite with urea is predicted using these extrema points in Table 2 and pointed as shown in Fig. 5. The extrema point always appears in the middle of the ring for both the Si-O surface and the Al-O surface. Maximum points are shown at the Al-O surface hydroxyl, specifically on top of hydrogens. As shown in Fig. 5, four hydroxyls exist in the middle of the kaolinite ring. However, only three hydroxyls had a maximum point which is OH₅₁₋₅₂, OH₁₃₋₁₄, and OH₁₉₋₃₆. As mentioned before, OH₂₀₋₂₈ is the hydroxyl that points to the middle of the kaolinite ring. Thus, at that site, the ESP energy on the surface is a combination of all-atoms at the hydroxyl side. The difference in orientation of hydroxyl affects their function as H-donor and H-acceptor. Minimum points are shown in the ring of Si-O, which was previously shown to act as a proton-acceptor when interacting with the guest molecule [29]. From this observation, it is predicted that the urea will interact at these extrema points. Thus, urea is placed on top of these extrema points and optimized. The proportion and energetic results are shown in Table 2 and Fig. 6.

Interaction of Kaolinite with Urea

Our qualitative and quantitative calculations of the ESP have confirmed preferential adsorption sites for urea on kaolinite surfaces. As mentioned in ESP results, the preferable interaction site is at the middle of the Al-O and

Si-O ring surface. Thus, urea was placed on the top of the surfaces and optimized. Optimized structures of urea and kaolinite are shown in Fig. 6, and energetic results are in Table 3. This study compares urea with individual Al-O and Si-O sheets and urea with kaolinite at different Al-O and Si-O surfaces. In Table 2, individual sheets of Si-O and Al-O interacting with urea are labeled as Si-O + urea and Al-O + urea. While kaolinite sheets interact with urea at the different surfaces are labeled as kaolinite + urea, with a bracket including the interaction surface (Al-O or Si-O).

Generally, Table 2 shows that all interaction involved has negative interaction energy, indicating that both surfaces can adsorb urea as suggested previously [2]. For the Al-O surface, interaction energy ranges from -0.9904 to -1.5825 eV, while -0.4252 to -0.6040 eV for the Si-O surface. Different energy shows that the Al-O surface has higher interaction energy than the Si-O surface, depicting that the urea prefers to attach at the Al-O sheet surface than the Si-O sheet surface. The previous experimental studies reported that urea prefers interaction at the Si-O sheets and suggest that it is due to the dual NH₂ of urea from the Raman and vibration view [31-32]. However, thermal study on this complex shows at the cooler temperature, the urea and hydroxyl surface of Al-O are brought closer together so that hydrogen bonding between the hydroxyls of the gibbsite-like layer of the Al-O sheet and the C=O group

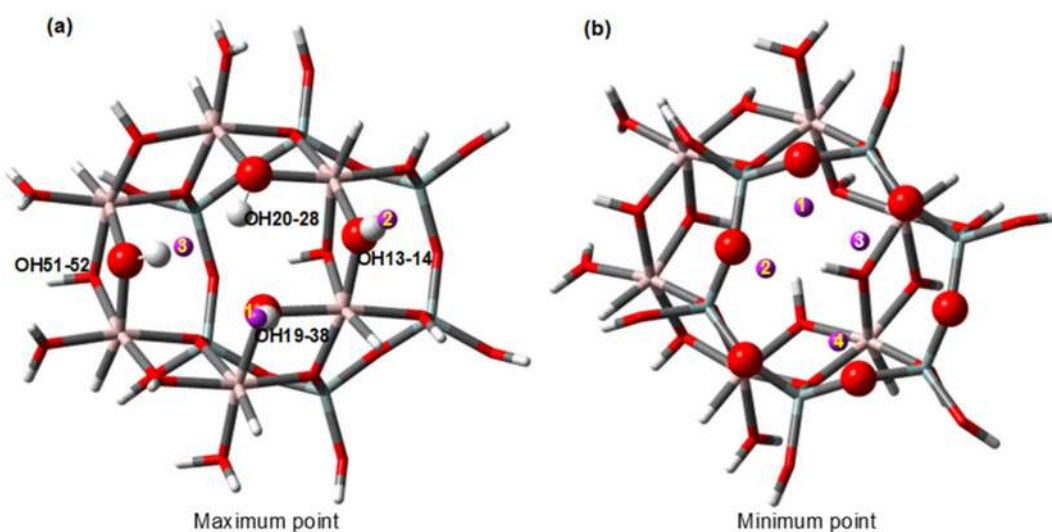


Fig 5. The minimum and maximum points on the Al-O, and Si-O surfaces. (Purple is the extrema point)

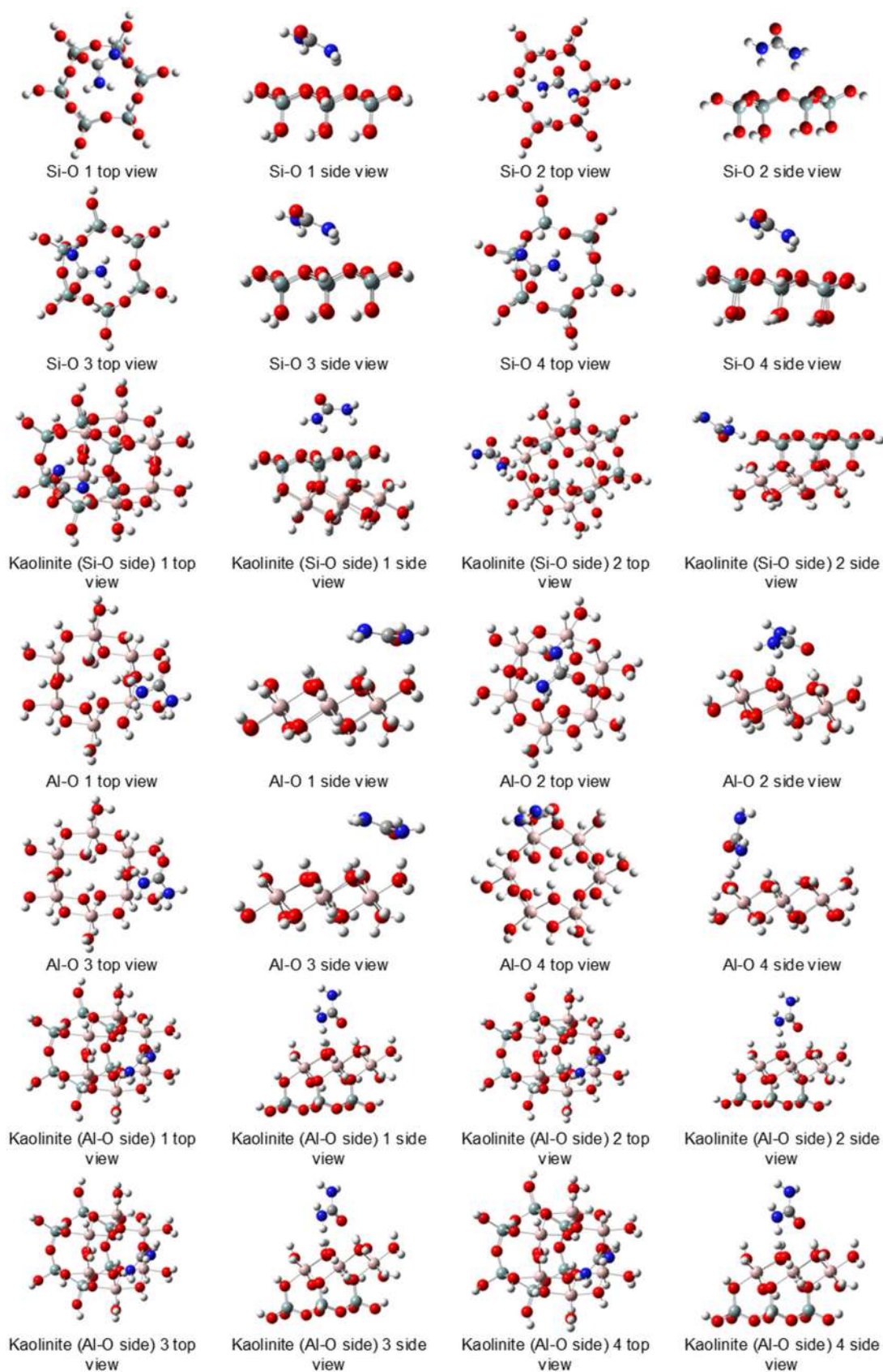


Fig 6. The optimized structures of kaolinite-urea clusters

Table 3. Interaction energy (IE) and the hydrogen bond

Structure	Position	eV	Bond Type	Bond Length (Å)
	1	-0.4529	N-H...O	2.6503
			N-H...O	2.6351
			N-H...O	2.3759
	2	-0.4252	N-H...O	2.2928
			N-H...O	2.4523
Si-O + urea	3	-0.4733	N-H...O	2.6474
			N-H...O	2.6891
			N-H...O	2.3613
	4	-0.5012	N-H...O	2.4520
			N-H...O	2.4132
			N-H...O	2.3130
Al-O + urea	1	-1.3835	O...H	1.7870
			N...H	1.7764
	2	-1.5825	O...H	1.7649
			N...H	2.2388
	3	-1.2458	N-H...O	1.9850
			N...H	1.8206
O...H			1.7319	
N...H			2.8443	
4	-0.9904	N...H	2.3649	
		O...H	1.8226	
Kaolinite (Si-O side) + urea	1	-0.5052	N-H...O	2.6066
			N-H...O	2.7972
			N-H...O	2.4232
	2	-0.6040	O...H	2.1182
			N-H...O	2.5268
			N-H...O	2.1877
Kaolinite (Al-O side) + urea	1	-0.4781	O...H	1.9694
			N-H...O	1.8706
			O...H	2.0968
	2	-1.0172	O...H	1.9690
			O...H	2.0971
			N-H...O	1.8704
3	-1.0013	O...H	1.9635	
		O...H	2.1318	
		N-H...O	1.8863	
4	-1.0170	O...H	1.9692	
		O...H	2.0967	
			N-H...O	1.8704

of urea can occur [32]. Simulation study on the different amide molecules attached at the kaolinite also shows that these molecules had higher interaction energy at the Al–O sheet than at the Si–O sheet [25,27,38]. As shown in Table 3, the bond length for urea interacting with the hydroxyl of Al–O is shorter than the bonding at the Si–O sheet. Primary interaction at the Al–O sheet is from the N–H of urea with oxygen from hydroxyl of gibbsite layer with bond length 1.87–1.99 Å. Secondary interaction is between oxygen and nitrogen atoms of the urea with the hydroxyl of the Si–O sheet.

The interaction sites are as conveyed by the ESP surface, where the red ESP map surface had attracted the dual NH₂ of the urea molecule to the basal oxygen on the siloxane surface (N–H··O). The hydrogen bonding of N–H··O bond length is in the range of 2.3–2.8 Å on the Si–O surface and did complement the previous study on the interaction between urea and kaolinite [2]. The ESP surface map had varying colors from blue to green on the Al–O sheet, which was predicted to act as H-donor and H-acceptor. The results from Table 3 and Fig. 6 had shown on the Al–O sheet, and both interactions are involved. The hydroxyl that points outward of the kaolinite sheet (appear blue in Fig. 4) acts as the H-acceptor by interacting with the oxygen and nitrogen from the urea molecules. At the same time, the other hydroxyl interacts with the NH₂ of the urea molecule as H-donor when they point to the middle of the kaolinite ring [2].

The previous studies had already discussed that the orientation of the guest molecule, when placed at the different sites of kaolinite, would appear differently. 2,4-dinitrotoluene on kaolinite surface change from dihedral angle 60° at Al–O sheet to 10° at the Si–O sheet, resulting from the hydrogen bond between the guest molecule and kaolinite sheets [29]. Fig. 6 shows that urea molecule orientation after optimization on top of the Si–O and Al–O appeared parallel or perpendicular to the kaolinite sheet. A simulation study using molecular dynamic simulation had reported in infinite structure, few urea molecules are nearly parallel to the basal surface of kaolinite, with the urea molecules situated closer to the silica tetrahedron sheet. Meanwhile, some urea molecules

are almost perpendicular to the basal surface of kaolinite [45]. Simulation study of bulk amount of urea on top of infinite Si–O sheet shows that final orientation of urea is always almost parallel to the sheets with the angle between 0°–20° [28]. Urea on top of the Si–O sheet, as shown in Fig. 6, also had a similar orientation as reported in previous experimental and simulation studies with dual hydrogen bonding [32]. The orientation at the Al–O had never been reported previously. This study simulated the closeness of both molecules oriented the urea perpendicular to the top of the Al–O surface. In this position, one N–H bond interacts with the hydroxyl of Al–O and the other N–H bond of urea free on the other side, as in Fig. 6.

Interaction between urea and kaolinite in simulation is scarce compared to other molecules. For other molecules studied in the finite structure of kaolinite, it always includes the single sheets of Al–O or Si–O to find the interaction between kaolinite and guest molecule [25-27,29]. Thus, this study compared the simulation result with previous research on urea and kaolinite. Results show that for the Si–O surface of kaolinite, urea is the least favorable to finalize on top of the Si–O surface when the single ring of kaolinite is introduced. However, the urea is consistently optimized in the middle of the siloxane ring when an individual Si–O sheet is used. All urea is also in the parallel orientation to the Si–O surface. The interaction energy is higher when a particular Si–O sheet is used due to the minor atom interacting with the urea. Urea had an inconsistent position when only the Al–O sheet was used. The urea tends to have a final position at the side of the kaolinite with both parallel and perpendicular orientation to the Al–O sheet. However, for urea introduced to the kaolinite (Al–O), it can consistently be optimized on the middle of the Al–O ring with perpendicular orientations.

■ CONCLUSION

This work aims to build a kaolinite cluster model and to explore the adsorption on the kaolinite surfaces. It is performed with updated functional and basis set for future references. For the geometry, among different

functionals and basis sets previously used, TPSS/TPSS combined with 6-311++G** showed the best result compared to the experimental result. As other studies always used the hydroxyl bond length as a benchmark of comparison, our result also has the hydroxyl bond length values in good agreement with the DFT computations of the previous finding, using bulk and cluster calculations. For the preferable sites of interactions with the guest molecules, Si-O was electron-deficient while the Al-O was an electron-abundant surface. Both Si-O and Al-O surfaces are suitable adsorbent surfaces for guest molecule interaction with kaolinite, compared to the energy of both surfaces interacting with urea. Interaction using urea as guest molecules shows that Si-O is an electron-deficient surface. Thus oxygen of urea is preferred to be attached to it, and Al-O is the dual adsorbent surface where it can interact with oxygen and hydrogen of urea.

■ ACKNOWLEDGMENTS

The Minister of Higher Education Malaysia financially supports this research through the Fundamental Research Grant Scheme (FRGS, project code 600-IRMI/FRGS 5/3 (115/2019)).

■ AUTHOR CONTRIBUTIONS

The authors contributed equally to this work.

■ REFERENCES

- [1] Zhang, S., Liu, Q., Cheng, H., and Zeng, F., 2015, Combined experimental and theoretical investigation of interactions between kaolinite inner surface and intercalated dimethyl sulfoxide, *Appl. Surf. Sci.*, 331, 234–240.
- [2] Zhang, S., Liu, Q., Gao, F., Li, X., Liu, C., Li, H., Boyd, S.A., Johnston, C.T., and Teppen, B.J., 2017, Mechanism associated with kaolinite intercalation with urea: Combination of infrared spectroscopy and molecular dynamics simulation studies, *J. Phys. Chem. C*, 121 (1), 402–409.
- [3] Makó, É., Kovács, A., Katona, R., and Kristóf, T., 2016, Characterization of kaolinite-cetyltrimethylammonium chloride intercalation complex synthesized through eco-friendly kaolinite-urea pre-intercalation complex, *Colloids Surf., A*, 508, 265–273.
- [4] Táborosi, A., Kurdi, R., and Szilágyi, R.K., 2014, Adsorption and intercalation of small molecules on kaolinite from molecular modelling studies, *Hung. J. Ind. Chem.*, 42 (1), 19–23.
- [5] Zhang, S., Gao, N., and Liu, K., 2021, Insights on the intercalation mechanism of the coal-bearing kaolinite intercalation based on experimental investigation and molecular dynamics simulations, *Chem. Pap.*, 75 (12), 6335–6344.
- [6] Azeem, B., KuShaari, K., Man, Z.B., Basit, A., and Thanh, T.H., 2014, Review on materials & methods to produce controlled release coated urea fertilizer, *J. Controlled Release*, 181, 11–21.
- [7] Roshanravan, B., Mahmoud-Soltani, S., Mahdavi, F., Abdul Rashid, S., and Yusop, M.K., 2014, Preparation of encapsulated urea-kaolinite controlled release fertiliser and their effect on rice productivity, *Chem. Speciation Bioavailability*, 26 (4), 249–256.
- [8] Sempeho, S.I., Kim, H.T., Mubofu, E., Pogrebnoi, A., Shao, G., and Hilonga, A., 2015, Dynamics of kaolinite-urea nanocomposites via coupled DMSO-hydroxyaluminum oligomeric intermediates, *Indian J. Eng. Mater. Sci.*, 2015, 920835.
- [9] Vejan, P., Khadiran, T., Abdullah, R., and Ahmad, N., 2021, Controlled release fertilizer: A review on developments, applications and potential in agriculture, *J. Controlled Release*, 339, 321–334.
- [10] Fariba, M., Suraya, A.R., and Yusop, M.K., 2014, Intercalation of urea into kaolinite for preparation of controlled release fertilizer, *Chem. Ind. Chem. Eng. Q.*, 20 (2), 207–213.
- [11] Roshanravan, B., Mahmoud-Soltani, S., Rashid, S.A., Mahdavi, F., and Yusop, M.K., 2015, Enhancement of nitrogen release properties of urea-kaolinite fertilizer with chitosan binder, *Chem. Speciat. Bioavailab.*, 27 (1), 44–51.
- [12] de Macedo Neto, J.C., do Nascimento, N.R., Bello, R.H., de Verçosa, L.A., Neto, J.E., da Costa, J.C.M., and Diaz, F.R.V., 2022, Kaolinite review:

- Intercalation and production of polymer nanocomposites, *Eng. Sci.*, 17, 28–44.
- [13] Brindley, G.W., and Robinson, K., 1946, The structure of kaolinite, *Mineral. Mag. J. Mineral. Soc.*, 27 (194), 242–253.
- [14] White, C.E., Provis, J.L., Riley, D.P., Kearley, G.J., van Deventer, J.S.J., 2009, What is the structure of kaolinite? reconciling theory and experiment, *J. Phys. Chem. B*, 113(19), 6756–6765.
- [15] Bish, D.L., 1993, Rietveld refinement of the kaolinite structure at 1.5 K, *Clays Clay Miner.*, 41 (6), 738–744.
- [16] Hess, A.C., and Saunders, V.R., 1992, Periodic ab initio Hartree-Fock calculations of the low-symmetry mineral kaolinite, *J. Phys. Chem.*, 96 (11), 4367–4374.
- [17] Balan, E., Saitta, A.M., Mauri, F., and Calas, G., 2001, First-principles modeling of the infrared spectrum of kaolinite, *Am. Mineral.*, 86 (11-12), 1321–1330.
- [18] Castro, E.A.S., and Martins, J.B.L., 2005, Theoretical study of kaolinite, *Int. J. Quantum Chem.*, 103 (5), 550–556.
- [19] Tosoni, S., Doll, K., and Ugliengo, P., 2006, Hydrogen bond in layered materials: Structural and vibrational properties of kaolinite by a periodic B3LYP approach, *Chem. Mater.*, 18 (8), 2135–2143.
- [20] Hu, X.L., and Michaelides, A., 2008, Water on the hydroxylated (001) surface of kaolinite: From monomer adsorption to a flat 2D wetting layer, *Surf Sci.*, 602 (4), 960–974.
- [21] Karmous, M.S., 2011, Theoretical study of kaolinite structure; Energy minimization and crystal properties, *World J. Nano Sci. Eng.*, 1 (2), 62–66.
- [22] Heimann, J.E., Grimes, R.T., Rosenzweig, Z., and Bennett, J.W., 2021, A density functional theory (DFT) investigation of how small molecules and atmospheric pollutants relevant to art conservation adsorb on kaolinite, *Appl. Clay Sci.*, 206, 106075.
- [23] Hobbs, J.D., Cygan, R.T., Nagy, K.L., Schultz, P.A., and Sears, M.P., 1997, All-atom ab initio energy minimization of the kaolinite crystal structure, *Am. Mineral.*, 82 (7-8), 657–662.
- [24] Zhang, Z., Liu, J., Yang, Y., Shen, F., and Zhang, Z., 2018, Theoretical investigation of sodium capture mechanism on kaolinite surfaces, *Fuel*, 234, 318–325.
- [25] Song, K.H., Zhong, M.J., Wang, L., Li, Y., and Qian, P., 2014, Theoretical study of interaction of amide molecules with kaolinite, *Comput. Theor. Chem.*, 1050, 58–67.
- [26] Zhang, C., Qi, Y.H., Qian, P., Zhong, M.J., Wang, L., and Yin, H.Z., 2014, Quantum chemical study of the adsorption of water molecules on kaolinite surfaces, *Comput. Theor. Chem.*, 1046, 10–19.
- [27] Song, K.H., Wang, X., Qian, P., Zhang, C., and Zhang, Q., 2013, Theoretical study of interaction of formamide with kaolinite, *Comput. Theor. Chem.*, 1020, 72–80.
- [28] Rutkai, G., Makó, É., and Kristóf, T., 2009, Simulation and experimental study of intercalation of urea in kaolinite, *J. Colloid Interface Sci.*, 334 (1), 65–69.
- [29] Wang, X., Qian, P., Song, K., Zhang, C., and Dong, J., 2013, The DFT study of adsorption of 2,4-dinitrotoluene on kaolinite surfaces, *Comput. Theor. Chem.*, 1025, 16–23.
- [30] Volkova, E., Narayanan Nair, A.K., Engelbrecht, J., Schwingenschlögl, U., Sun, S., and Stenichkov, G., 2021, Molecular dynamics modeling of kaolinite particle associations, *J. Phys. Chem. C*, 125 (43), 24126–24136.
- [31] Frost, R.L., Tran, T.H., and Kristof, J., 2018, The structure of an intercalated ordered kaolinite - A Raman microscopy study, *Clay Miner.*, 32 (4), 587–596.
- [32] Frost, R.L., Kristof, J., Rintoul, L., and Klopogge, J.T., 2000, Raman spectroscopy of urea and urea-intercalated kaolinites at 77 K, *Spectrochim. Acta, Part A*, 56 (9), 1681–1691.
- [33] Cheng, H., Liu, Q., Yang, J., Ma, S., and Frost, R.L., 2012, The thermal behavior of kaolinite intercalation complexes-A review, *Thermochim. Acta*, 545, 1–13.
- [34] Mohd Nabil, N.N.A., Mohd Zabidi, A.R., Abdullah, N.A.F., and Ang, L.S., 2017, Stability and electronic properties of urea in different arrangements: A DFT-based study, *Jurnal Intelek*, 12 (2), 44–54.
- [35] Mohd Nabil, N.N.A., and Ang, L.S., 2017, Theoretical investigation of the lattice energy of

- urea: Insight from DFT using systematic cluster method, *Malays. J. Fundam. Appl. Sci.*, 13 (4), 632–636.
- [36] Frisch, M.J., Trucks, G.W., Schlegel, H.B., Scuseria, G.E., Robb, M.A., Cheeseman, J.R., Scalmani, G., Barone, V., Mennucci, B., Petersson, G.A., Nakatsuji, H., Caricato, M., Li, X., Hratchian, H.P., Izmaylov, A.F., Bloino, J., Zheng, G., Sonnenberg, J.L., Hada, M., Ehara, M., Toyota, K., Fukuda, R., Hasegawa, J., Ishida, M., Nakajima, T., Honda, Y., Kitao, O., Nakai, H., Vreven, T., Montgomery Jr., J.A., Peralta, J.E., Ogliaro, F., Bearpark, M., Heyd, J.J., Brothers, E., Kudin, K.N., Staroverov, V.N., Kobayashi, R., Normand, J., Raghavachari, K., Rendell, A., Burant, J.C., Iyengar, S.S., Tomasi, J., Cossi, M., Rega, N., Millam, J.M., Klene, M., Knox, J.E., Cross, J.B., Bakken, V., Adamo, C., Jaramillo, J., Gomperts, R., Stratmann, R.E., Yazyev, O., Austin, A.J., Cammi, R., Pomelli, C., Ochterski, J.W., Martin, R.L., Morokuma, K., Zakrzewski, V.G., Voth, G.A., Salvador, P., Dannenberg, J.J., Dapprich, S., Daniels, A.D., Farkas, Ö., Foresman, J.B., Ortiz, J.V., Cioslowski, J., and Fox, D.J., 2013, *Gaussian-09 Revision D.01*, Gaussian, Inc., Wallingford, CT.
- [37] Yanai, T., Tew, D.P., and Handy, N.C., 2004, A new hybrid exchange–correlation functional using the Coulomb-attenuating method (CAM-B3LYP), *Chem. Phys. Lett.*, 393 (1-3), 51–57.
- [38] Michalkova, A., Robinson, T.L., and Leszczynski, J., 2011, Adsorption of thymine and uracil on 1:1 clay mineral surfaces: Comprehensive ab initio study on influence of sodium cation and water, *Phys. Chem. Chem. Phys.*, 13 (17), 7862–7881.
- [39] Zhao, Y., and Truhlar, D.G., 2008, The M06 suite of density functionals for main group thermochemistry, thermochemical kinetics, noncovalent interactions, excited states, and transition elements: two new functionals and systematic testing of four M06-class functionals and 12 other functionals, *Theor. Chem. Acc.*, 120 (1), 215–241.
- [40] Kruse, H., and Grimme, S., 2012, A geometrical correction for the inter- and intra-molecular basis set superposition error in Hartree-Fock and density functional theory calculations for large systems, *J. Chem. Phys.*, 136 (15), 154101.
- [41] Christensen, A.S., Kubař, T., Cui, Q., and Elstner, M., 2016, Semiempirical quantum mechanical methods for noncovalent interactions for chemical and biochemical applications, *Chem. Rev.*, 116 (9), 5301–5337.
- [42] Mohd Nabil, N.N.A., and Ang, L.S., 2019, Conformational and topology analysis of diphenylthiourea and diarylhalidethiourea compounds using DFT, *Indones. J. Chem.*, 20 (2), 264–275.
- [43] Benco, L., Tunega, D., Hafner, J., and Lischka, H., 2001, Orientation of OH groups in kaolinite and dickite: Ab initio molecular dynamics study, *Am. Mineral.*, 86 (9), 1057–1065.
- [44] Giese, R.F., and Datta, P., 1973, Hydroxyl orientation in kaolinite, dickite, and nacrite, *Am. Mineral.*, 58 (5-6), 471–479.
- [45] Liu, Q., Zhang, S., Cheng, H., Wang, D., Li, X., Hou, X., and Frost, R.L., 2014, Thermal behavior of kaolinite–urea intercalation complex and molecular dynamics simulation for urea molecule orientation, *J. Therm. Anal. Calorim.*, 117 (1), 189–196.

Antioxidant Analysis of Kawa Daun (*Coffea canephora*) Beverage by *In Vitro* and *In Silico* Approaches

Ifwarisan Defri^{1,2}, Nurheni Sri Palupi¹, Setyanto Tri Wahyudi³, and Nancy Dewi Yuliana^{1*}

¹Department of Food Science and Technology, IPB University, IPB Dramaga Campus, Bogor 16680, Indonesia

²Department of Food Technology, UPN "Veteran" Jawa Timur, Surabaya 60294, Indonesia

³Department of Physics, Faculty of Mathematical and Natural Sciences, IPB University, IPB Dramaga Campus, Bogor 16680, Indonesia

* **Corresponding author:**

tel: +62-81380035660

email: nancy_dewi@apps.ipb.ac.id

Received: September 27, 2021

Accepted: February 5, 2022

DOI: 10.22146/ijc.69422

Abstract: In Tanah Datar Regency, West Sumatra, Indonesia, the waste of pruning coffee leaves (*Coffea canephora*) is utilized as a traditional beverage called "Kawa Daun". For a consistent quality of Kawa Daun functional beverage, we evaluated the effect of different smoking times (0, 2, 4, and 6 h) on its *in vitro* DPPH antioxidant activity. Estimation of antioxidant components from the coffee leaf was conducted *in silico* using Peroxiredoxin V (PrxV) with 3MNG code as a receptor, and 33 phytochemicals were reported to be present in the coffee leaves as ligands. As a result, Kawa Daun, with a 2-h smoking time, had the highest antioxidant activity. Molecular docking between PrxV and the 33 compounds resulted in the ten most potential compounds based on the affinity energy. They were xanthone (-4.9 kcal/mol), uric acid (-4.8 kcal/mol), xanthosine (-4.8 kcal/mol), caffeine (-4.6 kcal/mol), 3-methylxanthine (-4.6 kcal/mol), 7-methylxanthosine (-4.6 kcal/mol), theobromine (-4.5 kcal/mol), theophylline (-4.5 kcal/mol), caffeic acid (-4.5 kcal/mol), and xanthine (-4.4 kcal/mol). These ten ligands had stronger interactions than the control ligand 1,2-dithiane-4,5-diol (-3.6 kcal/mol). This research showed the potential of Kawa Daun as a functional beverage with antioxidant activity. Further confirmation on the antioxidant potential of this beverage using an *in vivo* method is recommended.

Keywords: functional beverage; peroxiredoxin V; coffee leaves; Kawa Daun; smoking time

■ INTRODUCTION

Pruning the leaves of coffee plants is a common practice in coffee cultivation to stimulate the development of coffee beans, which leads to a shorter harvesting period. Coffee leaves from pruning are typically discarded as waste. The farmers in Batipuh Ateh, Tanah Datar Regency, West Sumatra Province, Indonesia, traditionally utilize the wasted coffee leaves, particularly the Robusta variety (*Coffea canephora*), in a traditional beverage known as "Kawa Daun." The term "Kawa" is derived from an Arabic term defined as brewed water from the coffee leaves. The distinctiveness of this beverage is in the drying methods of coffee leaves. There are two drying methods

commonly used by the local *Kawa Daun* industries: (1) using a *cabinet dryer* with a mechanically controlled temperature and (2) the traditional way by smoking the leaves in a fireplace of cinnamon wood for 2–4 h [1]. Empirically, Minang society believes that *Kawa Daun* beverage positively impacts their health. They feel that their bodies become fitter, stronger, and warmer after consuming the *Kawa Daun* beverage. Several studies reported the potency of functional characteristics of *Kawa Daun* since it contains bioactive components for antioxidants, such as 3-methylxanthine, xanthine, and theophylline [2], 7-methylxanthosine, xanthosine [3], caffeic acid [4], uric acid [5], caffeine, xanthone, and theobromine [6].

Most traditional *Kawa Daun* producers in Tanah Datar Regency produce the *Kawa Daun* beverage with inconsistent quality. Thus, the effect of different smoking times (0, 2, 4, and 6 h) on antioxidant activity must be evaluated. It is difficult to predict and identify the bioactive components of coffee leaves that are most beneficial as antioxidants. *In silico* is a computational method that can be implemented for such a purpose. *In silico* can provide preliminary information that can be utilized as the foundation for future strategy in developing *Kawa Daun* as a functional beverage. Target proteins (receptors) of Peroxiredoxin V (PrxV) with 3MNG code are used to investigate the antioxidant potential of the *Kawa Daun* beverage. Peroxiredoxin (Prxs) is an essential peroxidase involved in antioxidant and redox signaling protection in humans. It has a very high catalytic efficiency which dominates peroxide reduction in all body cells. At 1.45 Å resolution, the new structure of human PrxV has a dithiothreitol bond in the active site, with its diol moiety emulating the two oxygens of the peroxide substrate. This structure classifies the diol and related dioxygen as a new competitive inhibitor for Prxs. The PrxV protein developed into a suitable and efficient receptor to be used as the target receptor of antioxidant activity in the human body [7].

Protein function targeting is accomplished by substituting the native ligand of PrxV with 33 bioactive components previously reported to be identified in the coffee leaves as tested ligands. The binding mode of the ligand-receptor complex is interpreted by comparing the tested ligand to the original ligand as a control, specifically the competitive antioxidant inhibitor 1,2-dithiane-4,5-diol (D1D). The molecular docking method can predict the proper ligand by obtaining affinity energy and bond stability between the receptor and the ligand [7]. Molecular docking is a tool for studying the interactions within a molecular complex. Hydrophobic and hydrogen interactions classify interactive positions that will be potential ligand-binding sites at each possible position. *In silico* research on coffee leaves, particularly associated with antioxidant compounds, has never been conveyed. The interaction between methyl gallate with various antioxidant receptors was predicted while comparing it

with gallate acid as the main compound. The results showed that the affinity energy for the 3MNG receptor was 3.6 kcal/mol, which indicates that the methyl gallate had the potential as an antioxidant [8]. Another experiment showed that molecular docking on the meglumine catalyst exhibited the best docking results on the compound of 3,3'-((3,5-dimethoxyphenyl)methylene)bis(1*H*-indole), which had the strongest binding to 3MNG with an affinity energy of -7.6 kcal/mol. The binding energy value correlates with the highest value of the antioxidant activity, which was 78.48 µg/mL [9]. Meanwhile, *in vitro* antioxidant power of Robusta coffee leaves with water fractions at several concentrations, i.e., 100, 80, 60, 40, and 20 ppm, was reported. The IC₅₀ value was 73.62 ppm [10-11].

The combination of *in silico* and *in vitro* antioxidants is crucial to obtain more accurate data results regarding the potential of *Kawa Daun* beverage as a functional beverage with the best antioxidant potential, as well as the bioactive components of coffee leaves that play the most crucial role as antioxidants. This research aimed to find the smoking time which gave *Kawa Daun* the highest antioxidant activity and to identify the possible antioxidant compounds. The fresh coffee leaves were smoked using a cinnamon fireplace at different smoking times. The *in vitro* antioxidant activity of *Kawa Daun* methanolic extracts was measured using the 2,2-diphenyl-1-picrylhydrazyl (DPPH) method. In parallel, a literature study was conducted to list phytochemicals previously identified in the coffee leaves. *In silico* study was then conducted to analyze the interaction and the affinity energy of those bioactive components in coffee leaves as ligands to the target protein of PrxV (receptor) using molecular docking.

■ EXPERIMENTAL SECTION

Materials

Fresh coffee leaves of Robusta variety (*C. canephora*) were harvested from Mus's coffee plantation, Tanah Datar, West Sumatra, Indonesia, from August to January 2021. Only broad, green, and young and old aged leaves in pseudostem parts were selected. The coffee leaves were washed before being subjected to the

subsequent treatment. Cinnamon wood for the fireplace was freshly harvested from the Batipuh Ateh forest, Tanah Datar, West Sumatera, Indonesia. The chemicals used were DPPH (2,2-diphenyl-1-picrylhydrazyl), methanol, dimethyl sulfoxide (DMSO), and ascorbic acid. They were all analytical grade and acquired from Sigma-Aldrich (Darmstadt, Germany).

For *in silico* study, protein target 3D structure (receptor) of Peroxiredoxin V (PrxV) utilizing PDB code (3MNG) was retrieved from the Research Collaboratory for Structural Bioinformatics (RCSB), Protein Data Bank (PDB) (<https://www.rcsb.org/>) sites, which is in the .pdb format. Table 2 displays the 33 tested ligands. The D1D was used as a control ligand. All ligands acted as oxidation inhibitors and were obtained in the form of SDF from the PubChem database of chemical molecules (<https://pubchem.ncbi.nlm.nih.gov/>). The personal computer specification for *in silico* study was as follows: Intel 2Core N3350 2.4 Ghz, Intel HD Graphics, Endless OS, Windows Operation System 10 64-bit. The software used in this research comprised USCF Chimera 1.13.1, VMD version 1.9.3, Avogadro, Open Babel version 2.3.2, Autodock Tools (ADT) version 1.5.6, LigPlot+ version 2.1, and PyMOLMolecular Graphics System Version 2.4.0.

Procedure

Kawa Daun preparation [12]

Coffee leaves were smoked on a cinnamon wood fireplace with different smoking times (0, 2, 4, and 6 h at 70 °C). The 0-h sample (control sample) was the coffee leaves dried in a cabinet drier at 70 °C for 8 h. In a waring blender, all the dried coffee leaves were ground into very fine powder. The powder was then stored in airtight plastic containers. To prepare the *Kawa Daun* beverage, the powdered leaves were mixed with freshwater (1:100 b/v), boiled (100 °C, 15 min), and filtered. The resulting beverage was stored in a dark bottle and kept cold in the refrigerator (8 °C). For *in vitro* antioxidant activity measurement, the *Kawa Daun* beverage was dried in a freeze dryer for 72 h and stored in the freezer (-10 °C) before the measurement.

Antioxidant activities [13]

One hundred microliter of Kawa Daun solution at different concentrations (20, 40, 60, 80, and 100 ppm) were pipetted into 96 wells microplate, added by 100 µL DPPH (125 µM in methanol) incubated at room temperature in the dark condition (30 min). The absorbance reduction was measured using a microplate reader at 517 nm. The measurement was repeated two times.

$$\text{Percentage of antioxidant activity} = \frac{[(AB - AKB) - (AS - AKS)]}{(AB - AKB)} \times 100\%$$

where AB is blank absorbance, AKB is absorbance control blank, AS is sample absorbance, and AKS is sample control absorbance.

In silico computation [14]

The first step was gathering data on the bioactive components found in coffee leaves (*Coffea canephora*) based on the literature review. The obtained data were used to create ligand compounds, then examined via molecular docking. The molecular docking was carried out on the ligand test and the native ligand of D1D (from the 3D structure of 3MNG) was employed as a control. The second step involved preparing ligand tests using a Pubchem database (<https://pubchem.ncbi.nlm.nih.gov/>). The database contained 33 molecular structures of tested ligands in SDF files. The tested ligand molecules were geometrically adjusted to resemble their natural condition using OCRA2 software [15]. Peroxiredoxin V (PrxV) ID: 3MNG was acquired as the target protein molecules (receptor), which was taken from Protein Data Bank (<https://www.rcsb.org/>). The receptor docking was repeated using a native ligand of D1D to recognize the coordinate of the receptor's active site. The system was prepared using Chimera 1.14.0 version (<https://www.rbvi.ucsf.edu/chimera>) [16]. The target protein was reduced, then segregation was performed as a ligand and receptor using USCF-Chimera software version 1.14.0; furthermore, it was planned to get rid of the free ion and water included in the protein's initial structure. The magnetic field and water molecules were

also eliminated after the native ligands were combined with hydrogen atoms to create an electric charge. The third step consisted of molecular docking. Ligand and receptor whose initial form was .pdb were converted to .pdbqt using AutoDock Tools 1.5.6. The grid box dimensions were set at $x = 15$, $y = 15$, and $z = 15$. The x , y , and z docking centers of 91.788, 91.838, and 104.806, respectively, were used so that the active site where the ligand binding took place was appropriately positioned. The database then used Autodock Vina to perform molecular docking. The results of the top 10 ligands-receptor that had the most potential as antioxidants were seen based on the interactions and the resulting affinity energy. The top 10 tested ligands were finally visualized in the fourth stage using PyMOL Molecular Graphics System Version 2.4.0 (<https://pymol.org/>) [17] and LigPlot [18]. The pharmacokinetic properties of the ligand with the lowest values (most negative) would be evaluated using SwissADME (<http://www.swissadme.ch/>) based on Lipinski's rules. This website allows us to compute physicochemical descriptors and predict ADME parameters (absorption, distribution, metabolism, elimination), pharmacokinetic properties, druglike nature, and medicinal chemistry friendliness of one or multiple small molecules to support drug discovery. The complex bond of a receptor with the native ligand as the comparison (control) and the complex bond of a receptor with the ten most robust tested ligands were simulated.

RESULTS AND DISCUSSION

Antioxidant Activity

The antioxidant activity of *Kawa Daun* methanolic extract obtained from four different smoking times ranged from 22.58 to 81.40% (Fig. 1). Sample B (2 h smoking) had the highest antioxidant activity among other fractions at all concentrations tested, followed by sample A (the unsmoked control). In contrast, sample D (6 h smoking) had the lowest antioxidant activity. Samples A and B had a shorter high-temperature exposure, resulting in minimal damage to the bioactive components in the coffee leaves.

The IC_{50} results of the *Kawa Daun* beverage from each treatment are presented in Table 1. Samples A and B had the lowest IC_{50} value (< 20 ppm). The compound is said to have very strong antioxidant activity if the IC_{50} value is < 50 ppm, strong if it is 50 to 100 ppm, moderate if it is 100 to 150 ppm, and weak if it is 150 to 200 ppm [19]. Thus, samples A and B are classified as having very

Table 1. IC_{50} values of *Kawa Daun* beverage

Smoking duration	IC_{50} (ppm)
A (0 h)*	< 20
B (2 h)	< 20
C (4 h)	53.56 ± 0.04
D (6 h)	64.37 ± 0.74
Vitamin C (control)	4.48 ± 0.01

(*)Drying in cabinet dryer (70 °C, 8 h)

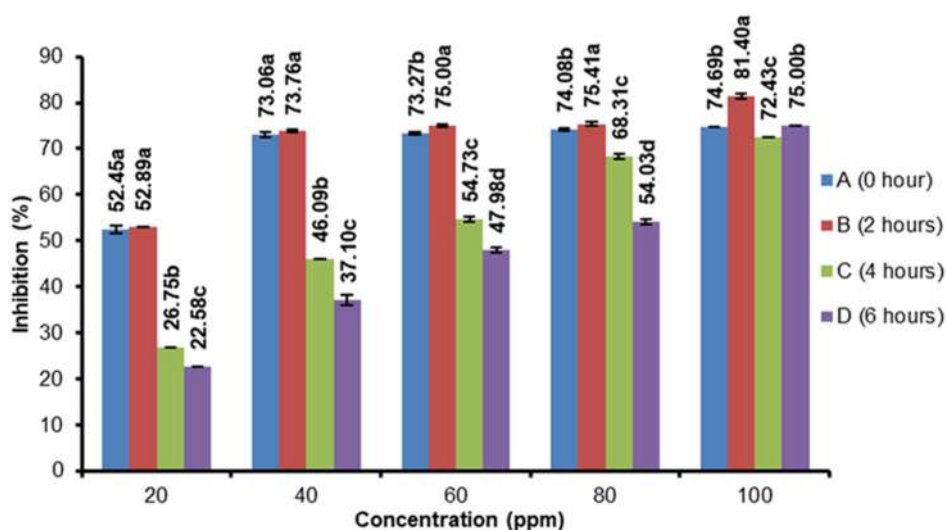


Fig 1. DPPH antioxidant activity profile of *Kawa Daun* beverage prepared with different smoking time

strong antioxidant activity. In contrast, sample C and D with the IC₅₀ values of 53.56 and 64.37 ppm is classified as having strong antioxidant activity. The difference between percentage values for inhibition and IC₅₀ values is due to the smoking time. The longer coffee leaves are smoked, the more likely it is that the bioactive substance of the coffee leaves will be damaged, affecting antioxidant activity. Several bioactive compounds are extremely temperature-sensitive and unstable.

The effect of temperature on bioactive components was reported—an increase in temperature that is not constant causes an increase in phenolic concentration to a specific temperature. However, the phenolic concentration then decreases with increasing smoking time and higher temperature [20]. The result was also in agreement with a previous study which reported that *in vivo* antioxidant activity of the coffee bean significantly decreased with the longer roasting time [21]. In another report, six flavonoids were reported to have antioxidant activities. The compounds, which consisted of rutin, naringin, eriodictyol, mesquitol, luteolin, and luteolin 7-O glucoside, were exposed to heat treatment (70–130 °C, 120 min). It was found that all were degraded at a different speed. The level of degradation increased with a higher temperature and longer heating duration [22]. Several factors may influence the phytochemical composition of plant samples and their biological activity, such as varieties, environmental changes during growth and harvest, post-harvest treatment, extraction, and sample preparation methods [23]. Sample preparation methods such as smoking and the brewing *Kawa Daun* beverage are also suggested to influence their antioxidant activity. The most recent study showed that DPPH radical scavenging activity, total phenolic content, and total procyanidins of *Coffea arabica* L. leaf were significantly increased with a higher drying temperature [24].

Molecular Docking

As previously discussed, coffee leaves contain bioactive components that act as antioxidants. A recent study mentioned that bioactive components in coffee leaves come from the alkaloid group, i.e., caffeine, theobromine, theophylline, and trigonelline. It also comes

from the phenolic compound group, i.e., caffeic acid, ferulic acid, sinapic acid, and chlorogenic acids (3-CQA, 4-CQA, 5-CQA, 3,4-diCQA, 3,5-diCQA, 4,5-diCQA). Quercetin, catechins, and kaempferol are examples of bioactive flavonoid phenolic compounds. Other phenolic compound group's bioactive components include xanthenes, such as mangiferin and isomangiferin [25]. Because of the current advancements in science and technology, the exploration of the bioactive components present in coffee leaves focuses not only on the refreshing impact but also on the potential for antioxidant content, which can be detected early using *in silico* method. *In silico* method can be used to support the data resulting from *in vitro* experiment, or vice versa. In our study, *in vitro* method was used to provide initial information on the antioxidant activity of the *Kawa Daun* beverage. *In silico* method was then used to obtain detailed information on which compounds might associate with the antioxidant activity of the beverage.

Molecular docking is used to examine the bioactivity of coffee leaves in the ligand and receptor complex. Molecular docking is essential for determining the conformation of the tested ligand interaction on the active site of the target protein receptor, as well as determining which tested ligand has the most significant negative affinity energy and interacts well with the target protein receptor. The human antioxidant receptor Peroxiredoxin V (PrxV) is chosen. It comprises essential cysteine residues as catalysts and thioredoxin as electron donors, which help scavenge peroxides and cellular metabolic responses to reactive oxygen species in the human body [7].

The docking results of 33 tested ligands and one native (control) ligand are well-ordered based on the ligand's binding strength to the receptor (Table 2). In Table 2, the top 10 ligands strongly bind the receptor. The binding strength is determined by whether the affinity energy value (kcal/mol) is more significant than the affinity energy value of the native ligand (control). If the affinity energy value is more negative, the ligand-receptor binding will be stronger. When the binding affinity energy is negative, it means that the bioactive

Table 2. The list of tested ligands and results of molecular docking between ligands and PrxV

No	Compounds identified in coffee leaves	References	PubChem CID	Affinity (kcal/mol)	Kd (M)
1	Xanthone	[6]	7020	-4.9	3.33E-04
2	Uric Acid	[5]	1175	-4.8	3.92E-04
3	Xanthosine	[3]	64959	-4.8	4.09E-04
4	Caffeine	[2,5,25]	2519	-4.6	5.23E-04
5	3-Methylxanthine	[2,5]	70639	-4.6	5.45E-04
6	7-Methylxanthosine	[3]	23724732	-4.6	5.68E-04
7	Theobromine	[2,6]	5429	-4.5	6.16E-04
8	Theophylline	[2,5]	2153	-4.5	6.16E-04
9	Caffeic Acid	[4]	689043	-4.5	6.42E-04
10	Xanthine	[2,5]	1188	-4.4	7.26E-04
11	Hypoxanthine	[6]	135398638	-4.4	7.26E-04
12	Methylxanthine	[2]	80220	-4.4	7.26E-04
13	7-Methylxanthine	[5]	68374	-4.4	7.26E-04
14	Allantoic	[5]	203	-4.4	7.57E-04
15	Allantoin	[5]	204	-4.3	8.56E-04
16	Ferulic acid	[11]	445858	-4.3	8.92E-04
17	Trigonelline	[24]	5570	-4.2	1.01E-03
18	Xanthosine-5-monophosphate	[3]	73323	-4.2	1.05E-03
19	D1D	[7]	3MNG	-3.6	2.70E-03
20	5-caffeoylquinic acid (5-CQA)	[24]	5280633	-3.4	4.08E-03
21	Quercetin	[24]	5280343	-3.3	4.42E-03
22	3-caffeoylquinic acid (3-CQA)	[24]	102111217	-2.8	1.09E-02
23	Chlorogenic Acid	[24]	1794427	-2.7	1.29E-02
24	4-caffeoylquinic acid (4-CQA)	[24]	9798666	-2.4	1.94E-02
25	Mangiferin	[24]	5281647	0.0	1.00E+00
26	3,4-dicaffeoylquinic acid (3,4-diCQA)	[24]	5281780	2.8	9.16E+01
27	Dicaffeoylquinic acid (diCQA)	[24]	12358846	3.5	3.14E+02
28	3,5-dicaffeoylquinic acid (3,5-diCQA)	[24]	6474310	5.5	8.39E+03
29	Hyperoside	[24]	5281643	6.4	3.83E+04
30	4,5-dicaffeoylquinic acid (4,5-diCQA)	[24]	10324242	8.9	2.33E+06
31	Isomangiferin	[24]	5318597	13.9	8.24E+09
32	Rutin	[24]	5280805	26.3	5.54E+18

component of coffee leaves used as the tested ligand requires less energy to attach or interact with the receptor. After all, if the resulting affinity energy value is lower/negative, the tested ligand has a higher chance of interacting with the protein receptor [26], as can be seen in Table 2.

Table 2 reveals that 32 bioactive components serve as ligands in the human receptor of Peroxiredoxin V (PrxV). Several compounds had more negative affinity energy than the D1D control ligand, namely xanthone,

uric acid, xanthosine, caffeine, 3-methylxanthine, 7-methylxanthosine, theobromine, theophylline, caffeic acid, xanthine, hypoxanthine, methylxanthine, 7-methylxanthine, allantoic, allantoin, ferulic, trigonelline, xanthosine-5-monophosphate (XMP), hydroxycinnamic acid, and sinapic acid. The affinity of a small molecule ligand for a macromolecule receptor is commonly used to define a compound's biological activity. Factors that may affect the ligand's affinity include electrostatic interactions between the ligand and acceptor, the

contributions of solvation and desiccation, and the steric complementation of the two binding partners. Changes in the number of degrees of freedom and changes in the structure of the ligand and acceptor during complex formation generate additional effects. Understanding the determining enthalpic and entropic contributions to binding is an initial step for predicting affinity [27].

Virtual simulation can be used to understand the characteristics of a molecule based on its structure and microscopic interactions between other molecules. Most ligand-binding interactions can be classified as binding affinity or affinities. The affinity value reflects whether a ligand can be tethered or connected to the receptor. At the affinity energy, the strength of the binding interaction between the protein and its ligand can be observed. The more negative value gives the greater chance of ligand to bind to the receptor, and vice versa. After acquiring the affinity energy, the tethering results are analyzed using the Ligplot software. Ligplot is a computer program that generates 2-dimensional (2D) graphics by automatically representing the interaction of protein-ligands [28]. Fig. 2 depicts the 2D structure of the top 10 most robust ligands with antioxidant capability.

Visual analysis is performed by comparing the positions and interactions between the ligands and protein residues on the PrxV receptor. The analysis is carried out to observe the type of interaction and the

residues involved. PyMOL software was used to see the binding distance. Generally, the ligands have occupied the appropriate active site at the PrxV receptor. A comparison of the molecular binding results between the top 10 ligand compounds and the most negative PrxV receptor can be seen in Table 3. Amino acid residues that interact using hydrogen bonding on native ligands are Glycine 46 and Threonine 44. The same things were also found in some test ligands such as caffeic acid hydrogen-bonded amino acid residues, such as Threonine 147 and Arginine 127. Based on the results of the hydrophobic interaction analysis, there was no significant difference between the tested and native ligands; the amino acids that appeared mainly were the same.

The affinity energy produced by the D1D-PrxV native ligand complex is -3.6 kcal/mol, which is lower than the energy produced by the top ten strongest PrxV-ligands. The lower energy value suggests that the natural D1D ligand has a weaker binding than the top ten ligand-receptor complexes, namely xanthenes, uric acid, xanthosine, caffeine, 3-methylxanthine, 7-methylxanthosine, theobromine, theophylline, caffeic acid, and xanthine. Table 2 shows that the interaction between the xanthone complex and the PrxV receptor has the most negative affinity energy value (-4.9 kcal/mol) and the lowest Kd value (3.33E-04). Based on

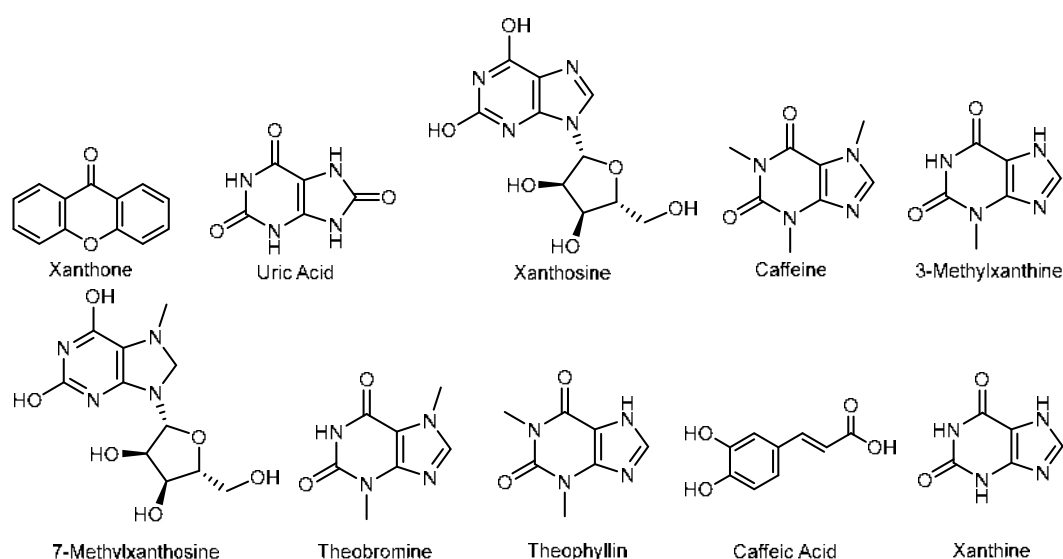


Fig 2. The 2D Structure of top 10 antioxidant ligands

Table 3. Comparison of strongest ligand-receptor complex compounds interaction

No	Complex compound ligand-receptor	Affinity (kcal/mol)	Hydrophobic interactions		Hydrogen bond	
			Total interactions	Amino acid residues	Total bond	Amino acid residues
1	Native ligand D1D-PrxV (Control)	-3.6	6	Proline 40, Threonine 147, Threonine 44, Phenylalanine 120, Cysteine 47, Arginine 127	2	Glycine 46, Threonine 44
2	Xanthone-PrxV	-4.9	7	Arginine 127, Leucine 116, Leucine 149, Glycine 46, Phenylalanine 120, Isoleucine 119, Threonine 147	1	Threonine 147
3	Uric acid-PrxV	-4.8	4	Proline 45, Phenylalanine 120, Threonine 147, Threonine 44	5	Threonine 44, Threonine 147, Glycine 46, Arginine 127, Cysteine 47
4	Xanthosine-PrxV	-4.8	7	Proline 45, Phenylalanine 120, Isoleucine 119, Glycine 148, Glycine 46, Leucine 149, Threonine 44	3	Threonine 44, Threonine 147, Arginine 127
5	Caffeine-PrxV	-4.6	6	Leucine 116, Leucine 149, Proline 40, Phenylalanine 120, Threonine 44, Threonine 147	3	Glycine 46, Threonine 147, Arginine 127
6	3-Methylxanthine-PrxV	-4.6	3	Cysteine 47, Phenylalanine 120, Threonine 147	4	Glycine 46, Cysteine 47, Threonine 147, Arginine 127
7	7methylxanthosine-PrxV	-4.6	6	Proline 40, Proline 45, Leucine 149, Glycine 46, Cysteine 47, Phenylalanine 120	3	Threonine 44, Threonine 147, Arginine 127
8	Theobromine-PrxV	-4.5	6	Threonine 147, Proline 40, Proline 45, Cysteine 47, Phenylalanine 120, Leucine 116	3	Glycine 46, Threonine 44, Threonine 147
9	Theophylline-PrxV	-4.5	4	Threonine 44, Threonine 147, Phenylalanine 120, Cysteine 47	3	Threonine 147, Arginine 127, Glycine 46
10	Caffeic acid-PrxV	-4.5	6	Proline 40, Proline 45, Cysteine 47, Isoleucine 119, Phenylalanine 20, Threonine 147	4	Threonine 44, Threonine 147, Arginine 127, Glycine 46
11	Xanthine-PrxV	-4.4	6	Threonine 44, Threonine 147, Phenylalanine 120, Proline 40, Proline 45, Arginine 127	3	Threonine 44, Cysteine 47, Glycine 46

this value, it can be concluded that the hydrophobic interaction and hydrogen bonding between the xanthenes ligand and the receptor is firmer as compared to those of other tested ligands, including D1D control. The interaction between rutin and the PrxV receptor, on the other hand, has the highest positive affinity energy value (26.3 kcal/mol) and the highest Kd value (5.54E+18). This high-affinity energy value implies that the hydrophobic interactions and hydrogen bonds formed between the

ligand and the receptor are weaker than those of other tested ligands including D1D control.

The visualization results of the molecular docking between the top 10 most potent ligand compounds and the PrxV receptor can be seen in Fig. 3. The involvement of the similar amino acid residue indicates the extent of the ligand-binding tendency to its receptor. The results of the tenth complex of the coffee leave tested ligands showed almost the same binding ability as the D1D control ligands

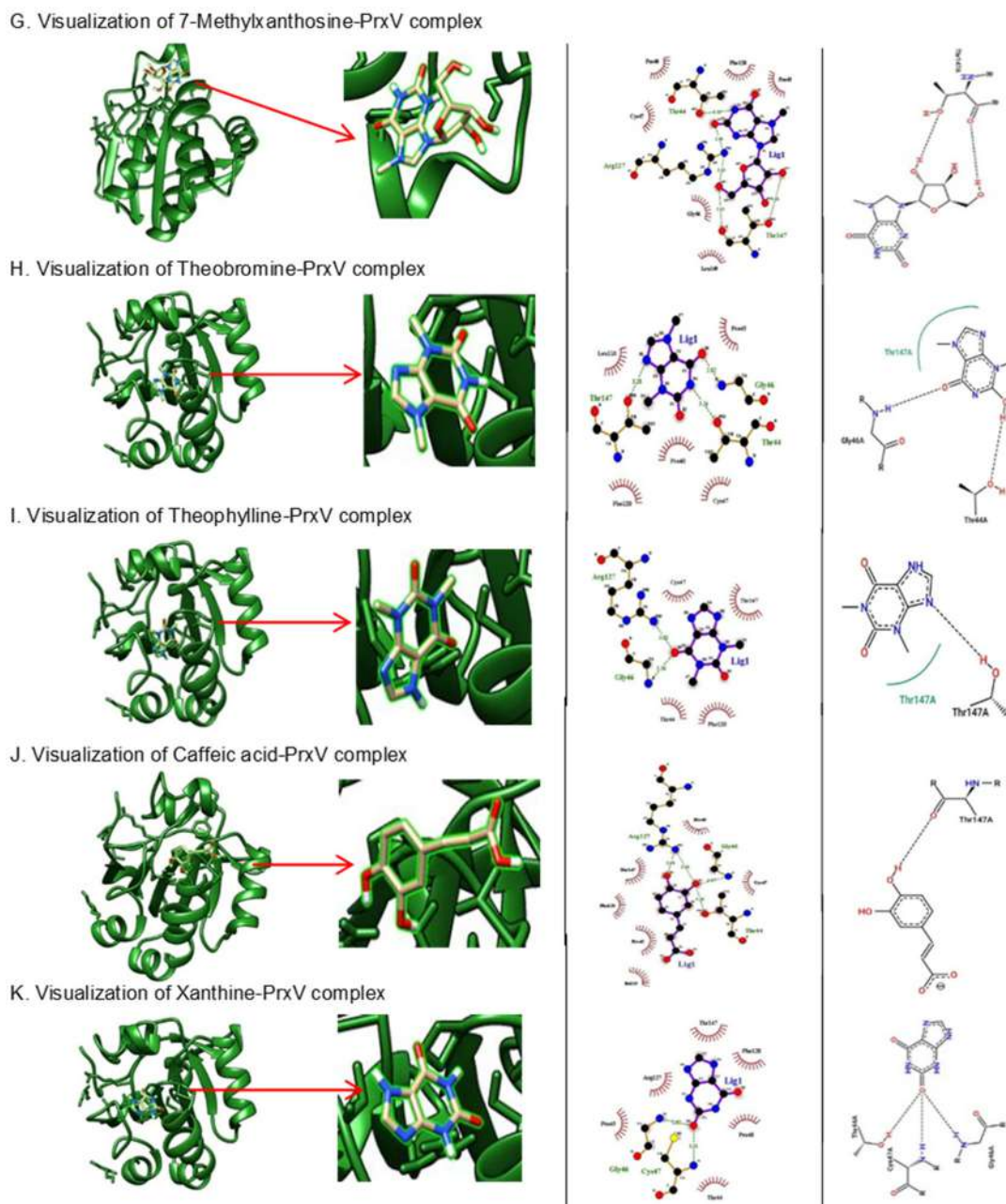


Fig 3. (A-K) Visualization of the 10 strongest ligand-receptor complexes using PyMOL Molecular Graphics System Software Version 2.4.0 and LigPlot and evaluated through www.swissadme.ch (*Continued*)

since they generally had the same binding sites in both hydrogen bonding and hydrophobic interactions. This similarity indicated that the ten bioactive components of coffee leaves have almost the same or even better antioxidant activity than the D1D control ligand. The affinity energy value determines the strength of the ligand-receptor complex interaction. If the affinity energy of the tested ligand is lower than that of the control ligand,

the results can be utilized to make an early prediction about the ligand's potential as an antioxidant. The ligands and bound residues are not stationary during the molecular docking simulation. Because the interactions influence each other, both are constantly in motion.

Consequently, these interactions will cause the atom to move from its initial position. The resulting interaction of the ligand and receptor can be either attraction or

repulsion. The bound residue tends to experience a slight shift due to the influence of the ligand [29].

The results of this research imply that the binding of these ten active compounds to the active site of PrxV, namely the active 2-Cys, will lead to an increase in the work selectivity of PrxV in catalyzing the reduction process of hydrogen peroxide substrate (H_2O_2) to become water (H_2O). Due to oxidative stress because of excessive ROS production, endogenous antioxidants must receive additional exogenous antioxidants from outside the body, such as bioactive components in the form of phenolic compounds, alkaloids, and flavonoids, which can be obtained from food or beverage intakes. The bioactive components of coffee leaves, such as xanthenes, caffeine, and chlorogenates, can increase the activity of PrxV's enzymatic antioxidant. Coffee leaf's phenol molecules can capture ROS and can form chelates with metals that encourage the generation of ROS, hence preventing lipid peroxidation and DNA damage. The $-OH$ group, which can contribute one molecule of hydrogen to make the ROS stable, is the active group that generally works as a catcher and inhibitor of free radical processes. Many $-OH$ groups in coffee leaf polyphenols are multifunctional. They can react with free radicals as reducing agents, free radical scavengers, metal chelating agents and boosting the work of the PrxV enzyme [30].

Finally, the results of our study emphasize the potential of coffee leaves as a source of antioxidant compounds. However, the composition of these antioxidant compounds might be changed when the leaves are subjected to different processing methods, especially those with prolong exposure to high temperature, as presented in this study. Several other recent reports also indicated similar trends, not only to the antioxidant activity of the coffee leaves but also to its anti-inflammatory activity [31-33]. *In vivo* antioxidant assessment of coffee leaf extract in experimental animals and human studies is also not as extensive as that of coffee beans, which should be highlighted in the future research direction.

■ CONCLUSION

The best antioxidant activity of the *Kawa Daun* beverage was obtained in *Kawa Daun* with smoking times

of 0 and 2 h (on the value of $IC_{50} < 20$ ppm). The results of molecular docking between the PrxV receptor and the studied ligands of 33 bioactive components of coffee leaves reveal that ten compounds have the most significant potential as antioxidants based on the most negative affinity energy, such as xanthone, uric acid, xanthosine, caffeine, 3-methylxanthine, 7-methylxanthosine, theobromine, theophylline, caffeic acid, and xanthine with affinity energy of -4.9, -4.8, -4.8, -4.6, -4.6, -4.6, -4.5, -4.5, -4.5, and -4.4 kcal/mol, respectively. Those top 10 ligands have more vital interaction from the control ligand of D1D, of which ligand has affinity energy (-3.6 kcal/mol). This study provided scientific evidence for using *Kawa Daun* is a traditional functional beverage. A short smoking time (2 h) is recommended for better antioxidant performance of the beverage. Further research to confirm the potential antioxidant of *Kawa Daun* by *in vivo* method is recommended.

■ ACKNOWLEDGMENTS

The authors wish to acknowledge the support of LPDP Scholarship 2020 to Ifwarisan Defri, with the contract number 201807110113078.

■ REFERENCES

- [1] Defri, I., Palupi, N.S., and Yuliana, N.D., 2021, Physicochemical and sensory characteristics of *Kawa Daun* from West Sumatra at different smoking time, *Proceedings of the International Seminar on Promoting Local Resources for Sustainable Agriculture and Development (ISPLRSAD 2020)*, Atlantis Press, 113–125.
- [2] Yin, Y., Katahira, R., and Ashihara, H., 2015, Metabolism of purine alkaloids and xanthine in leaves of maté (*Ilex paraguariensis*), *Nat. Prod. Commun.*, 10 (5), 707–712.
- [3] Mizuno, K., Kato, M., Irino, F., Yoneyama, N., Fujimura, T., and Ashihara, H., 2003, The first committed step reaction of caffeine biosynthesis: 7-Methylxanthosine synthase is closely homologous to caffeine synthases in coffee (*Coffea arabica* L.), *FEBS Lett.*, 547 (1-3), 56–60.
- [4] Nayeem, N., Denny, G., and Mehta, S.K., 2011, Comparative phytochemical analysis, antimicrobial

- and antioxidant activity of the methanolic extracts of the leaves of *Coffea Arabica* and *Coffea Robusta*, *Pharm. Lett.*, 3 (1), 292–297.
- [5] Vitória, A.P., and Mazzafera, P., 1999, Xanthine degradation and related enzyme activities in leaves and fruits of two *Coffea* species differing in caffeine catabolism, *J. Agric. Food Chem.*, 47 (5), 1851–1855.
- [6] Monteiro, Â., Colombari, S., Azinheira, H.G., Guerra-Guimarães, L., Do Céu Silva, M., Navarini, L., and Resmini, M., 2020, Dietary antioxidants in coffee leaves: Impact of botanical origin and maturity on chlorogenic acids and xanthones, *Antioxidants*, 9 (1), 6.
- [7] Hall, A., Parsonage, D., Poole, L.B., and Karplus, P.A., 2010, Structural evidence that peroxiredoxin catalytic power is based on transition-state stabilization, *J. Mol. Biol.*, 402 (1), 194–209.
- [8] Sutomo, S., and Pratama, M.R.F., 2020, Measuring the potential antioxidant activity of methyl gallate: Molecular docking study, *Thai J. Pharm. Sci.*, 44 (1), 14–22.
- [9] Nemallapudi, B.R., Zyryanov, G.V., Avula, B., Guda, M.R., Cirandur, S.R., Venkataramaiah, C., Rajendra, W., and Gundala, S., 2019, Meglumine as a green, efficient and reusable catalyst for synthesis and molecular docking studies of bis(indolyl)methanes as antioxidant agents, *Bioorg. Chem.*, 87, 465–473.
- [10] Hasanah, M., Maharani, B., and Munarsih, E., 2017, Daya antioksidan ekstrak dan fraksi daun kopi robusta (*Coffea robusta*) terhadap pereaksi DPPH (2,2-difenil-1-pikrilhidrazil), *IJPST*, 4 (2), 42–49.
- [11] Gómez-Ruiz, J.Á., Leake, D.S., and Ames, J.M., 2007, *In vitro* antioxidant activity of coffee compounds and their metabolites, *J. Agric. Food Chem.*, 55 (17), 6962–6969.
- [12] Novita, R., Kasim, A., Anggraini, T., and Putra, D.P., 2018, *Kahwa daun*: Traditional knowledge of a coffee leaf herbal tea from West Sumatera, Indonesia, *J. Ethn. Foods*, 5 (4), 286–291.
- [13] Salazar-Aranda, R., Pérez-López, L.A., López-Arroyo, J., Alanís-Garza, B.A., and Waksman de Torres, N., 2011, Antimicrobial and antioxidant activities of plants from northeast of Mexico, *Evidence-Based Complementary Altern. Med.*, 2011, 536139.
- [14] Hosseini, F.S., and Amanlou, M., 2020, Anti-HCV and anti-malaria agent, potential candidates to repurpose for coronavirus infection: Virtual screening, molecular docking, and molecular dynamics simulation study, *Life Sci.*, 258, 118205.
- [15] Boenzi, F., Digiesi, S., Mossa, G., Mummolo, G., and Romano, V.A., 2013, Optimal break and job rotation schedules of high repetitive - low load manual tasks in assembly lines: An OCRA - based approach, *IFAC Proc. Vol.*, 46 (9), 1896–1901.
- [16] Goddard, T.D., Huang, C.C., Meng, E.C., Pettersen, E.F., Couch, G.S., Morris, J.H., and Ferrin, T.E., 2018, UCSF ChimeraX: Meeting modern challenges in visualization and analysis, *Protein Sci.*, 27 (1), 14–25.
- [17] DeLano, W.L., and Bromberg, S., 2004, *PyMOL User's Guide*, Delano Scientific LLC, California.
- [18] Laskowski, R.A., and Swindells, M.B., 2011, LigPlot+: Multiple ligand-protein interaction diagrams for drug discovery, *J. Chem. Inf. Model.*, 51 (10), 2778–2786.
- [19] Badarinath, A.V., Rao, K.M., Madhusudhana, C.C., Ramkanth, S., Rajan, T.V.S., and Gnanaprakash, K., 2010, A review on *in-vitro* antioxidant methods: Comparisons, correlations and considerations, *Int. J. PharmTech Res.*, 2 (2), 1276–1285.
- [20] Defri, I., Rahmi, I.D., and Asben, A., 2019, The effect on extraction time of Kawa Daun grounds (*Coffea cannephora*) using ultrasonic towards bioactive components, *Seminar Nasional Bioteknologi IV Universitas Gadjah Mada*, Universitas Gadjah Mada, Yogyakarta, 2 November 2019, 72–90.
- [21] Choi, S., Jung, S., and Ko, K.S., 2018, Effects of coffee extracts with different roasting degrees on antioxidant and anti-inflammatory systems in mice, *Nutrients*, 10 (3), 363.
- [22] Chaaban, H., Ioannou, I., Chebil, L., Slimane, M., Gerardin, C., Paris, C., Charbonnel, C., Chekir, L., and Ghouil, M., 2017, Effect of heat processing on thermal stability and antioxidant activity of six flavonoids, *J. Food Process. Preserv.*, 41 (5), e13203.

- [23] Yuliana, N.D., Sugiharto, M.A., Lioe, H.N., Goto, M., and Ishikawa, Y.T., 2018, NMR metabolomics revealed metabolites and bioactivity variation in Torbangun leaves *Plectranthus amboinicus* L. with different origins, *Indones. J. Biotechnol.*, 23 (2), 91–101.
- [24] Ngamsuk, S., Huang, T.C., and Hsu, J.L. 2019, Determination of phenolic compounds, procyanidins, and antioxidant activity in processed *Coffea arabica* L. leaves, *Foods*, 8 (9), 389.
- [25] Chen, X., Mu, K., and Kitts, D.D., 2019, Characterization of phytochemical mixtures with inflammatory modulation potential from coffee leaves processed by green and black tea processing methods, *Food Chem.*, 271, 248–258.
- [26] Prieto-Martínez, F.D., Arciniega, M., and Medina-Franco, J.L., 2018, Acoplamiento molecular: Avances recientes y retos, *TIP*, 21, 65–97.
- [27] Gohlke, H., and Klebe, G., 2002, Approach to the description and prediction of the binding affinity of small-molecule ligands to macromolecular receptors, *Angew. Chem., Int. Ed.*, 41 (15), 2644–2676.
- [28] Syahbanu, F., Giriwono, P.E., Tjandrawinata, R.R., and Suhartono, M.T., 2020, Molecular analysis of a fibrin-degrading enzyme from *Bacillus subtilis* K2 isolated from the Indonesian soybean-based fermented food moromi, *Mol. Biol. Rep.*, 47 (11), 8553–8563.
- [29] Li, M.H., Luo, Q., Xue, X.G., and Li, Z.S., 2011, Molecular dynamics studies of the 3D structure and planar ligand binding of a quadruplex dimer, *J. Mol. Model.*, 17 (3), 515–526.
- [30] Akhlaghi, M., and Bandy, B., 2009, Mechanisms of flavonoid protection against myocardial ischemia-reperfusion injury, *J. Mol. Cell. Cardiol.*, 46 (3), 309–317.
- [31] Chen, X.M., Ma, Z., and Kitts, D.D., 2018, Effects of processing method and age of leaves on phytochemical profiles and bioactivity of coffee leaves, *Food Chem.*, 249, 143–153.
- [32] Segheto, L., Santos, B.C.S., Werneck, A.F.L., Vilela, F.M.P., de Sousa, O.V., and Rodarte, M.P., 2018, Antioxidant extracts of coffee leaves and its active ingredients 5-caffeoylquinic acid reduce chemically-induced inflammation in mice, *Ind. Crops Prod.*, 126, 48–57.
- [33] Ding, J., Mei, S., Gao, L., Wang, Q., Ma, H., and Chen, X., 2022, Tea processing steps affect chemical compositions, enzyme activities, and antioxidant and anti-inflammatory activities of coffee leaves, *Food Front.*, 00, 1–12.

Supplementary Data

This supplementary data is a part of paper entitled "Superparamagnetic Composite of Magnetite-CTAB as an Efficient Adsorbent for Methyl Orange".

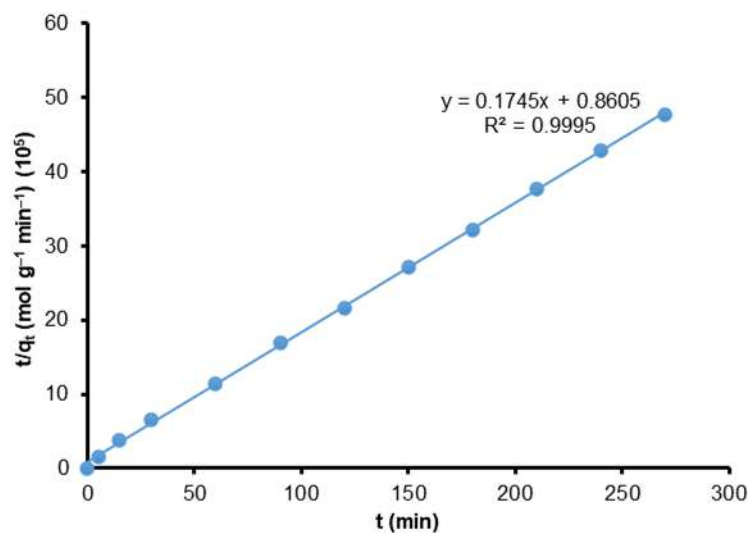


Fig S1. The curve of t/q_t vs. t is based on the Ho and McKay kinetic equations

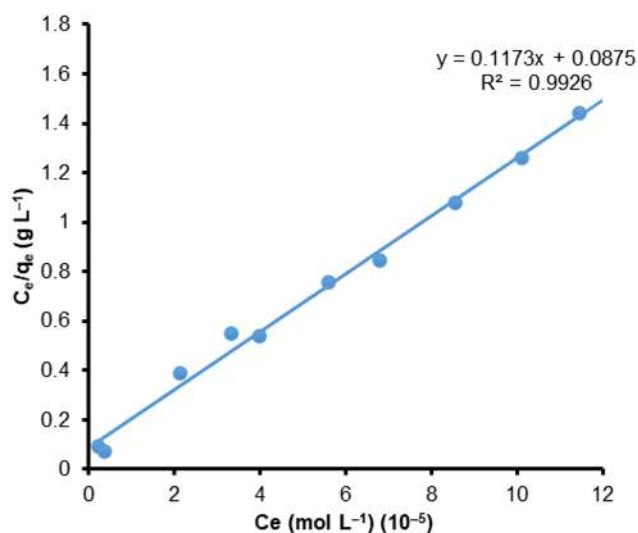


Fig S2. The linear curve of C_e/q_e vs. C_e related with Langmuir isotherms

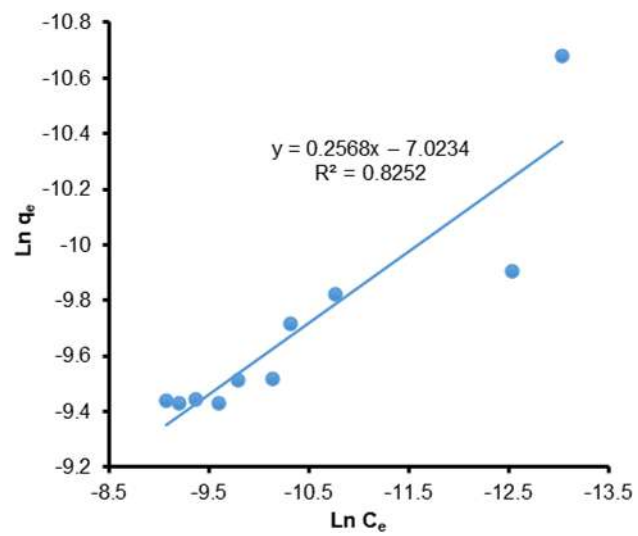


Fig S3. The linear curve of C_e/q_e vs. C_e related with Langmuir isotherms



Fig S4. Adsorbent recovery test with an external magnetic field

Superparamagnetic Composite of Magnetite-CTAB as an Efficient Adsorbent for Methyl Orange

Nor Harisah, Dwi Siswanta, Mudasir Mudasir, and Suyanta Suyanta*

Department of Chemistry, Faculty of Mathematics and Natural Sciences, Universitas Gadjah Mada, Sekip Utara, Yogyakarta 55281, Indonesia

* **Corresponding author:**

tel: +62-8568936689

email: suyanta_mipa@ugm.ac.id

Received: October 1, 2021

Accepted: January 4, 2022

DOI: 10.22146/ijc.69499

Abstract: In this study, a superparamagnetic composite of magnetite-cetyltrimethylammonium bromide (CTAB) has been prepared by the coprecipitation method and then applied as a charge-selective adsorbent of anionic methyl orange (MO). The VSM (Vibrating Sample Magnetometer) measurement suggests the superparamagnetic property of MNPs (Magnetite Nano Particles) with a magnetic saturation of 49.2 emu g^{-1} . The SEM image exhibits the significant difference in particle size from nanometers in uncoated magnetite to micrometers in magnetite-CTAB. Calculations with ImageJ software indicate that the diameter of the composite is in the range of 2–13 μm , with an average diameter of 6.56 μm , possibly consisting of hundreds to thousands of magnetite-CTAB micelles. The adsorption kinetics of MO over magnetite-CTAB follows the pseudo-second-order adsorption model of Ho and McKay with a rate constant (k_2) of $3.54 \times 10^3 \text{ g mol}^{-1} \text{ min}$. The adsorption isotherm is well described by the Langmuir model with a Langmuir constant (K_L) of $7.46 \times 10^4 \text{ L mol}$ and a maximum capacity (q_m) of 27.9 mg g^{-1} . The developed material is intriguing because it can be easily and quickly recovered using an external magnet after adsorption and selectively adsorbs anionic dyes.

Keywords: superparamagnetic; composite; magnetite-CTAB; adsorption; methyl orange

■ INTRODUCTION

Dyes are one of the primary sources of environmental contamination. The total amount of dyes used worldwide is estimated at over 10^7 kg per year, mainly originating from the textile industry [1]. Textile fibers have polar groups that can form a dipole-dipole bond with auxotrophic groups on dyes that are also polar [2]. Dyes are readily soluble in organic solvents or water, so they are difficult to remove by various physical, chemical, and biological methods [3]. The main problem with using reactive dyes in textiles is that not all of these dyes are adsorbed by the fabrics because the binding efficiency of fibers to the dyes is only 60–90%. The dyes that are not absorbed by the fibers are released into the environment and become hazardous waste [4].

Pollution of textile dyes in the water causes aesthetic damage, blocks light penetration, and interferes with the photosynthesis of aquatic plants, such as algae [5]. Textile

dyes are also toxic, mutagenic, and carcinogenic [6-7]. Based on the charge of the dye molecule when ionized in water, two types of dyes can be mentioned, e.g., cationic and anionic dyes [8]. Due to its dangerous effect on the environment, several techniques for dye removal from water have been proposed. These include coagulation/flocculation, ozonization, oxidation, filtering with membrane, electrochemical processes, photocatalytic degradation, and adsorption [9]. Among those various techniques, adsorption normally becomes the choice because it is the most practical, simple, efficient, and economical way. Various types of adsorbents have been reported to be used for the adsorption of dyes, including zeolite, bentonite, sepiolite, smectite, mesoporous silica, orange peel, chitosan, alginate, and magnetite (Fe_3O_4) [1]. Although most of these materials are effective and efficient as adsorbents for the dyes, their handling after the

adsorption process becomes a serious problem because they are not easily recovered and separated from the pollutants. Therefore, a new adsorbent that can be easily separated and recovered, such as magnetite materials, should be developed.

It has been well known that superparamagnetic materials, such as magnetite nanoparticles (MNPs) with a particle size of less than 25 nm can be attracted by magnetic fields. Still, their magnetic properties will be lost when the magnet is removed [10]. This unique property makes it suitable to be used as a dye adsorbent. After the adsorption process, the adsorbent can be separated quickly by an external magnetic field, so it does not require centrifugation or filtration, which is usually required when other non-magnetite adsorbents are used. However, superparamagnetic materials such as MNPs synthesized in this study have limitations. For example, they tend to attract each other and agglomerate to form a bulk phase due to their magnetic properties. One strategy that can be used to prevent the formation of agglomeration is to trap the MNPs using surfactants as soon as they are formed so that their superparamagnetic property can be maintained. Cetyltrimethylammonium bromide (CTAB) is one of the most widely used cationic surfactants for such purposes. It will be ionized in water, resulting in cationic CTA^+ and anionic Br^- . The cationic CTA^+ will interact with the surface of magnetite to form a positive layer on the surface of magnetite so that it can be used to adsorb selectively anionic dyes.

It has been previously reported that the isoelectric point of magnetite is at around $\text{pH} = 7$ [11-12]. The synthesis of magnetite is generally carried out at a relatively high pH, i.e., $\text{pH} = 11$ [13], so its surface will be negatively charged. In the case of magnetite-CTAB preparation, spherical micelles in which the double-layered CTA^+ becomes a shell covering the MNPs core can be produced under these circumstances if an appropriate amount of CTAB is introduced into the MNPs sol [14]. The positive head of the CTA^+ polar groups in the first layer will face the center of the sphere containing MNPs and interact electrostatically with the negatively charged MNPs surface. Meanwhile, the hydrophobic groups of CTA^+ interact hydrophobically

with other hydrophobic groups of CTA^+ positioned in the second layer [14]. The remaining polar groups of CTA^+ in the second layer are located on the surface of the spherical micelles, giving a positive charge to the double layer surface. Therefore, the material will adsorb anionic pollutants such as methyl orange (MO) by electrostatic interactions. So far, there have been extensive reports dealing with the synthesis and application of magnetite-CTAB composites [2-3,5-7]. However, to the best of our knowledge, there is still no work focusing on optimizing the CTAB mass in the synthesis. Yet, this parameter is crucial to be optimized to get the exact double-layer material with positively charged surfaces.

Furthermore, the application of these magnetite materials as charge-selective adsorbents of anionic dyes such as MO is also hardly reported, although the removal of MO by adsorption methods has been reported by many workers [10,15-18]. Chen et al. [10] have studied the kinetics and adsorption mechanism of methyl orange by surfactant modified *silkworm exuviae*. Protonated cross-linked chitosan has been used to adsorb MO [15], and the determination of biosorption conditions of MO by biomaterials of *humicola fuscoatra* has also been conducted [16]. The role of surface and pH on the adsorption behavior of MO onto wheat bran has been reported by Alzaydien [17], while an equilibrium, kinetic, and thermodynamic study of the removal of MO from aqueous solution via adsorption on cork as a natural and low-cost adsorbent has also been carried out [18]. None of the reported adsorbents used for this MO adsorption are magnetite materials.

Recently, Fisli et al. [19] have reported the synthesis of magnetite-CTAB and used the material for MO removal. However, the procedure used in this report did not control pH up to pH 11, did not optimize the mass of CTAB added, did not maintain the inert atmosphere, and used conventional mixing. As mentioned above, control of pH, as well as the amount of CTAB added to the reaction, are essential to get exactly a double layer with positively charged surfaces. Moreover, inert atmosphere control is also important to ensure that Fe^{2+} is not oxidized into Fe^{3+} during the

process. If this happens, magnetite will not be produced; instead, Fe_2O_3 will be obtained. In addition, conventional mixing by stirrer is also used in this report so that the reaction time is longer. In the present work, we introduce a new modified procedure for synthesizing magnetite-CTAB composite. The synthesis was done in the nitrogen atmosphere, and the addition of CTAB was optimized to get a double layer on the surface of magnetite so that the charge on the surface is positive. To speed up the reaction, ultrasonic mixing has also been used in the reaction. The obtained materials were characterized by FTIR, XRD, VSM, and SEM and then used for the adsorption of MO from aqueous samples. MO has been used as an anionic target in this study because it is extensively used in textile industries and is normally difficult to remove from water [1]. In the adsorption study, some parameters influencing the adsorption, including pH, contact time, and initial concentration, were optimized. Evaluation of kinetic adsorption was done by applying three types of kinetic models, e.g., Lagergren, Ho and McKay, and Langmuir-Hinshelwood, while for isotherm adsorption, Langmuir and Freundlich were applied, and the recovery of the adsorbent using an external magnet was determined after adsorption. Meanwhile, Fisli et al. [19] used only one model for each parameter in the adsorption study of MO, i.e., the Ho and McKay kinetic model and the Langmuir isotherm model, and no recovery of adsorbent was conducted. Moreover, as the magnetite (MNP) is positioned deep in the core of the micelle, it is expected that it will be more protected from oxidation. As a result, the composites will have a long duration or high stability magnetic properties.

■ EXPERIMENTAL SECTION

Materials

The materials used in this study included CTAB ($\geq 98\%$ purity Merck, Germany), $\text{FeSO}_4 \cdot 7\text{H}_2\text{O}$ ($\geq 99\%$ purity Merck, Germany), $\text{FeCl}_3 \cdot 6\text{H}_2\text{O}$ ($\geq 98\%$ purity Merck, Germany), NH_4OH (27% purity Merck, Germany), MO (85% purity Merck, Germany), and methyl violet (MV, 75% purity Merck, Germany). The chemicals were used as purchased, and no further purification was performed.

Distilled water was obtained from CV. Progo Mulyo Yogyakarta, Indonesia.

Instrumentation

The Bransonic 220 ultrasonic device was used as an ultrasonic beam source with a heating power of 100 W and a frequency of 48 kHz at 25–32 °C (room temperature). An X-ray diffractometer (XRD, Shimadzu XD-3H) was used to obtain the X-ray diffraction pattern, using $\text{Cu}_{\text{K}\alpha}$ powder irradiated at $\lambda = 0.15418$ nm. Shimadzu FTIR-8010PC was used for FTIR spectroscopic analysis, and the spectrum was recorded at a wavelength of 4000–400 cm^{-1} at room temperature using the KBr disc technique. A vibrating sample magnetometer (VSM Oxford 1.2H) was used to analyze the magnetic properties of the samples, using a magnetic field of up to 1.600 kA m^{-1} at room temperature. Scanning Electron Microscope (SEM, JEOL JSM-6510LA) was used to obtain the surface images of samples. The ImageJ software was used to process the obtained images. Spectrophotometer UV-Vis (Shimadzu UV-1700 E) was used to analyze the concentration of MO and MV at the λ_{max} of 464 nm and 582 nm, respectively.

Procedure

Synthesis of magnetite-CTAB

The new approach of magnetite-CTAB synthesis was developed by our groups here with the following procedure. Firstly, the nanocomposites of Magnetite-CTAB were synthesized by coprecipitation method, i.e., by adding NH_4OH (27%) solution dropwise into 100 mL of a solution containing $\text{FeCl}_3 \cdot 6\text{H}_2\text{O}$ (4.055 g), $\text{FeSO}_4 \cdot 7\text{H}_2\text{O}$ (2.085 g), and various masses of CTAB (0.365, 1.823, and 3.645 g) until the pH reached 11, and then the mixture was sonicated for 15 min. A flow of N_2 gas was continuously bubbled to the reactor to avoid oxidation by O_2 during the reaction. The precipitate was removed from the mixture by an external magnet, washed with distilled water to neutral pH, dried in an oven at 100 °C for 3 h, and stored in a desiccator. Each product was denoted as magnetite-CTAB-0.01, magnetite-CTAB-0.05, and magnetite-CTAB-0.10, respectively. A similar procedure but without CTAB was

used to synthesize the uncoated magnetite. All products were characterized by FTIR, XRD, and one product that gave the best performance during the preliminary test, e.g., magnetite-CTAB-0.10, was further characterized by SEM and VSM methods as an example.

Adsorption study

The determination of adsorption capacity as a preliminary test of different adsorbents was carried out by interacting the composite of magnetite-CTAB-0.01 (25 mg) with MO solution (10 mg L⁻¹, 20 mL) at pH 7. The mixture was then shaken for 2 h. The selection of pH 7 was based on the pH PZC of magnetite, which is around 7, so that the double layer of CTAB was maintained. After adsorption, the adsorbent was recovered using a magnetic bar, and the concentration of MO in the filtrate was analyzed by UV-Vis spectrophotometry at the λ_{\max} of 464 nm. Next, similar experiments were carried out using magnetite-CTAB-0.05, magnetite-CTAB-0.10, and uncoated magnetite, respectively, as an adsorbent. To test the selectivity of the adsorbent towards anionic dyes, similar experiments using cationic MV were also carried out using the same adsorbents and the same procedure as used for MO, except that the spectrometric analysis of MV in the filtrate was done at the λ_{\max} of 582 nm. The following Eq. (1) [20] was used to calculate the adsorption capacity of both MO and MV:

$$q_e = \frac{(C_o - C_t)V}{m} \quad (1)$$

in which q_e is the adsorption capacity (mg g⁻¹), C_o is the initial concentration (mg L⁻¹), C_t is the concentration at time t (mg L⁻¹), V is the volume of the solution (L), and m is the mass of the adsorbent (g).

Further experiments were the determination of optimum conditions for the adsorption MO, and it was done only to the adsorbent with the highest adsorption capacity of magnetite-CTAB. The effect of pH on the adsorption capacity was studied using the same experiments but with pH variations in the range 4–9. The adsorption kinetics was studied by doing the same experiments but with variations of contact time of 5, 10, 15, 30, 60, 90, 120, 150, 180, 210, 240, and 270 min at the optimum pH. The obtained data were evaluated using several kinetic models such as Lagergren, Ho-McKay, and

Langmuir-Hinshelwood models. For the adsorption isotherms study, the same experiments were also done but with variations of dye concentration, namely 5, 10, 15, 20, 25, 30, 35, 40, 45, and 50 mg L⁻¹ at the optimum pH and contact time. The data were evaluated using Langmuir and Freundlich Isotherms equations. The recovery test was carried out by separating the used adsorbent from outside the tube wall using an external magnet after the completion of the adsorption process.

RESULTS AND DISCUSSION

FTIR Analysis

FTIR spectra of uncoated magnetite, magnetite-CTAB-0.01, magnetite-CTAB-0.05, and magnetite-CTAB-0.10 (Fig. 1) show the peak at wavenumbers of 572, 586, 586, and 590 cm⁻¹, which is characteristic for the stretching vibration of the Fe–O bond on magnetite [21–22]. The shift of Fe–O absorption from 572 cm⁻¹ in uncoated magnetite to 586–590 cm⁻¹ in magnetite-CTAB indicates the alterations in the surface environment of MNPs caused by an interaction between the MNPs and the adsorbed CTAB molecules [3]. The weak adsorption at 3400 cm⁻¹ in all spectra was caused by stretching vibration of O–H⁻ adsorbed on the MNPs surface, while the peak at 1627 cm⁻¹ comes from the bending vibration of the hydroxyl group on the adsorbed water [22].

In Fig. 1(b-d), the peaks appearing at wavenumbers of 2924 and 2854 cm⁻¹ are due to the –CH and –CH₃ vibrations from CTAB, respectively [7,22]. Also, the bending vibration bands of the head [N(CH₃)₃] group at 1481 cm⁻¹ and (CN⁺) stretching vibrations at 904 cm⁻¹ are observed [23]. The intensity of peaks increases with the increase in the CTAB mass added. As the concentration of CTAB used in this synthesis was relatively small, the absorptions associated with CTAB in Fig. 1(b) are relatively weak, indicating that only a few portions of CTAB coat the magnetite particles.

XRD Analysis

The diffractograms of uncoated magnetite, magnetite-CTAB-0.01, magnetite-CTAB-0.05, and magnetite-CTAB-0.10 (Fig. 2) show multiple peaks at 2 θ

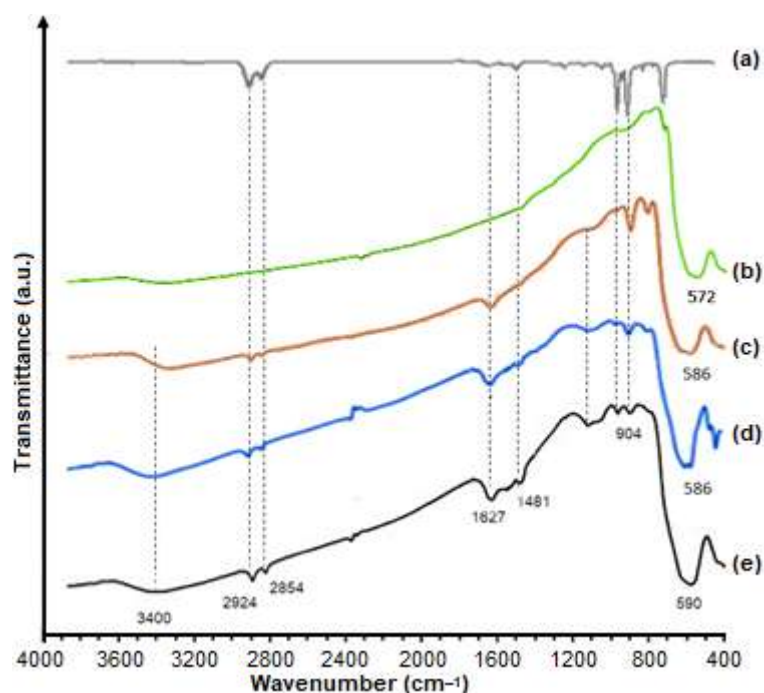


Fig 1. FTIR spectra of (a) CTAB, (b) uncoated magnetite, (c) magnetite-CTAB-0.01, (c) magnetite-CTAB-0.05, (d) magnetite-CTAB-0.10

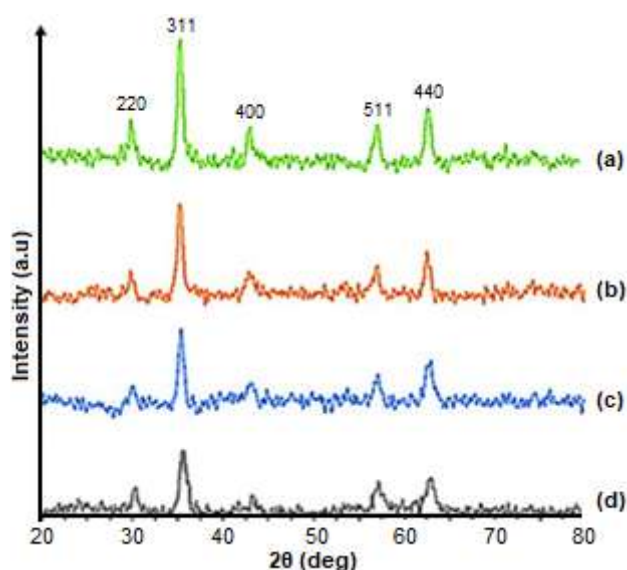


Fig 2. Diffractograms of (a) uncoated magnetite, (b) magnetite-CTAB-0.01, (c) magnetite-CTAB-0.05, and (d) magnetite-CTAB-0.10

30.5, 35.62, 43.07, 57.18, and 62.75° which correspond to *d*-spacing of 2.93, 2.52, 2.9, 1.61, and 1.48 Å, respectively. These peaks are the characteristics of the inverted spinel phase of magnetite, namely (220), (311), (400), (511), and (440) of magnetite (ICDD No.85-1436) [24], indicating

clearly that the four samples contain magnetite material. The identical diffraction angles among the diffractograms show that the CTAB coating does not affect the magnetite crystal structure. Hence, the CTA⁺ cation interacts electrostatically only with the surface charge of the MNPs and does not form covalent bonds with atoms in the magnetite crystal system. The decrease in peak intensity after the coating is caused by fewer X-rays reaching the MNP surface.

In the magnetite-CTAB-0.01 sample (Fig. 2(b)), the peak is still relatively high, indicating that only a few portions of the MNP were coated by CTAB, which matches the interpretation of FTIR spectra. In the magnetite-CTAB-0.05 sample (Fig. 2(c)), the diffractogram peaks were still observed, albeit at a lower intensity, indicating that the inverted spinel of magnetite is still present in the sample. Meanwhile, the intensity decreases significantly in the 0.10 magnetite-CTAB sample (Fig. 2(d)), indicating that the CTAB coating has been perfectly obtained. Based on the Scherrer Equation [25], namely $D = K\lambda/(\beta\cos\theta)$ where *K* is the constant (0.94), λ is the wavelength of X-ray (0.15418 nm), β is the FWHM of the (311) peak, and θ is the diffraction angle,

it is observed the average crystal sizes of magnetite decrease in the order of uncoated magnetite, magnetite-CTAB-0.01, magnetite-CTAB-0.05, and magnetite-CTAB-0.10, e.g., about 43, 35, 28, and 23 nm, respectively. This decrease in crystallite size with the increasing addition of CTAB is due to the role of CTAB in blocking the agglomeration among MNPs. Therefore, it is easily understood that increasing the addition of CTAB results in a smaller crystallite size of MNPs because the formation of agglomerates is hindered by CTAB.

VSM Analysis

VSM analysis was conducted only for the sample showing the best performance in the preliminary test (magnetite-CTAB-0.10) and uncoated magnetite for comparison. The hysteresis curves of uncoated magnetite and magnetite-CTAB-0.10 presented in Fig. 3 show that the saturation magnetization field (M_s) of the two samples are 72.8 and 49.2 emu g^{-1} , respectively. The M_s value of magnetite-CTAB-0.10 is smaller than that of uncoated magnetite due to the presence of non-magnetic coating materials, i.e., CTAB, that reduces the magnetic properties [26]. This VSM result is in line with the results of the diffractogram observations, showing the peak intensity of magnetite-CTAB-0.10 diffractogram is lower than that of uncoated magnetite. The magnetite-CTAB-0.10 composite has superparamagnetic properties, as indicated by the absence of loops in its hysteresis curve (Fig. 3(b)) [27]. Superparamagnetic materials arise from very small ferromagnetic materials ($< 25 \text{ nm}$) that form magnetic domains with high degrees of freedom. This result matches the estimated crystallite size of MNPs based on the previously stated Scherer Equation (23 nm). The uncoated magnetite in this study is ferrimagnetic, as indicated by the presence of loops on its hysteresis curve (Fig. 3(a)) [28]. This fact is due to the agglomeration of the existing MNPs so that the particle size becomes relatively large. Agglomeration between MNPs in magnetite-CTAB-0.10 composite does not occur because the CTAB layer blocks the formation of agglomerates.

SEM Analysis

Similar to VSM analysis, SEM analysis was also carried out to magnetite-CTAB-0.10 and uncoated

magnetite. The SEM image of uncoated magnetite (Fig. 4(a)) shows the presence of lumps of relatively large size in around $8\text{--}16 \mu\text{m}$ with an average of $9.94 \pm 0.38 \mu\text{m}$, resembling peeling bark and cast stone fragments. Meanwhile, the image of magnetite-CTAB-0.10 (Fig. 4(b)) shows relatively small grains ($2\text{--}13 \mu\text{m}$ with an average of $6.56 \pm 0.45 \mu\text{m}$) and resembling a pile of gravel mixed with sand. In uncoated magnetite, the magnetite particles are agglomerated because of their magnetic properties. In the magnetite-CTAB-0.10, however, XRD diffractogram data are corroborated by VSM data, confirming that the crystallite size of magnetite in the core of the particle was about 23 nm . On the other hand, the SEM image shows that the particle size of Magnetite-CTAB-0.10 is about $2\text{--}10 \mu\text{m}$ or $2,000\text{--}10,000 \text{ nm}$. Based on this finding, it is argued that what looks like a tiny grain in Fig. 4(b) is not just a magnetite-CTAB micelle but possibly an agglomeration of hundreds to thousands of magnetite-CTAB micelles.

Preliminary Determination of Adsorption Capacity

The adsorption capacity of MO and MV on uncoated magnetite, magnetite-CTAB-0.01, magnetite-CTAB-0.05, and magnetite-CTAB-0.10 are presented in

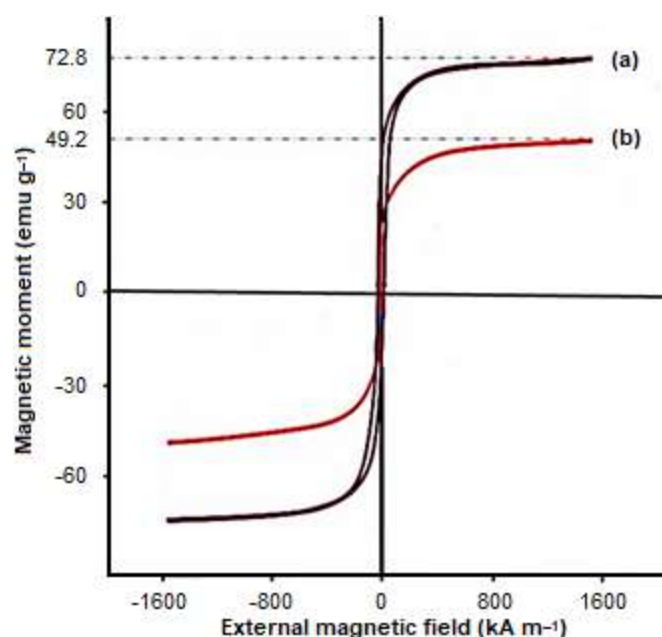


Fig 3. Magnetization curve of (a) uncoated magnetite and (b) magnetite-CTAB-0.10

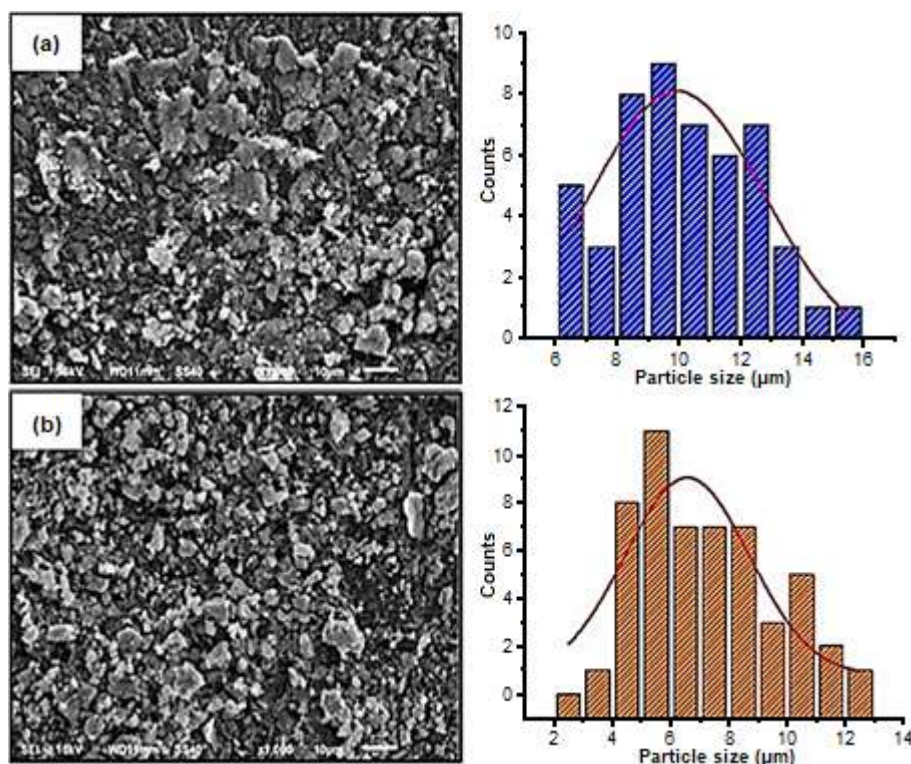


Fig 4. SEM images and the particle size distribution processed by ImageJ software: (a) uncoated magnetite and (b) magnetite-CTAB-0.10

Table 1. These data are needed to determine the optimum CTAB concentration in the synthesis of magnetite-CTAB composites. The magnetite-CTAB with a certain CTAB concentration with the highest adsorption capacity is considered the optimum CTAB addition concentration. The adsorption of the cationic dye of MV in this experiment was intended to check the selectivity of the adsorbents towards cationic and anionic dyes. From Table 1, it is found that increasing the concentration of CTAB in the synthesis of magnetite-CTAB gives rise to the increase in adsorption capacity. Based on these adsorption capacity data, the structure of magnetite-CTAB may be estimated. The uncoated magnetite provides a relatively small adsorption capacity because at the condition of adsorption, $\text{pH} = 7$ (a little bit higher than PZC), its surface has a negative charge so that it repels each other with an anionic dye of MO, while cationic dye of MV is sufficiently adsorbed because it has opposite charge with the surface of adsorbents.

Along with the increase in the concentration of CTAB, adsorption of anionic MO increases significantly

Table 1. Adsorption capacity (mg g^{-1}) and efficiency (%) of MO and MV on uncoated magnetite, magnetite-CTAB-0.01, magnetite-CTAB-0.05, and magnetite-CTAB-0.10

Adsorbent	Adsorption capacity, mg g^{-1} (% efficiency)	
	MO	MV
Uncoated magnetite	0.41 (5.20)	2.31 (28.9)
Magnetite-CTAB-0.01	5.48 (68.6)	0.50 (6.30)
Magnetite-CTAB-0.05	7.81 (97.6)	0.43 (5.38)
Magnetite-CTAB-0.10	7.94 (99.2)	0.14 (1.76)

while that of cationic MV sharply decreases. This is because the surface charge of the adsorbents changes gradually from negatively charged to positively charged surfaces as the double layer of CTAB is formed on the surface. The lower adsorption capacity of magnetite-CTAB-0.01 towards MO (5.48 mg g^{-1} or 68.55%) compared to the other two magnetite-CTAB adsorbents (almost 100% MO is adsorbed) indicates that the number of MNPs coated by CTAB is relatively still low or in other words, the concentration of CTAB in the

reaction system is still not enough to form a perfect double layer. This is consistent with the FTIR analysis that shows the absorption spectra of the CTA⁺ group to be relatively weak. Also, the high intensity of the XRD diffractogram indicates that only a few MNPs are coated by CTAB. On the other hand, the adsorption capacity of magnetite-CTAB-0.05 and magnetite-CTAB-0.10 is 7.81 mg g⁻¹ (97.6%) and 7.94 mg g⁻¹ (99.2%), respectively, meaning that all MO is adsorbed from the solution and that the double-layer micelles were fully formed.

The magnetite-CTAB has a positive charge of (CH₃)₃N⁺ group at the surface of adsorbents. This favorably interacts with anionic dyes of MO through electrostatic interaction [10]. The positive polar is formed on the surface of the Magnetite-CTAB composite because the CTA⁺ ions form double-layered spherical micelles with MNPs located in the core. In the first layer, the polar group of (CH₃)₃N⁺ from CTA⁺ interact electrostatically with the negative charge on the surface of MNPs, while the alkyl chain as the nonpolar group interacts hydrophobically with the alkyl chain of CTA⁺ in the second layer. The positive polar groups of the second layer point to the micelle surface to interact electrostatically with the anionic die of MO [23]. Fig. 5 presents the hypothetical structure of the double layer micelles on Magnetite-CTAB and the interactions that emerge between the positively charged surface of the adsorbent and the anionic adsorbate.

Table 1 clearly shows that the adsorption capacity of all adsorbents towards cationic MV is relatively low compared to the adsorption percentage of MO except uncoated magnetite. The relatively large adsorption capacity (2.31 mg g⁻¹ or 28.9%) of uncoated magnetite towards MV is due to electrostatic interaction between the negative charge of the uncoated magnetite surface with the positive charge of the MV. However, this adsorption capacity value is still much lower than the adsorption capacity of Magnetite-CTAB-0.10 towards MO (7.94 mg g⁻¹ or 99.21%). This is probably caused by steric hindrance between MV molecules due to the relatively small size of uncoated MNPs. In the case of magnetite-CTAB adsorbents, the greater the concentration of CTAB used in the magnetite-CTAB synthesis, the smaller its adsorption capacity towards cationic MV. It is because more positive charges are formed on the magnetite surface so that a stronger repulsion occurs between cationic MV and the surface of the adsorbent. MV dye in these conditions of experiment produces cationic dye. Therefore, the most suitable adsorbent to adsorb MV is an anionic adsorbent. This finding also indirectly confirms that the developed adsorbent of magnetite-CTAB is charge-selective adsorbent or cationic adsorbent. For this reason, further study of MO adsorption was conducted only on magnetite-CTAB-0.10.

Solution pH is an essential factor in the adsorption

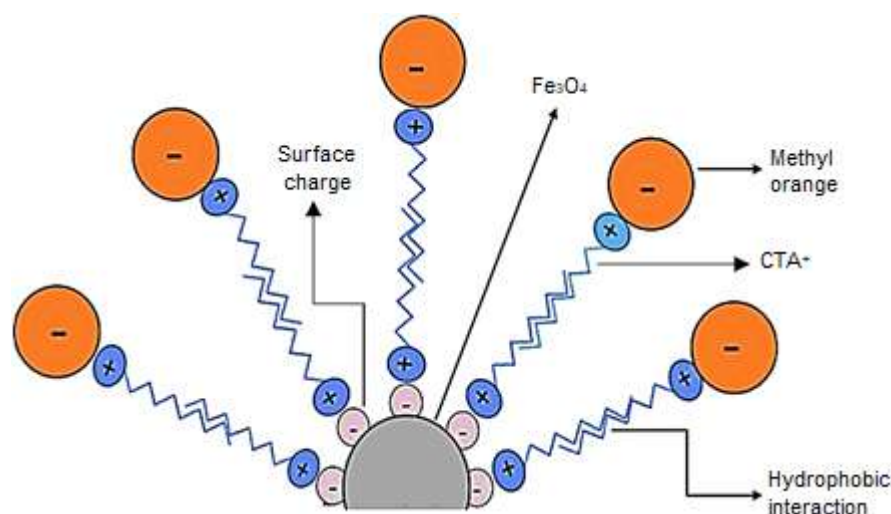


Fig 5. Hypothetical structure of double layer micelles on Magnetite-CTAB and its interaction with MO

process because it affects the surface charge of magnetite-CTAB composites and MO speciation [16]. Fig. 6 shows that the adsorption capacity increases with increasing pH of the solution from 4 to 7, then it continues to decrease from 7 to 9. The optimum adsorption occurs at pH 7 with an adsorption capacity of 7.27 mg g^{-1} (90.82%). Under acidic conditions, the MO molecule is protonated to form a quinoid structure with a positive charge on its NH_2 group (Fig. 7), while the surface of the adsorbent is also positively charged. Therefore, at low pH, repulsion between the protonated MO molecules and the positive charge of magnetite-CTAB-0.10 occurs, leading to lower adsorption of MO by magnetite-CTAB-0.10 with the decrease in solution pH from 7 to 4. Fig. 6 also shows that the adsorption capacity decreases significantly with increasing pH from 7 to 9. This is due to competition between the negatively charged MO molecules and OH^- ions to electrostatically interact with a positive charge at magnetite-CTAB-0.10 under alkaline conditions.

Adsorption Kinetics

The effect of contact time on the adsorption capacity of MO by magnetite-CTAB-0.10 is presented in Fig. 8. It is clearly shown the adsorption takes place very rapidly at the beginning. There are still plenty of active sites on the adsorbent that can interact with the MO, and the MO concentration in the solution is still high. The adsorption reaches its equilibrium after 120 min of mixing, where the amount of adsorbed MO no longer increases, meaning that the adsorption capacity (q_t) has reached its maximum value. There are two possible factors: saturation of the active sites or the exhaustion of adsorbent. As the concentration and volume of MO solution used in this

study are relatively low (20 mL of 10 mg L^{-1}), the second factor is more likely in this case.

Adsorption kinetics is used to predict the adsorption rate constant (k), providing important information about the mechanism and model of the adsorption process. In this study, three well-known adsorption kinetic models were applied to evaluate the most appropriate kinetic models: pseudo-first-order (Lagergren), pseudo-second-order (Ho and McKay), and Langmuir-Hinshelwood. The linear form of Lagergren's adsorption kinetics model is presented in Eq. (2) [30]:

$$\ln(q_e - q_t) = \ln q_e - k_1 t \quad (2)$$

where k_1 (min^{-1}) is the apparent first-order rate constant, q_e (mol g^{-1}) is the number of moles of adsorbate adsorbed by each gram of adsorbent at equilibrium, and q_t (mol g^{-1}) is the number of moles of adsorbate adsorbed by per gram of adsorbent at time t . If the plot of $\ln(q_e - q_t)$ versus t is constructed and the data fit the model, then a linear curve will be obtained with $\ln q_e$ as the intercept

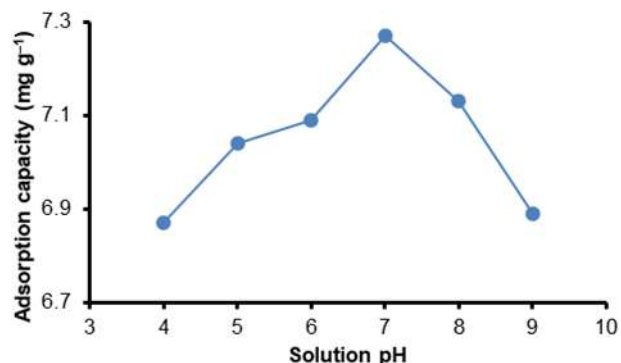


Fig 6. Effect of solution pH on the adsorption capacity of MO on magnetite-CTAB-0.10

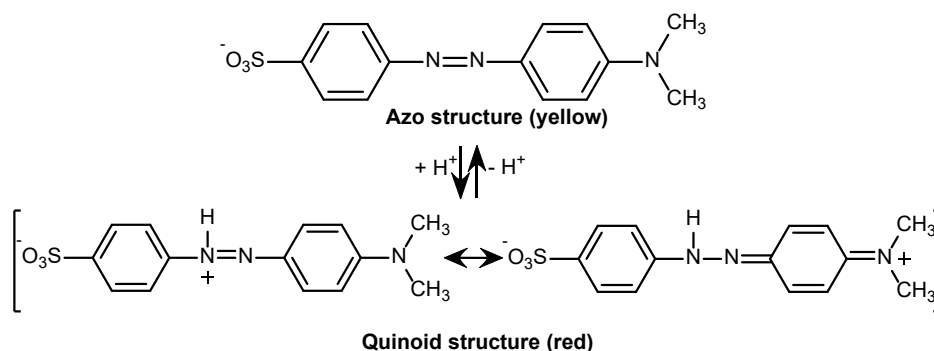


Fig 7. The resonance structure of MO as a function of pH [29]

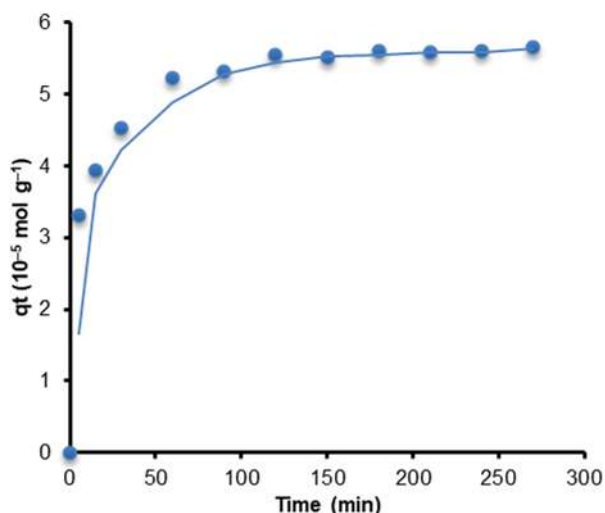


Fig 8. The effect of contact time on the adsorption capacity of MO

and k_1 as the slope.

The linear form of Ho and McKay's adsorption kinetics model is represented by Eq. (3) [31].

$$\frac{t}{q_t} = \frac{1}{k_2 q_e^2} + \frac{t}{q_e} \quad (3)$$

where k_2 is the adsorption rate constant of Ho and McKay ($\text{g mol}^{-1} \text{min}$), q_e is the amount of MO adsorbed at equilibrium (mol g^{-1}), and q_t is the amount of MO adsorbed at time t (mol g^{-1}). If t/q_t was plotted as a function of t and the data fit the model, then a linear curve will be obtained with $1/q_e$ as the intercept and $\frac{1}{k_2 q_e^2}$ as the slope so that the values of q_e and k_2 can be calculated.

Meanwhile, the linear form of the Langmuir-Hinshelwood adsorption kinetics model is expressed in Eq. (4) [32].

$$\frac{\ln\left(\frac{C_o}{C_t}\right)}{C_o - C_t} = k_1 \frac{t}{C_o - C_t} - k_o \quad (4)$$

where C_o (mol L^{-1}) is the initial concentration of adsorbate, C_t (mol L^{-1}) is the concentration of adsorbate remaining after adsorption for t time, k_1 (min^{-1}) is the adsorption rate constant, and k_o (L mol^{-1}) is the adsorption equilibrium constant. If a curve of $[\ln(C_o/C_t)]/(C_o - C_t)$ versus $t/(C_o - C_t)$ is constructed, then a linear curve with k_1 as the slope and $-k_o$ as the intercept will be obtained if the adsorption follows the kinetic adsorption model. Detailed results of the evaluation of the

kinetic model by the three equations are presented in Table 2.

From Table 2, it is easily seen that Ho and McKay's kinetic model gives the highest value of correlation coefficient (r^2), 0.9995, compared to those produced by the other two kinetic models, indicating that the MO adsorption on magnetite-CTAB-0.10 is best fitted to the Ho and McKay kinetic model. This suggests that at least two factors are involved in the mechanism of MO adsorption on the adsorbents, possibly the adsorbate and the active sites of the adsorbent and/or molecule of the solvent. Applying this model, it is found that the amount of MO adsorbed at equilibrium (q_e) is $5.73 \times 10^{-5} \text{ mol g}^{-1}$, and the adsorption rate constant (k_2) is $3.54 \times 10^3 \text{ g mol}^{-1} \text{ min}$. The linear curve of t/q_t versus t is attached as the Supporting Information (Fig. S1).

Adsorption Isotherms

The curve for the amount of MO adsorbed at equilibrium (q_e) as a function of initial concentration $[\text{MO}]$ is given in Fig. 9. It is observed that the q_e value increases with the increasing initial $[\text{MO}]$, then it reaches the saturation state at $[\text{MO}]$ of 35 mg/L, giving a maximum adsorption capacity of 26.33 mg g^{-1} . The MO adsorption isotherm on magnetite-CTAB-0.10 was studied using two types of well-known isotherm equation models, i.e., the Langmuir and Freundlich adsorption isotherm models.

The linear form of the Langmuir Isotherms equation is presented in Eq. (5) [33], where C_e (mol L^{-1}) is the concentration of adsorbate in the solution at

Table 2. Parameters of three kinetic models in MO adsorption on magnetite-CTAB-0.10

Kinetic models	Parameters	Values
Pseudo first order (Lagergren)	r^2	0.9639
	q_e (mol g^{-1})	2.389×10^{-5}
	k_1 (min^{-1})	2.83×10^{-2}
Pseudo second order (Ho and McKay)	r^2	0.9995
	q_e (mol g^{-1})	5.73×10^{-5}
	k_2 ($\text{g mol}^{-1} \text{ min}$)	3.54×10^3
Langmuir-Hinshelwood	r^2	0.6159
	k_1 (min^{-1})	6×10^{-3}

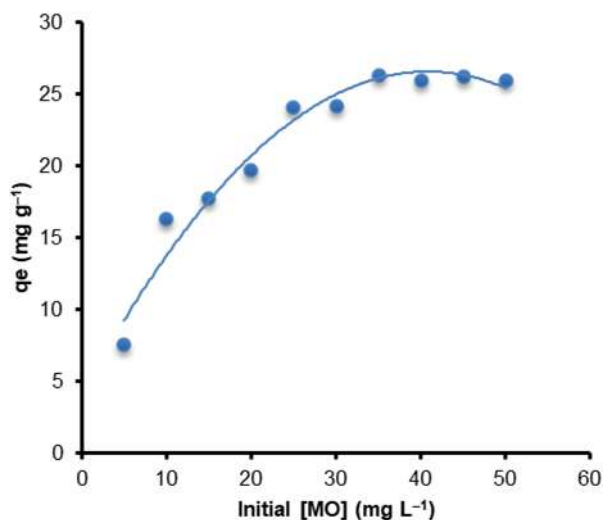


Fig 9. The curve of q_e as a function of the initial [MO]

equilibrium, q_e (mol g^{-1}) is the mole of adsorbate adsorbed by each gram of adsorbent at equilibrium, q_m (mol g^{-1}) is the maximum adsorption capacity, and K_L (L mol^{-1}) is the Langmuir constant. Based on Eq. (5), the plot of C_e/q_e vs. C_e will be linear with $1/q_m$ as the slope and $1/(q_m K_L)$ as the intercept if the adsorption follows this model so that the values of K_L and q_m can be obtained. An approximation of adsorption energy can be determined based on the standard Gibbs equation of $\Delta G_{\text{ads}}^0 = -RT \ln K_L$, where ΔG_{ads}^0 is the standard Gibbs free energy of adsorption, R is the universal gas constant ($8.314 \text{ J K}^{-1} \text{ mol}^{-1}$), and T is the temperature in Kelvin.

$$\frac{C_e}{q_e} = \frac{1}{q_m K_L} + \frac{1}{q_m} C_e \quad (5)$$

Meanwhile, the linear equation for Freundlich adsorption isotherms is expressed in Eq. (6) [34], where C_e is the concentration of adsorbate at equilibrium (mol L^{-1}), q_e is the amount of adsorbed substance in a gram of adsorbent (mol g^{-1}), K_F is the Freundlich adsorption capacity (mol g^{-1}) and n is a constant.

$$q_e = \log K_F + \frac{1}{n} \log C_e \quad (6)$$

The linear curves of the Langmuir and Freundlich Isotherms are attached in Fig. S2 and Fig. S3), respectively. Table 3 gives detailed isotherm parameter calculations for the two models used in this study. Because the value of r^2 for the Langmuir Isotherms (0.9926) is greater than that for the Freundlich Isotherms (0.8252), it can be concluded that the Langmuir Isotherm model best

describes the adsorption of MO on Magnetite-CTAB-0.10. These results suggest that the adsorption occurs on more homogeneous surfaces, probably due to the double-layer formation of CTAB, namely the polar group of CTA^+ on the core-shell of magnetite-CTAB. In addition, according to Fig. 9, the maximum adsorption is reached at a concentration of 35 mg L^{-1} , and, afterward, the adsorption tends to be constant. This indicates that the surface of the adsorbent experiences saturation when all of the active sites have been filled with MO, and the adsorption process will no longer occur even when the concentration of MO increases because adsorption is limited to one layer only.

Table 3 shows that the maximum adsorption capacity (q_{max}) of MO is 27.9 mg g^{-1} , meaning that every 1 g of the adsorbent can adsorb 27.9 mg of MO. This q_{max} value of MO is higher than those reported by previous studies that used various adsorbents. Table 4 gives the q_{max} of MO using the present adsorbent of Magnetite-CTAB-0.10 along with those obtained by other workers [17-19, 35-37] for comparison. It is clearly found that the adsorbent developed in this study, magnetite-CTAB-0.10, is superior and more efficient compared to previously reported adsorbents as it gives the highest value of q_{max} . Even more, it is almost four times higher than that of previously reported magnetite-CTAB [19], which was synthesized using the conventional method without optimization of the concentration of CTAB, without keeping the inert atmosphere, and using conventional magnetic mixing. The value of adsorption capacity obtained from this study is also compared to the results obtained from many studies using different magnetite adsorbents, as summarized in Table 5. It is

Table 3. Adsorption isotherm parameters of MO on Magnetite-CTAB-0.10

Isotherms model	Parameter	Value
Langmuir	r^2	0.9926
	q_{max} (mg g^{-1})	27.9
	K_L (L mol)	7.46×10^4
	ΔG_{ads}^0 (kJ mol^{-1})	-27.8
Freundlich	r^2	0.8252
	n	3.90
	K_F (L g^{-1})	8.91×10^{-4}

Table 4. Comparison of maximum adsorption capacities (q_{\max}) for MO on various types of adsorbents

Adsorbents	q_{\max} (mg g ⁻¹)	References
Copper oxide	1.2	[35]
Ammonium-functionalized MCM-41	1.12	[36]
Wheat Bran	12	[17]
Cork powder	16.8	[18]
Activated aluminas	9.8	[37]
Magnetite-CTAB	7.58	[19]
Magnetite-CTAB (modified method)*	27.9	This study

*CTAB concentration is optimized, synthesized in an inert atmosphere, and used ultrasonic mixing to speed up synthesis

Table 5. Comparison of maximum adsorption capacities (q_{\max}) for MO on various types of magnetite adsorbents

Adsorbent types	Optimum pH	Equilibrium time (min)	Q_{\max} (mg g ⁻¹)	Magnetization (emu g ⁻¹)	References
Magnetic hydroxyapatite	7	80	18.0	12.5	[38]
γ -Fe ₂ O ₃ /2C nanocomposite	4.5	60	42.34	30	[39]
Magnetic cellulose beads	7	180	1.47	40	[40]
Magnetic halloysite nanotubes/iron oxide composites	7	480	0.65	27.91	[41]
Rectorite/iron oxide nanocomposites	7	1	0.36	19.14	[42]
γ -Fe ₂ O ₃ crosslinked chitosan composite	6.6	100	29.46	4.36	[43]
Magnetite-CTAB	7	120	27.9	49.2	This study

observed that our results, in general, are higher or comparable to those previously reported in many kinds of literature [38-43].

Moreover, based on the equation of $\Delta G_{\text{ads}}^0 = -RT \ln K_L$ [44], where the values of $R = 8.314 \text{ J K}^{-1} \text{ mol}^{-1}$, $T = 298.15 \text{ K}$, and $K_L = 7.46 \times 10^4 \text{ L mol}^{-1}$, it has been found that the value of ΔG_{ads}^0 is $-27.8 \text{ kJ mol}^{-1}$. This result indicates that the adsorption of MO on Magnetite-CTAB-0.10 is dominated by both physisorption and chemisorption mechanisms (ΔG_{ads}^0 ranges from -20 to -80 kJ mol^{-1} [45-46]). It is predicted that the primary interaction in this adsorption is an electrostatic interaction between the positive surface charge on the adsorbent and the negative charge group on the adsorbate. Besides that, the relatively weak Van der Waals force may also be expected.

Recovery Test

The visualization (photograph) of the experimental bottle used in the recovery test after the separation process of the used adsorbent with an external magnetic field is

given in the Supporting Information (4). The adsorbent separation lasted only 1 min. The adsorbent magnetite-CTAB-0.10 and the adsorbed MO were attracted strongly by an external magnetic field and stuck to the bottle wall. This case matches the results of VSM measurements, which show that the magnetite-CTAB-0.10 composite is superparamagnetic with a large M_s of 68.88 emu g^{-1} . The orange solution containing MO becomes clear quickly because the composite rapidly adsorbs MO with a k_2 of $3.54 \times 10^3 \text{ g mol}^{-1} \text{ min}$ and a K_L of $7.46 \times 10^4 \text{ L mol}$. Furthermore, the adsorbent used and the adsorbed MO can be separated immediately by the external magnetic field.

CONCLUSION

Rapid synthesis of Magnetite-CTAB composites has been successfully developed by the coprecipitation method using ultrasonic mixing in an inert atmosphere. The use of 0.10 M CTAB produces the best performance of the magnetite-CTAB composite for the adsorption of methyl orange, probably due to the formation of a

double layer spherical micellar structure with MNPs as the core and a double layer of CTAB as the shell. The magnetite-CTAB composite obtained has a strong superparamagnetic property with a saturation magnetization field (Ms) of 49.2 emu g⁻¹. Adsorption study of MO using the developed adsorbent suggests the material can adsorb anionic dye of MO efficiently with the optimum conditions reached at pH 7 and 120 min of contact time. Kinetic study of the adsorption indicates that adsorption of MO on magnetite-CTAB fits well into the pseudo 2nd order kinetic model, meaning at least two factors are involved in the mechanism of adsorption, possibly the adsorbate itself and the active site and/or the molecules of solvent. The adsorption isotherms of MO by Magnetite-CTAB composite are best described by the Langmuir isotherm model, suggesting that the adsorption takes place on the homogenous active sites of the adsorbent surface and forms a monolayer. As the adsorbent selectively adsorbed anionic dyes (MO) over cationic ones (MV), it is predicted that the active sites are the positively charged group of CTA⁺ in the second layer facing outside the micellar. The developed Magnetite-CTAB composite is very prospective and promising because it selectively adsorbs anionic species and can be easily and quickly separated from the solution using an external magnetic field after the adsorption process. Therefore, it may be applied not only to anionic dyes but also to other hazardous anionic species in the environment.

■ ACKNOWLEDGMENTS

The first author (Nor Harisah) would like to acknowledge the Bureau of planning and overseas cooperation, The Ministry of Education and Culture of the Republic of Indonesia, for the financial support through “Beasiswa Unggulan” for M.Sc. Program in Chemistry at Universitas Gadjah Mada under the cooperation agreement letter No. 53960/A1.4/LL/2016 dated 30 September 2016.

■ REFERENCES

- [1] Mahdavi, M., Ahmad, M.B., Haron, M.J., Namvar, F., Nadi, B., Ab Rahman, M.Z., and Amin, J., 2013, Synthesis, surface modification and characterisation of biocompatible magnetic iron oxide nanoparticles for biomedical applications, *Molecules*, 18 (7), 7533–7548.
- [2] Gan, L., Lu, Z., Cao, D., and Chen, Z., 2018, Effects of cetyltrimethylammonium bromide on the morphology of green synthesized MNPs used to remove phosphate, *Mater. Sci. Eng., C*, 82, 41–45.
- [3] Khoshnevisan, K., Barkhi, M., Zare, D., Davoodi, D., and Tabatabaei, M., 2012, Preparation and characterization of CTAB-coated Fe₃O₄ nanoparticles, *Synth. React. Inorg., Met.-Org., Nano-Met. Chem.*, 42 (5), 644–648.
- [4] Lellis, B., Fávaro-Polonio, C.Z., Pamphile, J.A., and Polonio, J.C., 2019, Effects of textile dyes on health and the environment and bioremediation potential of living organisms, *Biotechnol. Res. Innovation*, 3 (2), 275–290.
- [5] Rajabi, A.A., Yamini, Y., Faraji, M., and Nourmohammadian, F., 2016, Modified magnetite nanoparticles with cetyltrimethylammonium bromide as superior adsorbent for rapid removal of the disperse dyes from wastewater of textile companies, *Nanochem. Res.*, 1 (1), 49–56.
- [6] Aquino, J.M., Rocha-Filho, R.C., Ruotolo, L.A.M., Bocchi, N., and Biaggio, S.R., 2014, Electrochemical degradation of a real textile wastewater using β-PbO₂ and DSA[®] anodes, *Chem. Eng. J.*, 251, 138–145.
- [7] Khatri, J., Nidheesh, P.V., Anantha Singh, T.S., and Kumar, M.S., 2018, Advanced oxidation processes based on zero-valent aluminium for treating textile wastewater, *Chem. Eng. J.*, 348, 67–73.
- [8] Sabna, V., Thampi, S.G., and Chandrakaran, S., 2018, Adsorptive removal of cationic and anionic dyes using graphene oxide, *Water Sci. Technol.*, 78 (4), 732–742.
- [9] Kasperchik, V.P., Yaskevich, A.L., and Bil'dyukevich, A.V., 2012, Wastewater treatment for removal of dyes by coagulation and membrane processes, *Pet. Chem.*, 52 (7), 545–556.
- [10] Estelrich, J., Escribano, E., Queralt, J., and Busquets, M.A., 2015, Iron oxide nanoparticles for

- magnetically-guided and magnetically-responsive drug delivery, *Int. J. Mol. Sci.*, 16 (4), 8070–8101.
- [11] Zemtsova, E.G., Ponomareva, A.N., Panchuk, V.V., Galiullina, L.F., and Smirnov, V.M., 2017, Synthesis, structure and magnetic properties of magnetite-SiO₂ nanocomposites with core-shell structures for targeted drug delivery, *Rev. Adv. Mater. Sci.*, 52, 82–90.
- [12] Kristianto, H., Reynaldi, E., Prasetyo, S., and Sugih, A.K., 2020, Adsorbed leucaena protein on citrate modified magnetite nanoparticles: Synthesis, characterization, and its application as magnetic coagulant, *Sustainable Environ. Res.*, 30 (1), 32.
- [13] Yew, Y.P., Shameli, K., Miyake, M., Kuwano, N., Bt Ahmad Khairudin, N.B., Bt Mohamad, S.E., and Lee, K.X., 2016, Green synthesis of magnetite (Fe₃O₄) nanoparticles using seaweed (*Kappaphycus alvarezii*) extract, *Nanoscale Res. Lett.*, 11 (1), 276.
- [14] El-Dib, F.I., Mohamed, D.E., El-Shamy, O.A.A., and Mishrif, M.R., 2020, Study the adsorption properties of magnetite nanoparticles in the presence of different synthesized surfactants for heavy metal ions removal, *Egypt. J. Pet.*, 29 (1), 1–7.
- [15] Huang, R., Liu, Q., Huo, J., and Yang, B., 2017, Adsorption of methyl orange onto protonated cross-linked chitosan, *Arabian J. Chem.*, 10, 24–32.
- [16] Subasioglu, T., and Bilkay, I.S., 2009, Determination of biosorption conditions of methyl orange by humicolafuscoatra, *J. Sci. Ind. Res.*, 68, 1075–1077.
- [17] Alzaydien, A.S., 2015, Adsorption behavior of methyl orange onto wheat bran: Role of surface and pH, *Orient. J. Chem.*, 31 (2), 643–651.
- [18] Krika, F., and Benlahbib, O.F., 2015, Removal of methyl orange from aqueous solution via adsorption on cork as a natural and low-cost adsorbent: Equilibrium, kinetic and thermodynamic study of the removal process, *Desalin. Water Treat.*, 53 (13), 3711–3723.
- [19] Fisli, A., Winatapura, D.S., and Alfian, A., 2018, The surface functionalization of Fe₃O₄ nanoparticles by CTAB as adsorbent for methyl orange elimination in water, *J. Phys.: Conf. Ser.*, 1091, 012002.
- [20] Edet, U.A., and Ifelebuegu, A.O., 2020, Kinetics, isotherms, and thermodynamic modeling of the adsorption of phosphates from model wastewater using recycled brick waste, *Processes*, 8 (6), 665.
- [21] Gaffer, A., Al Kahlawy, A.A., and Aman, D., 2017, Magnetic zeolite-natural polymer composite for adsorption of chromium (VI), *Egypt. J. Pet.*, 26 (4), 995–999.
- [22] Guivar, J.A.R., Sanches, E.A., Magon, C.J., and Fernandes, E.G.R., 2015, Preparation and characterization of cetyltrimethylammonium bromide (CTAB)-stabilized Fe₃O₄ nanoparticles for electrochemistry detection of citric acid, *J. Electroanal. Chem.*, 755, 158–166.
- [23] Elfeky, S.A., Mahmoud, S.E., and Youssef, A.F., 2017, Applications of CTAB modified magnetic nanoparticles for removal of chromium (VI) from contaminated water, *J. Adv. Res.*, 8 (4), 435–443.
- [24] Viana, R.B., da Silva, A.B.F., and Pimentel, A.S., 2012, Infrared spectroscopy of anionic, cationic, and zwitterionic surfactants, *Adv. Phys. Chem.*, 2012, 903272.
- [25] Muniz, F.T., Miranda, M.A.R., Dos Santos, C.M., and Sasaki, J.M., 2016, The Scherrer equation and the dynamical theory of X-ray diffraction, *Acta Crystallogr., Sect. A: Found. Adv.*, 72 (3), 385–390.
- [26] Liu, Y., 2013, Recent progress in Fourier transform infrared (FTIR) spectroscopy study of compositional, structural and physical attributes of developmental cotton fibers, *Materials*, 6 (1), 299–313.
- [27] Faghihian, H., Moayed, M., Firooz, A., and Iravani, M., 2014, Evaluation of a new magnetic zeolite composite for removal of Cs⁺ and Sr²⁺ from aqueous solutions: Kinetic, equilibrium and thermodynamic studies, *C.R. Chim.*, 17 (2), 108–117.
- [28] Baumgartner, J., Bertinetti, L., Widdrat, M., Hirt, A.M., and Faivre, D., 2013, Formation of MNPs at low temperature: from superparamagnetic to stable single-domain particles, *PLoS One*, 8 (3), e57070.
- [29] Kahlert, H., Meyer, G. and Albrecht, A., 2016, Colour maps of acid-base titrations with colour indicators: how to choose the appropriate indicator and how to estimate the systematic titration errors, *ChemTexts*, 2 (2), 7.

- [30] Kajjumba, G.W., Emik, S., Öngen, A., Özcan, H.K., Aydın, S., 2018, "Modelling of Adsorption Kinetic Processes—Errors, Theory, and Application" in *Advanced Sorption Process Applications*, Eds. Edebali, S., IntechOpen, Rijeka, Croatia.
- [31] Aliakbarian, B., Casazza, A.A., and Perego, P., 2015, Kinetic and isotherm modelling of the adsorption of phenolic compounds from olive mill wastewater onto activated carbon, *Food Technol. Biotechnol.*, 53 (2), 207–214.
- [32] Armenise, S., García-Bordejé, E., Valverde, J.L., Romeo, E., and Monzón, A., 2013, A Langmuir–Hinshelwood approach to the kinetic modelling of catalytic ammonia decomposition in an integral reactor, *Phys. Chem. Chem. Phys.*, 15 (29), 12104–12117.
- [33] Sauer, E., and Gross, J., 2019, Prediction of adsorption isotherms and selectivities: Comparison between classical density functional theory based on the perturbed-chain statistical associating fluid theory equation of state and ideal adsorbed solution theory, *Langmuir*, 35 (36), 11690–11701.
- [34] Obaid, S.A., 2020, Langmuir, Freundlich, Tamkin, Adsorption isotherms and kinetics for the removal *Aartichoke tournefortii* straw from agricultural waste, *J. Phys.: Conf. Ser.*, 1664, 012011.
- [35] Shiue, A., Ma, C.M., Ruan, R.T., and Chang, C.T., 2012, Adsorption kinetics and isotherms for the removal methyl orange from wastewaters using copper oxide catalyst prepared by the waste printed circuit boards, *Sustainable Environ. Res.*, 22 (4), 209–215.
- [36] Qin, Q., Ma, J., and Liu, K., 2009, Adsorption of anionic dyes on ammonium-functionalized MCM-41, *J. Hazard. Mater.*, 162 (1), 133–139.
- [37] Iida, Y., Kozuka, Tuziuti, T., and Yasui, K., 2004, Sonochemically enhanced adsorption and degradation of methyl orange with activated aluminas, *Ultrasonics*, 42 (1), 635–639.
- [38] Wang, X., 2011, Preparation of magnetic hydroxyapatite and their use as recyclable adsorbent for phenol in wastewater, *Clean: Soil, Air, Water*, 39 (1), 13–20.
- [39] Istratie, R., Stoia, M., Păcurariu, C., and Locovei, C., 2019, Single and simultaneous adsorption of methyl orange and phenol onto magnetic iron oxide/carbon nanocomposites, *Arabian J. Chem.*, 12 (8), 3704–3722.
- [40] Luo, X., and Zhang, L., 2009, High effective adsorption of organic dyes on magnetic cellulose beads entrapping activated carbon, *J. Hazard. Mater.*, 171 (1-3), 340–347.
- [41] Xie, Y., Qian, D., Wu, D., and Ma, X., 2011, Magnetic halloysite nanotubes/iron oxide composites for the adsorption of dyes, *Chem. Eng. J.*, 168 (2), 959–963.
- [42] Wu, D., Zheng, P., Chang, P.R., and Ma, X., 2011, Preparation and characterization of magnetic rectorite/iron oxide nanocomposites and its application for the removal of the dyes, *Chem. Eng. J.*, 174 (1), 489–494.
- [43] Zhu, H.Y., Jiang, R., Xiao, L., and Li, W., 2010, A novel magnetically separable γ -Fe₂O₃/cross-linked chitosan adsorbent: Preparation, characterization and adsorption application for removal of hazardous azo dye, *J. Hazard. Mater.*, 179, 251–257.
- [44] Chowdhury, Z.Z., Zain, S.M., Khan, R.A., and Islam, M.S., 2012, Preparation and characterizations of activated carbon from kenaf fiber for equilibrium adsorption studies of copper from wastewater, *Korean J. Chem. Eng.*, 29 (9), 1187–1195.
- [45] Jaycock, M.J., and Parfitt, G.D., 1981, *Chemistry of Interfaces*, Halstead Press, Ultimo, NSW, Australia.
- [46] Wu, L, Zhang, G., and Lin, J., 2020, The physiochemical properties and adsorption characteristics of processed pomelo peel as a carrier for epigallocatechin-3-gallate, *Molecules*, 25 (18), 4249.

Preparation of Iron-Doped SiO₂/TiO₂ Using Silica from Sugarcane Bagasse Ash for Visible Light Degradation of Congo Red

Nawwal Hikmah, Dewi Agustiningsih, Nuryono Nuryono, and Eko Sri Kunarti*

Department of Chemistry, Faculty Mathematics and Natural Sciences, Universitas Gadjah Mada, Sekip Utara, PO BOX BLS 21, Yogyakarta 55281, Indonesia

* Corresponding author:

email: eko_kunarti@ugm.ac.id

Received: October 1, 2021

Accepted: November 9, 2021

DOI: 10.22146/ijc.69501

Abstract: Iron(III)-doped SiO₂/TiO₂ composite (SiO₂/TiO₂-Fe) has been prepared from sugarcane bagasse ash for photocatalytic degradation of Congo Red. This research was initiated by preparing SiO₂ from sugarcane bagasse ash through a sol-gel method. The SiO₂/TiO₂-Fe was obtained by mixing SiO₂ gel with TiO₂-Fe sol which was produced with titanium tetraisopropoxide (TTIP) as precursor and FeCl₃·H₂O as the dopant source. Dopant concentration was varied by 0, 1, 3, 5, 7% (w/w). The prepared materials were characterized by FT-IR, XRD, SR-UV, XRF, SAA, and SEM-EDX. The photocatalytic activity was evaluated for Congo Red degradation in a closed reactor under visible light illumination. The degradation yield was determined by the UV-Visible spectrophotometry method. Results showed that SiO₂ was successfully extracted from bagasse ash with a silica content of 90.87%. The SiO₂/TiO₂-Fe composite was successfully prepared with the bandgap energy value (E_g) decreasing as the dopant concentration increased. The optimum E_g of 2.63 eV was obtained at the concentration of Fe was 5%. Under that condition, the SiO₂/TiO₂-Fe photocatalyst degraded Congo Red solution by 98.18 % under visible light at pH 3 with a mass of 30 mg for 90 min. The SiO₂/TiO₂-Fe composite is expected to be a photocatalyst material candidate for dye wastewater treatment.

Keywords: sugarcane bagasse ash; SiO₂/TiO₂-Fe; photocatalyst; Congo Red; degradation

■ INTRODUCTION

Textile industry waste in the form of dyes has recently become an environmental problem because of its increasing amount of disposal. One of these dye wastes is Congo Red. The existence of Congo Red waste generates some toxic impacts which are able to disrupt the aquatic ecosystem. Its toxic effects include causing oxygen depletion and reducing the amount of light penetrated to alter the photosynthetic activity of some aquatic living organisms, and it is known as one of the carcinogenic chemicals. Consequently, it is highly required to overcome these environmental problems caused by Congo Red waste [1].

Several ways have been done to overcome dye waste, one of which is adsorption [2], coagulation [3], and ozonation [4]. However, the dye is only adsorbed in the adsorption method without being degraded, released, and becoming a secondary pollutant. The photocatalysis

method using a semiconductor photocatalyst could be applied to remove dye waste [5], degrading dyes into simpler, safer, and economic components.

Photocatalyst is a material that can absorb light and carry out some chemical transformations by redox reaction [6]. One photocatalyst material that is commonly used is titanium dioxide (TiO₂). TiO₂ has a high oxidation capacity, high photostability, and is non-toxicity [7]. Hence, TiO₂ is widely used as a photocatalyst material. However, TiO₂ has a small specific surface area and easily forms agglomeration between its particle and recombination between its charge carriers. This weakness can be overcome by dispersing TiO₂ into a porous material, such as silica (SiO₂) [8]. The SiO₂ can reduce TiO₂ particle size and minimize agglomeration between TiO₂ particles to increase the surface area and catalytic activity. The silica used can be extracted from natural materials with high

silica content [9]. Recent studies state that one of the natural materials that have the potential as a source of silica is bagasse which has a silica content of 88.68% [10]. However, the $\text{SiO}_2/\text{TiO}_2$ composite photocatalyst needs UV radiation (≤ 390 nm) for dye degradation because of the significant bandgap energy of TiO_2 .

Based on previous research, it is known that TiO_2 has a value of bandgap energy of 3.26 eV [11-13]. It allows TiO_2 to absorb only UV lights for dye waste treatment, limiting the application of TiO_2 on an industrial scale [13-17]. Besides, another limitation is that UV light takes less than 5% of solar light irradiated on the earth's surface [18]. Therefore, it is necessary to extend the photo-response of the TiO_2 to the visible region by modifying its optical properties to achieve the more efficient photocatalytic activity. Li et al. [19] prepared Fe doped TiO_2 , which has photocatalytic activity under visible light. The Fe^{3+} ion is often used as a dopant because the ionic radius (0.690 Å) is closed to Ti^{4+} (0.745 Å). Therefore, Fe^{3+} can be easily incorporated into the TiO_2 crystal lattice [19]. This study reports the preparation of $\text{SiO}_2/\text{TiO}_2\text{-Fe}$ using sugarcane bagasse ash as the new potential of a silica source. This catalyst has not been synthesized and examined in the previous research. The effect of Fe(III) addition on the properties and photocatalytic activity of $\text{SiO}_2/\text{TiO}_2$ for the degradation of Congo Red was evaluated.

■ EXPERIMENTAL SECTION

Materials

The materials used in this research were in pro-analysis qualities obtained from Sigma-Aldrich and Merck, including NaOH, HCl 37%, NH_3 25%, $\text{Ti}(\text{OCH}(\text{CH}_3)_2)_4$ 97% (TTIP), $\text{C}_2\text{H}_5\text{OH}$ 99%, $\text{FeCl}_3\cdot\text{H}_2\text{O}$ 97%, and Congo Red. Other materials were technical grade, including deionized water and sugarcane bagasse waste collected from the sugarcane factory in Bantul, Yogyakarta. All reagents were used as received without further purification.

Instrumentation

The instrumentations used in this research were Fourier Transform Infrared Spectrophotometer (Nicolet Avatar 360 IR; Shimadzu 2450), X-Ray Diffractometer

(PANalytical: X'Pert PRO 2318), Scanning Electron Microscope with Energy Dispersive X-Ray (JEOL JED-2300; Hitachi SU 3500), X-Ray Fluorescence Spectrometer (S2 PUMA), Specular Reflectance Ultraviolet-Visible Spectrometer (Shimadzu 2450), and Surface Area Analyzer (Quantachrome Nova 4200e).

Procedure

Extraction of SiO_2 from sugarcane bagasse ash

Sugarcane bagasse (1 g) was washed with 100 mL water and dried at 100 °C for 4 h. Dried sugarcane bagasse was then combusted at 1000 °C for 4 h and dispersed in 10 mL HCl 1 M for 2 h at room temperature. Furthermore, the ash treated with acid was filtered, washed with distilled water, and dried for 24 h at 80 °C. The dried ash was then dispersed in 10 mL NaOH 2 M, stirred for 4 h at 80 °C and filtered to obtain filtrate of sodium silicate solution. The sodium silicate solution was then titrated with HCl 1 M to reach pH 7.0 and form SiO_2 sol. The sol was aged for 20 h at room temperature to produce SiO_2 gel. Finally, silica gel was washed with 5 mL distilled water, filtered, and dried at 70 °C for 24 h [20].

Preparation of $\text{SiO}_2/\text{TiO}_2\text{-Fe}$, $\text{SiO}_2/\text{TiO}_2$, TiO_2

$\text{SiO}_2/\text{TiO}_2\text{-Fe}$ was prepared with a modified method from previous studies of $\text{TiO}_2\text{-Fe}$ [21] and SiO_2 from sugarcane bagasse [20]. The $\text{SiO}_2/\text{TiO}_2\text{-Fe}$ was prepared with SiO_2 to TiO_2 mass ratio of 1:1. This ratio is based on previously unpublished optimization results. The first step was extracting SiO_2 from 1 g sugarcane bagasse ash to produce SiO_2 gel. TiO_2 sol was then prepared by stirring 4 mL (13.2 mmol) TTIP, 1 mL water, 2.3 mL $\text{C}_2\text{H}_5\text{OH}$, and 0.7 mL HCl (molar ratio of 1:4:3:0.01) for 3 h. The mixture was then added with 1 mL Fe(III) solution with a varied concentration (1, 3, 5, and 7% (w/w)) at stirring for 30 min. The mixture was then sonicated for 10 min and then added to SiO_2 gel. NH_4OH solution (20 mL) was added to the mixture then sonicated for 1 h to produce $\text{SiO}_2/\text{TiO}_2\text{-Fe}$ homogeneous sol. The sol was dried at 70 °C for 24 h, and the composite obtained was calcined at 500 °C for 4 h.

$\text{SiO}_2/\text{TiO}_2$ preparation was performed with a similar procedure to the $\text{SiO}_2/\text{TiO}_2\text{-Fe}$ without the

addition of Fe. The TiO₂ was synthesized by adding 2 mL (13.2 mmol) TTIP into 20 mL ethanol solution and then added dropwise with distilled water and sonicated for 1 h. The sol was dried at 70 °C for 24 h and calcined at 500 °C for 4 h to get TiO₂ as an anatase phase.

Photocatalytic activity

Experiments were performed by mixing an aqueous solution (20 mL) of Congo Red 10 mg/L at a pH 3 with 30 mg of photocatalysts (TiO₂, SiO₂/TiO₂, and SiO₂/TiO₂-Fe) in all variations of dopant concentration (1, 3, 5, and 7%). All the reactions were performed under stirring for 90 min with various conditions: dark and under visible illumination in a closed photoreactor equipped with LED 12 W Philips lamp ($\lambda = 483\text{--}595$ nm) as the light source. Then, the photocatalyst was separated through centrifugation with the type of the centrifuge is Gemmy PLC-025. The filtrate obtained was analyzed with a UV-visible spectrophotometer with the type of GENESYS 10S. The filtrate was scanned with a wavelength from 200 to 600 nm and the optimum wavelength obtained was 561 nm. The photocatalytic degradation percentage has been calculated as

$$\text{Degradation}(\%) = \frac{C_0 - C_e}{C_0}$$

where C_0 and C_e correspond to the initial and final concentration of dye before and after photo-irradiation.

RESULTS AND DISCUSSION

SiO₂ Extraction from Sugarcane Bagasse

In this research, silica (SiO₂) was obtained from sugarcane bagasse ash and used as the matrix in SiO₂/TiO₂-Fe. Sugarcane bagasse ash was utilized as the source of silica because it has a large amount of silica content after being combusted at 1000 °C and treated with acid. Sugarcane bagasse would undergo a pyrolysis process, which will reduce the organic and inorganic contents such as K⁺ and Ca²⁺ into its oxidized form. In addition, the acid treatment caused other minerals besides SiO₂ in sugarcane bagasse ash to dissolve, and their content would decrease relatively to SiO₂. The sugarcane bagasse ash was analyzed with XRF, and the result is presented in Table 1. The major component in sugarcane bagasse ash is SiO₂ with 90.87%.

Fig. 1 displays infrared spectra of raw sugarcane bagasse, sugarcane bagasse ash, and silica. From the raw sugarcane bagasse spectrum, it could be seen there are peaks at 3416 and 1326 cm⁻¹, which indicate the stretching and bending vibration of H–O–H. In addition, there were some peaks at 2909 and 1054 cm⁻¹ stretching of Csp³–H and stretching of C–O from primary alcohol, respectively. In addition, there are also peaks at 1250 and 1730 cm⁻¹, which indicate the existence of C–O, and C=O stretching vibration, respectively [22]. According to these data, the sugarcane bagasse may contain lignin and lignocellulose. From the sugarcane bagasse ash spectrum, some peaks could be seen at 3448, 1054, 786, and 497 cm⁻¹, which indicate stretching vibration of H–O–H, Si–O–Si asymmetric stretching, Si–O–Si symmetric stretching, and bending vibration of Si–O–Si, respectively [23]. There is also a peak with low intensity at 617 cm⁻¹, which shows the characteristic of silica cristobalite. Cristobalite is formed

Table 1. Composition of sugarcane bagasse ash

Component	Content (% mass)
SiO ₂	90.87
CaO	3.060
MgO	2.077
Na ₂ O	1.186
Al ₂ O ₃	1.003

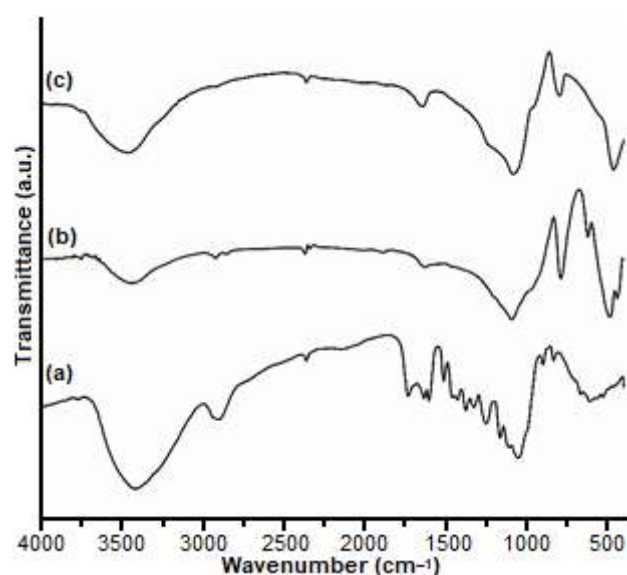


Fig 1. Infrared spectra of raw sugarcane bagasse (a), sugarcane bagasse ash (b), and extracted silica (c)

when silica is heated at 1000 °C. At this temperature, tridymite turns into cristobalite [24]. The silica spectrum shows peaks at 3467 and 1639 cm^{-1} , respectively, indicating adsorbed water's stretching and bending vibration on the SiO_2 surface. In addition, peaks at 1083, 954, and 462 cm^{-1} , indicate stretching vibration of Si–O–Si, stretching vibration of the non-bridging oxygen atom (Si–OH) [25] and bending vibration of Si–O–Si, respectively.

The X-ray diffraction pattern in Fig. 2 shows an amorphous pattern with a prominent peak at 2θ 22.16°, and a broad peak at 16–17° appears for the raw sugarcane bagasse ash. These peaks are typical peaks of cellulose corresponding to the Miller index in ICDD (International Center for Diffraction Data) number 00-003-0289 with the (hkl) values being: (-111) and (002). The XRD pattern of sugarcane bagasse ash shows peaks at 2θ 19.68, 21.83, 28.26, 31.39, and 36.07°. According to Miller's ICDD index number 00-039-1425, this is the diffraction pattern index of cristobalite with (hkl) of (101), (111), (102), and (112). Based on the diffraction pattern of silica, there is an amorphous pattern between 2θ 10–15° with a broad peak at 20.76°. There are also some sharp peaks at pada 28.16, 31.32, 40.45, 45.06, and 56.02°. This diffraction pattern was compared to Miller ICDD index number 00-003-0267, which is the diffraction pattern index of cristobalite.

Fig. 3(a) depicts an SEM image of extracted SiO_2 ; it can be explained that the surface of SiO_2 looks quite smooth even though there are some abrupt areas. Fig. 3(b) displays the SEM-EDX spectrum of SiO_2 , which shows that SiO_2 consists of O and Si elements on the material's surface. The SEM-EDX data confirm that the material is only composed of Si and O atoms as shown in Table 2.

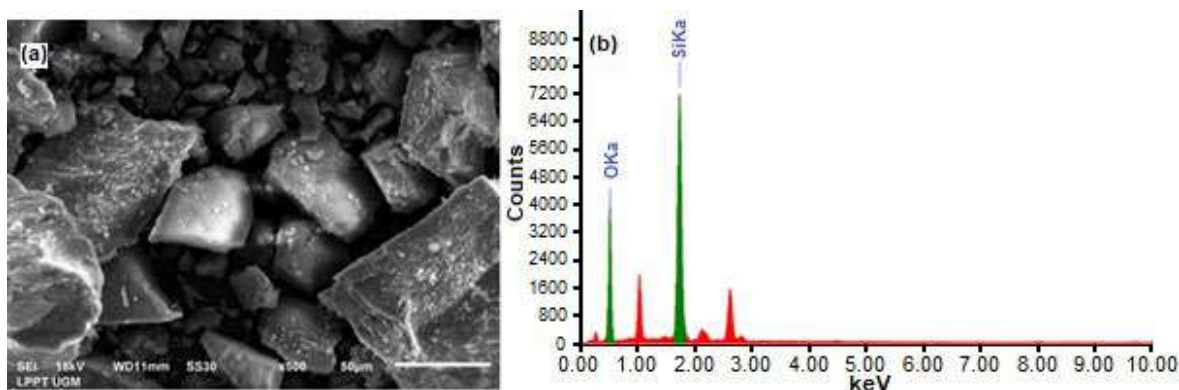


Fig 3. SEM image of SiO_2 (a) EDX spectrum of SiO_2 (b)

Characterization of $\text{SiO}_2/\text{TiO}_2\text{-Fe}$

Fig. 4 displays the infrared spectra of $\text{SiO}_2/\text{TiO}_2$ and $\text{SiO}_2/\text{TiO}_2\text{-Fe}$ with various dopant concentrations. The spectra show that in all variations, absorption peaks appear at 410–495, 500–600, 920–927, 1026–1050, and 2360–2370 cm^{-1} . These peaks indicate respectively the stretching vibration of Si–O–Si, bending vibration of Ti–O–Ti, stretching vibration of Ti–O–Si, bending vibration of Si–O–Si, and stretching vibration of Ti–O–Ti. Sharp

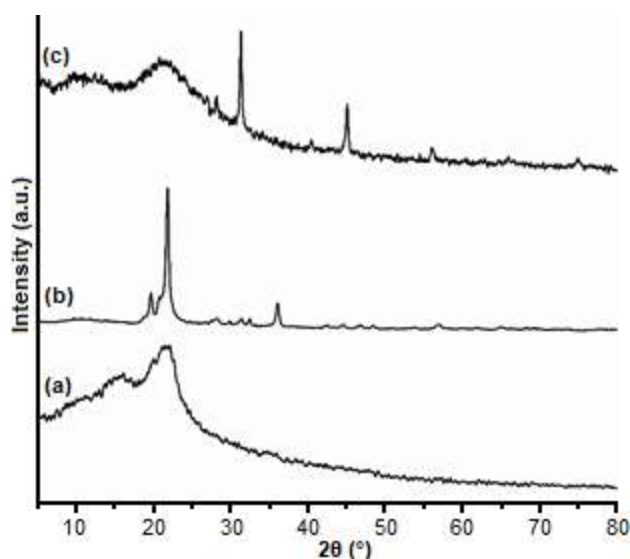


Fig 2. X-ray diffraction pattern of raw sugarcane bagasse (a), sugarcane bagasse ash (b), and extracted silica (c)

Table 2. Elements composition on the surface of SiO_2

Element	Atom%
O	79.94
Si	29.06
Total	100.00

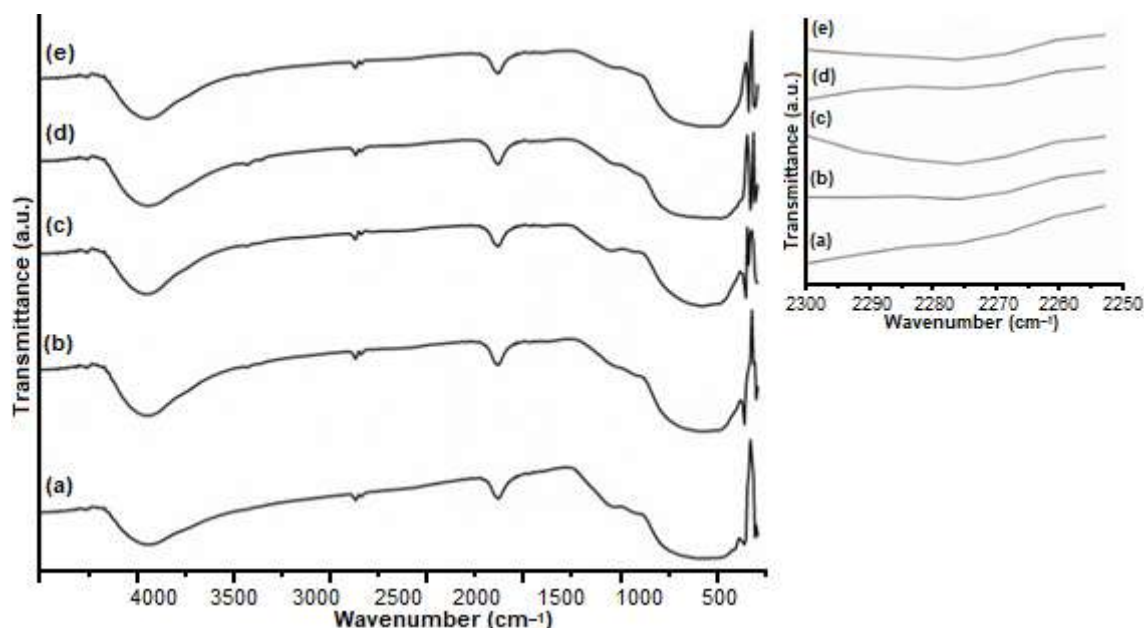


Fig 4. Infrared spectra of $\text{SiO}_2/\text{TiO}_2$ (a), and $\text{SiO}_2/\text{TiO}_2\text{-Fe}$ 1% (b), 3% (c), 5% (d), 7% (e)

peaks at 3400 and 1600 cm^{-1} also appear, indicating H–O–H's stretching and bending vibration. The addition of Fe(III) as a dopant gives a new peak at 2200 cm^{-1} with low intensity, as can be seen in inset spectra in Fig. 4. This peak is a characteristic of Ti–O–Fe vibration that Fe inserted into the TiO_2 crystal lattice [26].

Fig. 5 presents the X-ray diffraction pattern of $\text{SiO}_2/\text{TiO}_2$ and $\text{SiO}_2/\text{TiO}_2\text{-Fe}$ with various dopant concentrations of Fe(III). There are characteristic peaks of silica cristobalite and anatase of $\text{SiO}_2/\text{TiO}_2$ and $\text{SiO}_2/\text{TiO}_2\text{-Fe}$ samples. The peaks of silica cristobalite are shown at 2θ 28, 31, 40, 45, 56° according to ICDD number 00-003-0267. TiO_2 anatase is revealed at 25, 48, 75° according to ICDD number 00-002-0406. Table 3 shows that at 2θ of 25° of the $\text{SiO}_2/\text{TiO}_2\text{-Fe}$ is shifted toward a smaller 2θ than $\text{SiO}_2/\text{TiO}_2$. It denotes Fe^{3+} was successfully doped in interstitial mode, causing the distance between planes of $\text{SiO}_2/\text{TiO}_2\text{-Fe}$ to be greater than $\text{SiO}_2/\text{TiO}_2$. The Fe^{3+} radius is smaller than the Ti^{4+} radius, making it possible for Fe^{3+} ions to enter the crystal cell of TiO_2 on the interstitial mode within the crystal lattice [27]. It is noted that crystal size continues to decrease as the Fe^{3+} concentration increase implying the doped Fe^{3+} could inhibit the grain growth of TiO_2 .

The TiO_2 and $\text{TiO}_2\text{-Fe}$ were dispersed into the SiO_2

matrix to achieve a more significant surface area. Table 3 shows that $\text{SiO}_2/\text{TiO}_2$ has a greater surface area ($72.59\text{ m}^2/\text{g}$) than TiO_2 ($20.26\text{ m}^2/\text{g}$). It confirms that dispersing TiO_2 into the SiO_2 matrix would increase the surface area due to the presence of porous SiO_2 , which has a high specific surface area [28]. The $\text{SiO}_2/\text{TiO}_2\text{-Fe}$ also has a greater surface area than the undoped material. Therefore, Fe dopant can inhibit the growth of

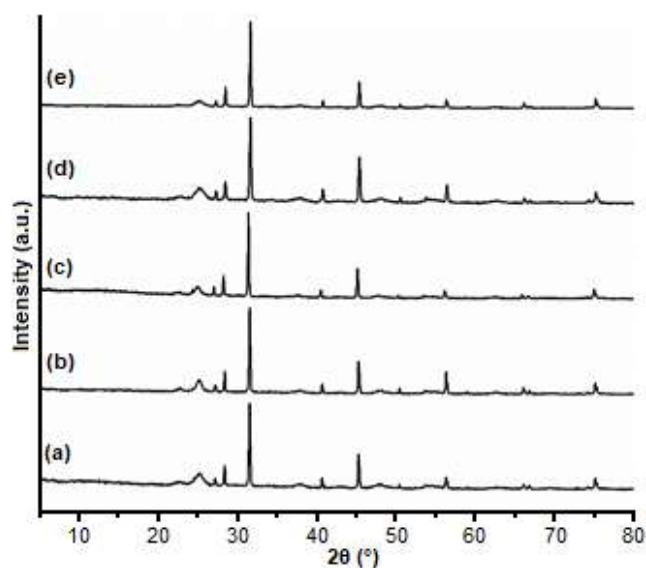


Fig 5. X-ray diffraction pattern of $\text{SiO}_2/\text{TiO}_2$ (a), and $\text{SiO}_2/\text{TiO}_2\text{-Fe}$ 1% (b), 3% (c), 5% (d), 7% (e)

TiO₂ crystal, crystal, reducing the crystal size and increasing the material surface area [29]. This fact correlates to the crystallite size data shown in Table 4 where SiO₂/TiO₂-Fe 5% has a smaller size than SiO₂/TiO₂.

The EDX was also carried out to determine the elements in SiO₂/TiO₂ and SiO₂/TiO₂-Fe. The EDX data of SiO₂/TiO₂ shows that SiO₂/TiO₂ contains O, Ti, and Si, meanwhile SiO₂/TiO₂-Fe consists of O, Ti, Si, and Fe. The element composition of both materials can be seen in Table 5. The result denotes that the surface of the materials is dominated by Ti, giving a better photocatalytic performance.

Fig. 6 shows SiO₂/TiO₂ and SiO₂/TiO₂-Fe SEM images, which show that compared to the SiO₂ surface, both materials have rougher surfaces caused by TiO₂ and TiO₂-Fe particles dispersed on the SiO₂ surface. SEM mapping was conducted to see the distribution of the atoms on the surface of SiO₂/TiO₂ (Fig. 7(a)) and SiO₂/TiO₂-Fe (Fig. 7(b)). It can be seen that Ti and Si atoms occupy the same position on both materials, indicating the formation of SiO₂/TiO₂ composite. Ti and Fe atoms also occupy the same position, indicating Fe doping into the TiO₂ crystal lattice.

Characterization using the SR UV-Visible method is aimed to determine the material's bandgap energy (E_g). Fig. 8 reveals a shift of absorption wavelength toward the visible light region with an increasing concentration of Fe. The E_g was calculated from the data using the Tauc plot. Table 6 demonstrates that SiO₂/TiO₂ has a slightly higher E_g than that of TiO₂. It might be caused by the quantum size effect, which inhibits the TiO₂ crystal growth [30]. The TiO₂ E_g 3.15 eV corresponds to the results reported

by Aguado [31] that TiO₂ anatase has the E_g value in the range of 3.08–3.35 eV. The E_g of the doped materials tends to decrease as the Fe concentration increase. It occurs because the distance between the valence and conduction bands is getting smaller due to forming a new energy level originating from the d orbitals of Fe metal dopant below the conduction band. The distance of the new energy level with the formed conduction band becomes smaller, and electron transfer requires lower energy.

Table 3. The surface area of materials

Material	SBET (m ² /g)
TiO ₂	10.26
TiO ₂ /SiO ₂	72.59
TiO ₂ /SiO ₂ -Fe 5%	108.6

Table 4. The d-space and crystallite size of materials

Material	2θ (°)	d (Å)	D (nm)
TiO ₂ /SiO ₂	25.38	3.507	19.34
TiO ₂ /SiO ₂ -Fe 1%	25.22	3.528	15.75
TiO ₂ /SiO ₂ -Fe 3%	24.94	3.567	11.81
TiO ₂ /SiO ₂ -Fe 5%	25.22	3.528	10.67
TiO ₂ /SiO ₂ -Fe 7%	25.32	3.515	10.64

Table 5. Elements composition on the surface of SiO₂/TiO₂ and SiO₂/TiO₂-Fe

Material	Element	Atom%
SiO ₂ /TiO ₂	O	67.97
	Si	3.97
	Ti	28.06
SiO ₂ /TiO ₂ -Fe 5%	O	67.36
	Si	2.21
	Ti	28.58
	Fe	1.85

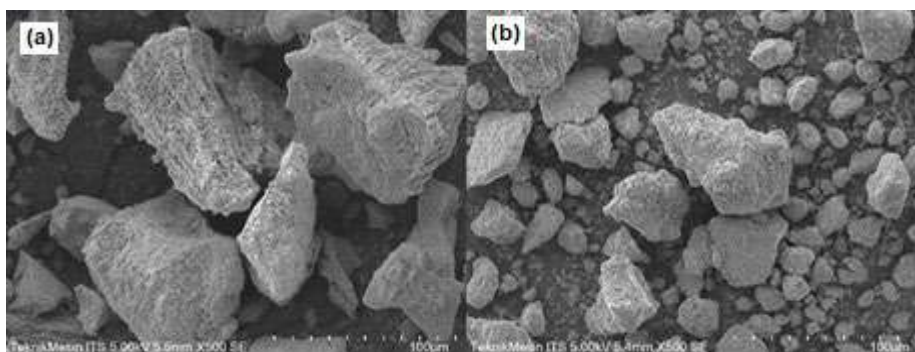


Fig 6. SEM image of SiO₂/TiO₂ (a) and SiO₂/TiO₂-Fe (b)

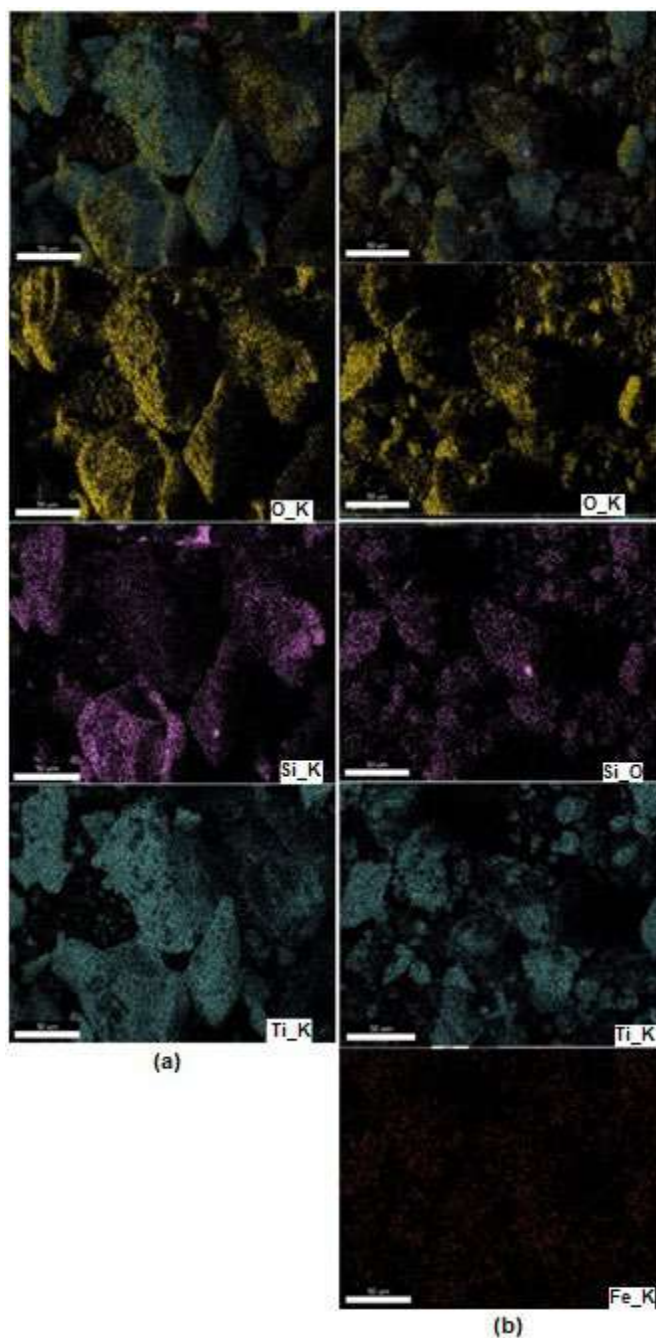


Fig 7. Elements mapping on the $\text{SiO}_2/\text{TiO}_2$ (a) and $\text{SiO}_2/\text{TiO}_2\text{-Fe}$ 5% (b) surface

It is noted that E_g is shifted towards higher energy at a dopant concentration of 7%. It might be caused by the Burstein-Moss effect, which stated that when the concentration of dopants is too abundant, the electrons occupying the conduction band will be excess so that it can push the Fermi level up. This increased fermi level results in an increase in the bandgap energy [32].

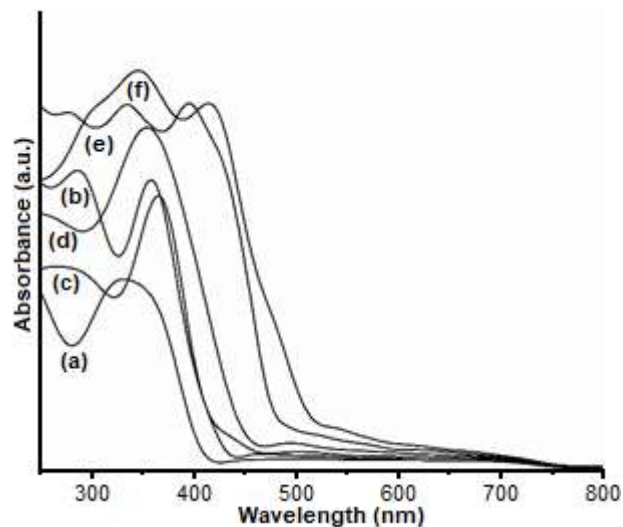


Fig 8. Specular Reflectance UV-Visible Spectra of TiO_2 (a), $\text{SiO}_2/\text{TiO}_2$ (b), $\text{SiO}_2/\text{TiO}_2\text{-Fe}$ 1% (c), $\text{SiO}_2/\text{TiO}_2\text{-Fe}$ 3% (d), $\text{SiO}_2/\text{TiO}_2\text{-Fe}$ 5% (e), and $\text{SiO}_2/\text{TiO}_2\text{-Fe}$ 7% (f)

Table 6. Bandgap energy of prepared material

Material	E_g (eV)
TiO_2	3.15
$\text{SiO}_2/\text{TiO}_2$	3.16
$\text{SiO}_2/\text{TiO}_2\text{-Fe}$ 1%	3.06
$\text{SiO}_2/\text{TiO}_2\text{-Fe}$ 3%	2.93
$\text{SiO}_2/\text{TiO}_2\text{-Fe}$ 5%	2.63
$\text{SiO}_2/\text{TiO}_2\text{-Fe}$ 7%	2.67

Photocatalytic Activity of $\text{SiO}_2/\text{TiO}_2\text{-Fe}$

The photocatalytic activity of $\text{SiO}_2/\text{TiO}_2\text{-Fe}$ was examined to degrade the Congo Red in the aqueous solution. Fig. 9 shows the photocatalytic activity under visible light illumination. The Fe doped $\text{SiO}_2/\text{TiO}_2$ material obtained the highest percentage of Congo Red degradation with a concentration of Fe(III) 5% (98.18%). It is related to the obtained E_g where $\text{SiO}_2/\text{TiO}_2\text{-Fe}$ (5%) has the lowest E_g value of 2.39 eV, requiring the smallest energy to excite electrons from the valence band to the conduction band. On the other hand, the $\text{SiO}_2/\text{TiO}_2\text{-Fe}$ photocatalysts with dopant concentrations of 1, 3, and 7% have larger E_g values shown in Table 6, so that it requires greater energy to excite the electrons. Thus, resulting in lower percentage degradation, as can be seen in Fig. 9. Even though some of these photocatalysts have a higher E_g value, they are still responsive to visible light.

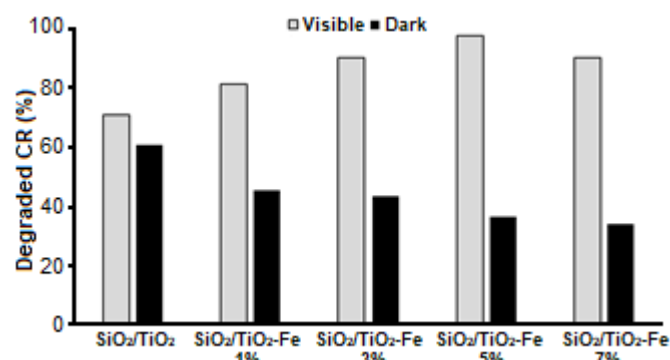
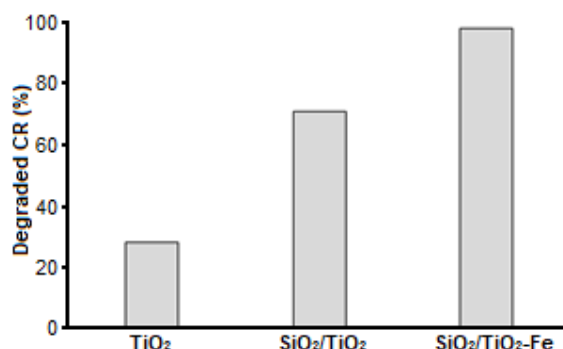
Table 7. Comparison of Congo Red degradation percentage with reported studies

Catalyst	Initial dye conc. (mg/L)	Light source	Time (min)	Degradation (%)	Ref
TiO ₂	4	58 W UV lamp	30	64.72	[33]
ZrO ₂ /TiO ₂ /ZnO	10	8 W UV lamp	15	97	[34]
TiO ₂ -Fe	20	250 W Xenon lamp	60	54.16	[35]
PVA/TiO ₂ /Chi/Chl	10	W70 LED lamp	210	94	[36]
Mn-TiO ₂ /Ti	1	150 W visible lamp	60	75.48	[37]
SiO ₂ /TiO ₂ -Fe	10	12 W LED lamp	90	98.18	This study

According to Fig. 9, it can be seen that SiO₂/TiO₂-Fe photocatalysts can reduce the concentration of Congo Red in dark conditions with no external energy source. In this condition, the reduction of Congo Red concentration is not caused by photocatalytic degradation but adsorption. The adsorption could occur due to the active sites on the surface of the photocatalysts. This process is recognized as decolorization. The SiO₂ can act as a suitable adsorbent that provides an adsorption site to support TiO₂ in capturing more target molecules.

Fig. 10 shows that SiO₂/TiO₂-Fe with Fe(III) 5% concentration gave the highest photocatalytic activity than pure TiO₂ and undoped SiO₂/TiO₂. The SiO₂/TiO₂-Fe can degrade more Congo Red due to the contribution of SiO₂, which acts as an adsorbent and gives a greater surface area as a result of TiO₂ dispersion into the SiO₂ matrix. The dopant added is responsive to visible light and improves photocatalyst's performance in the visible light region. The percentage degradation of SiO₂/TiO₂ is lower than SiO₂/TiO₂-Fe in visible light illumination due to the E_g compatibility. It can be concluded that SiO₂/TiO₂-Fe will be more effectively used as a photocatalyst than unmodified TiO₂.

Until the present day, there has not been any report of SiO₂/TiO₂-Fe with extracted silica from sugarcane bagasse ash for photocatalytic degradation of Congo Red. Therefore, earlier reported studies including various photocatalysts were compared with this study for Congo Red degradation. The comparisons data can be seen in Table 7. Compared to all the photocatalysts used, SiO₂/TiO₂-Fe has the highest activity within a relatively short period. Thus, it suggests that SiO₂/TiO₂-Fe may be a good choice for wastewater treatment.

**Fig 9.** Percentage degradation of Congo Red (CR) catalyzed by SiO₂/TiO₂ and SiO₂/TiO₂-Fe under visible light and dark condition**Fig 10.** Percentage degradation of Congo Red (CR) catalyzed by TiO₂, SiO₂/TiO₂, and SiO₂/TiO₂-Fe 5% under visible light irradiation

CONCLUSION

Silica was successfully extracted from sugarcane bagasse ash with a content of 90.87%. SiO₂/TiO₂-Fe photocatalysts were also successfully synthesized. The addition of SiO₂ gives a higher surface area on the SiO₂/TiO₂-Fe compared to the unmodified TiO₂. Furthermore, Fe(III) modification on SiO₂/TiO₂

influences the bandgap energy of TiO₂, resulting in a lower value of E_g from 3.15 to 2.63 eV. Therefore, the SiO₂/TiO₂-Fe can be used as a photocatalyst responsive to visible light for Congo Red degradation under visible light exposure. The Fe doped SiO₂/TiO₂ with a dopant concentration of 5% can degrade 10 mg/L of Congo Red dye solution with a degradation yield of 98.18% under the condition of pH 3, under visible light illumination for 90 min. This finding led to a conclusion of possible new materials for wastewater treatment.

■ ACKNOWLEDGMENTS

The authors acknowledge to Faculty of Mathematics and Natural Sciences, Universitas Gadjah Mada, for the financial support of this research (DAMAS 2021 internal research grant, with contract number: 163/J01.1.28/PL.06.02/2021).

■ REFERENCES

- [1] Hernández-Zamora, M., and Martínez-Jerónimo, F., 2019, Congo red dye diversely affects organisms of different trophic levels: A comparative study with microalgae, cladocerans, and zebrafish embryos, *Environ. Sci. Pollut. Res.*, 26 (12), 11743–11755.
- [2] Batool, M., Qureshi, M.Z., Hashmi, F., Mehboob, N., and Shah, A.S., 2019, Congo red azo dye removal and study of its kinetics by aloe vera mediated copper oxide nanoparticles, *Indones. J. Chem.*, 19 (3), 626–637.
- [3] Lindu, M., 2008, The effects of gradient velocity and detention time to coagulation– flocculation of dyes and organic compound in deep well water, *Indones. J. Chem.*, 8 (2), 146–150.
- [4] Karamah, E.F., and Nurcahyani, P.A., 2019, Degradation of blue KN-R dye in batik effluent by an advanced oxidation process using a combination of ozonation and hydrodynamic cavitation, *Indones. J. Chem.*, 19 (1), 41–47.
- [5] Zargoosh, K., Rostami, M., and Aliabadi, H.M., 2020, Eu²⁺- and Nd³⁺-doped CaAl₂O₄/WO₃/polyester nanocomposite as a sunlight-activated photocatalyst for fast removal of dyes from industrial wastes, *J. Mater. Sci.: Mater. Electron.*, 31 (14), 11482–11495.
- [6] Liu, L., and Li, Y., 2014, Understanding the reaction mechanism of photocatalytic reduction of CO₂ with H₂O on TiO₂-based photocatalysts: A review, *Aerosol Air Qual. Res.*, 14 (2), 453–469.
- [7] Tangale, N.P., Niphadkar, P.S., Samuel, V., Deshpande, S.S., Joshi, P.N., and Awate, S.V., 2016, Synthesis of Sn-containing anatase (TiO₂) by sol-gel method and their performance in catalytic water splitting under visible light as a function of tin content, *Mater. Lett.*, 171, 50–54.
- [8] Chen, J., Qiu, F., Xu, W., Cao, S., and Zhu, H., 2015, Recent progress in enhancing photocatalytic efficiency of TiO₂-based materials, *Appl. Catal., A*, 495, 131–140.
- [9] Manurung, P., Situmeang, R., Ginting, E., and Pardede, I., 2015, Synthesis and characterization of titania-rice husk silica composites as photocatalyst, *Indones. J. Chem.*, 15 (1), 36–42.
- [10] Rovani, S., Santos, J.J., Corio, P., and Fungaro, D.A., 2018, Highly pure silica nanoparticles with high adsorption capacity obtained from sugarcane waste ash, *ACS Omega*, 3 (3), 2618–2627.
- [11] Fonseca-Cervantes, O.R., Pérez-Larios, A., Romero Arellano, V.H., Sulbaran-Rangel, B., and Guzmán González, C.A., 2020, Effects in band gap for photocatalysis in TiO₂ support by adding gold and ruthenium, *Processes*, 8 (9), 1032.
- [12] Wan, H., Yao, W., Zhu, W., Tang, Y., Ge, H., Shi, X., and Duan, T., 2018, Fe-N co-doped SiO₂@TiO₂ yolk-shell hollow nanospheres with enhanced visible light photocatalytic degradation, *Appl. Surf. Sci.*, 444, 355–363.
- [13] D'Amato, C.A., Giovannetti, R., Zannotti, M., Rommozzi, E., Minicucci, M., Gunnella, R., and Di Cicco, A., 2018, Band gap implications on nano-TiO₂ surface modification with ascorbic acid for visible light-active polypropylene coated photocatalyst, *Nanomaterials*, 8 (8), 599.
- [14] Liu, J., Li, Y., Ke, J., Wang, S., Wang, L., and Xiao, H., 2018, Black NiO-TiO₂ nanorods for solar photocatalysis: Recognition of electronic structure and reaction mechanism, *Appl. Catal., B*, 224, 705–714.

- [15] Niu, X., Yan, W., Shao, C., Zhao, H., and Yang, J., 2019, Hydrothermal synthesis of Mo-C co-doped TiO₂ and coupled with fluorine-doped tin oxide (FTO) for high-efficiency photodegradation of methylene blue and tetracycline: Effect of donor-acceptor passivated co-doping, *Appl. Surf. Sci.*, 466, 882–892.
- [16] El Mragui, A., Logvina, Y., da Silva, L.P., Zegaoui, O., and da Silva, J.C.G.E., 2019, Synthesis of Fe⁻ and co-doped TiO₂ with improved photocatalytic activity under visible irradiation toward carbamazepine degradation, *Materials*, 12 (23), 3874.
- [17] Raza, W., Haque, M.M., Muneer, M., Fleisch, M., Hakki, A., and Bahnemann, D., 2015, Photocatalytic degradation of different chromophoric dyes in aqueous phase using La and Mo doped TiO₂ hybrid carbon spheres, *J. Alloys Compd.*, 632, 837–844.
- [18] Wu, J.C.S., and Chen, C.H., 2004, A visible-light response vanadium-doped titania nanocatalyst by sol-gel method, *J. Photochem. Photobiol., A*, 163 (3), 509–515.
- [19] Li, Z., Shen, W., He, W., and Zu, X., 2008, Effect of Fe-doped TiO₂ nanoparticle derived from modified hydrothermal process on the photocatalytic degradation performance on methylene blue, *J. Hazard. Mater.*, 155 (3), 590–594.
- [20] Norsuraya, S., Fazlena, H., and Norhasyimi, R., 2016, Sugarcane bagasse as a renewable source of silica to synthesize Santa Barbara Amorphous-15 (SBA-15), *Procedia Eng.*, 148, 839–846.
- [21] Anwar, D.I., and Mulyadi, D., 2015, Synthesis of Fe-TiO₂ composite as a photocatalyst for degradation of methylene blue, *Procedia Chem.*, 17, 49–54.
- [22] Kumar, A., Negi, Y.S, Choudhary, V., and Bhardwaj, N.K., 2014, Characterization of cellulose nanocrystals produced by acid-hydrolysis from sugarcane bagasse as agro-waste, *J. Mater. Phys. Chem.*, 2 (1), 1–8.
- [23] Worathanakul, P., Payubnop, W., and Muangpet, A., 2009, Characterization for post-treatment effect of bagasse ash for silica extraction, *World Acad. Sci. Eng. Technol.*, 3 (8), 398–400.
- [24] Dapiaggi, M., Pagliari, L., Pavese, A., Sciascia, L., Merli, M., and Francescon, F., 2015, The formation of silica high temperature polymorphs from quartz: Influence of grain size and mineralising agents, *J. Eur. Ceram. Soc.*, 35 (16), 4547–4555.
- [25] Rahman, N.A., Widhiana, I., Juliastuti, S.R., and Setyawan, H., 2015, Synthesis of mesoporous silica with controlled pore structure from bagasse ash as a silica source, *Colloids Surf., A*, 476, 1–7.
- [26] Luu, C.L., Nguyen, Q.T., and Ho, ST, 2010, Synthesis and characterization of Fe-doped TiO₂ photocatalyst by the sol-gel method, *Adv. Nat. Sci.: Nanosci. Nanotechnol.*, 1, 015008.
- [27] Yang, Y., Yu, Y., Wang, J., Zheng, W., and Cao, Y., 2017, Doping and transformation mechanisms of Fe³⁺ ions in Fe-doped TiO₂, *CrystEngComm*, 19 (7), 1100–1105.
- [28] Huynh, N.D.T., Vo, K.D., Nguyen, T.V., and Le, M.V., 2019, Enhancing the photoactivity of TiO₂/SiO₂ monolithic catalyst and its reusability for wastewater treatment, *MATEC Web Conf.*, 268, 07005.
- [29] Safari, M., Talebi, R., Rostami, M.H., Nikazar, M., and Dadvar, M., 2014, Synthesis of iron-doped TiO₂ for degradation of reactive orange 16, *J. Environ. Health Sci. Eng.*, 12 (1), 19.
- [30] Othman, S.H., Rashid, S.A., Mohd Ghazi, T.I., and Abdullah, N., 2011, Fe-doped TiO₂ nanoparticles produced via MOCVD: Synthesis, characterization, and photocatalytic activity, *J. Nanomater.*, 2011, 571601.
- [31] Aguado, J., van Grieken, R., López-Muñoz, M.J., and Marugán, J., 2006, A comprehensive study of the synthesis, characterization and activity of TiO₂ and mixed TiO₂/SiO₂ photocatalysts, *Appl. Catal., A*, 312, 202–212.
- [32] Munir, S., Shah, S.M., Hussain, H., and Ali khan, R., 2016, Effect of carrier concentration on the optical band gap of TiO₂ nanoparticles, *Mater. Des.*, 92, 64–72.
- [33] Harun, N.S., Rahman, M.N.A., Kamarudin, W.F.W., Irwan, Z., Muhammad, A., Akhir, N.E.F.M., and Yaafar, M.R., 2018, Photocatalytic degradation of Congo red dye based on titanium

- dioxide using solar and UV lamp, *J. Fundam. Appl. Sci.*, 10 (1S), 832–846.
- [34] Seyedi-Chokanlou, T., Aghabeygi, S., Molahasani, N., and Abrinaei, F., 2021, Applying Taguchi method to optimize the synthesis conditions of $ZrO_2/TiO_2/ZnO$ nanocomposite for high-performance photodegradation of Congo red, *Iran. J. Catal.*, 11 (1), 49–58.
- [35] Kaya, D., and Türkten, N., 2020, Preparation of doped TiO_2 photocatalysts and their decolorization efficiencies under solar light, *J. Eng. Sci. Des.*, 8 (3), 655–663.
- [36] Jo, W.K., and Tayade, R.J., 2014, New generation energy-efficient light source for photocatalysis: LEDs for environmental applications, *Ind. Eng. Chem. Res.*, 53 (6), 2073–2084.
- [37] Nurdin, M., Maulidiyah, M., Syahputra, R.A., Salim, L.O.A., Wati, I., Irwan, I., and Mustapa, F., 2021, Degradation test of organic congo red compounds using $Mn-TiO_2/Ti$ electrode by photocatalytic under the UV-visible irradiation, *J. Phys.: Conf. Ser.*, 1899, 012047.

Visible-Light-Driven Photocatalytic Degradation of Rhodamine B over Bimetallic Cu/Ti-MOFs

Hong Tham Thi Nguyen^{1,2}, Kim Ngan Thi Tran^{1,2}, Thuy Bich Tran³, Thanh Trung Nguyen^{4,5}, Sy Trung Do⁶, and Kim Oanh Thi Nguyen^{1,2*}

¹Institute of Environmental Technology and Sustainable Development, Nguyen Tat Thanh University, 298-300A Nguyen Tat Thanh, Ward 13, District 4, Ho Chi Minh City, 700000, Vietnam

²Faculty of Food and Environmental Engineering, Nguyen Tat Thanh University, 298-300A Nguyen Tat Thanh, Ward 13, District 4, Ho Chi Minh City, 700000, Vietnam

³Institute of Environmental Science, Engineering and Management, Industrial University of Ho Chi Minh City, 12 Nguyen Van Bao Street, Ward 4, Go Vap District, Ho Chi Minh City, Vietnam

⁴Nanomaterial Laboratory, An Giang University, 18 Ung Van Khienn St., Dong Xuyen Dist, Long Xuyen City, An Giang Province, Vietnam

⁵Vietnam National University Ho Chi Minh City, Linh Trung Ward, Thu Duc District, Ho Chi Minh City, Vietnam

⁶Institute of Chemistry, Vietnam Academy of Science and Technology (VAST), Hanoi City, Vietnam

* **Corresponding author:**

tel: +84-392073898

email: ntkoanh@ntt.edu.vn

Received: October 13, 2021

Accepted: December 15, 2021

DOI: 10.22146/ijc.69765

Abstract: The first copper-doped titanium-based amine-dicarboxylate metal-organic framework was synthesized by the solvothermal approach in this article, with a Cu²⁺/Ti⁴⁺ ratio of 0.15 (15% Cu/Ti-MOFs). X-ray diffraction (XRD), Fourier transform infrared spectroscopy (FTIR), Raman spectra, N₂ adsorption-desorption studies, and UV-Vis diffuse reflectance spectroscopy (UV-Vis DRS) were all used to identify the crystalline and properties of the semiconductors. The rate constants of 15% Cu/Ti-MOFs to degrade Rhodamine B (RhB) were roughly two times higher than NH₂-Ti-MOFs. Furthermore, 15% Cu/Ti-MOFs photocatalysts remained stable after three cycles. The trapping test revealed that the principal active species in the degradation performance were hydroxyl radicals and holes.

Keywords: bimetallic Cu/Ti-MOFs; photocatalytic; degradation; Rhodamine B; kinetic

■ INTRODUCTION

Organic dyes have been widely used in the textile and print industries. However, because these compounds are toxic, non-biodegradable, and potentially carcinogenic, their release into the water supply could endanger humans and the environment [1]. Rhodamine B (RhB) is an example of a highly toxic dye [2]. Nonetheless, RhB is still used as a fluorescent dye for staining in biology, sometimes in conjunction with auramine O to form the auramine-rhodamine stain [3]. As a result, there is a pressing need to design an effective dye wastewater treatment process.

Metal-organic frameworks (MOFs) have many possible uses due to their huge surface areas, homogeneous yet configurable cavities, and tailorable physicochemical features [4-6]. Gas adsorption and storage [7], separation [8], drug delivery [9], and catalysis [10] are a few typical examples. In addition, the cost-effective photocatalysis process has gained popularity due to its advantages, such as biodegradable and non-toxic end products.

Recently, the photoactive, crystalline, and highly porous titanium-oriented MOFs NH₂-MIL-125(Ti) exhibiting Ti₈O₈(OH)₄(O₂CC₆H₃(NH₂)CO₂)₆ have

received much attention in the photocatalysis domain [11-13]. $\text{NH}_2\text{-MIL-125(Ti)}$ is crystal titanium-based amine-dicarboxylate with excellent absorbance, encapsulation potential, and stability [14]. This material is also embellished with numerous inactive Ti sites. However, due to its exclusive activation in the UV light area and quick charge recombination, its employment in photocatalytic platforms is limited, resulting in poor photocatalytic efficiency [15].

When suitable energy light strikes the photocatalyst, the generated electron-hole pair participates in the reaction [16]. Electron-hole pair recombination must be avoided to be so large to promote photocatalysis. The photocatalytic activity of MOFs has been improved using various techniques, including coupling with noble metals [17-18] and forming heterojunctions with other semiconductors [19-20]. Furthermore, metal doping is a potential method for regulating the electronic structure and improving photocatalytic activity. For example, Hong Liu et al. used an in situ doping approach to create new copper-doped titanium-based amine-functionalized metal-organic frameworks ($\text{Cu-NH}_2\text{-MIL-125(Ti)}$).

In this work, the photocatalytic activity of produced samples was demonstrated through the degradation of methyl orange (MO) and phenol under visible light [21]. In 2019, Gómez-Avilés et al. synthesized mixed Ti-Zr-MOFs and tested them as photocatalysts under solar-simulated radiation using acetaminophen (ACE) as a target pollutant [22]. However, a full comprehensive determination of the structure and photocatalysis mechanism of these materials remains challenging. The photocatalytic performance of bimetallics strongly depends on their composition and microstructures. Herein, the scope for further investigation into the role played by Cu^{2+} in $\text{NH}_2\text{-MIL-125(Ti)}$, which is also rare recently.

This article reports a simple method of synthesizing $\text{NH}_2\text{-Ti-MOFs}$ and bimetallic 15% Cu/Ti-MOFs using the solvothermal method. The bare Ti-MOFs were prepared to compare with 15% Cu/Ti-MOFs to highlight the advantage of transition metal-based on its superior optical performance. Moreover, Cu^{2+} was also supposed to play a part in the structural adjustment of $\text{NH}_2\text{-Ti-MOFs}$.

■ EXPERIMENTAL SECTION

Materials

Titanium (IV) isopropoxide ($\text{TiOCH(CH}_3)_2$), 2-amino terephthalic acid ($\text{NH}_2\text{-BDC}$) were purchased from Sigma-Aldrich Co. (St. Louis, MO, USA), copper(II) chloride (CuCl_2) were obtained from Fisher Scientific (Fair Long, NJ, USA), N-dimethylformamide (DMF, 99.5%) and methanol (CH_3OH) were obtained from Xilong Chemical Co., Ltd (China).

Instrumentation

The catalysts were identified using the powder X-ray diffraction (PXRD) technique, which used a 600 XRD diffractometer (Shimadzu, Japan) with Cu K α radiation ($\lambda = 1.5418$) at a scan rate of $0.020^\circ/\text{s}$ in the 5–40 range of the 2-theta range. Raman spectroscopy was performed using a HORIBA Jobin Yvon spectrometer (Horiba Scientific, Japan) with a wavenumber range of $100\text{--}1000\text{ cm}^{-1}$ (633 nm of the laser beam). FTIR spectroscopy was performed on the sample KBr pellets using a Jasco-4700 FTIR Spectrometric Analyzer (Japan). Nitrogen physisorption was used to investigate the BET and pore size distributions using a Micromeritics Tristar 3000 analyzer. The UV-vis DRS was measured at wavelengths ranging from 200 to 800 nm (UV-2450, Shimadzu, Japan).

Procedure

Preparation of $\text{NH}_2\text{-Ti-MOFs}$ and 15% Cu/Ti-MOFs

$\text{NH}_2\text{-Ti-MOFs}$ were synthesized via the report of Hanna et al. (2020) [23]. Briefly, 0.504 g 2-amino-1,4-benzene dicarboxylate (BDC-NH_2) was dissolved in 12.1 mL N,N-dimethylformamide (DMF). 1.4 mL methanol was added to the mixture and magnetically stirred at room temperature for 30 min. Next, 0.26 mL of titanium isopropoxide was added to the mixture, with continued stirring until homogenous, and later added with 20 mg of CTAB surfactant. Then, the reaction mixture was transferred to a heat-resistant 100 mL Teflon and placed in a closed convection heat apparatus at $150\text{ }^\circ\text{C}$ for 24 h. The product was then cooled and refluxed overnight at $80\text{ }^\circ\text{C}$ to remove BDC-NH_2 from the pores. Next, the obtained material was centrifuged,

washed several times with DMF and methanol, and vacuum dried overnight at 150 °C. The mixed Cu/Ti-MOFs were synthesized according to the copper molar percentage of the ratio $\text{Cu}^{2+}/\text{Ti}^{4+}$ of 0.15.

Photocatalytic test

The ability of NH_2 -Ti-MOFs and 15% Cu/Ti-MOFs samples to degrade RhB with the help of H_2O_2 and the presence of visible light demonstrates their photocatalytic activity. The catalyst (5 mg) was combined with RhB (100 mL, 3×10^{-5} M) and 1 mL H_2O_2 (2 mM) in a 250 mL double-layer beaker. Before photocatalytic degradation, the suspensions were magnetically stirred for 1 h without light to achieve equilibrium adsorption and desorption. Herein, 4 mL of samples were removed during the photodegradation process and centrifuged at 6000 rpm at regular intervals for 10 min to separate the solid material. An Agilent Cary (USA) was used to measure dye concentration and absorption.

Trapping test

The RhB photodegradation of 15% Cu/Ti-MOFs was conducted using different scavenger compounds to obtain in-depth knowledge about the photocatalytic reaction mechanism. $\text{O}_2^{\cdot-}$, HO^{\cdot} and h^+ scavengers were inhibited by p-benzoquinone (BQ), tert-butanol (TBA), and EDTA-2Na, respectively. The concentrations of TBA and EDTA were fixed at 1 mM, while the concentration of BQ was fixed at 1 μM .

■ RESULTS AND DISCUSSION

Characterization of NH_2 -Ti-MOFs and 15% Cu/Ti-MOFs

The XRD patterns of NH_2 -Ti-MOFs and 15% Cu/Ti-MOFs are shown in Fig. 1(a). The diffraction peak intensity at $2\theta = 6.8^\circ$ is attributed to the NH_2 -Ti-MOFs bare [24-25]. Noticeably, the diffraction peaks are slightly moved to lower angles when doping with ionic Cu^{2+} into the titanium framework. This can be explained based on the difference of the ionic radius of Cu^{2+} and Ti^{4+} which are 0.72 and 0.68 Å, respectively [21]. The slight decrease observed is probably due to the thermal treatment following metal deposition [26]. However, the modification of ion Cu^{2+} had not changed the crystalline phase of NH_2 -Ti-MOFs.

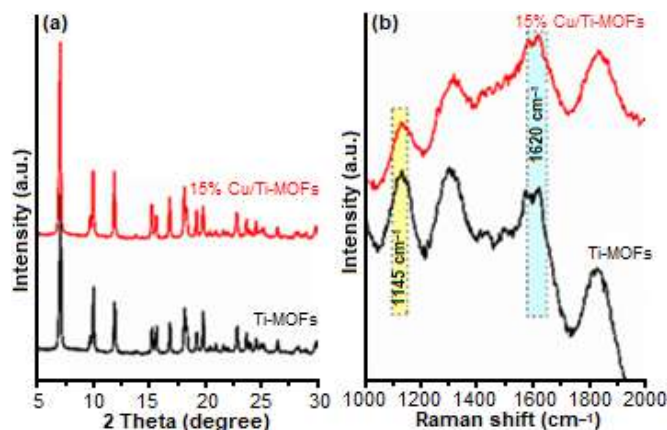


Fig 1. XRD pattern (a) and Raman spectra (b) of NH_2 -Ti-MOFs and 15% Cu/Ti-MOFs

Therefore, the formation of 15% Cu/Ti-MOFs was further confirmed.

Raman spectroscopy was used to investigate the bonding vibration of Ti-MOFs and 15% Cu/Ti-MOFs bimetallic materials (Fig. 1(b)). All of the spectra had the same characteristic peaks. The relatively strong bands observed at 325 nm at 546, 640, 1145, and 1620 cm^{-1} characterize NH_2 -MIL-125(Ti) materials [27]. The type of framework of titanium is responsible for the resonance-enhanced Raman band at 703 cm^{-1} . The N-H bond of the organic bridge is represented in the band at 1620 cm^{-1} [28]. The appearance of a band of symmetrical bending and elongation at 546 cm^{-1} is typical for octahedral Ti-O-Ti-O [29].

The nitrogen adsorption/desorption analyses at 77 K were used to explore the specific surface areas and porosity of MOF materials. As displayed in Fig. 2, all the samples exhibit the typical isotherms of IV, indicative of the presence of a large number of micropores with some small contribution of mesoporosity and high surface area values. The Brunauer-Emmett-Teller (BET) surface areas of the as-prepared NH_2 -Ti-MOFs and 15% Cu/Ti-MOFs were 970.23 and 1157.41 m^2/g , respectively. Therefore, as in the case of the crystalline structure, metal cluster modification did not provoke significant changes in the porous texture of the original NH_2 -Ti-MOFs.

The UV-Vis spectra of NH_2 -Ti-MOFs reveal two prominent absorption bands with maxima at 217 and 370 nm, which are caused by the Ti-O and ligand cluster transition. Furthermore, an absorption band extending

up to 500 nm can be observed due to the $\text{NH}_2\text{-BDC}$ ligand [30]. After incorporating transition metals into Ti-MOFs, the UV-Vis absorption band redshifted, and the visible region expanded noticeably (Fig. 3(a)). The bandgap energy of all obtained samples was calculated using the graph of $(h\nu)^2$ versus photon energy (h) shown in Fig. 3(b). The bandgap of $\text{NH}_2\text{-Ti-MOFs}$ and 15% Cu/Ti-MOFs were calculated from the absorption line intersection and are 2.56 and 2.42 eV, respectively.

Photocatalytic Test

The photocatalyst efficiency of the as-prepared samples was figured out via the degradation of Rhodamine B (RhB) dye under visible light irradiation (Fig. 4(a)). It was found that the rate of degradation of $\text{NH}_2\text{-Ti-MOFs}$ was prolonged after 120 min of irradiation. However, the degradation process significantly rose when doping Cu^{2+} ions into the $\text{NH}_2\text{-Ti-MOFs}$. Therefore, it is indicated that the Cu^{2+} ion helped the bandgap energy to narrow, which boosted the photocatalyst effect. Furthermore, as per the literature, $\cdot\text{OH}$ radicals were generated and acted as electron acceptors, which is the main factor in helping the MOFs generate more holes and encourage the photocatalysis process.

The kinetics of RhB degradation on $\text{NH}_2\text{-Ti-MOFs}$ and bimetallic 15% Cu/Ti-MOFs were also described via the pseudo-first-order (Fig. 4(b)). For 15% Cu/Ti-MOFs, the correlation coefficient (R^2) and the rate constant (k_1) for the pseudo-first-order kinetic model were the highest. Notably, the kinetic rate of 15% Cu/Ti-MOFs reached

10.23 (10^{-3} min^{-1}), which showed the highest photocatalytic performance. The UV-Vis absorption spectra of RhB to irradiation time over Ti-MOFs and 15% Cu/Ti-MOFs are also depicted in Fig. 4(c-d). The RhB dye solution's absorption peak was at 554 nm, and it gradually decreased due to dye degradation, reaching its lowest value at 120 min. The photocatalyst cleavage of the aromatic ring of the dye molecules is thought to cause a decrease in absorption peaks, which leads to the decomposition of the RhB dye [31].

The pH of the solution had a significant impact on the efficiency of the photocatalytic reactions (Fig. 5(a)). The free radicals attacked the dye molecules and caused them to degrade over time. Because of the electrostatic interaction between the negatively charged material surface (from the proton separation process) and the predominant positively charged dye cation at pH 2, the

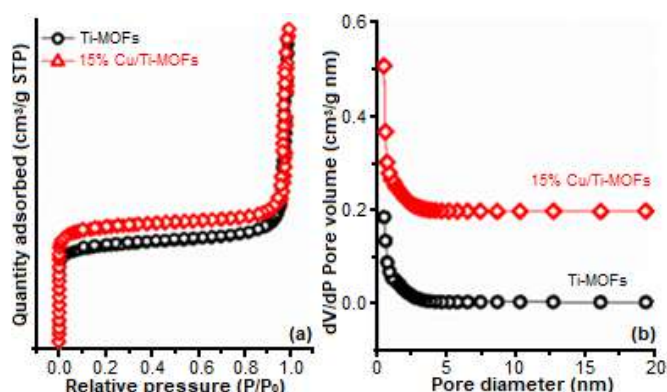


Fig 2. Adsorption-desorption isotherms of $\text{NH}_2\text{-Ti-MOFs}$ and 15% Cu/Ti-MOFs

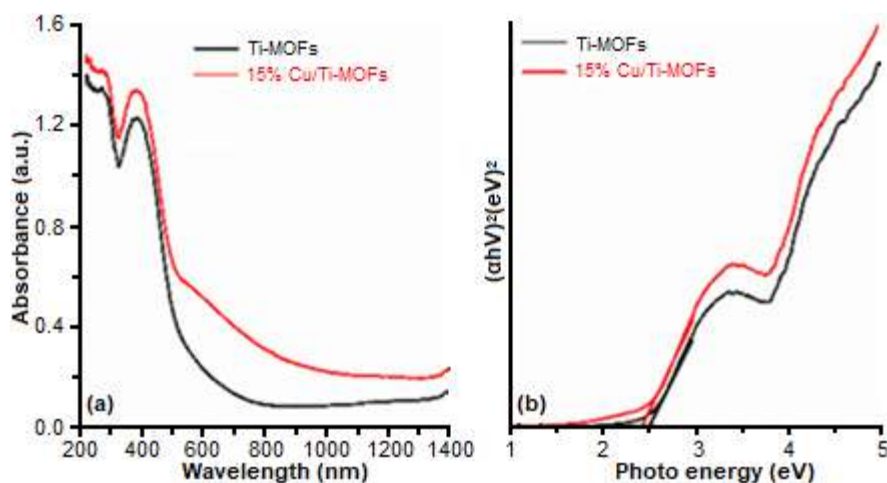


Fig 3. UV-Vis DRS (A) and Tauc plot (B) of $\text{NH}_2\text{-Ti-MOFs}$ and 15% Cu/Ti-MOFs

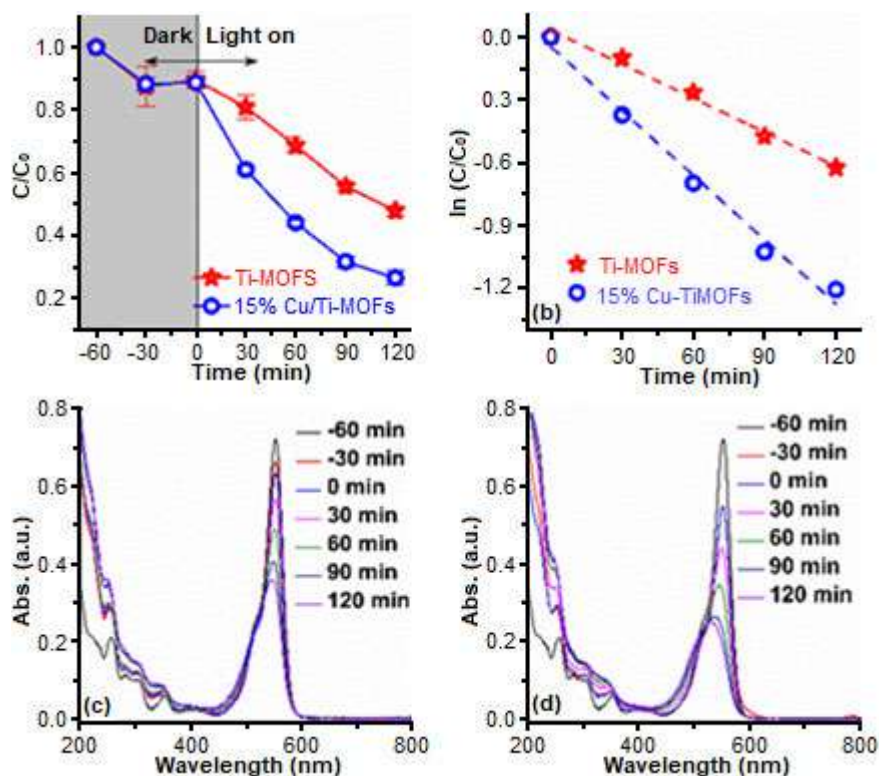


Fig 4. The removal efficiency of Rhodamine B (a) using different catalysts under visible light irradiation in the presence of H_2O_2 and (b) Pseudo first-order kinetic of the degradation process, (c, d) UV-Vis absorption spectra of RhB with respect to irradiation time over NH_2 -Ti-MOFs and 15% Cu/Ti-MOFs, respectively

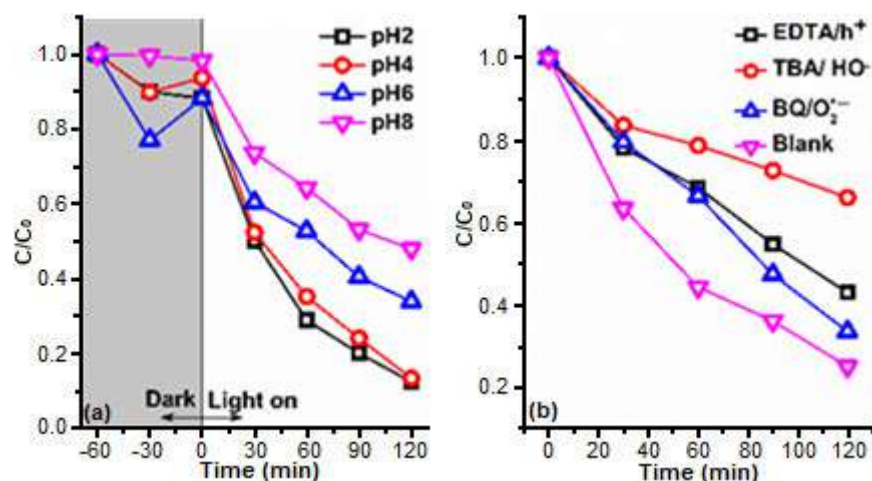


Fig 5. The effect of pH solution (a) and photocatalyst mechanism of 15% Cu/Ti-MOFs (b)

the photochemical degradation efficiency increased sharply, resulting in a sharp increase in absorbance as well as causing the photochemical reaction. When the pH rises above 8, RhB is deprotonated, and its zwitterion is formed. Furthermore, photochemical degradation was inhibited

because the hydroxyl ions competed with the RhB molecules for adsorption on the catalyst surface. This finding is consistent with the findings of Zhao et al. [32].

Reactive radicals ($\cdot OH$, $O_2^{\cdot -}$, h^+) are produced during the irradiation process and are responsible for

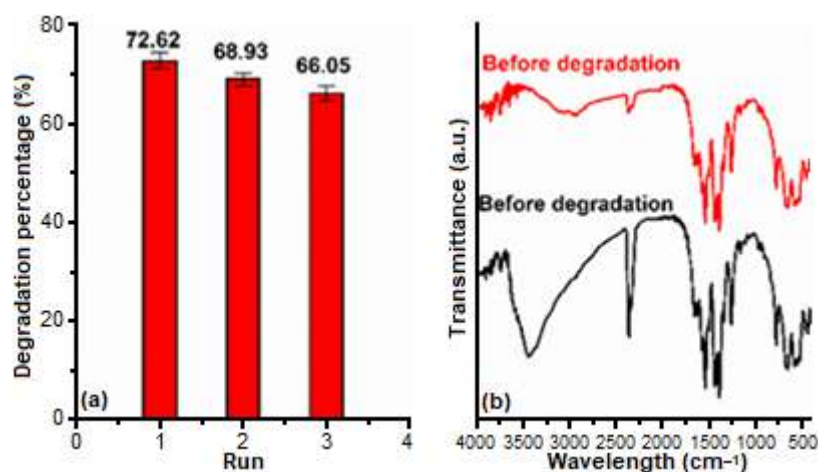


Fig 6. The reliability test of the degradation of RhB over 15% Cu/Ti-MOFs (a), FTIR spectra of 15% Cu/Ti-MOFs before and after degradation performance (b)

dye degradation. Trapping experiments were used to determine which radical was dominant. According to Fig. 5(b), the final degradation efficiency changed almost noticeably after 2 h of visible light irradiation when added with 1 mM TBA and 1 mM EDTA-2Na. Hence, $\cdot\text{OH}$ and h^+ were predominantly responsible for RhB degradation.

To investigate the stability of the photocatalyst, recycling experiments of 15% Cu/Ti-MOFs were performed under the same conditions. Fig. 6(a) depicts the photodegradation of RhB after three runs. The removal of RhB decreased from 72.62% to 66.05%, indicating that the catalyst can be used repeatedly with no discernible variation in photocatalytic performance. The FTIR spectra (Fig. 6(b)) of fresh and used catalyst (used three-times) proved the stability of 15% Cu/Ti-MOFs after the 3rd -run. The organic linkers C-C and N-H bonds bending vibrations were visible in the FTIR spectra of 15% Cu/Ti-MOFs, with peaks at 1500 and 1620 cm^{-1} , respectively [33-34]. Furthermore, the peaks at 1245 and 1414 cm^{-1} are associated with a Ti-O framework's bending and symmetric stretching [35]. According to this study, the organic linker's -COOH group was directly attached to the Ti-oxo cluster.

■ CONCLUSION

NH_2 -Ti-MOFs and 15% Cu/Ti-MOFs were successfully prepared via the solvothermal method and were used to degrade RhB dye efficiently. Compared to the individual Ti-MOFs, 15% Cu/Ti-MOFs exhibited

enhanced photocatalytic activity for RhB degradation. The promoted electron transfer by the $\text{Cu}^{2+}/\text{Cu}^+$ and $\text{Ti}^{4+}/\text{Ti}^{3+}$ redox cycles and the efficient separation of photo-excited electron-hole pairs by introducing H_2O_2 can be attributed to the accelerated photocatalytic degradation of RhB. The prepared 15% Cu/Ti-MOFs also demonstrated good reusability and stability. Further investigation revealed that the principal active species in the degradation process were hydroxyl radicals and holes. The 15% as-synthesized Cu/Ti-MOFs showed promise in the removal of organic contaminants from wastewater.

■ ACKNOWLEDGMENTS

This research was funded by the Center of Science and Technology Development for Youth, Ho Chi Minh City Communist Youth Union, Vietnam (No. 33/2020/HĐ-KHCN-VU).

■ REFERENCES

- [1] Wang, M., Yang, L., Guo, C., Liu, X., He, L., Song, Y., Zhang, Q., Qu, X., Zhang, H., Zhang, Z., and Fang, S., 2018, Bimetallic Fe/Ti-based metal-organic framework for persulfate-assisted visible light photocatalytic degradation of Orange II, *ChemistrySelect*, 3 (13), 3664-3674.
- [2] Vieira, Y., Leichtweis, J., Foletto, E.L., and Silvestri, S., 2020, Reactive oxygen species-induced heterogeneous photocatalytic degradation of

- organic pollutant rhodamine B by copper and zinc aluminate spinels, *J. Chem. Technol. Biotechnol.*, 95 (3), 791–797.
- [3] Tang, S.K., Teng, T.T., Alkarkhi, A.F.M., and Li, Z., 2012, Sonocatalytic degradation of rhodamine B in aqueous solution in the presence of TiO₂ coated activated carbon, *APCBEE Procedia*, 1, 110–115.
- [4] Shi, L., Wang, T., Zhang, H., Chang, K., Meng, X., Liu, H., and Ye, J., 2015, An amine-functionalized iron(III) metal-organic framework as efficient visible-light photocatalyst for Cr(VI) reduction, *J. Ye, Adv. Sci.*, 2 (3), 1500006.
- [5] Wu, Y.Y., Yang, C.X., and Yan, X.P., 2014, Fabrication of metal-organic framework MIL-88B films on stainless steel fibers for solid-phase microextraction of polychlorinated biphenyls, *J. Chromatogr. A*, 1334, 1–8.
- [6] Lin, K.Y.A., Chang, H.A., and Hsu, C.J., 2015, Iron-based metal-organic framework, MIL-88A, as a heterogeneous persulfate catalyst for decolorization of Rhodamine B in water, *RSC Adv.*, 5 (41), 32520–32530.
- [7] Li, H., Wang, K., Sun, Y., Lollar, C.T., Li, J., and Zhou, H.C., 2018, Recent advances in gas storage and separation using metal-organic frameworks, *Mater. Today*, 21 (2), 108–121.
- [8] Solanki, V.A., and Borah, B., 2019, Ranking of metal-organic frameworks (MOFs) for separation of hexane isomers by selective adsorption, *Ind. Eng. Chem. Res.*, 58 (43), 20047–20065.
- [9] Wang, L., Zheng, M., and Xie, Z., 2018, Nanoscale metal-organic frameworks for drug delivery: A conventional platform with new promise, *J. Mater. Chem. B*, 6 (5), 707–717.
- [10] Nguyen, H.T.T., Dinh, V.P., Phan, Q.A.N., Tran, V.A., Doan, V.D., Lee, T., and Nguyen, T.D., 2020, Bimetallic Al/Fe metal-organic framework for highly efficient photo-Fenton degradation of rhodamine B under visible light irradiation, *Mater. Lett.*, 279, 128482.
- [11] Kim, S.N., Kim, J., Kim, H.Y., Cho, H.Y., and Ahn, W.S., 2013, Adsorption/catalytic properties of MIL-125 and NH₂-MIL-125, *Catal. Today*, 204, 85–93.
- [12] Gómez-Avilés, A., Muelas-Ramos, V., Bedia, J., Rodríguez, J.J., and Belver, C., 2020, Thermal post-treatments to enhance the water stability of NH₂-MIL-125(Ti), *Catalysts*, 10 (6), 603.
- [13] Remiro-Buenamañana, S., Cabrero-Antonino, M., Martínez-Guanter, M., Álvaro, M., Navalón, S., and García, H., 2019, Influence of co-catalysts on the photocatalytic activity of MIL-125(Ti)-NH₂ in the overall water splitting, *Appl. Catal., B*, 254, 677–684.
- [14] Zhao, Y., Cai, W., Chen, J., Miao, Y., and Bu, Y., 2019, A highly efficient composite catalyst constructed from NH₂-MIL-125(Ti) and reduced graphene oxide for CO₂ photoreduction, *Front. Chem.*, 7, 789.
- [15] Hlophe, P.V., Mahlalela, L.C., and Dlamini, L.N., 2019, A composite of platelet-like orientated BiVO₄ fused with MIL-125(Ti): Synthesis and characterization, *Sci. Rep.*, 9 (1), 10044.
- [16] Rani, S., Aggarwal, M., Kumar, M., Sharma, S., and Kumar, D., 2016, Removal of methylene blue and rhodamine B from water by zirconium oxide/graphene, *Water Sci.*, 30 (1), 51–60.
- [17] Sun, D., Liu, W., Fu, Y., Fang, Z., Sun, F., Fu, X., Zhang, Y., and Li, Z., 2014, Noble metals can have different effects on photocatalysis over metal-organic frameworks (MOFs): A case study on M/NH₂-MIL-125(Ti) (M=Pt and Au), *Chem. Eur. J.*, 20 (16), 4780–4788.
- [18] Wang, D., and Li, Z., 2016, Coupling MOF-based photocatalysis with Pd catalysis over Pd@MIL-100(Fe) for efficient N-alkylation of amines with alcohols under visible light, *J. Catal.*, 342, 151–157.
- [19] Su, Y., Zhang, Z., Liu, H., and Wang, Y., 2017, Cd_{0.2}Zn_{0.8}S@UiO-66-NH₂ nanocomposites as efficient and stable visible-light-driven photocatalyst for H₂ evolution and CO₂ reduction, *Appl. Catal., B*, 200, 448–457.
- [20] Liang, R., Shen, L., Jing, F., Qin, N., and Wu, L., 2015, Preparation of MIL-53(Fe)-reduced graphene oxide nanocomposites by a simple self-assembly strategy for increasing interfacial contact: Efficient visible-light photocatalysts, *ACS Appl. Mater. Interfaces*, 7 (18), 9507–9515.

- [21] Ao, D., Zhang, J., and Liu, H., 2018, Visible-light-driven photocatalytic degradation of pollutants over Cu-doped NH₂-MIL-125(Ti), *J. Photochem. Photobiol., A*, 364, 524–533.
- [22] Gómez-Avilés, A., Peñas-Garzón, M., Bedia, J., Dionysiou, D.D., Rodríguez, J.J., and Belver, C., 2019, Mixed Ti-Zr metal-organic-frameworks for the photodegradation of acetaminophen under solar irradiation, *Appl. Catal., B*, 253, 253–262.
- [23] Hanna, L., Long, C.L., Zhang, X., and Lockard, J.V., 2020, Heterometal incorporation in NH₂-MIL-125(Ti) and its participation in the photoinduced charge-separated excited state, *Chem. Commun.*, 56 (78), 11597–11600.
- [24] Sun, D., Liu, W., Qiu, M., Zhang, Y., and Li, Z., 2015, Introduction of a mediator for enhancing photocatalytic performance via post-synthetic metal exchange in metal-organic frameworks (MOFs), *Chem. Commun.*, 51 (11), 2056–2059.
- [25] Zhu, S.R., Liu, P.F., Wu, M.K., Zhao, W.N., Li, G.C., Tao, K., Yi, F.Y., and Han, L., 2016, Enhanced photocatalytic performance of BiOBr/NH₂-MIL-125(Ti) composite for dye degradation under visible light, *Dalton Trans.*, 45 (43), 17521–17529.
- [26] Muelas Ramos, V., Belver, C., Rodríguez, J.J., and Bedia, J., 2021, Synthesis of noble metal-decorated NH₂-MIL-125 titanium MOF for the photocatalytic degradation of acetaminophen under solar irradiation, *Sep. Purif. Technol.*, 272, 118896.
- [27] Yuan, X., Wang, H., Wu, Y., Zeng, G., Chen, X., Leng, L., Wu, Z., and Li, H., 2016, One-pot self-assembly and photoreduction synthesis of silver nanoparticle-decorated reduced graphene oxide/MIL-125(Ti) photocatalyst with improved visible-light photocatalytic activity, *Appl. Organomet. Chem.*, 30 (5), 289–296.
- [28] Karthik, P., Vinoth, R., Zhang, P., Choi, W., Balaraman, E., and Neppolian, B., 2018, π - π Interaction between metal-organic framework and reduced graphene oxide for visible-light photocatalytic H₂ production, *ACS Appl. Energy Mater.*, 1 (5), 1913–1923.
- [29] Hu, S., Liu, M., Li, K., Zuo, Y., Zhang, A., Song, C., Zhang, G., and Guo, X., 2014, Solvothermal synthesis of NH₂-MIL-125(Ti) from circular plate to octahedron, *CrystEngComm*, 16 (41), 9645–9650.
- [30] Fiaz, M., Kashif, M., Majeed, S., Ashiq, M.N., Farid, M.A., and Athar, M., 2019, Facile fabrication of highly efficient photoelectrocatalysts M_xO_y@NH₂-MIL-125(Ti) for enhanced hydrogen evolution reaction, *ChemistrySelect*, 4 (23), 6996–7002.
- [31] Jia, K., Wang, Y., Pan, Q., Zhong, B., Luo, Y., Cui, G., Guo, X., and Sun, X., 2019, Enabling the electrocatalytic fixation of N₂ to NH₃ by C-doped TiO₂ nanoparticles under ambient conditions, *Nanoscale Adv.*, 1 (3), 961–964.
- [32] Zhao, H., Zhang, Y., Li, G., Tian, F., Tang, H., and Chen, R., 2016, Rhodamine B-sensitized BiOCl hierarchical nanostructure for methyl orange photodegradation, *RSC Adv.*, 6 (10), 7772–7779.
- [33] Shen, L., Liang, S., Wu, W., Liang, R., and Wu, L., 2013, Multifunctional NH₂-mediated zirconium metal-organic framework as an efficient visible-light-driven photocatalyst for selective oxidation of alcohols and reduction of aqueous Cr(VI), *Dalton Trans.*, 42 (37), 13649–13657.
- [34] Liang, R., Shen, L., Jing, F., Wu, W., Qin, N., Lin, R., and Wu, L., 2015, NH₂-mediated indium metal-organic framework as a novel visible-light-driven photocatalyst for reduction of the aqueous Cr(VI), *Appl. Catal., B*, 162, 245–251.
- [35] Yin, S., Chen, Y., Hu, Q., Li, M., Ding, Y., Di, J., Xia, J., and Li, H., 2020, Construction of NH₂-MIL-125(Ti) nanoplates modified Bi₂WO₆ microspheres with boosted visible-light photocatalytic activity, *Res. Chem. Intermed.*, 46 (7), 3311–3326.

Supplementary Data

This supplementary data is a part of paper entitled "Synthesis, Characterization, and Theoretical Study of Some New Organotellurium Compounds Derived from Camphor".

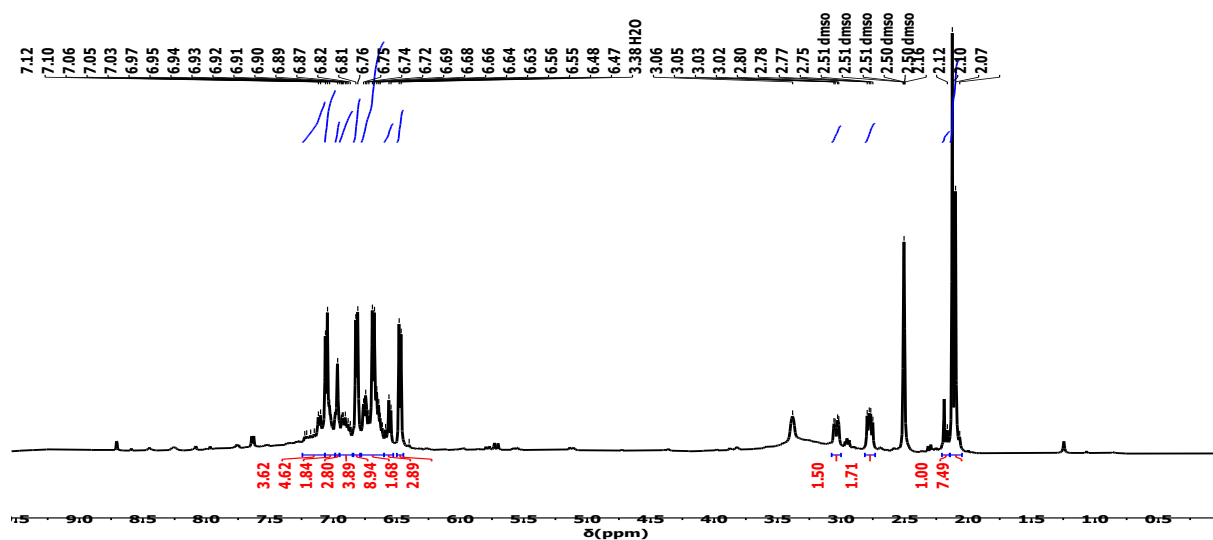


Fig S1. ¹H-NMR spectrum of compound A

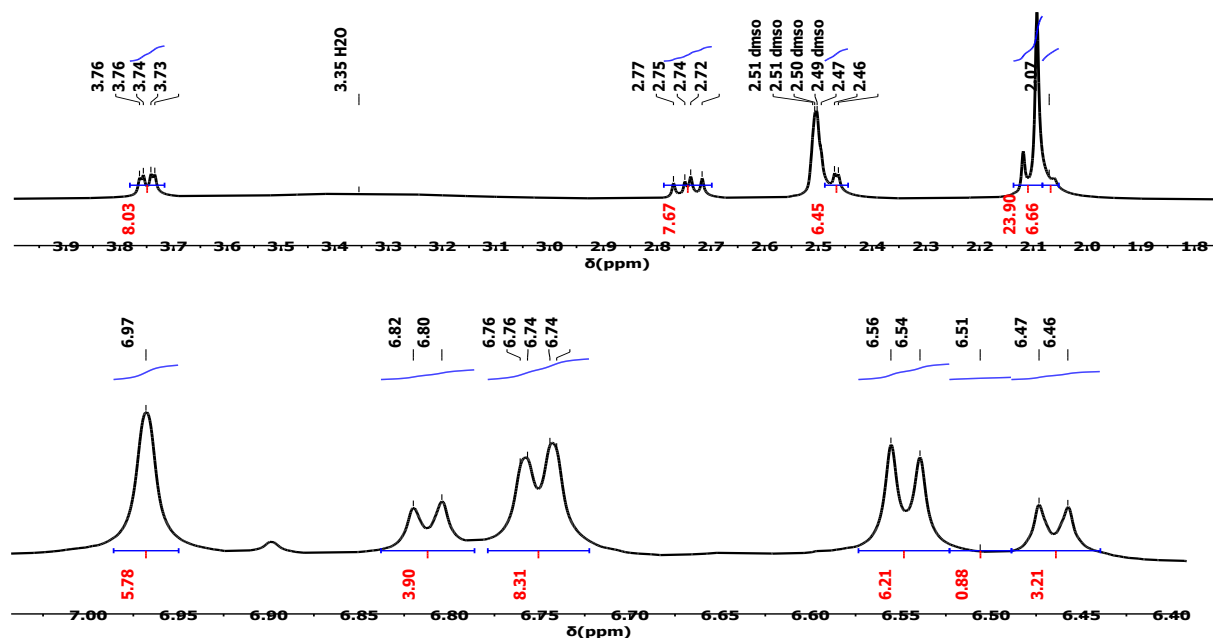
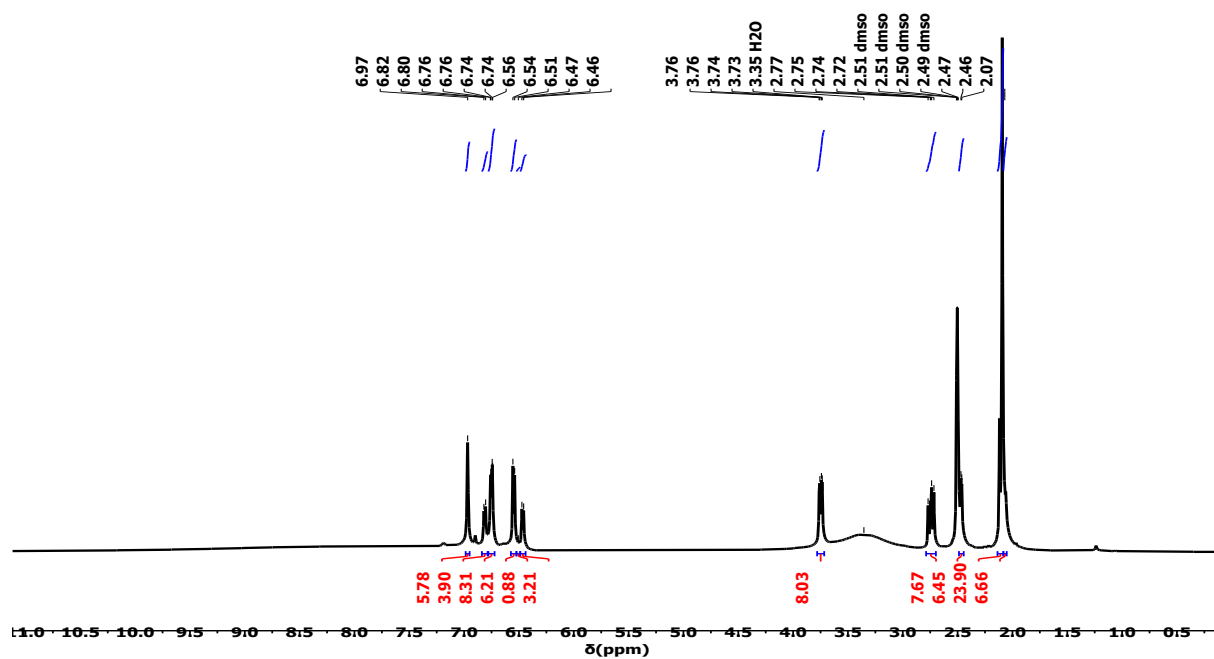
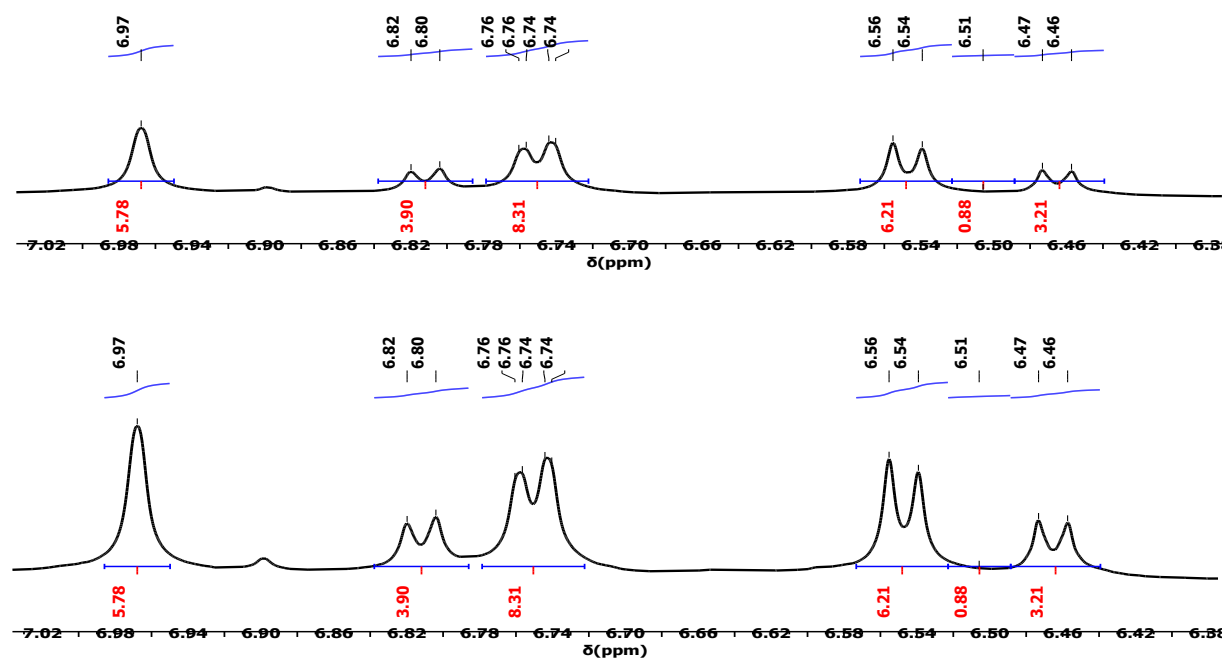


Fig S2. ¹H-NMR spectrum expansion of compound A

Fig S3. ¹H-NMR spectrum of compound BFig S4. ¹H-NMR spectrum expansion of compound B

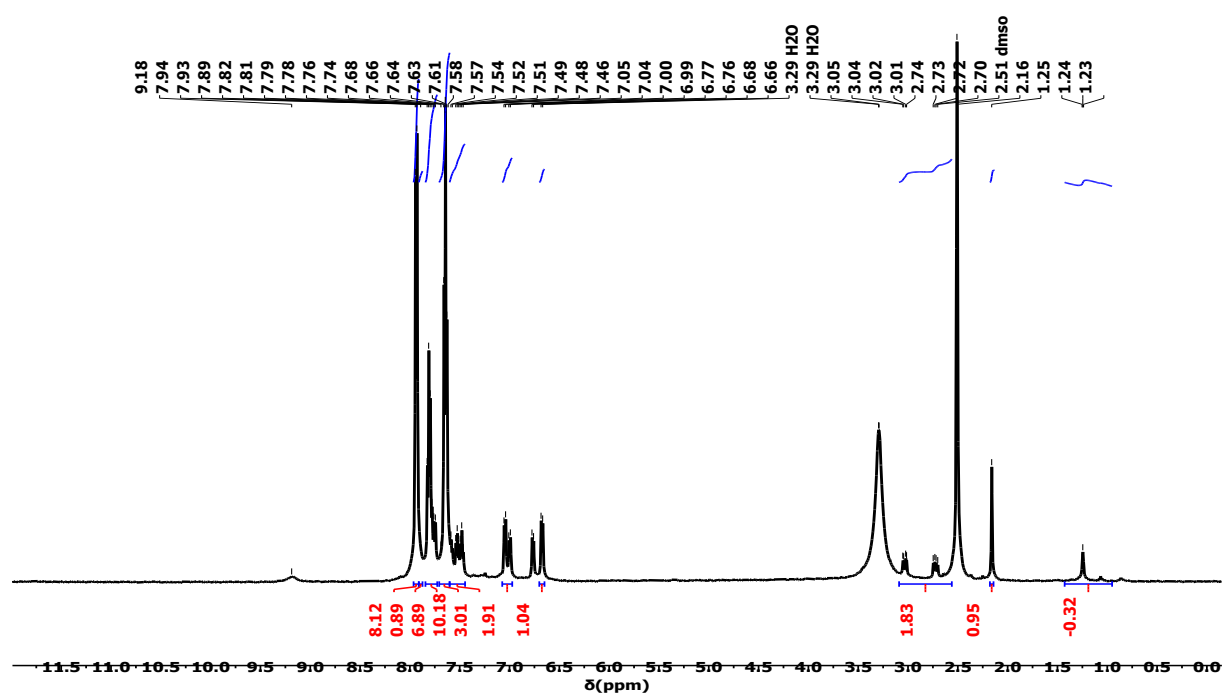


Fig S5. ¹H-NMR spectrum of compound C

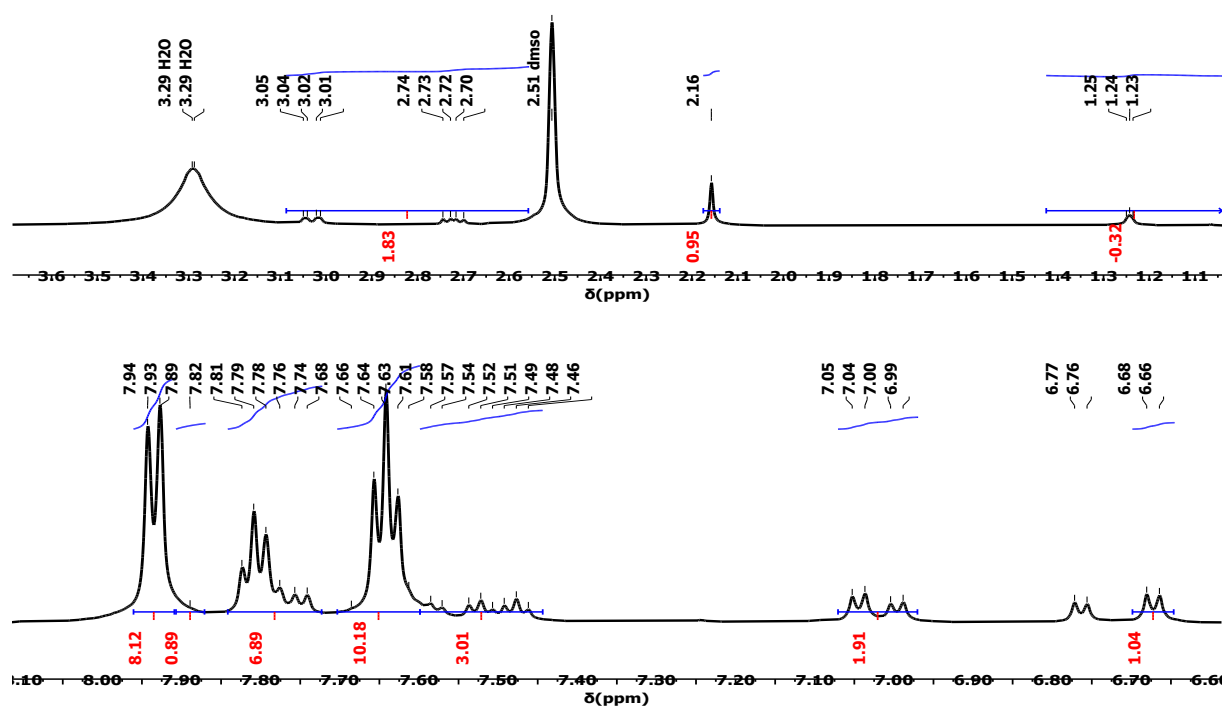
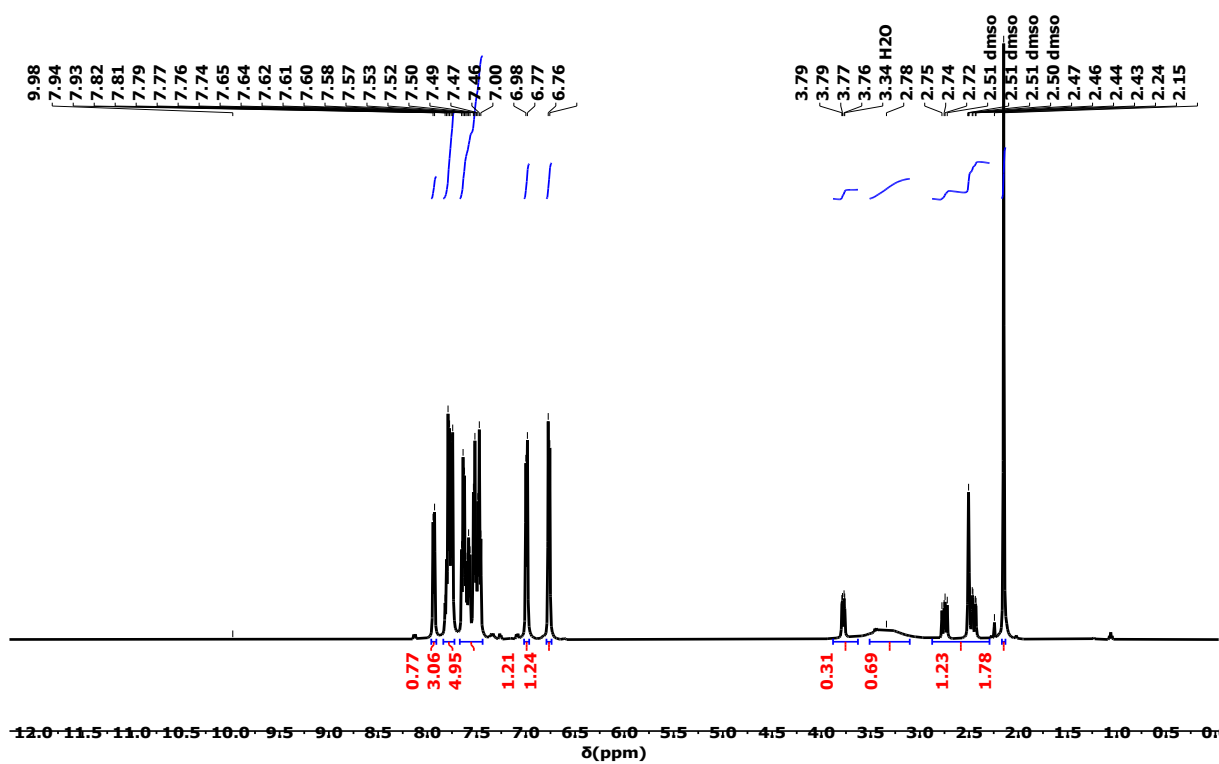
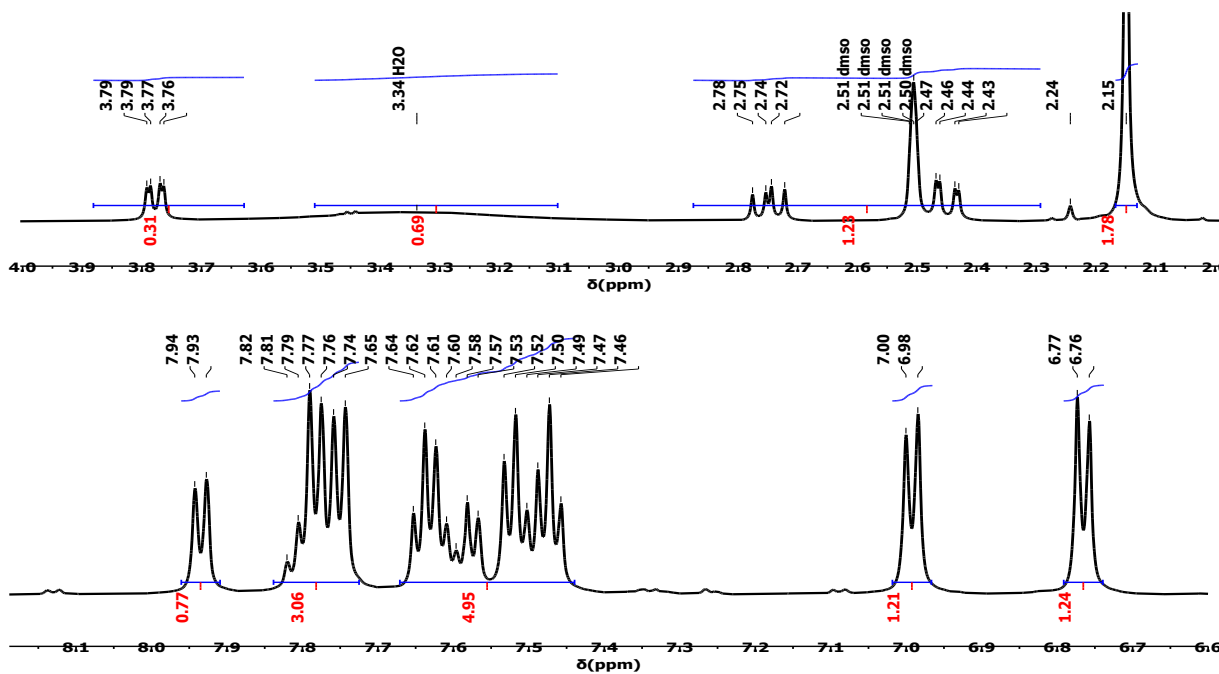


Fig S6. ¹H-NMR spectrum expansion of compound C

Fig S7. ¹H-NMR spectrum of compound DFig S8. ¹H-NMR spectrum expansion of compound D

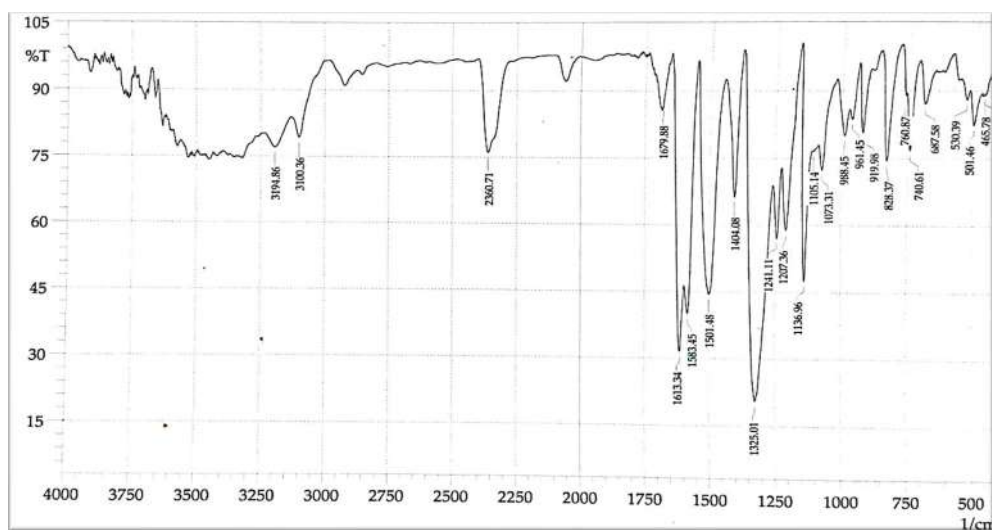


Fig S9. FT-IR spectrum of compound A

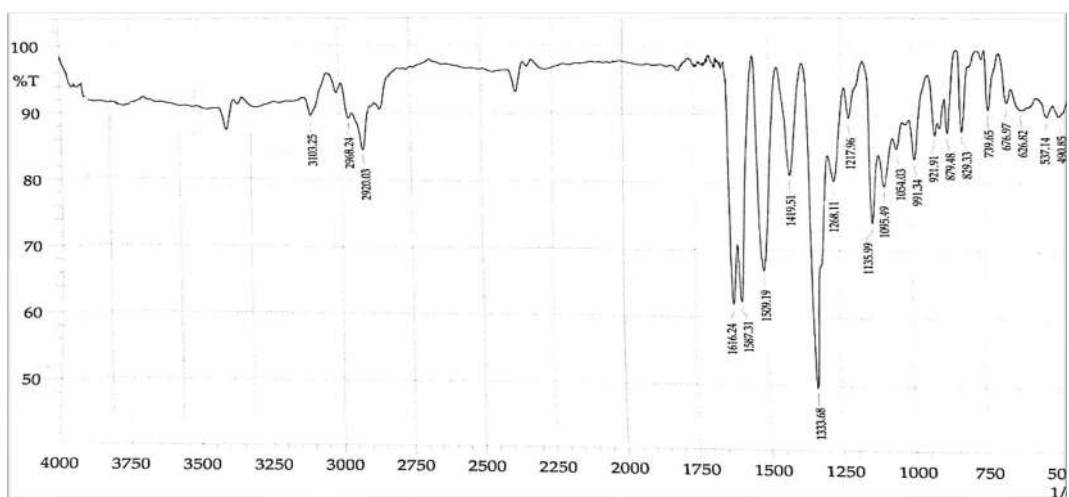


Fig S10. FT-IR spectrum of compound B

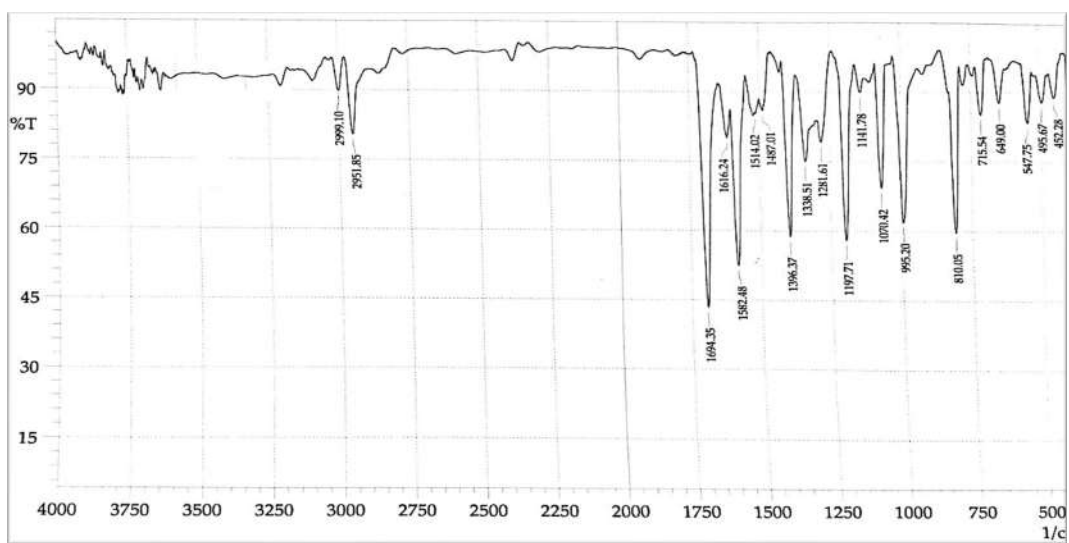


Fig S11. FT-IR spectrum of compound C

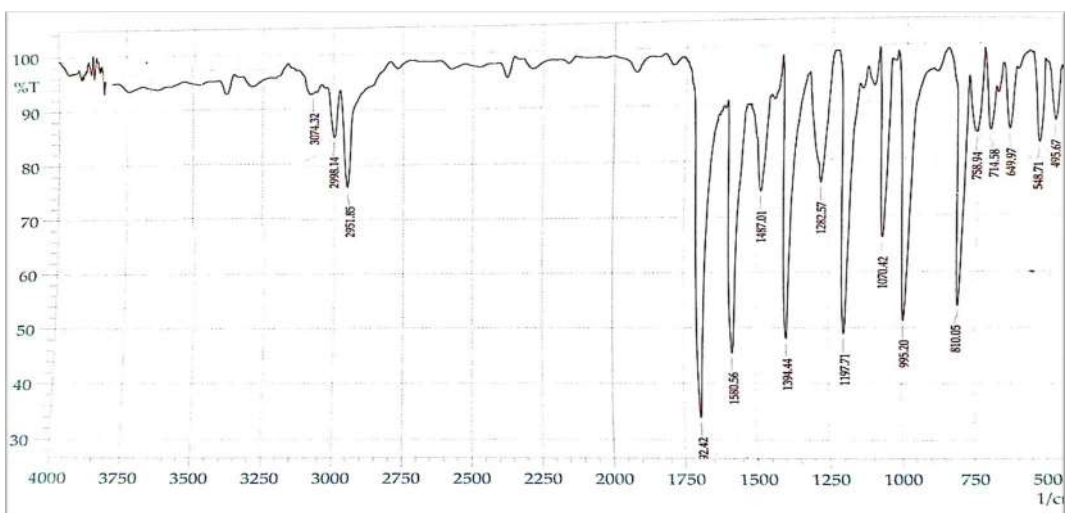


Fig S12. FT-IR spectrum of compound D

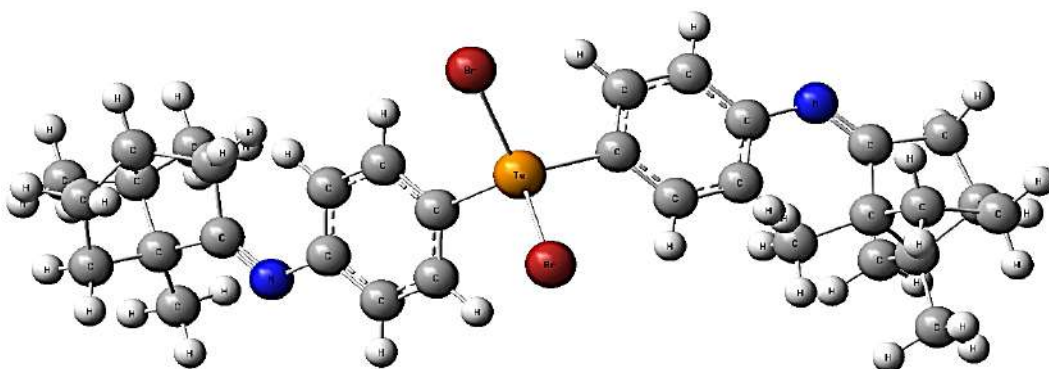


Fig S13. Molecular structure of compound A

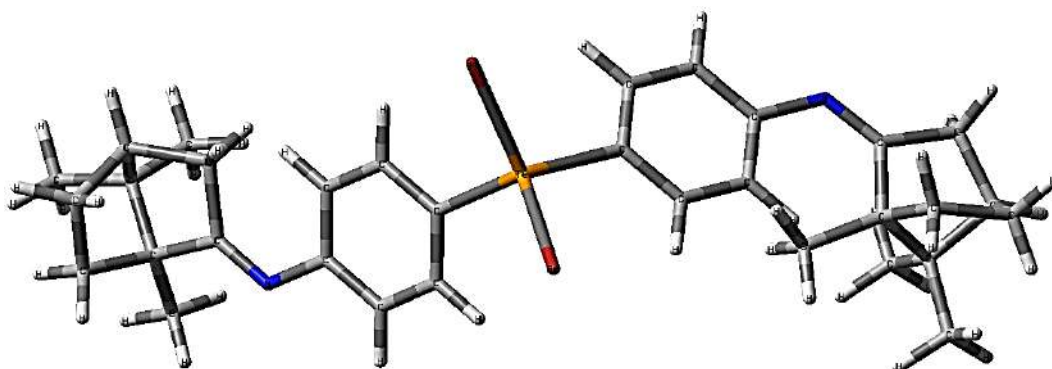


Fig S14. Sticks molecular model of compound A

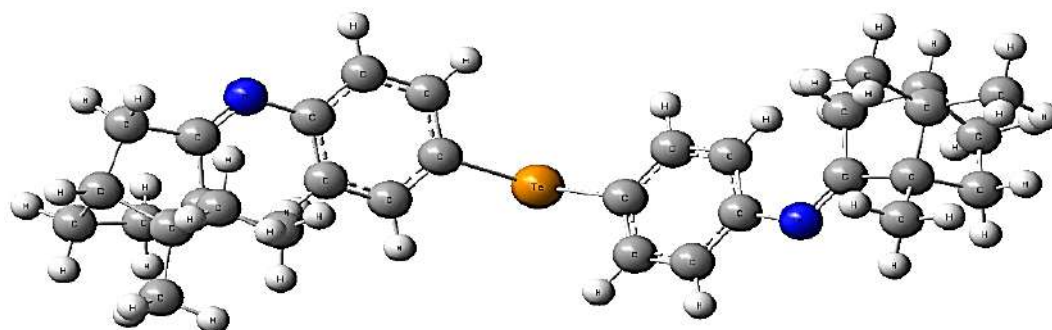


Fig S15. Molecular structure of compound B

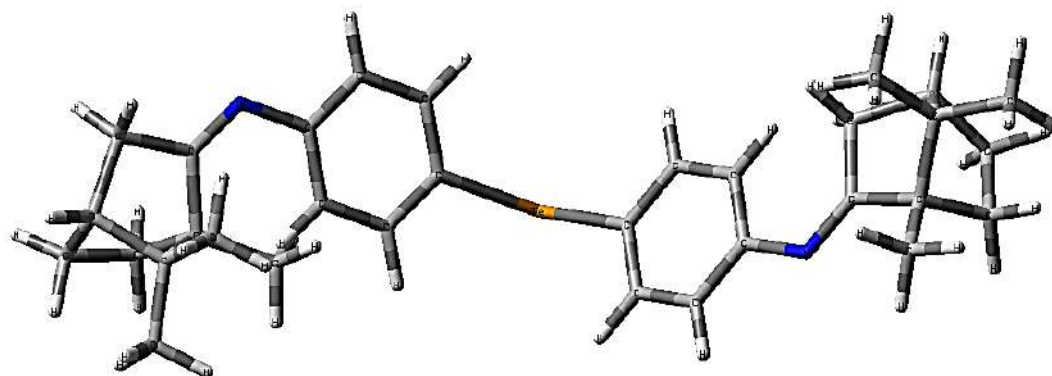


Fig S16. Sticks molecular model of compound B

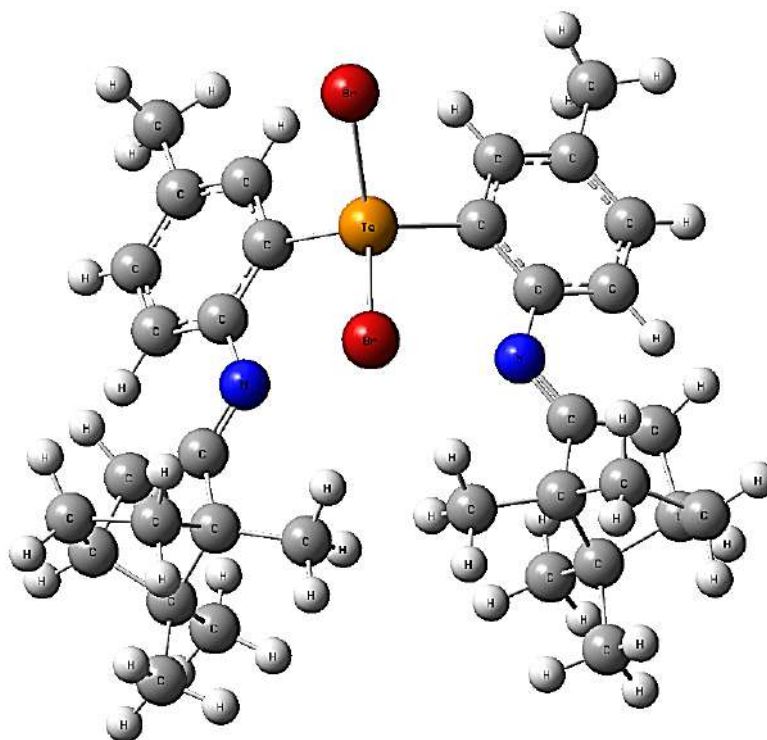


Fig S17. Molecular structure of compound C

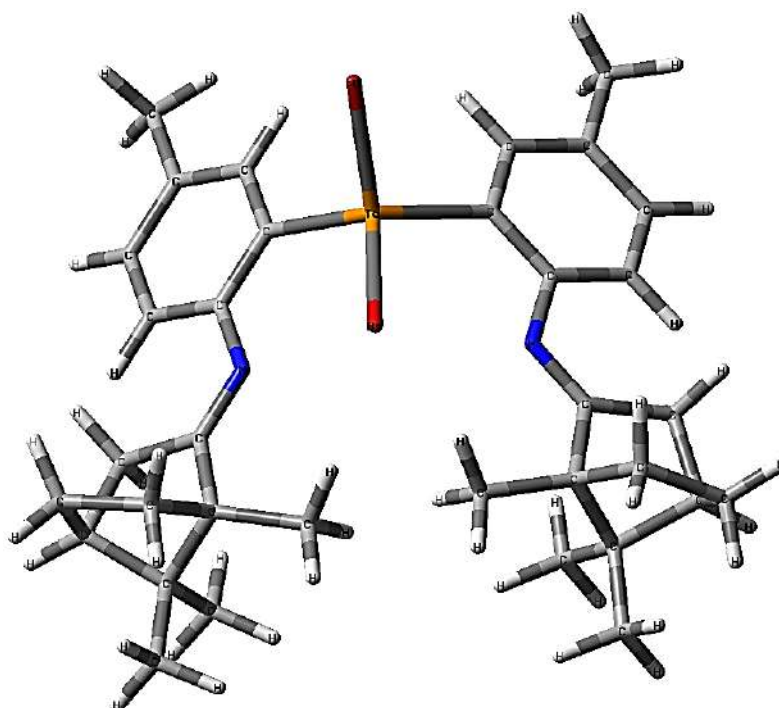


Fig S18. Sticks molecular model of compound C

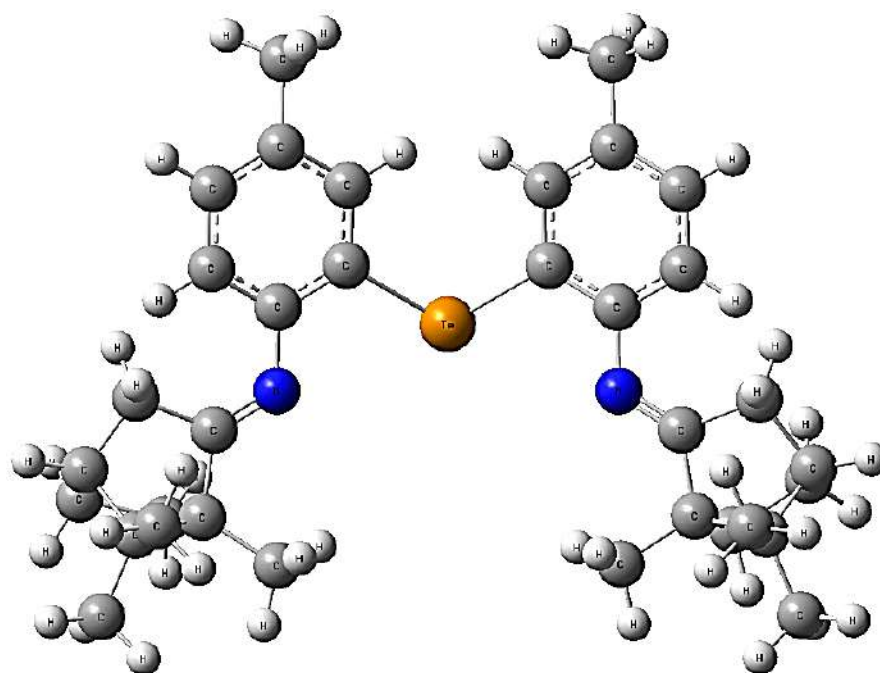


Fig S19. Molecular structure of compound D

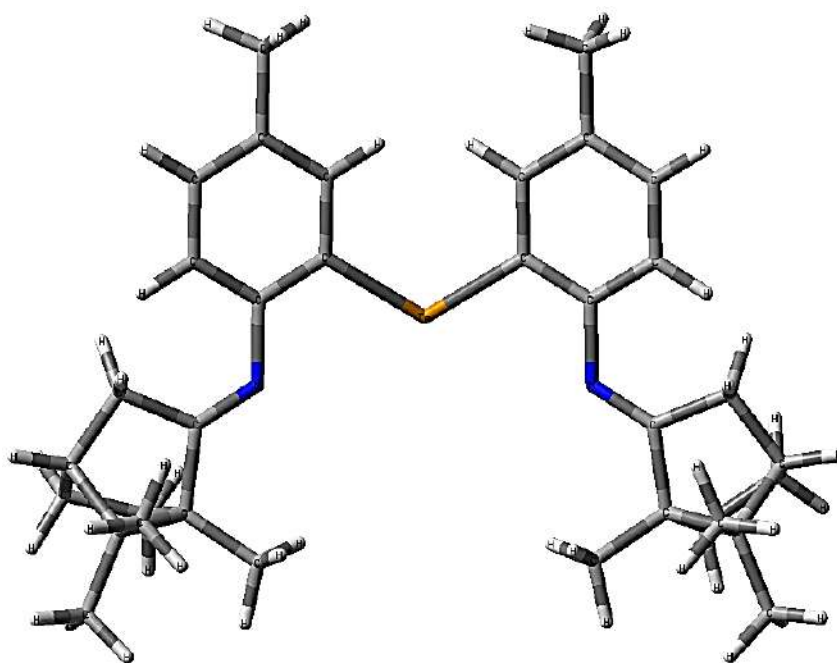


Fig S20. Sticks molecular model of compound D

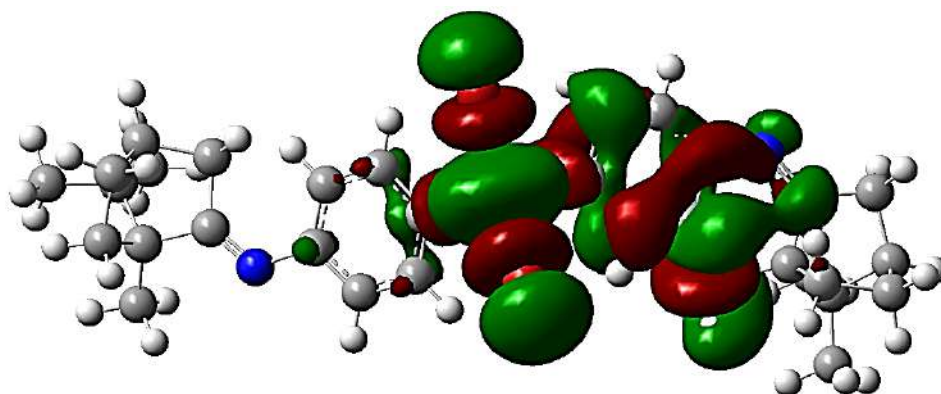


Fig S21. Molecular orbital (HOMO) of compound A

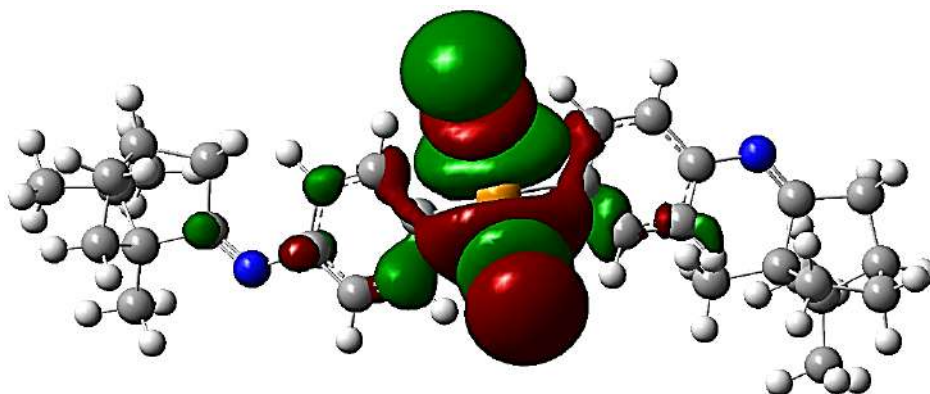


Fig S22. Molecular orbital (LUMO) of compound A

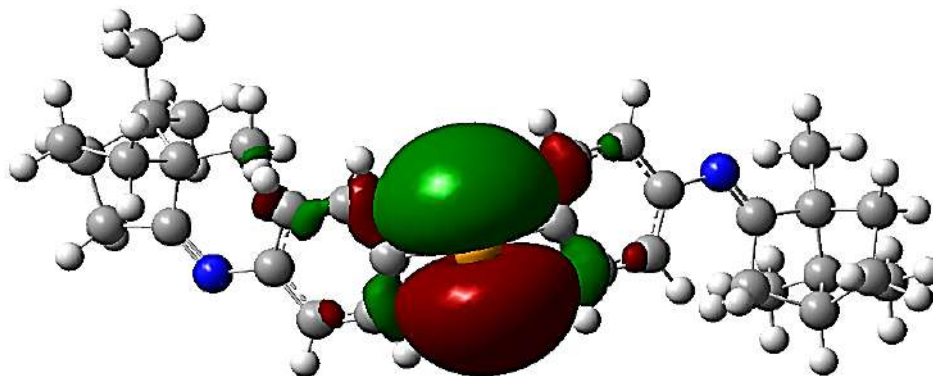


Fig S23. Molecular orbital (HOMO) of compound B

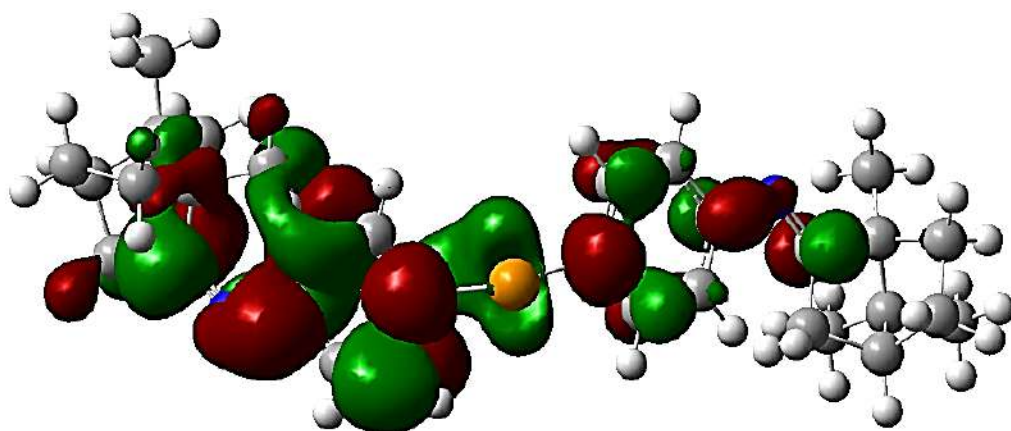


Fig S24. Molecular orbital (LUMO) of compound B

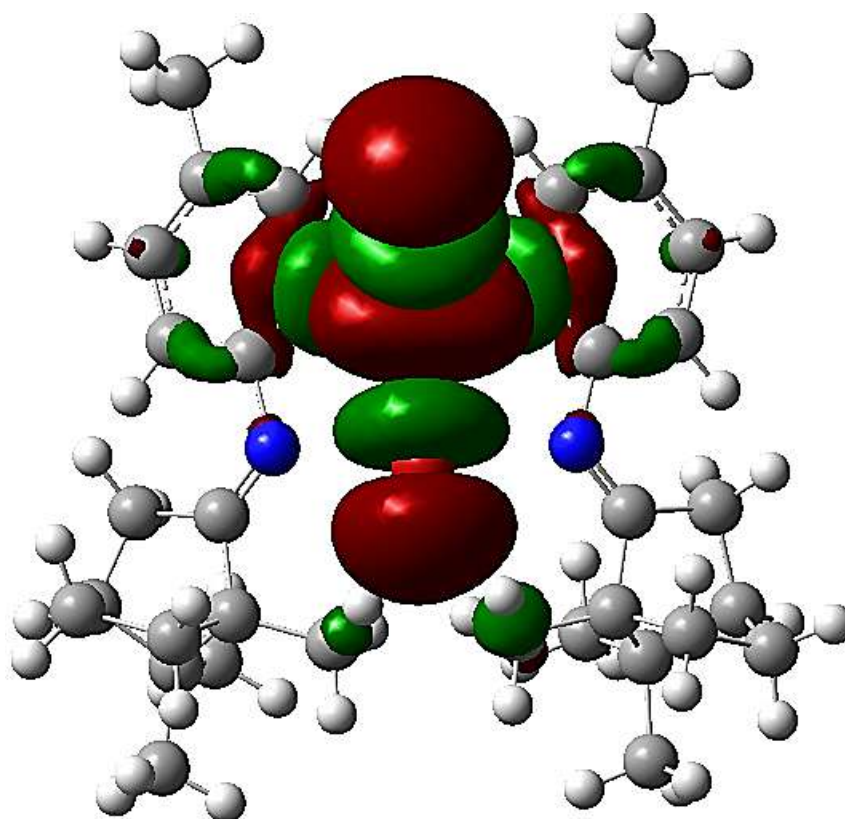


Fig S25. Molecular orbital (HOMO) of compound C

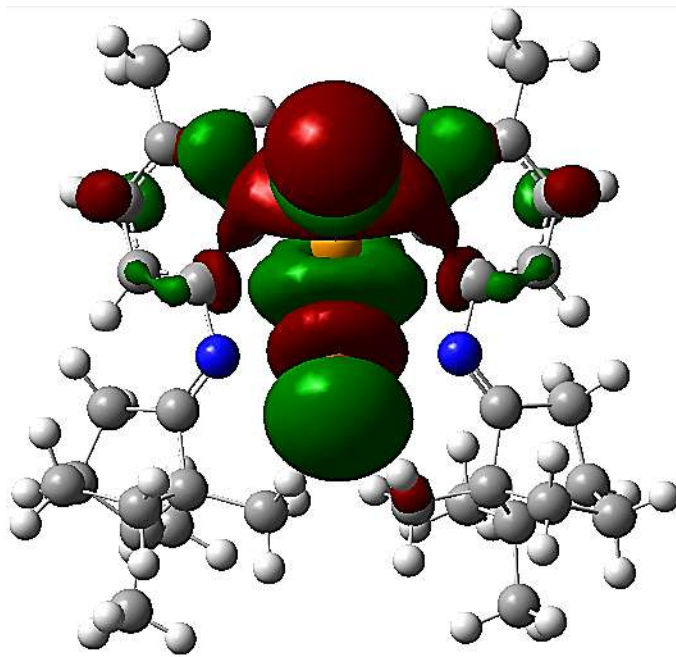


Fig S26. Molecular orbital (LUMO) of compound C

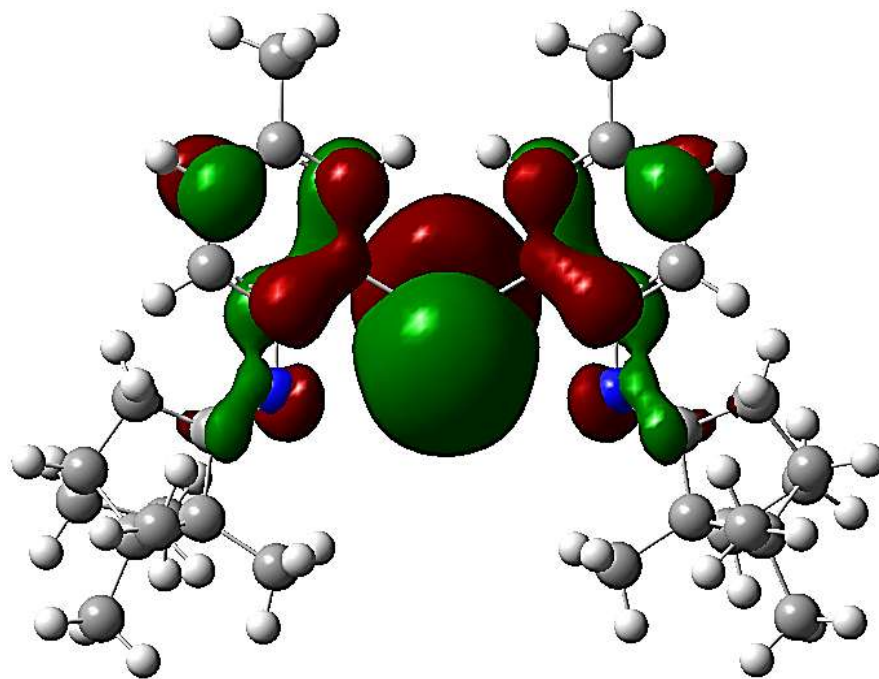


Fig S27. Molecular orbital (HOMO) of compound D

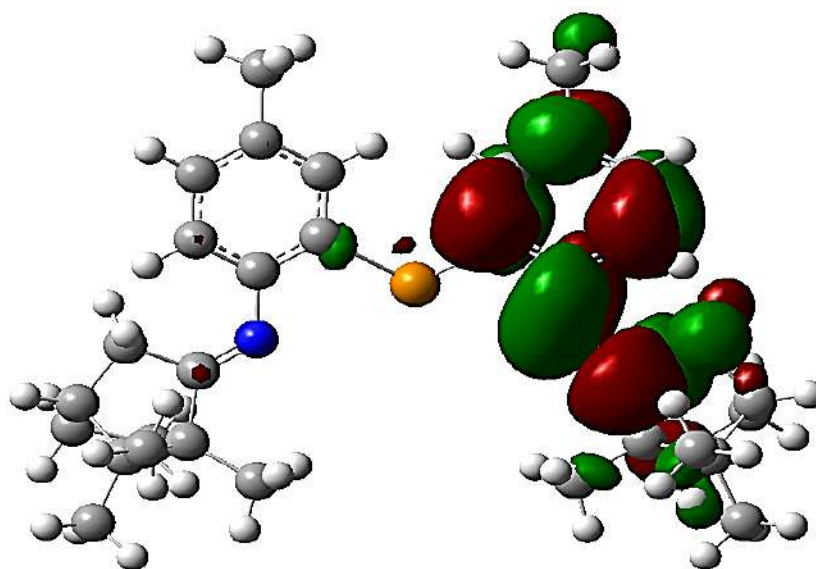


Fig S28. Molecular orbital (LUMO) of compound D

Synthesis, Characterization, and Theoretical Study of Some New Organotellurium Compounds Derived from Camphor

Nuha Hussain Al-Saadawy*

Department of Chemistry, College of Science, University of Thi-Qar, Thi-Qar, Iraq

* Corresponding author:

email: nuh.hussain@sci.utq.ed.iq

Received: October 15, 2021

Accepted: November 26, 2021

DOI: 10.22146/ijc.69805

Abstract: The present work describes the synthesis of a variety of organotellurium compounds. The first part describes the synthesis of a new series of organotellurium compounds containing azomethine groups. Reaction of (E)-(4-((1,7,7-trimethylbicyclo[2.2.1]heptan-2-ylidene)amino)phenyl)mercury(II)chloride and (E)-(5-methyl-2-((1,7,7-trimethylbicyclo[2.2.1]heptan-2-ylidene)amino)phenyl)mercury(II)chloride with tellurium tetrabromide in 2:1 mole ratio yielded the tellurated Schiff bases Ar_2TeBr_2 (where $Ar = 1-(C_9H_{16}C=N)C=N)C_6H_4$ and $1-(C_9H_{16}C=N)C=N)-4-CH_3C_6H_3$) respectively. Reduction of organyl tellurium dibromide Ar_2TeBr_2 by hydrazine hydrate obtained the corresponding tellurides (i.e., Ar_2Te) in good yields. Characterization of the prepared compounds was carried out using infrared spectrum (FT-IR), proton nuclear magnetic resonance spectrum (1H -NMR), and elemental analysis (CHN). The molecular structure of the organotellurium compounds was investigated using the density functional theory with hybrid functional (B3LYP), and the basis set 6-31G Geometrical structure, HOMO surfaces, LUMO surfaces, and energy gap have been produced throughout the geometry optimization. The molecular geometry and contours for the organotellurium compounds were investigated throughout the geometrical optimization. The donor and acceptor properties have been studied by comparing organotellurium compounds' highest occupied molecular orbital energies (HOMO). The present study aims to prepare organotellurium compounds derived from aniline, p-toluidine, and camphor and their derivatives using tellurated Schiff bases.

Keywords: organotellurium; telluride; organyl tellurium dibromide; HOMO and LUMO energies; camphor; density functional theory

■ INTRODUCTION

In recent years, there has been a great deal of interest in synthesizing organotellurium compounds containing amino [1-2], azomethine [3], pyridines, or acetamido group in 2-position of tellurium element [1]. The high stability of such compounds is due to the intramolecular interactions ($N \rightarrow Te$). There are few examples of tellurated derivatives of azobenzenes in the literature, although the first example was prepared in 1979 by trans-metallation of mercurated azobenzenes with tellurium tetrachloride [4-6]. In the last ten years, the field of organic tellurium chemistry has witnessed a vast development, and several review articles and books on the subject have been published [3,7-11]. Organotellurium compounds have

long proved to be valuable intermediate products in organic synthesis, are known to be convenient models for studying fundamental problems of theoretical chemistry, and are essential substances from the practical viewpoint [12-13]. Elemental tellurium provides a source of nucleophilic (chalcogenide and dichalcogenide ions) and electrophilic reagents, which may be generated in situ or prepared just before use [14-15]. Elemental tellurium can be brought into insertion reaction with organometallic compounds to afford the corresponding metal tellurolates, which are then involved in nucleophilic substitution and addition reactions [15]. Organotellurium compounds have been used as precursors for the preparative organic synthesis

and semiconducting metal tellurides. Organotellurium chemistry has become a trending topic [5,7-9,16].

The quantum mechanical wave function contains all the information about the given system [17]. In the case of a simple 2-D square potential or even a hydrogen atom, the Schrodinger equation may be solved to get the system's wave function, following which the allowed energy states of the system can be determined [11]. The simplest definition of density functional theory (DFT) is a technique used to approximate the Schrödinger equation of many-body systems [18]. Computational codes refer to DFT in the Gaussian 09 program. DFT is one of the most common methods of quantum mechanics. DFT exactly describes the rigid structure of the molecules throughout the geometrical optimization procedure. In application, it is used to investigate the structural, electronic, and physical properties of the molecules and materials, such as the binding energies of the molecules in chemistry, physics, and other areas [[19]]. For example, DFT aims to calculate the electronic ground state energy of a system of N electrons only through its density without prior well-known system wave function [11,17,18,20-23].

In the present work, attempts will be made to prepare several new organotellurium compounds containing group ($-C=N$). However, to the best of our knowledge, there is no method to prepare organotellurium compounds derived from camphor, aniline, and *p*-toluidine. Therefore, the current study aims at studying the biological activity of these new compounds.

■ EXPERIMENTAL SECTION

Materials

The chemicals used in this study included camphor, ethanol absolute, *p*-toluidine, glacial acetic acid, mercuric acetate, bromine, chloroform, dioxane, sodium metal, potassium hydroxide, hydrazine hydrate, aniline (Avantor), lithium chloride, tellurium powder, hydrochloric acid (HGB), and molecular sieves (ACS). All the chemicals in this study were used as obtained by the manufacturer with no further purification.

Instrumentation

The $^1\text{H-NMR}$ spectra were recorded on Bruker 500 MHz spectrometers with TMS as an internal reference, utilizing soluble $\text{DMSO-}d_6$. Elemental analysis for carbon, hydrogen, and nitrogen was performed using a Euro vector EA 3000A Elemental Analysis (Italy). Infrared spectra were recorded with KBr circles, utilizing an FTIR spectrophotometer Shimadzu model 8400 S in $4000\text{--}250\text{ cm}^{-1}$. This study begins by optimizing A, B, C, and D compounds using the DFT method, implemented in the Gaussian 09W package with the 6-31G basis set in its ground state. Depending on the first principle of DFT computations, the energy gaps (E_g) and frontier orbital distributions (HOMO and LUMO) are computed for all these systems. DFT using Becke and Lee-Yang-Parr exchange-correlation functional, with the 6-31G mention basis set were applied in the quantum-chemical evaluation.

Procedure

Synthesis of (2E,2'E)-N,N'-((dibromo- λ^4 -tellanediyl)bis(4,1-phenylene))bis(1,7,7-trimethylbicyclo[2.2.1]heptan-2-imine) (A)

Firstly, (5.5 mmol, 2.54 g) of (*E*)-(4-((1,7,7-trimethylbicyclo[2.2.1]heptan-2-ylidene)amino) phenyl) mercury(II) chloride was dissolved in 25 mL of dry dioxane. Then, (2.8 mmol, 1.25 g) of tellurium tetrabromide in 25 mL of dry dioxane was added to the mixture. The mixture was then refluxed for 14 h, the hot solution was filtered, and the filtrate was cooled to room temperature [1-2,11]. The filtrate was poured into 250 mL of cold distilled water to form reddish-brown crystals. Following recrystallization by ethanol, brown crystals were formed, yielding 63% and melting point $103\text{--}105\text{ }^\circ\text{C}$.

C.H.N.: theoretical % (practical %): C, 51.93 (51.64); H, 5.45 (5.33); N, 3.79 (3.47); FT-IR using KBr: $\nu(\text{C-H})$ Aliphatic = 3100 cm^{-1} , $\nu(\text{C-H})$ Aromatic = 3194 cm^{-1} , $\nu(\text{C=N})$ Aliphatic = 1679 cm^{-1} , $\nu(\text{C-N})$ Aromatic = 1325 cm^{-1} , $\nu(\text{C=C})$ Aromatic = 1404 cm^{-1} .

$^1\text{H-NMR}$ (500 MHz, $\text{DMSO-}d_6$) δ 6.97 (s, 6H), 6.81 (d, $J = 7.9\text{ Hz}$, 4H), 6.78–6.72 (m, 8H), 6.55 (d, $J = 8.0\text{ Hz}$, 6H), 6.51 (s, 1H), 6.47 (d, $J = 8.0\text{ Hz}$, 3H), 3.75 (dd,

$J = 10.6, 3.6$ Hz, 8H), 2.74 (dd, $J = 16.0, 10.6$ Hz, 8H), 2.47 (d, $J = 3.6$ Hz, 6H), 2.11 (d, $J = 12.8$ Hz, 24H), 2.07 (s, 7H). These data were shown in Scheme 1, Table 1 and 2, Fig. S1, S2 and S9.

Synthesis of (2E,2'E)-N,N'-((tellurobis(4,1-phenylene))bis(1,7,7-trimethylbicyclo[2.2.1]heptan-2-imine) (B)

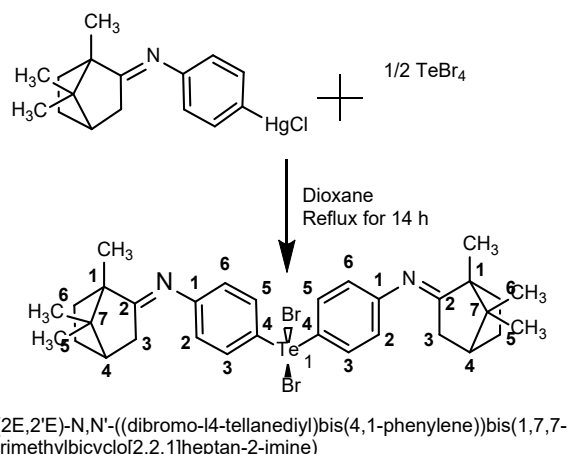
(2E,2'E)-N,N'-((dibromo- λ^4 -tellanediy)bis(4,1-phenylene))bis(1,7,7-trimethylbicyclo[2.2.1]heptan-2-imine) (5 mmol, 3.7 g) was dissolved in 25 mL of ethanol. The solution was then refluxed for 2 h, and the mixture was cooled to room temperature. To the mixture, hydrazine hydrate (5 mmol, 0.16 g) in 25 mL of ethanol was added dropwise and heated in the water bath to 70 °C. The resulting solution was evaporated using a rotary evaporator [1-2,11]. The brown solid that had formed was recrystallized by using chloroform to give brown crystals, with a yield of 55%, and melting point 88–90 °C.

C.H.N: theoretical % (practical %): C, 66.23 (66.45); H, 6.95 (6.83); N, 4.83 (4.11); FT-IR using KBr: $\nu(\text{C-H})$ Aliphatic = 2920 cm^{-1} , $\nu(\text{C-H})$ Aromatic = 3103 cm^{-1} , $\nu(\text{C=N})$ Aliphatic = 1616 cm^{-1} , $\nu(\text{C-N})$ Aromatic = 1333 cm^{-1} , $\nu(\text{C=C})$ Aromatic = 1419 cm^{-1} .

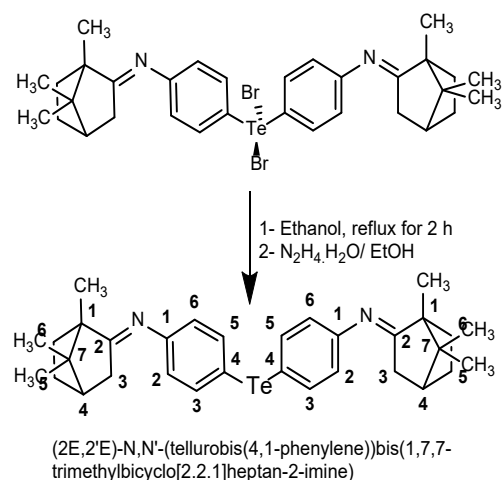
$^1\text{H-NMR}$ (500 MHz, DMSO- d_6) δ 6.97 (s, 6H), 6.81 (d, $J = 7.9$ Hz, 4H), 6.78–6.72 (m, 8H), 6.55 (d, $J = 8.0$ Hz, 6H), 6.51 (s, 1H), 6.47 (d, $J = 8.0$ Hz, 3H), 3.75 (dd, $J = 10.6, 3.6$ Hz, 8H), 2.74 (dd, $J = 16.0, 10.6$ Hz, 8H), 2.47 (d, $J = 3.6$ Hz, 6H), 2.11 (d, $J = 12.8$ Hz, 24H), 2.07 (s, 7H). These data were shown in Scheme 2, Table 1 and 2, Fig. S3, S4, and S10.

Synthesis of (E)-N-(2-(dibromo(5-methyl-2-((E)-1,7,7-trimethylbicyclo[2.2.1]heptan-2-ylidene)amino)phenyl)- λ^4 -tellaneyl)-4-methylphenyl)-1,7,7-trimethylbicyclo[3.1.1]heptan-6-imine (C)

(E)-(5-methyl-2-((1,7,7-trimethylbicyclo[2.2.1]heptan-2-ylidene)amino)phenyl)mercury(II) chloride (5.5 mmol, 2.62 g) was dissolved in 25 mL of dry dioxane. To the solution, (2.8 mmol, 1.25 g) of tellurium tetrabromide in 25 mL of dry dioxane was added and then refluxed for 14 h. Next, the hot solution was filtered, and the filtrate was cooled to room temperature [1-2,11]. The filtrate was poured into 250 mL of cold distilled water to form brown crystals, recrystallization by ethanol to give



Scheme 1. Preparation of diorganyl tellurium dibromide of aniline and camphor derivative

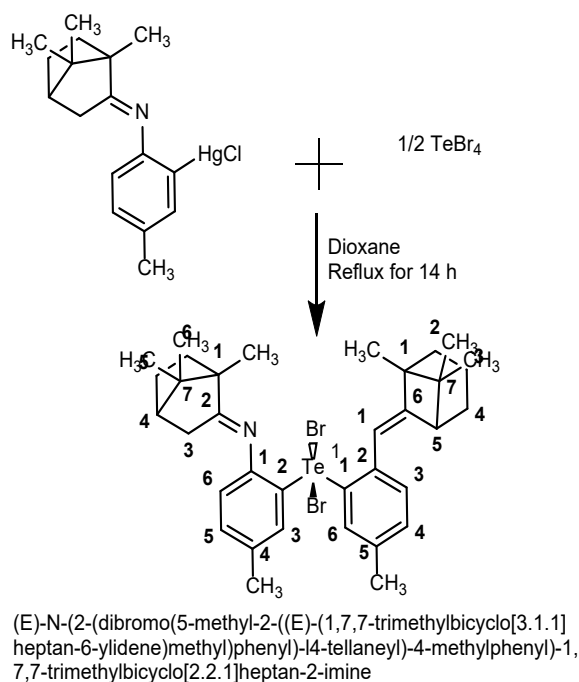


Scheme 2. Preparation of diorganyl telluride of aniline and camphor derivative

brown crystals, with a yield of 65%, and melting point 123–125 °C.

C.H.N: theoretical % (practical %): C, 53.16 (52.95); H, 5.77 (5.45); N, 3.79 (3.47); FT-IR using KBr: $\nu(\text{C-H})$ Aliphatic = 2951 cm^{-1} , $\nu(\text{C-H})$ Aromatic = 2999 cm^{-1} , $\nu(\text{C=N})$ Aliphatic = 1694 cm^{-1} , $\nu(\text{C-N})$ Aromatic = 1396 cm^{-1} , $\nu(\text{C=C})$ Aromatic = 1487 cm^{-1} .

$^1\text{H-NMR}$ (500 MHz, DMSO- d_6) δ 7.93 (d, $J = 7.8$ Hz, 8H), 7.89 (s, 1H), 7.78 (dt, $J = 26.1, 7.7$ Hz, 7H), 7.64 (t, $J = 7.6$ Hz, 10H), 7.60–7.44 (m, 3H), 7.02 (dd, $J = 24.2, 8.0$ Hz, 2H), 6.67 (d, $J = 8.0$ Hz, 1H), 2.16 (s, 1H). These data were shown in Scheme 3, Table 1 and 2, Fig. S5, S6, and S11.



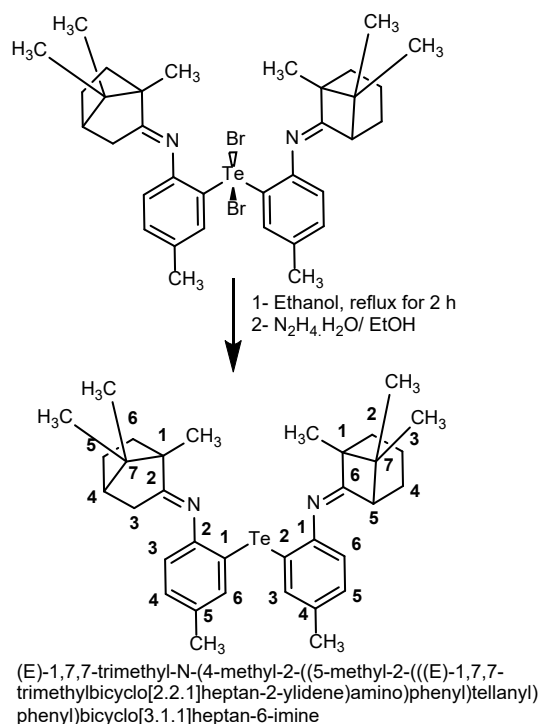
Scheme 3. Preparation of diorganyl tellurium dibromide of *p*-toluidine and a camphor derivative

Synthesis of (E)-1,7,7-trimethyl-N-(4-methyl-2-((5-methyl-2-(((E)-1,7,7-trimethylbicyclo[2.2.1]heptan-2-ylidene)amino)phenyl)tellanyl)phenyl)bicyclo[3.1.1]heptan-6-imine (D)

(E)-N-(2-(dibromo(5-methyl-2-((E)-(1,7,7-trimethylbicyclo[3.1.1]heptan-6-ylidene)methyl)phenyl)-4-tellanyl)-4-methylphenyl)-1,7,7-trimethylbicyclo[2.2.1]heptan-2-imine (5 mmol., 3.8 g) was dissolved in 25 mL of ethanol. Then, the solution was refluxed for 2 h, and the mixture was cooled to room temperature. To the mixture, hydrazine hydrate (5 mmol., 0.16 g) in 25 mL of ethanol was added dropwise and heated in a water bath to 70 °C. The resulting solution was evaporated using a rotary evaporator. The brown solid that had formed was recrystallized by using chloroform to give brown crystals [1,2,11], with a yield of 51%, melting point of 95–97 °C.

C.H.N: theoretical % (practical %): C, 67.13 (66.98); H, 7.29 (7.13); N, 4.60 (4.83); FT-IR using KBr: $\nu(\text{C-H})$ Aliphatic = 2951 cm^{-1} , $\nu(\text{C-H})$ Aromatic = 2998 cm^{-1} , $\nu(\text{C=N})$ Aliphatic = 1692 cm^{-1} , $\nu(\text{C-N})$ Aromatic = 1394 cm^{-1} , $\nu(\text{C=C})$ Aromatic = 1487 cm^{-1} .

$^1\text{H-NMR}$ (500 MHz, $\text{DMSO-}d_6$) δ 7.93 (d, $J = 7.7$ Hz, 1H), 7.78 (td, $J = 16.0, 15.5, 7.6$ Hz, 3H), 7.55 (ddt, $J = 54.8,$



Scheme 4. Preparation of diorganyl telluride of *p*-toluidine and a camphor derivative

22.5, 7.6 Hz, 5H), 6.99 (d, $J = 7.9$ Hz, 1H), 6.76 (d, $J = 7.9$ Hz, 1H), 2.15 (s, 2H). These data were shown in Scheme 4, Table 1 and 2, Fig. S7, S8, and S12.

RESULTS AND DISCUSSION

The present work included the preparation of organotellurium compounds such as Ar_2TeBr_2 and Ar_2Te (where $\text{Ar} = 1-(\text{C}_9\text{H}_{16}\text{C}=\text{N})\text{C}=\text{N})\text{C}_6\text{H}_4$ and $1-(\text{C}_9\text{H}_{16}\text{C}=\text{N})\text{C}=\text{N})-4-\text{CH}_3\text{C}_6\text{H}_3$, respectively) by tellurated Schiff base derived of camphor, aniline, and *p*-toluidine.

$^1\text{H-NMR}$ spectra of compounds (A–D) showed all the expected peaks. All spectrum [16,24–28] in $\text{DMSO-}d_6$ are given in Table 1 and explained in Fig. S1–S8.

IR spectra of the compounds under study displayed standard features in specific regions and characteristic bands in the other areas [24–29] (explained in Table 2). In all the compounds under study, the aromatic (C–H) bond appeared at the range (2998–3194 cm^{-1}) [24–29], whereas the aliphatic (C–H) bond appeared at the range of (2920–3100 cm^{-1}). The clear band at the range of (1616–1696 cm^{-1}) was attributed to the aliphatic bond (C=N) [24–29]. On the

Table 1. ¹H-NMR spectral data of selected compounds

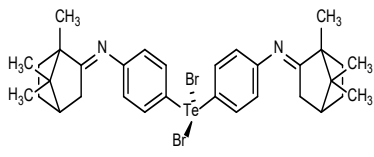
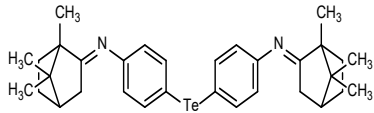
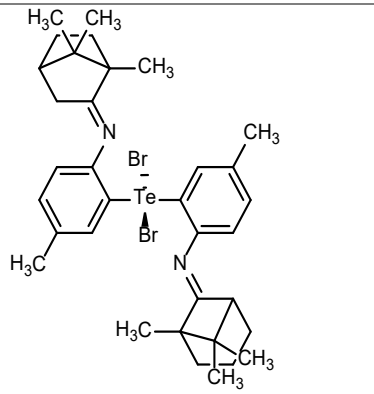
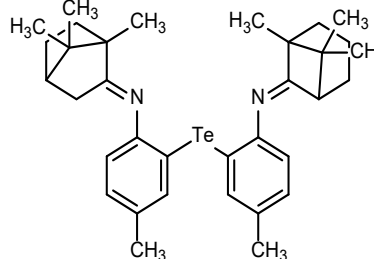
Structure for compound	¹ H-NMR (DMSO- <i>d</i> ₆); TMS = 0 ppm
<p>A</p> 	6.97 (s, 6H), 6.81 (d, <i>J</i> = 7.9 Hz, 4H), 6.78–6.72 (m, 8H), 6.55 (d, <i>J</i> = 8.0 Hz, 6H), 6.51 (s, 1H), 6.47 (d, <i>J</i> = 8.0 Hz, 3H), 3.75 (dd, <i>J</i> = 10.6, 3.6 Hz, 8H), 2.74 (dd, <i>J</i> = 16.0, 10.6 Hz, 8H), 2.47 (d, <i>J</i> = 3.6 Hz, 6H), 2.11 (d, <i>J</i> = 12.8 Hz, 24H), 2.07 (s, 7H)
<p>B</p> 	6.97 (s, 6H), 6.81 (d, <i>J</i> = 7.9 Hz, 4H), 6.78–6.72 (m, 8H), 6.55 (d, <i>J</i> = 8.0 Hz, 6H), 6.51 (s, 1H), 6.47 (d, <i>J</i> = 8.0 Hz, 3H), 3.75 (dd, <i>J</i> = 10.6, 3.6 Hz, 8H), 2.74 (dd, <i>J</i> = 16.0, 10.6 Hz, 8H), 2.47 (d, <i>J</i> = 3.6 Hz, 6H), 2.11 (d, <i>J</i> = 12.8 Hz, 24H), 2.07 (s, 7H)
<p>C</p> 	7.93 (d, <i>J</i> = 7.8 Hz, 8H), 7.89 (s, 1H), 7.78 (dt, <i>J</i> = 26.1, 7.7 Hz, 7H), 7.64 (t, <i>J</i> = 7.6 Hz, 10H), 7.60–7.44 (m, 3H), 7.02 (dd, <i>J</i> = 24.2, 8.0 Hz, 2H), 6.67 (d, <i>J</i> = 8.0 Hz, 1H), 2.16 (s, 1H)
<p>D</p> 	7.93 (d, <i>J</i> = 7.7 Hz, 1H), 7.78 (td, <i>J</i> = 16.0, 15.5, 7.6 Hz, 3H), 7.55 (ddt, <i>J</i> = 54.8, 22.5, 7.6 Hz, 5H), 6.99 (d, <i>J</i> = 7.9 Hz, 1H), 6.76 (d, <i>J</i> = 7.9 Hz, 1H), 2.15 (s, 2H)

Table 2. FT-IR spectral data of selected compounds

Compound	Aromatic	Aliphatic	Aliphatic	Aromatic	Aromatic
	C–H	C–H	C=N	C–N	C=C
A	3194	3100	1679	1325	1404
B	3103	2920	1616	1333	1419
C	2999	2951	1694	1396	1487
D	2998	2951	1692	1394	1487

other hand, the band at the range of 1325–1396 cm⁻¹ was attributed to the aromatic (C–N) bond for all the prepared compounds. The aromatic (C=C) bond appeared at the range of (1404–1487 cm⁻¹) [24–29], as shown in Table 2 and Fig. S9–S12.

Computational Study

The molecular structure for the organotellurium compounds was investigated using optimization plus frequency at the ground state level. In addition, density functional theory has been applied to optimize the

organotellurium compounds with Gaussian 09 software program [17,29-30] (see Fig. S13–S28).

HOMO (Highest Occupied Molecular Orbital) and LUMO (Lowest Unoccupied Molecular Orbital) energies are the electronic states, referring to certain places of the existence of the electrons with quantized energies, where the molecular orbitals are in linear combination to the atomic orbitals [17,30-31] (see Fig. S21–S28). The difference between HOMO provides the energy bandgap (E_g). The energy gap is a crucial property in solids as it allows the prediction of the material (whether it is a conductor, insulator, or semiconductor). Furthermore, it represents the energy difference between the lower virtual energy and the higher total energy levels [32-34] (see Fig. S21–S28 and Table 3).

$$E_g = E_{\text{LUMO}} - E_{\text{HOMO}} \quad (1)$$

In the present work, a comparison between the HOMO and LUMO energies is explained in Table 3. to find out that HOMO energy of organyl tellurium dibromide A and C compound where is C a greater than D compound, as, for diorganyl telluride B and D, D is higher than C compound [32-34]. as follows:

$$D > B > A > C$$

Therefore, the highest energy gap was observed by compound D, while the lowest value was observed by compound C (see Table 3 and Fig. S21–S28).

Electronegativity and electrophilicity

Electronegativity and electrophilicity can be calculated from [30,32-36] the relations 2 and 3 (see Table 4).

$$x = \frac{E_{\text{HOMO}} + E_{\text{LUMO}}}{2} \quad (2)$$

$$w = \frac{x^2}{2\eta} \quad (3)$$

In Table 4, the electronegativity of D was higher than the electronegativity of C and A. On the other hand, the electronegativity of compound B was the lowest.

$$D > C > A > B$$

Among the prepared compounds, compound B had the greatest electrophilicity, whereas compound D had the least.

$$B > A > C > D$$

Ionization potential and electron affinity

According to Koopman's theory, the following relations, 4 and 5 [29-30,37], can express the ionization potential and electron affinity, as shown in Table 5.

$$\text{I.P} = -E_{\text{HOMO}} \quad (4)$$

$$\text{E.A} = -E_{\text{LUMO}} \quad (5)$$

Table 5 demonstrates the ionization potential, and electron affinity values in (eV) for compounds A, B, C, and D. According to Koopman's theorem, the ionization potential, and electron affinity results depend on the energies in the valence band and the conduction band. The table demonstrates the arrangement of the prepared compounds according to the increase in their ionization potential [29,37]:

$$B > D > A > C$$

Hardness softness acid base (HSAB Principle)

The following equations 6 and 7 can express the hardness and softness [18,29,35,38]:

Table 3. The electronic states of the organotellurium compounds

Compound	HOMO (eV)	LUMO (eV)	E_g (eV)
A	-3.795	-1.950	1.845
B	-7.438	-5.519	1.910
C	-3.565	-1.820	1.740
D	-4.549	-0.639	3.910

Table 4. Electronegativity and electrophilicity of the organotellurium compounds

Compound	Electronegativity (eV) (X)	Electrophilicity (eV) (w)
A	-2.87	4.44
B	-6.47	21.76
C	-2.69	4.12
D	-2.58	1.66

Table 5. Ionization potential and electron affinity of the organotellurium compounds

Compound	Ionization potential (eV) (I.P)	Electron affinity (eV) (E.A)
A	3.79	1.95
B	7.43	5.52
C	3.56	1.82
D	4.55	0.64

Table 6. Chemical hardness and chemical softness of the organotellurium compounds

Compound	Chemical hardness (η)	Chemical softness (σ)
A	0.92	0.54
B	0.95	0.52
C	0.87	0.57
D	1.96	0.25

$$\eta = \frac{I.P - E.A}{2} \quad (6)$$

$$\sigma = \frac{1}{2\eta} \quad (7)$$

η refers to chemical hardness, and σ refers to chemical softness (see Table 6).

The comparison between A, B, C, and D shows that compound D was harder than compounds B, C, and A, respectively, indicating that compound D will behave as a hard base [29,35,38].

$D > B > C > A$

On the other hand, compound D was softer than compounds A, B, and C, indicating that compound C will behave as a soft base. Therefore, according to Table 6, the behavior of organotellurium compounds can be classified as donors or acceptors.

$C > A > B > D$

■ CONCLUSION

In the present study, compounds A, B, C, and D were obtained in a 51–65% yield. All the prepared compounds were characterized by the CHN elemental analysis, FTIR, and ¹H-NMR. Findings from this study were in concordance with previous research findings, confirming the correctness of the proposed structures for all the prepared compounds. Additionally, it is evident that the density functional theory used in this study was a powerful method, and B3LYP functional is a suitable and efficient function for studying the electronic properties of these structures.

■ REFERENCES

- [1] Al-Rubaie, A.Z., Al-Salim, N.I., and Al-Jadaan, S.A.N., 1993, Synthesis and characterization of new organotellurium compounds containing an *ortho*-amino group, *J. Organomet. Chem.*, 443 (1), 67–70.
- [2] Al-Rubaie, A.Z., Al-Masoudi, W.A., Al-Jadaan, S.A.N., Jalbout, A.F., and Hameed, A.J., 2008, Synthesis, characterization, and computational study of some new organotellurium compounds containing azomethine groups, *Heteroat. Chem.*, 19 (3), 307–315.
- [3] Yamago, S., 2021, Practical synthesis of dendritic hyperbranched polymers by reversible deactivation radical polymerization, *Polym. J.*, 53 (8), 847–864.
- [4] Al-Saadawy, N.H., 2021, Synthesis, characterization and theoretical studies of new organotellurium compounds based on (4-(((1S,E)-1,7,7-trimethyl bicyclo[2.2.1]heptan-2-ylidene)amino)phenyl) mercury(II) chloride, *Indones. J. Chem.*, 21 (6), 1443–1453.
- [5] Yousif, T.Y., 2020, Preparation of some new organotellurium compounds derived from 4,4-dihydroxy azobenzene, *Coll. Basic Educ. Res. J.*, 16 (3), 892–898.
- [6] Carrera Boutzis, E.I., 2017, Synthesis, Reactivity, and Photochemistry of π -Conjugated Tellurophenes, *Dissertation*, Department of Chemistry, University of Toronto, Canada.
- [7] Aziz, F.K., Gazar, S.H., and Al-Saadawy, N.H., 2020, Simple, selective, and sensitive spectrophotometric method for determination of trace amounts of lead(II), cadmium(II), cobalt(II) with organomercury compounds, *J. Global Pharma Technol.*, 12, 248–255.
- [8] Al-Asadi, R.H., 2020, Synthesis and molecular structure study of new organotellurium and organomercury compounds based on 4-bromonaphthalen-1-amine, *Russ. J. Gen. Chem.*, 90 (9), 1744–1749.
- [9] Ahmed, W.M., Al-Saadawy, N.H., and Abowd, M.I., 2021, Synthesis and characterization of a new organoselenium and organotellurium compounds depending on 9-chloro-10-nitro-9,10-dihydroanthracene, *Ann. Romanian Soc. Cell Biol.*, 25 (4), 11035–11043.

- [10] Kadhim, M.A., and Al-Saadawy, N.H., 2021, Synthesis and characterization for some new organoselenium compounds depending on 8-hydroxyquinoline, *Ann. Romanian Soc. Cell Biol.*, 25 (2), 2162–2172.
- [11] Al-Saadawy, N.H., 2022, New organotellurium compounds based on camphor, aniline and *p*-toluidine: Preparation, characterization and theoretical study, *Egypt. J. Chem.*, 65 (2), 19–27.
- [12] Pop, A., Silvestru, C., and Silvestru, A., 2019, Organoselenium and organotellurium compounds containing chalcogen-oxygen bonds in organic synthesis or related processes, *Phys. Sci. Rev.*, 4 (5), 20180061.
- [13] Pop, A., Silvestru, C., and Silvestru, A., 2019, "3. Organoselenium and Organotellurium Compounds Containing Chalcogen-Oxygen Bonds in Organic Synthesis or Related Processes" in *Selenium and Tellurium Reagents*, Eds. Laitinen, R., and Oilunkaniemi, R., De Gruyter, Boston, 61–122.
- [14] Tanini, D., and Capperucci, A., 2020, Unexpected ethyltellurenylation of epoxides with elemental tellurium under lithium triethylborohydride conditions, *Chemistry*, 2 (3), 652–661.
- [15] Tanini, D., and Capperucci, A., 2019, Ring-opening reactions of heterocycles with selenium and tellurium nucleophiles, *New J. Chem.*, 43 (29), 11451–11468.
- [16] Irfan, M., Rehman, R., Razali, M.R., Ur Rehman, S., Ur Rehman, A., and Iqbal, M.A., 2020, Organotellurium compounds: An overview of synthetic methodologies, *Rev. Inorg. Chem.*, 40 (4), 193–232.
- [17] Al-Asadi, R.H., 2019, Synthesis, DFT calculation and biological activity of some organotellurium compounds containing azomethine group, *Orbital: Electron. J. Chem.*, 11 (7), 402–410.
- [18] Panda, A., and Behera, R.N., 2014, Comparative study of E...N (E=Se/Te) intramolecular interactions in organochalcogen compounds using density functional theory, *J. Hazard. Mater.*, 269, 2–8.
- [19] Diki, N.Y.S., Coulibaly, N.H., Kambiré, O., and Trokourey, A., 2021, Experimental and theoretical investigations on copper corrosion inhibition by cefixime drug in 1 M HNO₃ solution, *J. Mater. Sci. Chem. Eng.*, 9, 11–28.
- [20] Zhang, Z., Hu, M., Zhang, W., and Zhang, X., 2022, Construction of tellurium-doped mesoporous bioactive glass nanoparticles for bone cancer therapy by promoting ROS-mediated apoptosis and antibacterial activity, *J. Colloid Interface Sci.*, 610, 719–730.
- [21] Arora, A., Oswal, P., Rao, G.K., Kumar, S., Singh, A.K., and Kumar, A., 2021, Tellurium-ligated Pd(II) complex of bulky organotellurium ligand as a catalyst of Suzuki coupling: First report on in situ generation of bimetallic alloy 'telluropalladinite' (Pd₉Te₄) nanoparticles and role in highly efficient catalysis, *Catal. Lett.*, 1–13.
- [22] Behera, R.N., and Panda, A., 2012, Nature of the Te...N intramolecular interaction in organotellurium compounds. A theoretical investigation by NBO and AIM methods, *Comput. Theor. Chem.*, 999, 215–224.
- [23] Kerbadou, R.M., Hadjadj Aoul, R., Benmaati, A., Taleb, A., Hacini, S., and Habib Zahmani, H., 2021, Identification of new biologically active synthetic molecules: Comparative experimental and theoretical studies on the structure-antioxidant activity relationship of cyclic 1,3-ketoamides, *J. Mol. Model.*, 27 (4), 109.
- [24] Silverstein, R.M., and Bassler, G.C., 1962, Spectrometric identification of organic compounds, *J. Chem. Educ.*, 39 (11), 546.
- [25] Bennett, A.J., Duke, C.B., and Silverstein, S.D., 1968, Theory of the tunneling spectroscopy of collective excitations, *Phys. Rev.*, 176 (3), 969.
- [26] Guthrie, R.D., 1978, Introduction to Spectroscopy (Pavia, Donald; Lampman, Gary M.; Kriz, George S., Jr.), *J. Chem. Educ.*, 56 (10), A323.
- [27] Scheinmann, F., 2013, An Introduction to Spectroscopic Methods for the Identification of Organic Compounds: Mass Spectrometry, Ultraviolet Spectroscopy, Electron Spin Resonance Spectroscopy, Nuclear Magnetic Resonance Spectroscopy (Recent Developments), Use of

- Various Spectral Methods Together, and Documentation of Molecular Spectra, Elsevier Science, Amsterdam, Netherlands.
- [28] Pavia, D.L., Lampman, G.M., Kriz, G.S., and Vyvyan, J.A., 2014, Introduction to Spectroscopy, Cengage Learning, Boston, US.
- [29] Oliveira, G.P., Barboza, B.H., and Batagin-Neto A., 2022, Polyaniline-based gas sensors: DFT study on the effect of side groups, *Comput. Theor. Chem.*, 1207, 113526.
- [30] Gusakova, J., Wang, X., Shiao, L.L., Krivosheeva, A., Shaposhnikov, V., Borisenko, V., Gusakov, V., and Tay, B.K., 2017, Electronic properties of bulk and monolayer TMDs: Theoretical study within DFT framework (GVJ-2e method), *Phys. Status Solidi A*, 214 (12), 1700218.
- [31] Fernandes, G.F.S., Pontes, M.A.P., Machado, F.B.C., and Ferrão, L.F.A., 2022, Electronic structure and stability of transition metal acetylacetonates $\text{TM}(\text{AcAc})_n$ (TM = Cr, Fe, Co, Ni, Cu; n = 1, 2, 3), *Comput. Theor. Chem.*, 1207, 113502.
- [32] Xavier, R.J., and Gobinath, E., 2012, FT-IR, FT-Raman, *ab initio* and DFT studies, HOMO-LUMO and NBO analysis of 3-amino-5-mercapto-1,2,4-triazole, *Spectrochim. Acta, Part A*, 86, 242–251.
- [33] Arivazhagan, M., Manivel, S., Jeyavijayan, S., and Meenakshi, R., 2015, Vibrational spectroscopic (FTIR and FT-Raman), first-order hyperpolarizability, HOMO, LUMO, NBO, Mulliken charge analyses of 2-ethylimidazole based on Hartree-Fock and DFT calculations, *Spectrochim. Acta, Part A*, 134, 493–501.
- [34] Sheela, N.R., Muthu, S., and Sampathkrishnan, S., 2014, Molecular orbital studies (hardness, chemical potential, and electrophilicity), vibrational investigation and theoretical NBO analysis of 4-4'-(1H-1,2,4-triazol-1-yl methylene) dibenzonitrile based on *ab initio* and DFT methods, *Spectrochim. Acta, Part A*, 120, 237–251.
- [35] Vennila, P., Govindaraju, M., Venkatesh, G., and Kamal, C., 2016, Molecular structure, vibrational spectral assignments (FT-IR and FT-RAMAN), NMR, NBO, HOMO-LUMO and NLO properties of O-methoxybenzaldehyde based on DFT calculations, *J. Mol. Struct.*, 1111, 151–156.
- [36] Muya, J.T., Donald, K.J., Ceulemans, A., and Parish, C., 2021, A comparison of the chemical bonding and reactivity of $\text{Si}_8\text{H}_8\text{O}_{12}$ and $\text{Ge}_8\text{H}_8\text{O}_{12}$: A theoretical study, *J. Chem. Phys.*, 154, 164305.
- [37] Vikramaditya, T., and Lin, S.T., 2017, Assessing the role of Hartree-Fock exchange, correlation energy and long-range corrections in evaluating ionization potential, and electron affinity in density functional theory, *J. Comput. Chem.*, 38 (21), 1844–1852.
- [38] Xu, H., Xu, D.C., and Wang, Y., 2017, Natural indices for the chemical hardness/softness of metal cations and ligands, *ACS Omega*, 2 (10), 7185–7193.

Synthesis of the Novel Nanocatalyst of Pt₃Mo Nanoalloys on Ti_{0.8}W_{0.2}O₂ via Hydrothermal and Microwave-Assisted Polyol Process

Anh Tram Ngoc Mai¹, Nguyen Khanh Pham¹, Kim Ngan Thi Tran², and Van Thi Thanh Ho^{3*}

¹Ho Chi Minh City University of Technology, Vietnam National University-Ho Chi Minh City, Ho Chi Minh City 700000, Vietnam

²Institute of Environmental Technology and Sustainable Development, Nguyen Tat Thanh University, Ho Chi Minh City 700000, Vietnam

³Ho Chi Minh City University of Natural Resources and Environment (HCMUNRE), Ho Chi Minh City 700000, Vietnam

* **Corresponding author:**

tel: +84-913603994

email: httvan@hcmunre.edu.vn

Received: October 23, 2021

Accepted: January 11, 2022

DOI: 10.22146/ijc.69928

Abstract: Direct methanol fuel cell (DMFC) attracts much attention due to its high abundance, environmental friendliness, and convenient transportation and storage. In this study, a novel catalyst of Pt₃Mo alloy nanoparticles (NPs) on non-carbon Ti_{0.8}W_{0.2}O₂ support was synthesized by microwave-assisted polyol process. The characteristic of Pt₃Mo NPS/Ti_{0.8}W_{0.2}O₂ catalyst was determined by X-ray diffraction (XRD), transmission electron microscopy (TEM), scanning electronic microscopy (SEM), energy-dispersive X-ray (EDX), and Brunauer-Emmett-Teller (BET) method. Pt₃Mo NPs had an average diameter of approximate 5.18 nm and were uniformly anchored on Ti_{0.8}W_{0.2}O₂ surface. The ratio of Mo in the Pt₃Mo alloy was consistent with the theoretical value, which supported the effectiveness of the synthesis method. In addition, Pt₃Mo/Ti_{0.8}W_{0.2}O₂ electrocatalysts exhibited higher CO-like tolerance in methanol oxidation reaction (MOR) than commercial electrocatalysts, excellent catalytic activity, and strong durability after 2000 cycles. The synergistic effect of Pt-Mo alloy, and the strong interaction between the bimetallic Pt-Mo alloy and the mesoporous Ti_{0.8}W_{0.2}O₂ support, could weaken the Pt-CO bond. Besides, the high corrosion resistance and superior electrochemical durability of TiO₂-based oxide also contribute to the excellent stability of Pt₃Mo/Ti_{0.8}W_{0.2}O₂ electrocatalyst in harsh electrochemical media. These results revealed that this material could be a potential catalyst in DMFC technology.

Keywords: bimetallic metal; Pt-Mo alloy; W-doped TiO₂; microwave-assisted polyol process; hydrothermal

■ INTRODUCTION

Using fossil fuels (oil, coal, etc.) for energy has caused severe effects on humanity and the environment, from air and water pollution to global warming. To reduce greenhouse gas emissions and economic dependence on petroleum, replacing fossil fuels with alternative energy resources is intensively studied worldwide. Fuel cell technology operating as energy conversion devices could be the answer to the world's pressing demand for clean and efficient power since it offers extremely low or even zero emissions of health-damaging pollutants [1-3]. Direct methanol fuel cell

technology exhibits a high energy density of liquid methanol used as an abundant fuel source, easy storage, relatively straightforward system design, and convenient operation. Therefore, it is a potential power source for automotive, portable power generating, and electronics industry applications [4]. Nevertheless, the greatest challenges which limit commercialization of fuel cells are that the systems involve high intrinsic costs and poor durability of catalysts, usually noble Pt-based materials. Literately, many previous studies have pointed out several factors reducing the lifetime of these electrocatalysts, such as carbon-support corrosion, Pt detachment, and agglomeration, and Pt poisoning

caused by carbon-containing intermediates (such as $-\text{CO}_{\text{ads}}$) [5-7].

It is generally recognized that alloying Pt with noble metals like Pd, Au, Ru, or less expensive 3d-transition metals, such as Mo, Ni, Co, Cu, is one feasible strategy for Pt-load reduction and activity enhancement in fuel cells, including DMFCs [8-10]. Among Pt-M alloys, the state-of-the-art Pt-Ru is found to be the most active and commonly used binary alloy catalyst and in MOR at the anode of DMFCs [4,11]. However, Pt-Ru alloy is severely subjected to Ru dissolution and migration, called "Ru crossover". It leads to poor performance by inhibiting or contaminating the oxygen reduction kinetics at the cathode and the potential stability of the cathode against the parasitic MOR [12-14]. For further investigation, some studies have focused on alloying platinum with molybdenum, which is inexpensive, widely available, and has outstanding potential as a promoter for enhancing Pt activity in the MOR [15]. It is reported that the PtMo/C catalyst exhibited a three-time better enhancement in CO tolerance as compared to Pt₅₀Ru₅₀/C and a greater than four-fold enhancement relative to Pt/C [16]. Another study indicated that Mo in Pt₃Mo alloy induced ligand effect on neighboring Pt atoms leads to weaker CO adsorption on Pt as compared to Ru in Pt₃Ru alloy [17]. Nevertheless, various synthesis methods of Pt-Mo alloy NPs have been surveyed, including arc melting of pure elements, wet impregnation, electrochemical deposition, that are subject to intrinsic drawbacks, such as (i) complicated multistep processes involving capping/surfactant agents, (ii) strict conditions required for alloying; and (iii) heat treatment at the high temperature employed afterward to archive true Pt-Mo alloy form [18-20]. These challenges are mainly due to the large negative redox potential of the Moⁿ⁺/Mo⁰ couple and the low miscibility of Pt and Mo [21-22].

With the purpose to solve mentioned issues, a novel Pt-based nanoalloy on robust non-carbon support was introduced. Non-carbon Ti_{0.8}W_{0.2}O₂ support was successfully synthesized via one-step low-temperature hydrothermal preparation, while the Pt₃Mo nanoalloy on Ti_{0.8}W_{0.2}O₂ support was fabricated by a simple microwave-assisted polyol route [23-24]. The synthesis

process in the present work did not include any surfactant or stabilizer. The characteristics of Pt₃Mo/Ti_{0.8}W_{0.2}O₂ electrocatalyst were measured by X-ray diffraction (XRD), transmission electron microscopy (TEM), BET measurement with N₂ adsorption isotherms, scanning electron microscopy (SEM), and energy-dispersive X-ray spectroscopy (EDX). The synthesized material showed a uniform diameter of ~5.18 nm and good dispersion on the surface of Ti_{0.8}W_{0.2}O₂ support. Pt₃Mo/Ti_{0.8}W_{0.2}O₂ electrocatalyst showed a high surface area (152.32 m²/g), a large pore diameter (2.46 nm). It exhibited superior CO-tolerance with the I_r/I_b ratio of Pt₃Mo/Ti_{0.8}W_{0.2}O₂ was up to 1.49. In addition, the Pt₃Mo/Ti_{0.8}W_{0.2}O₂ photocatalyst showed excellent catalytic activity compared to commercial catalysts.

■ EXPERIMENTAL SECTION

Materials

Tungsten (VI) chloride (WCl₆, 99.9%), Hexachloroplatinic acid (H₂PtCl₆·6H₂O, 99.9%, 38–40% Pt) were obtained from Sigma-Aldrich, USA. Titanium (IV) chloride (TiCl₄, 99.5%) was purchased from Shanghai, China. Ethanol (99.9%), ethylene glycol (EG, 99.5%), acetone (99.9%) were acquired from Merck, Belgium. Molybdenum (V) Chloride (MoCl₅) was bought from Sigma-Aldrich (99.99%). Distilled water was used throughout the experiments.

Instrumentation

Synthesizing process

Besides the common tools in the laboratory, Teflon-lined autoclave, microwave oven, and laboratory centrifuge were mainly used for synthesizing the materials via microwave-assisted polyol process in this study.

Characterization

To investigate the structural characterization of Pt₃Mo/Ti_{0.8}W_{0.2}O₂, Powder X-ray diffractometer (XRD, D2 PHASER-Brucker), transmission electron microscope (TEM, JEOL-JEM 1400), the nitrogen adsorption isotherms (NOVA 1000e), scanning electron microscopy (SEM), and the energy-dispersive X-ray

spectroscopy (EDX, EDX-JSM 6500F, JEOL) were used after synthesis process.

For electrochemical characterization, the CV test was performed in an acidic medium with methanol (N_2 -purged 10 v/v% $CH_3OH/0.5$ M H_2SO_4 solution; at a scan rate of 50 mV/s) to get access to the MOR activity of this material.

Procedure

Synthesis of $Ti_{0.8}W_{0.2}O_2$ nanoparticles

By approaching the solvothermal method applied in the previous studies [3-4], the non-carbon support $Ti_{0.8}W_{0.2}O_2$ NPs were synthesized without using surfactants or stabilizers and further heat treatment. After dissolving 0.159 g WCl_6 in 50 mL ethanol to generate a homogeneous solution, 0.176 mL $TiCl_4$ was added into the mixture. Then the mixture was put into a Teflon-lined autoclave and moved into an oven; the reaction condition was set at 200 °C for 10 h. Subsequently, the suspension was stored at ambient temperature to cool down naturally and rinsed several times with acetone and distilled water. After that, it was dried in the oven set up at 80 °C overnight. Finally, the obtained product was collected for the next synthesis.

Synthesis of the $Pt_3Mo/Ti_{0.8}W_{0.2}O_2$ nanoparticles

The 20 wt.% $Pt_3Mo/Ti_{0.8}W_{0.2}O_2$ were synthesized by a polyol process under microwave radiation. Firstly, 110 mg of the as synthesized $Ti_{0.8}W_{0.2}O_2$ was introduced in a beaker, followed by adding 25 mL EG and stirring for 15 min. This mixture was sonicated for 30 min at 5 °C to form a uniform suspension. The precursor solutions, including 2.422 mL H_2PtCl_6 0.05 M and 0.808 mL $MoCl_5$ 0.05 M, were added into the previous suspension to get a 3:1 atomic ratio of Pt:Mo. To achieve better dispersion, the stirring process was kept for 15 min. Afterward,

NaOH solution was slowly dropped into the mixture to adjust pH = 11, and then the suspension was moved into the microwave oven. The system was operated at a 50% power rate for 3 min. The resulted black product was collected by centrifuging and washing with distilled water 5 times at 6000 rpm. At the end of the process, the sample was dried at 80 °C for 12 h for analysis. The preparation steps of Pt_3Mo NPS/ $Ti_{0.8}W_{0.2}O_2$ schematically can be seen in Fig. 1. Similarly, the 20 wt.% $Pt/Ti_{0.8}W_{0.2}O_2$ NPs catalyst was prepared using the same procedure for further comparison.

Material characterization

The structure of Pt_3Mo nanoalloy on $Ti_{0.8}W_{0.2}O_2$ support was measured by X-ray diffraction (XRD) implemented on D2 PHASER-Brucker using $Cu K_{\alpha}$ X-ray source at 30 kV, in the angle between 20° and 80° with a sweep rate of 2°/min. The transmission electron microscopy (TEM) measurement was performed on JEOL-JEM 1400 microscope at an accelerating voltage of 3800 V to determine the particle size of the as-prepared support and catalyst. Furthermore, by means of EDX-JSM 6500F, JEOL machine operated at an accelerating voltage of 10 kV, the image analysis, elemental composition, and mapping of $Pt_3Mo/Ti_{0.8}W_{0.2}O_2$ nanoparticles are possible to be investigated. The specific surface area of the $Ti_{0.8}W_{0.2}O_2$ support was figured out by Brunauer-Emmett-Teller (BET) method using isothermal N_2 adsorption/desorption. Prior to the analysis test, the sample undergoes the outgassing process to clear away all adsorbed gases and water from material pores by heating at 250 °C for 3 h. The resistivity measurement of the sample has been implemented by preparing a four-point probe. The $Ti_{0.8}W_{0.2}O_2$ powder was placed into pellets of a size of

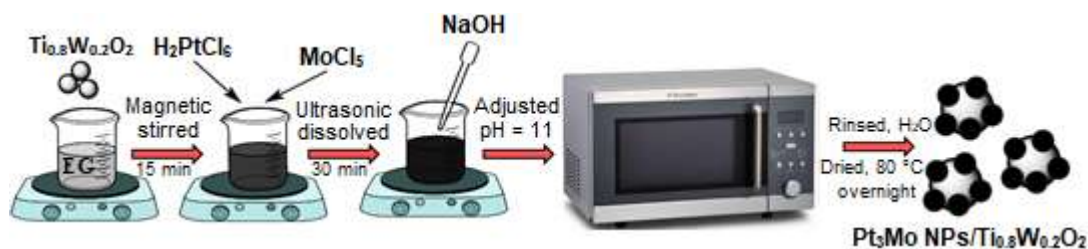


Fig 1. Schematic illustration of the preparation of the Pt_3Mo NPs/ $Ti_{0.8}W_{0.2}O_2$ catalyst

10 mm and ~1 mm in diameter and thickness, respectively, by hydraulic injection mold under pressure about 300 MPa.

RESULTS AND DISCUSSION

Characterization by X-ray diffraction (XRD) was used to verify the 20 wt.% Pt₃Mo/Ti_{0.8}W_{0.2}O₂ catalyst structure. As shown in Fig. 2, the diffraction peaks of the 20 wt.% Pt₃Mo/Ti_{0.8}W_{0.2}O₂ catalyst could be indexed to the (111), (200), and (220) planes of platinum metal (JCPDS 04-0820) with face-center cubic (fcc) structure at 2θ positions of approximate 39.76°, 46.24°, and 67.45°, respectively. Only the characteristic diffraction peaks of the fcc phase of Pt bulk, anatase Ti_{0.8}W_{0.2}O₂ and no single peaks for Mo were detected for the 20 wt.% Pt₃Mo/Ti_{0.8}W_{0.2}O₂ catalyst indicating that Pt and Mo had come into being alloy on the surface of the Ti_{0.8}W_{0.2}O₂ support together with the low mismatch between Pt and Mo atoms [25-26]. Furthermore, the 20 wt.% Pt₃Mo/Ti_{0.8}W_{0.2}O₂ catalyst presented well-matching XRD peak positions with the anatase Ti_{0.8}W_{0.2}O₂ suggesting that the support has a stable structure.

Fig. 3 presents the transmission emission micrograph (TEM) and the surface structure of the Ti_{0.8}W_{0.2}O₂ support. The mesoporous Ti_{0.8}W_{0.2}O₂ nanoparticles had an average diameter of about 9 nm

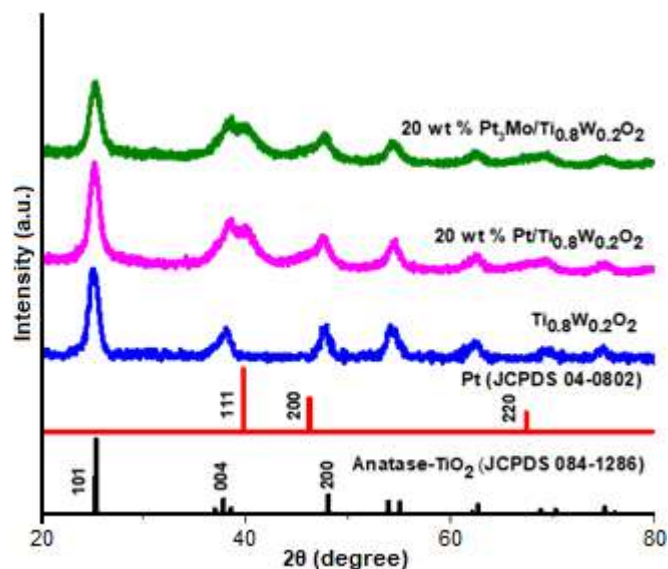


Fig 2. The XRD spectra of the 20 wt.% Pt₃Mo/Ti_{0.8}W_{0.2}O₂, 20 wt.% Pt/Ti_{0.8}W_{0.2}O₂ catalysts and Ti_{0.8}W_{0.2}O₂ support in the 2θ range of 20°–80°

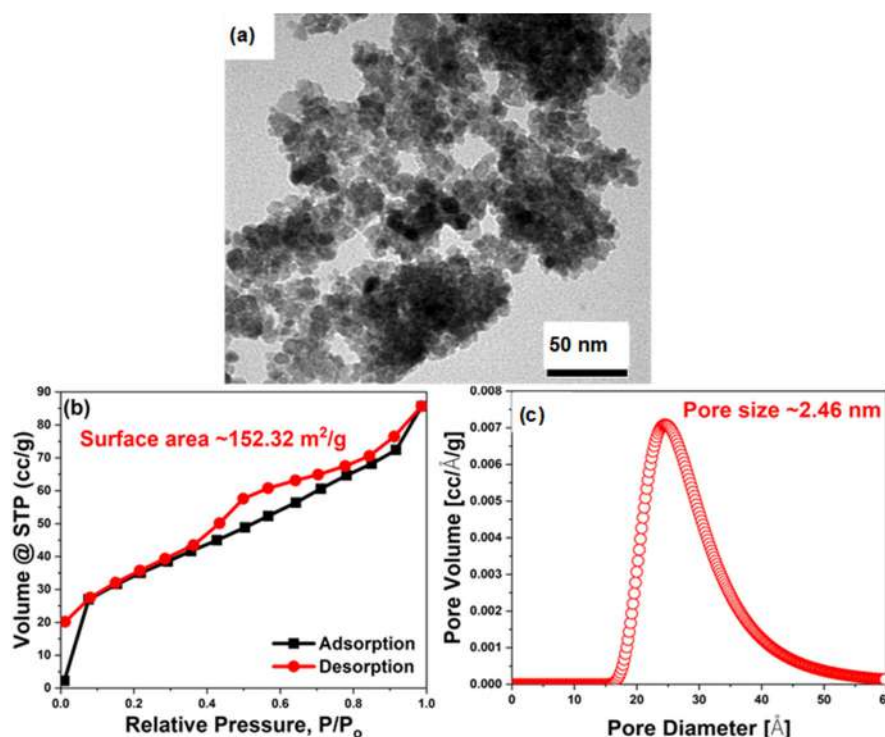


Fig 3. (a) The TEM image, (b) N₂ adsorption/desorption isotherms and (c) pore size distribution of the non-carbon Ti_{0.8}W_{0.2}O₂ support

(Fig. 3(a)), its BET surface area and pore size were measured about $152.32 \text{ m}^2/\text{g}$ and 2.46 nm (Fig. 3(b-c)), respectively, by implementing the N_2 adsorption/desorption isotherms coped with the Barrette–Joyner–Halenda (BJH) technique. Besides, the electrical conductivity of the as-prepared $\text{Ti}_{0.8}\text{W}_{0.2}\text{O}_2$ nanoparticles after using the four-point probe evaluation are near $1.90 \times 10^{-2} \text{ S/cm}$. These data are in good agreement with our previous study [24].

The morphology, the average size, and uniformity of the 20 wt.% $\text{Pt}_3\text{Mo}/\text{Ti}_{0.8}\text{W}_{0.2}\text{O}_2$ nanoparticles were evaluated by the TEM, as shown in Fig. 4. The Pt_3Mo alloy nanoparticles were nearly spherical with a uniform diameter of approximate 5.18 nm and well-dispersed on the surface of $\text{Ti}_{0.8}\text{W}_{0.2}\text{O}_2$ support. In comparison with commercial carbon-supported electrocatalyst (Pt/C, E-TEK), $\text{Pt}_3\text{Mo}/\text{Ti}_{0.8}\text{W}_{0.2}\text{O}_2$ showed the higher surface area

and pore volume, smaller pore diameter (Table 1).

The SEM-EDX elemental analyses are implemented to obtain the Pt-Mo alloy formation and composition (Fig. 5). As can be seen in Fig. 5(b), the Pt:Mo atomic ratio

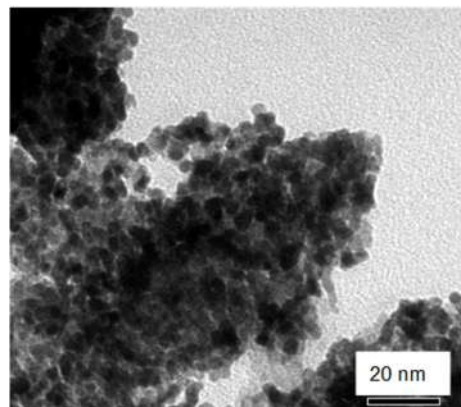


Fig 4. The TEM image of the 20 wt.% $\text{Pt}_3\text{Mo}/\text{Ti}_{0.8}\text{W}_{0.2}\text{O}_2$ catalyst

Table 1. Comparison in BET surface area and pore diameter of $\text{Pt}_3\text{Mo}/\text{Ti}_{0.8}\text{W}_{0.2}\text{O}_2$ and E-TEK commercial catalyst

Electrocatalyst	BET surface area (m^2/g)	Pore diameter (nm)	Reference
20 wt.% $\text{Pt}_3\text{Mo}/\text{Ti}_{0.8}\text{W}_{0.2}\text{O}_2$	153.32	2.46	Present work
E-TEK	69.21	9.8	[27]

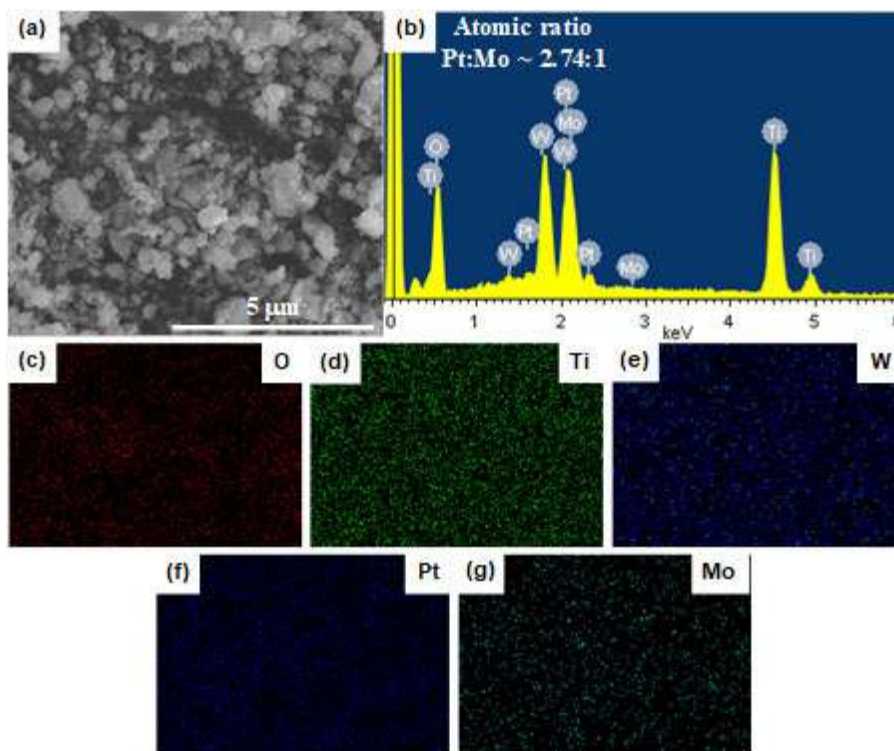


Fig 5. (a) SEM image and (b) EDX analysis and (c-g) elemental mapping of the 20 wt.% $\text{Pt}_3\text{Mo}/\text{Ti}_{0.8}\text{W}_{0.2}\text{O}_2$ catalyst

of the 20 wt.% Pt₃Mo/Ti_{0.8}W_{0.2}O₂ catalyst was found to be 2.74:1, which indicates that the real Mo contents in the binary alloy are slightly smaller than the theoretical value (3:1). It supports the 20 wt.% Pt₃Mo/Ti_{0.8}W_{0.2}O₂ catalyst suffered from a dissolution of some Mo species during the synthesis [15]. Additionally, the elemental mapping shows that the catalyst and support were localized uniformly, suggesting the effectiveness of the rapid microwave-assisted polyol reduction synthesis method.

To elucidate the electrical performance of the 20 wt.% Pt₃Mo/Ti_{0.8}W_{0.2}O₂ catalyst, cyclic voltammetry techniques were carried out in N₂-purged 0.5 M H₂SO₄ electrolyte at a sweep rate of 50 mV/s, as illustrated in Fig. 6. The Pt-H_{upd} region (0 to 0.37 V versus NHE) of Pt₃Mo/Ti_{0.8}W_{0.2}O₂ is not as well defined as those on the Pt/Ti_{0.8}W_{0.2}O₂ and Pt/C (E-TEK) electrodes, it suggesting the relatively low crystallinity of Pt₃Mo/Ti_{0.8}W_{0.2}O₂ than other catalysts. More importantly, the electrochemical specific area (ECSA) values, which were calculated after normalizing the double-layer and assuming a value of 210 (mC/cm²) for the adsorption of H₂ monolayer, of the three catalysts increased in the order: Pt₃Mo/Ti_{0.8}W_{0.2}O₂ (58.28 m²/g_{Pt}) < Pt/C (65.13 m²/g_{Pt}) < Pt/Ti_{0.8}W_{0.2}O₂ (120.16 m²/g_{Pt}). Albeit the ECSA of Pt₃Mo/Ti_{0.8}W_{0.2}O₂ was only half of ECSA of Pt/Ti_{0.8}W_{0.2}O₂, which was probably due to the reduction in Pt content and the presence of Mo in the alloy structure decreasing the interaction between hydrogen molecules and the Pt surface, it is comparable with that of Pt/C. This result could be ascribed to the well-distribution of Pt and the hydrogen spillover effect occurring on the W-doped

TiO₂ support surface.

Methanol Oxidation Reaction Investigation

To get access to the MOR activity of the as-synthesis catalyst, the CV test was performed in an acidic medium with methanol (N₂-purged 10 v/v% CH₃OH/0.5 M H₂SO₄ solution) at a scan rate of 50 mV/s (Fig. 7). As shown in Fig. 7(b), the Mo-containing electrocatalyst (Pt₃Mo/Ti_{0.8}W_{0.2}O₂) showed onset potential (E_{onset} = 0.29 V) at a higher value than the pure Pt electrocatalyst supported on Ti_{0.8}W_{0.2}O₂ (0.24 V) and lower than Pt/C (E-TEK) (0.32 V). Another interesting observation was made concerning the relative positions of the current density peak in the positive-going sweep. The forward peak of Pt₃Mo/Ti_{0.8}W_{0.2}O₂ is 21.16 mA/cm² which is lower than Pt/Ti_{0.8}W_{0.2}O₂ (23.29 mA/cm²) and nearly equal to Pt/C (21.01 mA/cm²). These results imply that the methanol oxidation reaction can occur more easily and faster on the Pt/Ti_{0.8}W_{0.2}O₂ surface rather than on Pt₃Mo/Ti_{0.8}W_{0.2}O₂ due to the higher Pt composition of the Pt nanoparticles in comparison with the binary Pt₃Mo alloy. Notably, the I_f/I_b ratio of Pt₃Mo/Ti_{0.8}W_{0.2}O₂ is up to 1.49, whilst those of Pt/Ti_{0.8}W_{0.2}O₂ and Pt/C are mere ~1.18 and ~0.69, respectively (Fig. 7(c)). The highest I_f/I_b ratio of Pt₃Mo/Ti_{0.8}W_{0.2}O₂ which can be considered an indication for better -CO_{ads} tolerance is attributable to the promotion of the removal of the surface-bound intermediates in the presence of Mo. The parameter comparison of Pt₃Mo/Ti_{0.8}W_{0.2}O₂ and Pt/Ti_{0.8}W_{0.2}O₂ to others reported previously is presented in Table 2.

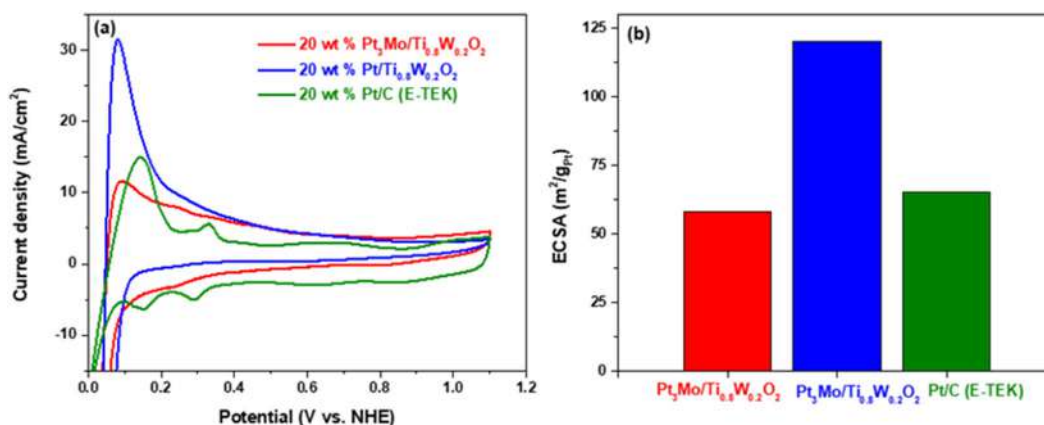


Fig 6. (a) CV curves and (b) ECSA values of the different catalysts in N₂-purged 0.5 M H₂SO₄ solution at a scan rate of 50 mV/s

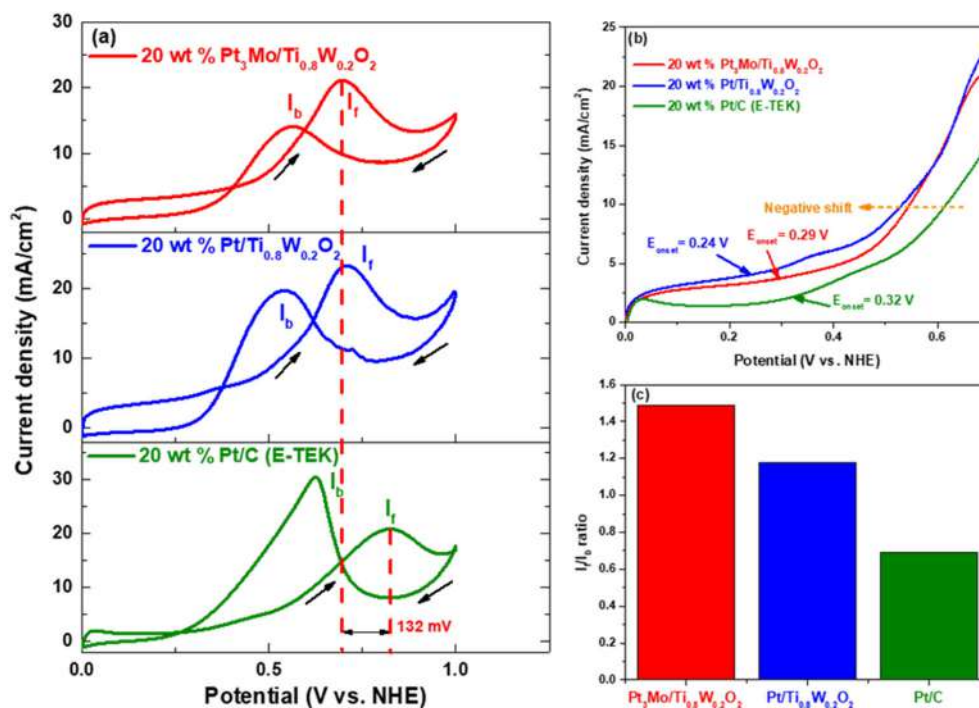


Fig 7. (a) CV curves; (b) the onset potential and (c) I_f/I_b values of the catalysts in N_2 -purged 10 v/v % $CH_3OH/0.5 M H_2SO_4$ solution at a scan rate of 50 mV/s

Table 2. Comparison of $Pt_3Mo/Ti_{0.8}W_{0.2}O_2$ and $Pt/Ti_{0.8}W_{0.2}O_2$ with other Pt-based electrocatalysts

Electrocatalyst	ECSA (m^2/g_{Pt})	Onset potential (V)	Specific MOR activity (mA/cm^2)	I_f/I_b	Ref
$Pt_3Mo/Ti_{0.8}W_{0.2}O_2$	58.28	0.29 V vs. NHE	21.16	1.49	This work
$Pt/Ti_{0.8}W_{0.2}O_2$	120.16	0.24 V vs. NHE	23.29	1.18	This work
Pt/C (E-TEK)	65.13	0.32 V vs. NHE	21.01	0.69	This work
Pt_1Ru_2/C	-	0.35 V vs. Ag/AgCl	-	1.22	[29]
PtRu/C	-	0.346 V vs. NHE	38.2	0.8	[30]
BPt NW/RGO	25.90	0.4 V vs. Ag/AgCl	1.154	1.01	[31]
$CuPt_3$ wavy NWs	18.0	0.48 V vs. SCE	2.80	1.67	[32]

Specifically, mechanisms for the higher CO tolerance of the alloy Pt_3Mo on $Ti_{0.8}W_{0.2}O_2$ material, as compared to only Pt on $Ti_{0.8}W_{0.2}O_2$ can be assigned to the major bifunctional and the minor electronic mechanisms. As for the bifunctional manner, the electro-oxidation of CO to CO_2 occurs more readily and easily with the presence of oxophilic Mo element after $-OH_{ads}$ species formed on Mo migrate to neighboring Pt sites where they react with $-CO_{ads}$. With regards to the electronic effect, the addition of Mo alters the Pt electronic properties and thus changes the CO chemisorption properties, consequently reducing the CO coverage and leaving freer Pt sites available for the

methanol oxidation. Also, other known ways to reduce catalyst poisoning is promoting CO-like poison oxidation by oxygen supplied in the fuel flow or arriving from the cathode after passing the membrane, and the occurrence of the water gas shift process (WGS) which correlates with the reaction of CO with water catalyzed by Pt-Mo. Furthermore, the dissociative adsorption of water molecules upon the anatase titania-based support, along with its spillover characteristic, facilitates the transfer of primary oxides (Pt-OH) to the reacting sites, otherwise being decisive for the electro-oxidation of CO and substantially enhancing CO tolerance.

■ CONCLUSION

In conclusion, the Pt₃Mo/Ti_{0.8}W_{0.2}O₂ electrocatalyst was successfully synthesized via a simple microwave-assisted polyol route without using any surfactant or stabilizer. The bimetallic Pt₃Mo nanoalloy particles were well-dispersed on the surface of robust non-carbon Ti_{0.8}W_{0.2}O₂ support. Electrochemical tests indicated that the Pt₃Mo/Ti_{0.8}W_{0.2}O₂ electrocatalyst showed higher CO-like tolerance and stability towards the methanol oxidation reaction than those of the commercial Pt/C electrocatalysts. The combination of the transition metal element Mo on the alloy structure shows that Pt₃Mo bi-component structure can not only reduce the amount of used Pt metal and the cost of catalysts but also provide notable catalytic activity for catalysts in MOR reactions. Therefore, Pt₃Mo/Ti_{0.8}W_{0.2}O₂ material has the potential to be a potential electrocatalyst for DMFC.

■ ACKNOWLEDGMENTS

This work is supported by L'Oreal - UNESCO for Women in Science National Fellowship, Vietnam 2019. Thanks to Dr. Huynh Thien Tai for your support for this work.

■ REFERENCES

- [1] Hsieh, B.J., Tsai, M.C., Pan, C.J., Su, W.N., Rick, J., Lee, J.F., Yang, Y.W., and Hwang, B.J., 2017, Platinum loaded on dual-doped TiO₂ as an active and durable oxygen reduction reaction catalyst, *NPG Asia Mater.*, 9 (7), e403.
- [2] Pan, C.J., Tsai, M.C., Su, W.N., Rick, J., Akalework, N.G., Agegnehu, A.K., Cheng, S.Y., and Hwang, B.J., 2017, Tuning/exploiting strong metal-support interaction (SMSI) in heterogeneous catalysis, *J. Taiwan Inst. Chem. Eng.*, 74, 154–186.
- [3] Salam, M.A., Habib, M.S., Arefin, P., Ahmed, K., Uddin, M.S., Hossain, T., and Papri, N., 2020, Effect of temperature on the performance factors and durability of proton exchange membrane of hydrogen fuel cell: A narrative review, *Mater. Sci. Res. India*, 17 (2), 179–191.
- [4] Shrivastava, N.K., and Harris, T.A.L., 2017, “Direct Methanol Fuel Cells” in *Encyclopedia of Sustainable Technologies*, Elsevier, Oxford, UK, 343–357.
- [5] Sharma, S., and Pollet, B.G., 2012, Support materials for PEMFC and DMFC electrocatalysts—A review, *J. Power Sources*, 208, 96–119.
- [6] Tamaki, T., Wang, H., Oka, N., Honma, I., Yoon, S.H., and Yamaguchi, T., 2018, Correlation between the carbon structures and their tolerance to carbon corrosion as catalyst supports for polymer electrolyte fuel cells, *Int. J. Hydrogen Energy*, 43 (12), 6406–6412.
- [7] Zhao, J., and Li, X., 2019, A review of polymer electrolyte membrane fuel cell durability for vehicular applications: Degradation modes and experimental techniques, *Energy Convers. Manage.*, 199, 112022.
- [8] You, H., Zhang, F., Liu, Z., and Fang, J., 2014, Free-standing Pt–Au hollow nanourchins with enhanced activity and stability for catalytic methanol oxidation, *ACS Catal.*, 4 (9), 2829–2835.
- [9] Lee, E., Kim, S., Jang, J.H., Park, H.U., Matin, M.A., Kim, Y.T., and Kwon, Y.U., 2015, Effects of particle proximity and composition of Pt–M (M = Mn, Fe, Co) nanoparticles on electrocatalysis in methanol oxidation reaction, *J. Power Sources*, 294, 75–81.
- [10] Huang, L., Zhang, X., Wang, Q., Han, Y., Fang, Y., and Dong, S., 2018, Shape-control of Pt–Ru nanocrystals: Tuning surface structure for enhanced electrocatalytic methanol oxidation, *J. Am. Chem. Soc.*, 140 (3), 1142–1147.
- [11] Manthiram, A., Zhao, X., and Li, W., 2012, “Developments in Membranes, Catalysts and Membrane Electrode Assemblies for Direct Methanol Fuel Cells (DMFCs)” in *Functional Materials for Sustainable Energy Applications*, Eds. Kilner, J.A., Skinner, S.J., Irvine, S.J.C., and Edwards, P.P., Woodhead Publishing, UK, 312–369.
- [12] Hartmann, P., and Gerteisen, D., 2012, Local degradation analysis of a real long-term operated DMFC stack MEA, *J. Power Sources*, 219, 147–154.
- [13] Moura, A.S., Fajín, J.L.C., Mandado, M., and Cordeiro, M.N.D.S., 2017, Ruthenium–platinum catalysts and direct methanol fuel cells (DMFC): A review of theoretical and experimental breakthroughs, *Catalysts*, 7 (2), 47.

- [14] Jing, F., Sun, R., Wang, S., Sun, H., and Sun, G., 2020, Effect of the anode structure on the stability of a direct methanol fuel cell, *Energy Fuels*, 34 (3), 3850–3857.
- [15] Hassan, A., and Ticianelli, E.A., 2018, Activity and stability of dispersed multi metallic Pt-based catalysts for CO tolerance in proton exchange membrane fuel cell anodes, *An. Acad. Bras. Cienc.*, 90, 697–718.
- [16] Liu, Z., Ma, L., Zhang, J., Hongsirikarn, K., and Goodwin, J.G., 2013, Pt alloy electrocatalysts for proton exchange membrane fuel cells: A review, *Catal. Rev. Sci. Eng.*, 55 (3), 255–288.
- [17] Liu, Y., Duan, Z., and Henkelman, G., 2019, Computational design of CO-tolerant Pt₃M anode electrocatalysts for proton-exchange membrane fuel cells, *Phys. Chem. Chem. Phys.*, 21 (7), 4046–4052.
- [18] Uwitonze, N., and Chen, Y.X., 2017, The study of Pt and Pd based anode catalysis for formic acid fuel cell, *Chem. Sci. J.*, 8 (3), 1000167.
- [19] Hassan, A., Carreras, A., Trincavelli, J., and Ticianelli, E.A., 2014, Effect of heat treatment on the activity and stability of carbon supported PtMo alloy electrocatalysts for hydrogen oxidation in proton exchange membrane fuel cells, *J. Power Sources*, 247, 712–720.
- [20] Bang, J.H., and Kim, H.S., 2011, CO-tolerant PtMo/C fuel cell catalyst for H₂ oxidation, *Bull. Korean Chem. Soc.*, 32 (10), 3660–3665.
- [21] Gao, J., Zou, J., Zeng, X., and Ding, W., 2016, Carbon supported nano Pt–Mo alloy catalysts for oxygen reduction in magnesium–air batteries, *RSC Adv.*, 6 (86), 83025–83030.
- [22] Hu, J.E., Liu, Z., Eichhorn, B.W., and Jackson, G.S., 2012, CO tolerance of nano-architected Pt–Mo anode electrocatalysts for PEM fuel cells, *Int. J. Hydrogen Energy*, 37 (15), 11268–11275.
- [23] Huynh, T.T., Pham, H.Q., Van Nguyen, A., Ngoc Mai, A.T., Nguyen, S.T., Bach, L.G., Vo, D.V.N., and Vo, D.V.N., 2019, High conductivity and surface area of Ti_{0.7}W_{0.3}O₂ mesoporous nanostructures support for Pt toward enhanced methanol oxidation in DMFCs, *Int. J. Hydrogen Energy*, 44 (37), 20933–20943.
- [24] Pham, H.Q., Huynh, T.T., Bich, H.N., Pham, T.M., and Nguyen, S.T., 2019, Tungsten-doped titanium-dioxide-supported low-Pt-loading electrocatalysts for the oxidation reaction of ethanol in acidic fuel cells, *C.R. Chim.*, 22 (11-12), 829–837.
- [25] Liu, Z., Hu, J.E., Wang, Q., Gaskell, K., Frenkel, A.I., Jackson, G.S., and Eichhorn, B., 2009, PtMo alloy and MoO_x@Pt core–shell nanoparticles as highly CO-tolerant electrocatalysts, *J. Am. Chem. Soc.*, 131 (20), 6924–6925.
- [26] Lu, S., Eid, K., Lin, M., Wang, L., Wang, H., and Gu, H., 2016, Hydrogen gas-assisted synthesis of worm-like PtMo wavy nanowires as efficient catalysts for the methanol oxidation reaction, *J. Mater. Chem. A*, 4 (27), 10508–10513.
- [27] Fıçıcılar, B., Bayrakçeken, A., and Eroğlu, İ., 2010, Pt incorporated hollow core mesoporous shell carbon nanocomposite catalyst for proton exchange membrane fuel cells, *Int. J. Hydrogen Energy*, 35 (18), 9924–9933.
- [28] Hu, Y., Zhu, A., Zhang, Q., and Liu, Q., 2016, Preparation of PtRu/C core–shell catalyst with polyol method for alcohol oxidation, *Int. J. Hydrogen Energy*, 41 (26), 11359–11368.
- [29] Chen, F., Ren, J., He, Q., Liu, J., and Song, R., 2017, Facile and one-pot synthesis of uniform PtRu nanoparticles on polydopamine-modified multiwalled carbon nanotubes for direct methanol fuel cell application, *J. Colloid Interface Sci.*, 497, 276–283.
- [30] Luo, Z., Yuwen, L., Bao, B., Tian, J., Zhu, X., Weng, L., and Wang, L., 2012, One-pot, low-temperature synthesis of branched platinum nanowires/reduced graphene oxide (BPtNW/RGO) hybrids for fuel cells, *J. Mater. Chem.*, 22 (16), 7791–7796.
- [31] Fu, G., Yan, X., Cui, Z., Sun, D., Xu, L., Tang, Y., Goodenough, J.B., and Lee, J.M., 2016, Catalytic activities for methanol oxidation on ultrathin CuPt₃ wavy nanowires with/without smart polymer, *Chem. Sci.*, 7 (8), 5414–5420.

Simple and Green Preparation of ZnO Blended with Highly Magnetic Silica Sand from Parangtritis Beach as Catalyst for Oxidative Desulfurization of Dibenzothiophene

Wega Trisunaryanti^{1*}, Safa Annissa Novianti¹, Dyah Ayu Fatmawati¹, Triyono Triyono¹, Maria Ulfa², and Didik Prasetyoko³

¹Department of Chemistry, Faculty of Mathematics and Natural Sciences, Universitas Gadjah Mada, Sekip Utara, Yogyakarta 55281, Indonesia

²Department of Chemistry Education, Faculty of Teacher Training and Education, Sebelas Maret University, Jl. Ir. Sutami 36A Surakarta 57126 Indonesia

³Department of Chemistry, Faculty of Science and Data Analytics, Sepuluh Nopember Institute of Technology, Keputih, Sukolilo, Surabaya 60111, Indonesia

* **Corresponding author:**

email: wegats@ugm.ac.id

Received: October 23, 2021

Accepted: December 16, 2021

DOI: 10.22146/ijc.69938

Abstract: Simple and green preparation of ZnO blended with Parangtritis beach sand (BS) catalysts for oxidative desulfurization of dibenzothiophene (ODS-DBT) has been conducted. The ZnO-BS catalysts were prepared by blending ZnO with beach sand under a weight ratio of 1:1, 1:2, and 1:4, and then heated by microwave (MW) at 540 watts for 30 min, resulting in BS-MW, ZnO-MW, ZnO-BS-1-MW, ZnO-BS-2-MW, and ZnO-BS-4-MW, respectively. As a comparison, the ZnO-BS-1 was also heated by oven at 100 °C for 30 min produced ZnO-BS-1-OV. Each product was characterized by XRF, XRD, FTIR, acidity test by NH₃ vapor adsorption, SAA, SEM-EDX, TEM, and magneticity test by an external magnetic field. Furthermore, each material was applied for ODS-DBT, and its product was analyzed by UV-Vis spectrophotometer and FTIR. The results showed that ZnO-BS-1-OV had the highest acidity of 2.3486 mmol/g and produced the highest DBT removal efficiency through the ODS reaction of 81.59%. The use of catalysts in ODS-DBT does not affect the main structure of the treated fuel. Therefore, the combination of ZnO with BS can provide good performance in ODS activity and facilitate the separation of catalysts after the reaction due to its magnetic iron oxide content.

Keywords: dibenzothiophene; magnetic; oxidative desulfurization; Parangtritis beach sand; ZnO

■ INTRODUCTION

One of the world's most critical issues is the depletion of petroleum-based resources due to extended industrialization and motorization. It has been stated that the transport sector uses 40% of the number one energy consumed worldwide [1]. The decline in oil reserves worldwide increases the dependence on heavy oils containing a heteroatom. Therefore, the trend towards converting heavy oil to light products as much as possible to compensate for this shortage has become a priority in energy research centers. Thus, the percentage of total sulfur content in these refined products increased [2].

The presence of sulfur compounds in transport fuels is undesirable from an environmental side. These sulfur compounds present in fuels such as gasoline and diesel result in harmful effects such as corrosion of engine parts, wear, deposits formation, and air pollution. These environmental risks have led the environmental protection agency (EPA) to set the maximum sulfur content in gasoline to less than 30 ppm. At the same time, this ratio was determined in diesel fuel below 15 ppm [3], and accordingly, refineries have adopted several techniques to meet these legislations. Complete knowledge regarding their structure and chemical nature is desirable to remove these sulfur compounds

from engine fuels by an appropriate refining process. Petroleum oil refineries convert many heavy oils into high-value products that can meet societal needs such as liquid petroleum gas, gasoline, diesel, and jet fuel through physical processes such as distillation or chemical processes such as catalytic reforming [4].

In industry, sulfur compounds are eliminated through the hydrodesulfurization (HDS) method. However, it has a few inherent issues in treating sulfur-containing aromatic hydrocarbon compounds, including dibenzothiophene (DBT) and its derivatives. It also requires harsh conditions, including high temperatures and pressures of hydrogen gas, to provide light oil with low levels of sulfur compounds. Because of this, it's been an urgent challenge to discover new methods for the desulfurization of fuel oils. Catalytic oxidative desulfurization (ODS) combined with extraction of oxygenated sulfur using a polar solvent is considered due to favorable operating conditions. Generally, ODS processes are achieved through the oxidation of sulfur compounds to sulfoxides and sulfones, followed by a separation process using appropriate extractants or adsorbents. ODS is capable of removing the widest possible sulfur compounds due to the nature of the reaction and the ability to operate under mild operating conditions with the presence of green oxidants [5]. According to the literature, various ODS systems have been developed, such as a series of heteropolyacid catalysts, ionic liquids systems, acetic acid catalyst [6-7], porous glass supported with titanium silicate particles [8], and ultrasound-assisted ODS processes [9].

Several solid catalysts had been examined for ODS reaction, including heteropoly acid, either alone or supported [10], and metal oxides, i.e., oxides of (Mo, Mn, Sn, Fe, Co, Zn) metals [11-13]. However, most of it either involved complicated and multistep synthesis techniques or was unrecyclable. The latest literature survey shows that ZnO as a catalyst has obtained significant interest due to its inexpensive, non-toxic, and environmental benefits, i.e., minimal execution time, low corrosion, waste minimization, recycling of the catalyst, clean delivery, and disposal of the catalyst [14]. Parangtritis beach sand is rich in iron, silica, and alumina oxide. It is selected as the

support material for ZnO catalyst since it is a reasonably-priced, environmentally friendly, natural active catalyst, and an example of higher use of natural resources [15].

Iron oxide can activate a considered clean oxidant such as H_2O_2 , producing active superoxide/peroxide species [16], while the ZnO was reported for adsorptive desulfurization [17]. ZnO is also found to be able to remove the sulfur content without changing the main hydrocarbon structure where non-sulfur-containing crude fuel oil mass remains unchanged. Thus, the combination of the adsorptive capability of zinc oxide and oxidant activated by rich iron oxide sand will enhance the possibility of efficient removal of a refractory sulfur compound through the ODS technique. In addition, iron-zinc oxide material was reported in the literature to have both hydrophobic-hydrophilic characteristics [16]. It has a great potential to act like a phase-transfer catalyst, which is further important for the reaction that consists of immiscible H_2O_2 containing H_2O and hydrocarbon solution.

Therefore, in this research, the ZnO-beach sand catalysts were prepared by the physical grinding (blending) method, which is a simple and easy method that can also provide magneticity properties that allow catalyst recovery at the end of the ODS-DBT reaction so that it can be easily separated from the product by an external magnetic bar. The comparison of catalysts' characteristics and activities heated by microwave at various weight ratios and heated by oven were also studied.

■ EXPERIMENTAL SECTION

Materials

The materials used in this research were sand obtained from Parangtritis Beach, Bantul Regency, Special Region of Yogyakarta with purity can be seen from the XRF data, zinc oxide (ZnO 99% purity, Merck), dibenzothiophene ($C_{12}H_8S$ 98% purity, Merck), *n*-hexane (C_6H_{14} 96% purity), 30% (w/w) hydrogen peroxide (H_2O_2 29–32% purity, Merck), acetonitrile (C_2H_3N 99.9% purity, Merck), distilled water (H_2O , technical grade), ice and filter paper (Whatman Filter Paper, Grade 42).

Instrumentation

Beach Sand (BS) was analyzed by an X-Ray Fluorescence spectrometer (XRF, RIGAKU-NEX QC+QuanTEZ). All catalysts (BS, BS-MW, ZnO, ZnO-MW, ZnO-BS-1-OV, ZnO-BS-1-MW, ZnO-BS-2-MW, and ZnO-BS-4-MW) were analyzed by X-Ray Diffractometer (XRD, Philips X'Pert MPD), Fourier-Transform Infrared Spectrometer (FTIR, Shimadzu IRPrestige-21), acidity test, and external magnetic field. ZnO-BS-1-OV and ZnO-BS-1-MW were analyzed by Surface Area Analyzer (SAA, JW-BK112) and Scanning Electron Microscope-Energy Dispersive X-Ray (SEM-EDX, Hitachi SU 3500). ZnO-BS-1-OV as the best catalyst was analyzed by Transmission Electron Microscopy (Jeol JEM-1400 TEM).

Procedure

Catalyst synthesis

The sand collected from Parangtritis Beach, Yogyakarta, Indonesia, was washed from any excess chloride (Cl⁻) using distilled water. It was then dried at 100 °C overnight to remove any excess water on the surface of the beach sand (BS). ZnO was blended with BS in different weight ratios of 1:1, 1:2, and 1:4 and then heated by microwave. The preparation of blended ZnO-BS was carried out as follows: 1 g of ZnO was added by 1, 2, and 4 g of BS and blended homogeneously. Distilled water (1 mL) was added to the mixture to form a paste and then microwaved at 540 watts for 30 min, producing ZnO-BS-1-MW, ZnO-BS-2-MW, and ZnO-BS-4-MW, respectively. BS and ZnO were also heated by a microwave that produced BS-MW and ZnO-MW. ZnO-BS-1 catalyst was also prepared without microwave irradiation (oven), producing ZnO-BS-1-OV.

Catalytic activity test

The model compound dibenzothiophene (DBT) was dissolved into *n*-hexane to make a stock solution of model fuel with a sulfur content of 500 ppm (DBT content = 2874.5 ppm). The oxidative desulfurization (ODS) experiment was performed in a three-necked 500 mL round-bottomed flask equipped with a condenser fitted with a magnetic stirrer and immersed in an oil bath controlled by a thermometer. The mixture of 25 mL DBT

and 0.15 g catalyst was then introduced and heated under vigorous stirring. Once the temperature reached 60 °C, 0.12 mL of 30% aqueous solution of H₂O₂ as oxidant was introduced for 20 min under stirring. The oxidized DBT solution was then transferred to a separating funnel followed by the addition of acetonitrile and extracted three times with the volume ratio of the total solvent to oxidized ODS solution of 1:1. The hydrocarbon layer of the oxidized DBT solution was then subjected to quantitative and qualitative analysis.

The hydrocarbon layer of the oxidized DBT solution after extraction was subjected to two different analysis methods. Ultraviolet-visible (UV-Vis) spectrophotometer was used to determine the efficiency of DBT removal. The removal percentage of DBT is calculated based on the following equation:

$$(\%) = \frac{C_0 - C_t}{C_0} \times 100\%$$

where C_0 is the DBT initial concentration in the stock solution and C_t is the DBT concentration of the oxidized DBT solution in the hydrocarbon layer after reaction time (t). In addition to UV-Vis spectrophotometry, the hydrocarbon layer after the reaction was also subjected to FTIR to determine the stability of DBT in *n*-hexane qualitatively.

RESULTS AND DISCUSSION

Catalysts Characterization

The crystallographic interpretations were performed by X-ray diffractometer (XRD) using Cu K α wavelength and scanning in 2θ range from 10° to 80° with a rate of 4°/min. Each diffractogram of the material is shown in Fig. 1.

BS and BS-MW spectra exhibit peaks at 2θ of 8.46, 18.53, 18.73, 22.39, 24.09, 24.62, 28.37, 29.37, 29.57, 29.80, 30.45, 31.04, 33.21, 34.27, 34.74, 35.04, 35.35, 36.37, 36.59, 37.21, 37.42, 37.77, 40.87, 43.38, 43.61, 47.70, 49.38, 53.96, 54.17, 56.21, 57.63, 62.07, 63.88, 64.25, 66.31, 69.42, 71.34, 72.08, 72.33, 74.85, 75.13, 75.28, 79.78, and 80 degrees confirmed that the sand is mainly containing Magnetite (Fe₃O₄), Hematite (Fe₂O₃), Schwertmannite (Fe₈O₈(OH)₆·*n*H₂O), and Lepidocrocite (γ -FeO(OH)) with the three strongest peaks showed as

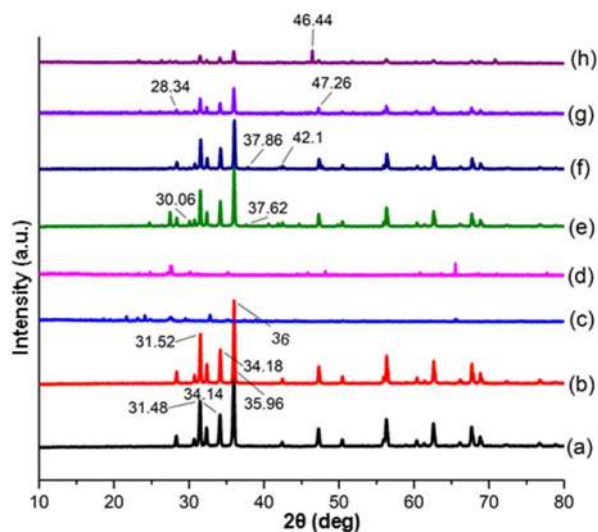


Fig 1. X-ray Diffractogram of (a) ZnO, (b) ZnO-MW, (c) BS, (d) BS-MW, (e) ZnO-BS-1-OV, (f) ZnO-BS-1-MW, (g) ZnO-BS-2-MW, and (h) ZnO-BS-4-MW

Schwertmannite, Lepidocrocite, and Hematite. The observed peak positions match the Crystallography Open Database (COD) File No. 00-101-1032, 00-101-1267, 00-901-5185, and 00-901-5156. ZnO-BS-4-MW material displays a clear appearance of the phase of cubic-ZnFe₂O₄ with peaks corresponding to hkl: (111), (220), (311), (222), (400), (331), (422), (531), (442), (620), (533), (642), and (731) with d values of 0.500, 0.300, 0.254, 0.244, 0.193, 0.172, 0.143, 0.141, 0.132, 0.128, 0.012, and 0.109 nm, respectively. The crystal structure of cubic-ZnFe₂O₄ is in accordance with the standard COD file no. 00-151-3087 (lattice constant: a = 0.843 nm) [18]. In ZnO-BS-2-MW, the diffractogram shows that the extra peaks also evolved corresponding to (220) (d = 0.302 nm), (331) (d = 0.196 nm), and (642) (d = 0.863 nm) of cubic-ZnFe₂O₄. The diffraction spectrums of the blended ZnO-BS-MW samples could not be assigned clearly as Fe₂O₃ due to the amount of Fe³⁺ of BS used in the mixture is very small. In ZnO-BS-1-MW, the diffractogram reveals that the particles form hexagonal-ZnO, also extra planes corresponding to (222) (d = 0.237 nm) and (400) (d = 0.214 nm) are also evolved. In addition to the hexagonal, the phase in ZnO-BS-1-OV develops as extra planes corresponding to (220) (d = 0.297 nm) and (222) (d = 0.238 nm) from cubic-ZnFe₂O₄. In the ZnO-MW, the most intense peaks were located at 2θ of 31.49, 34.14, and

35.98 degrees which corresponded to the Miller index of (100), (002), and (101), whereas ZnO lies at 2θ of 31.44, 35.93, and 56.30 degrees which correspond to the Miller index of (100), (101), and (2-10), respectively. The most intense and sharp peaks in Fig. 1 show that ZnO and ZnO-MW have high crystalline and purity. These peaks were identified by comparison with the ICDD powder diffraction file for ZnO (No. 10800075) which confirmed that the particles conform to the hexagonal structure of ZnO (wurtzite type: a = 0.32 nm, c = 0.52 nm). These hkl planes include (100), (002), (101), (102), (2-10), (103), (200), (2-12), (201), (202) with d values of 0.276, 0.262, 0.249, 0.192, 0.163, 0.148, 0.141, 0.138, 0.136, and 0.124 nm, respectively.

From Table 1, it can be seen that microwave treatment can reduce the crystallinity of the material as happened in BS→BS-MW, ZnO→ZnO-MW, and ZnO-BS-1-OV→ZnO-BS-1-MW. The decrease in crystallinity indicates the occurrence of crystalline amorphization. The level of crystallinity is also affected by the ratio of the weight of ZnO to BS. The greater content of ZnO in the mixture will increase the crystallinity. This is because ZnO dominates the crystals more than BS, which is an amorphous material.

The crystallite size of each material from XRD data was calculated using the Debye-Scherrer equation as follows:

$$D = \frac{K\lambda}{\beta \cos\theta}$$

where D is crystallite size in nm, K is Scherrer constant (0.89), λ is the X-ray wavelength for Cu-Kα in nm (λ = 1.54059 Å), β is the Full Width at Half Maximum (FWHM) in radian, and θ is the Bragg angle in radian.

From Table 1, it can be concluded that microwave heating can increase the crystallite size of the material, as happened in BS→BS-MW and ZnO→ZnO-MW. The increase in crystallite size is possible for sintering due to the large energy generated by the microwave. Although ZnO-BS-1-OV→ZnO-BS-1-MW has decreased, this value is considered consistent because its difference is very small (0.34 nm). When ZnO is blended with BS, the sintering can be prevented because the position of ZnO and BS could be distributed evenly. The lower the ZnO

Table 1. Crystallinity properties and acidity of materials

Material	Crystallinity (%)	Crystallite size (nm)	Acidity (mmol/g)
ZnO	96.87	38.70	2.1137
ZnO-MW	93.89	51.60	1.9963
BS	76.20	56.54	2.2312
BS-MW	66.00	127.89	2.1785
ZnO-BS-1-OV	90.36	51.22	2.3486
ZnO-BS-1-MW	88.34	50.88	1.7614
ZnO-BS-2-MW	74.91	49.96	1.7826
ZnO-BS-4-MW	74.81	85.21	1.9251

content in the mixture, the more evenly distributed on the BS surface, so the crystallite size will be smaller. On the other hand, the greater the ZnO content in the mixture, the greater the chance of forming aggregates on the BS surface so that the crystallite size increases. This argument does not occur in the case of ZnO-BS-4-MW because ZnO may not be homogeneously distributed on the BS surface.

All materials that have been prepared are tested for acidity using the gravimetric method by ammonia adsorption. The acidity value is expressed as the number of mmol of ammonia absorbed in grams of catalyst. Table 1 summarizes the order of the acidity of the material. Heating the material by microwave can reduce acidity, as happened in BS→BS-MW, ZnO→ZnO-MW, and ZnO-BS-1-OV→ZnO-BS-1-MW. This might happen due to ZnO's dielectric properties by microwave heating, as stated by Omran et al. [18]. The dielectric values of ZnO at room temperature were relatively low. The influence of temperature on the real (ϵ') and imaginary (ϵ'') permittivities indicated that temperature has a more significant effect on the imaginary permittivity than on the real permittivity, and the effect of temperature is more significant at higher temperatures. Due to the low dielectric values of the sample, ZnO is a poor microwave absorber which makes the acidity of the samples decrease when irradiated by microwave. In addition, acidity is also influenced by the weight ratio of ZnO to BS. The acidity will increase following the amount of BS content in the mixture. This is because the largest content in BS is Fe, where this metal contributes a lot of Lewis acid sites from its empty p orbitals. The large amount of ZnO in the mixture allows the formation of aggregates that cover the

acid sites of the pores of the material, thereby reducing the acidity.

XRF is used to determine the elemental composition contained in Parangtritis beach sand (BS). The analysis results are shown in Table 2, which implies that the largest elemental contents include Fe, Si, and Al. This proves that BS contains a lot of Fe, which can be applied as potential catalyst support for oxidative desulfurization (ODS) [19-20].

EDX was conducted to compare the elemental content in ZnO-BS-1-OV and ZnO-BS-1-MW. From Table 3, it can be seen that the content of Fe and Zn elements did not change, which indicates that the microwave treatment did not affect the content of both elements in the material. The second reason is possibly the EDX measurement area was not taken correctly, so it is not representative.

Table 2. XRF analysis result of beach sand (BS)

Element	Composition (wt.%)
Al	3.17
Si	11.85
Fe	27.79
Co	0.11
Ni	<0.1
Zn	0.04

Table 3. EDX analysis results of ZnO-BS-1-OV and ZnO-BS-1-MW

Material	Elemental content (wt.%)				
	O	Al	Si	Fe	Zn
ZnO-BS-1-OV	26.5	4	2.4	0.9	66.2
ZnO-BS-1-MW	24.5	4.3	4.1	0.9	66.2

FTIR analysis was applied to determine the functional groups present in the material. According to the literature, magnetite displays two strong absorption bands at 570 and 390 cm^{-1} leading to the Fe–O stretching mode of the tetrahedral and octahedral sites, respectively [21]. Whereas maghemite, a defective form of magnetite, has absorption bands at 630, 590, and 430 cm^{-1} . Geothite contains stretching vibrations of –OH at 3125 (ν -OH), 890 (δ -OH), and 800 (γ -OH) cm^{-1} [22], where the last two bands are important diagnostic bands of goethite as well as stretching Fe–O with weak intensity around 400 and 630 cm^{-1} [23]. Due to their differences, FTIR is considered as one of the suitable tools for confirming the purity of the pure or mixed iron oxide-based material.

By analyzing the spectrum in Fig. 2, it can be stated that the BS consists of a mixture of magnetite and maghemite, based on the fact that the band located at 540.07 cm^{-1} is not symmetric; some weak bands of maghemite may also be present. There is a shift to 524.64 cm^{-1} in BS when heated by microwave. The spectra of BS and BS-MW show water molecule stretching and bending vibrations of protons in hydroxyl at 3448.72 cm^{-1}

[24] and –OH vibration bands at 786.96 and 794.67 cm^{-1} . This can be due to the formation of metal hydroxides as an intermediate compound before the formation of ZnO. The C=O stretching between 1543.05 and 1635.64 cm^{-1} and the C–O asymmetric stretching between 1381.03 and 1388.75 cm^{-1} are also present [25]. The bands observed at 2337.72 and 2368.59 cm^{-1} are attributed to the C=O stretching mode, possibly due to the absorption of CO_2 from the air by the metallic cation [26-27]. The absorption band observed at 424.34–447.49 cm^{-1} is associated with the vibrational mode characteristic of Zn–O bonding [28].

In this research, an attempt was made to measure the infrared spectra of ammonia adsorbed on BS, BS-MW, ZnO, ZnO-MW, ZnO-BS-1-OV, ZnO-BS-1-MW, ZnO-BS-2-MW, and ZnO-BS-4-MW surfaces and to investigate the adsorbed state of ammonia on the surfaces of the catalysts. The bands observed at 3448.72–3456.44 cm^{-1} involve both the –OH stretching vibration of surface hydroxyls bonded to NH_3 molecules through hydrogen bonding and the –NH stretching vibration of the adsorbed NH_3 molecules. The absorption band at

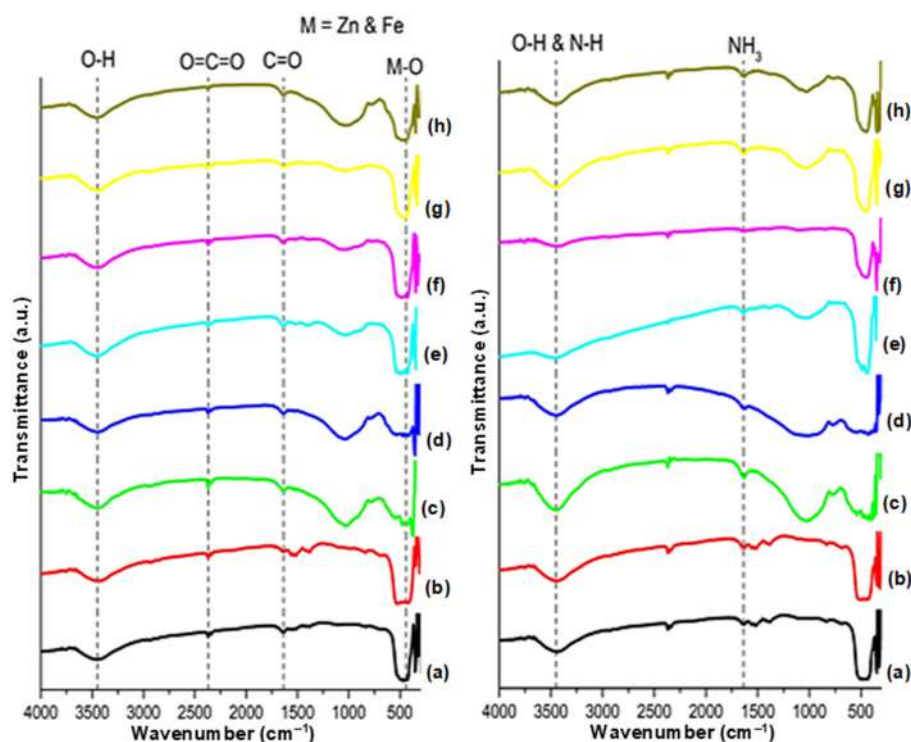


Fig 2. FTIR spectra (a) ZnO, (b) ZnO-MW, (c) BS, (d) BS-MW, (e) ZnO-BS-1-OV, (f) ZnO-BS-1-MW, (g) ZnO-BS-2-MW, and (h) ZnO-BS-4-MW before (left side) and after (right side) ammonia adsorption

1473.62–1635.64 cm^{-1} may be considered as the bending vibration of NH_3 molecules because it is identical to that found in the coordinately bonded NH_3 molecules. However, the intensity of this absorption band decreases in parallel with the decrease of the broadband at 3448.72–3456.44 cm^{-1} , which suggests that the bending vibration is of the weakly adsorbed NH_3 molecules. The appearance of the absorption band at 1473.62 cm^{-1} implies the formation of NH_4^+ ions on the surface of the catalyst. The situation resembles the case of the adsorption of NH_3 on the $\alpha\text{-Fe}_2\text{O}_3$ surface, where NH_4^+ ions are formed by the interaction of NH_3 molecules with physisorbed H_2O on $\alpha\text{-Fe}_2\text{O}_3$ [29]. This absorption appears in the same area as the $\text{C}=\text{O}$ vibration so that it is possible to overlap each other.

The surface morphology of ZnO-BS-1-OV and ZnO-BS-1-MW is illustrated in Fig. 3. These morphological structures can be the evidence to show that ZnO and sand have been mixed and interacted well. The materials proved to be hexagonal-cubic which supported the previous XRD data.

The TEM image of ZnO-BS-1-OV is shown in Fig. 4. TEM studies were carried out to understand the shape characteristics of the crystals. The image confirms that the particles are mostly cubic with slightly hexagonal, which corroborates the previous XRD and SEM data.

From Fig. 5, both materials exhibit Type IV isotherms related to the characteristics of mesoporous materials, according to the IUPAC classification. This typical mesoporous material is represented by the presence of a hysteresis loop at the isotherm. The type of hysteresis possessed by these materials follows the H3 pattern described by IUPAC. The desorption branch tends to be perpendicular to the adsorption branch in the closure region at lower relative pressures. In the hysteresis loop H3, the pores have a wedge or slit geometry, resulting from agglomerates of parallel plateshaped particles [30].

The surface area was calculated using the BET approach, while the pore diameter and volume were calculated using the BJH. Based on the calculation results in Table 4, the surface area of ZnO-BS-1-MW is

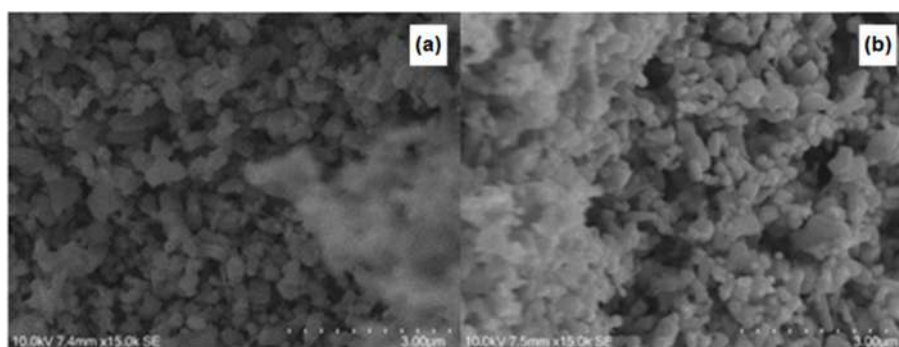


Fig 3. SEM micrographs of (a) ZnO-BS-1-OV and (b) ZnO-BS-1-MW

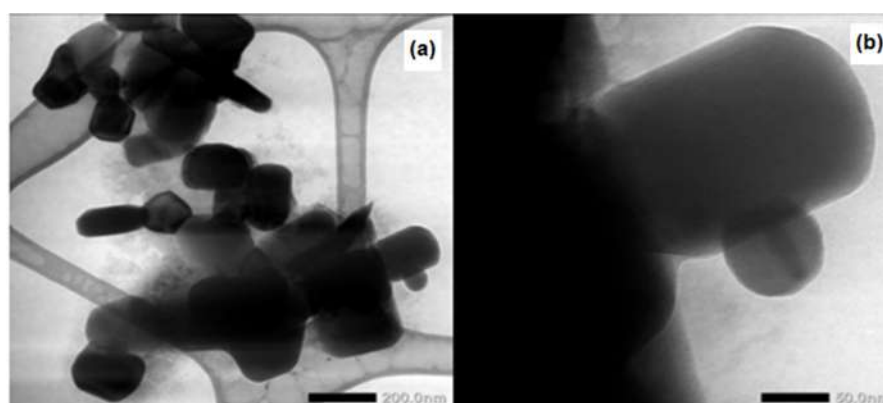


Fig 4. TEM image of ZnO-BS-1-OV in (a) 20,000 and (b) 80,000 times magnification

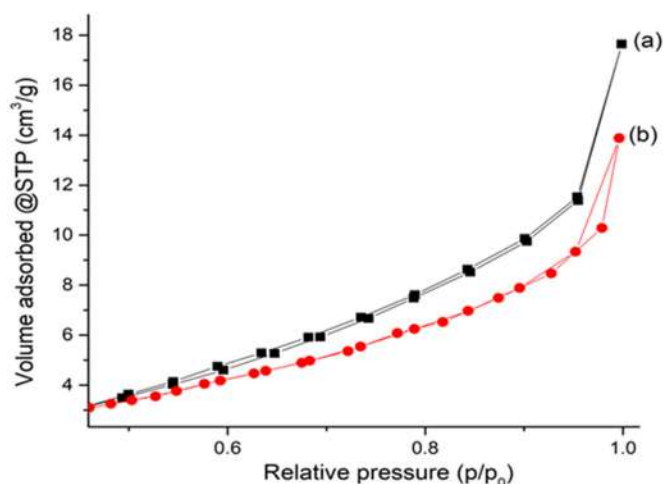


Fig 5. N₂ adsorption-desorption isotherm of (a) ZnO-BS-1-OV and (b) ZnO-BS-1-MW

larger than that of ZnO-BS-1-OV. This value follows the crystallite size of XRD, where a small crystal size will produce a large surface area. This indicates that heating by microwave also affects the textural properties of the material. The resulting pore diameter is also in the mesoporous range, which is between 2–50 nm. This value confirms the appearance of a hysteresis loop on the nitrogen isotherm curve.

The observation of magnetic properties was conducted by attracting each material using an external magnetic field. The more easily attracted indicates that the material is more easily separated from the reaction. Based on Fig. 6, materials containing more BS will be attracted more easily than pure ZnO. This is because the magnetic properties arise from the iron oxides naturally present in the BS material. These magnetic properties also offer benefits for catalyst separation and reuse for ODS to meet the principles of green chemistry. However, the ZnO-BS material was not completely attracted by the magnet. This is based on the method used, namely physical mixing, not chemical reactions so that the resulting interaction between ZnO and BS is only a physical bond.

Catalytic Activity Test

The reaction time chosen for the oxidative desulfurization of dibenzothiophene (ODS-DBT) was 20 min after the addition of H₂O₂. From the literature, insignificant sulfur removal was witnessed after 60 min of reaction time, exceeding to longest tested time (240 min). It was anticipated that at prolonged reaction

Table 4. Textural properties of ZnO-BS-1-OV and ZnO-BS-1-MW

Material	Surface area (m ² /g)	Pore volume (cm ³ /g)	Pore diameter (nm)
ZnO-BS-1-OV	6.649	0.025	15.259
ZnO-BS-1-MW	7.268	0.019	10.715

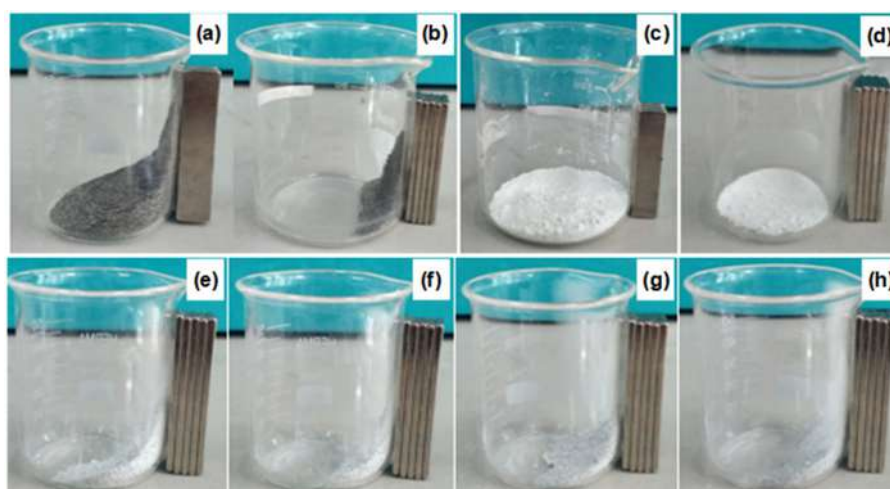


Fig 6. Magnetivity test of (a) BS, (b) BS-MW, (c) ZnO, (d) ZnO-MW, (e) ZnO-BS-1-OV, (f) ZnO-BS-1-MW, (g) ZnO-BS-2-MW, and (h) ZnO-BS-4-MW

time, the reaction does not affect the proportion of desulfurization due to the degradation of most oxidants. Quantitative analysis through titration method discovered that most of H_2O_2 were utilized after reaction, either through selective utilization or unselective utilization due to (i) decomposition to oxygen and water, (ii) hydrogenation to water, and (iii) direct non-selective formation of water.

The operation temperature chosen was 60 °C because the model fuel (*n*-hexane) is evaporated at higher temperatures. Besides, high temperatures will initiate the non-selective decomposition of H_2O to produce O_2 and H_2O , subsequently suppressing the oxidation capability [31]. Availability of the H_2O_2 throughout the reaction is crucial since it will form an active species that is capable of oxidizing sulfur to sulfoxide and sulfone. Another reason was the sulfur removal appeared to be unsatisfying at a temperature of 40 °C from Li and Liu's research, which may be because H_2O_2 and the catalyst cannot work efficiently under low reaction temperature [32]. Raising the reaction temperature from 40 to 60 °C led to a remarkable increase in sulfur removal. However, a further increase of the reaction temperature to 70 °C caused a decrease in the desulfurization efficiency. This is because the high temperature leads to the partial decomposition of H_2O_2 , which brings down the oxidation efficiency.

The concentrations of DBT were analyzed using a UV spectrophotometer. The phase fractional was taken from the *n*-hexane phase for DBT analysis. After the reaction, the oxidized DBT was separated by decantation after collecting the catalyst by an external magnetic field. Then, the DBT concentration in the hydrocarbon layer was calculated by UV-Vis spectrophotometer. The absorption at 279 nm was used to monitor the DBT concentration based on the scanning of DBT solution to find the maximum wavelength of DBT in *n*-hexane solution. The highest absorbance found was 3.629 in wavelength of 279 nm. Therefore, 279 nm was chosen as a maximum wavelength to further observe the absorbance found in oxidized DBT.

The catalytic ODS-DBT process consists of two steps. In the first step, sulfur-containing fuel oil (in this case, DBT in *n*-hexane solution) was subjected to catalytic

oxidation to produce oxidized sulfur compounds (sulfones/sulfoxides) in the presence of an oxidant (H_2O_2). In the second step, the oxidized sulfur compounds were removed from the reaction mixture using the liquid/liquid extraction method. In this research, a highly polar solvent, acetonitrile, was used to extract the sulfur compounds [33].

Table 5 shows that Microwave treatment on the material can reduce the catalytic activity as happened in $ZnO-BS-1-OV \rightarrow ZnO-BS-1-MW$, $BS \rightarrow BS-MW$, and $ZnO \rightarrow ZnO-MW$. In addition, the higher BS or lower ZnO content in the mixture was able to increase the catalytic activity. It might happen due to the availability of $Fe=O$ catalytic sites present in BS responsible for activating iron superoxide for the oxidation reaction. Other contents in BS, such as silica and alumina oxide, may also work synergistically with iron oxide. The highest DBT removal efficiency is shown by the use of $ZnO-BS-1-OV$ as a catalyst due to its highest acidity.

The $ZnO-BS-1-OV$ catalyst has shown to be efficient in the removal of DBT compounds. It is believed that the reaction was initiated by nucleophilic attack of H_2O_2 by the $Fe=O$ bond of $ZnO-BS-1-OV$ catalyst surface, which had generated active intermediate iron peroxides. Then, nucleophilic attack of the sulfur atom with higher electron density in DBT on iron peroxide was conducted to form sulfoxide and regenerated $Fe=O$ where the sulfoxide later undergoes further oxidation by using iron peroxide that converts it to a corresponding sulfone and regenerates $Fe=O$ for a close cycle of reaction. This mechanism demonstrates that the presence of active $Fe=O$ sites is important for an

Table 5. Catalytic activity in ODS and Non-ODS of DBT

Material	Removal of DBT (%)	
	ODS	Non-ODS
ZnO	74.17	-
ZnO-MW	73.61	-
BS	79.24	-
BS -MW	74.36	-
ZnO-BS-1-OV	81.59	75.27
ZnO-BS-1-MW	70.54	-
ZnO-BS-2-MW	71.53	-
ZnO-BS-4-MW	71.53	-

efficient ODS reaction. Thus, ZnO-BS-1-OV with a higher amount of Fe justifies the availability of more Fe=O sites compared to other ZnO-BS catalysts.

The efficiency of ODS-DBT was also known as the activity of the catalyst. It was shown that the efficiency of ODS-DBT increase with the increase of the acidity of the catalyst. Interaction between H₂O₂ and acidic sites of the catalyst improves the electrophilic attack of H₂O₂ on DBT as a weak nucleophile, forming intermediary peroxometallic complex on the catalyst surface, thus increasing the efficiency of ODS-DBT. The ZnO-BS-1-OV showed the highest catalytic activity because of its highest acidity, while the ZnO-BS-1-MW showed the lowest catalytic activity due to the lowest acidity.

Furthermore, the ZnO-BS-1-OV catalyst will be reused to compare its activity in ODS and non-ODS reactions. From the research results in Table 5, the addition of H₂O₂ as an oxidizing agent can increase the efficiency of DBT removal. This is supported by the presence of iron oxide contained in BS capable of activating oxidants. It is important to highlight that during the oxidation process, few bubbles were observed when the fresh catalyst was immersed in the DBT solution, indicating the presence of O₂ gas originated from the decomposition of hydrogen peroxide.

The ability to remove the sulfur compound without altering the hydrocarbon structure is crucial in preserving the quality of fuel. Detail analysis on FTIR had been discovered, and it confirmed that all the catalysts are not affecting the main structure of the treated fuel.

Fig. 7 shows the FTIR spectra comparison between the DBT and oxidized DBT. Both compounds show almost identical bands, except that the two new bands at nearly 964.61 cm⁻¹ at the ZnO-BS-1-OV that can be assigned as the asymmetrical and symmetrical stretching vibration modes of sulfoxide [34] and band at 1064.71 and 1056.99 cm⁻¹ in all samples correspond to the S=O bond of sulfone [35]. Thus, it confirmed that the oxidation process successfully occurred and produced an oxygenated sulfur compound. Some of these functional groups are still shown in the upper layer after the extraction process due to the removal of DBT is not 100% based on the results in UV-visible spectrometry. Other

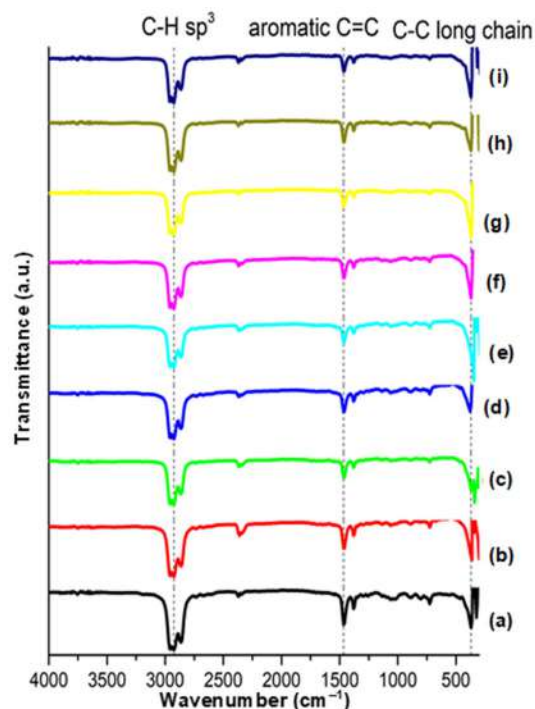


Fig 7. DBT solution (a) before ODS and after ODS using (b) ZnO (c) ZnO-MW (d) BS (e) BS-MW (f) ZnO-BS-1-OV (g) ZnO-BS-1-MW (h) ZnO-BS-2-MW (i) ZnO-BS-4-MW

bands shown in the FTIR spectra are 2954.95–2862.36 cm⁻¹ correspond to the C–H sp³, 1465.90–1381.03 cm⁻¹ correspond to the aromatic C=C, and 370.33–324.04 cm⁻¹ correspond to the C–C long-chain [36].

■ CONCLUSION

Microwave treatment on the material can reduce acidity and crystallinity level but increase the crystallite size. High BS content or low ZnO content in ZnO-BS-MW material can increase acidity and reduce crystallinity level as well as crystallite size. Although the surface area of ZnO-BS-1-OV is smaller than that of ZnO-BS-1-MW, the material can produce the highest catalytic activity in ODS-DBT. This proves that the acidity of the catalyst dramatically affects the efficiency of DBT removal. The presence of iron oxide in the beach sand (BS) material, in addition to functioning to activate oxidant H₂O₂, also offers benefits for the separation of catalysts after the ODS reaction.

■ ACKNOWLEDGMENTS

The authors would like to thank all the members involved in the *Program Penelitian Kolaborasi Indonesia* (PPKI) 2021 project collaboration between Sebelas Maret University, Sepuluh Nopember Institute of Technology, and Universitas Gadjah Mada. This research project is fully funded by Universitas Gadjah Mada under the scheme of *Program Penelitian Kolaborasi Indonesia* (PPKI) 2021 with the contact number: 1070/UN1/DITLIT/DITLIT/PT/2021 for Wega Trisunaryanti.

■ REFERENCES

- [1] Mohan, D., Pittman, C.U., and Steele, P.H., 2006, Pyrolysis of wood/biomass for bio-oil: A critical review, *Energy Fuels*, 20 (3), 848–889.
- [2] Betiha, M.A., Rabie, A.M., Ahmed, H.S., Abdelrahman, A.A., and El-Shahat, M.F., 2018, Oxidative desulfurization using graphene and its composites for fuel containing thiophene and its derivatives: An update review, *Egypt. J. Pet.*, 27 (4), 715–730.
- [3] Alizadeh, A., Fakhari, M., Khodeai, M.M., Abdi, G., and Amirian, J., 2017, Oxidative desulfurization of model oil in an organic biphasic system catalysed by Fe₃O₄@SiO₂-ionic liquid, *RSC Adv.*, 7 (56), 34972–34983.
- [4] Dutta, A.M., Saikia, B.K., and Baruah, B.P., 2012, Oxidative desulphurization of North-East Indian coals by using different metal ions/oxides as catalyst, *Int. J. Innovative Res. Dev.*, 1 (7), 214–220.
- [5] Tang, L., Luo, G., Zhu, M., Kang, L., and Dai, B., 2013, Preparation, characterization and catalytic performance of HPW-TUD-1 catalyst on oxidative desulfurization, *J. Ind. Eng. Chem.*, 19 (2), 620–626.
- [6] Yun, G.N. and Lee, Y.K., 2013, Beneficial effects of polycyclic aromatics on oxidative desulfurization of light cycle oil over phosphotungstic acid (PTA) catalyst, *Fuel Process. Technol.*, 114, 1–5.
- [7] Shen, C., Wang, Y.J., Xu, J.H., and Luo, G.S., 2015, Synthesis of TS-1 on porous glass beads for catalytic oxidative desulfurization, *Chem. Eng. J.*, 259, 552–561.
- [8] Xiao, J., Wu, L., Wu, Y., Liu, B., Dai, L., Li, Z., Xia, Q., and Xi, H., 2014, Effect of gasoline composition on oxidative desulfurization using a phosphotungstic acid/activated carbon catalyst with hydrogen peroxide, *Appl. Energy*, 113, 78–85.
- [9] Chen, Y., Zhao, S., and Song, Y.F., 2013, An efficient heterogeneous catalyst based on highly dispersed Na₇H₂LaW₁₀O₃₆·32H₂O nanoparticles on mesoporous silica for deep desulfurization, *Appl. Catal., A*, 466, 307–314.
- [10] Wan Abu Bakar, W.A., Ali, R., Abdul Kadir, A.A., and Wan Mokhtar, W.N.A., 2012, Effect of transition metal oxides catalysts on oxidative desulfurization of model diesel, *Fuel Process. Technol.*, 101, 78–84.
- [11] Guo, J.X., Fan, L., Peng, J.F., Chen, J., Yin, H.Q., and Jiang, W.J., 2014, Desulfurization activity of metal oxides blended into walnut shell based activated carbons, *J. Chem. Technol. Biotechnol.*, 89 (10), 1565–1575.
- [12] Hassanpour, A., Hosseinzadeh-Khanmiri, R., Babazadeh, M., and Edjlali, L., 2016, ZnO NPs: An efficient and reusable nanocatalyst for the synthesis of nitrones from DAG using H₂O as a solvent at room-temperature, *Res. Chem. Intermed.*, 42 (3), 2221–2231.
- [13] Dar, B.A., Mohsin, M., Basit, A., and Farooqui, M., 2013, Sand: A natural and potential catalyst in renowned Friedel Craft's acylation of aromatic compounds, *J. Saudi Chem. Soc.*, 17 (2), 177–180.
- [14] Arellano, U., Wang, J.A., Timko, M.T., Chen, L.F., Paredes-Carrera, S.P., Asomoza, M., González-Vargas, O.A., and Llanos, M.E., 2014, Oxidative removal of dibenzothiophene in a biphasic system using sol-gel Fe–TiO₂ catalysts and H₂O₂ promoted with acetic acid, *Fuel*, 126, 16–25.
- [15] Adeyi, A.A. and Aberuaga, F., 2012, Comparative analysis of adsorptive desulphurization of crude oil by manganese dioxide and zinc oxide, *Res. J. Chem. Sci.*, 2 (8), 14–20.
- [16] Tang, Q., Lin, S., Cheng, Y., Liu, S., and Xiong, J.R., 2013, Ultrasound-assisted oxidative desulfurization

- of bunker-C oil using *tert*-butyl hydroperoxide, *Ultrason. Sonochem.*, 20 (5), 1168–1175.
- [17] Omran, M., Fabritius, T., Heikkinen, E.P., and Chen, G., 2017, Dielectric properties and carbothermic reduction of zinc oxide and zinc ferrite by microwave heating, *R. Soc. Open Sci.*, 4 (9), 170710.
- [18] Teh, P.F., Pramana, S.S., Kim, C., Chen, C.M., Chuang, C.H., Sharma, Y., Cabana, J., and Madhavi, S., 2013, Electrochemical reactivity with lithium of spinel-type $\text{ZnFe}_{2-y}\text{Cr}_y\text{O}_4$ ($0 \leq y \leq 2$), *J. Phys. Chem. C*, 117 (46), 24213–24223.
- [19] Zhu, W., Wu, P., Yang, L., Chang, Y., Chao, Y., Li, H., Jiang, Y., Jiang, W., and Xun, S., 2013, Pyridinium-based temperature-responsive magnetic ionic liquid for oxidative desulfurization of fuels, *Chem. Eng. J.*, 229, 250–256.
- [20] Piscopo, C.G., Tochtermann, J., Schwarzer, M., Boskovic, D., Maggi, R., Maestri, G., and Loebbecke, S., 2018, Titania supported on silica as an efficient catalyst for deep oxidative desulfurization of a model fuel with exceptionally diluted H_2O_2 , *React. Chem. Eng.*, 3 (1), 13–16.
- [21] Ercuta, A., and Chirita, M., 2013, Highly crystalline porous magnetite and vacancy-ordered maghemite microcrystals of rhombohedral habit, *J. Cryst. Growth*, 380, 182–186.
- [22] Cambier, P., 1986, Infrared study of goethites of varying crystallinity and particle size: II. Crystallographic and morphological changes in series of synthetic goethites, *Clay Miner.*, 21 (2), 201–210.
- [23] Namduri, H., and Nasrazadani, S., 2008, Quantitative analysis of iron oxides using Fourier transform infrared spectrophotometry, *Corros. Sci.*, 50 (9), 2493–2497.
- [24] Long, T., Yin, S., Takabatake, K., Zhnag, P., and Sato, T., 2009, Synthesis and characterization of ZnO nanorods and nanodisks from zinc chloride aqueous solution, *Nanoscale Res. Lett.*, 4 (3), 247–253.
- [25] Khanna, L., and Verma, N.K., 2013, Size-dependent magnetic properties of calcium ferrite nanoparticles, *J. Magn. Magn. Mater.*, 336, 1–7.
- [26] Parvin, T., Keerthiraj, N., Ibrahim, I.A., Phanichphant, S., and Byrappa, K., 2012, Photocatalytic degradation of municipal wastewater and brilliant blue dye using hydrothermally synthesized surface-modified silver-doped ZnO designer particles, *Int. J. Photoenergy*, 2012, 670610.
- [27] Pholnak, C., Sirisathitkul, C., Suwanboon, S., and Harding, D.J., 2014, Effects of precursor concentration and reaction time on sonochemically synthesized ZnO nanoparticles, *Mater. Res.*, 17 (2), 405–411.
- [28] Franco, R.L.M., Oliveira, T.G., Pedrosa, A.M.G., Naviciene, S., and Souza, M.J.B., 2013, Textural properties of nickel, palladium and titanium oxides supported on MCM.41 materials and their application on oxidative desulfurization of dibenzothiophene, *Mater. Res.*, 16 (6), 1449–1456.
- [29] Adam, F., Jeannot, F., Dupre, B., and Gletzer, C., 1988, The remarkable effect of water vapour on the cracking of hematite during its reduction into magnetite, *React. Solids*, 5 (2-3), 115–127.
- [30] Thommes, M., Kaneko, K., Neimark, A.V., Olivier, J.P., Rodriguez-Reinoso, F., Rouquerol, J., and Sing, K.S.W., 2015, Physisorption of gases, with special reference to the evaluation of surface area and pore size distribution (IUPAC Technical Report), *Pure Appl. Chem.*, 87 (9-10), 1051–1069.
- [31] Zhang, X., Zhu, Y., Huang, P., and Zhu, M., 2016, Phosphotungstic acid on zirconia-modified silica as catalyst for oxidative desulfurization, *RSC Adv.*, 6 (73), 69357–69364.
- [32] Li, B., and Liu, Z., 2011, “Synthesis and Characterization of Ordered Mesoporous Silica Pillared Clay with HPW Heteropoly Acid Encapsulated into the Framework and Its Catalytic Performance for Deep Oxidative Desulfurization of Fuels” in *Metal, Ceramic and Polymeric Composites for Various Uses*, Eds. Cuppoletti, J., InTechOpen, Rijeka, 225–238.
- [33] Hossain, M.N., Choi, M.K., Park, H.C., and Choi, H.S., 2020, Purifying of waste tire pyrolysis oil using an S-ZrO₂/SBA-15-H₂O₂ catalytic oxidation method, *Catalysts*, 10 (4), 368.

- [34] Calligaris, M., 2004, Structure and bonding in metal sulfoxide complexes: An update, *Coord. Chem. Rev.*, 248 (3-4), 351–375.
- [35] Shakirullah, M., Ahmad, I., Ishaq, M., and Ahmad, W., 2009, Study on the role of metal oxides in desulphurization of some petroleum fractions, *J. Chin. Chem. Soc.*, 56 (1), 107–114.
- [36] Abdul-Kadhim, W., Deraman, M.A., Abdullah, S.B., Tajuddin, S.N., Yusoff, M.M., Taufiq-Yap, Y.H., and Rahim, M.H.A., 2017, Efficient and reusable iron-zinc oxide catalyst for oxidative desulfurization of model fuel, *J. Environ. Chem. Eng.*, 5 (2), 1645–1656.

Risk Assessment of Toxic Metals from Drinking Water of Taluka Ghorābāri, Sindh, Pakistan

Abdul Raheem Shar^{1*}, Ghulam Qadir Shar¹, Zulfiqar Ali Jumani¹, Aslam Khan Pathan¹, Zubeda Bhatti¹, Ali Raza Rind², and Ghulam Mujtaba Jogi¹

¹Institute of Chemistry, Shah Abdul Latif University Khairpur, Sindh 66020, Pakistan

²Institute of Physics, University of Sindh, Jamshoro 76080, Sindh, Pakistan

* **Corresponding author:**

tel: +92-3063402926

email: araheem.shar@salu.edu.pk

Received: November 10, 2021

Accepted: January 10, 2022

DOI: 10.22146/ijc.70345

Abstract: In the current study, the quality of groundwater used for drinking purposes was assessed in Taluka Ghorābāri, Sindh, Pakistan. Twenty-five sampling locations were selected for the collection of groundwater. Samples were analyzed for physicochemical and heavy metal analysis, followed by standard methods. Detection of heavy metals was conducted using Atomic Absorption Spectrophotometer. Heavy metals which exceeded the WHO safe limit included Cr (28%), Fe (16%), Mn (48%), and Ni (16%) from the drinking water of the study area. The Cu and Zn were found within the safe limit in all drinking water samples of the study area. The Daily Intake of heavy Metals (DIM) and Health Risk Indexes (HRI) Assessments were calculated to determine risk assessments; the order of mean DIM values was observed as Ni > Cu > Fe > Zn > Cr while HRI was observed in the order of Cu > Mn > Zn > Fe > Cr. The HRI values were observed less than one for both adults and children, which shows the lack of possible health hazards for the people of the study area.

Keywords: heavy metals; WHO; DIM; HRI; risk assessments

■ INTRODUCTION

Water is essential for all kinds of life. On the earth, about 3% of fresh water is available, out of which only 0.01% can be utilized for the use of people. Anthropogenic and lithogenic activities severely affect this little amount of freshwater, like vehicular emission, mining, urbanization, rapid population growth, and invalid development in industries and agriculture [1]. Most people of urban and rural areas of developing countries are unable to know the quality of groundwater they use. According to an estimation made by the WHO, yearly deaths of 842,000 took place in developing countries due to various reasons such as unsafe hygiene, sanitation, and water supply. Meanwhile, about 780 million people from the globe do not have access to safe drinking water because of chemical and bacteriological pollutants [2]. Reports reveal that presence of heavy metals in groundwater has enhanced threats in the world because

heavy metals may cause various types of diseases, including cancers.

So many drinking water sources are found, such as the accessibility of rivers, reservoirs, lakes, and aquifers. The severe natural disaster and health risk of people may arise from contamination of drinking water whose origin is found from geological variations and anthropogenic sources. Variation in water quality and contribution to water pollution arises mostly from the release of industrial wastewater [3]. The disease state and main health controlling factors are associated with water quality characteristics. Potentially toxic metals, physical, chemical, and biological parameters are included in water quality characteristics since heavy metals are more toxic because of their bio-accumulative, non-degradable and toxic nature. Non-essential or toxic and essential elements are included in heavy metals. Regular functioning of essential elements is extremely important in a particular quantity since their higher amount may

cause destructive consequences. Heavy metals, for instance, Pb, Cd, As, and Hg, are highly detrimental for life, even at trace levels. Unfavorable effects of toxic metals include carcinogenesis, cardiovascular disease, nerve disease, anemia, mental stoppage, liver, kidney and brain problems, nausea, hypertension, irritability, vomiting, abdominal pain, and headache [4].

Supportive information is obtained for regular monitoring of water quality. Hence, various investigations from developed and developing countries focused on drinking water quality on a regular basis. The more severe problem of water contamination is observed in developing countries because of the high growth rate of population and less cost on treatment features. Pakistan is also facing severe drinking water problems in super cities like other developing neighboring countries [5]. There are different pathways by which extremely poisonous heavy metals accumulate in the water system, for instance, water drainage, industrial effluents, agricultural runoffs, range of bedrock, and environmental deposition [6]. Furthermore, the high content of toxic metals contaminates the groundwater and surface water, badly affecting water quality and human health. Toxic metals occur naturally in the crust of the earth since variation in their concentrations does not remain the same in different locations [7]. Although heavy metals have distinctive atmospheric toxicity, therefore, they cannot be converted into a non-toxic structure. Surface water contamination occurring due to the discharges and runoff of groundwater has been a matter of universal ecological distress since the liberation of heavy metals once into the atmosphere through food, water, and air or synthetic chemicals are taken into the human body by dermal absorption, ingestion, and inhalation. In the case of surface water conditions, ingestion and dermal absorptions are major sources of introduction [8].

The steady increase of contaminants may take place in the human body if the accumulation and entering of these toxic metals occur faster as compared to the discard of the detoxification mechanisms. For toxicity in the body, higher content of toxins is not a requirement because in body tissues amassing heavy metals may be observed steady and eventually may get the concentration

much more than the allowable level. It is, therefore, necessary to determine a risk assessment of daily human purpose. For this purpose, it is important to characterize physical situations, recognition of potential exposure populations and mechanisms, as well as assess the chemical intakes and exposure concentrations. Since heavy metals are major atmospheric contaminants and their toxic nature is a threat of enhancing consequence for atmospheric, nutritional, evolutionary, and ecological reasons [9]. Some important heavy metals at lesser content are supposed to be very important in the metabolic movements of living things; their long-term exposure may cause cancers, kidney, and liver problems and therefore are believed to be harmful to human health. Severe health problems may be caused to humans due to toxic metals and may possibly cause numerous diseases derived from the concentration and kind of metal concerned [10]. Overuse of copper is a casual issue for kidney damage, Alzheimer's disease, mental diseases, and gastrointestinal cancers. The main purpose of this study was to analyze physicochemical and chemical parameters from rural areas of Taluka Ghorābāri as well as to determine human health risk assessments. Our focus is to assess drinking water quality and to aware the people of the area under study because contaminated drinking water may cause various diseases, including different types of cancers, kidney, liver, and cardiovascular problems.

■ EXPERIMENTAL SECTION

Study Area

Ghorābāri is the study area situated in the coastal area of district Thatta, Sindh, Pakistan. Coordinates of Ghorābāri are 24° 13' 0" N, 67° 34' 0" E (Fig. 1). Its population is about 174,088 residing in scattered towns form and the Sindhi is the local language spoken in the area. The land of the villages consists of large ploughed fields. Ghorābāri is less developed since roads are unpaved and cob houses made by the residents. Health care centers and personal care clinics are less in the area. Education of the area is poor. Since for three centuries, inhabitants of Sindhi and some Baloch tribes are settled in Ghorābāri. It was observed in the present study that

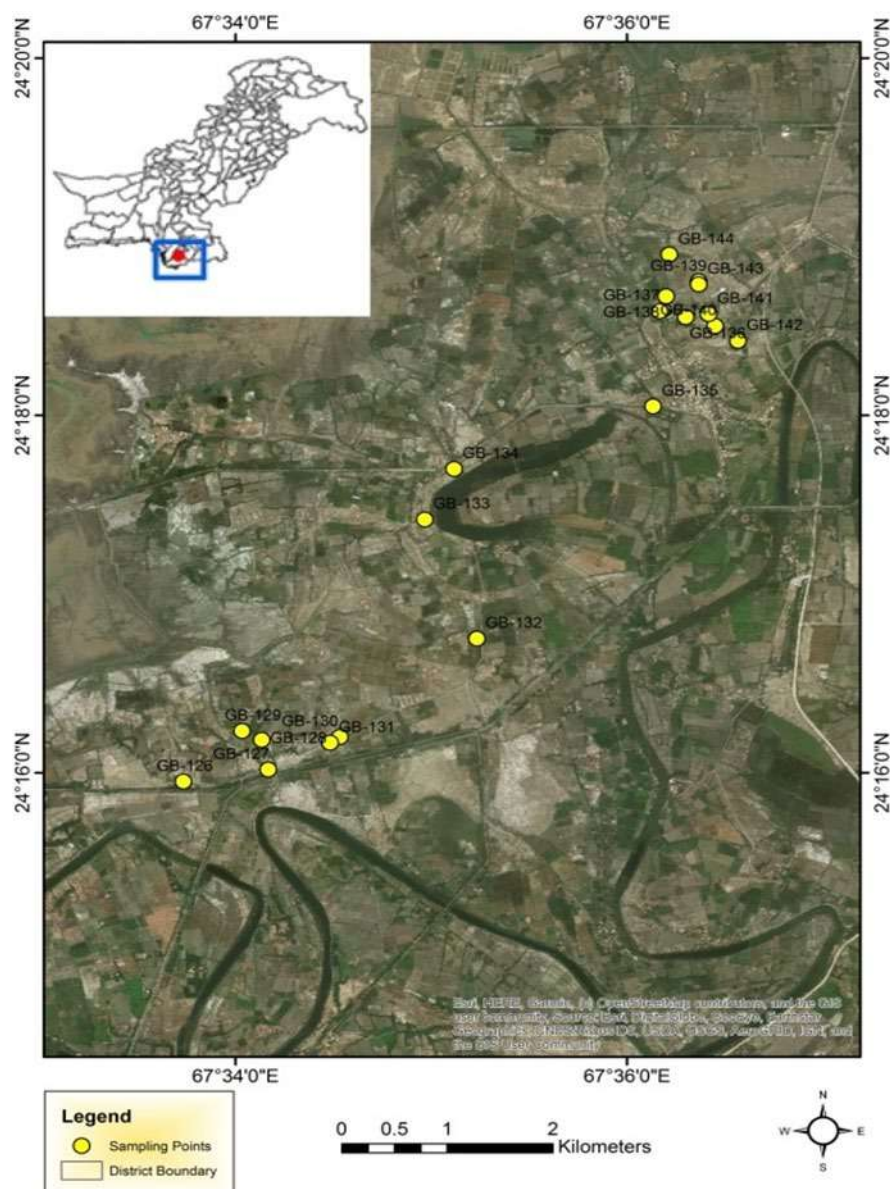


Fig 1. Sampling location map of the study area

people of the study area derived groundwater for drinking purposes from hand pumps situated mostly in rural areas of the Taluka Ghorābāri.

Materials

The spectroscopic purity of reagents and chemicals used in this study was about 99.9% (Merck Darmstadt, Germany). Standard solutions of all six heavy metals were prepared by successive dilution method from 1000 mg/L certified standard solution of corresponding heavy metals (FlukaKamica, Buchs, Switzerland).

Instrumentation

Heavy metals from drinking water samples were determined by standard methods. Atomic Absorption Spectrophotometer (Analytic Jena) was used to determine heavy metals such as chromium, nickel, copper, iron, manganese, and zinc under standard conditions. Prepared samples were transported to the Laboratory of Pakistan Council of Research in Water Resources (PCRWR) Government of Pakistan Ministry of Science & Technology National Water Quality Laboratory, Islamabad, for heavy metal analyses.

Procedure

Sampling

The 25 groundwater samples used for drinking purposes were collected from hand pumps fitted by the people of the rural areas of Taluka Ghorabari. Drinking water samples were collected after running the water sources for five minutes or till fresh water. Sampling bottles were labeled as GB-01 to GB-25. Most rural areas of the Taluka Ghorābāri were selected for sampling purposes. For heavy metals determination, water collected in sampling bottles was acidified with nitric acid. Samples were quickly shifted to the Shah Abdul Latif University Khairpur for further analytical processes and stored at 4 °C.

Health risk assessment for humans

The health risk for humans through consumption of heavy metals found in infected drinking water was assessed with the help of formulas for health risks like DIM and HRI.

Daily intake of metals (DIM)

There are various pathways through which heavy metals contact the human body, for instance, oral intake, ingestion, inhalation, food chain, and dermal interaction since the most important role is played by oral ingestion in amassing of heavy metals in humans. The following equation was used to calculate the DIM adapted from [11].

$$\text{DIM} = \frac{\text{Cm} \times \text{DIw}}{\text{BW}} \quad (1)$$

where Cm, DIw, and BW are the concentration of heavy metals in water, average daily intake of water (2 L per day for adults and 1 L per day for children) [12], and average body weight (72.0 and 23.7 kg for adult and children respectively).

Health risk indexes (HRIs) of heavy metals

Eq. (2) given below was used for the calculation of HRIs of toxic metals by ingestion of water [13].

$$\text{HRI} = \frac{\text{DIM}}{\text{RfD}} \quad (2)$$

where, DIM and RfD are average daily intake and toxicity oral reference dose of heavy metals. The RfD values of heavy metals were represented as; Cr (1.5 mg/kgbw/d), Ni

(0.02 mg/kgbw/d), Cu (0.04 mg/kgbw/d), Mn (0.033 mg/kgbw/d), Fe (0.7 mg/kgbw/d) and Zn (0.30 mg/kgbw/d). The level of selected metals is considered safe when HRIs are less than 1 [14].

RESULTS AND DISCUSSION

Little quantities of Cr(III) is present in food, wine, and water, whereas inhaled Cr(VI) is very toxic. Stomach tumors and allergic contact dermatitis may be caused when Cr(VI) is ingested through water [15]. The WHO guideline of Cr for potable water is 0.05 mg/L, since Cr was measured from 0.028 to 0.057 mg/L. The average content of Cr from potable water of the study area was determined as 0.044 mg/L. The higher limit of Cr as compared to prescribed limit was measured in samples GB-01 (0.055 mg/L), GB-03 (0.057 mg/L), GB-10 (0.055 mg/L), GB-16 (0.056 mg/L), GB-21 (0.055 mg/L), GB-24 (0.051 mg/L), and GB-25 (0.055 mg/L) (Table 1).

The dietary intake of Ni with a concentration of approximately 70–100 µg/day was prescribed with less than 10% may release in urine. Relatively high Ni content is observed above than assessed average intake due to stainless steel may release into food [16]. The concentration of Ni greater than allowable level of 0.02 mg/L was observed in potable water labelled as, G-08 (0.021 mg/L), G-19 (0.021 mg/L), G-20 (0.026 mg/L), and G-22 (0.024 mg/L). The minimum and maximum concentration of Ni was found as 0.010 and 0.026 mg/L, respectively, with a mean concentration of 0.017 mg/L (Table 1).

Copper is essential for the human being. The consequences of high Cu exposure on the well-being of people are most probably not known. Toxic effects of copper are recognized for high, acute Cu contact containing acute indications such as vomiting, nausea, and cramping in the gastrointestinal tract [17]. The concentration of Cu greater than 30 mg/L when utilized by polluted beverages or water causes copper-related diseases. The concentration of Cu > 1, when ingested by an adult, may cause acute toxemia and finally death. The WHO guideline of Cu in potable water is recommended as 2.0 mg/L, although all water samples showed the Cu

Table 1. Heavy metal contents in water collected from the area under study

Sample ID	Cr \pm SD	Cu \pm SD	Fe \pm SD	Mn \pm SD	Ni \pm SD	Zn \pm SD
G-1	0.055 \pm 0.001	0.900 \pm 0.003	0.150 \pm 0.002	0.020 \pm 0.002	0.018 \pm 0.002	0.190 \pm 0.005
G-2	0.040 \pm 0.001	0.040 \pm 0.001	0.110 \pm 0.002	0.050 \pm 0.002	0.016 \pm 0.001	0.064 \pm 0.004
G-3	0.057 \pm 0.002	0.110 \pm 0.005	0.060 \pm 0.002	0.040 \pm 0.003	0.017 \pm 0.001	0.066 \pm 0.005
G-4	0.045 \pm 0.001	0.140 \pm 0.005	0.370 \pm 0.003	0.030 \pm 0.003	0.011 \pm 0.001	0.064 \pm 0.006
G-5	0.039 \pm 0.001	0.120 \pm 0.005	0.090 \pm 0.002	0.310 \pm 0.005	0.014 \pm 0.001	0.060 \pm 0.003
G-6	0.046 \pm 0.001	0.800 \pm 0.005	0.170 \pm 0.001	0.040 \pm 0.003	0.020 \pm 0.000	0.210 \pm 0.005
G-7	0.028 \pm 0.002	0.740 \pm 0.008	0.140 \pm 0.002	0.060 \pm 0.003	0.020 \pm 0.000	0.061 \pm 0.005
G-8	0.04 \pm 0.0010	0.042 \pm 0.003	0.190 \pm 0.003	0.030 \pm 0.001	0.021 \pm 0.003	0.062 \pm 0.003
G-9	0.036 \pm 0.001	0.041 \pm 0.002	0.120 \pm 0.005	0.040 \pm 0.003	0.015 \pm 0.001	0.071 \pm 0.007
G-10	0.055 \pm 0.002	0.048 \pm 0.003	0.320 \pm 0.003	0.050 \pm 0.004	0.017 \pm 0.001	0.066 \pm 0.007
G-11	0.048 \pm 0.002	0.800 \pm 0.004	0.180 \pm 0.003	0.030 \pm 0.002	0.010 \pm 0.001	0.270 \pm 0.004
G-12	0.034 \pm 0.002	0.670 \pm 0.005	0.090 \pm 0.003	0.030 \pm 0.001	0.015 \pm 0.002	0.061 \pm 0.003
G-13	0.039 \pm 0.001	0.050 \pm 0.003	0.280 \pm 0.003	0.060 \pm 0.003	0.017 \pm 0.001	0.063 \pm 0.005
G-14	0.040 \pm 0.002	0.044 \pm 0.004	0.110 \pm 0.004	0.060 \pm 0.002	0.015 \pm 0.001	0.068 \pm 0.004
G-15	0.036 \pm 0.002	0.042 \pm 0.004	0.360 \pm 0.003	0.100 \pm 0.003	0.017 \pm 0.001	0.060 \pm 0.005
G-16	0.056 \pm 0.001	0.600 \pm 0.007	0.050 \pm 0.001	0.050 \pm 0.003	0.012 \pm 0.002	0.260 \pm 0.005
G-17	0.046 \pm 0.002	0.049 \pm 0.003	0.080 \pm 0.002	0.020 \pm 0.003	0.018 \pm 0.001	0.060 \pm 0.005
G-18	0.032 \pm 0.001	0.050 \pm 0.003	0.130 \pm 0.001	0.160 \pm 0.004	0.016 \pm 0.001	0.060 \pm 0.006
G-19	0.036 \pm 0.001	0.038 \pm 0.002	0.170 \pm 0.003	0.060 \pm 0.007	0.021 \pm 0.002	0.003 \pm 0.001
G-20	0.043 \pm 0.001	0.050 \pm 0.006	0.310 \pm 0.002	0.110 \pm 0.003	0.026 \pm 0.002	0.061 \pm 0.000
G-21	0.055 \pm 0.001	1.000 \pm 0.012	0.020 \pm 0.003	0.080 \pm 0.003	0.016 \pm 0.002	0.220 \pm 0.005
G-22	0.036 \pm 0.000	0.048 \pm 0.003	0.120 \pm 0.001	0.160 \pm 0.002	0.024 \pm 0.001	0.077 \pm 0.004
G-23	0.043 \pm 0.000	0.067 \pm 0.002	0.160 \pm 0.003	0.080 \pm 0.006	0.015 \pm 0.002	0.061 \pm 0.002
G-24	0.051 \pm 0.003	0.050 \pm 0.003	0.080 \pm 0.004	0.090 \pm 0.002	0.017 \pm 0.002	0.061 \pm 0.004
G-25	0.055 \pm 0.001	0.045 \pm 0.003	0.150 \pm 0.002	0.050 \pm 0.003	0.014 \pm 0.001	0.059 \pm 0.005

concentration below the prescribed limit. Since the range was observed as 0.040 to 1.000 mg/L, the mean Cu content of 0.239 mg/L was found in potable water samples of the study area (Table 1).

Iron is very important for life. The Nitrogenase enzyme is included in repetitive iron-sulfur clusters for the biological fixation of nitrogen. Iron-containing proteins carry out the use, transport, and storage of oxygen [18]. The concentration range of Fe from potable water was measured as 0.020 to 0.370 mg/L with an average content of 0.160 mg/L. The WHO allowable level of Fe is recommended as 0.3 mg/L, since samples in which higher Fe content was found comprise; GB-04 (0.37 mg/L), GB-10 (0.32 mg/L), GB-15 (0.36 mg/L), and GB-20 (0.31 mg/L) (Table1).

Manganese is believed to be important for growth and human health, metabolism as well as antioxidant

system. The neurogenerative disorder known as Parkinson's disease is observed due to ingestion of an excessive amount of Mn [19]. The permissible WHO limit of Mn is recommended as 0.05 mg/L, however, samples in which Mn content greater than allowable limit was found include; GB-05, G-07, G-13, G-14, G-15, G-18, G-19, G-20, G-21, G-22, G-23, and G-24 as; 0.31, 0.06, 0.06, 0.06, 0.10, 0.16, 0.06, 0.11, 0.08, 0.16, 0.08, and 0.09 mg/L, respectively (Table 1).

Zinc is extremely important for animals, humans, plants, microorganisms, and animals. Zinc is obligatory for the function of >300 enzymes and 1000 transcription factors that are transported and collected in metallothioneins. Zinc is 2nd most abundant trace metal after Fe in humans; zinc is present in approximately entire enzymes [20]. The WHO guideline of Zn for potable water is set as 3.0 mg/L, since all potable water

samples declared a safe limit of Zn from the area under study. The range was determined as 0.003 to 0.270 mg/L with mean Zn content of 0.094 mg/L (Table 1).

Daily Intake (DIM) of Heavy Metals

The DIM range of Cr in the drinking water of the study area was observed for adults as 0.0008–0.0016 mg/kgbw/d. For children, it was found as 0.0009–0.0017 mg/kgbw/d, while the mean DIM concentration of Cr for adults and children was determined as 0.0012 and 0.0013 mg/kgbw/d, respectively. For Ni, the DIM range was found for adults and children as; 0.2800–0.7200 and 0.3100–0.8000 mg/kgbw/d, respectively. Since the average DIM values were observed for adults and children as 0.4688 and 0.5168 mg/kgbw/d, respectively. For Cu DIM values for adults and children were measured as 0.0010 to 0.0280 mg/kgbw/d and 0.0010 to 0.0310 mg/kgbw/d, respectively with average level of Adult (0.0072 mg/kgbw/d) and Children (0.0080 mg/kgbw/d). The DIM

values of Mn for adults and children were measured as; for Adult (0.0006–0.0086 mg/kgbw/d) and for children (0.0008–0.0131 mg/kgbw/d) with mean content of 0.0020 and 0.0031 mg/kgbw/d for adults and children, respectively. The minimum and maximum DIM values of Fe for adults and children were determined as; 0.0006–0.0103 mg/kgbw/d and 0.0006–0.0113 mg/kgbw/d, respectively, since the average DIM values for both adults and children were found as 0.0045 and 0.0049 mg/kgbw/d, respectively. Minimum, maximum and mean DIM values of Zn for adults and children were measured as; 0.0001, 0.0075 and 0.0026 mg/kgbw/d, and 0.0001, 0.0083 and 0.0029 mg/kgbw/d, respectively (Table 2-5).

Health Risk Indexes of (HRIs) Heavy Metals

The minimum, maximum and mean HRI of Cr for adults and children were observed as 0.0005, 0.0011 and 0.0008; and 0.0006, 0.0012 and 0.0009, respectively. HRI

Table 2. The mean daily intakes (mg/kgbw/d) and Health risk indexes of Heavy Metals via absorption of polluted potable water

Sample ID	Cr				Ni			
	Adult		Children		Adult		Children	
	DIM	HRI	DIM	HRI	DIM	HRI	DIM	HRI
G-1	0.0015	0.0010	0.0017	0.0011	0.50	0.03	0.55	0.03
G-2	0.0011	0.0007	0.0012	0.0008	0.44	0.02	0.49	0.02
G-3	0.0016	0.0011	0.0017	0.0012	0.47	0.02	0.52	0.03
G-4	0.0013	0.0008	0.0014	0.0009	0.31	0.02	0.34	0.02
G-5	0.0011	0.0007	0.0012	0.0008	0.39	0.02	0.43	0.02
G-6	0.0013	0.0009	0.0014	0.0009	0.56	0.03	0.61	0.03
G-7	0.0008	0.0005	0.0009	0.0006	0.56	0.03	0.61	0.03
G-8	0.0013	0.0008	0.0014	0.0009	0.58	0.03	0.64	0.03
G-9	0.0010	0.0007	0.0011	0.0007	0.42	0.02	0.46	0.02
G-10	0.0015	0.0010	0.0017	0.0011	0.47	0.02	0.52	0.03
G-11	0.0013	0.0009	0.0015	0.0010	0.28	0.01	0.31	0.02
G-12	0.0009	0.0006	0.0010	0.0007	0.42	0.02	0.46	0.02
G-13	0.0011	0.0007	0.0012	0.0008	0.47	0.02	0.52	0.03
G-14	0.0011	0.0007	0.0012	0.0008	0.42	0.02	0.46	0.02
G-15	0.0010	0.0007	0.0011	0.0007	0.47	0.02	0.52	0.03
G-16	0.0016	0.0010	0.0017	0.0011	0.33	0.02	0.37	0.02
G-17	0.0013	0.0009	0.0014	0.0009	0.50	0.03	0.55	0.03
G-18	0.0009	0.0006	0.0010	0.0007	0.44	0.02	0.49	0.02
G-19	0.0010	0.0007	0.0011	0.0007	0.58	0.03	0.64	0.03
G-20	0.0012	0.0008	0.0013	0.0009	0.72	0.04	0.80	0.04

Table 3. The mean daily intakes (mg/kgbw/d) and Health risk indexes of Heavy Metals via absorption of polluted potable water (*Continued*)

Sample ID	Cr				Ni			
	Adult		Children		Adult		Children	
	DIM	HRI	DIM	HRI	DIM	HRI	DIM	HRI
G-21	0.0015	0.0010	0.0017	0.0011	0.44	0.02	0.49	0.02
G-22	0.0010	0.0007	0.0011	0.0007	0.67	0.03	0.73	0.04
G-23	0.0012	0.0008	0.0013	0.0009	0.42	0.02	0.46	0.02
G-24	0.0014	0.0009	0.0016	0.0010	0.47	0.02	0.52	0.03
G-25	0.0015	0.0010	0.0017	0.0011	0.39	0.02	0.43	0.02

Table 4. The mean daily intakes (mg/kgbw/d) and Health risk indexes of Heavy Metals via absorption of polluted potable water

Sample ID	Cu				Mn			
	Adult		Children		Adult		Children	
	DIM	HRI	DIM	HRI	DIM	HRI	DIM	HRI
G-1	0.025	0.625	0.028	0.688	0.0006	0.0168	0.0008	0.0256
G-2	0.001	0.028	0.001	0.031	0.0014	0.0421	0.0021	0.0639
G-3	0.003	0.076	0.003	0.084	0.0011	0.0337	0.0017	0.0511
G-4	0.004	0.097	0.004	0.107	0.0008	0.0253	0.0013	0.0384
G-5	0.003	0.083	0.004	0.092	0.0086	0.2609	0.0131	0.3964
G-6	0.022	0.556	0.024	0.612	0.0011	0.0337	0.0017	0.0511
G-7	0.021	0.514	0.023	0.566	0.0017	0.0505	0.0025	0.0767
G-8	0.001	0.029	0.001	0.032	0.0008	0.0253	0.0013	0.0384
G-9	0.001	0.028	0.001	0.031	0.0011	0.0337	0.0017	0.0511
G-10	0.001	0.033	0.001	0.037	0.0014	0.0421	0.0021	0.0639
G-11	0.022	0.556	0.024	0.612	0.0008	0.0253	0.0013	0.0384
G-12	0.019	0.465	0.020	0.512	0.0008	0.0253	0.0013	0.0384
G-13	0.001	0.035	0.002	0.038	0.0017	0.0505	0.0025	0.0767
G-14	0.001	0.031	0.001	0.034	0.0017	0.0505	0.0025	0.0767
G-15	0.001	0.029	0.001	0.032	0.0028	0.0842	0.0042	0.1279
G-16	0.017	0.417	0.018	0.459	0.0014	0.0421	0.0021	0.0639
G-17	0.001	0.034	0.001	0.037	0.0006	0.0168	0.0008	0.0256
G-18	0.001	0.035	0.002	0.038	0.0044	0.1347	0.0068	0.2046
G-19	0.001	0.026	0.001	0.029	0.0017	0.0505	0.0025	0.0767
G-20	0.001	0.035	0.002	0.038	0.0031	0.0926	0.0046	0.1406
G-21	0.028	0.694	0.031	0.765	0.0022	0.0673	0.0034	0.1023
G-22	0.001	0.033	0.001	0.037	0.0044	0.1347	0.0068	0.2046
G-23	0.002	0.047	0.002	0.051	0.0022	0.0673	0.0034	0.1023
G-24	0.001	0.035	0.002	0.038	0.0025	0.0758	0.0038	0.1151
G-25	0.001	0.031	0.001	0.034	0.0014	0.0421	0.0021	0.0639

values of Ni like minimum, maximum and mean for adults and children were found as; 0.0100, 0.0400 and 0.0232; and 0.0200, 0.0400 and 0.0260 respectively in the potable water of the area under study. The range of HRI

of Cu for adults and children in the study area were determined as 0.0260–0.6940 and 0.0290–0.7650, respectively, while the mean HRI value for adults and children was found as 0.1829 and 0.2014, respectively.

Table 5. The mean daily intakes (mg/kgbw/d) and Health risk indexes of Heavy Metals via absorption of polluted potable water

Sample ID	Fe				Zn			
	Adult		Children		Adult		Children	
	DIM	HRI	DIM	HRI	DIM	HRI	DIM	HRI
G-1	0.00417	0.005952	0.004587	0.006553	0.00528	0.017593	0.005810	0.019368
G-2	0.00306	0.004365	0.003364	0.004806	0.00178	0.005926	0.001957	0.006524
G-3	0.00167	0.002381	0.001835	0.002621	0.00183	0.006111	0.002018	0.006728
G-4	0.01028	0.014683	0.011315	0.016164	0.00178	0.005926	0.001957	0.006524
G-5	0.00250	0.003571	0.002752	0.003932	0.00167	0.005556	0.001835	0.006116
G-6	0.00472	0.006746	0.005199	0.007427	0.00583	0.019444	0.006422	0.021407
G-7	0.00389	0.005556	0.004281	0.006116	0.00169	0.005648	0.001865	0.006218
G-8	0.00528	0.00754	0.005810	0.008301	0.00172	0.005741	0.001896	0.006320
G-9	0.00333	0.004762	0.003670	0.005243	0.00197	0.006574	0.002171	0.007238
G-10	0.00889	0.012698	0.009786	0.01398	0.00183	0.006111	0.002018	0.006728
G-11	0.00500	0.007143	0.005505	0.007864	0.00750	0.025000	0.008257	0.027523
G-12	0.00250	0.003571	0.002752	0.003932	0.00169	0.005648	0.001865	0.006218
G-13	0.00778	0.011111	0.008563	0.012232	0.00175	0.005833	0.001927	0.006422
G-14	0.00306	0.004365	0.003364	0.004806	0.00189	0.006296	0.002080	0.006932
G-15	0.01000	0.014286	0.011009	0.015727	0.00167	0.005556	0.001835	0.006116
G-16	0.00139	0.001984	0.001529	0.002184	0.00722	0.024074	0.007951	0.026504
G-17	0.00222	0.003175	0.002446	0.003495	0.00167	0.005556	0.001835	0.006116
G-18	0.00361	0.005159	0.003976	0.005679	0.00167	0.005556	0.001835	0.006116
G-19	0.00472	0.006746	0.005199	0.007427	8.3E-05	0.000278	9.17E-05	0.000306
G-20	0.00861	0.012302	0.009480	0.013543	0.00169	0.005648	0.001865	0.006218
G-21	0.00056	0.000794	0.000612	0.000874	0.00611	0.020370	0.006728	0.022426
G-22	0.00333	0.004762	0.003670	0.005243	0.00214	0.007130	0.002355	0.007849
G-23	0.00444	0.006349	0.004893	0.006990	0.00169	0.005648	0.001865	0.006218
G-24	0.00222	0.003175	0.002446	0.003495	0.00169	0.005648	0.001865	0.006218
G-25	0.00417	0.005952	0.004587	0.006553	0.00164	0.005463	0.001804	0.006014

Table 6. Statistics with reference to daily intake and health risk indexes of heavy metals of potable water of area under study

	Daily Intake of Heavy Metals (DIM)											
	Cr		Ni		Cu		Mn		Fe		Zn	
	Adult	Children	Adult	Children	Adult	Children	Adult	Children	Adult	Children	Adult	Children
Min:	0.0008	0.0009	0.2800	0.3100	0.0010	0.0010	0.0006	0.0008	0.0006	0.0006	0.0001	0.0001
Max:	0.0016	0.0017	0.7200	0.8000	0.0280	0.0310	0.0086	0.0131	0.0103	0.0113	0.0075	0.0083
Mean	0.0012	0.0013	0.4688	0.5168	0.0072	0.0080	0.0020	0.0031	0.0045	0.0049	0.0026	0.0029
	Health Risk Indexes of Heavy Metals (HRIs)											
	Cr		Ni		Cu		Mn		Fe		Zn	
	Adult	Children	Adult	Children	Adult	Children	Adult	Children	Adult	Children	Adult	Children
Min:	0.0005	0.0006	0.0100	0.0200	0.0260	0.0290	0.0168	0.0256	0.0008	0.0009	0.0003	0.0003
Max:	0.0011	0.0012	0.0400	0.0400	0.6940	0.7650	0.2609	0.3964	0.0147	0.0162	0.0250	0.0275
Mean	0.0008	0.0009	0.0232	0.0260	0.1829	0.2014	0.0610	0.0926	0.0008	0.0070	0.0087	0.0096

The HRI range of Mn for adults and children was observed as; 0.0168–0.2609 and 0.0256–0.3964, respectively. Though, the average HRI value for adults and children was measured as 0.0610 and 0.0926, respectively. Minimum, maximum, and mean HRI values of Fe for adults and children were measured as 0.0008, 0.0147, and 0.006; and 0.0009, 0.0162, and 0.0070, respectively. For Zn, the minimum, maximum and mean HRI values for adults and children were determined as 0.0003, 0.0250, and 0.0087; and 0.0003, 0.0275, and 0.0096, respectively (Table 5).

■ CONCLUSION

The level of Cu and Zn were within the safe limit of the WHO, while Cr, Ni, Fe, Mn showed alarming levels in the drinking water of the study area. The DIM and HRI of heavy metals were measured for adults and children since the HRI values for all metals were < 1, which shows the lack of possible health hazards for the people of the study area. Finally, it can be concluded that groundwater used for drinking purposes must be treated before use. Otherwise, it may cause various diseases, for instance, heart disease, kidney failure, liver disease, blood pressure, hypertension, etc. it is, therefore, the responsibility of the government of Pakistan to provide either clean drinking water or to install reverse osmosis (RO) plants to clean drinking water before use for the people of the study area.

■ ACKNOWLEDGMENTS

The authors are highly thankful to the Pakistan Council of Research in Water Resources (PCRWR) Government of Pakistan Ministry of Science & Technology National Water Quality Laboratory, Islamabad, to analyze water samples for heavy metals.

■ AUTHOR CONTRIBUTIONS

Abdul Raheem Shar conducted the experiment, Ghulam Qadir Shar supervised the whole work, statistics of the data was carried out by Zulfiqar Jumani, Aslam Khan Pathan, Zubeda Bhatti corrected the grammatical mistakes, whereas Ali Raza Rind and Ghulam Mujtaba Jogi helped prepare the manuscript draft. All authors agreed to the final version of this manuscript.

■ REFERENCES

- [1] Cherfi, A., Achour, M., Cherfi, M., Otmani, S., and Morsli, A., 2015, Health risk assessment of heavy metals through consumption of vegetables irrigated with reclaimed urban wastewater in Algeria, *Process Saf. Environ. Prot.*, 98, 245–252.
- [2] Matta, G., and Kumar, A., 2017, Health risk, water hygiene, science and communication, *Essence*, 8 (1), 179–186.
- [3] Patel, P., Raju, N.J., Reddy, B.C.S.R., Suresh, U., Sankar, D.B., and Reddy, T.V.K., 2018, Heavy metal contamination in river water and sediments of the Swarnamukhi River Basin, India: Risk assessment and environmental implications, *Environ. Geochem. Health*, 40 (2), 609–623.
- [4] Riaz, A., Khan, S., Muhammad, S., Liu, C., Shah, M.T., and Tariq, M., 2018, Mercury contamination in selected foodstuffs and potential health risk assessment along the artisanal gold mining, Gilgit-Baltistan, Pakistan, *Environ. Geochem. Health*, 40 (2), 625–635.
- [5] Moynihan, M., 2016, Role of Diet in Heavy Metal Exposure and Toxicity during Prenatal and Peripubertal Periods, *Thesis*, University of Michigan, US.
- [6] Daud, M., Nafees, M., Ali, S., Rizwan, M., Bajwa, R.A., Shakoob, M.B., Arshad, M.U., Chatha, S.A.S., Deeba, F., Murad, W., Malook, I., and Zhu, S.J., 2017, Drinking water quality status and contamination in Pakistan, *BioMed. Res. Int.*, 2017, 7908183.
- [7] Khan, A., Khan, S., Khan, M.A., Qamar, Z., and Waqas, M., 2015, The uptake and bioaccumulation of heavy metals by food plants, their effects on plants nutrients, and associated health risk: A review, *Environ. Sci. Pollut. Res.*, 22 (18), 13772–13799.
- [8] Rezapour, M., Rezapour, H.A., Chegeni, M., and Khanjani, N., 2021, Exposure to cadmium and head and neck cancers: A meta-analysis of observational studies, *Rev. Environ. Health*, 36 (4), 577–584.
- [9] US-EPA, 2015, *Guidelines for Carcinogen Risk Assessment*, US Environmental Protection Agency, EPA/630/P-03/001F, Washington, DC.

- [10] Jaishankar, M., Mathew, B.B., Shah, M.S., Krishna Murthy, T.P., and Sangeetha Gowda, K.R., 2014, Biosorption of few heavy metal ions using agricultural wastes, *J. Environ. Pollut. Hum. Health*, 2 (1), 1–6.
- [11] Mehmood, A., Mirza, M.A., Choudhary, M.A., Kim, K.H., Raza, W., Raza, N., Lee, S.S., Zhang, M., Lee, J.H., and Sarfraz, M., 2019, Spatial distribution of heavy metals in crops in a wastewater irrigated zone and health risk assessment, *Environ. Res.*, 168, 382–388.
- [12] Muhammad, S., Shah, M.T., and Khan, S., 2011, Health risk assessment of heavy metals and their source apportionment in drinking water of Kohistan region, northern Pakistan, *Microchem. J.*, 98 (2), 334–343.
- [13] US-EPA, 2011, *Exposure Factors Handbook 2011 Edition (Final Report)*, US Environmental Protection Agency, EPA/600/R-09/052F, Washington, DC.
- [14] Nawab, J., Ali, S., Rauf, A., Ur Rehman, U., Khan, A.A., Sajjad, M., and Khan, W., 2015, Health risk associated with heavy metals via consumption of surface and groundwater in district Shangla, Pakistan, *J. Himalayan Earth Sci.*, 48 (2), 62–73.
- [15] Shekhawat, K., Chatterjee, S., and Joshi, B., 2015, Chromium toxicity and its health hazards, *Int. J Adv. Res.*, 3 (7), 167–172.
- [16] Vincent, J.B., 2015, Is the pharmacological mode of action of chromium (III) as a second messenger?, *Biol. Trace Elem. Res.*, 166 (1), 7–12.
- [17] Kamerud, K.L., Hobbie, K.A., and Anderson, K.A., 2013, Stainless steel leaches nickel and chromium into foods during cooking, *J. Agric. Food Chem.*, 61 (39), 9495–9501.
- [18] Seetharaman, J., and Sarma, M.S., 2021, Chelation therapy in liver diseases of childhood: Current status and response, *World J. Hepatol.*, 13 (11), 1552–1567.
- [19] Greenwood, N.N., and Earnshaw, A., 2012, *Chemistry of the Elements*, 2nd Ed., Elsevier, Oxford, Massachusetts, US.
- [20] Erikson, K.M., and Aschner, M., 2019, Manganese: Its Role in Disease and Health, in *Therapeutic Use and Toxicity of Metal Ions in the Clinic*, De Gruyter, Berlin.

Solubility Enhancement and Characterization of Tamoxifen Citrate Using Co-crystallization

Dolih Gozali, Iyan Sopyan, Hairunnisa Hairunnisa, and Siska Sari Marvita*

Department of Pharmaceutics and Pharmaceutical Technology, Faculty of Pharmacy, Padjadjaran University, West Java 45363, Indonesia

* Corresponding author:

email: siska20005@mail.unpad.ac.id

Received: December 1, 2021

Accepted: January 30, 2022

DOI: 10.22146/ijc.70891

Abstract: Tamoxifen citrate (TC) is one of the anti-estrogen agents which has low solubility in the water. As TC is still used as the main therapy in breast cancer treatment, modifications are still being made to increase the solubility of TC for a successful treatment. In this research, co-crystallization of TC was performed using Nicotinamide (NIC), Isonicotinamide (ISO), Saccharin (SAC), Aspartame (ASP), and Benzoic Acid (BNZ) as a cofomer with the molar ratio of 1:1, 1:2, and 2:1. Co-crystal was prepared by solvent drop grinding (SDG) and solvent evaporation (SE) methods using methanol. The results of the solubility test showed that TC-NIC and TC-ISO co-crystals with a 1:2 molar ratio made using the SDG and SE methods gave the best results. Meanwhile, the best dissolution test results were shown by TC-ISO co-crystals with a ratio of 1:2. Based on the characterization of physical stability, the SDG method resulted in more stable TC co-crystals than the SE method. Therefore, in this case, the SDG method could be more advantageous to be used for development in the field of co-crystallization.

Keywords: tamoxifen citrate; co-crystallization; solubility

INTRODUCTION

Since 2018, breast cancer cases in America have reached around 266,120 cases with a death rate of 72,590 [1]. Breast cancer is a disease diagnosed in women and ranks second as a cause of cancer death [2]. One of the treatments is chemotherapy using tamoxifen citrate (TC) [3]. TC (Fig. 1) is a salt form of tamoxifen consisting of tamoxifen and citric acid, a poorly soluble compound. Poor solubility based on physicochemical properties, namely solubility in water at a temperature of 20 °C (pH 3.0–3.5) reaching 0.3 mg/L and in HCl 0.02 M at 37 °C reaching 0.2 mg/mL, soluble in ethanol and methanol, and slightly soluble in acetone and chloroform. In addition, the bioavailability of tamoxifen citrate is in the range of 20–30% [4].

The success of a drug in achieving a therapeutic effect is influenced by its physicochemical properties, especially its solubility. Therefore, the solubility of the active substance greatly affects the performance of a drug [5]. Active substances with low solubility are a challenge in the pharmaceutical field in drug development and drug

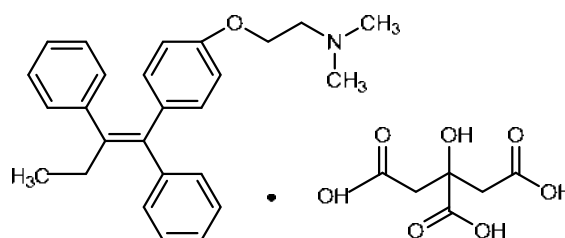


Fig 1. Structure of tamoxifen citrate (TC) [6]

dosage forms so that they can show a good profile in terms of solubility, dissolution, and bioavailability of a drug.

Previous studies reported efforts made to increase the efficiency of TC performance through the inclusion of TC complexes with cyclodextrins [6]. Subsequent studies observed PLGA nanoparticles containing TC as an anticancer drug [7], as well as increasing the solubility of TC through solid dispersion [2,4]. Some of the methods that have been carried out still have some drawbacks, such as the use of a lot of matrices, low drug loading, quite high process energy, and difficulties in the up-scaling process [8]. Thus, it is still possible to develop

methods with simple processes with considered results such as co-crystals.

Co-crystal is an approach that can be used to improve the physicochemical properties of an active substance (such as solubility, dissolution, bioavailability, and stability) without affecting the pharmacological activity of the active substance [9-10]. Co-crystallization can also be applied to acidic, basic, neutral, and ionic compounds [11], so it can be used on TC to increase its solubility. Several methods are used to produce co-crystals, namely solution-based crystallization (addition of solids to a crystallized solution, cooling crystallization, and solvent evaporation) and milling (dry or wet conditions) [9].

To achieve good results, the co-crystallization technique relies heavily on accuracy in coformer selection. The cofomers used must have a synthon supramolecular group in order to interact with the active pharmaceutical ingredients to form hydrogen bonds. Requirements cofomers must be inert and have low toxicity [12]. Some examples of commonly used cofomers that successfully form co-crystals with active drug substances are nicotinamide-trimethoprim [12], isonicotinamide-furosemide [13], saccharin-ibuprofen [9], aspartame-glibencalamide [14], and benzoic acid-theophylline [15]. The chemical structure of TC, which has four hydrogen bond donors and nine hydrogen bond acceptors, opens the opportunity for co-crystal formation when interacting with co-crystal cofomers, which also have synthon supramolecular groups. The interaction of co-crystal synthons with cofomers can be predicted using a computational method approach (in-silico) [16].

So far, not much has been reported regarding the co-crystallization approach to increase the solubility of TC. Therefore, this study was carried out to increase the solubility of TC by using a co-crystallization approach using nicotinamide, isonicotinamide, saccharin, aspartame, and benzoic acid as cofomers using solvent drop grinding and solvent evaporation methods, followed by evaluation of physicochemical properties and characterization using Fourier Transform Infrared Spectrophotometry (FTIR), Differential Scanning

Calorimetry (DSC), Powder X-Ray Diffraction (PXRD), and Scanning Electron Microscopy (SEM).

■ EXPERIMENTAL SECTION

Materials

The materials for the experiment include Tamoxifen citrate (TC) (Pharmaceutical Industries Ltd., China), ethanol pro analysis (Merck), nicotinamide (Sigma Aldrich), isonicotinamide (Sigma Aldrich), benzoic acid (Sigma Aldrich), saccharin (Sigma Aldrich), aspartame (Sigma Aldrich), distilled water, and potassium bromide (pro analysis (brand).

Instrumentation

The instruments included UV-Vis spectrophotometer (Specord 205 Analytical Jena), USP dissolution apparatus type 2 (SotaX AT7 Smart dissolution tester), X-ray diffractometer (Pan-Analytical), Differential Scanning Calorimetry (DSC) (Linseis PTA ST 1600), Fourier-Transformed Infrared Spectrophotometer (FTIR) (Specord 100), and Scanning Electron Microscope (SEM) (SU3500 SEM, HITACHI).

Procedure

Screening in-silico

Initial screening of co-crystals was carried out based on predicting hydrogen bond formation between TC and cofomers. The two-dimensional structure of TC and cofomers were obtained from PubChem Database and then converted into pdb format using Discovery Studio Visualizer v.16.1.0.15350. The interaction of two molecules (TC with each cofomer) was observed using the AutoDockTools version 1.6 program. The parameters observed were the type of interaction such as hydrogen bonds, van der Waals bonds or π electron bonds and Gibbs free energy, and the distance of the bonds that occurred.

Polarizing microscope

Pure TC powder, pure cofomer powder, and physical mixture were observed with a polarizing microscope. About 3 mg of TC powder and cofomers (nicotinamide, isonicotinamide, saccharin, aspartame, and benzoic acid) were each placed in an object glass,

dropped with methanol, and left in contact until the methanol evaporated (supersaturated). The results of the interactions that occur are observed under a polarizing microscope equipped with a digital camera.

Co-crystal preparation

Before the co-crystallization process, a phase solubility test was carried out by making a series of ratios of active pharmaceutical ingredients (API) and cofomers from 1:9 to 9:1 and then put into a vial containing 25 mL of distilled water. Then the sample was stirred using a mechanical stirrer at 25 °C for 24 h. The sample was then filtered, and dissolved API levels were measured and analyzed by UV-Vis spectrophotometry.

The phase solubility test was carried out to determine the ratio or the right number of cofomers in the formation of co-crystals so that it is expected to change the physicochemical properties of the active substance, especially its solubility. The obtained phase solubility curves are used to describe the concentration of solutes in various concentrations of cofomers. Thus, the solvent drop grinding and the solvent evaporation processes use a ratio of 1:1, 1:2, and 2:1.

Solvent drop grinding (SDG). TC and cofomer were mixed with a molar ratio of 1:1, 1:2, and 2:1; and then grinded together in a mortar for 5–10 min while dripping with a suitable solvent (such as methanol), drop by drop until it looks wet during the grinding process. Then the obtained co-crystals were stored at room temperature for 24 h to obtain a dry crystal precipitate [17].

Solvent evaporation (SE). TC and cofomer were mixed with a molar ratio of 1:1, 1:2, and 2:1; and dissolved in a suitable solvent such as methanol, shaken for 10 min, then evaporated in a water bath at 30 °C for 24 h to obtain a dry crystalline solid. Thus, the obtained co-crystals are stored at room temperature [18].

Co-crystal evaluation

Solubility test. Saturated solubility was measured by the shake flask method. 100 mg of co-crystal TC was mixed with 50 mL of distilled water in an Erlenmeyer flask. Then the sample was stirred using a mechanical stirrer at 25 °C for 24 h. The sample was then centrifuged at 5000 rpm for 10 min. The supernatant was then separated by filtering

using filter paper, then diluted and analyzed using a UV-Vis spectrophotometry at a wavelength of 200–800 nm. After obtaining the maximum wavelength of TC, the concentration of dissolved in the filtrate is determined from the results of the solubility test by looking at the absorption of UV-Vis light in the sample solution.

Dissolution test. The dissolution test was carried out on the co-crystals formed and showed the best solubility results, using a type 2 dissolution test apparatus with 900 mL HCl pH 1.2 at a rotation speed of 50 rpm for 60 min at 37 °C. The sample was weighed carefully then compacted to form a tablet. The tablets were then put into the media, then 10 mL of the sample solution was taken periodically at intervals of 10, 20, 30, 45, and 60 min, and each intake was replaced with new media and the same volume. The sample was then filtered using filter paper and analyzed using UV spectrophotometer at a wavelength of 200–300 nm. Then the dissolved TC levels were calculated at each collection time interval with a sampling factor.

Characteristics of co-crystal

Powder X-ray diffraction (PXRD). Diffractogram patterns of co-crystal, physical mixture, and pure TC were obtained using an X-ray diffractometer with Cu K α radiation ($\lambda = 1.54 \text{ \AA}$) and a voltage of 40 kV and a current of 30 mA. The slit width is 0.2 inches, with a scanning speed of 0.2–0.5°/min and a scanning distance of $2\theta = 5\text{--}50^\circ$ (organic compounds). Samples were measured then the results obtained were compared with the pure TC and TC co-crystals formed.

Differential scanning calorimetry (DSC). Thermal analysis of co-crystal, physical mixture, and pure TC were carried out with 3–5 mg of sample put into an aluminum pan, then measured on a programmed DSC device with a temperature range of 50–300 °C with a heating rate of 10°C/min. The thermogram results obtained will be compared with the pure TC thermogram to see any differences before and after treatment.

Fourier transform infrared (FT-IR) spectrophotometry. The IR spectra of co-crystal, physical mixture, and pure TC were analyzed at wavenumbers of 4000–400 cm^{-1} . 1 mg of sample was

mixed with 10 mg of KBr until homogeneous and then pellets were formed with a pressure of 20 psi using a KBr plate press. This procedure was carried out to see the functional groups of pure TC and TC co-crystals formed, the functional groups present in TC must also be present in TC co-crystals.

Scanning electron microscopy (SEM). SEM was used to study the morphology of co-crystals, physical mixtures, and pure TC. The light sample was sprinkled over an aluminum chamber and then covered with platinum 10 Å thick under an argon atmosphere using a mas module placed in a high vacuum evaporator. After that, the container containing the sample is placed on a scanning electron microscope.

Physical stability test

Physical stability testing was carried out on TC co-crystals which showed an increase in the solubility and dissolution profile and showed the typical characteristics of the co-crystals. Physical stability test was carried out at 40 °C and 75% relative humidity using a climatic chamber, by observing changes in the diffractogram pattern and comparing it with the initial storage conditions.

RESULTS AND DISCUSSION

Initial Characterization of TC

The diffraction pattern of tamoxifen citrate (TC) in Fig. 2 shows the form II polymorph. This is confirmed by the report of Gamberini et al. [19], with the characteristic high-intensity diffraction peak form II detected at $2\theta = 5.69^\circ, 13.15^\circ, 14.05^\circ, 21.01^\circ, 24.15^\circ,$ and 28.40° . TC, which is widely used as a pharmaceutical ingredient, exists in two main polymorphic forms, and the relatively stable

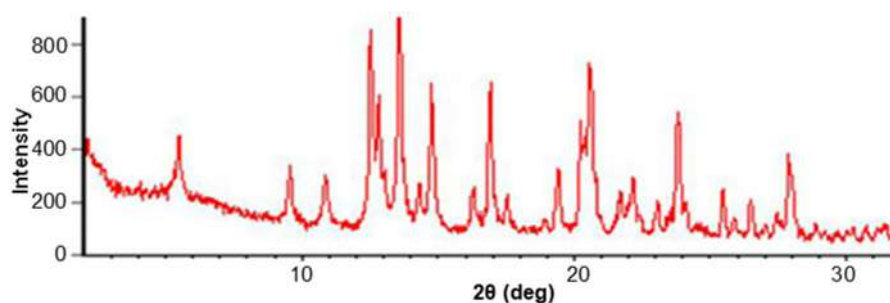


Fig 2. Diffractogram pattern of form II polymorphic form TC

polymorphic form is in form II.

Coformer Screening with *In-Silico*

TC has a structure containing functional groups as proton acceptors and donors. TC has nine functional groups that act as acceptors with acting atoms namely oxygen and nitrogen, and four functional groups that act as proton donors (Fig. 3).

The coformers selected for the formation of tamoxifen citrate co-crystals must be inert, have no pharmacological effects, and have hydrogen acceptor or donor groups that will form hydrogen bonds with TC. The coformers used were nicotinamide (NIC), isonicotinamide (ISO), saccharin (SAC), aspartame (ASP), and benzoic acid (BNZ). Table 1 shows the results of *in-silico* screening, which predicts the hydrogen bonds formed in the formation of co-crystals between the active substance and the coformer. Prediction results show that hydrogen bonds are only formed in the NIC and ISO coformers. The hydrogen bond formed between TC and NIC occurs between the amide group ($-\text{CO}-\text{NH}_2$) on the NIC with the ether group ($-\text{O}-$) on the TC, so the synthon formed $\text{N}-\text{H}\cdots\text{O}-\text{C}$ is called a monomer heterosynthon. Meanwhile, with ISO coformers, hydrogen bonds that occur between the amide group in ISO and the amine group (R_3N) in TC, so that the synthon

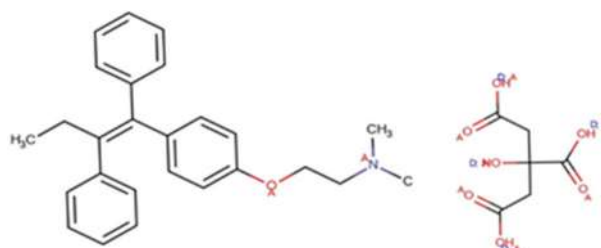


Fig 3. Donors and acceptors of TC

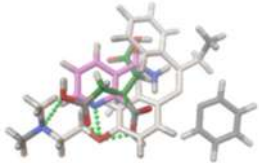
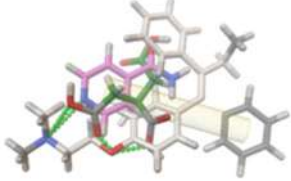
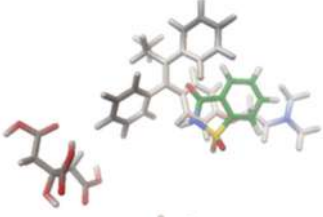
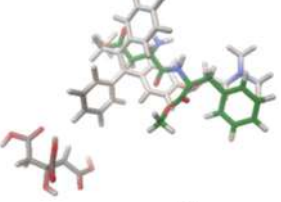
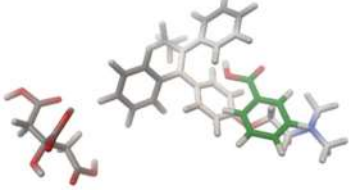
formed N-H...N-C is called a homosynthon monomer [20].

The Gibbs free energy formed from the NIC and ISO cofomer is -1.3 kcal/mole (Table 1), this indicates an interaction (hydrogen bond between cofomers and TC), and the bond distance formed by each cofomer is 2.34 and 2.20 Å, respectively. A good hydrogen bond has a distance of 2.8 Å. The number and distance of hydrogen bonds will affect the strength of the binding affinity between the ligand and the receptor [21]. Hydrogen bonds are said to be weak bonds, but in complex structures, these hydrogen bonds are strong enough to form supramolecular synthon in the co-crystal system

and stabilize the molecular structure [10]. Hydrogen interactions between TC with NIC and ISO form parameters to increase the solubility of TC.

In the other three cofomers SAC, ASP, and BNZ, no hydrogen bonds are formed. However, it has a smaller Gibbs free energy value compared to the formation by the NIC and ISO cofomers. The formation of hydrogen bonds is not caused by the distance between the atoms that are too far apart. The bond free energy indicates the ability of the ligands to interact. A compound is said to have a good interaction if the value of free energy is lower so that the bond that occurs is more stable [21].

Table 1. Simulation results of interaction of TC and cofomers with *in-silico*

Compounds	2D interaction	Bond interaction	Gibbs energy (kcal/mol)	Bond distance
Tamoxifen citrate–nicotinamide (TC-NIC)		4 hydrogen interactions	-1.3	2.34 Å
Tamoxifen citrate–isonicotinamide (TC-ISO)		4 hydrogen interactions, and 1 π - π interaction	-1.3	2.20 Å
Tamoxifen citrate–saccharin (TC-SAC)		No hydrogen interaction	-1.7	–
Tamoxifen citrate–aspartame (TC-ASP)		No hydrogen interaction	-2.5	–
Tamoxifen citrate–benzoic acid (TC-BNZ)		No hydrogen interaction	-1.2	–

Polarizing Microscope

Fig. 4 is the result of polarization microscopy between the TC mixture and the five cofomers, which shows the presence of a new crystal habit only in the NIC and ISO cofomers, while the other three cofomers (SAC, ASP, and BNZ) show mixing with TC, but do not produce new crystal habits. If the crystal habit obtained through recrystallization of the API mixture is significantly different from the single habit, then the mixture is indicated to show interaction. Differences in crystal habit and thermal behavior indicate a solid interaction between the two components of the active substance and the conformer.

Co-crystal Preparation

The results of the TC *in-silico* test with five cofomers were then made *in-vitro* co-crystals using solvent drop grinding (SDG) and solvent evaporation

(SE) methods with molar ratios of TC and cofomers of 1:1, 1:2, and 2:1 (30 variations), which resulted in a solid powder according to provided that the co-crystal form is a solid powder at room temperature. Co-crystallization using SDG does not require a lot of solvent so this method is environmentally friendly [22]. The purpose of adding solvent (methanol) in this method is to accelerate the interaction of the two components, which will accelerate the achievement of an amorphous state in each component so that both components become more reactive.

Co-crystallization using SE method using the principle of dissolving API and cofomer with a suitable solvent. Molecular interactions are expected to occur in the dissolution process of the two compounds so that hydrogen bonds are formed, where this interaction is expected to occur in the co-crystallization process. The SE

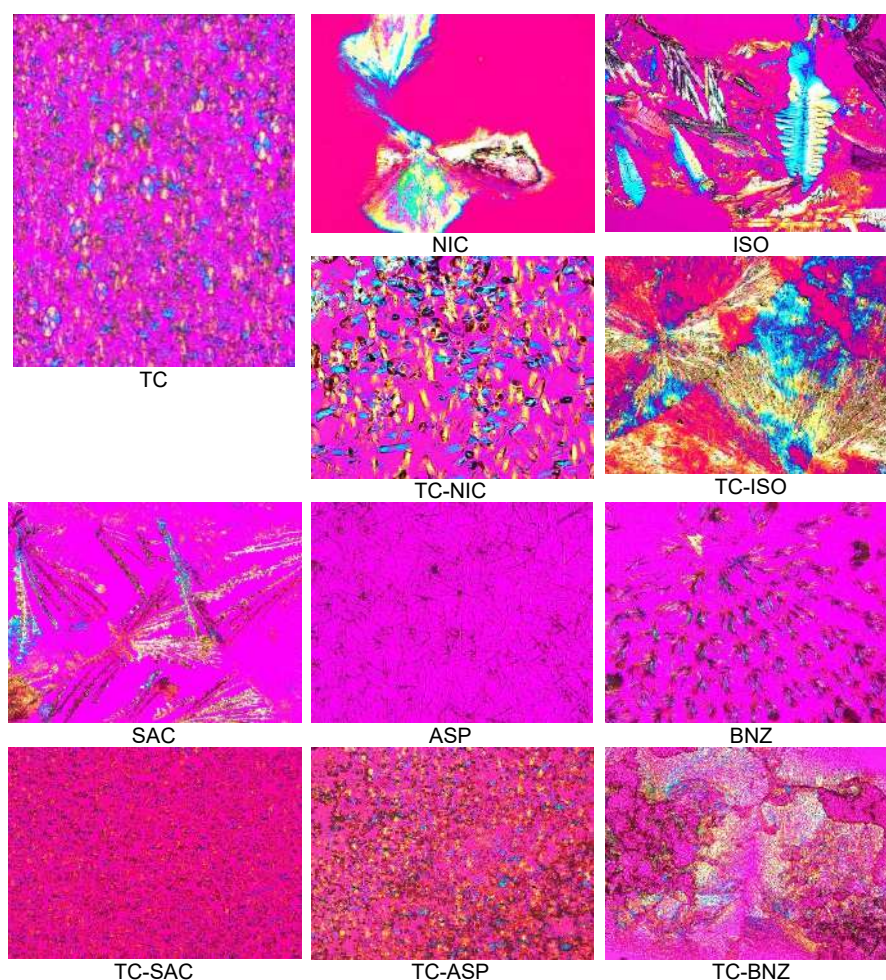


Fig 4. Polarizing microscopy of mixed TC and cofomers

process aims to remove the solvent so as to form a crystalline solid that has different physicochemical properties from the pure substance. Methanol is used as a solvent, because each material is soluble in the solvent and the result is solid at room temperature. Dissolution with organic solvents can affect changes in the crystal structure of a substance. This change in crystal structure will affect changes in the physicochemical properties of the substance [23].

Co-crystal Evaluation

The TC co-crystal approach was carried out to improve the solubility properties and dissolution profile of TC. Therefore, solubility and dissolution tests were carried out to find the best co-crystal variation, in terms of molar ratio, type of coformer, and method of preparation.

Solubility test

Fig. 5 shows the solubility results of TC co-crystals from the SDG method. The increase in solubility in TC-ISO co-crystals reached 55–74% with a ratio of 1:1, 1:2, and 2:1, respectively 368.184, 367.448, and 327.807 mg/mL compared to the saturated solubility of pure TC (211.940 mg/mL). Theoretically, coformers that have high solubility in water will affect the solubility of the active ingredient, the higher the hydrophilic nature of a material, the co-crystals formed will show high solubility [24]. The SDG method shows that the increase in saturation solubility is relatively small compared to the SE method, this may be due to the less solvent catalytic process at the time of manufacture.

The increase in the saturation solubility of TC co-crystals from the SE method also occurred in TC-ISO co-crystals reaching 61-103% from the ratios of 1:1, 1:2, and 2:1, respectively, for 347.333, 430.666, and 342.175 mg/L (Fig. 6). The increase in solubility that occurs is due to the hydrogen bonds formed in the TC-ISO co-crystal. Besides being able to change the crystal lattice, it can also increase the solubility by attracting more solvent so that the interaction of TC with the solvent is more. The increase in solubility was due to the increase in solvent affinity for TC due to the presence of coformers. Coformers are compounds that are polar so they will be linear with

affinity for water. With this, the NIC and ISO coformers provide effectiveness in increasing the solubility of TC through the co-crystallization technique. In another study, co-crystallization with NIC coformer was reported to increase trimethoprim [12]. In addition, ISO coformer was also used to increase the solubility of furosemide which showed an increase of 5.6 times higher than pure furosemide [13].

Dissolution test

The drug dissolution profile was studied for TC-NIC and TC-ISO co-crystals which showed increased solubility of TC. Fig. 7 shows the dissolution profile of the TC-NIC co-crystal drug. Increased dissolution occurred in TC-NIC 1:2 co-crystals prepared by the SE method. In the SDG method, the drug dissolution profile is not higher than pure TC. The choice of the molar ratio

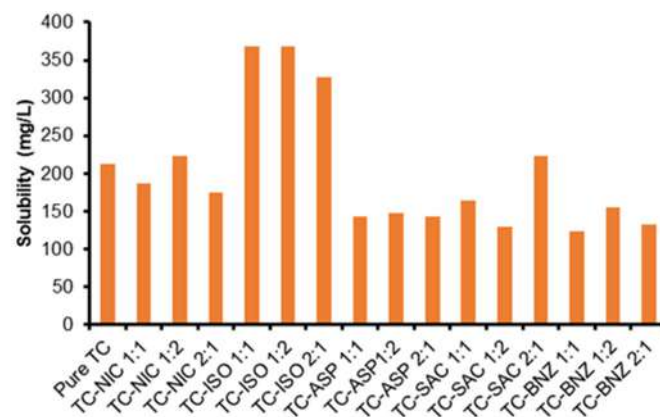


Fig 5. Comparison of solubility of TC co-crystal with SDG method

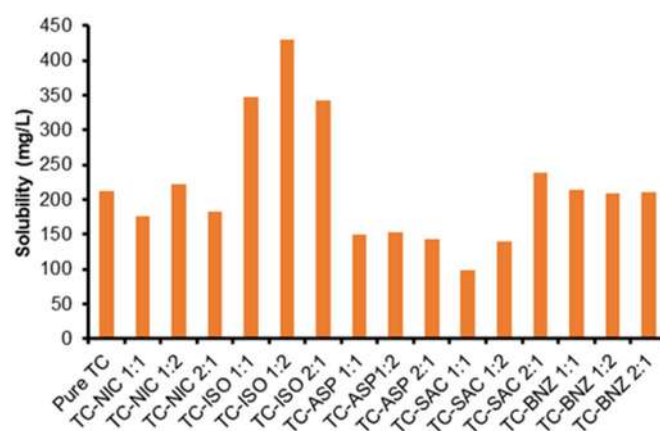


Fig 6. Comparison of solubility of co-crystal TC with SE method

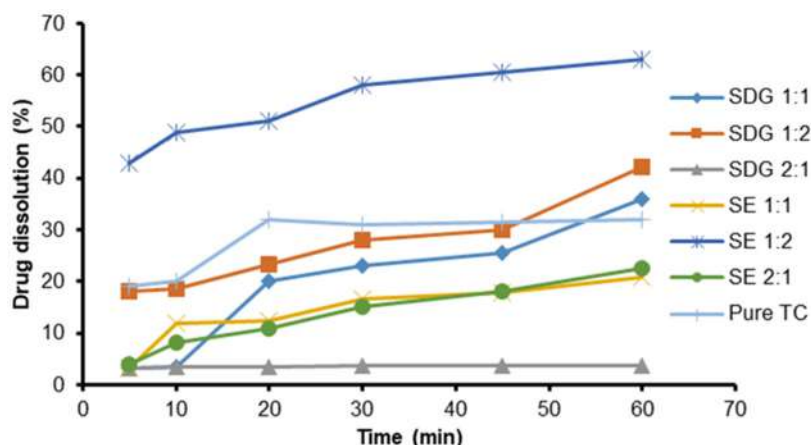


Fig 7. Dissolution profile of pure TC and TC-NIC co-crystal

also greatly determines the success of co-crystal formation. If the correct molar ratio is used, there will be an increase in solubility caused by several mechanisms, including the formation of a new co-crystal crystalline phase which can change the physicochemical properties (e.g., solubility). The increase in dissolution in the process with the NIC cofomer occurs due to the formation of hydrogen bonds between the amide functional group and the nicotinamide carboxyl group. Therefore, in relation to TC, it increases the polarity of the hydro-carboxyl hydroxyl thereby increasing its solubility [25].

The dissolution profile of the TC-ISO co-crystal drug is presented in Fig. 8. Like drug release in TC-NIC co-crystals, increased drug release occurred in TC-ISO 1:2 co-crystals using the SE method. However, the release that occurred was higher than that of TC-NIC co-crystals. ISO is reported to increase the dissolution rate because it

forms complexes with drug compounds through a mechanism as a donor and acceptor in the formation of hydrogen bonds. It also causes an increase in solubility through the formation of co-crystal complexes [17]. ISO is a hydrophilic conformer, that causes increased wetting of hydrophobic drug particles with the dissolution medium and has a positive effect on the dissolution profile. The results of the dissolution test have a linear relationship with the saturated solubility test and *in-silico* test where there is an increase in the solubility and dissolution profile of the TC-NIC and TC-ISO co-crystals with a molar ratio of 1:2 due to hydrogen bond interactions between the TC and NIC and ISO cofomers.

Co-crystal Characterization

TC-ISO co-crystals with a ratio of 1:2 made by SDG and SE methods showed that the best solubility and

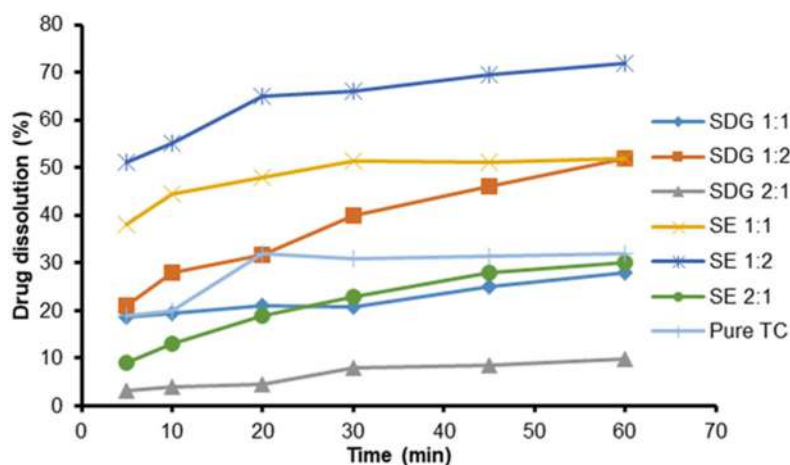


Fig 8. Dissolution Profile of pure TC and TC-ISO co-crystal

dissolution profiles were followed by characterization stages, namely PXRD, DSC, FTIR, and SEM.

Powder X-ray diffraction (PXRD)

The results of the TC, ISO, and TC-ISO co-crystal diffractograms with a ratio of 1:2 made by SE and SDG methods are presented in Fig. 9. The TC diffractogram shows the highest intensity at an angle of $2\theta = 5.47^\circ, 9.56^\circ, 10.80^\circ, 12.51^\circ, 13.57^\circ, 14.75^\circ, 17.57^\circ, 19.41^\circ, 20.59^\circ, 23.86^\circ,$ and 28.90° indicates that TC is a crystal. Meanwhile, ISO shows the highest intensity at $2\theta = 17.31^\circ, 17.50^\circ, 17.62^\circ, 20.69^\circ, 23.11^\circ, 23.19^\circ; 24,15^\circ, 25,60^\circ; 26.18^\circ, 29.66^\circ, 31.16^\circ,$ and 32.16° . The diffraction pattern of TC-ISO 1:2 co-crystal with SDG has almost the same diffraction as the physical mix (PM), but there are several new peaks at $2\theta = 11.08^\circ, 13.05^\circ, 13.84^\circ, 15.00^\circ, 17.03^\circ,$ and 20.77° which indicates the new crystal phase of TC. Meanwhile, in the TC-ISO 1:2 co-crystal with SE method, several new peaks were seen at $2\theta = 3.33^\circ, 4.98^\circ, 5.18^\circ, 6.50^\circ, 7.99^\circ,$ and 8.38° which also shows the phase change of the formed crystals.

The phenomenon of decreasing the degree of crystallinity that occurs in co-crystals is also one of the causes of the increased solubility and dissolution of TC. Changes in the crystalline phase in each of these co-crystals will affect the physicochemical properties (such as solubility and dissolution) and mechanical properties. X-ray diffraction is a commonly used technique to confirm the shape of new solids from multicomponent crystals, because the crystal shape of each compound will give a distinctive characteristic to the diffractogram pattern [26].

Differential scanning calorimetric (DSC)

The decrease in the melting point of the co-crystal is directly correlated with the increase in the solubility value of the active substance in the co-crystal. The melting point of the co-crystal will be between or below the melting point of the active substance and its cofomer so that the physicochemical properties of the co-crystal can be predicted from the polarity of the conformer. Based on Fig. 10, lower melting point values of pure TC and ISO are seen in TC-ISO 1:2 co-crystals with the SE method. The endothermic peak is in the temperature range of $81.71\text{--}104.05^\circ\text{C}$ with a sharp peak at 90.50°C , which is the melting point. Meanwhile, TC-ISO 1:2 co-crystal with SDG method showed an endothermic peak in

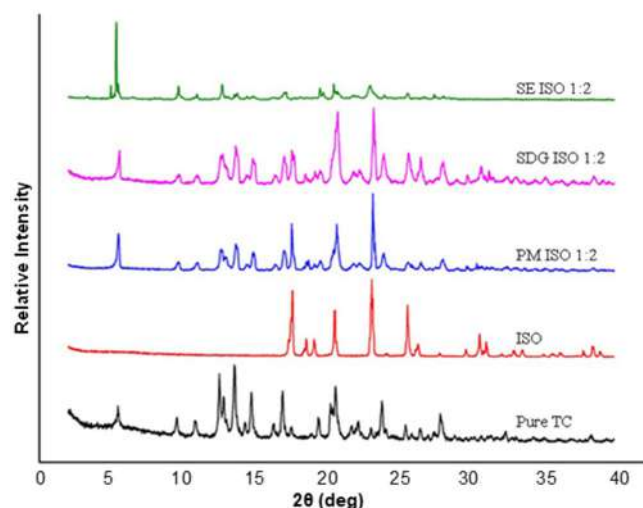


Fig 9. Comparison of pure TC and TC-ISO co-crystal diffractograms

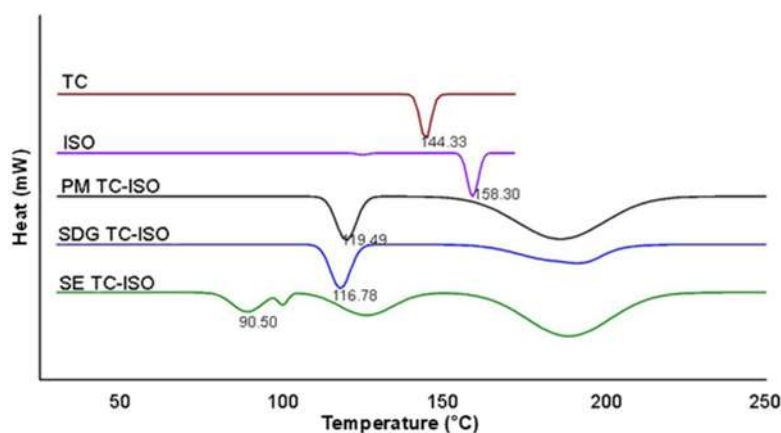


Fig 10. Thermogram profile of TC and TC-ISO 1:2 co-crystal

the range of 113.70–135.11 °C with a melting point of 116.78 °C, which was indicated by a sharp peak. Not much different from the physical mixture (PM), the endothermic peak is found at a temperature of 114.19–124.77 °C with a sharp peak as the melting point at 119.49 °C. TC-ISO co-crystal with PM and SDG method showed a similar thermogram profile. In the process, PM and SDG methods involve a mechanical process to mix the coformer and TC. In this case, it is possible in the PM mechanical process involving strong pressure, which results in the similarity of the thermogram profile. Meanwhile, the TC-ISO co-crystal with the SE method doesn't involve a mechanical process but uses a solvent to mix the coformer and TC as well as solvent evaporation. The solvent evaporation process is considered imperfect, resulting in a different shape of the thermogram profile.

When the melting point of the co-crystal solid mixture decreases, the TC-ISO 1:2 co-crystal has a higher solubility than pure TC. The endothermic peak that appears has the possibility of transforming in the co-crystals formed. The shift is caused by the interaction between TC and coformers, which changes the shape of the crystal lattice and forms a relatively different internal crystal structure, as shown in the diffractogram pattern [18]. The co-crystals formed have different melting point characteristics from the starting material.

Fourier transform infrared (FTIR) spectrophotometry

To confirm the formation of co-crystals, FTIR analysis was used to evaluate the changes in the vibrational frequencies of the specific functional groups of the crystals compared to their constituent components. Changes in hydrogen bonds at the intermolecular level provide a marked shift in the vibration frequency [27]. The FTIR spectrum of the TC crystal can be seen in Fig. 11. In the form II IR TC spectrum, it can be seen that there is a stretch of OH group at a wavenumber of 3400 cm^{-1} . In addition, the peaks at 2800 and 2600 cm^{-1} are due to the OH stretching of the citric acid carboxylic group forming two distinct hydrogen bonds. Peaks indicating C=O strain were also observed at 1738 cm^{-1} with new peaks at 1720 and 1703 cm^{-1} , indicating the presence of two carboxylic groups with different bonds.

ISO has an aromatic ring and an amide group in its

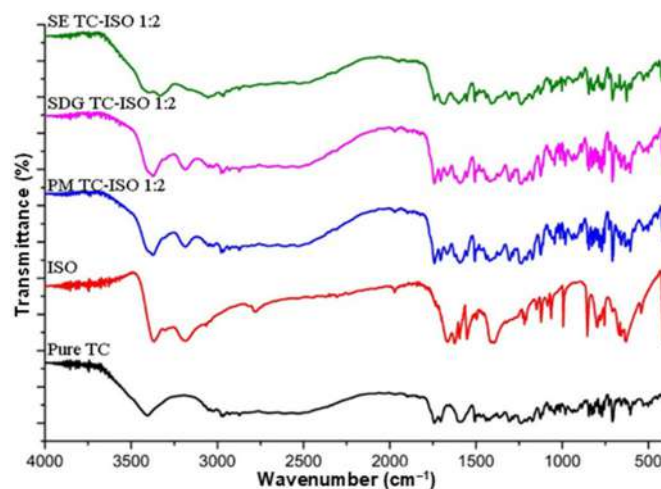


Fig 11. IR spectrum of pure TC and TC-ISO 1:2 co-crystal

molecular structure which gives it its characteristics in the IR spectrum (Fig. 11). The C-H stretching vibration on the aromatic ring is seen at 3160 cm^{-1} , and the C=C-C vibration on the aromatic ring is seen at 1618 cm^{-1} . The presence of nitrogen atoms in the aromatic ring gives a C-N vibration (stretch) at the peak of 1404 cm^{-1} . While the carbonyl group on the amide is shown at 1680 cm^{-1} with high intensity, and the strain vibration N-H is shown at 3364 cm^{-1} [25].

The IR spectrum of the TC-ISO 1:2 co-crystal (Fig. 11) shows a similar pattern to the two constituent components. Based on the *in-silico* simulation, TC and ISO form hydrogen bonds between nitrogen atoms. In the spectrum, it can be seen that there is a shift in the N-N strain vibration in the TC-ISO 1:2 co-crystal. The hydrogen bonds formed were indicated by a shift in the vibration of the N atom from 3198 to 3329 cm^{-1} in the TC-ISO 1:2 co-crystal. Another characteristic pattern of the FTIR spectrum is a shift from the carbonyl group, which usually appears at wavenumber 1760 to 1620 cm^{-1} .

Scanning electron microscopy (SEM)

The morphology of the active ingredient includes changes in the crystal habit of an active ingredient so that it can affect the physicochemical properties and ultimately affect the performance of the preparations made. The results of the SEM analysis (Fig. 12) show a change in the crystal habit of the co-crystals of its constituent components. TC crystal habit has a beam-like

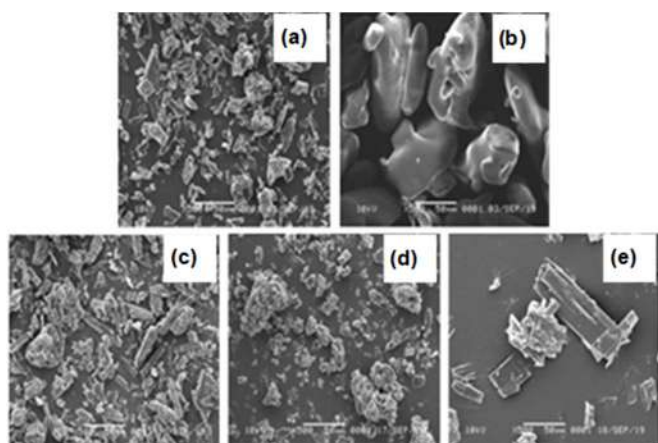


Fig 12. SEM Photomicrographs of (a) TC, (b) ISO, (c) PM TC-ISO 1:2, (d) SDG TC-ISO 1:2, and (e) SE TC-ISO 1:2

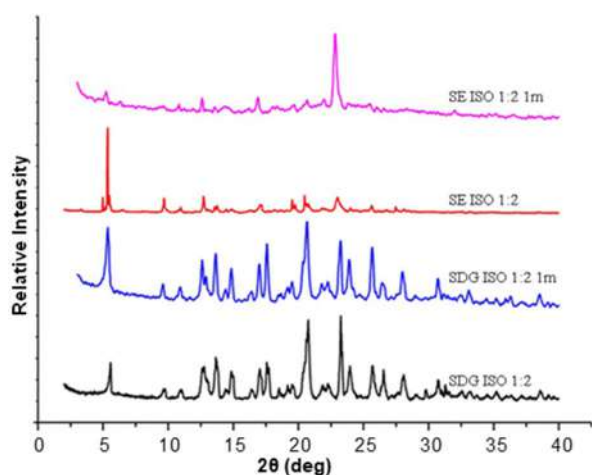


Fig 13. Comparison of diffractogram from before and after storage

shape at 500 \times magnification, while ISO forms irregular lumps. Morphological analysis of co-crystals showed a more compact structure with a higher density and combined to form larger molecules. This phenomenon is caused by the interaction of hydrogen bonds of TC and cofomers in supramolecular synthons.

Physical Stability Test

Physical observations were made to observe the physical stability of the co-crystals before and after storage, resulting in a diffraction pattern (Fig. 13). TC-ISO co-crystal with drop grinding dissolution did not change from the aspect of peak number and peak shift at an angle of 2θ , as well as peak intensity. This indicates that the stability of the TC-ISO co-crystal is relatively stable.

However, at co-crystal TC-ISO 1:2 with the SE method, changes are seen in the aspect of peak number and peak shift at an angle of 2θ . At angles of 3.33° and 4.98° , they were not seen after co-crystal storage for one month. Therefore, the SDG method is more stable than the SE method. Stability examination by x-ray diffraction is a very sensitive method to see changes in the three-dimensional structure of a molecule [18].

CONCLUSION

Increasing the solubility of TC through the co-crystallization approach in this study showed success using the NIC and ISO cofomers. Through the in-silico approach, only the two cofomers exhibit hydrogen interactions. However, based on the evaluation of solubility and dissolution tests, TC-ISO co-crystal showed the best results than TC-NIC at a ratio of 1:2. The formation of TC co-crystals will decrease the degree of crystallinity of TC, so that it becomes one of the causes of increased solubility and dissolution of TC. The increase in solubility was also caused by a decrease in the melting point value of TC after the formation of TC co-crystals. In addition, the morphology of TC co-crystals is more compact with higher density. In the physical stability test, the manufacture of co-crystals using the SDG method resulted in the stability of TC co-crystals which were more stable than the SE method.

REFERENCES

- [1] American Cancer Society, 2018, *Cancer Facts & Figures 2018*, American Cancer Society, Atlanta, US.
- [2] Chowdhury, N., Vhora, I., Patel, K., Bagde, A., Kutlehria, S., and Singh, M., 2018, Development of hot melt extruded solid dispersion of tamoxifen citrate and resveratrol for synergistic effects on breast cancer cells, *AAPS PharmSciTech*, 19 (7), 3287–3297.
- [3] Nasr, M., Hashem, F., Abdelmoniem, R., Tantawy, N., and Teiama, M., 2020, *In vitro* cytotoxicity and cellular uptake of tamoxifen citrate-loaded polymeric micelles, *AAPS PharmSciTech*, 21 (8), 306.

- [4] SreeHarsha, N., Hiremath, J.G., Chilukuri, S., Aitha, R.K., Al-Dhubiab, B.E., Venugopala, K.N., Alzahrani, A.M., and Meravanige, G., 2019, An approach to enhance dissolution rate of tamoxifen citrate, *Biomed Res. Int.*, 2019, 2161348.
- [5] Dengale, S.J., Ranjan, O.P., Hussien, S.S., Krishna, B.S.M., Musmade, P.B., Shenoy, G.G., and Bhat, K., 2014, Preparation and characterization of co-amorphous Ritonavir-Indomethacin systems by solvent evaporation technique: Improved dissolution behavior and physical stability without evidence of intermolecular interactions, *Eur. J. Pharm. Sci.*, 62, 57–64.
- [6] Metilda, G.M., and Kumari, J.P., 2016, Physicochemical characterization of α -cyclodextrin complexes of tamoxifen citrate and phase solubility studies, *Int. J. Pharm. Sci. Res.*, 7 (2), 681–688.
- [7] Mirzajani, F., Rafati, H., and Atyabi, F., 2010, Fabrication of biodegradable poly(d,l-co-glycolide) nanoparticles containing tamoxifen citrate, *Iran. Polym. J.*, 19 (6), 437–446.
- [8] Bestari, A.N., 2014, Penggunaan siklodekstrin dalam bidang farmasi, *Majalah Farmaseutik*, 10 (1), 197–201.
- [9] Abd Hashib, S., Anuar, N., Jamburi, N., Ahmad, N.F., and Abd Rahim, S., 2015, Screening for ibuprofen-sachharin co-crystal formation in wet milling, *Appl. Mech. Mater.*, 754-755, 1002–1006.
- [10] Sathisaran, I., and Dalvi, S.V., 2018, Engineering co-crystals of poorly water-soluble drugs to enhance dissolution in aqueous medium, *Pharmaceutics*, 10 (3), 108.
- [11] Aakeröy, C.B., Fasulo, M.E., and Desper, J., 2007, Co-crystal or salt: Does it really matter?, *Mol. Pharmaceutics*, 4 (3), 317–322.
- [12] Zaini, E., Halim, A., Soewandhi, S.N., and Setyawan, D., 2011, Peningkatan laju pelarutan trimetoprim melalui metode ko-kristalisasi dengan nikotinamida, *Jurnal Farmasi Indonesia*, 5 (4), 205–212.
- [13] Kerr, H.E., Softley, L.K., Suresh, K., Nangia, A., Hodgkinson, P., and Evans, I.R., 2015, A furosemide-isonicotinamide co-crystal: An investigation of properties and extensive structural disorder, *CrystEngComm*, 17 (35), 6707–6715.
- [14] Budiman, A., Megantara, S., and Apriliani, A., 2019, Solid dosage form development of glibenclamide-aspartame co-crystal using the solvent evaporation method to increase the solubility of glibenclamide, *Int. J. Appl. Pharm.*, 11 (3), 150–154.
- [15] Huang, Y., Zhou, L., Yang, W., Li, Y., Yang, Y., Zhang, Z., Wang, C., Zhang, X., and Yin, Q., 2019, Preparation of theophylline-benzoic acid co-crystal and on-line monitoring of co-crystallization process in solution by raman spectroscopy, *Crystals*, 9 (7), 329.
- [16] Zaworotko, M., 2008, Crystal engineering of co-crystals and their relevance to pharmaceuticals and solid-state chemistry, *Acta Crystallogr., Sect. A: Found. Crystallogr.*, 64 (a1), C11–C12.
- [17] Gozali, D., Bahti, H.H., Soewandhi, S.N., and Abdassah, M., 2014, Pembentukan kokristal antara kalsium atorvastatin dengan isonikotinamid dan karakterisasinya, *JUSAMI*, 15 (2), 103–110.
- [18] Hiendrawan, S., Widjojokusumo, E., Veriansyah, B., and Tjandrawinata, R.R., 2017, Pharmaceutical salts of carvedilol: Polymorphism and physicochemical properties, *AAPS PharmSciTech*, 18 (4), 1417–1425.
- [19] Gamberini, M.C., Baraldi, C., Tinti, A., Palazzoli, F., and Ferioli, V., 2007, Vibrational study of tamoxifen citrate polymorphism, *J. Mol. Struct.*, 840 (1-3), 29–37.
- [20] Qiao, N., Li, M., Schlindwein, W., Malek, N., Davies, A., and Trappitt, G., 2011, Pharmaceutical co-crystals: An overview, *Int. J. Pharm.*, 419 (1-2), 1–11.
- [21] Fadhilah, Q., and Tjahjono, D.H., 2012, Hubungan kuantitatif struktur dan aktivitas senyawa turunan 3-haloasilaminobenzoilurea sebagai inhibitor pembentukan mikrotubulus, *Acta Pharm. Indones.*, 37 (3), 76–82.
- [22] Alatas, F., Soewandhi, S.N., and Sasongko, L., 2014, Kelarutan dan stabilitas kimia kompleks didanosin dengan nikotinamid atau L-arginin, *JUSAMI*, 15 (2), 94–102.

- [23] Pagire, S.K., Korde, S.A., Whiteside, B.R., Kendrick, J., and Paradkar, A., 2013, Spherical crystallization of carbamazepine/saccharin co-crystals: Selective agglomeration and purification through surface interactions, *Cryst. Growth Des.*, 13 (10), 4162–4167.
- [24] Sanphui, P., Babu, N.J., and Nangia, A., 2013, Temozolomide co-crystals with carboxamide cofomers, *Cryst. Growth Des.*, 13 (5), 2208–2219.
- [25] Fernandes, G.J., Rathnanand, M., and Kulkarni, V., 2019, Mechanochemical synthesis of carvedilol cocrystals utilizing hot melt extrusion technology, *J. Pharm. Innovation*, 14 (4), 373–381.
- [26] Parmar, V.K., and Shah, S.A., 2013, Hydrochloride salt co-crystals: Preparation, characterization and physicochemical studies, *Pharm. Dev. Technol.*, 18 (2), 443–453.
- [27] Bolla, G., Sanphui, P., and Nangia, A., 2013, Solubility advantage of tenoxicam phenolic co-crystals compared to salts, *Cryst. Growth Des.*, 13 (5), 1988–2003.

The Optimization of Silica-Based Composite Membrane from Volcanic Ash of Mount Sinabung, Titanium Dioxide, and Polyvinyl Alcohol for River Water Treatment through Photocatalyst Process

Moraida Hasanah^{1,2}, Timbangan Sembiring¹, Zuriah Sitorus¹, Syahrul Humaidi^{1*}, Fynnisa Zebua³, and Rahmadsyah Rahmadsyah²

¹Postgraduate Program (Physics), Faculty of Mathematics and Natural Sciences, Universitas Sumatera Utara, Jl. Bioteknologi No. 1 Padang Bulan, Medan 20155, Indonesia

²Department of Mechanical Engineering, Universitas Asahan, Kisaran Timur, Kisaran 21216, Indonesia

³Department of Civil Engineering, Universitas Asahan, Kisaran Timur, Kisaran 21216, Indonesia

* **Corresponding author:**

tel: +62-82361351902

email: syahrul1@usu.ac.id

Received: December 5, 2021

Accepted: February 3, 2022

DOI: 10.22146/ijc.70989

Abstract: The application of composite membranes consisting of SiO₂ from the volcanic ash of Mount Sinabung, TiO₂, and PVA on a laboratory scale has been investigated to improve the Silau River's water quality in Asahan Regency. The purpose of this study is to determine the optimal combination of SiO₂, TiO₂, and PVA for treating river water to minimize its heavy metal content and color intensity to achieve clean water requirements. The membranes were prepared by drop-casting with varied compositions of PVA/40TiO₂/60SiO₂, PVA/60TiO₂/40SiO₂, PVA/80TiO₂/20SiO₂, and PVA/100TiO₂/0SiO₂. PVA was dissolved in aquadest, mixed with SiO₂ and TiO₂, then imprinted and dried for 24 h at 50 °C. A photocatalyst test was performed on each composition variation to see how the Silau River water's color changed over time. The PVA/80TiO₂/20SiO₂ membrane's composition fluctuated the highest during photocatalyst testing, with 45.95% degradation. The parameter results on the Silau River water test, namely turbidity, color, and chromium values, were reduced by photocatalysis of a PVA/80TiO₂/20SiO₂ composite membrane to 16 NTU, 30 TCU, and 0.013 mg/L, respectively. These results met the clean water quality criteria specified by Minister of Health of the Republic of Indonesia Decree No. 416/MENKES/PER/IX/1990.

Keywords: silica-based composite membrane; photocatalyst; river water treatment

■ INTRODUCTION

The Silau River is a vast river that flows from Asahan Regency's southern edge to the city of Tanjung Balai. The Silau River is the second biggest river in Indonesia, next to Asahan, and plays a significant role in the people who live along its banks. The Silau River benefits from abundant agricultural goods such as sand mining, fish, and shellfish. The Silau River watershed is also adjacent to community settlements and numerous community activities that significantly influence the Silau River water as a source of pollution. The Silau watershed provides numerous benefits to the surrounding community. However, it is feared that the Silau watershed area and its

surroundings will become polluted due to community and industrial activities near the river. Hence, monitoring and evaluation of the condition of the waters in the community are necessary as a form of prevention [1].

According to the Ministry of the Environment of the Republic of Indonesia data year 2014, residential garbage contaminated more than 60% of waterways [2]. Numerous techniques for resolving the pollution problem caused by liquid waste are being explored, one of which is the photocatalyst process. Photocatalysis is a chemical reaction that happens in the interaction between light and a photocatalyst. Due to its efficacy and

adaptability, photocatalytic degradation has become an increasingly attractive solution for water pollution concerns [3-4]. Photocatalysts are a favorable method in treating dirty water and textile waste. Titanium dioxide (TiO₂) is a frequently used photocatalyst material due to its high stability and non-toxicity. TiO₂ is a photocatalyst that stands out for its photodegradation of organic dyes [4].

TiO₂ with an anatase structure has high photocatalytic activity [5-7]. One of the properties of TiO₂ is determined by its crystallinity, crystal size, and crystal phase. Increasing the capability of TiO₂ material can be done by adding oxides substances such as Fe₂O₃ [6], SiO₂ [8], and other oxides. Since TiO₂ has a limited surface area, it can affect the performance of TiO₂ materials [9]. To address this issue, it is required to incorporate an oxide material with a high surface area, such as SiO₂. Silica with the chemical formula of SiO₂ may be produced by extracting volcanic ash from Mount Sinabung, where it is known that the silica concentration after extraction is 48% [10]. SiO₂ that is combined with TiO₂ has several benefits, including being one of the most promising heterogeneous photocatalytic options for the degradation of various chemical molecules, heavy metal reduction, and selective oxidative processes [9].

■ EXPERIMENTAL SECTION

Materials

The materials used to fabricate SiO₂ composite membranes included volcanic ash extracted from Mount Sinabung as a silica source, polyvinyl alcohol (PVA; Sigma-Aldrich, Mw = 145,000) as a matrix, TiO₂ (Sigma-Aldrich) as an active photocatalyst, and Silau River water from Asahan Regency, North Sumatera as a sample in the photocatalyst process.

Instrumentation

Fourier transform infrared (FTIR) spectroscopy (Shimadzu, IR Prestige 21), scanning electron microscope-energy dispersive X-ray (SEM-EDX, FEI, Inspect-S50), and X-ray diffractometer (XRD, PANalytical, X'Pert PRO) were employed to characterize the composite membrane samples. Furthermore,

ultraviolet-visible (UV-Vis) spectrophotometer (Analytik Jena, Specord 200 Plus) was used to monitor the degradation process.

Procedure

A 10% PVA solution was prepared by dissolving 1.111 g of PVA in 10 mL of distilled water and heating it for 1 h at 90 °C. Then, using a 100-mesh sieve, SiO₂ and TiO₂ were sieved. As a filler, SiO₂ was combined with TiO₂ in this research. PVA and filler are combined in a 4:1 ratio. The mixture was then molded and dried for 24 h at 50 °C. The following table summarizes the differences in the composition of the filling material (Table 1).

After fabricating the PVA/TiO₂/SiO₂ composite membrane, the next stage was to test the membrane material, precisely the degree of the swelling test, which was used to determine the membrane's resistance to water absorption. The degree of swelling was determined by submerging it in aquadest for varying periods. Additionally, FTIR and SEM analyses were performed to identify the functional groups and morphology of the PVA/TiO₂/SiO₂ composite membrane.

Additionally, the photocatalyst test was conducted to ascertain how the color content of Silau River water may be decreased by adding a PVA/TiO₂/SiO₂ composite membrane. The photocatalyst process was carried out in a box fitted with a ten-watt ultraviolet lamp for 1, 2, 3, 4, 5, 6, and 8 h. The solution's absorbance was determined following the treatment using a UV-Vis spectrometer. Eq. (1) was applied to calculate the percentage of watercolor decrease in the water sample.

$$\% \text{ Decrease in water content} = \frac{c_0 - c_t}{c_0} \times 100 \quad (1)$$

Table 1. Variations of Filler Composition as TiO₂:SiO₂

Sample	TiO ₂ (%)	SiO ₂ (%)
I	100	0
II	80	20
III	60	40
IV	40	60

where c_0 denotes the initial concentration of Silau River water, and c_t is the concentration after t time of the photocatalyst process.

The characterization of river water was conducted at the Environmental Health Engineering Center of Class I in Medan. The purpose of this test was to investigate the effect of adding a PVA/TiO₂/SiO₂ composite membrane towards river water content parameters.

RESULTS AND DISCUSSION

FTIR Characterization

FTIR was used to visualize the composite membrane's functional groups. A functional group is a collection of one or more atoms with distinct chemical characteristics covalently connected to other compounds [11]. The FTIR spectra are presented in Fig. 1. The band around 3500 and 1700 cm⁻¹ corresponds to the absorption of the O-H stretching and bending functional groups, which are the hydroxyl groups present in PVA [12]. A C-H stretching functional group with an absorbance of around 2900 cm⁻¹ suggests the existence of residual organic molecules. An absorption at a wavenumber of around 1100 cm⁻¹ was assigned to C-O bonds from PVA

[13]. This peak overlap with Si-O-Si asymmetric stretching vibration [14]. The absorption of about 960 cm⁻¹ is owing to the stretching of Si-O-Ti, which suggests the presence of a covalent bond between TiO₂ and SiO₂, rather than Van der Waals attraction [6]. However, this peak fuses with other peaks so that it looks unclear. Moreover, absorption at approximately 770 cm⁻¹ is due to the Si-O stretching functional group as well as Ti-O [14-15].

SEM-EDX Characterization

The morphology of the PVA/TiO₂/SiO₂ composite membrane was observed using SEM. The SEM test results are depicted in Fig. 2. The PVA/TiO₂/SiO₂ composite membrane appears to have a uniform distribution of TiO₂ and SiO₂ fillers [16]. The morphology of the PVA/60TiO₂/40SiO₂ and PVA/80TiO₂/20SiO₂ samples was more homogenous than that of the filler material, whereas the PVA/40TiO₂/60SiO₂ and PVA/100TiO₂/0SiO₂ samples exhibited an agglomeration [17].

Agglomeration may occur due to the uneven mixing of the PVA matrix with the TiO₂ and SiO₂ fillers [18]. Agglomeration decreased the surface area of TiO₂

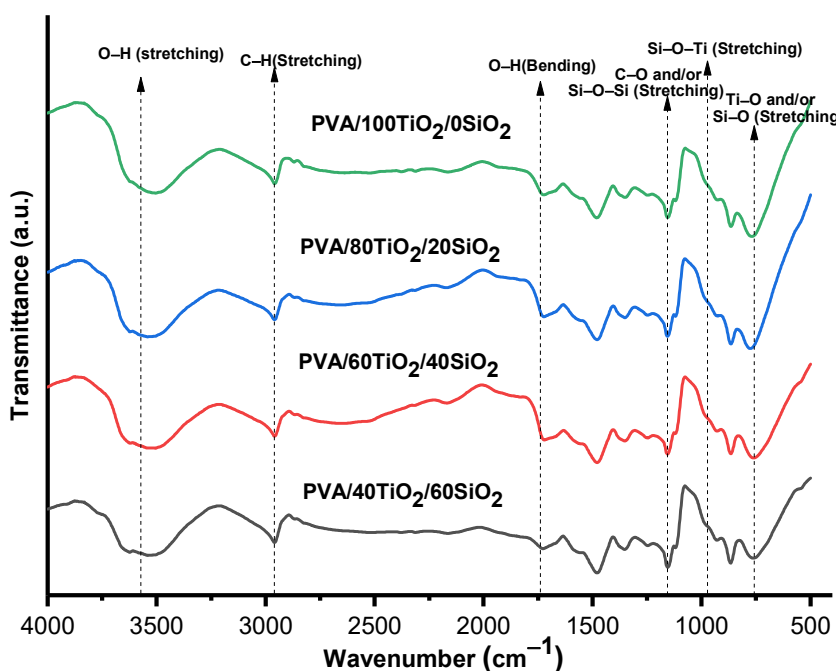


Fig 1. FTIR spectra of (a) PVA/40TiO₂/60SiO₂, (b) PVA/60TiO₂/40SiO₂, (c) PVA/80TiO₂/20SiO₂, and (d) PVA/100TiO₂/0SiO₂ composite membrane

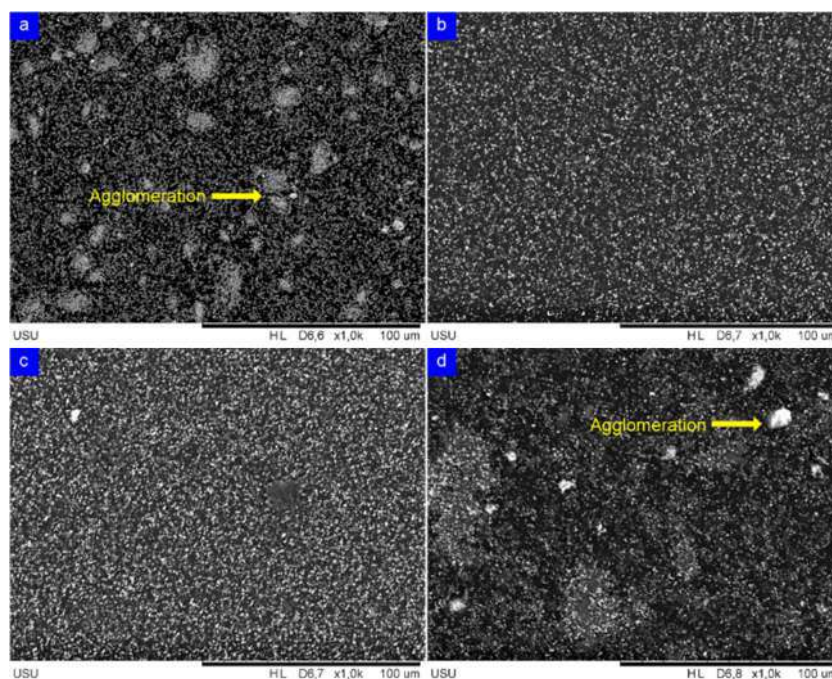


Fig 2. SEM images of (a) PVA/40TiO₂/60SiO₂, (b) PVA/60TiO₂/40SiO₂, (c) PVA/80TiO₂/20SiO₂, and (d) PVA/100TiO₂/0SiO₂ composite membrane

and SiO₂, both of which act as degrading agents in river water. This can affect the membrane's performance during the photocatalytic testing process. The bigger the surface area of the particles, the higher the surface area of contact between the membrane and the test sample in the form of river water, resulting in a quicker rate of color degradation of river water.

The distribution of the components that comprise the PVA/TiO₂/SiO₂ composite membrane is depicted in Fig. 3. As can be observed, the filler in TiO₂ and SiO₂ particles is dispersed equally. This will impact the photocatalyst process's outcome later. PVA/TiO₂/SiO₂ composite membranes are composed mainly of C and O elements, also found in PVA [16]. The contents of the membrane elements are determined using EDX, as stated in Table 2.

XRD Characterization

The crystal structure of the PVA/TiO₂/SiO₂ composite membrane was characterized using XRD. The diffractogram in Fig. 4 illustrates the XRD test results. Two crystal structures were identified in the XRD analysis, namely the Anatase and PVA peaks.

The XRD analysis reveals a crystal structure in the form of anatase for TiO₂ [19]. Anatase's crystal structure in Fig. 4 shows a tetragonal crystal system with lattice parameters of $a = 3.7845$ and $c = 9.5143$ Å, corresponding to COD:9015929. According to Jiang et al. [20], the anatase phase was found in this study at angles of $2\theta = 25.12^\circ$; 36.80° ; 37.64° ; 38.48° ; 47.98° ; and 53.70° with Miller indices of (011), (013), (004), (112), (020), and (015). As indicated by the XRD pattern,

Table 2. Composition of PVA/TiO₂/SiO₂ Composite Membrane

Composite Membrane	Percentage (%)			
	C	O	Si	Ti
PVA/40TiO ₂ /60SiO ₂	59.58	35.26	2.74	2.43
PVA/60TiO ₂ /40SiO ₂	63.94	32.33	0.72	3.01
PVA/80TiO ₂ /20SiO ₂	62.26	33.97	0.07	3.70
PVA/100TiO ₂ /0SiO ₂	62.78	33.17	NA*	4.05

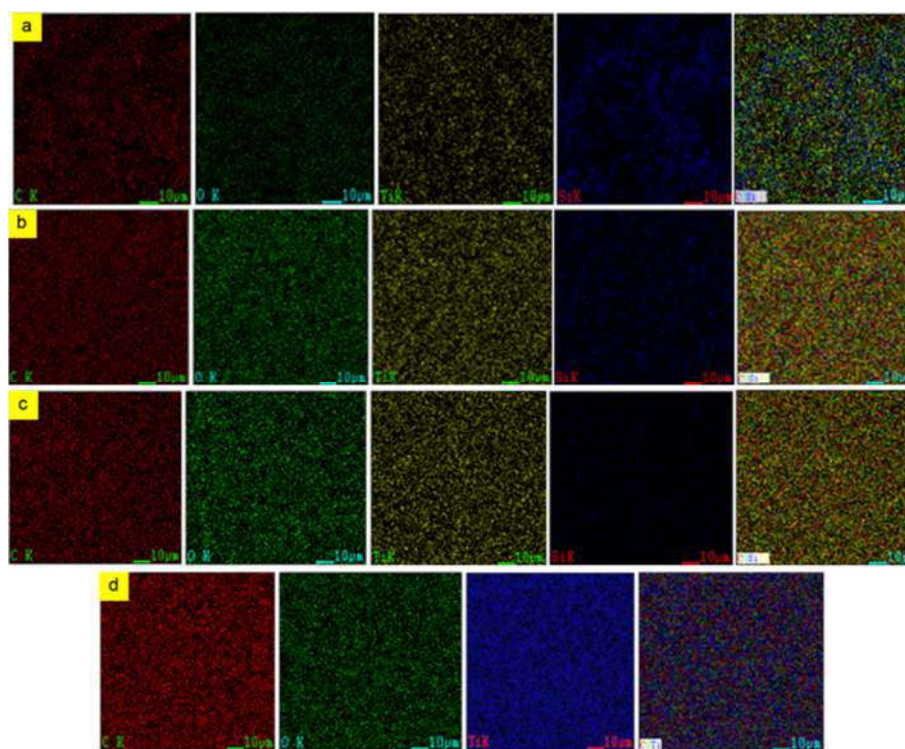


Fig 3. Elemental mapping of (a) PVA/40TiO₂/60SiO₂, (b) PVA/60TiO₂/40SiO₂, (c) PVA/80TiO₂/20SiO₂, and (d) PVA/100TiO₂/0SiO₂ composite membrane

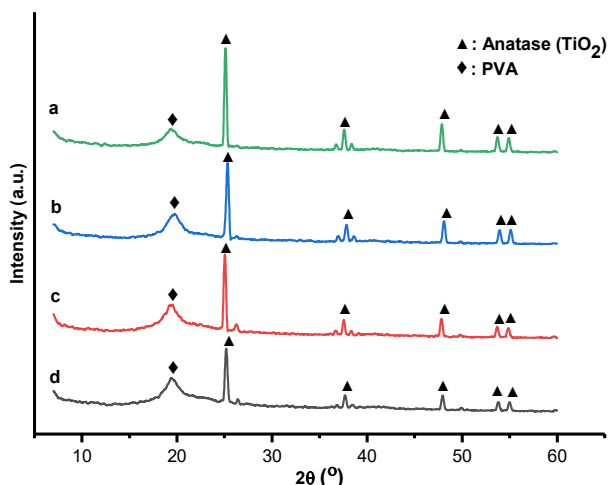


Fig 4. XRD patterns of (a) PVA/100TiO₂/0SiO₂, (b) PVA/80TiO₂/20SiO₂, (c) PVA/60TiO₂/40SiO₂, and (d) PVA/40TiO₂/60SiO₂

no peak indicates the structure of SiO₂. The structure of SiO₂ is amorphous, and as a result, the peak does not exist in this diffractogram. This is consistent with the findings in Ref. [21].

Meanwhile, the amorphous peak visible in the XRD

results corresponds to the PVA peak. PVA is an amorphous polymer. With a Miller index of (101), PVA was found at an angle of $2\theta = 21.92^\circ$. These findings were supported by the previous research [22]. Moreover, the intensity of the anatase was observed to increase with the addition of TiO₂.

Swelling Characterization

Swelling is a property that may be used to assess the rate of membrane absorption and the saturation point of solution absorption [23]. The swelling test results are depicted in Fig. 5.

After adding SiO₂ to the membrane composition, the degree of swelling was relatively modest. This demonstrates that the membrane is superior in terms of resistance to absorption but affects the photocatalytic process [23] since the catalyst process requires strong absorption when the membrane is put into the test solution to initiate a photocatalytic process [24-25]. The swelling values for the PVA/100TiO₂/0SiO₂ and the PVA/40TiO₂/60SiO₂ membrane composition were 171%

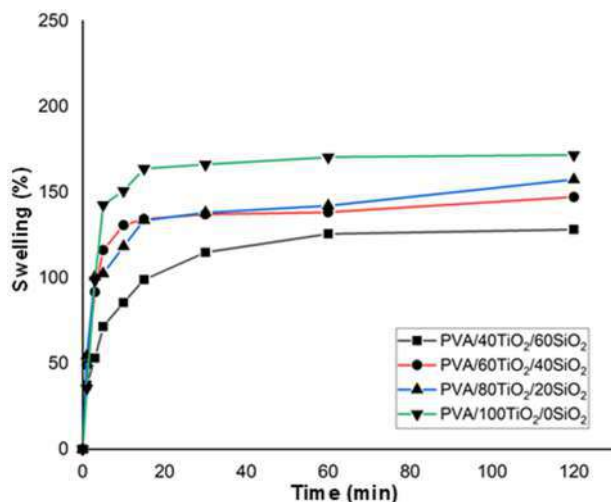


Fig 5. Swelling test of PVA/TiO₂/SiO₂ composite membrane

and 128%, respectively. It is reasonable to suppose that the amount of SiO₂ added is proportionate to the degree of swelling reduced [26]. The increased surface area of the

PVA/TiO₂/SiO₂ composite membrane contributes significantly to its increased processing and swelling rates. Swelling also affects the membrane's mechanical properties [9].

UV-Vis Analysis

UV-Vis spectroscopy was used to examine the color degradation. Water samples from the Silau River were passed over a membrane having a surface area of 1.5 × 1.5 cm². The water added to the membrane is then placed in a box equipped with a UV lamp, and the irradiation procedure is repeated for a specific duration. Fig. 6 illustrates the test results.

UV-Vis spectroscopy was used to measure the degree of color degradation in river water. The measurement results indicate that the optimal composition is PVA/80TiO₂/20SiO₂. As seen in Fig. 6, the cleanest water appears after 8 h, while the PVA/40TiO₂/60SiO₂ composite membrane produced the



Fig 6. Images of Silau River water treated using (a) PVA/40TiO₂/60SiO₂, (b) PVA/60TiO₂/40SiO₂, (c) PVA/80TiO₂/20SiO₂, and (d) PVA/100TiO₂/0SiO₂ for 1–8 h (from left to right)

lowest yield. The longer the photocatalyst process continues, the more significant the decrease in watercolor levels [6], resulting in cleaner Silau River water.

Fig. 7 shows the percentage of color degradation of river water. The most optimum degradation occurs at a rate of 45.95% by PVA/80TiO₂/20SiO₂ composite membrane. According to the graph in the illustration, degradation will occur at a maximum rate over time.

The length of irradiation in the photocatalyst process indicates the time required for the PVA/TiO₂/SiO₂ composite membrane to interact with the inner light and form •OH radicals from river water. With increasing duration, the PVA/TiO₂/SiO₂ composite membrane absorbs more proton energy, making it simpler to lower the color content of river water. The longer the irradiation period, the more the photocatalyst process will continuously operate until the optimum condition is reached [27].

The matrix plays a role as a support for dye absorption in the absence of decomposition. Increased dye decomposition efficiency might be attributed to improved TiO₂ dispersion. Additionally, photodegradation's efficacy depends on the degree of swelling, enabling the lower TiO₂ concentration to degrade the color efficiently and rapidly. Moreover, the carboxylate anions increase the electrostatic and hydrophilic repulsion of the hydrogel's polymer chains. As a result, the PVA membrane increases

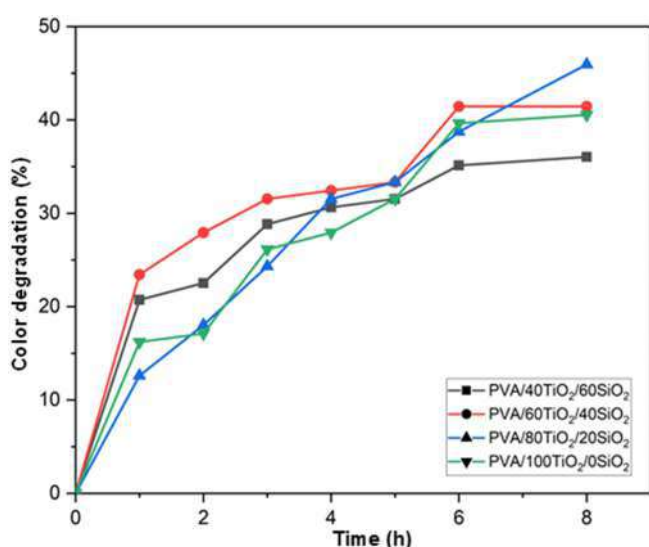


Fig. 7. Color degradation of the river water after photocatalytic process

the surface area, allowing TiO₂ particles to come into contact with a greater degree of swelling [28]. On the other hand, excessive TiO₂ can cause this compound coating to thicken, which can cause obstruct light transmission and reduce the specific surface area [6].

River Water Characterization Before and After Treatment by PVA/TiO₂/SiO₂ Composite Membranes

Following the photocatalyst test on river water, the best composition was used to determine its composition. Table 3 summarizes the test results. They can absorb heavy metals from river water due to the presence of SiO₂ particles. SiO₂ is a porous solid. The porous structure is proportional to the surface area: the smaller the silica particle, the higher the surface area. Hence, the more significant the adsorption capacity.

From the results of the FTIR characterization, there are silanol (Si–OH) and siloxane (Si–O–Si) groups that can bind specific metal ions [15] so that the levels of heavy metals dissolved in river water decrease. This silanol group has low acidity and oxygen as a weak donor atom. Two groups, namely straight-chain Si–O–Si, and siloxane groups, form a circular structure. Straight chain siloxanes are unreactive with common reagents but are highly reactive to alkali metal compounds. The siloxane group with a circular shape has high reactivity and can absorb water, ammonia, as well as methanol. The reaction of those with water will produce the Si–OH group [6].

Changes in functional groups are due to the transformation of certain silanol groups into others. Other groups should give advantages, such as interactions during the adsorption process. Other groups facilitate adsorption by creating compounds with metal ions. Adsorption can occur by ion exchange if the replacement group is ionic. This transformation enables interaction with metal ions. Adsorption of metal ions on SiO₂ can be used to separate metal ions present in a solution, such as industrial waste or wastewater [6].

Table 3 demonstrates that the test results indicate a change in the value of each parameter. The initial turbidity, color, and chromium parameter values were 115 NTU, 63 TCU, and 0.389 mg/L, respectively, which initially did not meet the clean water standard. After

Table 3. Characterization of river water before and after treatment by PVA/80TiO₂/20SiO₂ composite membranes

Parameters	Units	Test results before treatment	Test results after treatment	Maximum content
Turbidity	NTU	115	16	25
Color	TCU	63	30	50
Dissolved solid	mg/L	70.6	69	1000
Taste	-	Tasteless	Tasteless	Tasteless
Scent	-	Odorless	Odorless	Odorless
Fe	mg/L	0.19002	0.09002	1
Hardness	mg/L	67.02	59.1	500
Mn	mg/L	0.12451	0.11893	0.5
Nitrite	mg/L	3.3	2.3	10
Detergent	mg/L	< 0.5	< 0.5	< 0.05
Hg	mg/L	0.00079	0.00043	0.001
As	mg/L	0.00024	0.00018	0.05
Cd	mg/L	0.00043	0.00037	0.005
Cr(IV)	mg/L	0.389	0.013	0.05
Se	mg/L	0.00093	0.00089	0.01
Zn	mg/L	0.00191	0.00178	15
Pb	mg/L	0.00067	0.00058	0.05
Organic substance	mg/L	15.848	2.139	10

treatment, the parameters of turbidity, color, and chromium values were reduced to 16 NTU, 30 TCU, and 0.013 mg/L, respectively, following the treatment with a PVA/80TiO₂/20SiO₂ composite membrane using the photocatalyst method. It demonstrates that after treatment, the test results for river water fulfilled the criteria for clean water quality established by Minister of Health of the Republic of Indonesia Decree No. 416/MENKES/PER/IX/1990 dated September 3, 1990.

■ CONCLUSION

The composition of the PVA/80TiO₂/20SiO₂ membrane showed the most optimum composition in this study throughout photocatalyst testing. Degradation occurs at a rate of 45.95%. The membrane can effectively degrade the color of river water in this composition after 8 h. As for the Silau River water test results, it can be seen that each parameter has changed. The initial turbidity, color, and chromium parameter values were 115 NTU, 63 TCU, and 0.389 mg/L, respectively, which initially did not meet clean water standards. After being treated with a PVA/80TiO₂/20SiO₂ composite membrane by photocatalyst method, the turbidity, color, and chromium

parameter values were changed to 16 NTU, 30 TCU, and 0.013 mg/L, respectively. These results indicate that the Silau River water test satisfied the clean water quality criteria established by Minister of Health of the Republic of Indonesia Decree No. 416/MENKES/PER/IX/1990 dated September 3, 1990. Additionally, given the results of this study shown that the watercolor could be degraded, it is expected that this composite membrane might be used to clean dye waste in regions with high river flow, such as Asahan Regency.

■ ACKNOWLEDGMENTS

The authors would like to thank Universitas Sumatera Utara and Universitas Asahan for their support throughout this research.

■ AUTHOR CONTRIBUTIONS

The first author prepared materials and conducted experiments. The second, third, and fourth authors applied the concepts and methodology, while the fifth and sixth authors processed and analyzed the data. The manuscript was written and revised by the first and fourth authors. All authors evaluated and discussed the

results. All authors have approved the final version of this manuscript.

■ REFERENCES

- [1] Nasution, H.A., and Sihombing, A.T., 2017, Analisis kandungan logam berat timbal (Pb) dalam air sungai silau di kota kisaran, *Seminar Nasional Multidisiplin Ilmu 2017*, Universitas Asahan, September 22, 2017.
- [2] Asadiya, A., and Karnaningroem, N., 2018, Pengolahan air limbah domestik menggunakan proses aerasi, pengendapan, dan filtrasi media zeolit-arang aktif, *Jurnal Teknik ITS*, 7 (1), D18–D22.
- [3] Chau, J.H.F., Lee, K.M., Pang, Y.L., Abdullah, B., Juan, J.C., Leo, B.F., and Lai, C.W., 2021, Photodegradation assessment of RB5 dye by utilizing WO₃/TiO₂ nanocomposite: A cytotoxicity study, *Environ. Sci. Pollut. Res.*, 29 (15), 22372–22390.
- [4] Gopinath, K.P., Madhav, N.V., Krishnan, A., Malolan, R., and Rangarajan, G., 2020, Present applications of titanium dioxide for the photocatalytic removal of pollutants from water: A review, *J. Environ. Manage.*, 270, 110906.
- [5] Purbia, R., Borah, R., and Paria, S., 2017, Carbon-doped mesoporous anatase TiO₂ multi-tubes nanostructures for highly improved visible light photocatalytic activity, *Inorg. Chem.*, 56 (16), 10107–10116.
- [6] Yang, Y., Zhang, Q., Deng, Y., Zhu, C., Wang, D., and Li, Z., 2017, Synthesis of Nano TiO₂-Fe₂O₃ Photocatalyst and Photocatalytic Degradation Properties on Oxytetracycline Hydrochloride, *Proceedings of the 2017 7th International Conference on Manufacturing Science and Engineering (ICMSE 2017)*, Atlantis Press, Paris, France., 216–219.
- [7] Fayrus, M., Putra Santoso, A.Y., and Muljani, S., 2020, Sintesis komposit titania-silika dengan proses sol gel, *ChemPro*, 1 (1), 36–40.
- [8] Hakki, A., Yang, L., Wang, F., and Macphee, D.E., 2017, The effect of interfacial chemical bonding in TiO₂-SiO₂ composites on their photocatalytic NO_x abatement performance, *J. Visualized Exp.*, 125, e56070.
- [9] Rasheed, T., Adeel, M., Nabeel, F., Bilal, M., and Iqbal, H.M.N., 2019, TiO₂/SiO₂ decorated carbon nanostructured materials as a multifunctional platform for emerging pollutants removal, *Sci. Total Environ.*, 688, 299–311.
- [10] Hasanah, M., Sembiring, T., Sebayang, K., Humaidi, S., Rahmadsyah, Saktisahdan, T.J., Handoko, F., and Ritonga, S.I., 2021, Extraction of silica dioxide (SiO₂) from mount Sinabung volcanic ash with coprecipitation method, *IOP Conf. Ser.: Mater. Sci. Eng.*, 1156, 012015.
- [11] Kariminejad, M., Zibaei, R., Kolahdouz-Nasiri, A., Mohammadi, R., Mortazavian, A.M., Sohrabvandi, S., Khanniri, E., and Khorshidian, N., 2021, Chitosan/polyvinyl alcohol/SiO₂ nanocomposite films: Physicochemical and structural characterization, *Biointerface Res. Appl. Chem.*, 12 (3), 3725–3734.
- [12] Huang, F., Hao, H., Sheng, W., and Lang, X., 2021, Dye-TiO₂/SiO₂ assembly photocatalysis for blue light-initiated selective aerobic oxidation of organic sulfides, *Chem. Eng. J.*, 423, 129419.
- [13] Rodrigues, I.R., de Camargo Forte, M.M., Azambuja, D.S., and Castagno, K.R.L., 2007, Synthesis and characterization of hybrid polymeric networks (HPN) based on polyvinyl alcohol/chitosan, *React. Funct. Polym.*, 67 (8), 708–715.
- [14] Mirabedini, A., Mirabedini, S.M., Babalou, A.A., and Pazokifard, S., 2011, Synthesis, characterization and enhanced photocatalytic activity of TiO₂/SiO₂ nanocomposite in an aqueous solution and acrylic-based coatings, *Prog. Org. Coat.*, 72 (3), 453–460.
- [15] Yudo, S., and Said, N.I., 2019, Kondisi kualitas air sungai Surabaya studi kasus: Peningkatan kualitas air baku PDAM Surabaya, *JTL*, 20 (1), 19–28.
- [16] Khalil, A., Aboamera, N.M., Nasser, W.S., Mahmoud, W.H., and Mohamed, G.G., 2019, Photodegradation of organic dyes by PAN/SiO₂-TiO₂-NH₂ nanofiber membrane under visible light, *Sep. Purif. Technol.*, 224, 509–514.
- [17] Azari, M., Sadeghi, M., Aroon, M., and Matsuura, T., 2019, Polyurethane mixed matrix membranes for gas separation: A systematic study on effect of

- SiO₂/TiO₂ nanoparticles, *J. Membr. Sci. Res.*, 5 (1), 33–43.
- [18] Soudagar, M.E.M., Nik-Ghazali, N.N., Kalam, M.A., Badruddin, I.A., Banapurmath, N.R., Yunus Khan, T.M., Bashir, M.N., Akram, N., Farade, R., and Afzal, A., 2019, The effects of graphene oxide nanoparticle additive stably dispersed in dairy scum oil biodiesel-diesel fuel blend on CI engine: Performance, emission and combustion characteristics, *Fuel*, 257, 116015.
- [19] Yun, J., Im, J.S., Oh, A., Jin, D.H., Bae, T.S., Lee, Y.S., and Kim, H.I., 2011, pH-sensitive photocatalytic activities of TiO₂/poly(vinyl alcohol)/poly(acrylic acid) composite hydrogels, *Mater. Sci. Eng., B*, 176 (3), 276–281.
- [20] Jiang, Q., Huang, J., Ma, B., Yang, Z., Zhang, T., and Wang, X., 2020, Recyclable, hierarchical hollow photocatalyst TiO₂@SiO₂ composite microsphere realized by raspberry-like SiO₂, *Colloids Surf., A*, 602, 125112.
- [21] Takari, A., Ghasemi, A.R., Hamadian, M., Sarafrazi, M., and Najafidoust, A., 2021, Molecular dynamics simulation and thermo-mechanical characterization for optimization of three-phase epoxy/TiO₂/SiO₂ nano-composites, *Polym. Test.*, 93, 106890.
- [22] de Lima, G.G., Ferreira, B.D., Matos, M., Pereira, B.L., Nugent, M.J.D., Hansel, F.A., and Magalhães, W.L.E., 2020, Effect of cellulose size-concentration on the structure of polyvinyl alcohol hydrogels, *Carbohydr. Polym.*, 245, 116612.
- [23] Wang, C., Feng, Z., Zhao, Y., Li, X., Li, W., Xie, X., Wang, S., and Hou, H., 2017, Preparation and properties of ion exchange membranes for PEMFC with sulfonic and carboxylic acid groups based on polynorbornenes, *Int. J. Hydrogen Energy*, 42 (50), 29988–29994.
- [24] Zhang, Z., Hu, L., Zhang, H., Yu, L., and Liang, Y., 2020, Large-sized nano-TiO₂/SiO₂ mesoporous nanofilm-constructed macroporous photocatalysts with excellent photocatalytic performance, *Front. Mater. Sci.*, 14 (2), 163–176.
- [25] Zhang, M., E, L., Zhang, R., and Liu, Z., 2019, The effect of SiO₂ on TiO₂-SiO₂ composite film for self-cleaning application, *Surf. Interfaces*, 16, 194–198.
- [26] Wang, P., Wang, C., Wang, H., Long, H., and Zhou, T., 2022, Effects of SiO₂, CaO and basicity on reduction behaviors and swelling properties of fluxed pellet at different stages, *Powder Technol.*, 396, 477–489.
- [27] Azzaz, A.A., Jellali, S., Hamed, N.B.H., El Jery, A., Khezami, L., Assadi, A.A., and Amrane, A., 2021, Photocatalytic treatment of wastewater containing simultaneous organic and inorganic pollution: competition and operating parameters effects, *Catalysts*, 11 (7), 855.
- [28] Schraufnagel, D.E., 2020, The health effects of ultrafine particles, *Exp. Mol. Med.*, 52 (3), 311–317.

Profiling Metabolites through Chemometric Analysis in *Orthosiphon aristatus* Extracts as α -Glucosidase Inhibitory Activity and *In Silico* Molecular Docking

Faizal Maulana¹, Alfari Andiqa Muhammad², Ali Umar¹, Fachrur Rizal Mahendra², Muhammad Musthofa², and Waras Nurcholis^{2,3*}

¹Department of Chemistry, Faculty of Mathematics and Natural Sciences, IPB University, Jl. Tanjung Kampus IPB Dramaga, Bogor 16680, Indonesia

²Department of Biochemistry, Faculty of Mathematics and Natural Sciences, IPB University, Jl. Tanjung Kampus IPB Dramaga, Bogor 16680, Indonesia

³Tropical Biopharmaca Research Center, IPB University, Jl. Taman Kencana Kampus IPB Taman Kencana, Bogor 16128, Indonesia

* **Corresponding author:**

tel: +62-8179825145

email: wnurcholis@apps.ipb.ac.id

Received: December 18, 2021

Accepted: January 26, 2022

DOI: 10.22146/ijc.71334

Abstract: *Orthosiphon aristatus* (called *kumis kucing* in Indonesia) is a valuable herb for diabetes mellitus treatment. In this study, LC-MS/MS and PCA analyses were used to investigate the metabolite profile, classify *O. aristatus* extracts, and assess the inhibitory activity of α -glucosidase and the probable bioactive compounds through *in silico* study. Results showed that the methanol and ethanol extracts of *O. aristatus* were active in α -glucosidase inhibitory activity. Both extracts contained 86 compounds as known from the LC-MS/MS analysis. PCA analysis identified 10 metabolites that correlated with α -glucosidase inhibitory activity. Results of *in silico* analysis obtained rosmarinic acid compound potentially act as anti-diabetic activity, which can be developed for further research.

Keywords: *diabetic*; *in silico*; *Orthosiphon aristatus*; *metabolomics*; *PCA*

■ INTRODUCTION

The International Diabetes Federation reported that in 2019, 463 million people were suffering from diabetes mellitus (DM) in the world. It is predicted that this number will continue to increase to reach 700 million people by 2045 [1]. Indonesia's position is in the top 10 under China, America, Pakistan, Brazil, and Mexico. The population of Indonesian people affected by DM is 10.7 million people. According to the Ministry of Health of the Republic of Indonesia, DM is the number 3 cause of death in Indonesia [2]. Even so, about 30–50% of diabetics are not aware of it [3], so the disease condition develops into complications, such as nephropathy [4], cardiovascular [5], gangrene, or impaired wound healing, to stroke [6]. DM is divided into two, namely, type 1 DM and type 2 DM. Type 1 DM occurs due to damage to the β -pancreatic cells that cannot produce insulin properly. In contrast,

type 2 DM is caused by the ineffectiveness of the insulin hormone production process.

DM conditions can be determined by calculating blood sugar levels that exceed normal conditions (hyperglycemia). The chronic phase of hyperglycemia causes some of the glucose to undergo auto-oxidation. Glucose auto-oxidation creates reactive oxygen species that act as free radicals, significantly affecting vascular endothelial disorders and leading to complications [7–8]. One way to prevent hyperglycemia is to inhibit the α -glucosidase enzyme [9]. Determination of the target of α -glucosidase enzymes has been commonly used, and several drugs that have been developed are acarbose and voglibose. However, there are reported adverse effects from the usage of the standard drugs, namely gastrointestinal disturbances in diarrhea, dizziness, nausea, vomiting, liver disorders, and central nervous system disorders [10–11]. Therefore, alternative

compounds are needed that can inhibit the activity of the α -glucosidase enzyme.

It was known that bioactive compounds from plants are able to prevent diabetes due to fewer side effects [12]. One of the plants with antioxidant activity tested for α -glucosidase inhibition activity is *Orthosiphon aristatus*. Research from Mohamed et al. [13] has proven the antidiabetic activity of *O. aristatus* by *in vitro* study against the α -glucosidase enzyme. Sinensetin is thought to play a role in the inhibitory activity of *O. aristatus* extract. Although a lot of *O. aristatus*-based research has been performed, a clear classification of the natural compounds based on their polarity and α -glucosidase inhibition activity has not been established. In addition, there may also be other active compounds in *O. aristatus* leaves that have antidiabetic activity, inducing insulin secretion. Based on this research, further investigations are needed to determine the bioactive compounds that play a role in the antidiabetic activity of *O. aristatus*. A metabolomics approach based on a statistical analysis of chemometric complex datasets can be used to obtain information on the role of active chemical compounds [14-16].

This study used Principal Component Analysis (PCA) as the chemometric technique. PCA is a multivariate approach to analyze data tables where many correlated quantitative dependent variables determine observations. The aim is to extract important information from statistical data, express it as a new set of orthogonal variables called principal components, and visualize patterns of similarity between observations and variables [17]. By reducing the number of variables, PCA helps overcome the problem of data overfitting. PCA generates many variations, which will help visualize the data while eliminating related factors such as noise and outliers that have nothing to do with the data. Furthermore, the best compounds that act as the antidiabetic agent will be searched using *in silico* studies. Therefore, the purpose of this research was to determine the metabolite profile of the methanol and ethanol extracts of the *O. aristatus* using LC-MS/MS, classify them using PCA, to determine the inhibitory activity of α -glucosidase, and to study the potential active compounds of *O. aristatus* by *in silico* approach.

■ EXPERIMENTAL SECTION

Research Time and Location

This research was carried out in August–October 2021. This type of research is empirical research in blended activities, online and offline. Offline activities at the IPB Leadership Dormitory, Food Process Engineering laboratory, Tropical Biopharmaca Research Center (Trop-BRC), and IPB Advanced Laboratory and online using supporting media such as WhatsApp, zoom, and google meet applications for three months.

Materials

The main ingredients used in this study were *O. aristatus* powder consisting of leaves, twigs, and flowers obtained from Trop-BRC in powder form, *O. aristatus* compound ligands, filter paper, ethanol, methanol, KH_2PO_4 , KHPO_4 , *p*-nitrophenyl- α -D-glucopyranoside, dimethylsulfoxide (DMSO), acarbose, sodium carbonate, α -glucosidase enzyme, PTFE membrane filter, aquades, and three-dimensional structure of α -glucosidase enzyme (PDB 2QMJ).

Instrumentation

The tools used in this research are cabinet dryer, blender, freezer, rotary evaporator, freeze dryer, 100 mL beaker, 250 and 500 mL Erlenmeyer flasks, stir bar, funnel, analytical balance, incubator, microplate reader, LC-MS/MS (Liquid Chromatography-Mass Spectrometry/Mass Spectrometry) UHPLC Vanquish Tandem Q Exactive Plus Orbitrap HRMS (ThermoScientific, Germany), computer set, software e.g., YASARA Structure, Discovery Studio Visualizer, Avogadro, and PyMol.

Procedure

O. aristatus extraction

O. aristatus powder from Trop-BRC will be stored in the freezer until extraction is carried out. Extraction simplicia *O. aristatus* (50 g) 6 samples with each 3 to solvent of ethanol and methanol is made by the method of maceration add solvent until the tera in Erlenmeyer flasks of 250 mL. The mouth of the flask was covered with aluminium foil and then allowed to stand for one

day. Furthermore, the filtrate is filtered. Extraction was repeated three times (triplo). The extract is concentrated with a rotary evaporator. The results of the concentration are then weighed and separated into different vials.

α-Glucosidase enzyme activity inhibition test

Procedure modified from Aziz et al. [18]. A total of 50 μL 0.1 M phosphate buffer pH 6.9, 25 μL *p*-nitrophenyl- α -D-glucopyranoside solution (dissolved in 0.1 M phosphate buffer pH 6.9), 10 μL *O. aristatus* extract was dissolved in DMSO. Acarbose as a positive control was dissolved in distilled water, 25 μL α -glucosidase 0.04 U/mL in 0.1 M buffer solution pH 6.9 was mixed. This reaction was incubated at 37 °C for 30 min. The reaction was stopped by adding 100 μL of 0.2 M sodium carbonate solution. The enzymatic hydrolysis reaction was measured at a wavelength of 410 nm using a microplate reader. The test was carried out two times. The α -glucosidase inhibitory activity was expressed as percent inhibition and was calculated as follows:

$$\% \text{ Inhibition} = \frac{[(AB - ACS) - (AS - ACS)]}{(AB - ACB)} \times 100\%$$

whereas AB = absorbance of the blank, ACB = absorbance of control blank, AS = absorbance of the sample, and ACS = absorbance of the control sample.

Identification of O. aristatus extract compounds with LC-MS/MS and PCA multivariate data analysis

Procedure modified from Elhawary et al. [19]. A total of 10 mg of sample extract was dissolved in 5 mL of LC-MS/MS grade methanol. The extract dissolution process was carried out with an ultrasonicator for 30 min at room temperature. Then the solution was filtered using a 0.2 μm PTFE filter membrane, and 5 μL of the filtrate was injected in LC-MS/MS. The composition of the mobile phase is adjusted to the best composition of the mobile phase. Raw data *.RAW analysis results from LC-MS/MS can be processed with Compound Discoverer 3.2. After processing, identification was carried out by matching the MS and MS2 spectra of the analyzed compounds with online databases (PubChem, ChemSpider, HMDB, and literature).

The *O. aristatus* extract whose metabolites have been identified are then classified based on the solvent

using PCA. The peak area values of the 86 identified compounds were used as variables. The data were imported into excel form, then transposed on the data. After that, they were pre-processed in a center and scaled on the transposed data. Center and scale data are grouped using PCA to obtain at least 70% of the two PCs. The results of the identification of compounds that have been carried out will be continued by *in silico* studies to see the compounds with the most potential as antidiabetics associated with *in vitro*.

In silico studies

Procedure modified from Rather et al., Zafar et al., Krieger and Vriend [20-22]. The protein used has a PDB code of 2QMJ with a resolution of 1.90 Å, with a natural ligand on the catalytic site in the form of a complex molecule of acarbose with *N*-acetylglucosamine. Receptor preparation by adding hydrogen atoms, removing water molecules, and not using ligands was carried out using the YASARA Structure software. Then the grid box validation was carried out by redocking 999 times against the 2QMJ receptor until the best grid box validation was obtained at 3 Å. Ligand preparation is done by minimizing the bond energy of the ligand molecules by adding solvent molecules (water) in the system, then saving the files in *.pdb and *.sdf formats. After that, all ligands were collected in one *.sdf file as input for virtual screening with menus (join > object) and atomic coordinates equalization with menus (transfer > all).

After obtaining the best gridbox size from the structure (Table 1), a screening analysis of the *O. aristatus* test ligand was carried out for the receptor. The molecular screening method is carried out by preparing the *_receptor.sce and *_complex.sce files and then preparing the dock_runscreening file with *.mcr format as the command to run the screening process. The prepared ligand file is uploaded before starting the virtual screening process. From virtual screening analysis, the ligands which have higher affinity energy than acarbose was taken. Pharmacokinetic predictions can be made on the webserver provider http://biosig.unimelb.edu.au/pkcsml/prediction_single/adme_1633876478.78.

Table 1. Gridbox area and binding energy

Gridbox (Å)	Binding energy (kcal/mol)
1	1.668
1.5	1.806
2	2.673
2.5	2.276
3	3.216
3.5	-8.259

Molecular docking using YASARA Structure software. The protein and ligand docking process were carried out 100 times to obtain *.yob and *.txt files containing free energy values (ΔG), inhibition constants (K_i), and amino acid residues. The analysis of the docking results was carried out by comparing the highest free energy, the value of the inhibition constant, and the interaction of amino acid residues using excel. Analysis of bond types using Discovery Studio Visualizer software and 3D visualization using PyMol software.

Data analysis

The data was collected primary data obtained from research and research in the laboratory and computationally. The problems found were analyzed qualitatively and quantitatively based on the results of data collection. Quantitative data were obtained and analyzed from *in silico* data and LC-MS/MS instruments. Qualitative data were analyzed to determine the *O. aristatus* active compounds that potentially as an inhibitor of α -glucosidase. The data is processed, and then conclusions are drawn from the results of the study.

RESULTS AND DISCUSSION

O. aristatus Extract

This study used ethanol and methanol as solvents to

compare the types of compounds dissolved in 2 different organic solvents. Based on the data below, it can be concluded that the ethanol and methanol extracts of herbal formulations started with simplicia weights approaching 50 g. The simplicia was then macerated in ethanol and methanol in a 250 mL volumetric flask. The weight of the extract obtained from the ethanol solvent is shown in Table 2.

α -Glucosidase Enzyme Inhibition

Percent inhibition of *O. aristatus* extract is shown in Table 3 for various concentrations. *In vitro* results shown in Fig. 1 showed that the higher the concentration, the higher the inhibition percentage. Differences can influence these results in geographical origin where they grow, the type of solvent, and the part of the plant used to affect the bioactive content to cause differences in the biological activity of the *O. aristatus* plant [23]. The percentage yield that is not too high can be caused by the extract used being still in a crude form where there are still many compounds in the extract. The use of methanol as a solvent for the extraction of the *O. aristatus* plant is known to extract more active compounds and has a higher phytochemical constituent as well as total phenolic content than other solvents [24].

Table 2. Extract yield with ethanol and methanol solvent

Label	Simplicia weight (g)	Extract weight (g)	% Yield
E1	50.01	2.54	5.08
E2	49.78	2.52	5.07
E3	49.78	3.58	7.17
M1	50.01	3.42	6.83
M2	50.16	3.70	7.38
M3	49.96	3.36	6.73

Table 3. %Inhibition of *O. aristatus* extract

Concentration (ppm)	%Inhibition					
	E1	E2	E3	M1	M2	M3
1250	12.096	10.603	13.650	17.946	15.296	9.537
1000	8.775	5.728	8.592	14.473	13.193	5.210
750	6.399	3.778	7.313	9.537	5.424	3.077
500	5.667	2.864	7.130	2.468	4.906	2.468
250	2.651	2.438	5.698	0.030	3.504	-1.158

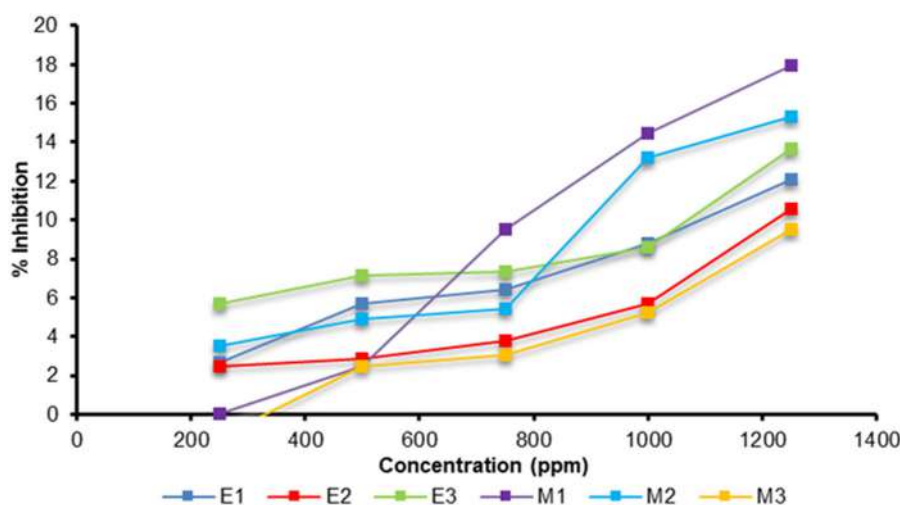


Fig 1. Graph of % inhibition at all concentrations

O. aristatus plant is rich in phenolic compounds, including flavonoids [25]. Some literatures stated that compounds inhibiting the activity of α -glucosidase belong to this group [26]. Therefore, in the next stage, metabolite analysis of ethanol and methanol extracts was carried out to see the differences in the content of the compounds by classifying them using PCA, which would then look for compounds that play a role in α -glucosidase inhibition in the *in silico* study.

Compound Profile and PCA Classification

LC-MS/MS is an analytical technique that combines the separation capabilities of liquid chromatography with the specificity of mass spectrophotometric detection. Data in the form of chromatograms of each plant sample based on different solvents were combined into a chromatogram as shown in Fig. 2. The results of the chromatograms have different patterns, which explain the differences in the composition of compounds detected in each solvent. The chromatogram was processed using Compound Discoverer software and obtained 86 compounds identified in the *O. aristatus* plant extract with various solvents. These compounds result from MS-MS fragmentation compared with the literature, so the identification of these components is putative. These compounds consist of alkaloids, phenolic acids, flavonoids, coumarins, steroids, and other group compounds (Table 4).

Analysis with PCA aims to summarize complex data

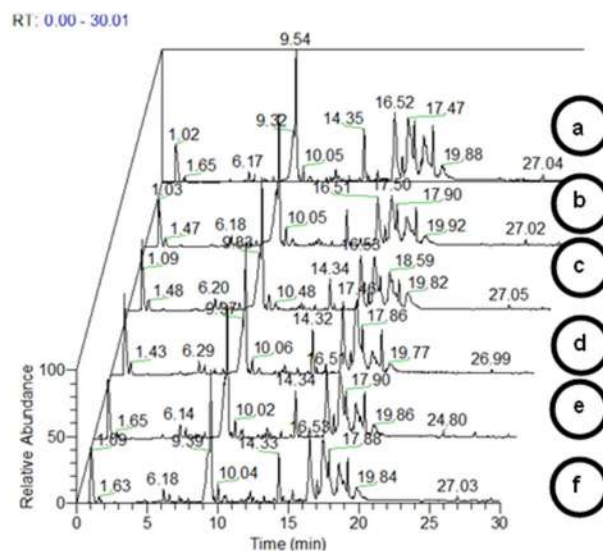


Fig 2. LC-MS/MS chromatogram results, (a) E1, (b) E2, (c) E3, (d) M1, (e) M2, (f) M3

and show the variance and how the sample is different from other samples. Cluster formation on a particular PC is the most influential function in this analysis. The PCA score plot shows the grouping of each sample based on the variable peak area of the chromatogram (Fig. 3(a)). This PCA analysis aims to see that the metabolite profile of each sample can be distinguished by solvent. The most frequently used components in PCA analysis are component 1 (PC1) and component 2 (PC2). The plot of scores generated from this study resulted in a diversity of data from both PCs of 70.3%. This shows that 70.3% of the data diversity can be explained by the

Table 4. *O. aristatus* compound identification using LC-MS/MS

Peak	Compound	Formula	Molecular weight	Rt [min]	E1	E2	E3	M1	M2	M3
1	3-Amino-2,3-dideoxy-scylo-inosose	C ₆ H ₁₁ NO ₄	161.06868	1.003	√	√	√		√	√
2	Kanosamine	C ₆ H ₁₃ NO ₅	179.07926	1.004	√	√	√	√	√	√
3	Linamarin	C ₁₀ H ₁₇ NO ₆	247.10535	1.025		√	√	√	√	
4	γ-Aminobutyric acid	C ₄ H ₉ NO ₂	103.06354	1.028	√	√	√	√	√	
5	N-Acetyl-L-ornithine	C ₇ H ₁₄ N ₂ O ₃	174.10029	1.036	√	√	√	√	√	√
6	Adenosine	C ₁₀ H ₁₃ N ₅ O ₄	267.09610	1.039	√			√	√	√
7	Lotaustralin	C ₁₁ H ₁₉ NO ₆	261.12114	1.040		√	√		√	√
8	Cytidine	C ₉ H ₁₃ N ₃ O ₅	243.08537	1.045			√			
9	L-glutamine	C ₅ H ₁₀ N ₂ O ₃	146.06902	1.048			√			
10	5-Oxo-L-proline	C ₅ H ₇ NO ₃	129.04262	1.050		√		√		
11	5-aminopentanoate	C ₅ H ₁₁ NO ₂	117.07900	1.055	√	√	√	√	√	√
12	N-Dimethylethanolamine phosphate	C ₄ H ₁₂ NO ₄ P	169.05042	1.060					√	
13	3,6-dihydronicotinate	C ₆ H ₇ NO ₂	125.04767	1.063	√	√	√	√	√	√
14	Phenylglyoxylate	C ₈ H ₆ O ₃	150.03147	1.106	√					
15	(R)-1-Amino-2-propanol O-2-phosphate	C ₃ H ₁₀ NO ₄ P	155.03477	1.106	√		√	√	√	√
16	Adenine	C ₅ H ₅ N ₅	135.05442	1.120			√			√
17	Sucrose	C ₁₂ H ₂₂ O ₁₁	359.14216	1.174	√	√	√	√	√	√
18	4-O-Acetyl-N-acetylmannosamine	C ₁₀ H ₁₇ NO ₇	263.10034	1.227	√	√		√	√	
19	Nicotinic acid	C ₆ H ₅ NO ₂	123.03207	1.316	√	√	√	√	√	
20	Uridine	C ₉ H ₁₂ N ₂ O ₆	244.06926	1.385				√		
21	Uracil	C ₄ H ₄ N ₂ O ₂	112.02753	1.387		√				
22	L-Pyroglutamic acid	C ₅ H ₇ NO ₃	129.04253	1.387	√			√	√	√
23	Adenine	C ₅ H ₅ N ₅	135.05442	1.389	√				√	
24	Adenosine	C ₁₀ H ₁₃ N ₅ O ₄	267.09617	1.402		√	√	√		√
25	L-tyrosine	C ₉ H ₁₁ NO ₃	181.07388	1.440	√	√	√	√		
26	L-isoleucine	C ₆ H ₁₃ NO ₂	131.09453	1.549	√	√	√	√	√	√
27	Adenine	C ₅ H ₅ N ₅	135.05446	1.551					√	√
28	Adenosine	C ₁₀ H ₁₃ N ₅ O ₄	267.09612	1.573	√				√	√
29	(S)-2-Amino-6-oxohexanoate	C ₆ H ₁₁ NO ₃	145.07370	1.599	√	√	√	√	√	√
30	D-proline	C ₅ H ₉ NO ₂	115.06341	1.727	√	√	√	√	√	√
31	L-pipecolate	C ₆ H ₁₁ NO ₂	129.07898	1.853	√	√	√	√	√	√
32	L-phenylalanine	C ₉ H ₁₁ NO ₂	165.07884	2.130	√	√	√		√	
33	Pantothenate	C ₉ H ₁₇ NO ₅	219.11060	2.411					√	
34	L-tryptophan	C ₁₁ H ₁₂ N ₂ O ₂	204.08970	4.307	√	√	√			
35	Kynurenate	C ₁₀ H ₇ NO ₃	189.04246	4.878	√	√	√	√	√	√
36	Kaempferol 7-O-glucoside	C ₂₁ H ₂₀ O ₁₁	448.09977	7.763	√	√	√	√	√	√
37	Methyl eugenol	C ₁₁ H ₁₄ O ₂	178.09932	8.648						√
38	Kaempferol 7-O-glucoside	C ₂₁ H ₂₀ O ₁₁	448.09963	8.985	√	√	√	√	√	√
39	Caffeic acid	C ₉ H ₈ O ₄	180.04188	9.526	√	√	√	√	√	√
40	Rosmarinic acid	C ₁₈ H ₁₆ O ₈	360.08328	9.528	√	√	√	√	√	√
41	Umbelliferone	C ₉ H ₆ O ₃	162.03130	9.529	√	√	√	√	√	√
42	Versiconal	C ₁₈ H ₁₄ O ₈	358.06844	9.978	√	√	√	√	√	√
43	Versicolorin B	C ₁₈ H ₁₂ O ₇	340.05786	9.978	√	√	√	√	√	√
44	Salvianolic acid B	C ₂₆ H ₃₀ O ₁₆	718.15274	10.050	√	√	√	√	√	√
45	Damascenone	C ₁₃ H ₁₈ O	190.13564	11.020	√	√	√	√	√	√
46	Kaempferol	C ₁₅ H ₁₀ O ₆	286.04750	12.470		√				
47	5-Hydroxy-6,7,3',4'-tetramethoxyflavone	C ₁₉ H ₁₈ O ₇	358.10407	12.595	√	√	√	√	√	√
48	(3r)-sophorol	C ₁₆ H ₁₂ O ₆	300.06291	13.884	√	√				
49	Sinensetin	C ₂₀ H ₂₀ O ₇	372.11952	14.021	√	√	√	√	√	√
50	2-hydroxyformononetin	C ₁₆ H ₁₂ O ₅	284.06786	14.265			√	√		

Table 4. *O. aristatus* compound identification using LC-MS/MS (Continued)

Peak	Compound	Formula	Molecular weight	Rt [min]	E1	E2	E3	M1	M2	M3
51	Eupatorin	C ₁₈ H ₁₆ O ₇	344.08837	14.347	√	√	√	√	√	√
52	Aflatoxin B2	C ₁₇ H ₁₄ O ₆	314.07792	14.474	√	√	√	√	√	√
53	Scutellarein 5,6,7,4'-tetramethyl ether	C ₁₉ H ₁₈ O ₆	342.10913	15.143	√	√	√	√	√	√
54	(1's,5's)-hydroxyaverantin	C ₂₀ H ₂₀ O ₈	388.11527	15.307	√	√				√
55	Gibberellin A36	C ₂₀ H ₂₆ O ₆	362.17207	15.309	√	√	√	√	√	√
56	2-hydroxyformononetin	C ₁₆ H ₁₂ O ₅	284.06801	15.402	√	√				√
57	Aflatoxin G2	C ₁₇ H ₁₄ O ₇	330.07303	15.863	√	√	√	√	√	√
58	(9s)-hpode	C ₁₈ H ₃₂ O ₄	312.22963	15.896	√	√				
59	Curcumin	C ₂₁ H ₂₀ O ₆	368.12532	16.376	√					
60	Hyperxanthone E	C ₁₈ H ₁₆ O ₆	328.09345	17.378	√	√	√	√	√	√
61	Orthosiphols R	C ₃₆ H ₄₂ O ₁₀	634.27567	17.600	√	√		√	√	√
62	Neoorthosiphol A	C ₃₈ H ₄₄ O ₁₂	692.28068	17.714	√	√		√	√	
63	Gibberellin A24	C ₂₀ H ₂₆ O ₅	346.17718	17.903	√		√	√	√	√
64	Orthosiphols S	C ₃₄ H ₃₆ O ₉	588.23481	18.363	√	√	√	√	√	√
65	Norstaminols C	C ₃₀ H ₃₆ O ₁₀	556.22938	18.375	√	√	√	√	√	√
66	Norstaminolactone A	C ₃₈ H ₄₅ NO ₁₂	707.29349	18.736			√	√	√	√
67	Estrone	C ₁₈ H ₂₂ O ₂	270.16144	18.854	√	√	√	√	√	√
68	Androsta-1,4-diene-3,17-dione	C ₁₉ H ₂₄ O ₂	284.17705	18.854	√	√	√	√	√	√
69	Indole	C ₈ H ₇ N	117.05784	19.233	√	√	√	√		√
70	Orthosiphonone A	C ₃₈ H ₄₂ O ₁₁	674.27064	19.235	√	√	√	√	√	√
71	9α-Hydroxyandrosta-1,4-diene-3,17-dione	C ₁₉ H ₂₄ O ₃	300.17193	19.236	√	√	√	√	√	√
72	9,10-Epoxy-10,12Z,15Z-octadecatrienoate	C ₁₈ H ₂₈ O ₃	292.20319	19.323	√	√	√	√	√	√
73	Demethylphyloquinone	C ₃₀ H ₄₄ O ₂	436.33339	19.437	√	√	√	√	√	√
74	β-Ionone	C ₁₃ H ₂₀ O	192.15125	19.659	√	√	√	√	√	√
75	A-Linolenate	C ₁₈ H ₃₀ O ₂	278.22398	19.696	√	√	√	√	√	√
76	Colneleate	C ₁₈ H ₃₀ O ₃	294.21877	20.283	√	√	√	√	√	√
77	Hydroxybetulinic acid	C ₃₀ H ₄₈ O ₄	472.35439	20.347	√	√	√	√	√	√
78	17-β-Hydroxy-5-α-androstan-3-one	C ₁₉ H ₃₀ O ₂	290.22392	21.901	√	√	√	√	√	√
79	4α-Hydroxymethyl-4β-methyl-5α-cholesta-8,24-dien-3β-ol	C ₂₉ H ₄₈ O ₂	428.36455	24.347		√				
80	Violaxanthin	C ₄₀ H ₅₆ O ₄	600.41643	24.464	√	√				
81	4,4-Dimethyl-cholesta-8,12,24-trienol	C ₂₉ H ₄₆ O	410.35380	24.514	√	√	√	√	√	
82	Linoleate	C ₁₈ H ₃₂ O ₂	280.23965	25.427	√	√				
83	Ent-kaurene	C ₂₀ H ₃₂	272.24986	26.009	√	√	√	√	√	√
84	Cycloeucalenone	C ₃₀ H ₄₈ O	424.36959	26.353	√	√	√	√	√	√
85	14-hydroxylanosterol	C ₃₀ H ₅₀ O ₂	442.38044	26.353	√	√			√	√
86	4α-Hydroxymethyl-4β-methyl-5α-cholesta-8,24-dien-3β-ol	C ₂₉ H ₄₈ O ₂	428.36391	27.260				√		

Rt: Retention time in min

E1: Ethanol sample 1

M1: Methanol sample 1

E2: Ethanol sample 2

M2: Methanol sample 2

E3: Ethanol sample 3

M3: Methanol sample 3

variable area of the peak chromatogram of *O. aristatus* plant based on the solvent. The value of the two PCs shows a fairly good two-dimensional visualization because the diversity value of PC1 and PC2 is greater than 70% [27].

Biplot of the PCA is a multivariate method that uses rows and columns in a chart. This method displays the object and the variables with the object under study [28]. Based on Fig. 3(b), the compound that plays a role in the inhibitory activity of α-glucosidase is the number

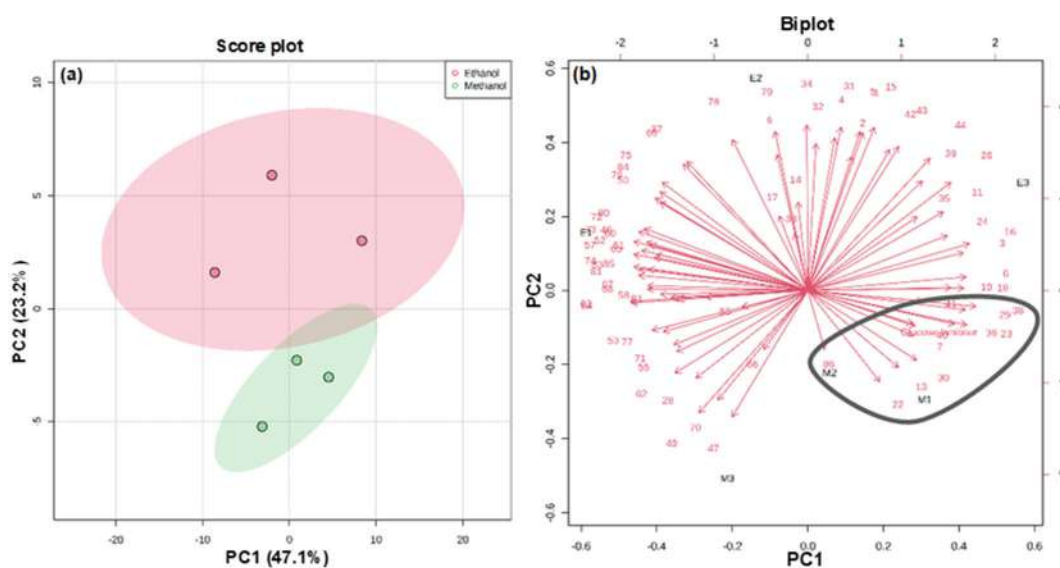


Fig 3. PCA results, (a) Score plot, (b) Biplot

Table 5. Virtual screening of *O. aristatus* extract

No.	Ligands	Effi [kcal/(mol*Atom)]	Bind. energy [kcal/mol]	Dissoc. constant [μM]
1	Rosmarinic acid	0.3153	8.197	0.01
2	Kaemferol 7-O-glucoside	0.2521	8.066	0.98
3	Acarbose	0.1770	7.787	1.96
3	4α-Hydroxymethyl-4β-methyl-5α-cholesta-8,24-dien-3β-ol	0.2266	7.025	7.08
5	Uridine	0.3882	6.599	14.50
6	Umbelliferone	0.5126	6.151	30.99
7	5-Oxo-L-proline	0.6683	6.015	38.89
8	(S)-2-Amino-6-oxohexanoate	0.5849	5.849	51.59
9	Nicotinic acid	0.6216	5.594	79.34
10	Lotaustralin	0.3102	5.584	80.70

of compounds that approach glucose inhibitors. The number of compounds that can be seen on the document the results of the identification of compound LC-MS/MS (Table 5) with 10 compounds. The tenth compounds further studies will be carried out *in silico*.

***In silico* Study**

Receptor protein structure stability

The structure of the receptor used in this study is a complex of α-glucosidase and acarbose enzymes with the code 2QMJ. The technique used to determine the 3D structure of this enzyme is X-ray diffraction with a resolution value of 1.90, which is relatively high [29]. The following analysis is the stability of the receptor. The analysis carried out on the PROCHECK page produces a

Ramachandran plot with the percentage of residues in quadrant I (most favored regions) of 87.2% with 654 residues, quadrant II (additional allowed regions) of 11.6% with 87 residues, quadrant III (generously allowed regions) of 0.8% with six residues, and quadrant IV (disallowed regions) of 0.4% with three residues. The quality of the protein structure is said to be good if it has a percentage of residues in the preferred region > 90% [28].

Grid box validation

Validation of the 2QMJ receptor was carried out by first cleaning water and natural ligands attached to its structure, such as sulfate ions and glycerol. Acarbose (AC1) binds to *N*-acetyl D-glucosamine to form an

inhibitor complex used as a comparison. AC1 and *N*-acetyl-D-glucosamine, which have been attached to the receptor, are separated and prepared. The anchoring validation was carried out by re-docking the complex molecule of AC1 and *N*-acetyl-D-glucosamine to the enzyme 999 times, and the best pose was taken. Validation was carried out by testing the molecular anchoring of the grid box from size 1 to 5 Å. The increase in grid box size was based on an interval value of 0.5 Å. The highest affinity energy value was obtained when the grid box size was 3 Å.

Virtual screening

The inhibition constant is proportional to the bond free energy value, the greater the bond free energy value, the greater the inhibition constant and vice versa. The value of the binding free energy and the inhibition constant obtained by each ligand is influenced by the interaction between the ligand and the receptor [30]. Therefore, visualization of molecular docking was carried out to determine the various types of interactions with amino acid residues. In addition, there is a ligand

efficiency parameter that interprets the ratio of the average binding energy value per atom obtained from the free Gibbs energy divided by the number of atomic weights ($LE = -\Delta G/N$) with units of (kcal/(mol.Atom)). Fragments with the high-efficiency value of ligand are directly proportional to the strength of the binding affinity of the ligand and receptor to guide the discovery of potential compounds [31].

Virtual screening with the YASARA structure filters and determines the interaction between ligands and receptors as drug candidates. Two ligand identifiers that have the best results against acarbose are kaempferol 7-O-glucoside and rosmarinic acid. The binding energy value (ΔG) of rosmarinic acid, kaempferol 7-O-glucoside, and acarbose was 8.197, 8.066, and 7.787 kcal/mol, respectively. In addition, the obtained values of K_i of each of 0.0081, 0.980, and 1.9595 μM , and the value of the efficiency of the ligand respectively 0.3153, 0.2521, and 0.177 kcal/(mol*Atom), respectively.

Acarbose as a ligand comparison has interactions with amino acid side active, i.e., Tyr299, Asp327, Asp443,

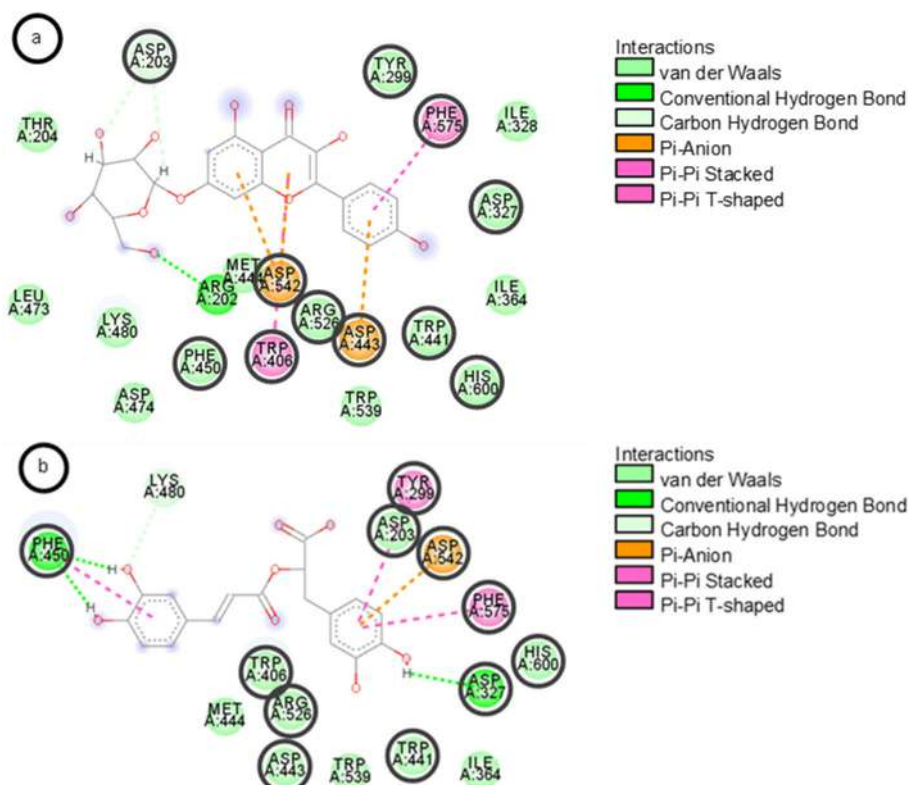


Fig 4. Amino acid residue, (a) kaempferol 7-O-glucoside, (b) rosmarinic acid, (c) acarbose

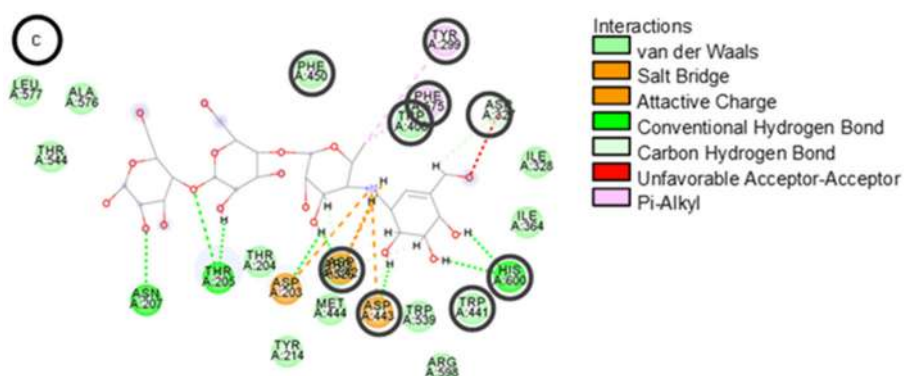


Fig 4. Amino acid residue, (a) kaempferol 7-O-glucoside, (b) rosmarinic acid, (c) acarbose (Continued)

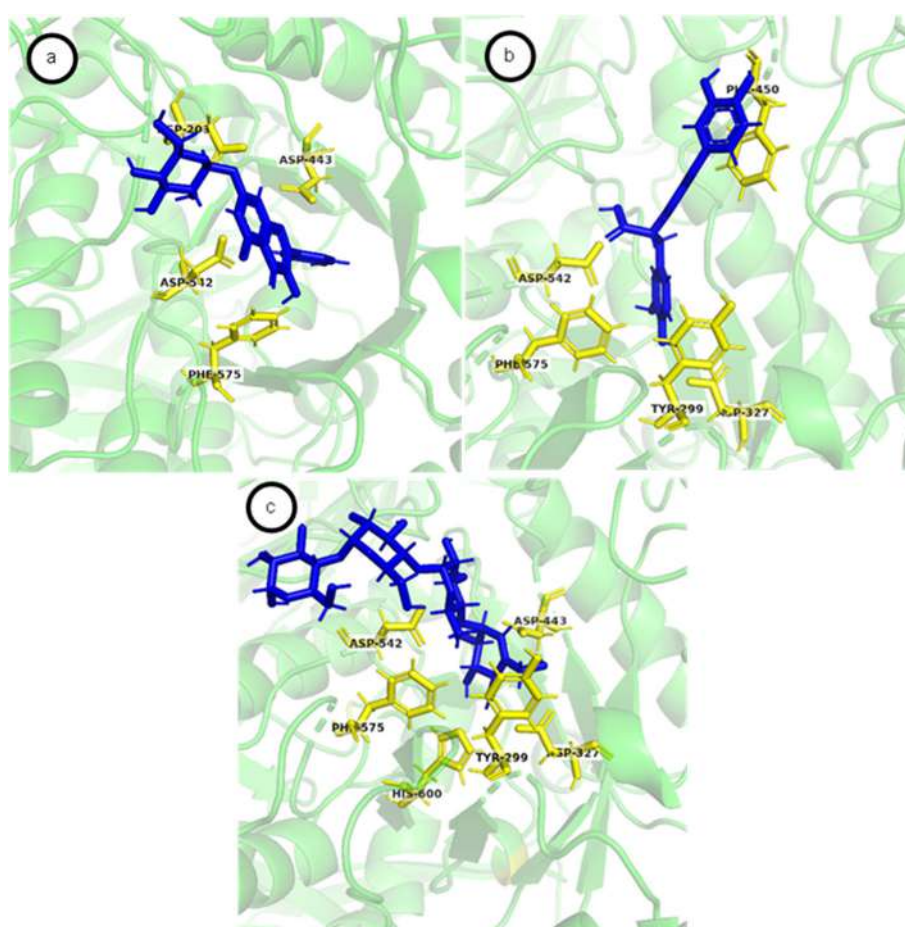


Fig. 5. 3D structure of α -GOX, (a) kaempferol 7-O-glucoside, (b) rosmarinic acid, (c) acarbose

Asp542, Phe575, His600 (hydrogen bond) and Trp406, Trp441, Phe450, Arg526 (Van der Waals bond). Rosmarinic acid interacts with residues Tyr299, Asp327, Phe450, Asp542, Phe575 (hydrogen bond) and Asp203, Trp406, Trp441, Asp443, Arg526, His600 (Van der Waals bond) (Fig. 4(b)). Kaempferol 7-O-glucoside interacts with

residues Asp203, Asp443, Asp542, Phe575 (hydrogen bond) and Tyr299, Asp327, Trp406, Trp441, Phe450, Arg526, His600 (Van der Waals bond) (Fig. 4(a)). This interaction is also presented in 3D, as shown in Fig. 5.

The correlation analysis between binding energy, inhibition constant, and ligand efficiency as shown in

Fig. 6 shows a negative correlation (purple color) between the binding energy value and the inhibition constant. Still, there was no correlation whatsoever to the efficiency value. This is because many other factors are involved in determining the value of the efficiency of the ligand, such as the number of atomic weights in the ligand [31].

Regression analysis showed a correlation between the binding energy of the ligands and the inhibition constant (Fig. 7). The decrease in the value of the inhibition constant is inversely proportional to the increase in the binding energy of the ligand, so the smaller the value of the inhibition constant indicates the stronger the ligand is attached to the receptor and vice versa, the greater the inhibition constant, the weaker the ligand is bound to the receptor. This result is in accordance with the research by Iman and Saadabadi [30].

Ligand bioavailability analysis

The two best compounds, rosmarinic acid and kaempferol 7-O-glucoside were analyzed bioavailability is based on the rules of Lipinski [32]. Five parameters that are used, among others, molecular weight ≤ 500 Da, hydrogen acceptors ≤ 10 , hydrogen donors ≤ 5 , $\log P \leq 5$, the value of PSA ≤ 140 A, and the number of rotatable bonds ≤ 10 [33-34]. On pharmacokinetic analysis, the ligand that violates more than two rules of Lipinski otherwise does not qualify and does not proceed to subsequent analysis [35]. In addition, the ligand with a value of $\log P < 0$ marked shows the value of which is less than ideal in the rules of Lipinski, so that did not pass the test analysis of the pharmacokinetic [36].

Rosmarinic acid has a molecular weight of 360 g/mol, hydrogen acceptors 8, hydrogen donors 5, $\log P$ value equal to 1.65, the value of PSA 144 A, and the number of the rotatable bond as much as 7. In comparison, kaempferol 7-O-glucoside has a molecular weight of 448 g/mol, hydrogen acceptors 11, donor hydrogen 7, the value of $\log P$ -0.23, the value of PSA 190, and rotatable bond as much as 4. Ligand rosmarinic acid violates the rules of Lipinski, while for the ligand kaempferol 7-O-glucoside breaking the $\log P \leq 0$, then it is not suitable to be used as an oral drug.

O. aristatus has a high rosmarinic acid content with 53–299 mg/g among other herbal plants [37]. Antidiabetic activity of this compound showed that treatment with rosmarinic acid (120–200 mg/kg) for 7 days fixed the

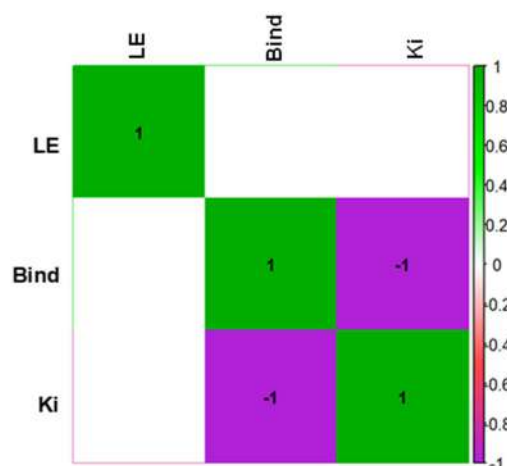


Fig 6. Result of correlation analysis between binding energy (Bind), inhibition constant (Ki), ligand efficiency (LE)

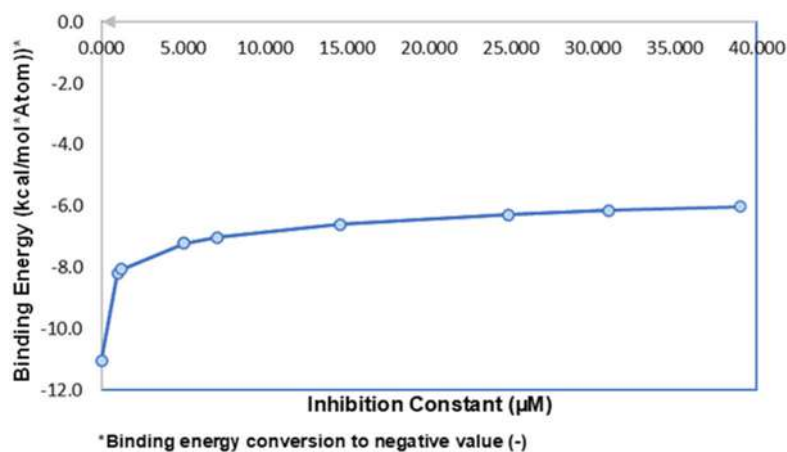


Fig 7. Regression analysis of binding energy and inhibition constant

hypoglycemic effect of rat type 1 diabetes induced by streptozocin. Experiments also showed an increase in glucose absorption from the 5.71 be about 7.42 mmol/L, and insulin sensitivity from 36.60 to 74.76 μ U/mL in mice with type 2 diabetes induced by a high-fat diet [38]. Therefore, the compound rosmarinic acid into compounds of potential developed as a new herbal remedy.

■ CONCLUSION

Extracts of *O. aristatus* plant in methanol and ethanol solvents have different compositions of the existing compounds using PCA chemometrics with the diversity of PC data was 70.3%. *O. aristatus* plant is proven to inhibit the activity of the α -glucosidase enzyme. To find the compounds that play a role in the antidiabetic activity, *in silico* test found the best compounds to be developed into a new herbal remedy, namely rosmarinic acid. This study is still in the *in vitro* and *in silico* stages. Therefore, more procedures, such as *in vivo* as pre-clinical and toxicity tests, are required before it can be proceeded into clinical trials.

■ ACKNOWLEDGMENTS

The author would like to thank the Tanoto Foundation, the Directorate of Student Affairs and Career Development of IPB for TSRA program in 2021. The author expresses his gratitude to the Department of Biochemistry of IPB, Department of Chemistry of IPB, Leadership Dormitory, Tropical Biopharmaca Research Center (Trop-BRC), and Advanced Research Laboratory IPB, who helped with this research.

■ AUTHOR CONTRIBUTIONS

Waras Nurcholis conducted design experiment and analysis data, and also revised the manuscript. Alfari Andiq Muhammad, Ali Umar, Fachrur Rizal Mahendra, and Muhammad Musthofa conducted the experiment, Faizal Maulana conducted the PCA calculations, Fachrur Rizal Mahendra conducted the molecular docking calculations, Alfari Andiq Muhammad, Ali Umar, and Muhammad Musthofa wrote and revised the manuscript. All authors agreed to the final version of this manuscript.

■ REFERENCES

- [1] International Diabetes Federation, 2019, *IDF Diabetes Atlas*, 9th Ed., International Diabetes Federation, Belgium.
- [2] Aquarista, N.C., 2016, Differences characteristics patients diabetes mellitus type 2 with and without coronary heart disease, *JBE*, 5 (1), 37–47.
- [3] Beagley, J., Guariguata, L., Weil, C., and Motala, A.A., 2014, Global estimates of undiagnosed diabetes in adults, *Diabetes Res. Clin. Pract.*, 103 (2), 150–160.
- [4] Miranda-Díaz, A.G., Pazarín-Villaseñor, L., Yanowsky-Escatell, F.G., and Andrade-Sierra, J., 2016, Oxidative stress in diabetic nephropathy with early chronic kidney disease, *J. Diabetes Res.*, 2016, 7047238.
- [5] Lathifah, N.L., 2017, Hubungan durasi penyakit dan kadar gula darah dengan keluhan subyektif penderita diabetes melitus, *JBE*, 5 (2), 231–239.
- [6] Ullah, F., Afridi, A.K., Rahim, F., Ashfaq, M., Khan, S., Shabbier, G., and Ur Rahman, S., 2015, Knowledge of diabetic complication in patients with diabetes mellitus, *J. Ayub Med. Coll. Abbottabad*, 27 (2), 360–363.
- [7] Arman, M.S.I., Al Mahmud, A., Mahmud, H.R., and Reza, A.S.M.A., 2019, Free radical, oxidative stress and diabetes mellitus: A mini review, *Discovery Phytomed.*, 6 (3), 99–101.
- [8] Tiwari, B.K., Pandey, K.B., Abidi, A.B., and Rizvi, S.I., 2013, Markers of oxidative stress during diabetes mellitus, *J. Biomarkers*, 2013, 378790.
- [9] Chatsumpun, N., Sritularak, B., and Likhitwitayawuid, K., 2017, New bioflavonoids with α -glucosidase and pancreatic lipase inhibitory activities from *Boesenbergia rotunda*, *Molecules*, 22 (11), 1862.
- [10] Dhahi, A.S., Bhatt, N.R., and Shah, M., 2013, Voglibose: An alpha glucosidase inhibitor, *J. Clin. Diagn. Res.*, 7 (12), 3023–3027.
- [11] Hasimun, P., Adnyana, I.K., Valentina, R., and Lisnasari, E., 2016, Potential alpha glucosidase inhibitor from selected zingiberaceae family, *Asian J. Pharm. Clin. Res.*, 9 (1), 164–167.

- [12] Yuan, H., Ma, Q., Ye, L., Piao, G., 2016, The traditional medicine and modern from natural products. *Molecules*, 21 (559), 1–18.
- [13] Mohamed, E.A.H., Siddiqui, M.J.A., Ang, L.F., Sadikun, A., Chan, S.H., Tan, S.C., Asmawi, M.Z., and Yam, M.F., 2012, Potent α -glucosidase and α -amylase inhibitory activities of standardized 50% ethanolic extracts and sinensetin from *Orthosiphon stamineus* Benth as anti-diabetic mechanism, *BMC Complementary Altern. Med.*, 12 (1), 176.
- [14] Ashraf, K., Sultan, S., and Adam, A., 2018, *Orthosiphon stamineus* Benth. is an outstanding food medicine: Review of phytochemical and pharmacological activities, *J. Pharm. BioAllied Sci.*, 10 (3), 109–118.
- [15] Murugesu, S., Ibrahim, Z., Ahmed, Q.U., Nik Yusoff, N.I., Uzir, B.F., Perumal, V., Abas, F., Saari, K., El-Seedi, H., and Khatib, A., 2018, Characterization of α -glucosidase inhibitors from *Clinacanthus nutans* Lindau leaves by gas chromatography-mass spectrometry-based metabolomics and molecular docking simulation, *Molecules*, 23 (9), 2402.
- [16] Guedes, J.A.C., Filho, E.G.A., Silva, M.F.S., Rodrigues, T.H.S., Ramires, C.M.C., Lima, M.A.C., Silva, G.S., Pessoa, C.O., Canuto, K.M., Brito, E.S., Alves, R.E., Nascimento, R.F., and Zocolo, G.J., 2020, GC-MS-based metabolomic profiles combined with chemometric tools and cytotoxic activities of non-polar leaf extract of *Spondias mombin* L. and *Spondias tuberosa* Arr. Cam, *J. Braz. Chem. Soc.*, 31 (2), 331–340.
- [17] Mishra, S., Sarkar, U., Taraphder, S., Datta, S., Swain, D.P., Saikhom, R., Panda, S., and Laishram, M., 2017, Multivariate statistical data analysis- Principal component analysis, *Int. J. Livest. Res.*, 7 (5), 60–78.
- [18] Aziz, Z., Yuliana, D.N., Simanjuntak, P., Rafi, M., Mulatsari, E., and Abdilah, S., 2021, Investigation of yacon leaves (*Smallanthus sonchifolius*) for α -glucosidase inhibitors using metabolomics and *in silico* approach, *Plant Foods Hum. Nutr.*, 76 (4), 487–493.
- [19] Elhawary, S.S., Younis, Y.I., Bishbishy, E.H.M., and Khattab, R.A., 2018, LC-MS/MS-based chemometric analysis of phytochemical diversity in 13 *Ficus* spp. (Moraceae): Correlation to their *in vitro* antimicrobial and *in silico* quorum sensing inhibitory activities, *Ind. Crops Prod.*, 126, 261–271.
- [20] Rather, M.A., Dutta, S., Guttula, P.K., Dhandare, B.C., Yusufzai, S.I., and Zafar, M.I., 2020, Structural analysis, molecular docking and molecular dynamics simulations of G-protein-coupled receptor (kisspeptin) in fish, *J. Biomol. Struct. Dyn.*, 38 (8), 2422–2439.
- [21] Zafar, M., Khan, H., Rauf, A., Khan, A., and Lodhi, M.A., 2016, *In silico* study of alkaloid as α -glucosidase inhibitors: Hope for the discovery of effective lead compounds, *Front. Endocrinol.*, 7, 153.
- [22] Krieger, E., and Vriend, G., 2015, New ways to boost molecular dynamics simulations, *J. Comput. Chem.*, 36 (13), 996–1007.
- [23] Rafi, M., Purwakusumah, E.D., Ridwan, T., Barus, B., Sutandi, A., and Darusman, L.K., 2015, Geographical classification of Java tea (*Orthosiphon stamineus*) from Java Island by FTIR spectroscopy combined with canonical variate analysis, *JSM*, 23 (1), 25–31.
- [24] Truong, D.H., Nguyen, D.H., Ta, N.T., Bui, A.V., Do, T.H., and Nguyen, H.C., 2019, Evaluation of the use of different solvents for phytochemical constituents, antioxidants, and *in vitro* anti-inflammatory activities of *Severinia buxifolia*, *J. Food Qual.*, 2019, 8178294.
- [25] Himani, B., Seema, B., Bhole, N., Mayank, Y., Vinod, S., and Mamta, S., 2013, Misai kuching: A glimpse of maestro, *Int. J. Pharm. Sci. Rev. Res.*, 22 (2), 55–59.
- [26] Şöhretoğlu, D., and Sari, S., 2019, Flavonoids as α -glucosidase inhibitors: Mechanistic approaches merged with enzyme kinetics and molecular modelling, *Phytochem. Rev.*, 19 (5), 1081–1092.
- [27] Jolliffe, I.T., and Cadima, J., 2016, Principal component analysis: A review and recent developments, *Philos. Trans. R. Soc., A*, 374 (2065), 20150202.
- [28] Zobayer, N., and Aowlad Hossain, A.B.M., 2018, *In silico* characterization and homology modelling of histamine receptors, *J. Biol. Sci.*, 18 (4), 178–191.

- [29] Ueno, G., Shimada, A., Yamashita, E., Hasegawa, K., Kumasaka, T., Shinzawa-Itoh, K., Yoshikawa, S., Tsukihara, T., and Yamamoto, M., 2019, Low-dose X-ray structure analysis of cytochrome c oxidase utilizing high-energy X-rays, *J. Synchrotron Radiat.*, 26 (4), 912–921.
- [30] Iman, M., Saadabadi, A., and Davood, A., 2015, Molecular docking analysis and molecular dynamics simulation study of ameltolide analogous as a sodium channel blocker, *Turk. J. Chem.*, 39, 306–316.
- [31] Chen, H., Zhou, X., Gao, Y., Chen, H., and Zhou, J., 2017, “Fragment-Based Drug Design: Strategic Advances and Lessons Learned” in *Comprehensive Medicinal Chemistry III*, Eds. Chackalamannil S., Rotella D., Ward S.E., Elsevier, Oxford, 212–232.
- [32] Lipinski, C.A., Lombardo, F., Dominy, B.W., and Feeney, P.J., 2012, Experimental and computational approaches to estimate solubility and permeability in drug discovery and development settings, *Adv. Drug Delivery Rev.*, 64 (Suppl.), 4–17.
- [33] Bickerton, G.R., Paolini, G.V., Besnard, J., Muresan, S., and Hopkins, A.L., 2012, Quantifying the chemical beauty of drugs, *Nat. Chem.*, 4 (2), 90–98.
- [34] Doak, B.C., Over, B., Giordanetto, F., and Kihlberg, J., 2014, Oral druggable space beyond the rule of 5: Insights from drugs and clinical candidates, *Chem. Biol.*, 21 (9), 1115–1142.
- [35] Benet, L.Z., Hosey, C.M., Ursu, O., and Oprea, T.I., 2016, BDDCS, the Rule of 5 and drugability, *Adv. Drug Delivery Rev.*, 101, 89–98.
- [36] Chagas, C.M., Moss, S., and Alisaraie, L., 2018, Drug metabolites and their effects on the development of adverse reactions: Revisiting Lipinski’s Rule of Five, *Int. J. Pharm.*, 549 (1-2), 133–149.
- [37] Chua, S.L., Lau, C.H., Chew, C.Y., Ismail, N.I.M., and Sootorgun, N., 2017, Phytochemical profile of *Orthosiphon aristatus* extracts after storage: Rosmarinic acid and other caffeic acid derivatives, *Phytomedicine*, 39, 49–55.
- [38] Runtuwene, J., Cheng, K.C., Asakawa, A., Amitani, H., Amitani, M., Morinaga, A., Takimoto, Y., Kairupan, B.H.R., and Inui, A., 2016, Rosmarinic acid ameliorates hyperglycemia and insulin sensitivity in diabetic rats, potentially by modulating the expression of PEPCK and GLUT4, *Drug Des., Dev. Ther.*, 10, 2193–2202.

Supplementary Data

This supplementary data is a part of paper entitled “Computational Design of Nanobody Binding to Cortisol to Improve Their Binding Affinity Using Molecular Docking and Molecular Dynamics Simulations”.

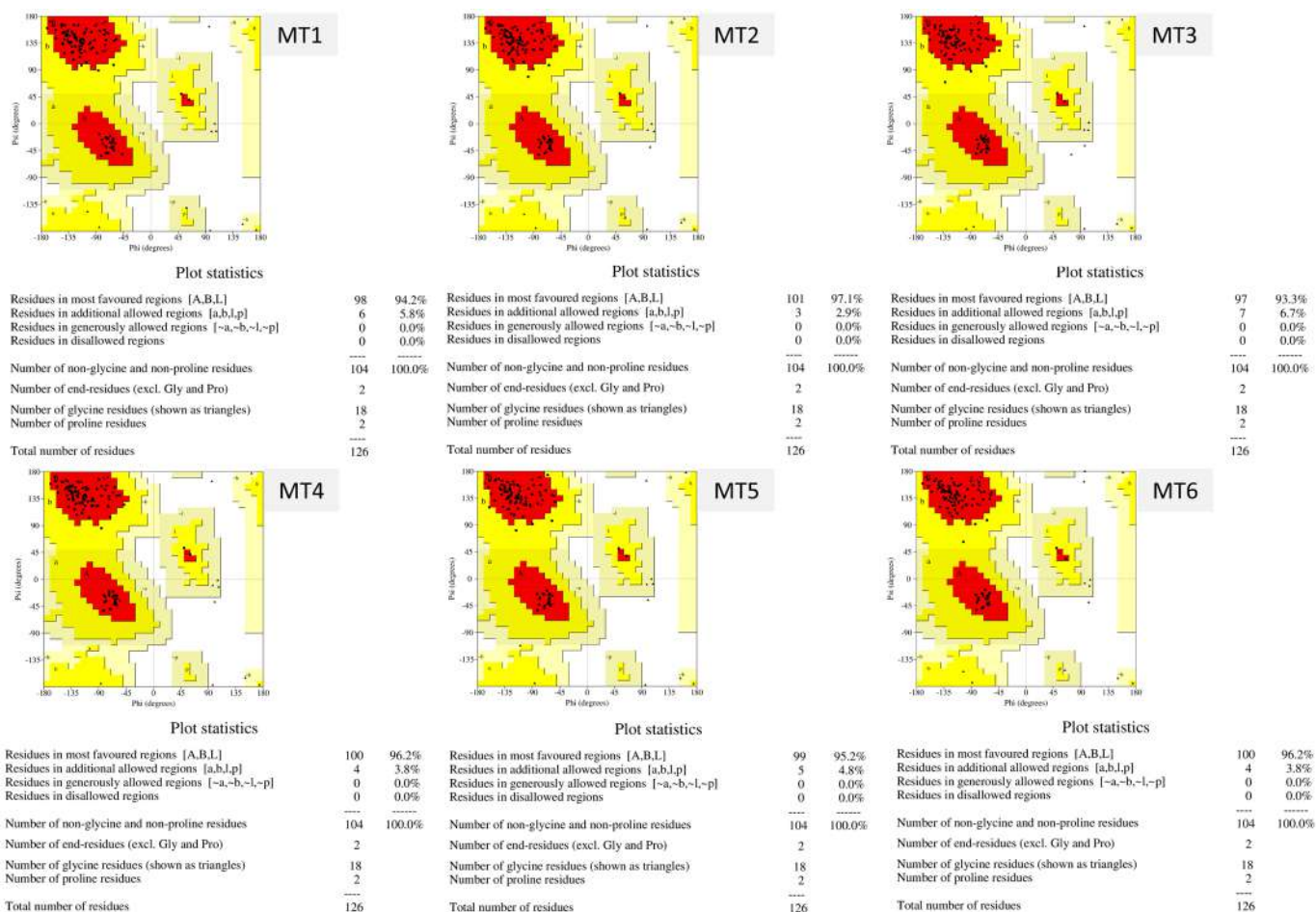


Fig S1. Ramachandran plot of all models

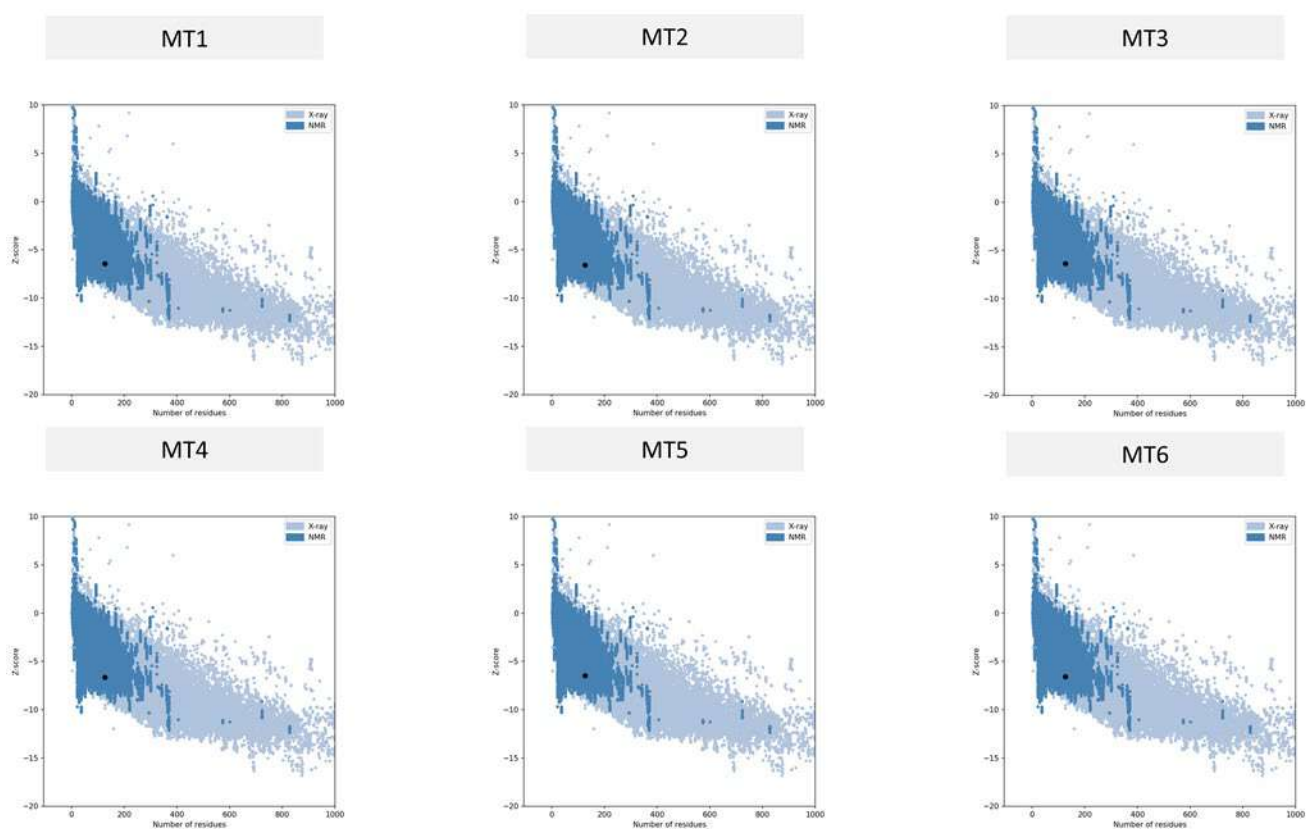


Fig S2. Z-score off all models

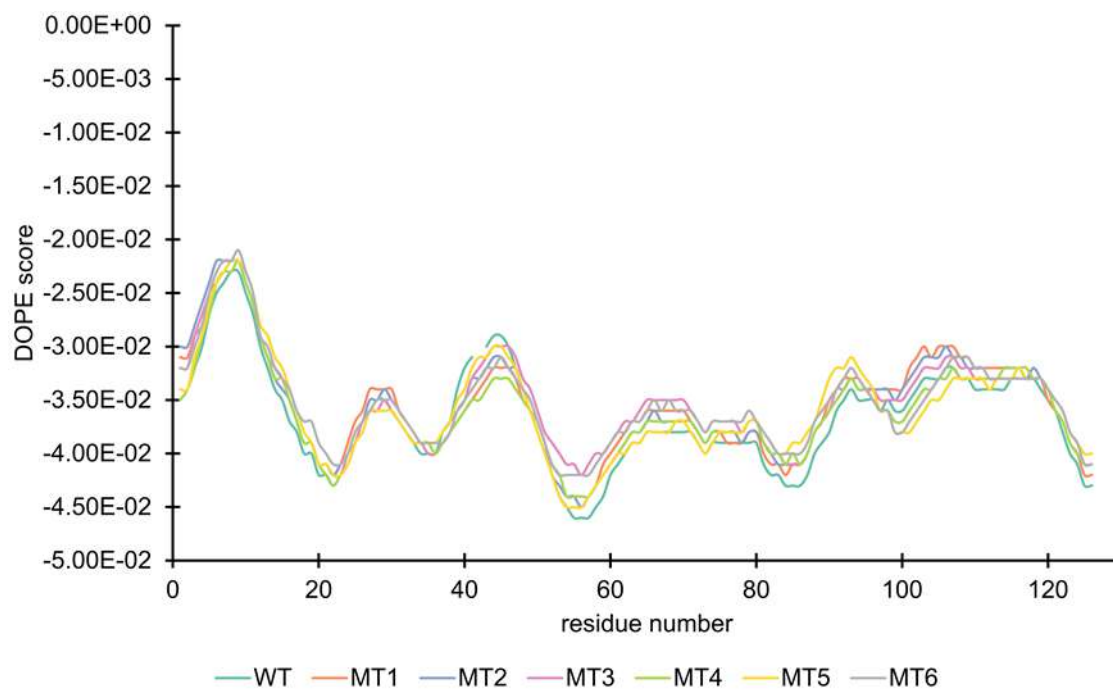


Fig S3. DOPE score of all models and template

Computational Design of Nanobody Binding to Cortisol to Improve Their Binding Affinity Using Molecular Docking and Molecular Dynamics Simulations

Umi Baroroh^{1*}, Nur Asni Setiani¹, Irma Mardiah¹, Dewi Astriany², and Muhammad Yusuf^{3,4}

¹Department of Biotechnology Pharmacy, Indonesian School of Pharmacy, Bandung, 40266, West Java, Indonesia

²Department of Pharmacy, Indonesian School of Pharmacy, Bandung, 40266, West Java, Indonesia

³Department of Chemistry, Faculty of Mathematics and Natural Sciences, Universitas Padjadjaran, Sumedang, 45363, West Java, Indonesia

⁴Research Center for Molecular Biotechnology and Bioinformatics, Jl. Singaperbangsa No. 2, Bandung 40133, West Java, Indonesia

* **Corresponding author:**

email: umibaroroh@stfi.ac.id

Received: December 23, 2021

Accepted: January 14, 2022

DOI: 10.22146/ijc.71480

Abstract: Currently, nanobody binding cortisol has been deposited in the database. Unfortunately, the affinity is still in micromolar order. Substituting hydrophobic residues in the binding pocket and utilizing CDR2 and CDR3 is the strategy to improve the affinity. A single and double substitution at positions 53 and 101 have been introduced to the nanobody structure through molecular modeling. The affinity toward cortisol was evaluated using molecular docking to get the binding pose. The highest binding energy pose was used as the initial coordinate to analyze further using 100 ns molecular dynamics simulations. The binding affinities calculated by MMGBSA showed that MT3, MT5, and MT6 have better binding affinity than WT. In contrast, the ligand movement through MD simulations reveals that MT1, MT3, and MT5 are relatively stable. Hence, docking and MD simulations showed that MT3 is the best mutant than others. This mutant is substituting the threonine to isoleucine at position 53. New hydrophobic interactions occurred and caused the increase of binding. Eventually, this study provides valuable structural information to improve the binding affinity of nanobody binding cortisol for further development of this molecule to antibody-based biosensor design.

Keywords: nanobody; cortisol; molecular dynamics simulations; molecular docking

■ INTRODUCTION

Antibodies play a crucial role in the immune system. The molecule produced by B lymphocytes recognizes the foreign biological or chemical substance in high specificity [1]. They have a high affinity and selectivity for a molecule with low molecular weight (hapten) [2-3]. Antibodies are widely used in various applications, including diagnostic, therapy, and research. Unfortunately, their significant molecular weight (MW: 150,000 g/mol) and the high total number of disulfide bonds make them challenging to produce in bacteria or eukaryotic cells' cytoplasm [4-5]. The small molecule of the single-chain variable fragment (scFv), which consists of the variable domain of the heavy and light polypeptide chains joined together with a synthetic linker to form a

single polypeptide chain, has several advantages. For example, bacteria can produce it because of its low molecular weight (MW: 30,000 g/mol). However, their fragile behavior leading to denaturation or aggregation or a spontaneous dimerization into diabodies remains an obvious flaw that complicates further application [6].

Fortunately, *Camelidae* family members (e.g., camels, llamas, and alpaca) have a subset of IgG antibodies that lack light chains, resulting in antibodies with only a single variable domain, VHH, that bind target molecules. This nanometer-sized antibody, approximately 2.5 nm in diameter and 4.2 nm in length, is called nanobodies (Nb) [7]. Aside from its small molecular size, some advantages include resistance to organic solvent, high solubility, and ease of production

in bacteria as a recombinant protein. This molecule is widely used in basic life science research, drug discovery, cancer diagnosis and treatment, and neurodegenerative and infectious diseases [8]. Some VHH bound to haptens have been reported to date: Spinelli et al. [9] determined the complex structure of azo-dye bound by VHH antibody; Fanning et al. [3] determined the structure of nanobodies attached to methotrexate (MTX); Rosa et al. [2] determined the structure of nanobodies bound to triclocarban (TCC), and Ding et al. [10] determined the structure of nanobodies attached to cortisol.

Cortisol, a steroid hormone, is a biomarker for some diseases and is essential in regulating psychological processes such as blood pressure, glucose levels, and carbohydrate metabolism [11]. Cortisol deficiency can result in Addison's disease. On the other hand, a persistent cortisol excess can result in Cushing's syndrome, leading to severe fatigue, depression, anxiety, cognitive difficulties, obesity, and cardiovascular disease [12-13]. Cortisol is commonly referred to as the "stress hormone" because of its fluctuating levels [14]. Continuous monitoring of cortisol levels is essential to preserve good health. Lately, cortisol measurements have been developed to determine whether variations in cortisol levels can be used as precursors for medically and psychologically relevant events like stress and, more recently, post-traumatic stress disorder (PTSD) [15-16].

Total cortisol is currently defined as the sum of the free cortisol and the protein-bound fraction. However, free cortisol is the only biologically active fraction [17-18] and is responsible for all cortisol-related activities in the body. As a result, regular estimation of free cortisol is required for accurate diagnosis and treatment. For the most part, current strategies are still limited to laboratory techniques such as chromatography, immunoassay, or electrochemical immuno-sensing [19] that are laborious, time-consuming, require large sample sizes, are expensive, and cannot be implemented as rapid test kits [20-21]. However, because of its high stability and tolerance to highly concentrated organic solvents, VHH antibodies can displace fragile traditional IgG antibodies in an ELISA and chip-based micro-detection system. Ding et al. determined the crystal structure of the VHH

complex with cortisol [10]. Cortisol mainly binds to the CDR1 of the VHH antibody. The interaction occurred in forming a hydrophobic pocket into which the majority of the hydrophobic portion of cortisol molecule inserted itself. Unfortunately, the binding affinity was not sufficiently high.

Therefore, we designed new mutants to improve the binding affinity by replacing amino acids at CDR2 and CDR3 with hydrophobic amino acids in the present study. The binding affinity was addressed using molecular docking and molecular dynamics (MD) simulations. It is hoped that the results will aid in developing Nb with a higher affinity to cortisol for diagnostic purposes.

■ COMPUTATIONAL METHODS

Modeling of Mutants

All mutants were built using the comparative modeling method using MODELLER 9.19 [22]. As a starting point, the structure of Nb-Cor (PDB ID: 6ITP) was used as a modeling template. The selection of the template is an essential step in comparative modeling. The quality of the template's structure is 1.57 Å resolution, and the quality of mutants was assessed using the Discrete Optimized Protein Energy (DOPE) score, Ramachandran plot, and Z-score. All mutants were designed based on the initial interaction observed in WT and substituted hydrophobic amino acids at residue numbers 53 and 101. All mutants are listed in Table 1.

Molecular Docking

The structure of Nb and its mutants were prepared using BIOVIA Discovery Studio 2017 Visualizer by separating the cortisol ligand, discarding the water molecules, and completing the structure by adding

Table 1. List of mutants

No.	Mutant	Description
1	MT1	T53V
2	MT2	T53L
3	MT3	T53I
4	MT4	S101V
5	MT5	T53V/S101V
6	MT6	T53L/S101V

hydrogen atoms. AutoDockTools-1.5.6 was used to convert all structures into PDBQT format. The crystal structure of Nb-Cor (PDB ID 6ITP) was redocked to validate the molecular docking method. The grid box size of $50 \times 50 \times 50$ points with a spacing of 0.375 \AA was placed in the center of the Nb binding site. The pre-calculated binding affinity of the ligand's atom type was prepared using Autogrid [23].

AutoDock program is responsible for conformational search and energy evaluation. The Lamarckian Genetic Algorithm (LGA) parameter was set at 100 runs, elitism of 1, the mutation rate of 0.02, the population size of 150, a crossover rate of 0.800, and energy evaluation of 2,500,000 [24]. The resulting docked conformations were clustered using a root-mean-square deviation (RMSD) tolerance of 1.0 \AA . The ligand conformational with the lowest free energy of binding (ΔG) was selected for further MD simulations.

Molecular Dynamics Simulations

The ligand conformational obtained from molecular docking was used as an initial coordinate. MD simulations were used to evaluate the binding of cortisol. MD simulations were carried out on a computer running Ubuntu 20.04.2.0 LTS and equipped with an Intel Xeon® CPU E5-2678 v3 @2.5 GHz \times 24, a GPU NVIDIA GeForce RTX 2080Ti 6 GB, and 16 GB of RAM. The MD simulations procedure was adapted from our prior research [25]. In brief, the ligand (cortisol) parameter was calculated using the AM1-BCC approach by antechamber program [26]. The other parameter was calculated using Generalized Amber Force Fields 2 (GAFF2) [27], while FF19SB was assigned to Nb and its mutants' amino acid residues. All complex system was prepared using tleap program in AmberTools20. The solvent system of a box TIP3P water was added to the solute with the shortest distance of 10 \AA between the protein and the box edge. To neutralize the system, the chloride ion was added. GPU-accelerated Particle-Mesh Ewald Molecular Dynamics (PMEMD) and periodic boundary conditions, as implemented in Amber20, were applied for each protein-ligand complex. Initially, energy minimization was implemented in three stages. First, 1,000 steps of the

steepest gradient algorithm followed by 2,000 steps of conjugate gradient minimization with a harmonic restraint of $500 \text{ kcal/mol \AA}^2$ were applied to the backbone atoms. A final 1,000 steps of unrestrained conjugate gradient minimization were performed to remove any sterically clashes among the atoms.

The system was gradually heated to room temperature (298 K) over 60 ns in the NVT ensemble. In this stage, a harmonic restraint of 5 kcal/mol \AA^2 on the complex was applied to the complex. In addition, 1 ns of NPT equilibration was conducted. Harmonic restraint is gradually reduced by 1 kcal/mol \AA^2 at this stage until it reaches zero. The production stage was run in the NPT ensemble for 100 ns. The time step at the production run was 2 fs since the SHAKE algorithm was used. Langevin thermostat was used to control the temperature. The collision frequency was set to 1 ps^{-1} . The pressure was controlled using a Berendsen barostat. The coupling constant parameter and target pressure were set to 1 ps and 1 bar, respectively. The nonbonded cutoff value was set to 9 \AA . Particle Mesh Ewald was activated to treat the long-range electrostatics.

Trajectory Analysis

We utilized the *cpptraj* program in AmberTools20 to analyze MD trajectories. The analysis includes computation of Root-Mean-Square Fluctuation (RMSF), Root-Mean-Square Deviation (RMSD), and H-bond conservation.

Binding Energy Calculation

We used the MMPBSA.py program to calculate the pairwise interaction energy using a single trajectory method [28]. Binding free energy (ΔG_{bind}) between nanobody and cortisol was calculated based on MM/GBSA method:

$$\begin{aligned}\Delta G_{\text{bind}} &= \Delta H - T\Delta S \approx \Delta E_{\text{MM}} + \Delta G_{\text{sol}} - T\Delta S \\ \Delta E_{\text{MM}} &= \Delta E_{\text{internal}} + \Delta E_{\text{electrostatic}} + \Delta E_{\text{vdw}} \\ \Delta G_{\text{sol}} &= \Delta G_{\text{GB}} + \Delta G_{\text{SA}}\end{aligned}$$

In these equations, ΔH denotes enthalpy, and T denotes temperature (K). ΔE_{MM} is the molecular mechanical (MM) energy change in the gas phase, which comprises of $\Delta E_{\text{internal}}$ (internal energy), $\Delta E_{\text{electrostatic}}$ (Coulomb electrostatics term), and ΔE_{vdw} (van der Waals

interaction term). ΔG_{sol} is the solvation free energy, consists of ΔG_{GB} (electrostatic solvation energy or polar contribution calculated by GB method) and ΔG_{SA} (non-electrostatic solvation component or nonpolar contribution). The interval step and salt concentrations were 1 ns and 150 mM in the binding energy calculation, respectively.

RESULTS AND DISCUSSION

Nanobody, which are small antibody derivatives made up of only the heavy chains of camelid antibodies, have a wide range of applications, including diagnostic, therapeutic, and research [1]. Nb can be designed to have a high binding affinity to cortisol to diagnose cortisol. Based on the initial non-bonding interaction in the crystal structure, hydrophobic interaction between V24 and W34 to the cortisol in CDR1 occurred (Fig. 1). To improve the binding affinity of cortisol, other CDR should be utilized by modifying the amino acid to interact with cortisol. The anti-MTX-VHH was modified by introducing five residues from the original CDR4 loop into the CDR1-3 graft, resulting in a 1,000-fold increase in affinity. The non-hypervariable loop of CDR4 is well-posed for direct interaction with the MTX ligand. The five replaced residues were located in residues number 76 to 80 [3].

Based on the size of the binding pocket of Nb, cortisol already fits into the pocket. Hence, the substitution amino acid was selected to be the same size but more hydrophobic. Threonine 53 and serine 101 have the shortest distance with the ligand at approximately 3 Å. These polar residues should be in an h-bond interaction, but their orientation did not support the h-bond interaction. Besides, ligand and amino acid orientation are relatively meaningless in hydrophobic interaction. The interaction of antigen-antibody is mainly contributed by hydrophobic interaction [29]. As a result, we designed six mutants with single and double substitutions. Valine, isoleucine, and leucine are hydrophobic amino acids composed mostly of carbon and hydrogen, have very small dipole moments, and tend to be repelled from water. Threonine 53 and serine 101 are not exposed to the surface protein either. Hence substitution in this position will not disturb the overall structure. The size of replaced

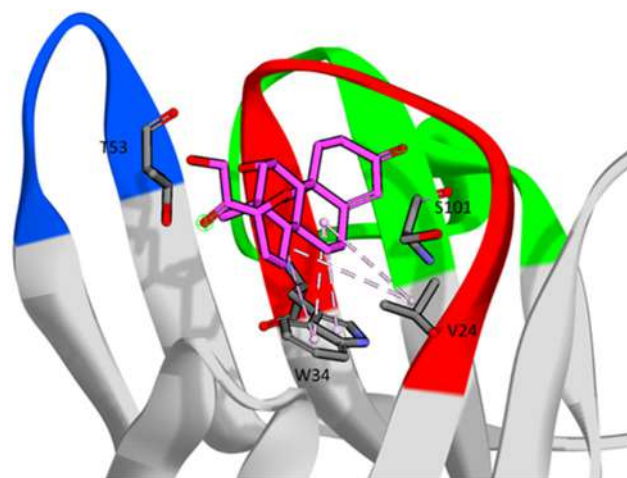


Fig 1. Initial interaction between Nb and cortisol. The red, blue, and green ribbons show the CDR1, CDR2, and CDR3, respectively. Cortisol is visualized in the pink stick, hydrophobic interaction in the pink dashed line, and residues around cortisol in the grey stick

amino acid is relatively not much different than previous. This was chosen to accommodate the ligand-binding pocket. Molecular docking and MD simulations were applied to evaluate and validate our design.

Modeling of Mutants

The mutant models were constructed from the WT structure. The crystal structure of Nb was resolved at good resolution, i.e., 1.57 Å. Because there were only one and/or two different amino acids, the identity of template and mutants was high.

The DOPE score, Ramachandran plot, and z-score were used to evaluate the quality of the mutants' model. According to the DOPE profile, all mutants have the same pattern as the template. Furthermore, the Ramachandran plot revealed that more than 90% of the residues in all mutants were located in the most favored regions, with no residues located in the disallowed region. A protein structure with more than 90% of its residues in the allowed region is classified as a good model [30]. In addition, the z-score of all mutants was equal to the quality of the structure source from X-ray and NMR (Fig. S1-S3).

Ligand Binding

To validate the methods, complex Nb-cortisol was

redocked. The binding energy was found to be -9.05 kcal/mol with an RMSD of 1.16 Å (Fig. 2). The low RMSD score (< 2 Å) indicated that this pose was similar to the pose found in the crystal structure [31]. In contrast, the binding energy of all mutants varied in the score. MT1 and MT3 had higher affinity than WT with the binding energies of -9.12 and -9.87 , respectively, compared to -9.05 kcal/mol. These mutants have CDR2 mutations. MT1 formed new hydrogen bonds with S30 and N77 and a new hydrophobic interaction with V53. While in MT3, a new hydrogen bond formed with S30 and K80 and a hydrophobic interaction with I53 (Fig. 3). It was indicated that our modification could generate new interactions.

MD simulations revealed that the WT, MT1, MT2, MT3, and MT5 are relatively stable, as evidenced by ligand snapshot every 20 ns and ligand's RMSD (Fig. 4). Furthermore, it showed that the ligand could maintain its conformation throughout the simulations. MT1 and MT3 also showed a stable RMSD, although a fluctuation was around 30–40 ns. Nonetheless, both systems can maintain the ligand's binding. Interestingly, MT5 showed stable movement although having the highest docking score than other mutants, -7.03 kcal/mol. The RMSD graph at around 40 ns indicates that almost all systems have a high deviation when viewed as a whole.

The binding energy calculated from molecular

docking and MD simulations revealed an interesting value. Although MT1 and MT3 have better binding affinity calculated from molecular docking, the affinity calculated from MD simulations showed differently. MT3, MT5, and MT6 were higher affinity than WT in MD simulations (Table 2). The Spearman's rank correlation coefficient of the binding energy from docking and MD simulation is -0.07 . It revealed that there was no correlation between the value. Hence, it was suggested that MD simulations are necessary to evaluate the binding from molecular docking. Interestingly, after MD simulations, MT5 and MT6, which demonstrated lower binding affinity in molecular docking, have a higher affinity than WT. Nevertheless, the RMSD of the

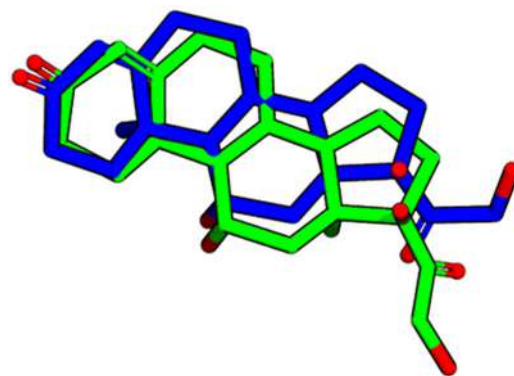


Fig 2. Superimpose of the docked pose (blue) and crystal structure (green)

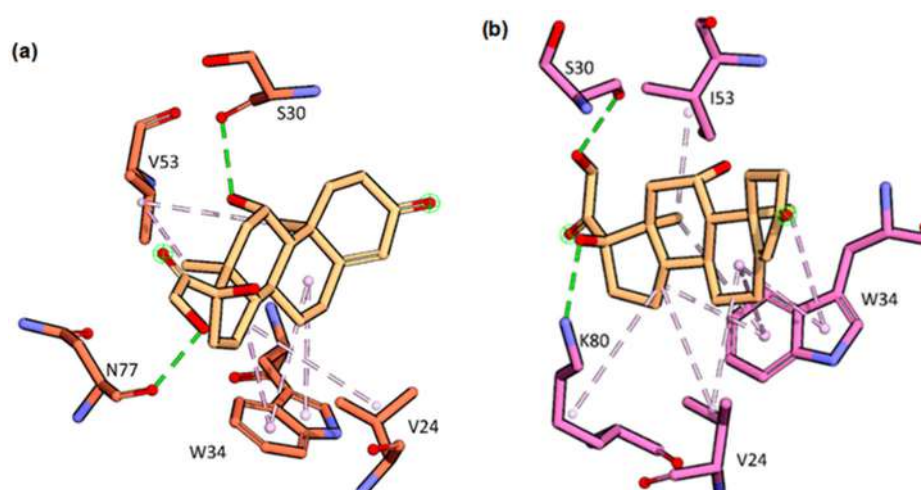


Fig 3. Interaction of cortisol and receptor in MT1 (a) and MT3 (b). Cortisol is represented in brown stick, the amino acid around ligand is shown in orange (MT1) and pink (MT3) stick, respectively, while the hydrogen bond and hydrophobic interaction are represented in green and pink dashed lines, respectively

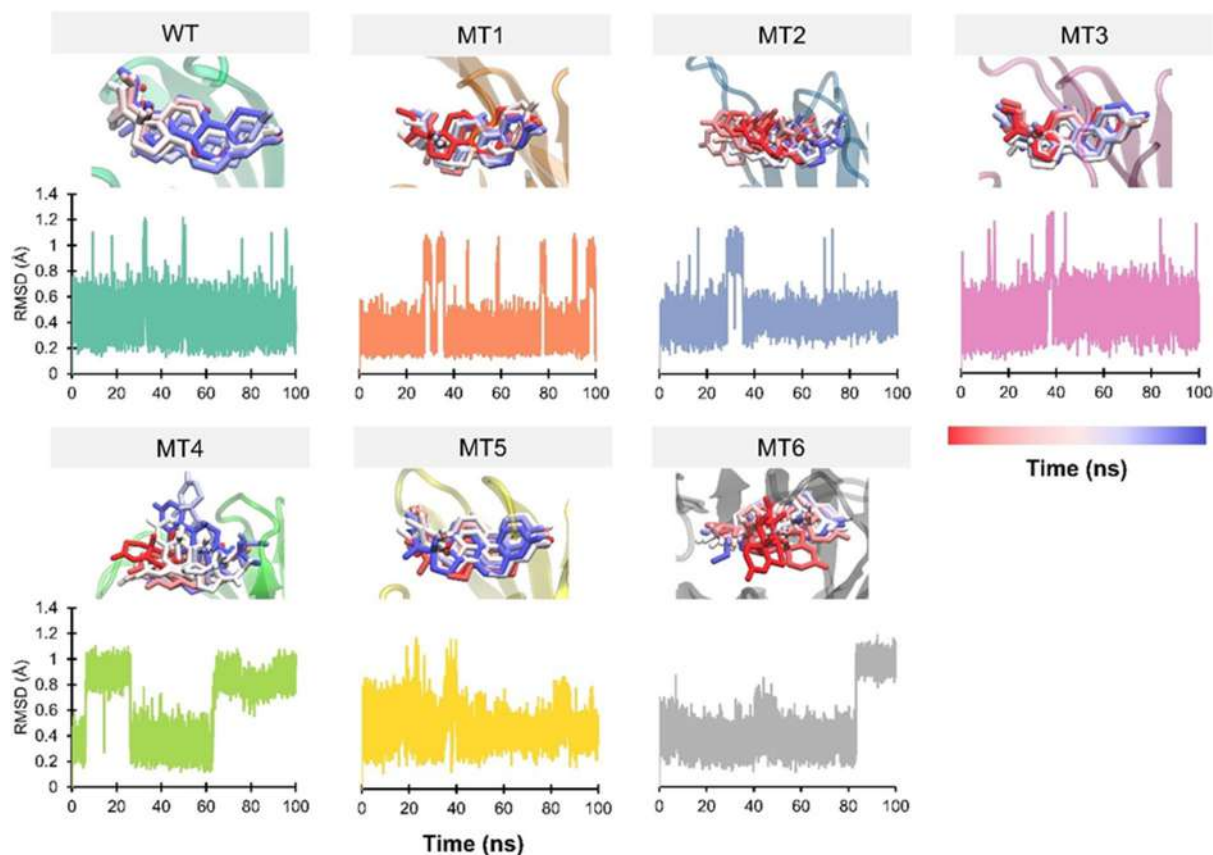


Fig 4. Timestep evolution snapshot and RMSD of ligand every 20 ns throughout MD simulations

Table 2. Binding energy calculation from molecular docking and MD simulations

System	Docking	MD Simulations			
	Binding energy (kcal/mol)	Binding energy (kcal/mol)	Std. Deviation	Average RMSD receptor	Average RMSD ligand
WT	-9.05	-35.03	3.56	1.82	0.45
MT1	-9.12	-33.68	3.48	1.98	0.37
MT2	-8.99	-30.02	7.05	2.09	0.45
MT3	-9.87	-36.84	3.24	1.94	0.49
MT4	-8.51	-26.09	5.01	2.07	0.64
MT5	-7.03	-35.75	7.71	2.15	0.49
MT6	-8.44	-37.61	6.94	2.29	0.49

ligand in MT6 revealed the conformational changes at 80 ns indicating the ligand is unstable.

MMGBSA calculated every 20 ns cumulative, computed from a single trajectory every 1 ns, showed that MT3 has a stable value in the average of -36 kcal/mol and has a better value than WT, -35.03 kcal/mol, although at 100 ns MT6 has lower energy binding, -37.61 kcal/mol

(Fig. 5). A stable value implied that the ligand could bind to the receptor in a stable conformation required for ligand binding. In addition, a stable molecule indicates a fit interaction between the detected molecule with the capture molecule and is required for diagnostic purposes.

The intramolecular interaction was calculated from all systems showed differences in interaction from

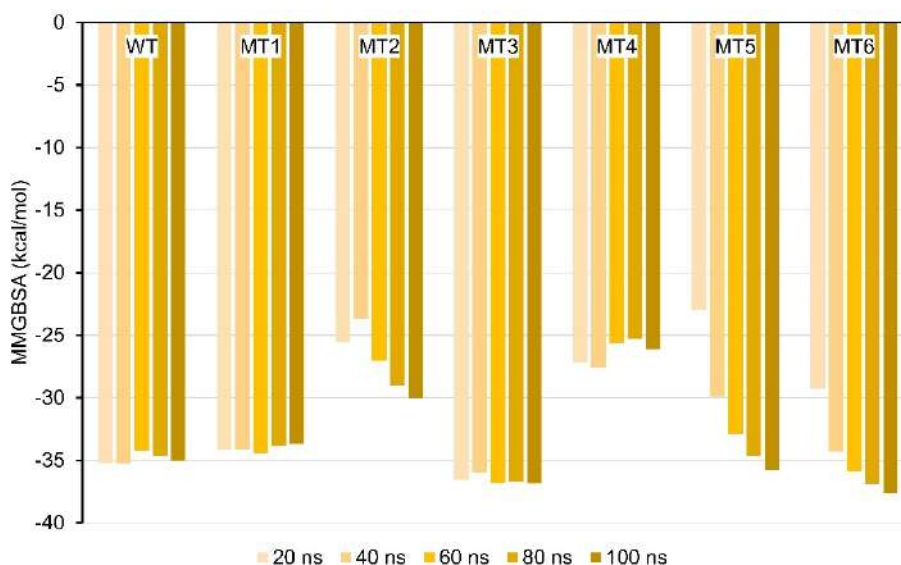


Fig 5. Binding energy trajectory of cortisol bound receptor in every 20 ns cumulative

Table 3. Nonbonded interaction between cortisol and Nb reveal from molecular docking (D) and at the end of MD simulations

Interaction	WT		MT1		MT2		MT3		MT4		MT5		MT6	
	D	MD	D	MD	D	MD	D	MD	D	MD	D	MD	D	MD
H-Bond		1	2	2		2	2	2	6	3	6		6	3
Carbon H-bond		1				2		2				1	2	1
Alkyl	2	2	3	2	4	2	4	2	1		2	4	3	2
Pi-Alkyl	2	5	3	2	5	1	5	6	2	1		1	2	
Pi-sigma				1										

Note: in MD simulations, the nonbonded interaction was extracted from the last frame of MD trajectories

molecular docking and MD simulations. MT3, MT5, and MT6 were found to have better binding energy from MD simulations showed that there were only 2 hydrogen bonds occurred in MT3, 3 h-bond in MT6, and there was no h-bond occurred in MT5. In addition, hydrophobic interaction occurred the most in MT3. This hydrophobic interaction is described in the alkyl, pi-alkyl, and pi-sigma interaction. Besides, MT4, MT5, and MT6, which have the highest sum of H-bond in molecular docking, decreased interaction at the end of MD simulations (Table 3).

H-bond interaction from MD simulations is shown in Table 4. MT1, MT2, MT3, and MT6 showed longer h-bond occurrences than WT. Although MT4 has the largest number of interactions, it was not strong enough to keep the ligand in place when it only occurred for 1 ns. This finding is also in line with the RMSD of ligand that showed fluctuating value. Surprisingly, MT3, which

demonstrated the better binding energy from docking or MD, only has seven atoms that contribute to H-bond.

Nevertheless, this h-bond was occupied for 57 ns with S30, also occupied in WT for 45 ns. According to our findings, hydrophobic interaction donates a lot in the binding energy calculation. It is in line with the fact that hydrophobic interaction is the most common non-covalent interaction observed in protein-ligands from PDB [32]. In addition, VDW interaction energy calculated along MD simulations revealed that MT3 was lower than others (Table 5). This finding corresponded well to the interaction at the last frame of MD trajectories.

Structural Effect

The substitution made on the WT structure can alter the overall conformation. Therefore, we evaluate the

Table 4. Hydrogen bond formation in Nb-cor complex throughout 100 ns of MD simulations

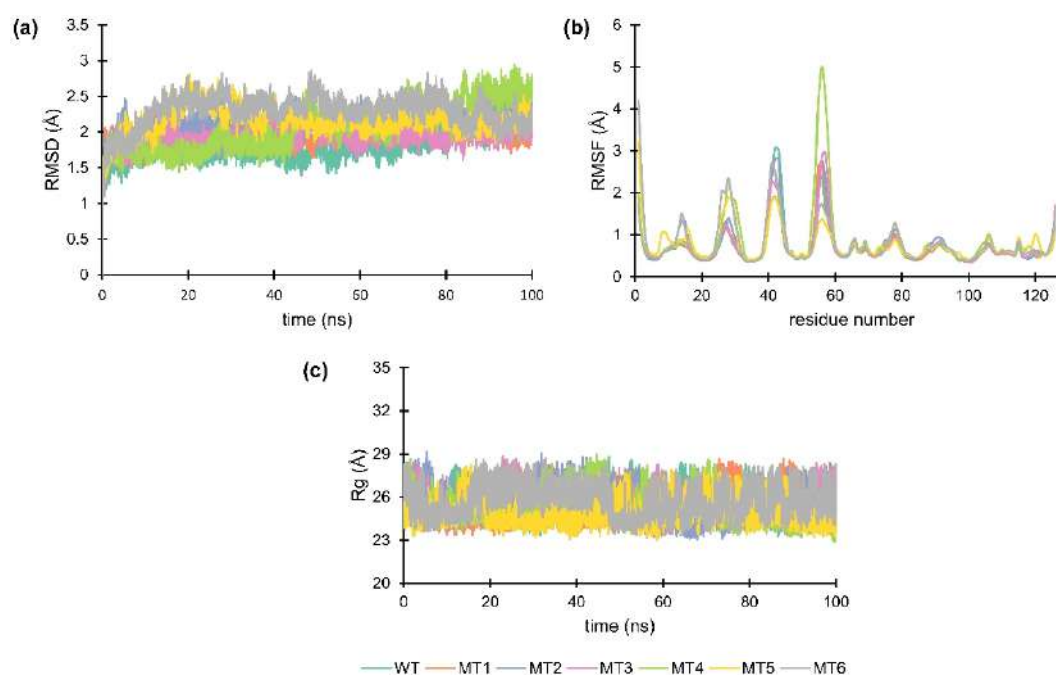
System	Acceptor	Donor	Occ (ns)	System	Acceptor	Donor	Occ (ns)
WT	SER_30@O	HCY_127@O2	45	MT1	SER_30@O	HCY_127@O2	55
	HCY_127@O1	SER_101@OG	14		HCY_127@O4	ASN_77@ND2	16
	HCY_127@O4	ASN_77@ND2	6		ASN_77@OD1	HCY_127@O3	7
	HCY_127@O4	GLN_75@NE2	4		HCY_127@O4	GLN_75@NE2	6
	ASN_77@OD1	HCY_127@O3	2		HCY_127@O1	SER_101@OG	1
				HCY_127@O4	ASN_77@ND2	1	
				ASN_77@OD1	HCY_127@O5	1	
MT2	SER_30@O	HCY_127@O2	52	MT3	SER_30@O	HCY_127@O2	57
	SER_101@OG	HCY_127@O3	12		HCY_127@O4	ASN_77@ND2	12
	THR_28@O	HCY_127@O5	9		HCY_127@O4	GLN_75@NE2	8
	GLY_29@O	HCY_127@O2	7		ASN_77@OD1	HCY_127@O3	4
	HCY_127@O1	GLN_75@NE2	3		ASN_77@OD1	HCY_127@O5	3
	TYR_33@O	HCY_127@O3	3		HCY_127@O1	SER_101@OG	2
	GLY_29@O	HCY_127@O5	3		HCY_127@O3	THR_28@OG1	1
	ALA_54@O	HCY_127@O2	3				
MT4	HCY_127@O4	THR_28@N	23	MT5	SER_30@OG	HCY_127@O2	39
	GLY_32@O	HCY_127@O5	17		HCY_127@O5	GLY_29@N	25
	SER_30@O	HCY_127@O3	13		HCY_127@O1	GLN_75@NE2	22
	SER_30@O	HCY_127@O2	13		HCY_127@O2	SER_30@OG	12
	THR_28@OG1	HCY_127@O3	12		HCY_127@O5	THR_28@N	7
	THR_31@OG1	HCY_127@O2	10		ASN_77@OD1	HCY_127@O2	3
	HCY_127@O3	GLN_75@NE2	8		HCY_127@O2	ASN_77@ND2	2
	ASN_77@OD1	HCY_127@O3	7		THR_28@OG1	HCY_127@O3	2
	THR_28@OG1	HCY_127@O5	7		GLY_29@O	HCY_127@O3	1
	HCY_127@O5	THR_28@OG1	6		HCY_127@O1	THR_51@OG1	1
	HCY_127@O5	THR_53@OG1	6	VAL_24@O	HCY_127@O3	1	
	THR_31@O	HCY_127@O5	5	HCY_127@O3	THR_28@N	1	
	SER_30@O	HCY_127@O5	3				
	HCY_127@O5	THR_53@N	3	MT6	GLN_75@OE1	HCY_127@O3	60
	HCY_127@O4	GLY_29@N	3		HCY_127@O4	GLN_75@NE2	18
	HCY_127@O4	SER_30@N	2		ASN_77@OD1	HCY_127@O2	8
	HCY_127@O5	GLY_32@N	2		HCY_127@O4	ASN_77@ND2	7
	GLY_29@O	HCY_127@O2	1		ASN_77@OD1	HCY_127@O3	6
	THR_31@OG1	HCY_127@O3	1		GLN_75@OE1	HCY_127@O5	4
	HCY_127@O4	THR_28@OG1	1		HCY_127@O3	GLN_75@NE2	3
TYR_33@O	HCY_127@O5	1	HCY_127@O4		ASN_77@ND2	3	

structural effect to ensure that the protein's conformation remains unchanged. RMSD, RMSF, and radius of gyration (Rg) were calculated from all systems and showed a similar trend (Fig. 6). The RMSD graphic

displayed an excellent value, which shows that all systems have a value lower than 2.5 Å. In contrast, the RMSF graphic revealed some high fluctuation in the same position across the entire system. The highest fluctuation

Table 5. VDW and electrostatic interaction calculated from MD simulations

System	VDW (kcal/mol)	Electrostatic (kcal/mol)
WT	-44.58	-16.55
MT1	-43.25	-17.29
MT2	-38.27	-17.88
MT3	-45.20	-17.85
MT4	-33.82	-15.16
MT5	-41.09	-17.79
MT6	-44.91	-18.56

**Fig 6.** Profile of RMSD (A), RMSF (B), and radius of gyration (C) of receptor throughout 100 ns MD simulations, respectively

occurs around residues number 30, 40, and 60 ns which describe a flexible loop. Residue around 30 is the CDR1, a flexible loop to which the ligand bind, while residue around 40 is a loop located far from the ligand binding. Besides, the residues around 60 are the CDR2. The highest fluctuation in MT4 at residue was around 60 (CDR2), flexible loop, which corresponds to the ligand-binding, indicating that the ligand is not stable in MT4 and could not maintain its conformation. Other analyses showed that the Rg of all systems showed the same trend. Rg is defined as a protein's atom distribution around its axis [33]. All systems have a linear graph that indicates the compactness of protein structure throughout MD simulations. As a result, these findings implied that our

modification had no effect on the conformational structure but did affect ligand binding.

CONCLUSION

Increasing the affinity of Nb-cortisol is quite challenging. The CDR is the main area that contributes to the ligand binding. Because CDR1 plays an important in ligand binding, therefore our modification did not affect it. The addition of hydrophobic amino acids to CDR2 and CDR3 can improve the affinity, particularly at MT3, MT5, and MT6. Based on the docking energy, MM/GBSA energy, and ligand movement, MT3 has the highest binding affinity and is relatively more stable than others. The new hydrophobic interaction contributed to

the VDW energy calculation, which yielded the highest value compared to the others. It has been proposed that MT3 can increase the binding affinity of cortisol and is relatively stable. These results can guide the production of Nb in a recombinant laboratory.

■ ACKNOWLEDGMENTS

Yayasan Hazanah supported this work through Fundamental Internal Grant No. 008/SPK/YHZ/III/2021, and also, we want to thank the Indonesian School of Pharmacy for supporting this research.

■ AUTHOR CONTRIBUTIONS

UB and NAS designed the experiments. UB conducted the experiment. UB, MY, NAS analyzed the data. UB, NAS, IM, DA, and MY wrote and revised the manuscript. All authors agreed to the final manuscript.

■ REFERENCES

- [1] Hassanzadeh-Ghassabeh, G., Devoogdt, N., De Pauw, P., Vincke, C., and Muyldermans, S., 2013, Nanobodies and their potential applications, *Nanomedicine*, 8 (6), 1013–1026.
- [2] Tabares-da Rosa, S., Wogulis, L.A., Wogulis, M.D., González-Sapienza, G., and Wilson, D.K., 2019, Structure and specificity of several triclocarban-binding single domain camelid antibody fragments, *J. Mol. Recognit.*, 32 (1), e2755.
- [3] Fanning, S.W., and Horn, J.R., 2011, An anti-hapten camelid antibody reveals a cryptic binding site with significant energetic contributions from a nonhypervariable loop, *Protein Sci.*, 20 (7), 1196–1207.
- [4] Huston, J.S., Levinson, D., Mudgett-Hunter, M., Tai, M.S., Novotný, J., Margolies, M.N., Ridge, R.J., Bruccoleri, R.E., Haber, E., Crea, R., and Oppermann, H., 1988, Protein engineering of antibody binding sites: Recovery of specific activity in an anti-digoxin single-chain Fv analogue produced in *Escherichia coli*, *Proc. Natl. Acad. Sci. U. S. A.*, 85 (16), 5879–5883.
- [5] Rosano, G.L., and Ceccarelli, E.A., 2014, Recombinant protein expression in *Escherichia coli*: Advances and challenges, *Front. Microbiol.*, 5, 172.
- [6] Löfblom, J., Frejd, F.Y., and Ståhl, S., 2011, Non-immunoglobulin based protein scaffolds, *Curr. Opin. Biotechnol.*, 22 (6), 843–848.
- [7] Muyldermans, S., 2013, Nanobodies: Natural single-domain antibodies, *Annu. Rev. Biochem.*, 82 (1), 775–797.
- [8] Bever, C.S., Dong, J.X., Vasylieva, N., Barnych, B., Cui, Y., Xu, Z.L., Hammock, B.D., and Gee, S.J., 2016, VHH antibodies: Emerging reagents for the analysis of environmental chemicals, *Anal. Bioanal. Chem.*, 408 (22), 5985–6002.
- [9] Spinelli, S., Frenken, L.G.J., Hermans, P., Verrips, T., Brown, K., Tegoni, M., and Cambillau, C., 2000, Camelid heavy-chain variable domains provide efficient combining sites to haptens, *Biochemistry*, 39 (6), 1217–1222.
- [10] Ding, L., Wang, Z., Zhong, P., Jiang, H., Zhao, Z., Zhang, Y., Ren, Z., and Ding, Y., 2019, Structural insights into the mechanism of single domain VHH antibody binding to cortisol, *FEBS Lett.*, 593 (11), 1248–1256.
- [11] Corbalán-Tutau, D., Madrid, J.A., Nicolás, F., and Garaulet, M., 2014, Daily profile in two circadian markers “melatonin and cortisol” and associations with metabolic syndrome components, *Physiol. Behav.*, 123, 231–235.
- [12] Pasha, S.K., Kaushik, A., Vasudev, A., Snipes, S.A., and Bhansali, S., 2014, Electrochemical immunosensing of saliva cortisol, *J. Electrochem. Soc.*, 161 (2), B3077.
- [13] McEwen, B.S., 2002, Editorial: Cortisol, Cushing's syndrome, and a shrinking brain - New evidence for reversibility, *J. Clin. Endocrinol. Metab.*, 87 (5), 1947–1948.
- [14] Kaushik, A., Vasudev, A., Arya, S.K., Pasha, S.K., and Bhansali, S., 2014, Recent advances in cortisol sensing technologies for point-of-care application, *Biosens. Bioelectron.*, 53, 499–512.
- [15] Dalirirad, S., and Steckl, A.J., 2019, Aptamer-based lateral flow assay for point of care cortisol detection in sweat, *Sens. Actuators, B*, 283, 79–86.
- [16] Dikme, O., and Dikme, O., 2019, Serum cortisol level as a useful predictor of surgical disease in

- patients with acute abdominal pain, *Signa Vitae*, 15 (1), 27–31.
- [17] le Roux, C.W., Chapman, G.A., Kong, W.M., Dhillon, W.S., Jones, J., and Alaghband-Zadeh, J., 2003, Free cortisol index is better than serum total cortisol in determining hypothalamic-pituitary-adrenal status in patients undergoing surgery, *J. Clin. Endocrinol. Metab.*, 88 (5), 2045–2048.
- [18] Rice, P., Upasham, S., Jagannath, B., Manuel, R., Pali, M., and Prasad, S., 2019, CortiWatch: Watch-based cortisol tracker, *Future Sci. OA*, 5 (9), FSO416.
- [19] Kaushik, A., Yndart, A., Jayant, R.D., Sagar, V., Atluri, V., Bhansali, S., and Nair, M., 2015, Electrochemical sensing method for point-of-care cortisol detection in human immunodeficiency virus-infected patients, *Int. J. Nanomedicine*, 10, 677–685.
- [20] Frasconi, M., Mazzarino, M., Botrè, F., and Mazzei, F., 2009, Surface plasmon resonance immunosensor for cortisol and cortisone determination, *Anal. Bioanal. Chem.*, 394 (8), 2151–2159.
- [21] Zainol Abidin, A.S., Rahim, R.A., Md Arshad, M.K., Fatin Nabilah, M.F., Voon, C.H., Tang, T.H., and Citartan, M., 2017, Current and potential developments of cortisol aptasensing towards point-of-care diagnostics (POTC), *Sensors*, 17 (5), 1180.
- [22] Fiser, A., and Šali, A., 2003, MODELLER: Generation and refinement of homology-based protein structure models, *Methods Enzymol.*, 374, 461–491.
- [23] Morris, G.M., Goodsell, D.S., Halliday, R.S., Huey, R., Hart, W.E., Belew, R.K., and Olson, A.J., 1998, Automated docking using a Lamarckian genetic algorithm and an empirical binding free energy function, *J. Comput. Chem.*, 19 (14), 1639–1662.
- [24] Morris, G.M., Huey, R., Lindstrom, W., Sanner, M.F., Belew, R.K., Goodsell, D.S., and Olson, A.J., 2009, AutoDock4 and AutoDockTools4: Automated docking with selective receptor flexibility, *J. Comput. Chem.*, 30 (16), 2785–2791.
- [25] Baroroh, U., Yusuf, M., Rachman, S.D., Ishmayana, S., Hasan, K., and Subroto, T., 2019, Molecular dynamics study to improve the substrate adsorption of *Saccharomycopsis fibuligera* R64 alpha-amylase by designing a new surface binding site, *Adv. Appl. Bioinf. Chem.*, 12, 1–13.
- [26] Jakalian, A., Jack, D.B., and Bayly, C.I., 2002, Fast, efficient generation of high-quality atomic charges. AM1-BCC Model: II. Parameterization and validation, *J. Comput. Chem.*, 23 (16), 1623–1641.
- [27] Wang, J., Wolf, R.M., Caldwell, J.W., Kollman, P.A., and Case, D.A., 2004, Development and testing of a general amber force field, *J. Comput. Chem.*, 25 (9), 1157–1174.
- [28] Miller, B.R., Mcgee, T.D., Swails, J.M., Homeyer, N., Gohlke, H., and Roitberg, A.E., 2012, MMPBSA.py: An efficient program for end-state free energy calculations, *J. Chem. Theory Comput.*, 8 (9), 3314–3321.
- [29] van Oss, C.J., Absolom, D.R., and Neumann, A.W., 1980, The “hydrophobic effect”: Essentially a van der Waals interaction, *Colloid Polym. Sci.*, 258 (4), 424–427.
- [30] Laskowski, R., MacArthur, M., Moss, D., and Thornton, J., 1993, PROCHECK: A program to check the stereochemical quality of protein structures, *J. Appl. Crystallogr.*, 26 (2), 283–291.
- [31] Hernández-Santoyo, A., Tenorio-Barajas, A.Y., Altuzar, V., Vivanco-Cid, H., and Mendoza-Barrera, C., 2013, "Protein-Protein and Protein-Ligand Docking" in *Protein Engineering: Technology and Application*, Eds. Tomohisa Ogawa, T., IntechOpen, London, 21.
- [32] de Freitas, R.F., and Schapira, M., 2017, A systematic analysis of atomic protein-ligand interactions in the PDB, *MedChemComm*, 8 (10), 1970–1981.
- [33] Sneha, P., and Priya Doss, C.G., 2016, Molecular dynamics: New frontier in personalized medicine, *Adv. Protein Chem. Struct. Biol.*, 102, 181–224.

Identification α -Amylase Inhibitors of *Vernonia amygdalina* Leaves Extract Using Metabolite Profiling Combined with Molecular Docking

Norainny Yunitasari*, Tri Joko Raharjo, Respati Tri Swasono, and Harno Dwi Pranowo

Department of Chemistry, Faculty of Mathematics and Natural Sciences, Universitas Gadjah Mada, Sekip Utara, PO BOX BLS 21, Yogyakarta 55281, Indonesia

* **Corresponding author:**

email:

yunitasari060688@mail.ugm.ac.id

Received: December 23, 2021

Accepted: February 23, 2022

DOI: 10.22146/ijc.71499

Abstract: *Vernonia amygdalina* was reported to be used as a therapy for Diabetes Mellitus (DM). One of the mechanisms of therapy DM was to inhibit the action of the α -amylase enzyme. This study aimed to prove the presence of compounds that could inhibit the action of α -amylase. *Vernonia amygdalina* leaves were macerated with methanol and partitioned into n-hexane, dichloromethane (DCM), and ethyl acetate (EtOAc). Furthermore, they were tested for α -amylase inhibitory activity and analyzed using liquid chromatography-high resolutions mass spectrometry (LC-HRMS). Molecular docking and molecular dynamics simulation (MD simulation) examined unique compounds in the extract with good activity and chromatogram results. The EtOAc extracts showed potential as α -amylase inhibitors indicated by their IC_{50} values, namely 3.0 μ g/mL. There are five unique compounds in the EtOAc extract predicted as 3-[(2Z)-3,7-dimethylocta-2,6-dien-1-yl]-2,4-dihydroxy-6-(2-phenylethyl)benzoic acid (compound 1), 2-hexylpentanedioic acid (compound 2), (2E,4E)-5-[1-hydroxy-2,6-dimethyl-4-oxo-6-({3,4,5-trihydroxy-6-(hydroxymethyl)oxan-2-yl}oxy)methyl)cyclohex-2-en-1-yl]-3-methylpenta-2,4-dienoic acid (compound 3), 3,5,5-trimethyl-4-(3-{{3,4,5-trihydroxy-6-(hydroxymethyl)oxan-1-yl}oxy}butyl)cyclohex-2-en-1-one (compound 4), and 2-{{(6E)-2,10-dihydroxy-2,6,10-trimethyldodeca-6,11-dien-3-yl}oxy}-6-(hydroxymethyl)oxane-3,4,5-triol (compound 5). The molecular docking analysis showed that compound 3 had better interaction energy (E_i) (-8.59 kcal/mol) and inhibition constant (K_i) values (0.503 μ M) than acarbose. These data were supported by MD simulations based on the parameters of RMSD value, the radius of gyration, and protein-ligand interaction energy.

Keywords: ethyl acetate extract; diabetes mellitus; LC-HRMS; protein 4GQR; molecular dynamic simulation

■ INTRODUCTION

Indonesia is one of the countries with the highest diabetes cases, particularly type 2 diabetes mellitus (T2DM) [1]. One of the mechanisms for treating DM is to suppress the hydrolysis of glucose from carbohydrates by inhibiting the action of digestive enzymes, such as α -amylase and α -glucosidase [2]. The α -amylase is the first digestive enzyme that breaks down dietary carbohydrates such as starch into simpler parts in the digestive system, which would then be degraded further by the α -glucosidase into glucose which is readily absorbed and enters the bloodstream [3]. Inhibition of the α -amylase is

an important molecular target for the treatment of type 2 DM [4]. Acarbose is one of the DM medicines that act as an α -glucosidase inhibitor [5]. A combination of α -amylase and α -glucosidase could be a potential approach to treat DM. However, none of the DM medicine has been reported to inhibit α -amylase.

Vernonia amygdalina leaves or often known as insulin leaves, are believed to be diabetes mellitus drugs. *Vernonia amygdalina* plant, commonly known as African leaves, is consumed by people with diabetes for therapeutic purposes in African countries [6]. The use of *Vernonia amygdalina* leaves for the treatment of DM is also carried out by people in Central Indonesia

(Makassar). Drinking tea from *Vernonia amygdalina* has been reported to be successful in lowering blood glucose levels [7]. This plant is also reported to treat various diseases other than DM [8]. These biological effects could be attributed to polyphenols in the extract, especially dicaffeoyl-quinic acid and its isomers [9]. In other studies, *Vernonia amygdalina* leaves were also shown to have the potential as a natural source for managing diabetes. In vitro, the extract of this plant was proven to contain a lot of mineral elements (potassium, magnesium, and calcium) and a little content of chromium through the microwave-assisted extraction method [10].

Phytochemicals in plants are very complex, with various concentrations. High-resolution MS was reported can be employed to do a high throughput metabolite profile. LC-HRMS was reported to identify compounds in large quantities in a short time. LC-HRMS was a high-resolution mass spectrometry linked to a database of compounds. Previous research identified 120 compounds from *Diaphragma juglandis*, of which 20 compounds are bioactive compounds, using LC-HRMS [11]. From the results of the analysis with LC-HRMS, it could be seen the structure of the identified compounds. This information helped perform in silico tests. An in-silico approach, namely through molecular docking, could be used to see if a compound had the potential to act as an α -amylase inhibitor [8-7,11]. In silico research had been conducted to prove to inhibit the work of α -amylase and α -glucosidase by several compounds. Several compounds were able to inhibit the work of α -amylase in silico, including Luteolin (LUT), Hesperetin (HES), and Quercetin (QUE) [12]. The compounds that could inhibit the action of α -glucosidase in silico were myricetin-3-O-rhamnoside (myricitrin) and epigallocatechin-3-gallate (EGCG) [1]. Molecular docking could be a valuable tool for proving an activity [13] and facilitating the discovery of new compounds in inhibiting α -amylase [14].

This study aimed to identify the secondary metabolites of *Vernonia amygdalina* that could be responsible for the antidiabetic activity, especially as an α -amylase inhibitor. Metabolite profile of the active extract followed by docking the discovered compounds from the

profile used as tools to accomplish the goal.

■ EXPERIMENTAL SECTION

Materials

Fresh leaves of *Vernonia amygdalina* were obtained from a self-grown plant. The authenticity of the plant was confirmed by The Plants Systematics Laboratory, Faculty of Biology, Universitas Gadjah Mada. All chemicals used were the analytical reagent grade, such as methanol (MeOH), n-hexane, dichloromethane (DCM), and ethyl acetate (EtOAc), and were commercially purchased from Merck (Darmstadt, Germany). α -amylase from hog pancreas was purchased from Sigma USA. Dimethyl sulfoxide (DMSO) and 3,5-dinitrosalicylic acid (DNSA) were purchased from Sigma-Aldrich.

Instrumentation

The instruments used were rotary evaporator (Buchi), incubator oven (Mettler), LC-HRMS Thermo Exactive Orbitrap (Thermo Scientific), and spectrophotometer UV-vis (Thermo Fisher Scientific G10S). Molecular docking assay was implemented using AutoDock Tools (ADT, version: 1.5.7), provided with the AutoDock 4.2 package (Autodock 4.2, Autogrid 4.2, AD4.1_bound, and AD4_parameters). Docking and MD simulation were running in a PC Computer using an AMD ThreadRipper 3970X processor.

Procedure

Plant extract preparation

Fresh leaves were dried in the shade with the sunlight exposure and aerated for 3-4 days. The dried leaves were powdered using a blender machine (Philips). Powdered leaves (500 g) of *Vernonia amygdalina* were macerated with 2000 mL methanol (MeOH) at room temperature for 3×24 h for each extraction. The MeOH extracts were concentrated by a rotary evaporator at 40 °C to 100 mL. The concentrated methanol extracts were partitioned with hexane-water (1:1) followed by n-hexane, DCM-water (3:1), and DCM. All extracts of partition were evaporated under vacuum at 40 °C. All extracts were stored in the refrigerator until further use.

In vitro α -amylase inhibitory studies

The method used for the α -amylase inhibition assay was the 3,5-dinitrosalicylic acid (DNSA) method [13-14]. Each extract was dissolved in a minimum amount of 10% DMSO and was further dissolved in buffer ((Na₂HPO₄/NaH₂PO₄ (0.02 M), NaCl (0.006 M) at pH 6.9). The 200 μ L of α -amylase solution (5 units/mL) was mixed with 200 μ L of the extract in a test tube and was incubated at 30 °C for 10 min. The test tubes were added 200 μ L of the starch solution (1% in water (w/v)) and incubated for 3 min. The reaction was terminated by adding 200 μ L DNSA reagent (12 g of sodium potassium tartrate tetrahydrate in 8.0 mL of 2 M NaOH and 20 mL of 96 mM of 3,5-dinitrosalicylic acid solution) and boiled at 85–90 °C for 10 min. The mixture was cooled to ambient temperature and was diluted with 5 mL of distilled water, and the absorbance was measured at 540 nm using a UV-Visible spectrophotometer. The blank with 100% enzyme activity was prepared by replacing the plant extract with 200 μ L of the buffer. A blank sample was prepared using the plant extract at each concentration in the absence of the enzyme solution, while acarbose (100 μ g/mL–2 μ g/mL) was used as a positive control. The α -amylase inhibitory activity was expressed as percent inhibition and was calculated using the equation given below: The % α -amylase inhibition was plotted against the extract concentration, and the IC₅₀ values were obtained from the graph.

$$\% \alpha \text{ amylase inhibiton} = 100 \times \frac{\text{Abs}_{100\% \text{ Control}} - \text{Abs}_{\text{Sample}}}{\text{Abs}_{100\% \text{ Control}}}$$

Using LC-HRMS analysis

The methanol extract, *n*-hexane extract, DCM extract, and EtOAc extract were analyzed using LC-HRMS. Five mg of extract dissolved in 5 mL of methanol then filtered with 0.2 μ m PTFE membrane and 5 μ L sample was injected. The LC-HRMS employed UHPLC Vanquish Tandem Q Exactive Plus Orbitrap LC-HRMS ThermoScientific. The column used was Accucore C18, 100 \times 2.1 mm, 1.5 μ m (ThermoScientific). The eluents used were H₂O with 0.1% formic acid (A) and acetonitrile with 0.1% formic acid (B). The flow rate was 0.2 mL/min. used gradient 5–60% B (0–15 min), flowed by 60–95% B (15–22 min), and kept until 25 min before finally

returning to 5%B (25–30 min). The MS/MS scan was set at *m/z* = 200–2000 with full scan and ddMS2 using positive and negative mode. The raw data was then analyzed using compound discoverer 2.0 software using untargeted metabolomics. The precursor ions and their fragmentation pattern of particular peaks on the sample chromatogram were matched with the mzCloud compound database during the identification process. The results of LC-HRMS were clarified by comparing the measured molecular weight with the proposed molecular weight. After that, check the molecular formula at www.chemcals.com and the structural formula at www.pubchem.com.

Molecular docking studies

Ligand preparation. The ligand structure of compounds 1 to 5 was obtained from the results of the LC-HRMS analysis. These structures were drawn using Marvin [15] in 2D format, and the clean 3D structure was optimized using the Orca program [16]. A Density functional theory (DFT) based on the proposed three-fold corrected (3c) Hartree-Fock method, termed PBEh-3c, was applied to optimize geometry ligand structure [17]. The optimized structure of the ligand was loaded partial charge by Gasteiger charge and kept in *.pdbqt format using AutodockTools 1.5.7.

Receptor preparation. The protein structure was downloaded from the protein data bank with PDB ID 4GQR. For docking purposes, water molecules were clean, and the Co-Crystal ligand code in Myricetin (MYC) was separate. Hydrogen atoms were added to the protein structure using the PyMOL program. Partial charges using the Gasteiger charge were loaded into the structure by AutodockTools 1.5.7. The Final file *.pdbqt was ready for docking.

Grid and docking parameter File. Using MYC ligand reference, the grid box for the search location was centered at [13.047 14.631 39.633] coordinate. The grid box dimensions were 60 \times 60 \times 60 Å with a 0.375 Å spacing. Autodock 4.2.6 was used as a docking program. Lamarckian Genetic Algorithm was used as a search parameter with *ga_run* was 100 times running, *ga_pop_size* was set to 300 and *ga_num_evals* using comprehensive evaluation, 25000000. Docking results

are visualized using Ligplot software version 4.4.2 (EMBL-EBI, Cambridgeshire, UK).

Molecular dynamics (MD) simulation

MD preparation. Complex structure from the best results of the docking step was used as the initial structure for MD simulation. Preparation uses the pdb4amber module for checking gaps, adding hydrogen, and missing atoms and residues. The protonation state (pK) of amino acid was computed using H++ Web Service (<http://newbiophysics.cs.vt.edu/H++/>). Ligands were parameterized using semi-empirical AM1-BCC methods using the Antechamber program. The complex protein-ligand was solvated using the TIP3P water model in a 14 Å cubic box. The final topology file (*.top) and coordinate file (*.crd) were built using the LEap module from AMBER20.

MD step. Molecular dynamics simulation consists of four steps. They are minimization of energy, heating, equilibration, and production. Energy minimization is needed to eliminate steric hindrance and bad contact. Energy minimization consists of 5 stages. Each stage has a different constraint value that gradually decreases. The last stage of minimization was set to be free from constraint. The combined algorithm, Steepest Descent, and Conjugate Gradient were used in the minimization step. The heating step is needed to make the solvent reach the final temperature, 300 K. The simulation system was set to the NVT ensemble when entering the heating step, and a small constraint of about 10 kcal/mol was applied only for C-alpha atoms. The Langevin method was used with γ_{ln} 1 for the heating process. The Equilibration step was to get the appropriate density of the system. In this step, an NPT ensemble was used, and a constraint from the heating process was released gradually. The final step, production run, was the molecular dynamics without any constraint and in natural conditions. The NPT ensemble was used from the equilibration step. The Periodic Boundary Condition was set to on, 9 Å was used as a cutoff, and 2 fs was used as timestep. Production of data evaluations was divided into 50 parts. Each part equals 2 ns simulation time and gives 100 ns in total. All MD step was carried out using the pmemd module as part of the AMBER program [18].

RESULTS AND DISCUSSION

α -Amylase Inhibition Activity

The inhibitory ability of the extract was observed from their IC₅₀ value. The smaller IC₅₀ value indicated a higher ability to inhibit α -amylase. Acarbose, a widely used and marketed antidiabetic drug, was used as a positive control. Acarbose worked by inhibiting α -glycosidase and was chosen as a positive control because no commercial anti-DM worked by inhibiting α -amylase [14]. Acarbose as a positive control in α -amylase inhibition was not as good as a positive control in α -glucosidase inhibition. In the study on *Vitex doniana* leaf extract, the IC₅₀ value of α -glucosidase inhibition was smaller than when inhibited α -amylase, namely 55.59 μ g/mL and 256.66 μ g/mL, respectively [19].

The results of the α -amylase inhibition assay of the four types of extracts are shown in Table 1. The EtOAc extract was the extract that had the smallest IC₅₀ value, namely 3.0 μ g/mL. This extract had a smaller IC₅₀ value than the positive control. These findings indicated that the EtOAc from *Vernonia amygdalina* was potent to be further studied in searching for the compounds for the α -amylase inhibitor. In another study, EtOAc extract from *Eugenia dysenterica* leaves exhibited inhibitory capability against α -amylase, with an inhibitory ability of above 50% at 10 μ g/mL [20]. Similar results were also found in the study on *Vitex doniana* leaf extract, where the EtOAc extract had the smallest IC₅₀ value [19]. The IC₅₀ value of α -amylase inhibition from the *Vernonia amygdalina* leaf extract was not as strong as the α -amylase inhibition from the *Vitex doniana* leaf extract, the IC₅₀ values were 3.0 μ g/mL and 1.67 μ g/mL, respectively.

Table 1. The results of α -amylase inhibition assay on various extracts of *Vernonia amygdalina* and acarbose

No.	Extract	IC ₅₀ (μ g/mL)
1	Methanol	5.0
2	<i>n</i> -hexane	29.3
3	DCM	6.7
4	EtOAc	3.0
5	Acarbose	23.6

Profiling of Compounds Using LC-HRMS Analysis

LC-HRMS results showed that 7 compounds only appeared in the EtOAc extract. There were 5 of them had good chromatogram results; namely, a single signal only appeared in the sample (Table 2). These compounds had not been reported as inhibitors of α -amylase.

The peak at RT 10.005 min identified the presence of compound 1 and was characterized by fragment ions at m/z 99.87447 and 136.13499. At the RT 11.347 min, compound 2 was identified and indicated by the fragment

ions at m/z 57.03340, 61.98717, and 85.51666. Compound 3 was identified at RT 7.722 min and characterized by the fragment ions at m/z 135.08040 and 83.02869. Fragment ions at m/z 101.02333, 137.02327, and 161.02336 indicated the presence of compound 4 and exited at RT 8.290 min. Compound 5 was characterized by the presence of fragment ions at m/z 68.86910, 145.20244, and 163.03885 and exited at RT 8.739 min. One of the LC-HRMS results could be seen in Fig. 1.

Table 2. LC-HRMS data of unique compounds in the EtOAc extract

RT (min)	Compounds		Formula	Molecular weight (MW)	Production (m/z)
	No.	Name			
10.005	Compound 1	3-[(2Z)-3,7-dimethylocta-2,6-dien-1-yl]-2,4-dihydroxy-6-(2-phenylethyl)benzoid acid	C ₂₅ H ₃₀ O ₄	394.21441	99.87447; 136.13499
11.347	Compound 2	2-hexylpentanedioic acid	C ₁₁ H ₂₀ O ₄	216.13616	57.03340; 61.98717; 85.51666
7.722	Compound 3	(2E,4E)-5-[1-hydroxy-2,6-dimethyl-4-oxo-6-({3,4,5-trihydroxy-6-(hydroxymethyl) oxan-2-yl] oxy} methyl) cyclohex-2-en-1-yl]-3-methylpenta-2,4-dienoic acid	C ₂₁ H ₃₀ O ₁₀	442.1839	135.08040; 83.02869
8.290	Compound 4	3,5,5-trimethyl-4-(3-{{3,4,5-trihydroxy-6-(hydroxymethyl) oxan-1yl} oxy} butyl) cyclohex-2-en-1-one	C ₁₉ H ₃₂ O ₇	372.214805	101.02333; 137.02327; 161.02336
8.739	Compound 5	2-[[{(6E)-2,10-dihydroxy-2,6,10-trimethyldodeca-6,11-dien-3-yl] oxy]-6-(hydroxymethyl) oxane-3,4,5-triol	C ₂₁ H ₃₈ O ₈	418.25667	68.86910; 145.20244; 163.03885

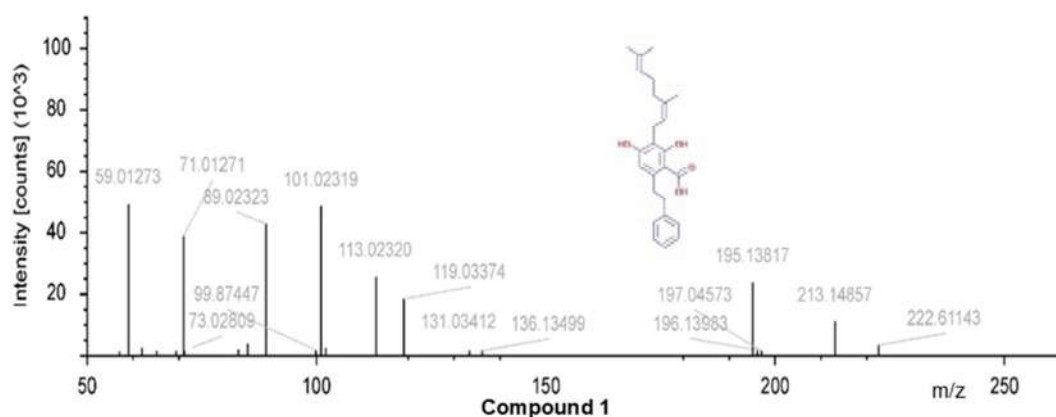


Fig 1. The LC-HRMS results in EtOAc extract

Docking results

The docking results of 5 unique compounds in the EtOAc extract can be seen in Fig. 4. These results indicated that not all the docked compounds occupied the active site of the human pancreas α -amylase (Table 3). Human pancreas α -amylase had an active site on Asp197, Glu233, and Asp300 [21]. At the same time, acarbose (as a positive control and as a diabetes drug) inhibited the action of α -amylase through its active site, which was attached to amino acid residues Asp197, Glu233, and Asp300 (Fig. 5).

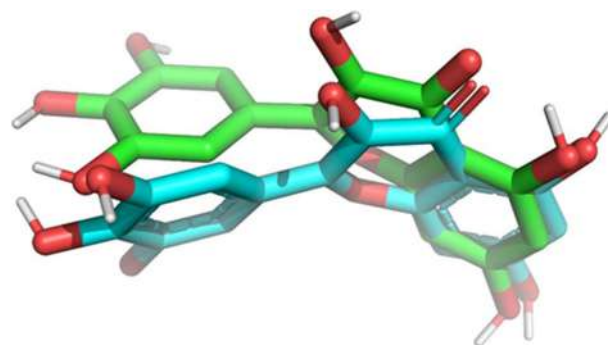


Fig 2. Re-docking MYC ligand

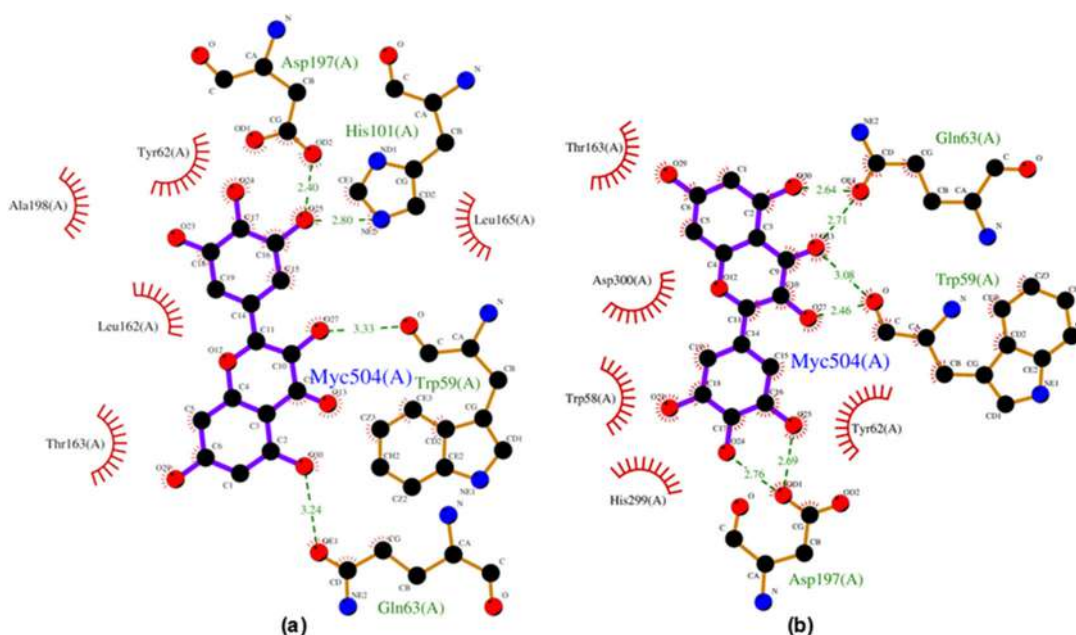


Fig 3. (a) Complex between 4GQR and MYC co-crystals, and (b) Complex between 4GQR and MYC (re-docking)

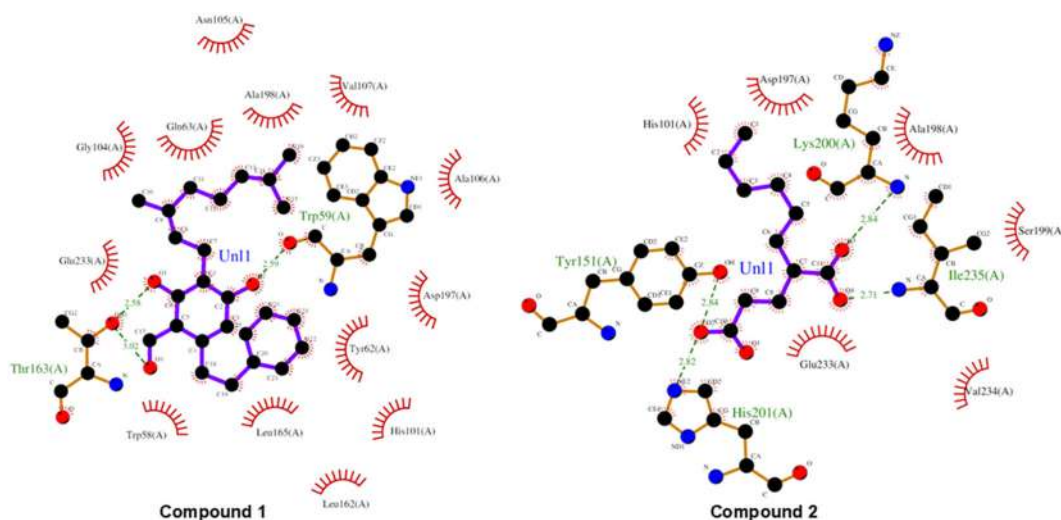


Fig 4. Docking of the unique compounds in the EtOAc extract

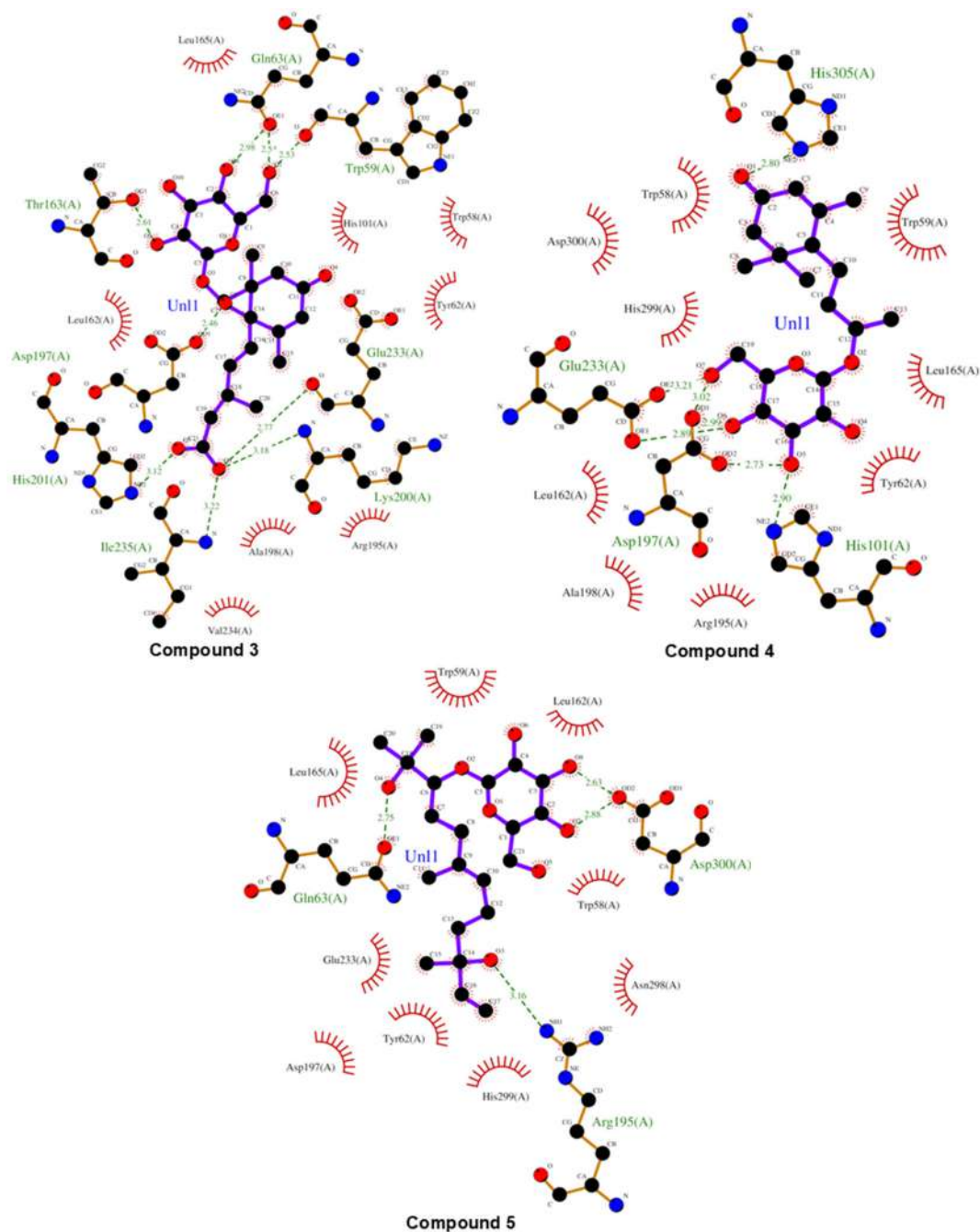


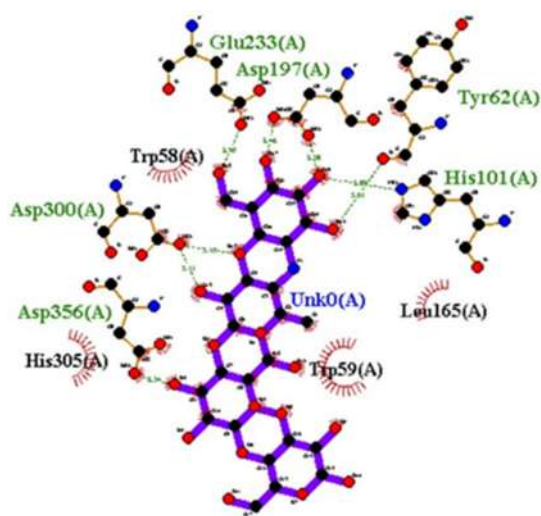
Fig 4. Docking of the unique compounds in the EtOAc extract (Continued)

Based on E_i and K_i values, there were two of five unique compounds in the EtOAc extract, which had a better value than the E_i and K_i values of the original ligand and acarbose, namely compound 3 and compound 4 (Table 4). A drug candidate could be better than the standard drug if E_i and K_i were lower than the standard drug [22]. The more negative the interaction energy, the

more stable the ligand interaction with the protein. A negative value of the interaction energy indicated that the binding of the ligand to the protein was a spontaneous process [23]. The value of the inhibition constant could be said to be proportional to the IC_{50} value with the assumptions: 1) for competitive inhibition, the substrate concentration is close to zero;

Table 3. The hydrogen bond distance of each compound in the molecular docking analysis

	Acarbose	Compound 1	Compound 2	Compound 3	Compound 4	Compound 5	
Distance to amino acid residues (Å)	Asp197	2.38; 2.46	-	-	3.12	3.02	-
	Asp300	3.11; 3.15	-	-	-	-	2.63; 2.88
	Glu233	2.95	-	-	2.77	2.89; 3.21	-
	Asp356	2.34	-	-	-	-	-
	Tyr62	3.01	-	-	-	-	-
	His101	2.89	-	-	-	2.90	-
	Thr163	-	2.58; 3.02	-	2.61	-	-
	Lys200	-	-	2.84	3.18	-	-
	Ile235	-	-	2.71	3.22	-	-
	Gln63	-	-	-	2.54; 2.98	-	2.75
	Trp59	-	2.59	-	2.53	-	-
	Tyr151	-	-	2.82	-	-	-
	His201	-	-	2.82	3.12	-	-
	His305	-	-	-	-	2.80	-
	Arg195	-	-	-	-	-	3.16

**Fig 5.** Results of docking acarbose with alpha-amylase (PDB ID 4GQR)**Table 4.** List of interaction energy values and inhibition constants

Name	Interaction energy/ E_i (kcal/mol)	Inhibition constants/ K_i (μM)
Acarbose	-6.44	19.09
Compound 1	-6.15	31.14
Compound 2	-4.34	659.75
Compound 3	-8.59	0.503
Compound 4	-7.26	4.75
Compound 5	-5.70	66.76

and 2) for non-competitive inhibition, the substrate concentration is infinite. For K_i , smaller values denote tighter binding [24].

The location of the hydrogen bond formed between compound 3 and α -amylase was on the active site of α -amylase, namely on the amino acid residues Asp197 and Glu233 and in the amino acid residues Thr163, Lys200, Ile235, Gln63, Trp59, and His201. Compound 4 inhibited the protein's active site, notably the Asp197 and Glu233 amino acid residues, and established hydrogen bonds with the His101 and His305 amino acid residues. The number of hydrogen bonds formed between compounds 3 and 4 with α -amylase was what causes compounds 3 and 4 to have the most negligible interaction energy and inhibition constant compared to other ligands.

The value of the interaction energy and the inhibition constant of compounds 1, 2, and 5 was less good than acarbose. These facts were possible due to the absence of hydrogen bonds formed with the active site of α -amylase.

Molecular Dynamics Simulation Analysis

This MD simulation analysis was helpful in the analysis of molecular docking results [25]. There were

several parameters in the MD simulation, including Root Mean Square Deviation (RMSD), Radius of Gyration, Root Mean Square Fluctuation (RMSF), and Protein-Ligand Interaction Energy.

Root mean square deviation (RMSD)

RMSD was a measure of conformational change concerning the reference conformation. In this simulation, the reference used was the initial confirmation at the start of the production run stage. The conformational changes of the five ligands are shown in Fig. 6. Compound 5 had a high fluctuation at 10 ns. There were also high fluctuations in compound 2 when after 40 ns. However,

compound 3 has relatively no high fluctuations. At 20 ns to 40 ns, the five compounds converged in 1.25 to 1.5 Å. Overall the RMSD of all compounds/ligands was stable in the change range of 1.5 Å. This RMSD result showed that the presence of the bound ligand did not significantly change the conformation of the protein, so it did not change the protein's function.

Radius of gyration

The radius of gyration showed the compactness of the structure and could see whether the structure was swelling or shrinking. The value of the radius of gyration of the five compounds can be seen in Fig. 7. The radius

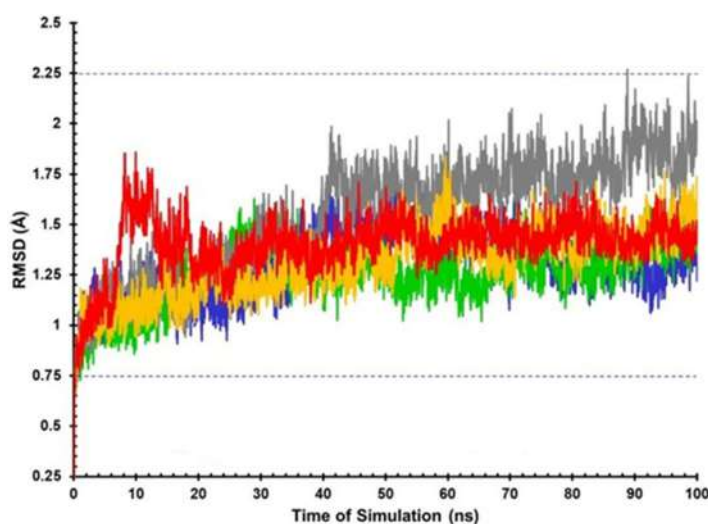


Fig 6. The conformational change of the five compounds during simulation time 100ns (blue: compound 1; grey: compound 2; green: compound 3; yellow: compound 4; and red: compound 5)

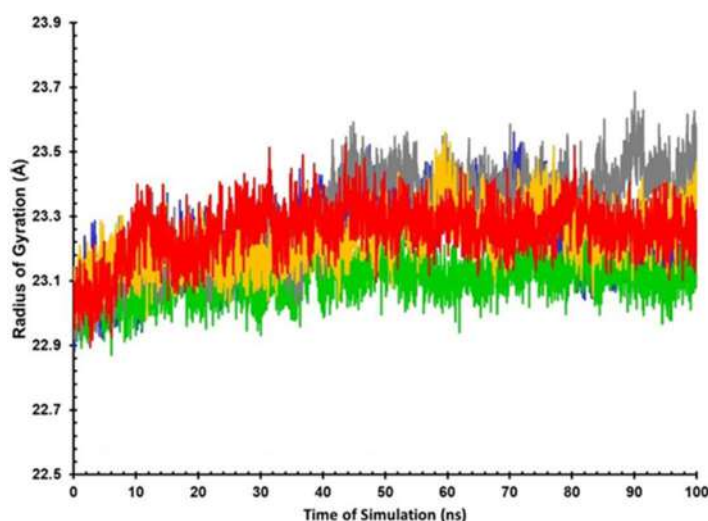


Fig 7. The radius of gyration of the five compounds during simulation time 100 ns (blue: compound 1; grey: compound 2; green: compound 3; yellow: compound 4; and red: compound 5)

of gyration showed the globular shape of the protein structure. The graph showed the shape of the globular structure was not swelling. The value of the radius of gyration had a slight difference in the conformational system of compound 3. The results of the radius of gyration analysis were in line with the results of the RMSD analysis, which showed that compound 3 did not have high fluctuations.

Root mean square fluctuation (RMSF)

RMSF was the dynamic fluctuation of each amino acid residue in the protein structure. This fluctuation

indicated a particular part of a protein structure that could have certain flexibility. Fluctuations that were not high allow for relatively easy interactions with ligands (Fig. 8). The RMSF graph showed the portion of amino acid residues that could have hydrogen bond interaction and other interactions, including Asp197, Glu233, Ala198, Leu162, His101, Trp59, and Tyr62. Furthermore, these residues could be considered when designing drugs targeting α -amylase. According to the docking results, compound 3 could form a hydrogen bond with amino acid residues Asp197, Glu233, and Trp59. Compound 4

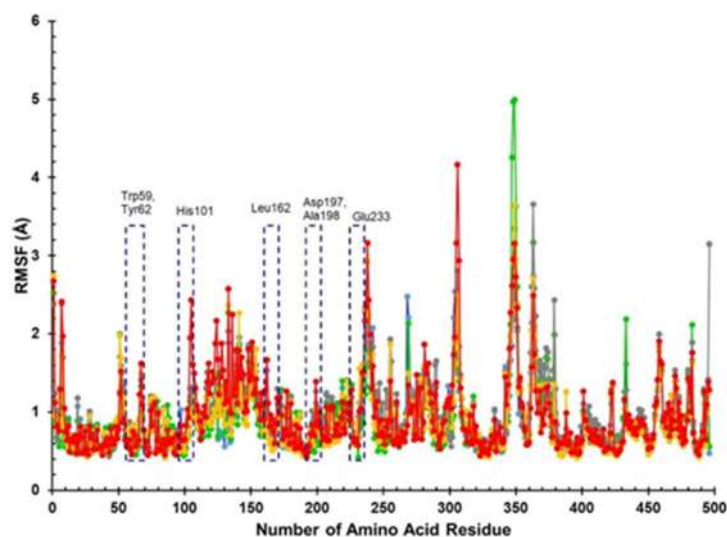


Fig 8. RMSF data (blue: compound 1; grey: compound 2; green: compound 3; yellow: compound 4; and red: compound 5)

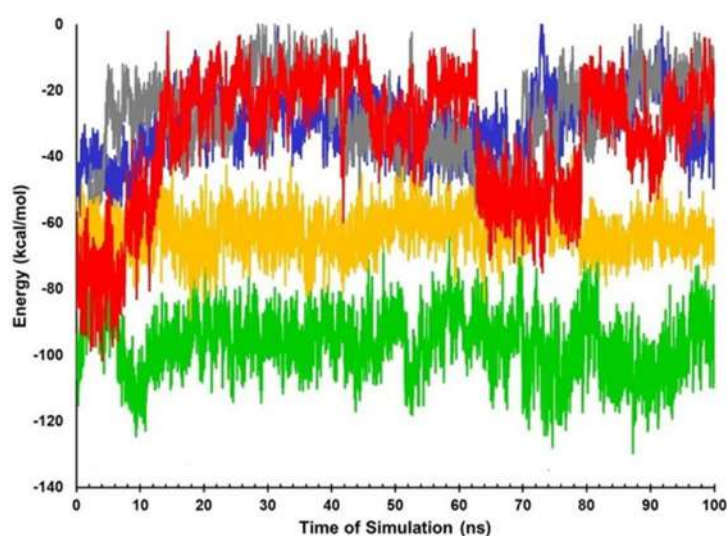


Fig 9. Protein-ligand interaction energy (blue: compound 1; grey: compound 2; green: compound 3; yellow: compound 4; and red: compound 5)

could form hydrogen bonds with amino acid residues Asp197, Glu233, and His101.

Protein-ligand interaction energy

The interaction energy was calculated using NamdEnergy from the NAMD program by looking at the non-bond interaction between protein and ligands. The calculated interactions included Van der Waals and electrostatic interactions. The total energy was the sum of the two energies—the more negative, the stronger the interaction between the ligand and the receptor (Fig. 9). Compounds 3 and 4 had the most substantial interaction energy values, with an average of -96.45 and -62.92 kcal/mol, respectively. Based on the graph, the interaction of the two ligands was relatively stable, only slightly experiencing insignificant fluctuations. The other three ligands appeared to be binding unstable.

CONCLUSION

The extract with the most potential as an α -amylase inhibitor was the EtOAc extract. From the LC-HRMS analysis, the EtOAc extract contained seven unique compounds. Five of the seven unique compounds had good chromatograms and were analyzed by molecular docking and MD simulations. This analysis could prove compounds with potential as α -amylase inhibitors, including compound 3.

ACKNOWLEDGMENTS

This work was supported by Lembaga Pengelola Dana Pendidikan (LPDP). This study is part of dissertation research.

AUTHOR CONTRIBUTIONS

The first author worked in the laboratory. The second author was the supervisor of the LC-HRMS analysis. The third author was the supervisor of the extraction process. The fourth author was the supervisor in the docking analysis and MD simulation.

REFERENCES

- [1] Syabana, M.A., Yuliana, N.D., Batubara, I., and Fardiaz, D., 2022, α -Glucosidase inhibitors from *Syzygium polyanthum* (Wight) Walp leaves as revealed by metabolomics and in silico approaches, *J. Ethnopharmacol.*, 282, 114618.
- [2] Liu, S., Yu, Z., Zhu, H., Zhang, W., and Chen, Y., 2016, *In vitro* α -glucosidase inhibitory activity of isolated fractions from water extract of Qingzhuan dark tea, *BMC Complementary Altern. Med.*, 16 (1), 378.
- [3] Alqahtani, A.S., Hidayathulla, S., Rehman, M.T., ElGamal, A.A., Al-Massarani, S., Razmovski-Naumovski, V., Alqahtani, M.S., El Dib, R.A., and AlAjmi, M.F., 2020, Alpha-amylase and alpha-glucosidase enzyme inhibition and antioxidant potential of 3-oxolupenal and katononic acid isolated from *Nuxia oppositifolia*, *Biomolecules*, 10 (1), 61.
- [4] Ganesan, M.S., Raja, K.K., Narasimhan, K., Murugesan, S., and Kumar, B.K., 2020, Design, synthesis, α -amylase inhibition and *in silico* docking study of novel quinoline bearing proline derivatives, *J. Mol. Struct.*, 1208, 127873.
- [5] Wyne, K., and Bakris, G.L., 2007, "Control of Blood Glucose and Insulin Resistance" in *Comprehensive Hypertension*, Eds. Lip, G.Y.H., and Hall, J.E., Mosby, Philadelphia, US, 1105–1112.
- [6] Ndip, R.N., Tanih, N.F., and Kuete, V., 2013, "Antidiabetes Activity of African Medicinal Plants" in *Medicinal Plant Research in Africa*, Eds. Kuete, V., Elsevier, Oxford, 753–786.
- [7] Halim, A.M., Sirajuddin, S., Bahar, B., Jafar, N., Syam, A., and Masni, 2020, The effect of African leaf herbal tea on fast blood glucose on centration of prediabetes teachers in Makassar city, *Enferm. Clin.*, 30, 261–264.
- [8] Egharevba, G.O., Dosumu, O.O., Oguntoye, S.O., Njinga, N.S., Dahunsi, S.O., Hamid, A.A., Anand, A., Amtul, Z., and Priyanka, U., 2019, Antidiabetic, antioxidant and antimicrobial activities of extracts of *Tephrosia bracteolata* leaves, *Heliyon*, 5 (8), e02275.
- [9] Ong, K.W., Hsu, A., Song, L., Huang, D., and Tan, B.K.H., 2011, Polyphenols-rich *Vernonia amygdalina* shows antidiabetic effects in streptozotocin-induced diabetic rats, *J. Ethnopharmacol.*, 133 (2), 598–607.

- [10] Alara, O.R., and Abdurahman, N.H., 2019, Antidiabetic activity and mineral elements evaluation of *Vernonia amygdalina* leaves obtained from Malaysia, *J. Res. Pharm.*, 23 (3), 514–521.
- [11] Martinez-Gonzalez, A.I., Díaz-Sánchez, Á.G., de la Rosa, L.A., Bustos-Jaimes, I., and Alvarez-Parrilla, E., 2019, Inhibition of α -amylase by flavonoids: Structure activity relationship (SAR), *Spectrochim. Acta, Part A*, 206, 437–447.
- [12] Miller, G.L., 1959, Use of dinitrosalicylic acid reagent for determination of reducing sugar, *Anal. Chem.*, 31 (3), 426–428.
- [13] Wickramaratne, M.N., Punchihewa, J.C., and Wickramaratne, D.B.M., 2016, *In-vitro* alpha amylase inhibitory activity of the leaf extracts of *Adenantha pavonina*, *BMC Complementary Altern. Med.*, 16 (1), 466.
- [14] Almeida, A.R.R.P., and Monte, M.J.S., 2017, Vapour pressures and phase transition properties of four substituted acetophenones, *J. Chem. Thermodyn.*, 107, 42–50.
- [15] Neese, F., Wennmohs, F., Becker, U., and Riplinger, C., 2020, The ORCA quantum chemistry program package, *J. Chem. Phys.*, 152 (22), 224108.
- [16] Grimme, S., Brandenburg, J.G., Bannwarth, C., and Hansen, A., 2015, Consistent structures and interactions by density functional theory with small atomic orbital basis sets, *J. Chem. Phys.*, 143 (5), 054107.
- [17] Case, D.A., Cheatham III, T.E., Darden, T., Gohlke, H., Luo, R., Merz Jr., K.M., Onufriev, A., Simmerling, C., Wang, B., and Woods, R.J., 2005, The Amber biomolecular simulation programs, *J. Comput. Chem.*, 26 (16), 1668–1688.
- [18] Ibrahim, M.A., Koorbanally, N.A., and Islam, M.S., 2016, Anti-oxidative, α -glucosidase and α -amylase inhibitory activity of *Vitex doniana*: Possible exploitation in the management of type 2 diabetes, *Acta Pol. Pharm.*, 73 (5), 1235–1247.
- [19] Justino, A.B., Guerra Silva, H.C., Franco, R.R., de Oliveira Cavalcante Pimentel, I., Silva, N.F., Saraiva, A.L., and Espindola, F.S., 2022, Flavonoids and proanthocyanidins-rich fractions from *Eugenia dysenterica* fruits and leaves inhibit the formation of advanced glycation end-products and the activities of α -amylase and α -glucosidase, *J. Ethnopharmacol.*, 285, 114902.
- [20] Williams, L.K., Li, C., Withers, S.G., and Brayer, G.D., 2012, Order and disorder: Differential structural impacts of myricetin and ethyl caffeate on human amylase, an antidiabetic target, *J. Med. Chem.*, 55 (22), 10177–10186.
- [21] Sari, B.L., Mun'im, A., Yanuar, A., and Riadhi, R., 2016, Screening of α -glucosidase inhibitors from *Terminalia catappa* L. Fruits using molecular docking method and in vitro test, *Int. J. Pharm. Pharm. Sci.*, 8 (12), 184–189.
- [22] Vaezi, M., Behbehani, G.R., Gheibi, N., and Farasat, A., 2020, Thermodynamic, kinetic and docking studies of some unsaturated fatty acids-quercetin derivatives as inhibitors of mushroom tyrosinase, *AIMS Biophys.*, 7 (4), 393–410.
- [23] Burlingham, B.T., and Widlanski, T.S., 2003, An intuitive look at the relationship of K_i and IC_{50} : A more general use for the Dixon plot, *J. Chem. Educ.*, 80 (2), 214–218.
- [24] Singh, S., Bani Baker, Q., and Singh, D.B., 2022, “Molecular Docking and Molecular Dynamics Simulation” in *Bioinformatics*, Eds. Singh, D.B., and Pathak, R.K., Academic Press, London, UK, 291–304.

Microstructural Analysis and Antibacterial Response of Zn²⁺/Mg²⁺ Dual Doped β -Tricalcium Phosphate Bioceramics

Ammar Zeidan Alshemary^{1,2*}, Huda Basim Qasim³, and Ali Taha Saleh⁴

¹Department of Biomedical Engineering, Faculty of Engineering, Karabuk University, Karabuk 78050, Turkey

²Biomedical Engineering Department, Al-Mustaqbal University College, Hillah, Babil 51001, Iraq

³Al-Manara College for Medical Sciences, Misan 62001, Iraq

⁴Department of Chemistry, College of Science, University of Misan, Misan 62001, Iraq

* **Corresponding author:**

email: ammar.zeidan@mustaqbal-college.edu.iq

Received: January 16, 2022

Accepted: February 17, 2022

DOI: 10.22146/ijc.72286

Abstract: This article evaluates the impact of the addition of zinc (Zn) and magnesium (Mg) on the structural, morphological, and antibacterial characteristics of β -tricalcium phosphates (hereafter called Zn/Mg- β TCP) prepared using the microwave (MW) assisted wet precipitation method in which the Ca deficient apatite [$Ca_{9-(x+y)}Mg_xZn_y(HPO_4)(PO_4)_5(OH)$] was calcined for 2 h at 1000 °C. The prepared samples were characterized using XRD, FTIR, and FESEM measurements. The XRD patterns of the samples showed a steady decrease in the lattice parameters with an increase in Mg²⁺ and Zn²⁺ content. The FESEM images of the samples disclosed the morphological changes due to the Mg²⁺/Zn²⁺ co-doping. The inclusion of Mg²⁺ and Zn²⁺ into the β TCP was shown to induce excellent bioactivities that were absent in the pristine β TCP. Enhancement, coupled with good antimicrobial properties against Escherichia coli (E. coli), suggests that Mg²⁺/Zn²⁺ co-doping TCP can be developed further into antibacterial bone cement. As synthesized, it would be considered a potential biomaterial for orthopedic applications.

Keywords: β -tricalcium phosphates; Co-doping; microstructure; phase purity; antibacterial

■ INTRODUCTION

Microbes infecting the bone create osteomyelitis, an inflammation of the bone that may be fatal. Osteomyelitis is often treated with basic surgical debridement of diseased bones, appropriate soft tissue covering, and antibiotics. Long-term antibiotic medication is necessary, usually lasting 4–6 weeks but sometimes much longer [1]. Oral antibiotics may cause systemic toxicity, including renal and hepatic problems, and have low penetration into the targeted region [2-4]. It is thus necessary to investigate other methods of administering antibiotics. The unique bioactivities, biocompatibilities, and osteoconductive traits of the calcium phosphates (CPs) based materials make them ideal for a wide range of biomedical uses. They are very effective for implant-bone tissues in dental and orthopedic reconstructive medicines [5-8]. Presently, Hydroxyapatite (HA) and β -tricalcium

phosphates (β TCP) are extensively used for bone tissue grafting due to their non-stimulating nature of bone generation and resorption inhibition [9-10]. β TCP and HA-based materials doped with trace elements such as Zinc (Zn) and Magnesium (Mg) have been shown to stimulate exceptional bioactivities that are missing in their parent counterparts [11-12].

In recent years, the inclusion of different dopants (Mg²⁺, Sr²⁺, and Zn²⁺) ions into the structure of the CPs received focused attention due to their significant role in diverse biological processes [13]. Zn is one of the most vital trace elements responsible for various cellular processes in the human body, such as DNA replication, behavioral responses, reproductions, virilities, bone generation, bone growth, and wound healing. Furthermore, Zn is essential in genetic expression, cellular growth regulation, and cell differentiation [14].

A recent study revealed a clinical correlation between osteoporosis and a deficiency of Zn in the human body [15]. The main reason for the biocompatibility of Zn is due to its matching ionic radius (0.075 nm) with the bone tissue element. Meanwhile, the bone tissues' slow resorption of the β TCP ceramics makes them highly biocompatible [16]. Chen et al. synthesized nanorods of Zn doped HA and found that the presence of Zn inhibited the growth of *Aggregatibacter actinomycetemcomitans*, *Fusobacterium nucleatum*, and *Streptococcus mutant* bacteria [17]. Bhattacharjee et al. demonstrated that incorporation of Zn improved the antibacterial efficacy of HA against *Escherichia coli* and *Staphylococcus aureus* bacteria [18].

The element of Mg participates in diverse biological activities of humans, such as cellular proliferation and differentiation, cell-matrix interactions, and the usual functions of the organs [19]. The significance of Mg concerning the human bone structures is well-known, especially the prevention of the potential risks related to osteoporosis [20]. On top of that, Mg is crucial for the calcification processes, bone fragility, and minerals' metabolic activities [21]. Synthetic materials containing metal ions can be destructive if the ions are highly concentrated and are poisonous to human cells in high concentrations [8]. Materials containing metal ions such as Zn^{2+} , Ag^+ , and Cu^{2+} can be used to combat post-operative infections, as these ions exhibit antimicrobial activity and are non-cytotoxic at low concentrations. Because of the significance of the indispensable elements Zn and Mg in the human body's functioning, some Zn/Mg co-doped β TCP were synthesized via the microwave (MW) assisted wet precipitation technique and characterized using different analytical tools. The structures and morphologies of the as-prepared samples were evaluated as a function of varying Zn/Mg contents to determine the feasibility of improving bioactivities. The antibacterial efficiency results were analyzed, interpreted, and discussed.

■ EXPERIMENTAL SECTION

Materials

The Zn/Mg-TCP was prepared using analytical grade high purity chemical reagents (Qrec, New Zealand)

of calcium nitrate [$Ca(NO_3)_2 \cdot 4H_2O$], diammonium hydrogen phosphate [$(NH_4)_2HPO_4$], magnesium nitrate [$(Mg(NO_3)_2 \cdot 6H_2O)$], zinc nitrate [$Zn(NO_3)_2$], and ammonium hydroxide [(NH_4OH)].

Instrumentation

The samples crystal structures and purity of the phases were examined using the X-ray diffractometer (Bruker D8 Advance XRD). The samples morphology was imaged via a field emission scanning electron microscope (FESEM, Zeiss-LEO 1530). The elemental compositional analyses of the samples were carried out using an energy dispersive X-ray spectrometer (EDX, Swift ED 3000 from the Oxford Instruments, operated at 20 kV). The chemical functional groups in the samples were detected using Fourier transform infrared spectroscopy (FTIR, Nicolet iS50 spectrometer) following the classic KBr pellet technique. The FTIR spectra (in the transmission mode) were recorded in the range of 400–4000 cm^{-1} with 32 scans at a resolution of 4 cm^{-1} . All the characterizations of the calcined samples (at 1000 °C) were performed at room temperature.

Procedure

The experimental steps, including the preparation of Zn/Mg- β TCP and antimicrobial test, as a flowchart, are presented in Fig. 1.

Preparation of Zn/Mg- β TCP materials

The pristine β TCP and Zn/Mg- β TCP were made via the MW-assisted wet precipitation technique where the Ca/P and (Ca+Mg+Zn)/P molar ratio was kept at 1.5. The [$Ca(NO_3)_2 \cdot 4H_2O$] (4.250 g) was first dissolved in 100 mL of double-distilled water (DDW), then drops of [$(NH_4)_2HPO_4$] were added, and the mixture was continuously stirred. The pH of the mixture was set at 7.4 via the addition of NH_4OH solution (8 M). Next, the resultant mixture was processed for 5 min in an MW oven (SHARP, model R-218LS, operated at 800 W) before being filtrated and rinsed using DDW. Then, the filtered specimen was dried for 17 h in an oven at 80 °C, then calcinated for 2 h at 1000 °C to achieve the β TCP. The Zn/Mg-TCP was prepared in the same manner, using the appropriate amounts of [$Mg(NO_3)_2 \cdot 6H_2O$]

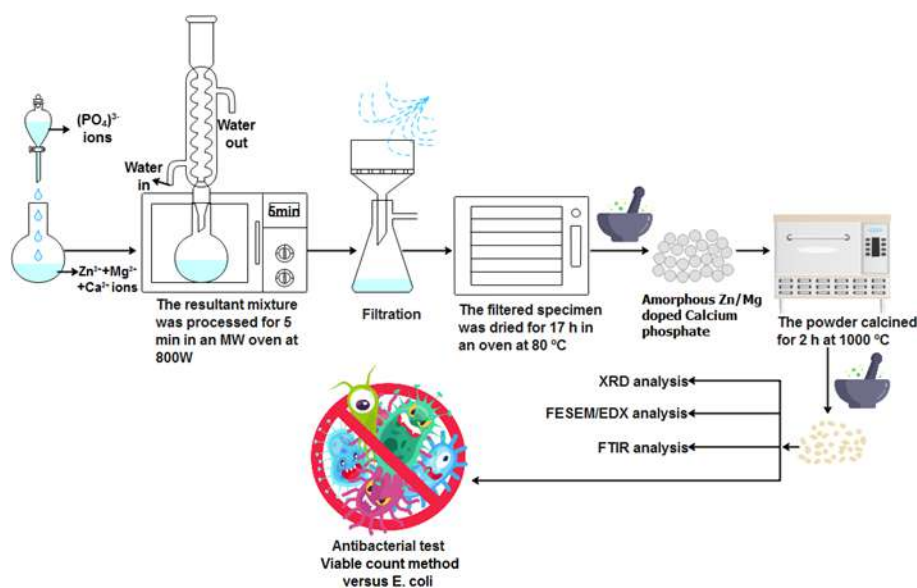
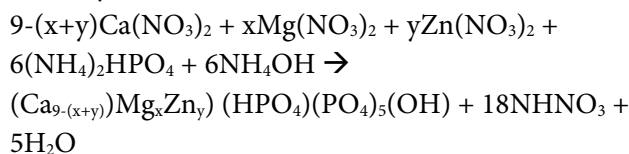


Fig 1. Experiment flow chart

(0.2, 0.3, 0.4, 0.5 M) (0.780, 1.170, 1.561, 1.951 g respectively), $[\text{Zn}(\text{NO}_3)_2]$ (0.2, 0.3, 0.4, 0.5 M) (0.757, 1.136, 1.515 and 1.894 g respectively), and $[\text{Ca}(\text{NO}_3)_2 \cdot 4\text{H}_2\text{O}]$ (8.6, 8.4, 8.2 and 7 M) (4.061, 3.967, 3.872 and 3.306 g respectively). Table 1 enlists the chemical compositions (in mol) of the produced samples with various concentrations of Zn and Mg with their respective codes. The production of the β TCP and Zn/Mg- β TCP can be described using the following chemical reaction pathways:

Pathway I:



Pathway II:

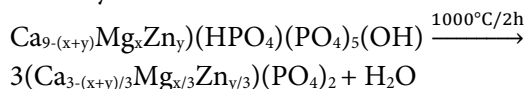


Table 1. Chemical compositions (in mol) of the obtained samples with their codes

Sample code	Ca ²⁺	PO ₄ ³⁻	Mg ²⁺	Zn ²⁺	Mg+Zn
β TCP	9	6	0.0	0.0	0.0
(0.4)Zn/Mg- β TCP	8.6	6	0.2	0.2	0.4
(0.6)Zn/Mg- β TCP	8.4	6	0.3	0.3	0.6
(0.8)Zn/Mg- β TCP	8.2	6	0.4	0.4	0.8
(1.0)Zn/Mg- β TCP	7.0	6	0.5	0.5	1.0

Antimicrobial tests

The antibacterial efficiency of pure and Zn/Mg doped

β TCP materials were evaluated quantitatively through the viable count method versus *Escherichia coli* (*E. coli*, ATCC 25922 strains). A standard mixture of 1 mL *E. coli* and 9 mL Luria-Bertani (LB) broth was incubated at 37 °C for a day, shaking at 250 rpm. The materials were sterilized and blended with the standard solution. The sterilized mixture (0.10 mL) was immunized on LB agar plates, then brooded at 37 °C. Lastly, the number of colonies developing units was tallied.

RESULTS AND DISCUSSION

Fig. 2 displays the XRD patterns of the produced samples, which consisted of several crystalline peaks at 25.82°, 27.77°, 29.64°, 31.02°, 32.4756°, and 34.38° corresponding to the growth along the (1 0 1 0), (2 1 4), (3 0 0), (0 2 1 0), (1 2 8), and (2 2 0) lattice plane orientations. The observed indexed peaks were matched with JCPDS card number of 09-0169 for the crystalline β TCP. Table 2 shows the lattice parameters, cell volume, and degree of crystallinity of the studied samples obtained from the XRD data analyses. The lattice plane directions for the pristine β TCP verified the growth of

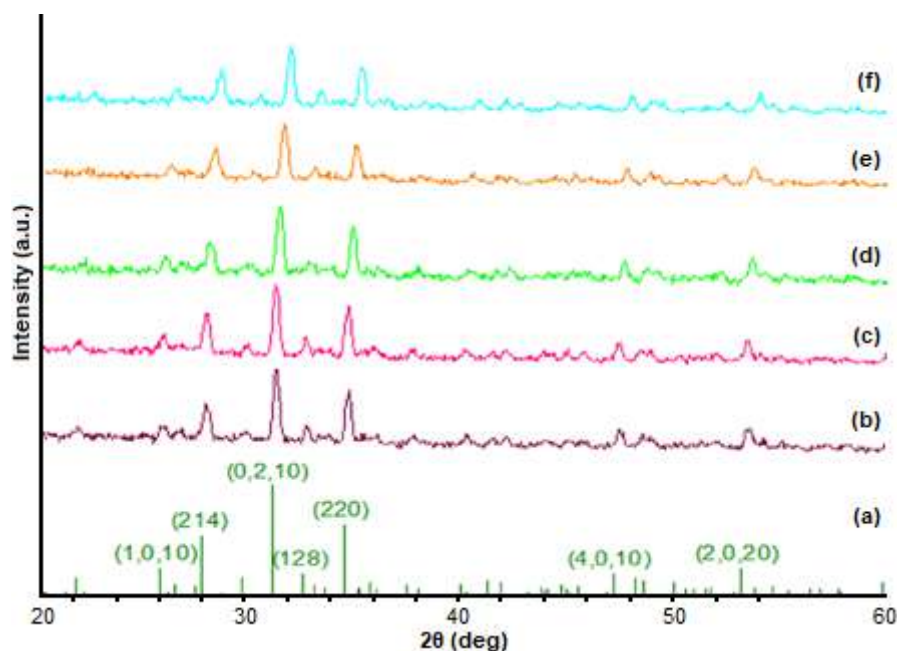


Fig 2. XRD patterns of the β TCP (JCPDS 09-0169) (a), β TCP (b), (0.4)Zn/Mg- β TCP (c), (0.6)Zn/Mg- β TCP (d), (0.8)Zn/Mg- β TCP (e), and (1.0)Zn/Mg- β TCP (f)

Table 2. Lattice parameters, cell volume, and degree of crystallinity of the studied samples

Samples code	Chemical formula	Lattice parameters			DC*
		a(Å)	c(Å)	V(Å) ^{3**}	
β TCP (JCPDS 09-0169)	Ca ₃ (PO ₄) ₂	10.429	37.380	3520.9	---
β TCP	Ca ₉ (PO ₄) ₆	10.460	37.391	3532.6	88
(0.4)Zn/Mg- β TCP	Ca _{8.6} Mg _{0.2} Zn _{0.2} (PO ₄) ₆	10.445	37.360	3529.7	81
(0.6)Zn/Mg- β TCP	Ca _{8.4} Mg _{0.3} Zn _{0.3} (PO ₄) ₆	10.421	37.354	3524.0	77
(0.8)Zn/Mg- β TCP	Ca _{8.2} Mg _{0.4} Zn _{0.4} (PO ₄) ₆	10.415	37.254	3521.5	69
(1.0)Zn/Mg- β TCP	Ca _{7.0} Mg _{0.5} Zn _{0.5} (PO ₄) ₆	10.410	37.222	3514.2	64

*Degree of crystallinity, **Cell volume

the hexagonal crystals with the lattice constants of $a = b = 10.4592$ Å and $c = 37.3914$ Å as depicted in Table 2. The inclusion of Mg^{2+}/Zn^{2+} into the β TCP lattice structures diminished the intensity of the Bragg's peaks accompanied by a shift toward higher diffraction angles (values of 2θ), as indicated in Fig. 2. The observed reduction in the sample's degree of crystallinities (from 88 to 64) was due to the replacement of the Ca^{2+} ions, which have larger ionic radii (0.99 Å) by the Mg^{2+} (0.65 Å) ions and Zn^{2+} (0.74 Å) which they have smaller ionic radii.

Furthermore, the XRD pattern did not reveal any other crystalline phases, confirming the purity of the sample [13]. The intense XRD peak calculated the mean crystallite diameter following the Debye-Scherrer

formula. The mean size of the β TCP and Zn/Mg- β TCP was 36 nm and 28 nm, respectively. The lattice values of a and c were gradually decreased with a rise in Mg^{2+} and Zn^{2+} contents (Table 2). These shortening in the lattice constants were mainly due to the substitution of the Ca^{2+} by Mg^{2+}/Zn^{2+} , where the disparity in their ionic radii played a significant role. The values of a and c were reduced from 10.4452–10.4101 Å and 37.2217–37.3598 Å, respectively, with the addition of Mg^{2+}/Zn^{2+} into the β TCP structures. Meanwhile, cell volumes of the samples were reduced from 3529.7 to 3514.2 with the increase in Mg^{2+}/Zn^{2+} doping levels into the β TCP structures.

Fig. 3 illustrates the FTIR spectra of all the prepared samples, which consisted of several

characteristic vibration bands of the phosphate groups and water molecules. The pristine β TCP revealed a broad vibration band at around 3440 cm^{-1} due to the OH^- from adsorbed water. The bands at approximately 1020 and 558 cm^{-1} were due to the vibration of the PO_4^{3-} units. The bands at around 618 and 548 cm^{-1} were related to the bending vibrations (ν_4) of the O–P–O linkages. The bands due to the stretching vibrations (ν_3 and ν_1) of the P–O bond occurred at approximately 955 cm^{-1} , 1033 , and 1135 cm^{-1} . The bands appeared at around 1643 and 3448 cm^{-1} due to the adsorbed water's bond vibrations. The characteristics bands at 962 cm^{-1} , 1122 cm^{-1} to 939 cm^{-1} , and 1150 cm^{-1} corresponding to the phosphate vibrations were broadened and shifted as the doping contents of $\text{Mg}^{2+}/\text{Zn}^{2+}$ were increased, implying the decrease in the crystallinity of the sample, which is consistent with the XRD results (Fig. 2). The nonexistence of the characteristic bands at 630 and 3570 cm^{-1} in the produced samples validated the complete absence of any HA as the secondary phase. The band assignments are summarized in Table 3.

Fig. 4 depicts the FESEM images of all the produced samples. The microstructures of the β TCP were comprised of dense (compact with nearly spherical crystallites without voids and cracks) aggregated particles with irregular morphology (Fig. 4(a)). Moreover, the morphologies of the $\text{Mg}^{2+}/\text{Zn}^{2+}$ co-doped β TCP specimens were appreciably altered into interconnected structures (less compact and ginger-like pattern with many voids) with a clustering tendency (Fig. 4(b-e)). The

particle size of β TCP materials gradually decreased with the addition of $\text{Mg}^{2+}/\text{Zn}^{2+}$ ions.

Table 4 compares the chemical composition of various products obtained from the EDX elemental analyses with the theoretical estimates. The close

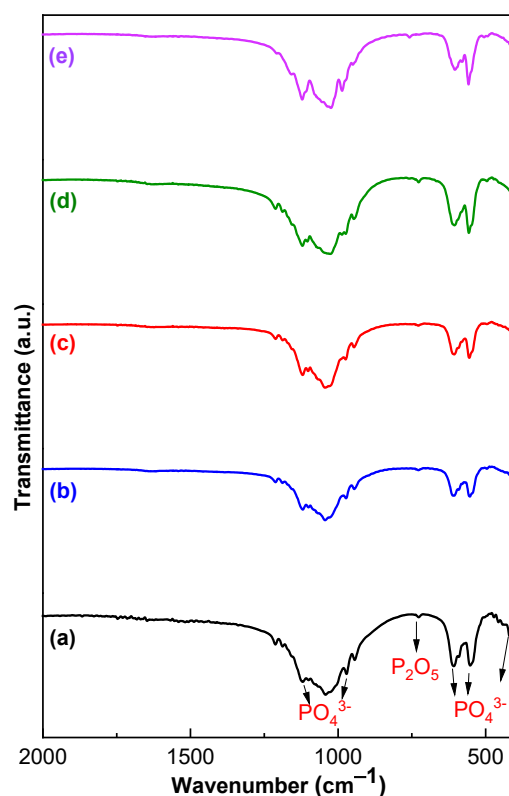


Fig 3. FTIR spectra of (a) β TCP, (b) (0.4) Zn/Mg- β TCP, (c) (0.6)Zn/Mg- β TCP, (d) (0.8)Zn/Mg- β TCP, and (e) (1.0)Zn/Mg- β TCP

Table 3. Band assignments for β TCP and $\text{Zn}^{2+}/\text{Mg}^{2+}$ doped β TCP materials [22]

Peak number	Wavenumber (cm^{-1})	Band assignment
1	427	Stretching mode of PO_4^{3-} group (ν_2)
2	545–601	Bending mode of the PO_4^{3-} group (ν_4)
3	727–1212	Stretching modes of P–O–P and P=O in P_2O_7 group
4	941–971	Stretching mode of PO_4^{3-} group (ν_1)

Table 4. Chemical composition of various products obtained from the EDX analyses compared with the theoretical estimates

Samples code	Theoretical ratios		Measured ratios	
	Zn+Mg/Ca= X_{MgZn}		Zn+Mg/Ca= X_{MgZn}	
β TCP	0.000		0.000	
(0.4)Zn/Mg- β TCP	0.040		0.038	
(0.6)Zn/Mg- β TCP	0.060		0.059	
(0.8)Zn/Mg- β TCP	0.080		0.078	
(1.0)Zn/Mg- β TCP	0.100		0.099	

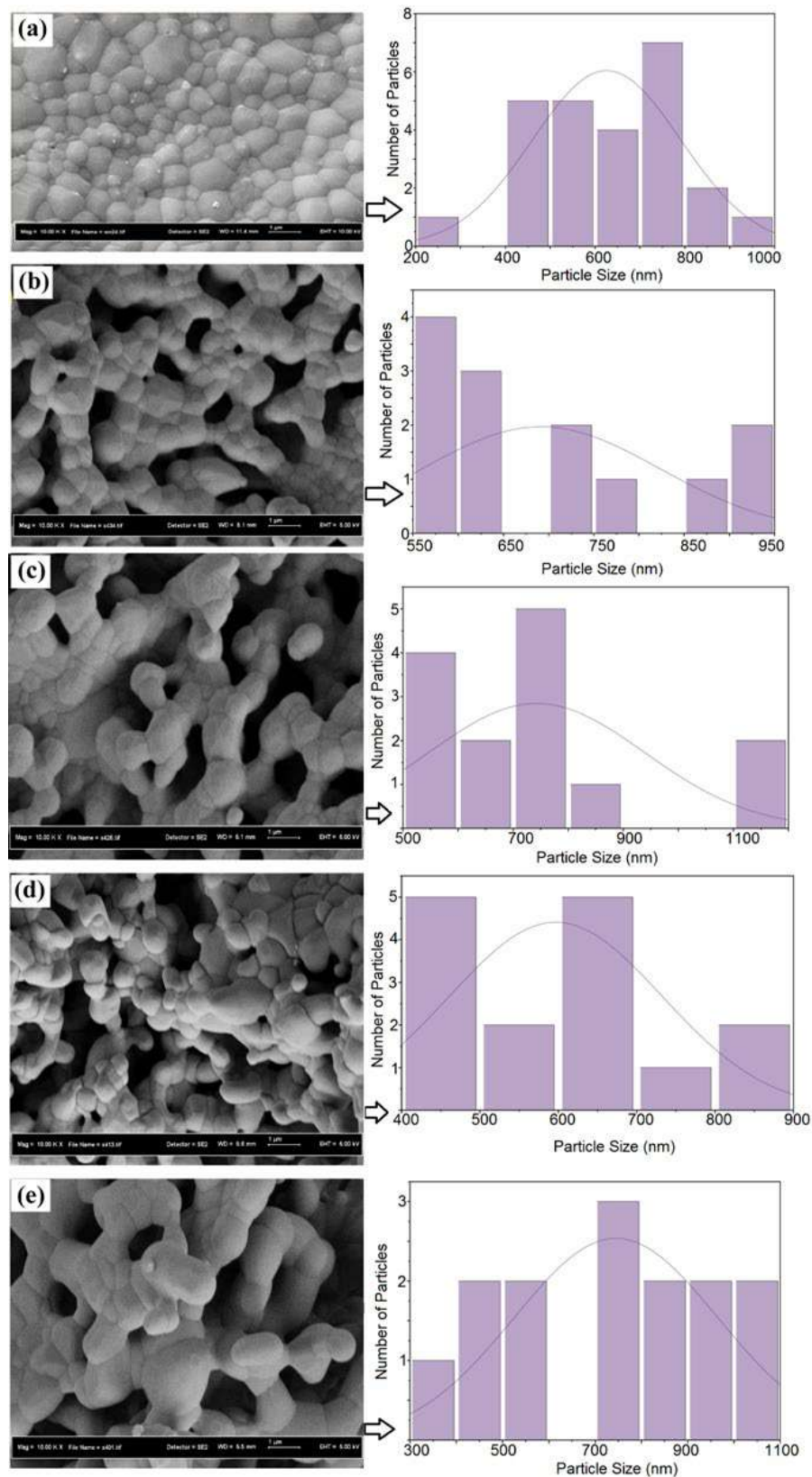


Fig 4. FESEM images of (a) β TCP, (b) (0.4)Zn/Mg- β TCP, (c) (0.6)Zn/Mg- β TCP, (d) (0.8)Zn/Mg- β TCP, and (e) (1.0)Zn/Mg- β TCP. Particles size distribution attached with the SEM images

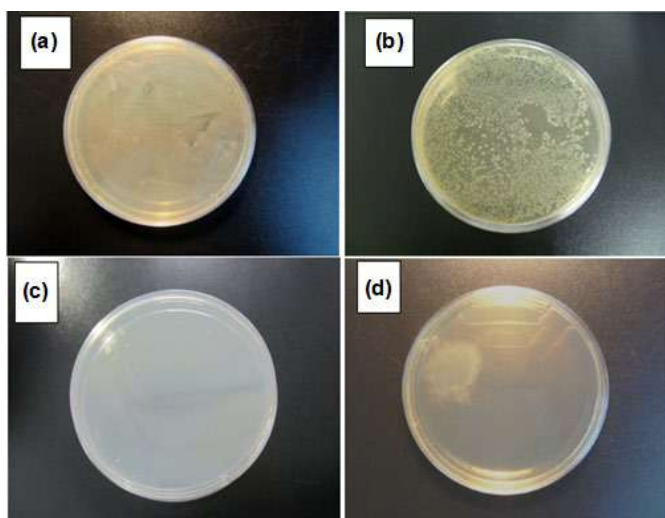


Fig 5. Descriptive photos of *E. coli* colonies on (a) (0.4)Zn/Mg- β TCP, (b) (0.6)Zn/Mg- β TCP, (c) (0.8)Zn/Mg- β TCP, and (d) (1.0)Zn/Mg- β TCP

agreement between the theoretical and experimental values of the trace elemental ratios confirmed the successful incorporation of the Mg^{2+}/Zn^{2+} into the β TCP crystal structure. In short, the inner consistency among the XRD, FTIR, and EDX results authenticated the adequate replacement of Ca^{2+} by the Mg^{2+}/Zn^{2+} dopants in the β TCP lattice sites.

The antibacterial activity of the Mg^{2+}/Zn^{2+} discharged from the Zn/Mg- β TCP was studied against the spread of *E. coli*. In this research, the viable count method assessed the antibacterial properties of Zn/Mg- β TCP materials. All samples were incubated with *E. coli* (ATCC 25922 strains) suspension for a day. Fig. 5 shows the substantial variance in bactericidal effect. The pure phase of β TCP materials has no ability to inhibit the growth of *E. coli* [23]. However, bacterial growth was inhibited by Zn/Mg-TCP nanocomposites. The number of *E. coli* colonies dwindled with an increase in the content of Mg^{2+}/Zn^{2+} . After a day of incubation in the plate containing (0.4) Zn/Mg-TCP and (0.6) Zn/Mg-TCP, hundreds of *E. coli* colonies were observed (Fig. 4(a, b)). However, a few bacterial colonies were observed in the agar plate containing (0.4) Zn/Mg-TCP. In contrast, no bacterial colonies were observed in the agar plates containing (0.8) Zn/Mg- β TCP and (1.0) Zn/Mg- β TCP (Fig. 4(c, d)).

■ CONCLUSION

Following the standard MW-assisted wet precipitation method, some Mg^{2+}/Zn^{2+} co-activated β TCP were produced. Thorough characterization was used to determine the Mg^{2+}/Zn^{2+} concentration-dependent structures and morphologies of dry and calcined (1000 °C) powdered specimens. The XRD analyses of the pristine and co-doped β TCP verified their hexagonal structure with phase purity where the lattice constants, cell volume, crystallinity, and crystallite size were found to decrease with the increase in the Mg^{2+}/Zn^{2+} concentrations. The FTIR spectral vibration bands revealed the existence of various characteristic functional groups related to β TCP and Zn/Mg- β TCP. The EDX analyses of the samples confirmed the appropriate elemental traces, thereby successfully incorporating the Mg^{2+}/Zn^{2+} dopants into the β TCP lattice. The FESEM surface morphologies of the sample manifested significant structural changes due to the substitution of Mg^{2+}/Zn^{2+} dopants, were more compact, void-free, and dense agglomerated irregular structures were gradually transformed into less compact and interconnected cluster-like networks with many voids. The results for the structures and morphologies were in good agreement. All these observations were ascribed to the replacement of the Ca^{2+} with larger ionic radii by the Mg^{2+}/Zn^{2+} having smaller ionic radii. The presented results suggest that the Mg^{2+}/Zn^{2+} containing β TCP cement is a very promising material for rapid antibacterial bone repair purposes. It is established that by selectively adjusting the Mg^{2+}/Zn^{2+} contents, the overall traits of the Zn/Mg- β TCP can be tailored, suggesting their suitability for diverse biomedical applications.

■ ACKNOWLEDGMENTS

Dr. Ammar Z. Alshemary would like to thank Al-Mustaqbal University College. Dr. Ali Taha Saleh would like to thank the University of Misan, Department of Chemistry, for supporting this work.

■ REFERENCES

- [1] Kumar, G.S., Govindan, R., and Girija, E., 2014, *In*

- situ* synthesis, characterization and *in vitro* studies of ciprofloxacin loaded hydroxyapatite nanoparticles for the treatment of osteomyelitis, *J. Mater. Chem. B*, 2 (31), 5052–5060.
- [2] Shefy-Peleg, A., Foox, M., Cohen, B., and Zilberman, M., 2014, Novel antibiotic-eluting gelatin-alginate soft tissue adhesives for various wound closing applications, *Int. J. Polym. Mater. Polym. Biomater.*, 63 (14), 699–707.
- [3] Mouriño, V., and Boccaccini, A.R., 2010, Bone tissue engineering therapeutics: controlled drug delivery in three-dimensional scaffolds, *J. R. Soc. Interface*, 7 (43), 209–227.
- [4] Feng, W., Geng, Z., Li, Z., Cui, Z., Zhu, S., Liang, Y., Liu, Y., Wang, R., and Yang, X., 2016, Controlled release behaviour and antibacterial effects of antibiotic-loaded titania nanotubes, *Mater. Sci. Eng., C*, 62, 105–112.
- [5] Dai, J., Fu, Y., Chen, D., and Sun, Z., 2021, A novel and injectable strontium-containing hydroxyapatite bone cement for bone substitution: A systematic evaluation, *Mater. Sci. Eng., C*, 124, 112052.
- [6] Han, B., Ma, P.W., Zhang, L.L., Yin, Y.J., Yao, K.D., Zhang, F.J., Zhang, Y.D., Li, X.L., and Nie, W., 2009, β -TCP/MCPM-based premixed calcium phosphate cements, *Acta Biomater.*, 5 (8), 3165–3177.
- [7] Wang, S., Liu, R., Yao, J., Wang, Y., Li, H., Dao, R., Guan, J., and Tang, G., 2013, Fabrication of mesoporous magnesium substituted β -tricalcium phosphate nanospheres by self-transformation and assembly involving EDTA ions, *Microporous Mesoporous Mater.*, 179, 172–181.
- [8] Prakash, C., Singh, S., Pabla, B.S., Sidhu, S.S., and Uddin, M.S., 2019, Bio-inspired low elastic biodegradable Mg-Zn-Mn-Si-HA alloy fabricated by spark plasma sintering, *Mater. Manuf. Processes*, 34 (4), 357–368.
- [9] Horiuchi, S., Hiasa, M., Yasue, A., Sekine, K., Hamada, K., Asaoka, K., and Tanaka, E., 2014, Fabrications of zinc-releasing biocement combining zinc calcium phosphate to calcium phosphate cement, *J. Mech. Behav. Biomed. Mater.*, 29, 151–160.
- [10] Kaygili, O., Keser, S., Bulut, N., and Ates, T., 2018, Characterization of Mg-containing hydroxyapatites synthesized by combustion method, *Physica B*, 537, 63–67.
- [11] Calasans-Maia, M., Calasans-Maia, J., Santos, S., Mavropoulos, E., Farina, M., Lima, I., Lopes, R.T., Rossi, A., and Granjeiro, J.M., 2014, Short-term *in vivo* evaluation of zinc-containing calcium phosphate using a normalized procedure, *Mater. Sci. Eng., C*, 41, 309–319.
- [12] Shahmohammadi, P., and Khazaei, B.A., 2021, Characterization of Zn/Mg-enriched calcium phosphate coating produced by the two-step pulsed electrodeposition method on titanium substrate, *Surf. Interfaces*, 22, 100819.
- [13] Saleh, A.T., Ling, L.S., and Hussain, R., 2016, Injectable magnesium-doped brushite cement for controlled drug release application, *J. Mater. Sci.*, 51 (16), 7427–7439.
- [14] Tas, A.C., Bhaduri, S.B., and Jalota, S., 2007, Preparation of Zn-doped β -tricalcium phosphate (β -Ca₃(PO₄)₂) bioceramics, *Mater. Sci. Eng., C*, 27 (3), 394–401.
- [15] Mahdavi-Roshan, M., Ebrahimi, M., and Ebrahimi, A., 2015, Copper, magnesium, zinc and calcium status in osteopenic and osteoporotic post-menopausal women, *Clin. Cases Miner. Bone Metab.*, 12 (1), 18–21.
- [16] Fadeeva, I.V., Gafurov, M.R., Kiaeva, I.A., Orlinskii, S.B., Kuznetsova, L.M., Filippov, Y.Y., Fomin, A.S., Davydova, G.A., Selezneva, I.I., and Barinov, S.M., 2017, Tricalcium phosphate ceramics doped with silver, copper, zinc, and iron (III) ions in concentrations of less than 0.5 wt.% for bone tissue regeneration, *BioNanoScience*, 7 (2), 434–438.
- [17] Chen, X., Tang, Q.L., Zhu, Y.J., Zhu, C.L., and Feng, X.P., 2012, Synthesis and antibacterial property of zinc loaded hydroxyapatite nanorods, *Mater. Lett.*, 89, 233–235.
- [18] Bhattacharjee, A., Gupta, A., Verma, M., Murugan, P.A., Sengupta, P., Matheshwaran, S., Manna, I., and Balani, K., 2019, Site-specific antibacterial

- efficacy and cyto/hemo-compatibility of zinc substituted hydroxyapatite, *Ceram. Int.*, 45 (9), 12225–12233.
- [19] Hofmann, M.P., Mohammed, A.R., Perrie, Y., Gbureck, U., and Barralet, J.E., 2009, High-strength resorbable brushite bone cement with controlled drug-releasing capabilities, *Acta Biomater.*, 5 (1), 43–49.
- [20] Frasnelli, M., Pedranz, A., Biesuz, M., Dirè, S., and Sglavo, V.M., 2019, Flash sintering of Mg-doped tricalcium phosphate (TCP) nanopowders, *J. Eur. Ceram. Soc.*, 39 (13), 3883–3892.
- [21] Saleh, A.T., and Alameri, D., 2021, Microwave-assisted preparation of zinc-doped β -tricalcium phosphate for orthopedic applications, *Indones. J. Chem.*, 21 (2), 376–382.
- [22] Motameni, A., Dalgic, A.D., Alshemary, A.Z., Keskin, D., and Evis, Z., 2020, Structural and biological analysis of mesoporous lanthanum doped β TCP for potential use as bone graft material, *Mater. Today Commun.*, 23, 101151.
- [23] Qin, L., Yi, J., Xuefei, L., Li, L., Kenan, X., and Lu, X., 2020, The preparation of a difunctional porous β -tricalcium phosphate scaffold with excellent compressive strength and antibacterial properties, *RSC Adv.*, 10, 28397–28407.

Short Communication:**Silicon Carbide/Polysilazane Composite: Effect of Temperature on the Densification, Phase, and Microstructure Evolution****Fiqhi Fauzi¹, Alfian Noviyanto^{1,2*}, Pipit Fitriani¹, Amirudin Wibowo³, Toto Sudiro⁴, Didik Aryanto⁴, and Nurul Taufiqu Rochman⁵**¹Nano Center Indonesia, Jl. PUSPIPTEK, South Tangerang, Banten 15314, Indonesia²Department of Mechanical Engineering, Mercu Buana University, Jl. Meruya Selatan, Kebun Jeruk, Jakarta 11650, Indonesia³Research Center, Mercu Buana University, Jl. Meruya Selatan, Kebun Jeruk, Jakarta 11650, Indonesia⁴Research Center for Physics, National Research and Innovation Agency, PUSPIPTEK, South Tangerang, Banten 15314, Indonesia⁵Research Center for Metallurgy and Materials, National Research and Innovation Agency, PUSPIPTEK, South Tangerang, Banten 15314, Indonesia*** Corresponding author:**

email: a.noviyanto@nano.or.id

Received: September 14, 2021

Accepted: October 29, 2021

DOI: 10.22146/ijc.69118

Abstract: This paper reports a route to suppress the grain growth in silicon carbide (SiC) during its sintering by combining it with polysilazane (PSZ). SiC was mixed with PSZ in a 1:1 weight ratio and sintered at 1600, 1700, and 1800 °C in a hot-pressing furnace. A satisfactory density was obtained at sintering temperatures > 1600 °C. The grain sizes of the SiC/PSZ composites sintered at 1700 and 1800 °C were 112 and 125 nm, respectively. The grain shape of the SiC/PSZ composite sintered at 1700 °C was circular and mainly similar to the initial shape of the SiC powder. Grain shape accommodation was observed at a sintering temperature of 1800 °C. It is suggested that different sample shapes were affected by different liquid phase formations. Silicon oxynitride (Si₂N₂O) was formed and played an important role in densification and microstructure generation.

Keywords: silicon carbide; polysilazane; sintering; microstructure

■ INTRODUCTION

Silicon carbide (SiC) is being studied as a non-oxide ceramic engineering material. SiC has high thermal conductivity, low thermal expansion, resistance to oxidation and corrosion, and high hardness. Owing to its strong covalent bonding, SiC has excellent properties. In particular, given that the hardness of SiC is lower than those of diamond and cubic boron nitride, SiC is widely used as an abrasive material. However, the sintering of SiC is complex, requiring a high temperature and pressure to obtain a dense microstructure. For instance, the sintering of SiC through solid-state requires temperatures ≥ 1900 °C [1-13], whereas liquid-phase sintering requires a temperature range of 1750–1900 °C [14-20]. Although a dense SiC body can be achieved under such sintering conditions, the microstructure of SiC undergoes

coarsening. According to the Hall–Petch relationship, a fine microstructure is proportional to high hardness; therefore, there is a need to minimize grain coarsening during its high-temperature sintering.

Typically, there are two approaches for minimizing the grain coarsening of the microstructure of SiC produced by high-temperature sintering. First, high pressure can be applied. For instance, Xie et al. reported that nanograin SiC could be successfully obtained at 1300 °C by applying a pressure of 4.5 GPa [21]. The second approach is a two-step sintering process; Lee et al. reported that SiC with a grain size of 43 nm could be obtained by two-step sintering [22]. However, the first approach requires ultra-high pressure, and the second one is time-consuming. The other method is the use of sintering additives that hinder the grain growth of SiC

during sintering. For example, Noviyanto et al. reported that a scandium-based additive could help minimize the grain growth in SiC [23]. Other reports show that polysilazane (PSZ, $[-SiR_1R_2NH-]_n$) can suppress the grain growth of alumina dan hafnia [24-25]. Noviyanto et al. examined a SiC/PSZ composite [26]. However, the effect of temperature on the SiC/PSZ composite was not elucidated.

In this study, SiC/PSZ composites were sintered using a hot-pressing furnace in the temperature range of 1600–1800 °C for 1 h under an applied pressure of 20 MPa in a nitrogen atmosphere. In addition, the effects of polysilazane on the densification, phase, and microstructure were thoroughly investigated. Finally, a mechanism to suppress grain growth with polysilazane was proposed in this study.

■ EXPERIMENTAL SECTION

Materials

β -SiC powder ($D_m = 52$ nm, 4620KE, 97.5% purity, NanoAmor Inc., USA), polysilazane (KiON Ceraset Polysilazane 20, USA), Al_2O_3 (99.9% purity, Baikowski, Japan) and Y_2O_3 (99.99% purity, Across Organic, USA) were used in this study.

Instrumentation

X-ray diffraction (XRD: X'Pert-PRO MPD, PANalytical, The Netherlands) and scanning electron microscope (SEM: S-4800, Hitachi, Japan) were used in this study.

Procedure

Prior to mixing with β -SiC powder, polysilazane was dissolved in acetone. Subsequently, β -SiC powder was added, and the solution was homogenized using an ultrasonicator for 45 min. The weight ratio of polysilazane to β -SiC powder was 1:1. Next, the homogenized slurry was dried and cross-linked on a hot plate at 200 °C for 90 min to obtain a powder containing β -SiC and polysilazane. After grinding and sieving, the powder was pyrolyzed in a tube furnace at 1300 °C for 2 h in a nitrogen atmosphere to transform the polysilazane into amorphous powder. This temperature was chosen

because the crystallization of amorphous polysilazane starts at 1400 °C [27-28].

Furthermore, the powder containing β -SiC and amorphous polysilazane was ground and sieved, followed by mixing with sintering additives (Al_2O_3 and Y_2O_3 , with a weight ratio of 60:40). The amount of sintering additives was 5 wt.% with respect to the total mass of the powder. Ball milling was used to mix the powder and sintering additives for 24 h and was made from SiC to prevent contamination. The sintering was performed in a hot-pressing furnace at various temperatures for 1 h under an applied pressure of 20 MPa in a nitrogen atmosphere. The samples were named SiCPSZ1600, SiCPSZ1700, and SiCPSZ1800, corresponding to the mixture containing β -SiC powder and polysilazane sintered at 1600, 1700, and 1800 °C, respectively. For comparison, the sintered SiC without adding polysilazane and sintered amorphous polysilazane were also prepared at 1750 and 1800 °C, respectively, named SiC and PSZ.

The weight of the sintered samples was measured at room temperature and when immersed in distilled water. The data were used to estimate the density of the sintered samples using the Archimedes principle. Furthermore, the sintered samples were characterized by room-temperature XRD to observe the crystalline phase formed after sintering. The qualitative and quantitative analyses of the XRD pattern were performed by XRD software analysis to determine the phases and their composition. Finally, the sintered samples were crushed, and the fractured surface was observed using SEM. The average grain size was estimated by calculating 100 grains from the SEM images and analyzed statistically.

■ RESULTS AND DISCUSSION

Fig. 1 shows the XRD patterns of the SiC/PSZ composite after sintering. The patterns of β -SiC and α -SiC can be detected at 1600 °C (Fig. 1(a)). As listed in Table 1, the major phases detected in SiCPSZ1600 were α -SiC (COD #96-900-0037) and β -SiC (COD #96-101-0966), accounting for 57.1% and 35.2%, respectively. To understand the phase transformation of β - and α -SiC in SiCPSZ1600, we need to compare with the sintering of

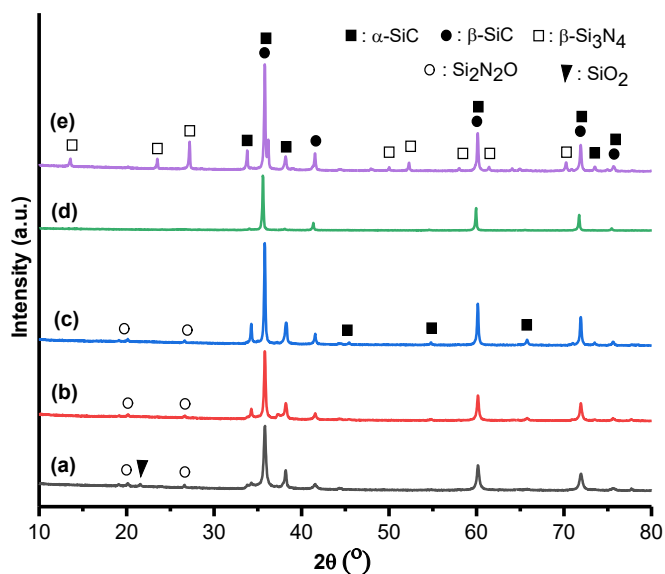


Fig 1. XRD patterns of the sintered sample (a) SiCPSZ1600, (b) SiCPSZ1700, (c) SiCPSZ1800, (d) SiC, and (e) PSZ

SiC and PSZ, as shown in Fig. 1(d) and 1(e), respectively. Sintering of the β -SiC powder resulted in a β -SiC phase; however, small peaks of α -SiC were detected, as shown in Fig. 1(d). The α -SiC phase in sintered SiC is more likely from the transformation of β - to α -SiC phase, which typically occurs in high-temperature sintering [29]. The quantity of α -SiC in the sintered SiC was 20.6% (Table 1).

In contrast, the sintering of PSZ results in a predominant α -SiC phase (55.6%) along with β -SiC and Si_3N_4 (COD #96-100-1245), as shown in Fig. 1(e). Thus, the main source of α -SiC in SiCPSZ1600 is more likely from polysilazane that tends to form α -SiC instead of β -SiC. The other phases detected in SiCPSZ1600 were $\text{Si}_2\text{N}_2\text{O}$ (COD #96-901-2533) and SiO_2 (COD #96-100-1245). Polysilazane might form SiC, Si_3N_4 , or SiO_2

depending on the temperature and atmosphere condition. This $\text{Si}_2\text{N}_2\text{O}$ phase is the product of a reaction between Si_3N_4 and SiO_2 [30]. Subsequently, the source of SiO_2 derives from polysilazane itself or SiC that has a small thin layer of oxide on the surface. According to the Gibbs free energy, the existence of Si_3N_4 from polysilazane is more favorable at < 1500 °C compared with SiC. Fig. 1(b) shows that the presence of SiO_2 could not be detected in SiCPSZ1700. SiO_2 completely reacted with Si_3N_4 to form $\text{Si}_2\text{N}_2\text{O}$ or decomposed at high temperatures and nitrogen atmosphere.

As listed in Table 1, the proportion of $\text{Si}_2\text{N}_2\text{O}$ in SiCPSZ1700 increases. Furthermore, $\text{Si}_2\text{N}_2\text{O}$ phase decreased in SiCPSZ1800. $\text{Si}_2\text{N}_2\text{O}$ is thermally unstable and starts to decompose at a high temperature of 1850 °C [30]. A similar phenomenon has been reported for LaTiO_2N , which decomposed during high-temperature sintering to La_2O_3 and TiN [31]. The final composition of the phases in SiCPSZ1800 are α -SiC, β -SiC, and $\text{Si}_2\text{N}_2\text{O}$, with the major phase being α -SiC, as listed in Table 1. On the other hand, the sintering of PSZ led to the formation of a SiC/ Si_3N_4 composite, as shown in Fig. 1(e). No trace of $\text{Si}_2\text{N}_2\text{O}$ could be detected in the sintering of SiC and PSZ. The absence of SiO_2 phase in PSZ and Si_3N_4 phase in SiC makes the formation of $\text{Si}_2\text{N}_2\text{O}$ unattainable.

Table 1 shows the quantitative analysis of the sintered samples' XRD, density, and relative density. The density increased with increasing temperature. However, the densification of the SiC/PSZ composite requires temperatures > 1600 °C. The density of SiCPSZ1600 was 2.48 g/cm^3 , corresponding to 77.2% of the relative density. Although the sintered sample was mixed with 5 wt.% of

Table 1. Quantitative analysis of the XRD patterns, density, and relative density of sintered samples

Sample	Phase composition (wt.%)					Density (g/cm^3)	Relative density (%) [*]
	β -SiC	α -SiC	$\text{Si}_2\text{N}_2\text{O}$	SiO_2	Si_3N_4		
SiCPSZ1600	35.2	57.1	7.2	0.3	-	2.48 ± 0.18	78.1
SiCPSZ1700	31.4	56.3	12.3	-	-	3.02 ± 0.01	95.5
SiCPSZ1800	27.8	69.4	2.8	-	-	3.05 ± 0.07	95.5
SiC	79.4	20.6	-	-	-	3.19 ± 0.01	99.3
PSZ	11.8	55.6	-	-	32.6	3.17 ± 0.04	98.7

^{*}Relative density was calculated by comparing the density of samples with their theoretical density, according to the rule of mixture

additives, it seems that the temperature was too low for liquid-phase formation; therefore, the density of SiCPSZ1600 did not increase. In contrast, the density of the samples sintered at temperatures > 1600 °C significantly increased, as listed in Table 1. The density and relative density of SiCPSZ1700 were 3.02 g/cm^3 and 94.1%, respectively. No significant increase in the density of the samples sintered at 1800 °C was observed, i.e., the density of SiCPSZ1800 was 3.05 g/cm^3 . Therefore, a liquid-phase formation is believed to have occurred in SiCPSZ1700 and SiCPSZ1800, causing densification.

The source of the liquid phase is generally the sintering additives. The sintering additives, i.e., $\text{Al}_2\text{O}_3\text{-Y}_2\text{O}_3$, form a liquid phase at 1760 °C [32]. Therefore, the

densification of SiCPSZ1700 is more likely due to another liquid phase, not $\text{Al}_2\text{O}_3\text{-Y}_2\text{O}_3$. As reported, the formation of $\text{Si}_2\text{N}_2\text{O}$ occurs through a liquid phase [30,33-36]; hence, the liquid phase enhances the densification in SiCPSZ1700.

Fig. 2 shows the SEM images of the sintered SiC/PSZ composites at various temperatures. Clearly, pores were observed in the composite SiCPSZ1600 (Fig. 2(a)), which showed a low sintered solid body. On the other hand, dense sintered bodies were obtained from SiCPSZ1700 and SiCPSZ1800. Remarkably, the average grain sizes of SiCPSZ1700 and SiCPSZ1800 were 112 ± 40 and 125 ± 62 nm, respectively, which increased by a factor of two from the initial particle size of the $\beta\text{-SiC}$

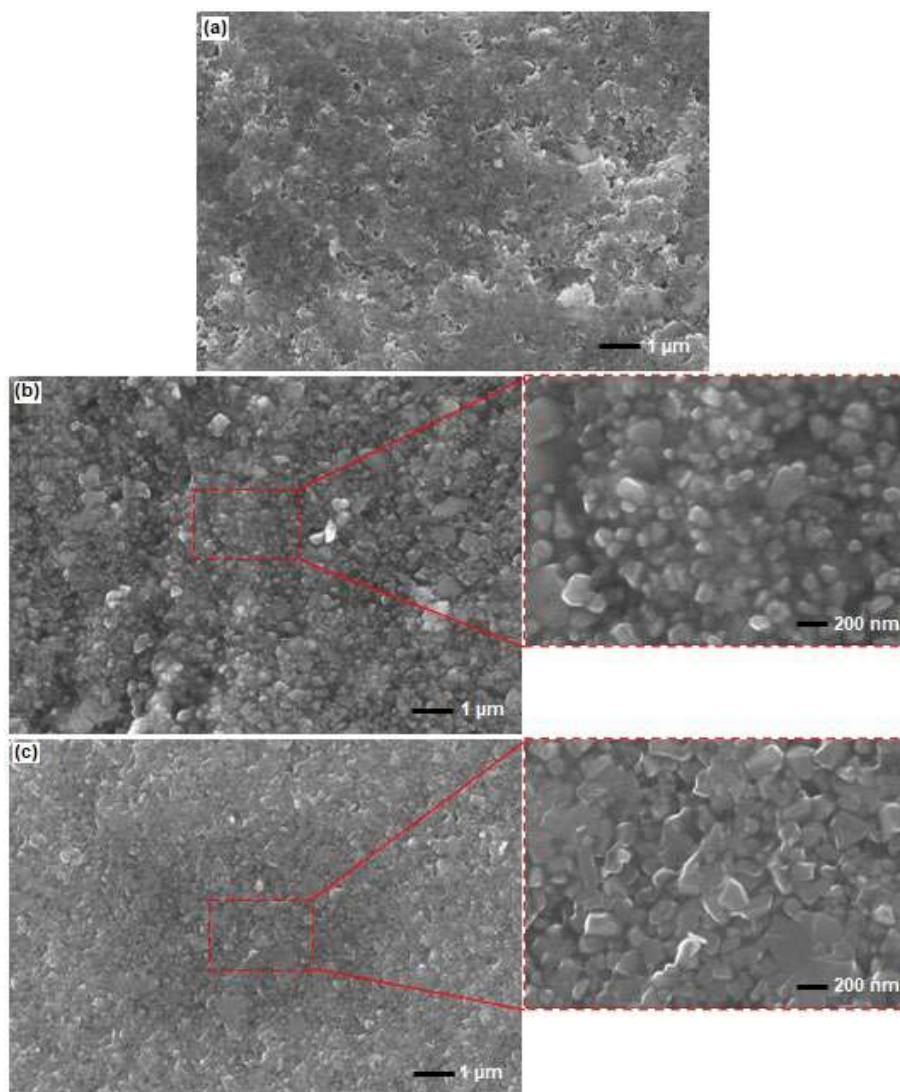


Fig 2. SEM images of SiC/PSZ composites sintered at temperatures of (a) 1600, (b) 1700, and (c) 1800 °C

powder. Although the densities of SiCPSZ1700 and SiCPSZ1800 were similar, the microstructures of the prepared samples were considerably different. The grain shape of SiCPSZ1700 (Fig. 2(b)) was close to the initial shape of SiC, i.e., round, whereas an equiaxed grain was observed in SiCPSZ1800 (Fig. 2(c)). The difference in the microstructures is more likely induced by the liquid phase that forms during sintering. As explained previously, the liquid phase of $\text{Si}_2\text{N}_2\text{O}$ appears at a lower temperature than the liquid phase of $\text{Al}_2\text{O}_3\text{-Y}_2\text{O}_3$. Hence, the microstructure in SiCPSZ1700 is more likely influenced by the presence of liquid-phase $\text{Si}_2\text{N}_2\text{O}$. Meanwhile, equiaxed grain in SiCPSZ1800 is affected by the presence of liquid-phase $\text{Al}_2\text{O}_3\text{-Y}_2\text{O}_3$. A similar microstructure with SiCPSZ1800 is also observed for SiC and PSZ, as shown in Fig. 3(b) and 3(c), respectively. Therefore, it seems that the densification process of SiCPSZ1700 occurs because of the rearrangement stage without proceeding to the shape accommodation stage.

In contrast, SiCPSZ1800 reaches the shape accommodation stage, even though it seems to be at the beginning of the stage, owing to which the relative density slightly improves compared with SiCPSZ1700. Densification via the rearrangement stage is possible because of the high capillary force for a small particle size

system [37]. Fig. 3(b) shows a typical SiC microstructure with the addition of $\text{Al}_2\text{O}_3\text{-Y}_2\text{O}_3$ sintered at 1750 °C. Grain coarsening can be observed in the sintering of SiC. A finer microstructure was obtained when sintering with PSZ (Fig. 3(c)). However, the SiC and PSZ microstructures are larger than that of SiCPSZ1800, as shown in Fig. 3(a). Since the difference in these samples is the presence of $\text{Si}_2\text{N}_2\text{O}$, $\text{Si}_2\text{N}_2\text{O}$ plays an important role in inhibiting excessive grain growth, as in SiC without polysilazane. The densities of SiC and PSZ were 3.19 and 3.17 g/cm^3 , respectively, higher than that of the SiC/PSZ composite. Subsequently, the liquid phase of $\text{Al}_2\text{O}_3\text{-Y}_2\text{O}_3$ is more effective in enhancing densification than liquid $\text{Si}_2\text{N}_2\text{O}$. The liquid formation is not the only factor affecting densification. Other factors, such as the low contact angle, low dihedral angle, volume fraction of liquid, the high solubility of solid in liquid, homogenous packing of the particulate solid, homogenous distribution of the liquid phase, and fairly fine particle size are also important for densification [38].

Fig. 4 shows a schematic of the densification of the SiC/PSZ composite at different temperatures. Under the initial condition, the $\beta\text{-SiC}$ powder is covered by a thin layer of SiO_2 on the SiC surface. Furthermore, after mixing with dissolved polysilazane, it is assumed that an

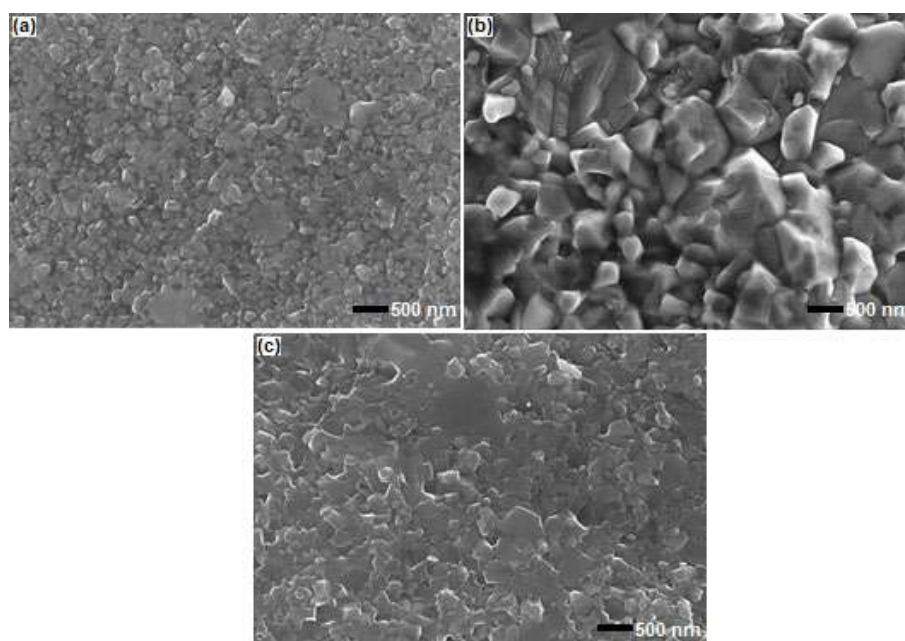


Fig 3. SEM images of sintered (a) SiCPSZ1800, (b) SiC, and (c) PSZ

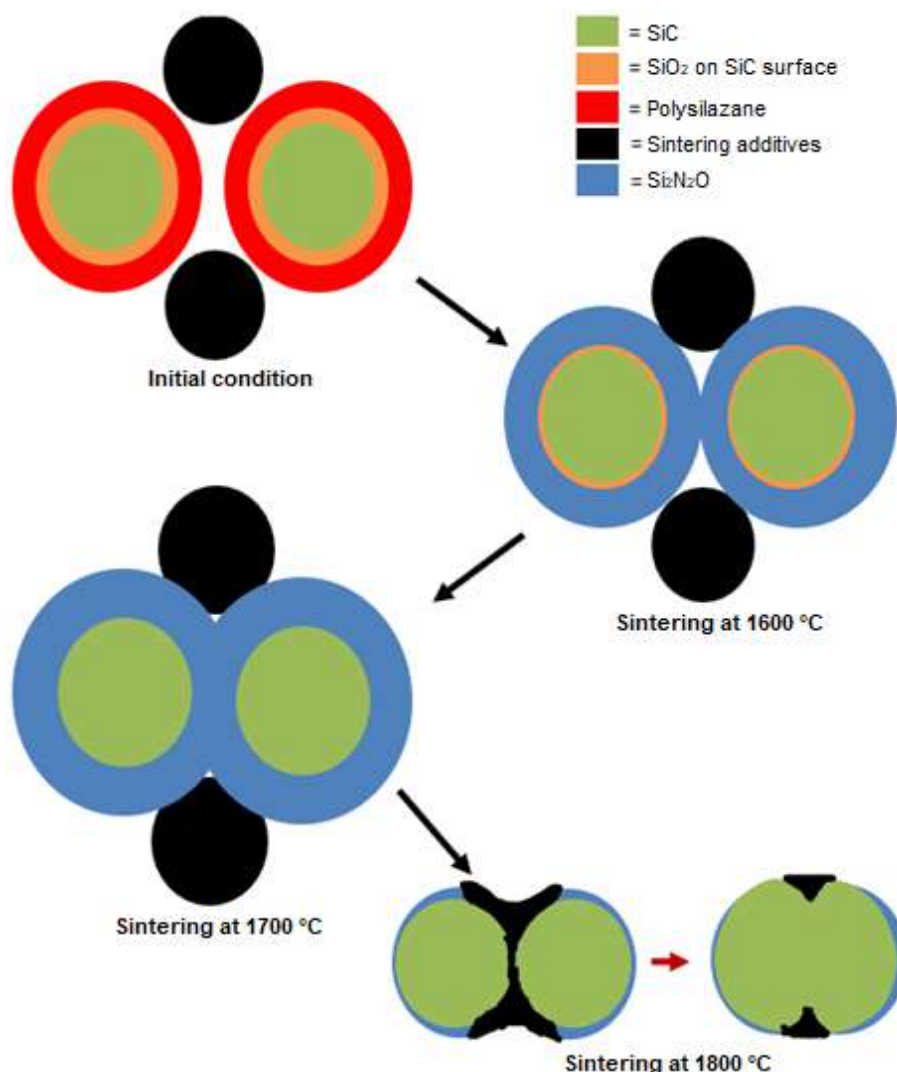


Fig 4. Schematic of the densification of SiC/PSZ composite at different temperatures

amorphous layer of polysilazane also completely covers the β -SiC powder. Si₂N₂O is detected at 1600 °C, with a small amount of SiO₂ still detected. Although the liquid phase of Si₂N₂O is already formed at this temperature, the amount of Si₂N₂O is insufficient to aid the densification, resulting in a low relative density. The relative density considerably increased to 94.1% at 1700 °C owing to the sufficient amount of Si₂N₂O. In this state, densification occurs without any change in the initial shape of SiC. The sintering additives, i.e., Al₂O₃-Y₂O₃, maintain their shape since the melting point of these additives is 1760 °C. Shape accommodation occurs at 1800 °C, and the role of sintering additives appears at this temperature.

CONCLUSION

SiC/PSZ composites were successfully sintered at various temperatures. A density higher than 90% could be achieved at temperatures > 1600 °C. Phase generation during sintering played a significant role in the densification process. The formation of liquid-phase Si₂N₂O was responsible for enhancing the densification of the SiC/PSZ composite at temperatures as low as 1700 °C. Moreover, densification at 1700 °C helped minimize grain growth. The grain size of the SiC/PSZ composite at 1700 °C only increased by a factor of two from the initial particle size of the SiC powder. Sintering at higher temperatures increased the density as well as the grain

growth. However, the grain size was considerably finer compared with that obtained after the sintering of SiC or PSZ. Therefore, SiC/polysilazane is suitable to obtain the dense body and fine microstructure ceramic compared to monolithic SiC sinter at 1750 °C with coarse microstructure. Indeed, the fine microstructure is essential to enhance the mechanical properties of ceramics.

■ ACKNOWLEDGMENTS

This work was financially supported by Kerjasama Dalam Negeri Scheme (KDN) [grant number 02-5/531/B-SPK/II/2021], Mercuru Buana University.

■ AUTHOR CONTRIBUTIONS

FF: Writing the original draft. AN: Conceptualization, methodology, conducted the experiment, formal analysis, visualization, supervision, writing - review & editing. PF: Formal analysis. AW: Project administration. TS: Formal analysis. DA: Formal analysis and resources. NTR: Resources. All authors agreed to the final version of this manuscript.

■ REFERENCES

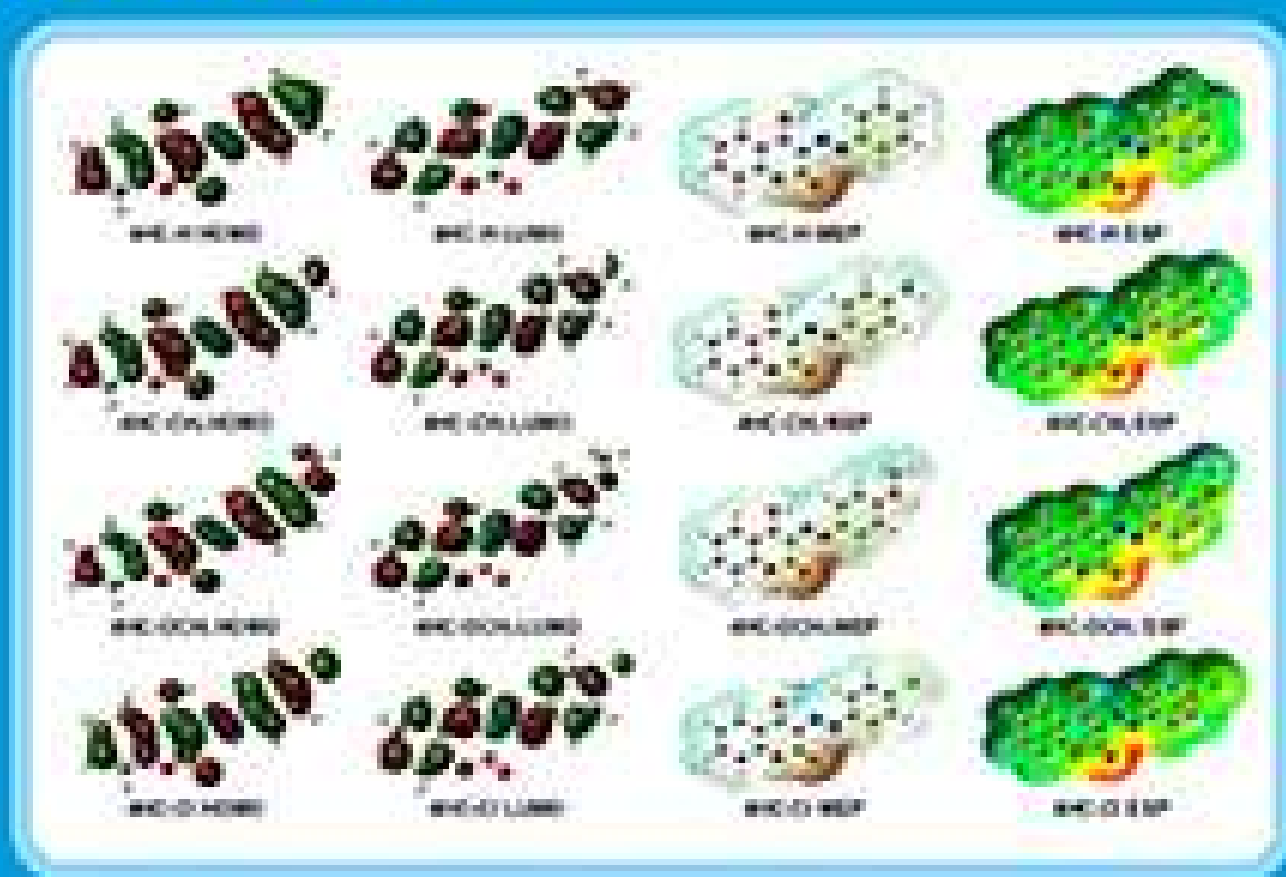
- [1] Malik, R., and Kim, Y.W., 2021, Pressureless solid-state sintering of SiC ceramics with BN and C additives, *J. Asian Ceram. Soc.*, 9 (3), 1165–1172.
- [2] Grasso, S., Saunders, T., Porwal, H., and Reece, M., 2015, Ultra-high temperature spark plasma sintering of α -SiC, *Ceram. Int.*, 41 (1), 225–230.
- [3] Kultayeva, S., Kim, Y.W., and Song, I.H., 2021, Effects of dopants on electrical, thermal, and mechanical properties of porous SiC ceramics, *J. Eur. Ceram. Soc.*, 41 (7), 4006–4015.
- [4] Petrus, M., Wozniak, J., Jastrzębska, A., Kostecki, M., Cygan, T., and Olszyna, A., 2018, The effect of the morphology of carbon used as a sintering aid on the sinterability of silicon carbide, *Ceram. Int.*, 44 (6), 7020–7025.
- [5] Aygüzer Yaşar, Z., DeLucca, V.A., and Haber, R.A., 2021, Effect of boron carbide additive and sintering temperature - Dwelling time on silicon carbide properties, *Ceram. Int.*, 47 (5), 7177–7182.
- [6] Liu, M., Yang, Y., Wei, Y., Li, Y., Zhang, H., Liu, X., and Huang, Z., 2019, Preparation of dense and high-purity SiC ceramics by pressureless solid-state-sintering, *Ceram. Int.*, 45 (16), 19771–19776.
- [7] Gross, E., Dahan, D.B., and Kaplan, W.D., 2015, The role of carbon and SiO₂ in solid-state sintering of SiC, *J. Eur. Ceram. Soc.*, 35 (7), 2001–2005.
- [8] Li, Y., Wu, H., Liu, X., Huang, Z., and Jiang, D., 2019, Microstructures and properties of solid-state-sintered silicon carbide membrane supports, *Ceram. Int.*, 45 (16), 19888–19894.
- [9] Jana, D.C., Sundararajan, G., and Chattopadhyay, K., 2018, Effective activation energy for the solid-state sintering of silicon carbide ceramics, *Metall. Mater. Trans. A*, 49 (11), 5599–5606.
- [10] Wu, H., Yan, Y., Liu, G., Liu, X., Zhu, Y., Huang, Z., Jiang, D., and Li, Y., 2015, Effects of grain grading on microstructures and mechanical behaviors of pressureless solid-state-sintered SiC, *Int. J. Appl. Ceram. Technol.*, 12 (5), 976–984.
- [11] Malinge, A., Coupé, A., Le Petitcorps, Y., and Pailler, R., 2012, Pressureless sintering of beta silicon carbide nanoparticles, *J. Eur. Ceram. Soc.*, 32 (16), 4393–4400.
- [12] Malinge, A., Coupé, A., Jouannigot, S., Le Petitcorps, Y., Pailler, R., and Weisbecker, P., 2012, Pressureless sintered silicon carbide tailored with aluminium nitride sintering agent, *J. Eur. Ceram. Soc.*, 32 (16), 4419–4426.
- [13] Zapata-Solvas, E., Bonilla, S., Wilshaw, P.R., and Todd, R.I., 2013, Preliminary investigation of flash sintering of SiC, *J. Eur. Ceram. Soc.*, 33 (13-14), 2811–2816.
- [14] Ribeiro, S., Gênova, L.A., Ribeiro, G.C., Oliveira, M.R., and Bressiani, A.H.A., 2016, effect of heating rate on the shrinkage and microstructure of liquid phase sintered SiC ceramics, *Ceram. Int.*, 42 (15), 17398–17404.
- [15] Noviyanto, A., and Yoon, D.H., 2013, Rare-earth oxide additives for the sintering of silicon carbide, *Diamond Relat. Mater.*, 38, 124–130.
- [16] Noviyanto, A., and Yoon, D.H., 2013, Metal oxide additives for the sintering of silicon carbide: Reactivity and densification, *Curr. Appl Phys.*, 13 (1), 287–292.

- [17] Liang, H., Yao, X., Zhang, J., Liu, X., and Huang, Z., 2014, Low temperature pressureless sintering of α -SiC with Al_2O_3 and CeO_2 as additives, *J. Eur. Ceram. Soc.*, 34 (3), 831–835.
- [18] Liang, H., Yao, X., Zhang, J., Liu, X., and Huang, Z., 2014, The effect of rare earth oxides on the pressureless liquid phase sintering of α -SiC, *J. Eur. Ceram. Soc.*, 34 (12), 2865–2874.
- [19] Candelario, V.M., Moreno, R., Shen, Z., Guiberteau, F., and Ortiz, A.L., 2017, Liquid-phase assisted spark-plasma sintering of SiC nanoceramics and their nanocomposites with carbon nanotubes, *J. Eur. Ceram. Soc.*, 37 (5), 1929–1936.
- [20] Yang, Z., Li, B., Zhang, P., Chu, M., Bai, B., Tang, H., Zhong, Y., Liu, X., Gao, R., Liu, T., and Huang, H., 2020, Microstructure and thermal physical properties of SiC matrix microencapsulated composites at temperature up to 1900 °C, *Ceram. Int.*, 46 (4), 5159–5167.
- [21] Xie, M.L., Luo, D.L., Xian, X. Bin, Leng, B.Y., Chang'an, C., and Lu, W.Y., 2010, Densification of nano-SiC by ultra-high pressure effects of time, temperature and pressure, *Fusion Eng. Des.*, 85 (7-9), 964–968.
- [22] Lee, Y.I., Kim, Y.W., Mitomo, M., and Kim, D.Y., 2003, Fabrication of dense nanostructured silicon carbide ceramics through two-step sintering, *J. Am. Ceram. Soc.*, 86 (10), 1803–1805.
- [23] Noviyanto, A., Han, S.W., Yu, H.W., and Yoon, D.H., 2013, Rare-earth nitrate additives for the sintering of silicon carbide, *J. Eur. Ceram. Soc.*, 33 (15-16), 2915–2923.
- [24] Brahmandam, S., and Raj, R., 2007, Novel composites constituted from hafnia and a polymer-derived ceramic as an interface: Phase for severe ultrahigh temperature applications, *J. Am. Ceram. Soc.*, 90 (10), 3171–3176.
- [25] Castellan, E., Shah, S.R., and Raj, R., 2010, Compression creep of alumina containing interfacial silicon, carbon, and nitrogen, derived from a polysilazane precursor, *J. Am. Ceram. Soc.*, 93 (4), 954–958.
- [26] Noviyanto, A., Yoon, D.H., Han, Y.H., and Nishimura, T., 2016, effect of sintering atmosphere on the grain growth and hardness of SiC/polysilazane ceramic composites, *Adv. Appl. Ceram.*, 115 (5), 272–275.
- [27] Zambotti, A., Biesuz, M., Campostrini, R., Carturan, S.M., Speranza, G., Ceccato, R., Parrino, F., and Sorarù, G.D., 2021, Synthesis and thermal evolution of polysilazane-derived SiCN(O) aerogels with variable C content stable at 1600 °C, *Ceram. Int.*, 47 (6), 8035–8043.
- [28] Mainzer, B., Lin, C., Jemmali, R., Frieß, M., Riedel, R., and Koch, D., 2019, Characterization and application of a novel low viscosity polysilazane for the manufacture of C- and SiC-fiber reinforced SiCN ceramic matrix composites by PIP process, *J. Eur. Ceram. Soc.*, 39 (2-3), 212–221.
- [29] Santoro, U., Novitskaya, E., Karandikar, K., Khalifa, H.E., and Graeve, O.A., 2019, Phase stability of SiC/SiC fiber reinforced composites: The effect of processing on the formation of α and β phases, *Mater. Lett.*, 241, 123–127.
- [30] Zhang, X.Y., Li, N., Lan, T., Lu, Y.J., Gan, K., Wu, J.M., Huo, W.L., Xu, J., and Yang, J.L., 2017, In-situ reaction synthesis of porous $\text{Si}_2\text{N}_2\text{O}$ - Si_3N_4 multiphase ceramics with low dielectric constant via silica poly-hollow microspheres, *Ceram. Int.*, 43 (5), 4235–4240.
- [31] Li, D., Li, W., Fasel, C., Shen, J., and Riedel, R., 2014, Sinterability of the oxynitride LaTiO_2N with perovskite-type structure, *J. Alloys Compd.*, 586, 567–573.
- [32] Gomez, E., Echeberria, J., Iturriza, I., and Castro, F., 2004, Liquid phase sintering of SiC with additions of Y_2O_3 , Al_2O_3 and SiO_2 , *J. Eur. Ceram. Soc.*, 24 (9), 2895–2903.
- [33] Fan, B., Chen, Y., Wang, Y., Liu, G., Zheng, H., Li, H., and Zhang, R., 2021, Preparation of $\text{Si}_2\text{N}_2\text{O}$ wave-transparent and thermal insulation materials with Na_2CO_3 and BN as aids by pressureless sintering, *Ceram. Int.*, 47 (17), 24306–24312.
- [34] Jin, H., Jia, D., Yang, Z., and Zhou, Y., 2021,

- Mechanical and dielectric properties of direct ink writing $\text{Si}_2\text{N}_2\text{O}$ composites, *J. Eur. Ceram. Soc.*, 41 (4), 2579–2586.
- [35] Li, Y., Liu, D., Ge, B., Shi, Z., and Jin, Z., 2018, Fabrication of $\text{Si}_2\text{N}_2\text{O}$ ceramic with silicon kerf waste as raw material, *Ceram. Int.*, 44 (5), 5581–5586.
- [36] Lee, S.J., and Baek, S., 2016, Effect of SiO_2 content on the microstructure, mechanical and dielectric properties of Si_3N_4 ceramics, *Ceram. Int.*, 42 (8), 9921–9925.
- [37] Bordia, R.K., Kang, S.J.L., and Olevsky, E.A., 2017, Current understanding and future research directions at the onset of the next century of sintering science and technology, *J. Am. Ceram. Soc.*, 100 (6), 2314–2352.
- [38] German, R.M., Farooq, S., and Kipphut, C.M., 1988, Kinetics of liquid sintering, *Mater. Sci. Eng., A*, 105-106, 215–224.

Indonesian Journal of Chemistry

Vol. 22, No. 2, April 2022



Approved journal by
INDONESIAN